THE UNIVERSITY OF CHICAGO

SPECTROSCOPY OF H_3^+ IN LABORATORY AND ASTROPHYSICAL PLASMAS

A DISSERTATION SUBMITTED TO
THE FACULTY OF THE DIVISION OF THE PHYSICAL SCIENCES
IN CANDIDACY FOR THE DEGREE OF
DOCTOR OF PHILOSOPHY

DEPARTMENT OF CHEMISTRY
AND
DEPARTMENT OF ASTRONOMY & ASTROPHYSICS

BY
BENJAMIN J. MCCALL

CHICAGO, ILLINOIS
JUNE 2001

To Birgit, who suffered many lonely evenings while this dissertation was written.

ABSTRACT

H_3^+ is the simplest and most fundamental polyatomic molecule, consisting of only three protons and two electrons. As such, it plays important roles in the laboratory spectroscopy of hydrogen-rich plasmas, the theoretical calculation of rotation-vibration energy levels, and also the chemistry of interstellar clouds. This dissertation touches on all three of these areas.

High resolution spectroscopy of H_3^+ has been performed in a positive column discharge. The combination bands $\nu_1 + 2\nu_2 \leftarrow 0$ and $2\nu_1 + \nu_2 \leftarrow 0$ have been observed with a diode laser, and reach the highest energy vibrational states yet studied. The initial detection of the fourth overtone band ($5\nu_2 \leftarrow 0$, which reaches above the barrier to linearity) with a Titanium-Sapphire laser is also discussed.

A comprehensive re-evaluation of all previous laboratory spectroscopy of H_3^+ has been conducted in order to obtain a reliable linelist and derive experimentally determined energy levels. These energy levels have been compared with the most recent variational calculations on *ab initio* potential energy surfaces. It is hoped that this comparison will permit further refinements in the theoretical calculations.

H_3^+ has been detected (using absorption lines of the ν_2 fundamental band) in several dense interstellar clouds, where it serves as the universal protonator, initiating a chain of ion-neutral reactions that is responsible for the production of the variety of molecules observed by radioastronomers. In dense clouds, measurements of H_3^+ provide direct estimates of the clouds' path lengths, average number densities, and kinetic temperatures.

H_3^+ has also been observed in several diffuse interstellar clouds, where it is supposed to be two to three orders of magnitude less abundant due to the efficiency of electron recombination. This observational result suggests a serious general problem with the models of diffuse cloud chemistry. The most likely solution is that the ratio of the cosmic ray ionization rate (ζ) to the dissociative recombination rate (k_e) is at least one to two orders of magnitude higher than has been generally assumed. This implies that the laboratory measurement of k_e is not applicable to interstellar conditions, and/or that H_2 ionization is enhanced in diffuse clouds relative to dense clouds.

ACKNOWLEDGEMENTS

My thanks go first and foremost to my thesis advisor, Takeshi Oka. Oka has been, from my perspective, the perfect advisor — he has allowed me the freedom to spend my time on the work I found most interesting, but also has provided much-needed guidance on many occasions. He has been incredibly supportive of both my laboratory and my observational work, even when one of them lagged behind at the expense of the other. Through the course of my graduate career, his role has evolved from that of an advisor to that of an enthusaistic collaborator.

Second, I wish to thank the other members of my dissertation committee, John Carlstrom, Robert Clayton, Don Levy, and Don York, for agreeing to serve on my dissertation committee, and for their helpful feedback on the dissertation.

Third, I would like to acknowledge the people who have played an important role in the observational work described in this thesis. This includes Tom Geballe and Ken Hinkle (our main collaborators in the search for interstellar H_3^+), Don York, Lew Hobbs, and Julie Thorburn (our collaborators in visible spectroscopy with the Apache Point Observatory), Verne Smith (who taught me how to use the echelle at McDonald), Neal Evans (who obtained CO spectra for the Cygnus OB2 sources at CSO), Gerard Moriarty-Schieven (who obtained CO spectra at JCMT), and Shuro Takano and Kentarou Kawaguchi (who obtained CO spectra at Nobeyama). John Maier and his group at Basel have been instrumental in the analysis of the diffuse bands attributed to C_7^-. Also, I wish to thank Eric Herbst, John Black, Ewine van Dishoeck, and Ted Snow for many helpful discussions through the course of my work.

Fourth, I must acknowledge the many people who played important roles in my laboratory work. In terms of the actual lab work, I'd like to thank Daniel Hullah for helping set up the Titanium:Sapphire laser, Jennifer Gottfried for her hard work making the $5\nu_2$ experiment possible, and Mike Lindsay for many helpful suggestions over the years. Also, I'd like to acknowledge Guy Guelachvilli for providing the NH_3 reference spectrum which enabled accurate frequency measurements of the $\nu_1 + 2\nu_2$ band. I am also grateful to Jim Watson, Jonathan Tennyson, Ralph Jaquet, and Alex Alijah for providing us with their theoretical calculations for H_3^+, in many cases in

advance of publication.

Finally, I wish to express my appreciation to the Fannie and John Hertz Foundation, which supported all six years of my graduate work in both departments. Also, I am grateful to the National Optical Astronomy Observatory and the Sigma Xi Scientific Research Society for supporting my travel to observatories. This work was also supported by grants from the National Science Foundation and the National Aeronautics and Space Administration.

TABLE OF CONTENTS

LIST OF FIGURES

LIST OF TABLES

CHAPTER 1
INTRODUCTION

H_3^+, the simplest polyatomic molecule, plays important roles in laboratory, theoretical, and astronomical spectroscopy. This section gives a brief sketch of each of these areas, in order to place the work in this dissertation in a broader context.

Laboratory Work

H_3^+ was first discovered in 1911 by J. J. Thomson [1] during the course of his experiments on "rays of positive electricity." Since that time, various mass spectrometric studies had verified that H_3^+ is the dominant charge carrier in pure hydrogen plasmas. However, the fact that the equilibrium structure of H_3^+ is an equilateral triangle implies that the molecule has no (allowed) rotational spectrum. Furthermore, H_3^+ does not possess a sharp electronic spectrum, so that the comparatively weak vibrational spectrum is its only accessible spectroscopic signature.

The detection of the infrared spectrum of H_3^+ [2] was not possible until the widely-tunable difference frequency laser system was developed. Since the initial discovery of the ν_2 fundamental band, laboratory spectroscopists have been gradually probing higher and higher energy vibrational states. These include the doubly excited vibrational states, which were reached using hot bands ($2\nu_2^2 \leftarrow \nu_2$, $2\nu_2^0 \leftarrow \nu_2$, and $\nu_1 + \nu_2 \leftarrow \nu_1$) as well as the overtone band $2\nu_2^2 \leftarrow 0$. The first triply excited vibrational state ($3\nu_2^1$) was reached in 1991 [3] using the second overtone $3\nu_2^1 \leftarrow 0$. The previous laboratory spectroscopic work on H_3^+ is reviewed in Appendices B.2 and D.

In this dissertation (Section 3.2) I discuss the detection of two other triply excited states using the combination bands $\nu_1 + 2\nu_2^2 \leftarrow 0$ and $2\nu_1 + \nu_2 \leftarrow 0$. These states were, at the time, the highest energy states yet studied. In Section 3.3, I discuss our detection of the fourth overtone band $5\nu_2^1 \leftarrow 0$ and the search for other vibrational bands which lie above the theoretically challenging barrier to linearity.

The initial motivation for much of the laboratory spectroscopy of H_3^+ was to facilitate the astronomical study of H_3^+, as discussed below. However, since then we have reached energies that are unlikely to be significantly populated in astronomical

plasmas (so that emission spectra are improbable). Furthermore, the transitions to the energy levels now being studied are so weak that detection of absorption spectra in astronomical plasmas seems almost impossible. The primary motivation for continuing to study even higher energy levels of H_3^+ is to facilitate the development of theoretical calculations for polyatomic molecules.

Theoretical Work

H_3^+, as the simplest polyatomic, has served as a benchmark for the theoretical calculation of ro-vibrational energy levels of polyatomic molecules — much as H_2 was long a benchmark for diatomics, and H itself a benchmark for atoms. Because it only has three protons and two electrons, H_3^+ is a tractable problem that can be used to develop the computational techniques which can then be applied to more complicated molecules (such as H_2O).

A theoretical explanation of the equilateral triangle structure of H_3^+ was first given by Coulson [4] in 1935 using molecular orbital theory, although it was not until 1964 [5] that the structure was verified by more complete numerical calculations. By 1976, the vibrational energies of H_3^+ were calculated by Carney and Porter [6] from an *ab initio* potential energy surface, and by 1980, the complete rotation-vibration spectrum could be calculated [7], with an accuracy of a few cm^{-1}.

Agreement with experiment was considerably improved following the development of a better *ab initio* potential surface by Meyer, Botschwina, and Burton [8] and application of the variational formalism of Sutcliffe and Tennyson [9] to H_3^+. The resulting calculations [10] were key in the understanding of laboratory spectra involving doubly-excited vibrational states.

The residual deviations from experimental transition frequencies led to the development of "spectroscopically adjusted" potential energy surfaces, in which the parameters of the fit to the *ab initio* points were adjusted so as to optimize the agreement between laboratory and calculated frequencies. This approach was very useful for predicting new transitions, but did not provide any new insights into the physics of H_3^+, or into how the calculations might be improved.

Recently, *ab initio* potential energy surfaces have become substantially more accurate, such that variational calculations on these surfaces show good agreement with experiment (see Appendix D). The remaining differences with experiment are almost certainly due not to flaws in the potential energy surface, but rather to the failure of the Born-Oppenheimer approximation (and to relativistic corrections). New experiments, such as that discussed in Section 3.2, as well as the re-evaluation of previous spectroscopic work (discussed in Appendix D), give theorists the ability to compare and evaluate different methods of calculating the various corrections to the Born-Oppenheimer approximation.

An additional challenge for theorists is presented by energies above the barrier to linearity, where the approaches traditionally used in variational calculations become ineffective. New calculations using hyperspherical coordinates should be able to surmount this problem — the detection of the $5\nu_2 \leftarrow 0$ band (Section 3.3) is particularly important in this respect, as $5\nu_2$ is fully above the linearity barrier.

Astronomical Work

The first suggestion that H_3^+ might play an important role in astronomy seems to be that of Martin, McDaniel, and Meeks in 1961 [11], who suggested that the efficiency of the reaction $H_2^+ + H_2 \rightarrow H_3^+ + H$ meant that any H_2^+ produced in the interstellar medium would be promptly converted to H_3^+. When the ion-neutral reaction scheme for molecular clouds was introduced [12, 13], H_3^+ took center stage as the universal protonator and the initiator of interstellar chemistry.

As mentioned above, a major motivation in the laboratory search for the infrared spectrum of H_3^+ was to enable an astronomical search, and indeed the astronomical search began immediately once the transition frequencies were known. The search continued for many years, but astronomical infrared spectrometers were not yet efficient enough to detect the small ($\sim 1\%$) absorptions of H_3^+ in molecular clouds.

The big surprise came in the late 1980s, when a series of unidentified lines in the 2μm region were found in emission on Jupiter. These lines were eventually assigned to the overtone band of H_3^+, and H_3^+ became an important probe of planetary

ionospheres. The fundamental band of H_3^+ was later detected from Jupiter, Saturn, and Uranus — in the case of Jupiter, the spectral region of the ν_2 fundamental is background-free, such that the distribution of H_3^+ in the ionosphere can be imaged using a simple bandpass filter and an infrared camera.

Meanwhile, the search for interstellar H_3^+ continued, and was eventually successful. In 1996, Geballe and Oka reported [14] the first detections toward the molecular clouds AFGL 2136 and W33A. In this dissertation, I discuss the extension of this work to a small survey of molecular clouds (Section 4.2 and Appendix A.4). Observations of H_3^+ in dense clouds permit direct estimates of the clouds' path lengths, average number densities, and temperatures. The fact that the derived values are in accord with the canonical values for dense clouds represents a confirmation of the general picture of ion-neutral chemistry in this environment.

During the course of our dense cloud survey, we detected unusually strong absorption lines of H_3^+ in two lines of sight toward the Galactic Center, as described in Appendix A.3. The fact that the line of sight toward the Galactic Center crosses both dense and diffuse clouds prompted us to try a purely diffuse line of sight — that towards Cygnus OB2 12. Much to our surprise, we found that Cygnus OB2 12 has a similar column density of H_3^+ to dense clouds (see Appendices A.1 and A.3), despite the fact that models of diffuse cloud chemistry suggest H_3^+ should be two to three orders of magnitude less abundant in diffuse clouds!

We have followed up on the initial detection of H_3^+ in diffuse clouds with a small survey of diffuse cloud sightlines, as described in Section 4.3. This survey yielded detections in the more usual diffuse cloud sources HD 183143 and HD 20041, which suggests that there is a general problem with the chemical models of diffuse clouds. In this sense, the H_3^+ enigma is reminiscent of the problems of CH^+ and the Diffuse Interstellar Bands (Appendix A.5).

CHAPTER 2
THEORETICAL BACKGROUND OF H_3^+

For any molecule, the only truly rigorous quantum numbers are the total angular momentum (F) and the parity ($\pm$). These two quantum numbers are rigorous because they arise from the properties of space (isotropy and inversion symmetry) rather than from the properties of the molecule. To an extremely good approximation (due to the weakness of the nuclear spin–rotation and spin–spin interactions), we can separate the total angular momentum F into the nuclear spin angular momentum I and the "motional" angular momentum J. The three resulting quantum numbers I, J, and $\pm$ are the only good quantum numbers for H_3^+ at arbitrarily high energies.

At sufficiently low energies, there are other approximately good quantum numbers that are helpful in understanding the behavior of H_3^+. In this chapter, I describe these approximate quantum numbers using the permutation-inversion group, which describes the symmetry of H_3^+ that results from the equivalence of its three protons and the inversion symmetry of space.

2.1 The Permutation-Inversion Group S_3^*

Because protons are indistinguishable particles, the wavefunctions of H_3^+ must possess a definite symmetry with respect to interchanges of the protons. For a system of three equivalent protons, there are three sets of permutation symmetry operations: the identity E, the three permutations of two protons (12), and the two cyclic permutations of three protons (123). These six symmetry operations form the permutation group S_3. The inversion operation produces a group called E^*, with the two symmetry operations E and E^*. Since H_3^+ has both permutation and inversion symmetries, its wavefunctions must be described by the group $S_3^* = S_3 \otimes E^*$. The character tables for these three groups are shown in Table 2.1.

According to Dirac's statement of the Pauli principle [15], the total wavefunction must be antisymmetric with respect to the interchange of two protons and symmetric with respect to cyclic permutation of three protons (since the latter operation is

S_3	E	3(12)	2(123)
A_1	1	1	1
A_2	1	-1	1
E	2	0	-1

$\otimes$

E^*	E	E^*
A'	1	1
A''	1	-1

$=$

S_3^*	E	3(12)	2(123)	E^*	3(12)*	2(123)*
A_1'	1	1	1	1	1	1
A_2'	1	-1	1	1	-1	1
E'	2	0	-1	2	0	-1
A_1''	1	1	1	-1	-1	-1
A_2''	1	-1	1	-1	1	-1
E''	2	0	-1	-2	0	1

Table 2.1 Character tables for three equivalent protons.

S_3^*	A_1'	A_2'	E'	A_1''	A_2''	E''
A_1'	A_1'	A_2'	E'	A_1''	A_2''	E''
A_2'	A_2'	A_1'	E'	A_2''	A_1''	E''
E'	E'	E'	$A_1' \oplus A_2' \oplus E'$	E''	E''	$A_1'' \oplus A_2'' \oplus E''$
A_1''	A_1''	A_2''	E''	A_1'	A_2'	E'
A_2''	A_2''	A_1''	E''	A_2'	A_1'	E'
E''	E''	E''	$A_1'' \oplus A_2'' \oplus E''$	E'	E'	$A_1' \oplus A_2' \oplus E'$

Table 2.2 Product table for S_3^*.

equivalent to two interchanges of pairs of protons). From Table 2.1, this requirement implies that the H_3^+ total wavefunction must be of symmetry A_2' or A_2''.

The total wavefunction Ψ is often considered as the product of separate electronic (Ψ_{el}), rotation-vibration (Ψ_{rv}), and nuclear spin (Ψ_{ns}) wavefunctions, $\Psi = \Psi_{el}\Psi_{rv}\Psi_{ns}$. The separation of Ψ_{el} from Ψ_{rv} is the basis of the Born-Oppenheimer approximation, and the separation of $\Psi_{el}\Psi_{rv}$ from Ψ_{ns} is based on the fact that the former involves spatial coordinates and the latter involves spin coordinates (and their interaction is very small). The representation Γ of the total wavefunction can be expressed as the direct product $\Gamma = \Gamma_{el} \otimes \Gamma_{rv} \otimes \Gamma_{ns}$.

The requirement of the Pauli principle that the representation Γ of the total wavefunction must be A_2' or A_2'' imposes restrictions on the allowable combinations of the representations Γ_{el}, Γ_{rv}, and Γ_{ns}. These restrictions can be derived using the product table of S_3^* shown in Table 2.2, and will be considered in the following sections.

2.2 Electronic Symmetry

Without recourse to detailed calculations, we can infer the symmetry of the ground electronic state of H_3^+ from general considerations. It can be proven from the variational principle [16, p. 59] that in general the lowest energy state of a system has no nodes, so long as such a configuration is allowed by the requirements imposed by the identity of particles. In the case of H_3^+, the two electrons do allow such a configuration, so Ψ_{el} must have no nodes. If Ψ_{el} has no nodes, it certainly cannot change sign with any symmetry operation, which implies that it must belong to the totally symmetric represtation, $\Gamma_{el} = A_1'$. This further implies that $\Gamma_{rv} \otimes \Gamma_{ns} \supset A_2'$ or A_2''.

The determination of the symmetries of electronically excited states of H_3^+ requires *ab initio* theory. The lowest excited state is a triplet (as one of the two electrons is promoted to a higher molecular orbital) and is found to lie above the energy for the process $H_3^+ \rightarrow H_2 + H^+$, although below the energy for $H_3^+ \rightarrow H_2^+ + H$, which is $(15.4 - 13.6) = 1.8$ eV higher. However, this triplet ($^3\Sigma_u^+$) state cannot access the H_2 ($^1\Sigma_g^+$) + H^+ dissociation pathway due to symmetry restrictions [17]. Recent calculations [18] show that this triplet state is barely bound, with a well depth of 2951 cm^{-1} and a zero-point energy of 1722 cm^{-1} (the well can support only a single vibrational excitation). It is interesting to note that the equilibrium structure of H_3^+ in the triplet state is linear.

The consequence of this triplet state being the lowest excited state is that if H_3^+ does have a sharp electronic spectrum, it will lie deep in the ultraviolet, will be extremely weak (because of the singlet-triplet nature of the transition, as well as the unfavorable Franck-Condon overlap), and might be broadened by predissociation. As a result, electronic spectroscopy is not a useful tool for the spectroscopy of H_3^+, and we must resort to using vibrational spectroscopy.

2.3 Rotation-Vibrational Symmetry

2.3.1 Vibrational modes

A molecule with N nuclei has $3N$ nuclear coordinates. Three of the coordinates are used to define the position of the center of mass of the molecule with respect to the laboratory frame of reference. Three more coordinates are needed to describe the rotational motion of the molecule's frame (two if the molecule is linear). Thus, $3N-6$ ($3N-5$ for linear molecules) coordinates remain to describe the internal ("vibrational") motions of a molecule.

In the case of H_3^+, there are $3 \cdot 3 - 6 = 3$ internal coordinates. A convenient choice for these coordinates is one where r_1 is the distance between protons 2 and 3, r_2 that between 1 and 3, and r_3 that between 1 and 2. In this scheme, the permutation operation (12) leads to a swapping of $r_1 \leftrightarrow r_2$, and (123) leads to $r_1 \rightarrow r_2 \rightarrow r_3 \rightarrow r_1$. Since the coordinates are invariant to inversion, they transform according to the S_3 group.

While any combination of these three internal coordinates can be taken to describe the vibrational motion of H_3^+, the most natural combinations to consider are the "normal" modes of vibration — those combinations of the internal coordinates which transform according to one of the representations (A_1, A_2, E) of the S_3 permutation group.

One obvious combination is $r_1 + r_2 + r_3$, which is symmetric with respect to the (12) and (123) permutations, and therefore belongs to the totally symmetric A_1 representation. This normal mode corresponds to a "breathing" motion of the molecule, where all of the internuclear distances expand and contract in unison. The A_1 mode is referred to as ν_1, and is infrared inactive. The other two "symmetry adapted" linear combinations[1] are $r_1 + \epsilon r_2 + \epsilon^2 r_3$ and $r_1 + \epsilon^2 r_2 + \epsilon r_3$, where $\epsilon \equiv e^{2\pi i/3}$.

[1]The coefficients of the three symmetry adapted linear combinations of the internal coordinates can be obtained from the character table for the C_3 point group [16, p. 379]. It is also interesting to note that these three expressions appear in the solution of the cubic equation $x^3 - (r_1 + r_2 + r_3)x^2 + (r_1 r_2 + r_2 r_3 + r_3 r_1)x - r_1 r_2 r_3 = 0$ whose roots are r_1, r_2, and r_3. The solution $x = \frac{1}{3}\left[(r_1 + r_2 + r_3) + \sqrt[3]{(r_1 + \epsilon r_2 + \epsilon^2 r_3)^3} + \sqrt[3]{(r_1 + \epsilon^2 r_2 + \epsilon r_3)^3}\right]$ can be evaluated because the expressions $u = (r_1 + \epsilon r_2 + \epsilon^2 r_3)^3$ and $v = (r_1 + \epsilon^2 r_2 + \epsilon r_3)^3$ can be determined from the

These two combinations transform together according to the E representation of S_3, and represent the doubly degenerate ν_2 mode. This mode is infrared active and is the basis for both laboratory and astronomical spectroscopy of H_3^+.

Like any degenerate mode, ν_2 possesses vibrational angular momentum [20, p. 75 *ff.*]. This can be visualized by considering the equilateral triangle configuration of H_3^+ in Figure 2.1. Because the two components ν_{2x} and ν_{2y} are degenerate, we can just as well consider any linear combinations of these two components. In particular, if we form a combination with ν_{2y} 90° out of phase, we obtain ν_{2+}, in which each proton executes a circular motion, which evidently has a unit of angular momentum. With a different choice of phase we obtain ν_{2-}, which has angular momentum in the opposite sense. Thus the degenerate ν_2 mode has a *vibrational angular momentum* ℓ which is ± 1. The equilateral triangle triatomic molecule is unique in that the vibrational angular momentum has a unit value of $\hbar$ [21]. For any other symmetric top molecule, the vibrational angular momentum is less than $\hbar$ and is given by $\zeta\hbar$, where the Coriolis coupling constant $|\zeta| < 1$ [20, p. 402].

The general vibrational motion of H_3^+ may be a combination of the two normal modes, which is usually represented by the notation $v_1\nu_1 + v_2\nu_2^\ell$. For v_2 quanta of ν_2, the vibrational angular momentum quantum number ℓ can take on the values $\ell = -v_2, -v_2 + 2, \ldots, v_2 - 2, v_2$. As discussed in Section 2.3.4 below, the symmetry of the vibrational state is entirely determined by ℓ.

2.3.2 Pure rotational wavefunctions

Before tackling the full rotation-vibrational wavefunctions, let us consider the symmetry of the pure rotational wavefunctions $|J, k, m\rangle$. J is the "motional" angular momentum, which in the case of H_3^+ (with no electronic angular momentum) is simply the angular momentum of nuclear motion. The signed quantum number k is the projection of J onto the molecular axis, and m is the projection of J onto a space-fixed axis. In the absence of an external field, the energy of a rotational state is

fact that uv and $u + v$ are totally symmetric to permutations of r_1, r_2, and r_3 and therefore can be written in terms of the coefficients of the cubic. (This theory, developed by Lagrange, is explained in detail in [19].)

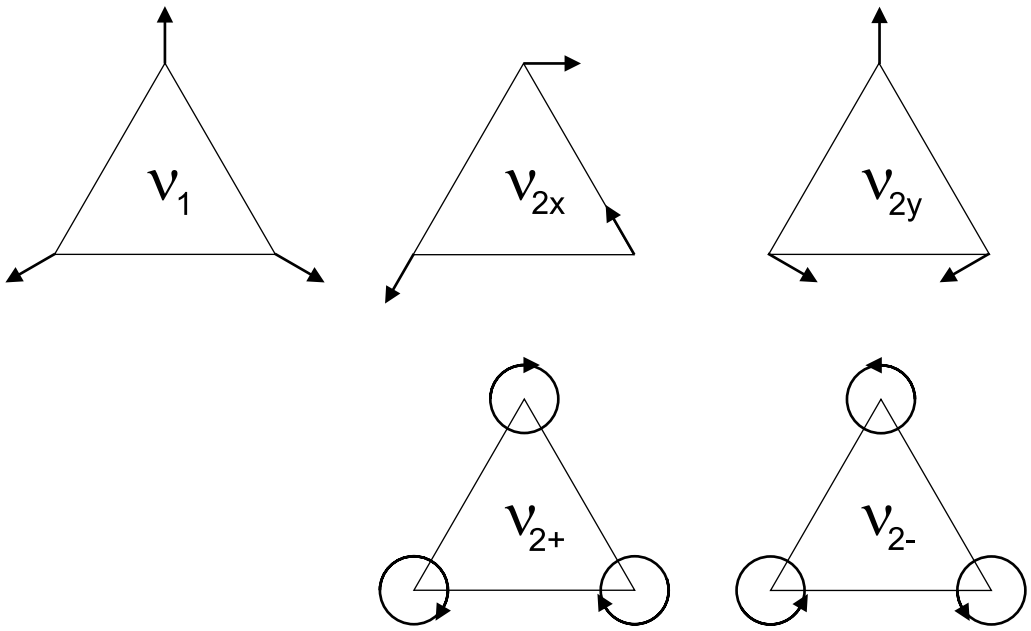

Figure 2.1 Vibrational angular momentum for H_3^+.

independent of m, so that m contributes only a $(2J+1)$-fold degeneracy.

To determine the effect of the symmetry operations on the rotational wavefunction, we must first consider the effect of each symmetry operation on the relationship between the space-fixed and the molecule-fixed axes, as this relationship defines the angular momentum operators in the molecule-fixed system and therefore the ladder operators which affect k. This relationship is described by the Eulerian angles (see Figure 2.2, which is adapted from [22, pp. 285–286]). The effect of a symmetry operation on the Eulerian angles can be described in terms of an "equivalent rotation" [23, p. 156,234]. In Bunker's notation, R_z^β is a rotation about the molecule-fixed z-axis by β radians (i.e. the $C_{2\pi/\beta}^{(z)}$ operation), and R_α^π is a rotation by π radians about an axis in the xy-plane making an angle α with the x-axis (i.e. the $C_2^{(x)}$ if $\alpha = 0$ or $C_2^{(y)}$ if $\alpha = \pi/2$). The symmetry operations in S_3^* have the equivalent rotations $E \mapsto R^0$, $(12) \mapsto R_0^\pi$, $(123) \mapsto R_z^{2\pi/3}$, $E^* \mapsto R_z^\pi$, $(12)^* \mapsto R_{\pi/2}^\pi$, and $(123)^* \mapsto R_z^{-\pi/3}$. The effects of the general equivalent rotations on the Eulerian angles and the angular momentum operators are shown in Table 2.3 [23, p. 155]. From this table, one can derive the effect of the equivalent rotations on $J_\pm = J_x \mp iJ_y$, namely that $R_z^\beta J_+ = e^{i\beta} J_+ R_z^\beta$ and

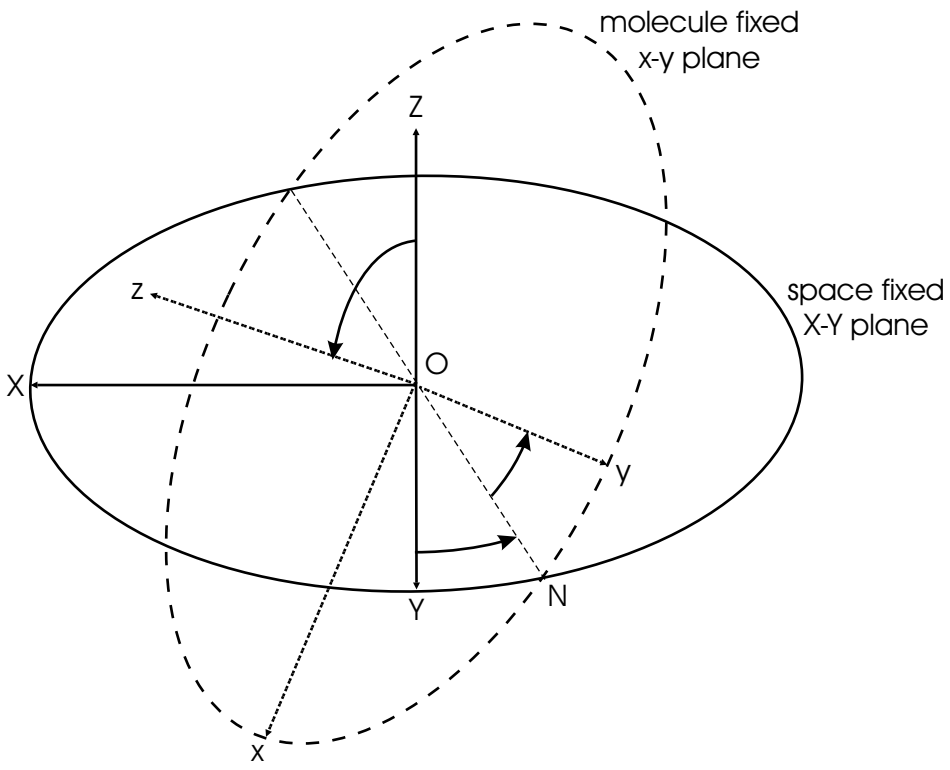

Figure 2.2 Euler angles θ, ϕ, and χ.

$R_\alpha^\pi J_+ = e^{-2i\alpha} J_- R_\alpha^\pi$.

Now we are ready to determine the effect of the equivalent rotations on the rotational wavefunctions $|J,k,m\rangle$. We begin with $|J,0,0\rangle$, which is simply proportional to $\frac{d^J}{(d\cos\theta)^J}(\cos^2\theta - 1)^J$. Since R_z^β has no effect on θ, $R_z^\beta|J,0,0\rangle = |J,0,0\rangle$. Since R_α^π maps θ to $\pi - \theta$, it maps $\cos\theta$ to $-\cos\theta$, and $R_\alpha^\pi|J,0,0\rangle = (-1)^J|J,0,0\rangle$.

We can now derive[2] the effect of R_z^β on $|J,k,0\rangle$

$$\begin{aligned} R_z^\beta J_+|J,0,0\rangle &= e^{i\beta} J_+ R_z^\beta|J,0,0\rangle \\ &= e^{i\beta} J_+|J,0,0\rangle \\ R_z^\beta|J,1,0\rangle &= e^{i\beta}|J,1,0\rangle \\ &\vdots \\ R_z^\beta|J,k,0\rangle &= e^{ik\beta}|J,k,0\rangle \end{aligned}$$

[2]Similar expressions can be derived for negative values of k using J_-.

	R_α^π	R_z^β
θ	$\pi - \theta$	θ
ϕ	$\pi + \phi$	ϕ
χ	$-2\alpha - \chi$	$\chi + \beta$
J_x	$J_x \cos 2\alpha + J_y \sin 2\alpha$	$J_x \cos\beta + J_y \sin\beta$
J_y	$J_x \sin 2\alpha - J_y \cos 2\alpha$	$-J_x \sin\beta + J_y \cos\beta$
J_z	$-J_z$	J_z

Table 2.3 Effect of equivalent rotations on Eulerian angles and angular momentum operators.

	E	(123)	(12)	E^*	$(123)^*$	$(12)^*$
	R^0	$R_z^{2\pi/3}$	R_0^π	R_z^π	$R_z^{-\pi/3}$	$R_{\pi/2}^\pi$
$\|J,0\rangle$	$\|J,0\rangle$	$\|J,0\rangle$	$(-1)^J\|J,0\rangle$	$\|J,0\rangle$	$\|J,0\rangle$	$(-1)^J\|J,0\rangle$
$\|J,k\rangle$	$\|J,k\rangle$	$e^{\frac{2ik\pi}{3}}\|J,k\rangle$	$(-1)^J\|J,-k\rangle$	$(-1)^k\|J,k\rangle$	$e^{\frac{-ik\pi}{3}}\|J,k\rangle$	$(-1)^{J-k}\|J,-k\rangle$
$\|J,-k\rangle$	$\|J,-k\rangle$	$e^{\frac{-2ik\pi}{3}}\|J,-k\rangle$	$(-1)^J\|J,k\rangle$	$(-1)^k\|J,-k\rangle$	$e^{\frac{ik\pi}{3}}\|J,-k\rangle$	$(-1)^{J+k}\|J,k\rangle$

Table 2.4 Effect of symmetry operations on $|J,\pm k\rangle$.

and similarly, the effect of R_α^π on $|J,k,0\rangle$

$$\begin{aligned} R_\alpha^\pi J_+|J,0,0\rangle &= e^{-2i\alpha}J_-R_\alpha^\pi|J,0,0\rangle \\ &= e^{-2i\alpha}J_-(-1)^J|J,0,0\rangle \\ R_\alpha^\pi|J,1,0\rangle &= (-1)^J e^{-2i\alpha}|J,-1,0\rangle \\ &\vdots \\ R_\alpha^\pi|J,k,0\rangle &= (-1)^J e^{-2ik\alpha}|J,-k,0\rangle \end{aligned}$$

Because the rotations R have no effect on the space-fixed axes, they commute with the ladder operators for the space-fixed projection m. Consequently, the preceding results are equally valid for $m \neq 0$. The effects of the symmetry operations of S_3^* on $|J,k\rangle$ and $|J,-k\rangle$ are summarized in Table 2.4. In this table and in the following discussion, m is omitted for brevity.

We now need to evaluate the character of the wavefunctions. This can be done by inspection for $|J,0\rangle$, since it always transforms into a constant times itself. On the other hand, $|J,\pm k\rangle$ are best handled as a pair, which is only natural because the energy does not depend on the sign of k. The character of the set $\{|J,k\rangle, |J,-k\rangle\}$ for

	E	(123)	(12)	E^*	$(123)^*$	$(12)^*$	Γ
$\|J,0\rangle$	1	1	$(-1)^J$	1	1	$(-1)^J$	
$\left\{ \begin{array}{c} \|J,k\rangle \\ \|J,-k\rangle \end{array} \right\}$	2	$2\cos\frac{2k\pi}{3}$	0	$2(-1)^k$	$2\cos\frac{k\pi}{3}$	0	
$\|J \text{ even},0\rangle$	1	1	1	1	1	1	A_1'
$\|J \text{ odd},0\rangle$	1	1	-1	1	1	-1	A_2'
$\|J,\pm(6n+6)\rangle$	2	2	0	2	2	0	$A_1' \oplus A_2'$
$\|J,\pm(6n+3)\rangle$	2	2	0	-2	-2	0	$A_1'' \oplus A_2''$
$\|J,\pm(6n\pm2)\rangle$	2	-1	0	2	-1	0	E'
$\|J,\pm(6n\pm1)\rangle$	2	-1	0	-2	1	0	E''

Table 2.5 Characters and representations of $|J,k\rangle$.

a given symmetry operation can be defined as the trace of the matrix which represents the effect of that symmetry operation on the set. For example, the identity operation E has a character of 2:

$$E \begin{bmatrix} |J,k\rangle \\ |J,-k\rangle \end{bmatrix} = \begin{bmatrix} |J,k\rangle \\ |J,-k\rangle \end{bmatrix} = \begin{bmatrix} 1 & 0 \\ 0 & 1 \end{bmatrix} \begin{bmatrix} |J,k\rangle \\ |J,-k\rangle \end{bmatrix}$$

Following this process, the characters for $|J,k\rangle$ with respect to all of the symmetry operations are shown in Table 2.5, along with the representation of each $|J,k\rangle$.

2.3.3 Rotation-vibrational wavefunctions

So far we have only considered the effect of the symmetry operations on the pure rotational wavefunctions $|J,k\rangle$. Since the symmetry operations have no effect on the quantum numbers v_1 and v_2 (the number of quanta in the ν_1 and ν_2 modes), we only need to examine the effect of the symmetry operations on the vibrational angular momentum ℓ.

The $q_\pm$ ladder operators for ℓ can be constructed from the two vibrational coordinates q_{2x} and q_{2y} of the degenerate ν_2 mode: $q_\pm = q_{2x} \pm iq_{2y}$. The vibrational coordinates transform just as the molecule-fixed Cartesian coordinates $\{x,y,z\}$, which transform the same way as the angular momenta $\{J_x, J_y, J_z\}$ for permutation oper-

	E	(123)	(12)	E^*	$(123)^*$	$(12)^*$
	R^0	$R_z^{2\pi/3}$	R_0^π	R_z^π	$R_z^{-\pi/3}$	$R_{\pi/2}^\pi$
J_x	J_x	$J_x \cos\frac{2\pi}{3} + J_y \sin\frac{2\pi}{3}$	J_x	$-J_x$	$J_x \cos\frac{-\pi}{3} + J_y \sin\frac{-\pi}{3}$	$-J_x$
J_y	J_y	$-J_x \sin\frac{2\pi}{3} + J_y \cos\frac{2\pi}{3}$	$-J_y$	$-J_y$	$-J_x \sin\frac{-\pi}{3} + J_y \cos\frac{-\pi}{3}$	J_y
J_z	J_z	J_z	$-J_z$	J_z	J_z	$-J_z$
x	x	$x \cos\frac{2\pi}{3} + y \sin\frac{2\pi}{3}$	x	x	$-x \cos\frac{-\pi}{3} - y \sin\frac{-\pi}{3}$	x
y	y	$-x \sin\frac{2\pi}{3} + y \cos\frac{2\pi}{3}$	$-y$	y	$x \sin\frac{-\pi}{3} - y \cos\frac{-\pi}{3}$	$-y$
z	z	z	$-z$	$-z$	$-z$	z
q_+	q_+	$q_+ e^{\frac{-2\pi i}{3}}$	q_-	q_+	$q_+ e^{\frac{-2\pi i}{3}}$	q_-

Table 2.6 Effect of symmetry operations on angular momenta and coordinates.

ations but with the opposite sign for permutation-inversion operations.[3] The effects of the symmetry operations on the angular momenta, coordinates, and q_+ operator are summarized in Table 2.6.

Following a similar argument to that used for the $|J,k\rangle$ wavefunctions, we can derive the effect of the symmetry operations on $|\ell\rangle$. The results are shown in Table 2.7.

We can then compute the character of $|J,\pm k,\pm\ell\rangle$, which is shown in Table 2.8. Comparing this table with the character table (Table 2.1) of S_3^*, we see that the wavefunctions $\{|J,k,\ell\rangle, |J,-k,-\ell\rangle\}$ belong to representation $A_1 \oplus A_2$ if $(k-\ell) = 3n$, and belong to E if $(k-\ell) = 3n \pm 1$. Because of the importance of the quantity $(k-\ell)$ in determining the symmetry of the wavefunction, it is given its own (signed) quantum number, g. The symmetry with respect to inversion is controlled by the parity of k: if k is even, then the representation is $'$ (prime), if k is odd, then it is $''$ (double-prime). The representations are summarized in Table 2.9.

2.3.4 Rotationless symmetry

A special case of the symmetries derived above is the "rotationless" symmetry — the symmetry of the pure vibrational state. This can be derived by setting[4] $J = k = 0$.

[3] This is because the inversion operation reverses the sign of all coordinates but leaves angular momenta ($\vec{r} \times \vec{p}$) unchanged.

[4] Although the $J = k = 0$ state is not always allowed (see Section 2.5), the state is still used in determining the "rotationless" symmetry.

	E	(123)	(12)	E^*	$(123)^*$	$(12)^*$
$\|\ell\rangle$	$\|\ell\rangle$	$e^{\frac{-2\pi i\ell}{3}}\|\ell\rangle$	$\|-\ell\rangle$	$\|\ell\rangle$	$e^{\frac{-2\pi i\ell}{3}}\|\ell\rangle$	$\|-\ell\rangle$
$\|-\ell\rangle$	$\|-\ell\rangle$	$e^{\frac{2\pi i\ell}{3}}\|-\ell\rangle$	$\|\ell\rangle$	$\|-\ell\rangle$	$e^{\frac{2\pi i\ell}{3}}\|-\ell\rangle$	$\|\ell\rangle$
$\|J,k,\ell\rangle$	$\|J,k,\ell\rangle$	$e^{\frac{2\pi i(k-\ell)}{3}}\|J,k,\ell\rangle$	$(-1)^J\|J,-k,-\ell\rangle$	$(-1)^k\|J,k,\ell\rangle$	$(-1)^k e^{\frac{2\pi i(k-\ell)}{3}}\|J,k,\ell\rangle$	$(-1)^{J-k}\|J,-k,-\ell\rangle$
$\|J,-k,-\ell\rangle$	$\|J,-k,-\ell\rangle$	$e^{\frac{-2\pi i(k-\ell)}{3}}\|J,-k,-\ell\rangle$	$(-1)^J\|J,k,\ell\rangle$	$(-1)^k\|J,-k,-\ell\rangle$	$(-1)^k e^{\frac{-2\pi i(k-\ell)}{3}}\|J,-k,-\ell\rangle$	$(-1)^{J+k}\|J,k,\ell\rangle$

Table 2.7 Effect of symmetry operations on $|\ell\rangle$ and $|J,k,\ell\rangle$.

	E	(123)	(12)	E^*	$(123)^*$	$(12)^*$
$\|J, \pm k, \pm\ell\rangle$	2	$2\cos\left[\frac{2\pi}{3}(k-\ell)\right]$	0	$2(-1)^k$	$2(-1)^k\cos\left[\frac{2\pi}{3}(k-\ell)\right]$	0
$(k-\ell) = 3n$	2	2	0	$2(-1)^k$	$2(-1)^k$	0
$(k-\ell) = 3n \pm 1$	2	-1	0	$2(-1)^k$	$-(-1)^k$	0

Table 2.8 Character of $|J, \pm k, \pm\ell\rangle$

	k even	k odd
$g = 3n$	$A_1' \oplus A_2'$	$A_1'' \oplus A_2''$
$g = 3n \pm 1$	E'	E''

Table 2.9 Representation of $|J, \pm k, \pm\ell\rangle$ in S_3^* as a function of k and $g \equiv (k-\ell)$

Since $k = 0$ is even, and $g = -\ell$ for $k = 0$, the symmetry depends only on the quantity (ℓ mod 3): if ℓ is a multiple of 3, then the vibrational state is of $A_1' \oplus A_2'$ symmetry; otherwise it is of E' symmetry. In the case $\ell = 0$, the vibrational symmetry is A_1', as can be seen from Table 2.7.

2.4 Nuclear Spin Symmetry

The character of the nuclear spin wavefunctions for a set of identical particles in a permutation-inversion group can be determined by counting the number of spin configurations that are mapped onto themselves by a given symmetry operation, as shown in Table 2.10. For example, if $\begin{matrix} 3 \\ 1\ \ 2 \end{matrix} = \begin{matrix} \uparrow \\ \downarrow\ \ \downarrow \end{matrix}$, then this configuration is mapped onto itself by E and (12), but not by (123).

Operation	$\begin{matrix} 3 \\ 1\ \ 2 \end{matrix}$	$\begin{matrix} 3 \\ 1\ \ 2 \end{matrix}$	$\begin{matrix} 3 \\ 1\ \ 2 \end{matrix}$	$\begin{matrix} 3 \\ 1\ \ 2 \end{matrix}$	$\begin{matrix} 3 \\ 1\ \ 2 \end{matrix}$	$\begin{matrix} 3 \\ 1\ \ 2 \end{matrix}$	$\begin{matrix} 3 \\ 1\ \ 2 \end{matrix}$	$\begin{matrix} 3 \\ 1\ \ 2 \end{matrix}$	Γ_{ns}
E	$\begin{matrix} \uparrow \\ \uparrow\ \ \uparrow \end{matrix}$	$\begin{matrix} \uparrow \\ \downarrow\ \ \uparrow \end{matrix}$	$\begin{matrix} \uparrow \\ \uparrow\ \ \downarrow \end{matrix}$	$\begin{matrix} \uparrow \\ \downarrow\ \ \downarrow \end{matrix}$	$\begin{matrix} \downarrow \\ \uparrow\ \ \uparrow \end{matrix}$	$\begin{matrix} \downarrow \\ \downarrow\ \ \uparrow \end{matrix}$	$\begin{matrix} \downarrow \\ \uparrow\ \ \downarrow \end{matrix}$	$\begin{matrix} \downarrow \\ \downarrow\ \ \downarrow \end{matrix}$	8
(12)	$\begin{matrix} \uparrow \\ \uparrow\ \ \uparrow \end{matrix}$			$\begin{matrix} \uparrow \\ \downarrow\ \ \downarrow \end{matrix}$	$\begin{matrix} \downarrow \\ \uparrow\ \ \uparrow \end{matrix}$			$\begin{matrix} \downarrow \\ \downarrow\ \ \downarrow \end{matrix}$	4
(123)	$\begin{matrix} \uparrow \\ \uparrow\ \ \uparrow \end{matrix}$							$\begin{matrix} \downarrow \\ \downarrow\ \ \downarrow \end{matrix}$	2

Table 2.10 Determination of the character of the nuclear spin wavefunctions in S_3^*.

The resulting representation for the nuclear spin wavefunctions Γ_{ns} can be decomposed into the irreducible representations of the S_3^* group using the usual methods, to yield $\Gamma_{ns} = 4A_1' \oplus 2E'$. The A_1' representation corresponds to the *ortho* spin configuration (with all three spins aligned), and E' corresponds to the *para* configuration (with one spin antiparallel to the other two). The statistical weight ratio for *ortho*:*para* is 4:2.

2.5 Symmetry Restrictions on Total Wavefunction

As mentioned in Section 2.1, the Pauli principle imposes the requirement that the total wavefunction belong to the A_2' or A_2'' representations. Since the symmetry of the ground electronic state $\Gamma_{el} = A_1'$, the product table (Table 2.2) tells us that the product $\Gamma_{rv} \otimes \Gamma_{ns} \supset A_2'$ or A_2''.

If the nuclear spin representation is $\Gamma_{ns} = A_1'$ (*ortho*), the product table implies that the rovibrational symmetry must be $\Gamma_{rv} \in \{A_2', A_2''\}$. On the other hand, if the nuclear spin symmetry is $\Gamma_{ns} = E'$ (*para*), then the rovibrational symmetry must be $\Gamma_{rv} \in \{E', E''\}$.

Recalling from Table 2.9 that the rovibrational symmetry A_2 corresponds to $g = 3n$ and that E corresponds to $g = 3n \pm 1$, we have the following correspondence between nuclear spin and the g quantum number:

$$\begin{aligned} ortho &\leftrightarrow g = 3n \\ para &\leftrightarrow g = 3n \pm 1 \end{aligned}$$

In addition to this fundamental link between the spin configuration and the g quantum number, the Pauli principle also implies that the rovibrational A_1 symmetry is not allowed. This means that of the two $g = 3n$ states, which have symmetry $A_1 \oplus A_2$, only one of them (A_2) is allowed. Furthermore, rovibrational levels with $k = \ell = g = 0$ and J even, which have symmetry A_1' (see Table 2.4), are not allowed. In particular, the ground rotational level ($J = k = 0$) of the ground vibrational state

($v_1 = v_2 = \ell = 0$) of the ground electronic state (A_1') is of A_1' symmetry and therefore does not exist! A system like H_3^+ is therefore unusual in the sense that the molecule is never at "rest."

2.6 Electric Dipole Selection Rules

The space-fixed electric dipole moment operator $\hat{\mu}$ is invariant to permutations (since identical particles have the same charge) but changes sign with the inversion operation ($\vec{r} \rightarrow -\vec{r}$). Therefore $\hat{\mu}$ belongs to the A_1'' representation (cf. Table 2.1). The strength of a dipole-allowed transition is proportional to $\langle \psi_f | \hat{\mu} | \psi_i \rangle^2$, which is non-zero only if the integrand is totally symmetric. This implies that $\Gamma_f \otimes \Gamma_{\hat{\mu}} \otimes \Gamma_i \supset A_1'$. Since $\Gamma_{\hat{\mu}} = A_1''$, the product table (Table 2.2) implies that $\Gamma_f \otimes \Gamma_i \supset A_1''$.

However, the Pauli principle requires that the representations of the total wavefunctions Γ_f and Γ_i belong to A_2' or A_2''. By looking at the product table, we see that the requirements that $\Gamma_f \otimes \Gamma_i \supset A_1''$ and $\Gamma_f, \Gamma_i \in \{A_2', A_2''\}$ imply a selection rule $A_2' \leftrightarrow A_2''$ for the total final and initial wavefunctions. This is equivalent to the statement that the parity must change in an electric dipole transition. Because the parity is determined (see the character of $|J, k, \ell\rangle$ with respect to inversion in Table 2.7) by $(-1)^k$, we can also say that k must go from even $\leftrightarrow$ odd, or $\Delta k = 2n + 1$.

Another important selection rule can be derived by directly considering the transformation properties of $\langle \psi_f | \hat{\mu} | \psi_i \rangle$. For allowed transitions, this quantity must be a non-zero number, so that any symmetry operation acting on it returns itself. In particular in the case of the (123) operation,

$$\begin{aligned}
(123)\langle J'k'\ell'|\hat{\mu}|Jk\ell\rangle &= \{(123)\langle J'k'\ell'|\}\,\{(123)\hat{\mu}\}\,\{(123)|Jk\ell\rangle\} \\
&= \left\{e^{\frac{-2\pi i}{3}(k'-\ell')}\langle J'k'\ell'|\right\}\,\{\hat{\mu}\}\,\left\{e^{\frac{2\pi i}{3}(k-\ell)}|Jk\ell\rangle\right\} \\
&= e^{\frac{2\pi i}{3}\{(k-\ell)-(k'-\ell')\}}\langle J'k'\ell'|\hat{\mu}|Jk\ell\rangle
\end{aligned}$$

This implies the selection rule $\Delta(k - \ell) = \Delta g = 3n$, where n is an integer. Because of the link between g and spin modification, this further implies that the

Selection Rule	Origin
$\Delta k = 2n \pm 1$	parity
$\Delta I = 0$, $\Delta g = 3n$	nuclear spin
$\Delta J = 0, \pm 1$	angular momentum
$J = 0 \leftrightarrow\!\!\!\!\!\!+\!\!\!\!\!\!\rightarrow J = 0$	angular momentum

Table 2.11 Electric dipole selection rules for H_3^+.

spin modification does not change during the absorption of radiation.[5]

Finally, we have a selection rule on J, the total (non-spin) angular momentum. An absorption is governed by the interaction between the space-fixed dipole moment $\hat{\mu}$ and the electric field $\vec{E}$. The dipole moment operator $\hat{\mu}$ is a first rank tensor, and therefore [16, p. 442] the rule for addition of angular momentum requires that J, J', and 1 form the three sides of a triangle (the "triangle rule"). This implies the selection rules on J: $\Delta J = 0, \pm 1$ and $0 \leftrightarrow\!\!\!\!\!\!+\!\!\!\!\!\!\rightarrow 0$. The dipole selection rules for H_3^+ are summarized in Table 2.11.

2.7 Vibrational Structure

2.7.1 Energy levels

The vibrational energy level structure of H_3^+ is shown in Figure 2.3, along with a one-dimensional slice of the potential energy surface. The ground vibrational state (more specifically, the theoretical $J = k = 0$ level of the ground state) lies about 4362 cm^{-1} above the bottom of the potential curve [25]. This vibrational zero point energy is roughly equal to half of ν_1 (3178.29 cm^{-1}) plus two halves (due to the degeneracy) of ν_2 (2521.31 cm^{-1}). The fact that the zero point energy is slightly larger than expected is due to the large anharmonicity of the potential surface. Also shown in Figure 2.3, by the dashed line, is the "barrier to linearity" — the energy necessary to achieve a linear configuration ($\theta = \pi$, where θ is the angle between two H–H bonds in C_{2v} geometry).

[5] This discussion has implicitly assumed that the off-diagonal spin–rotation interaction is negligible. This is an extremely good approximation because the inhomogeneous nuclear spin interaction ($\sim$ kHz) is much smaller than the rotational spacing ($\sim$40 cm^{-1}). [24]

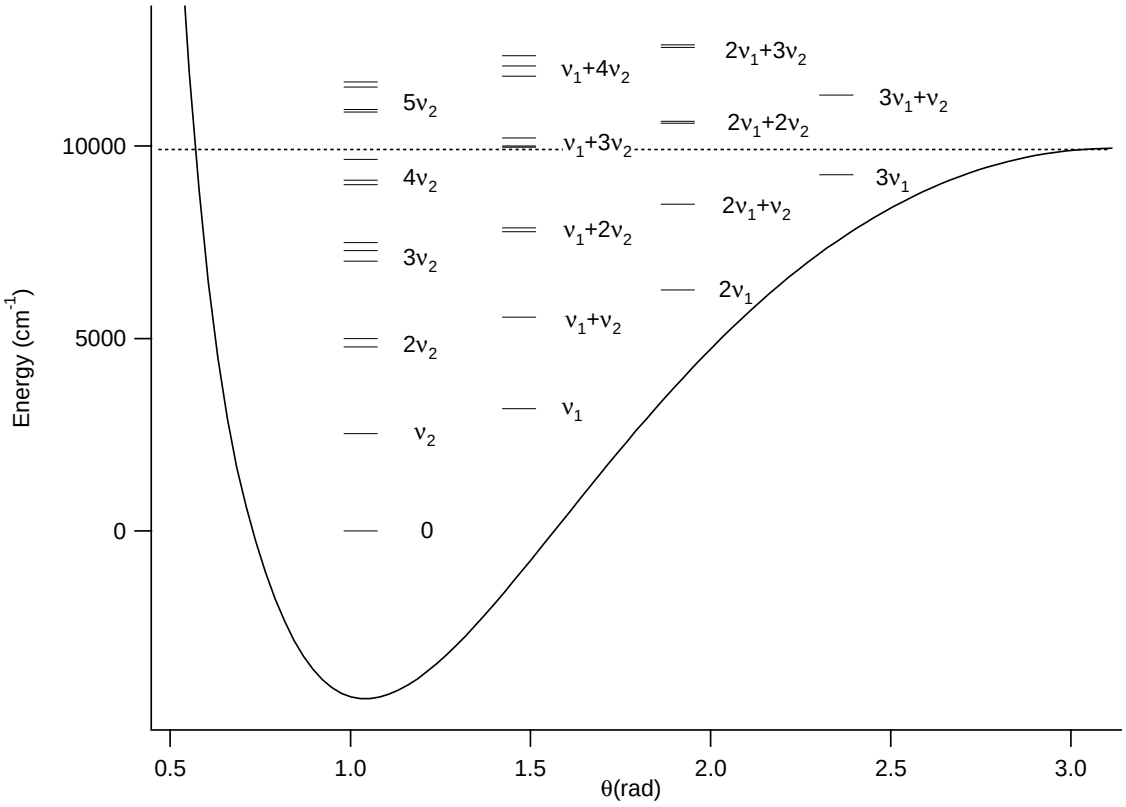

Figure 2.3 Vibrational energy level structure of H_3^+.

if $\Delta\ell = 0$	$\rightarrow$	$\Delta k = \pm 3$	$\Delta g = \pm 3$
if $\Delta\ell = \pm 1$	$\rightarrow$	$\Delta k = \pm 1$	$\Delta g = 0$
if $\Delta\ell = \pm 2$	$\rightarrow$	$\Delta k = \pm 1$	$\Delta g = \pm 3$
if $\Delta\ell = \pm 3$	$\rightarrow$	$\Delta k = \pm 3$	$\Delta g = 0$

Table 2.12 Approximate vibrational sub-band selection rules for H_3^+.

2.7.2 Selection rules

While there are no rigorous selection rules for the vibrational quantum numbers, there are approximate selection rules for vibrational sub-bands, to the extent that ℓ is an approximately good quantum number. These result from combining the selection rules $\Delta(k - \ell) = 3n$ and $\Delta k = 2m + 1$, as shown in Table 2.12.

As can be seen from the table, vibrational bands with $\Delta\ell = 3n$ are forbidden because they violate the traditional selection rule $\Delta k = 1$, which arises from the triangle rule for angular momentum addition (for the unmixed wavefunctions). However, due to mixing between states and resulting intensity borrowing, these (sub)bands do have a small intensity and are observable.

2.7.3 Transition strengths

If one considers absorption spectroscopy from the ground vibrational state of H_3^+ (as is most relevant to astronomical spectroscopy and a great deal of laboratory spectroscopy of cold discharges), and keeping in mind that the strongest bands will be those with $\Delta\ell = 1$ or 2, the following bands might be observed:

Single excitation :	$\nu_2 \leftarrow 0$		
Double excitaiton :	$2\nu_2^2 \leftarrow 0$	$\nu_1 + \nu_2 \leftarrow 0$	
Triple excitation :	$3\nu_2^1 \leftarrow 0$	$\nu_1 + 2\nu_2^2 \leftarrow 0$	$2\nu_1 + \nu_2 \leftarrow 0$
$\vdots$			

In the first-order, harmonic oscillator approximation, only the fundamental band $\nu_2 \leftarrow 0$ is allowed. In particular, ν_1 is forbidden because it does not induce a change

Band	(cm^{-1})	A (s^{-1})	μ^2 (D^2)	Relative Intensity
$\nu_2 \leftarrow 0$	2521	128.8	0.0256	1
$2\nu_2^2 \leftarrow 0$	4997	144.6	0.0037	1/7
$3\nu_2^1 \leftarrow 0$	7003	15.7	0.000146	1/175
$4\nu_2^2 \leftarrow 0$	9108	6.75	0.0000285	1/898
$5\nu_2^1 \leftarrow 0$	10884	2.46	0.00000557	1/4596

Table 2.13 Intensities of various vibrational bands of H_3^+.

in the dipole moment. Although the harmonic oscillator approximation is a poor approximation for H_3^+ because of the large anharmonicity of the potential, the fundamental band $\nu_2 \leftarrow 0$ is by far the strongest band.

In ordinary molecules, a given vibrational band has a squared dipole moment (μ^2) whose order of magnitude is proportional to $\kappa^{2\Delta v}$, where the Born-Oppenheimer parameter $\kappa \equiv \sqrt[4]{\frac{m_e}{m_N}}$. In the case of H_3^+, with the nuclear mass $m_N = m_p$, $\kappa^{-1} \cong 6.5$, so one would expect the first overtone ($\Delta v = 2$) to be about 42 (κ^{-2}) times weaker than the fundamental ($\Delta v = 1$). However, the large anharmonicity leads the overtones to be much stronger than expected, as shown in Table 2.13. [In this table, band origins and Einstein coefficients A are from [26], except in the case of $5\nu_2$, for which values were calculated from data provided by J. K. G. Watson (private communication).] It is interesting to note that the emission of $2\nu_2^2 \rightarrow 0$ is actually stronger than that of $\nu_2 \rightarrow 0$, due to the ν^3 factor in the formula for the Einstein coefficient of spontaneous emission.

2.8 Rotational Structure

2.8.1 $\ell = 0$ levels

The calculated rotational structure of the vibrational ground state of H_3^+ is shown in Figure 2.4. This structure is characteristic of all vibrational bands with $\ell = 0$. The energy levels can be fit with high accuracy to the usual formula for an oblate symmetric top:

$$E(J,k) \;=\; BJ(J+1) + (C-B)k^2$$

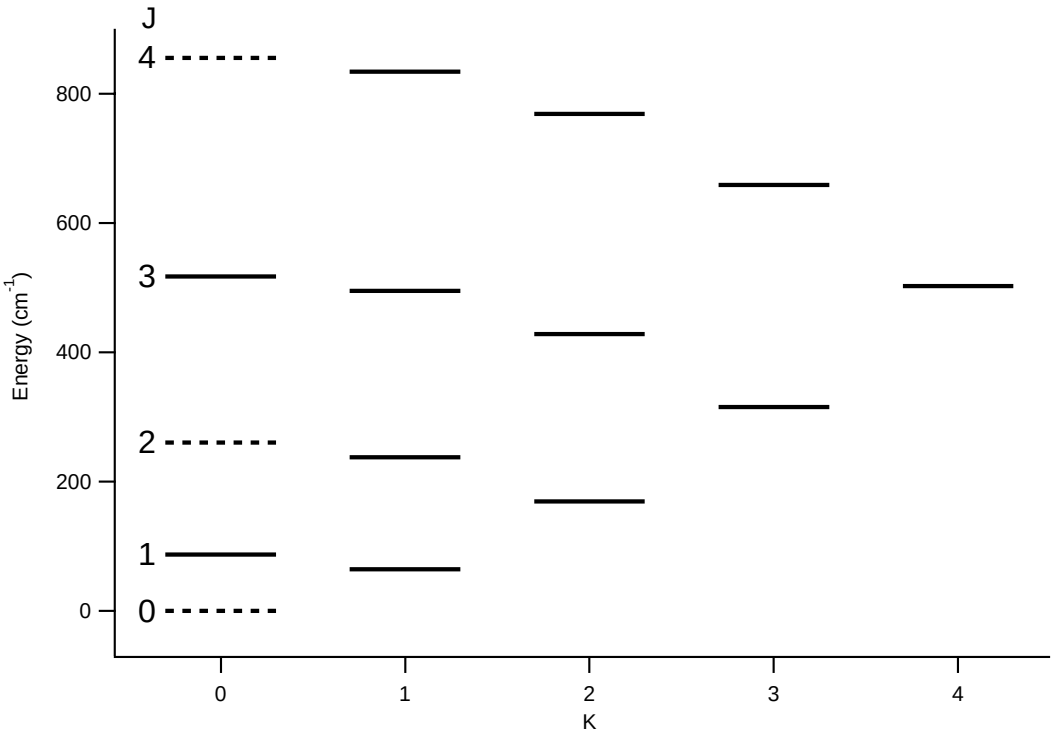

Figure 2.4 Ground state energy level structure of H_3^+.

$$
\begin{aligned}
&-D_{JJ}J^2(J+1)^2 - D_{Jk}J(J+1)k^2 - D_{kk}k^4 \\
&+H_{JJJ}J^3(J+1)^3 + H_{JJk}J^2(J+1)^2k^2 + H_{Jkk}J(J+1)k^4 + H_{kkk}k^6 \\
&-(-1)^J\delta_{k3}h_3\frac{(J+3)!}{(J-3)!}
\end{aligned}
$$

where the first line contains the principal terms, the second line contains first-order (quartic) centrifugal distortion terms, the third line contains second-order (sextic) distortion terms, and the fourth line contains the term which splits the $k = \pm 3$ levels, only one of which is allowed [27, 28]. Note that the energy levels are independent of the sign of k, so that the unsigned K can be used.

As discussed in Section 2.5, the Pauli principle causes the $k = 0$, J even levels to be forbidden. In particular the ground state $|J, k\rangle = |0, 0\rangle$ is missing, leaving $|1, 0\rangle$ and $|1, 1\rangle$ as the lowest energy levels.

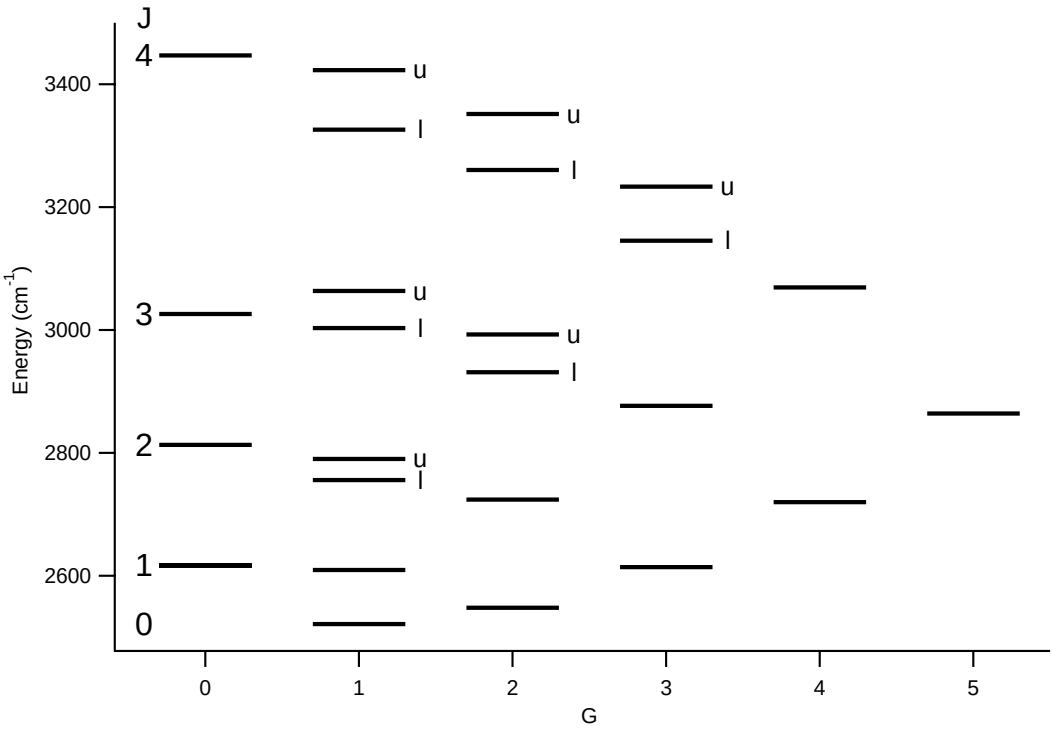

Figure 2.5 ν_2 state energy level structure of H_3^+.

2.8.2 $|\ell| = 1$ levels

The levels with $|\ell| = 1$ (for example the ν_2 state, shown in Figure 2.5), have a more complicated energy level structure. The zero-order energy level expression is $BJ(J+1) + (C-B)k^2 - 2C\zeta k\ell$. A quick calculation shows that the energy of the $|J, k, \ell\rangle = |J, k+1, +1\rangle$ and $|J, k-1, -1\rangle$ states is $4k[C - B - C\zeta]$. This energy difference is nearly zero because $B \cong 2C$ and $\zeta = -1$ for the triatomic equilateral triangle symmetric top. Hence the states $|J, k+1, +1\rangle$ and $|J, k-1, -1\rangle$ are nearly degenerate and will be mixed together. The term in the effective Hamiltonian which will couple these two states is

$$\tilde{H}_{22} = \frac{q}{4}\left(q_{2+}^2 J_{2+}^2 + q_{2-}^2 J_{2-}^2\right)$$

A fit of the experimental spectra [2] shows that the parameter q is quite large (-5.4 cm^{-1}), so that the two states will be mixed very badly. For this reason, we

need to use the $g \equiv (k - \ell)$ quantum number rather than k to describe the states.[6] The resulting two states after mixing will have the same g but will differ in energy, and they are labelled with a u or l to denote the upper or lower member of the pair, as shown in Figure 2.5. This "doubling" of levels will occur for all levels for which $J - 1 \geq |g| \geq 1$ — that is, whenever there are two sets of $\{k, \ell\}$ with the same g.

The energy levels are independent of the sign of g, and thus $G \equiv |g|$ is more often used. This can be understood by considering the invariance of the energy of the system with respect to time reversal: the time reversal operation reverses all angular momenta, so that $k \to -k$ and $\ell \to -\ell$. Consequently, $g = (k - \ell) \to (-k - -\ell) = -(k - \ell) = -g$, and therefore the energy is invariant to a change in the sign of g.

Complicated energy level expressions can be written in a polynomial form for the $|\ell| = 1$ states [28], but at higher energies one finds that an adequate fit requires nearly as many parameters as data points. Ultimately, variational calculations are the only reliable way to calculate the energy levels (see Appendix D).

2.8.3 $|\ell| = 2$ levels

An energy level diagram for the $2\nu_2^2$ state (representative of states with $|\ell| = 2$) is shown in Figure 2.6. The structure is generally similar to the case of $|\ell| = 1$, except that the doubling occurs for $J - 2 \geq G \geq 1$. In general, there will be doubling for levels with $J - |\ell| \geq G \geq 1$. Unlike the case of the ground state or the ν_2 state, for the $2\nu_2^2$ state it is not fruitful to attempt to use polynomial energy level expressions. We must rely on variational calculations, as discussed in more detail in Appendix D.

2.9 Notation for Rotation-Vibration Transitions

Since H_3^+ was first spectroscopically observed in the laboratory by Oka in 1980 [2], there have been many variations in the notation used to describe its ro-vibrational transitions. These notations have suffered from various problems, primarily that most of them are not easily extendable to high energy transitions. In addition, the symbols

[6] Note that we can also use g instead of k in the ground state, because $g = k$ when $\ell = 0$.

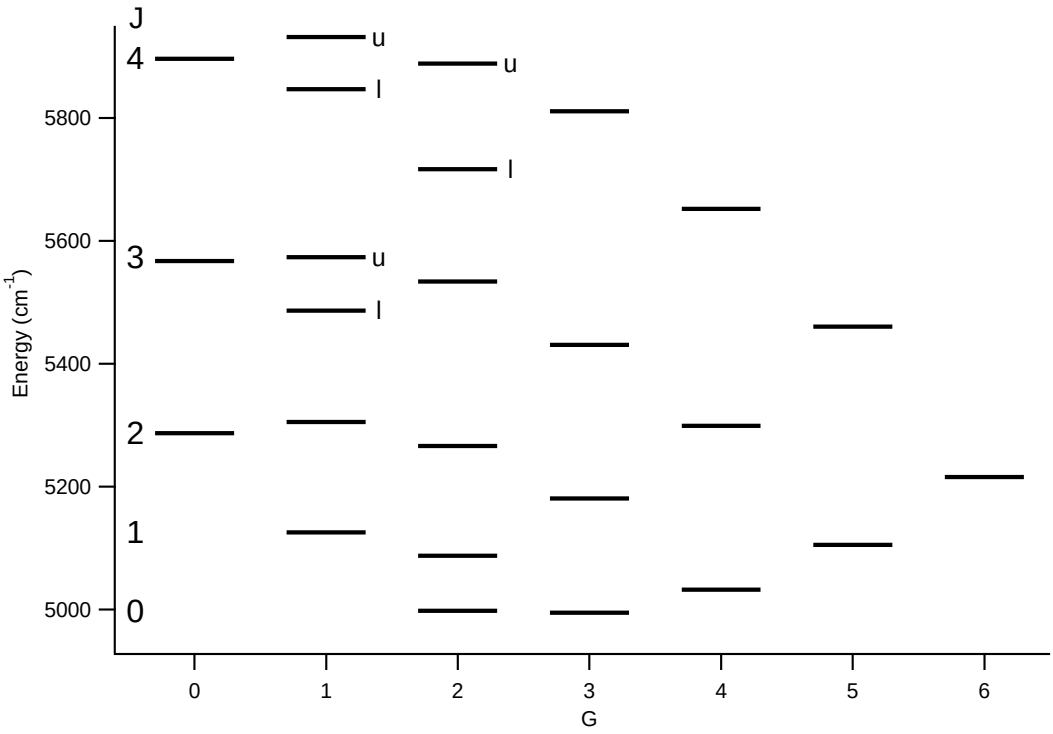

Figure 2.6 $2\nu_2^2$ state energy level structure of H_3^+.

+ and − were frequently used for the upper and lower levels of a doublet, which led to confusion with parity.

We have recently introduced [30, 31] a new notation scheme which overcomes these problems. It is imperfect in the sense that it relies on quantum numbers that are only approximately good ($v_1, v_2, |\ell|$, and to a lesser extent G), however this is done to retain an approximate understanding of the behavior of the molecule. We have shown (see Appendix D) that this notation suffices to describe transitions between all energy levels below 9000 cm^{-1}, and therefore it will be suitable for all astronomical work and the vast majority of laboratory work.[7]

The notation consists of two parts, the band symbol and the branch symbol. The band symbol is simply the usual $v_1'\nu_1 + v_2'\nu_2^{|\ell'|} \leftarrow v_1''\nu_1 + v_2''\nu_2^{|\ell''|}$, which can be abbreviated as $v_1'v_2'^{|\ell'|} \leftarrow v_1''v_2''^{|\ell''|}$. The branch symbol can be described as:

$$^{[\Delta g]}\{P|Q|R\}(J,G)^{\{u|l\}}_{\{u|l\}}$$

The P, Q, or R is used as usual to describe a transition of $\Delta J = -1, 0$, or $+1$. The (J, G) refers to the J and G quantum numbers of the lower level of the transition. The appropriate u or l is appended as a superscript if the upper level of the transition belongs to a doublet, and is appended as a subscript if the lower level belongs to a doublet. Finally, a superscript is prepended to the branch symbol when $\Delta g \neq 0$. If $\Delta g = \pm 3$, then an n is used if $\Delta G = -3$ and a t is used if $\Delta G = +3$.[8] In cases where $\Delta g = \pm 3m$ $(m > 1)$, as caused by mixing, the superscript used is the signed value of $|\Delta g|$, where the sign is that of ΔG.[9] Examples of this notation used in practice can be found in the following sections, especially in Appendix D.

[7] In fact, its failure above 9000 cm^{-1} will be primarily in very strongly mixed states, which are not those most likely to be observed in future experiments.

[8] Note that if $G'' = 1$ or 2, then the n transition will formally appear as $\Delta G = +1$ or -1, as G "wraps around" zero ($1 \rightarrow -2$ or $2 \rightarrow -1$).

[9] Except, as above, when G "wraps around" zero.

CHAPTER 3
LABORATORY SPECTROSCOPY OF H_3^+

This chapter begins with an overview of the experimental methods used for producing and detecting H_3^+ in laboratory plasmas. Section 3.2 discusses my work on the $\nu_1 + 2\nu_2 \leftarrow 0$ and $2\nu_1 + \nu_2 \leftarrow 0$ bands using a near-infrared diode laser, and Section 3.3 discusses our work on the $5\nu_2 \leftarrow 0$ band. In addition, Appendix D reviews my effort with Mike Lindsay to compile and re-evaluate all previous laboratory spectroscopy of H_3^+ and compute experimentally determined energy levels for comparsion with theoretical calculations. For a comprehensive review of the previous laboratory spectroscopy of H_3^+, see Appendix B.2 [30].

3.1 Production and Detection of H_3^+

3.1.1 Plasma cell

A diagram of the "Black Widow" cell used for the production of H_3^+ is shown in Figure 3.1. This cell ($\sim$ 1.4 m in length) features a "triple jacket" design: the innermost tube (18 mm diameter) contains the reagent gases, the middle jacket holds the coolant (in this case, liquid nitrogen), and the outer jacket holds an insulating vacuum.

The reagent gases (mixed externally) flow through the gas inlet on top of the cell, and then through eight inlets spaced throughout the length of the cell. The lengths of all inlet tubes are the same in order to ensure a uniform flow of gas into the discharge cell. The reagent gases flow out through four outlet tubes spaced along the length of the cell, which lead to a mechanical pump (Alcatel 2004A). An additional port to the inner tube of the cell is available for a pressure gauge (MKS Barotron 222CA). Typically the discharge is operated with about 0.5 Torr (760 Torr = 1 atm) of pure H_2, or a mixture of about 0.5 Torr of H_2 and 10 Torr of He.

The plasma is produced by applying a high-voltage alternating current potential between two water-cooled electrodes which are located off the axis of the discharge cell. An ordinary function generator is used to produce a high frequency ($\sim$ 18 kHz) sine wave, which is amplified by a power amplifier (Techron 7780). The resulting high

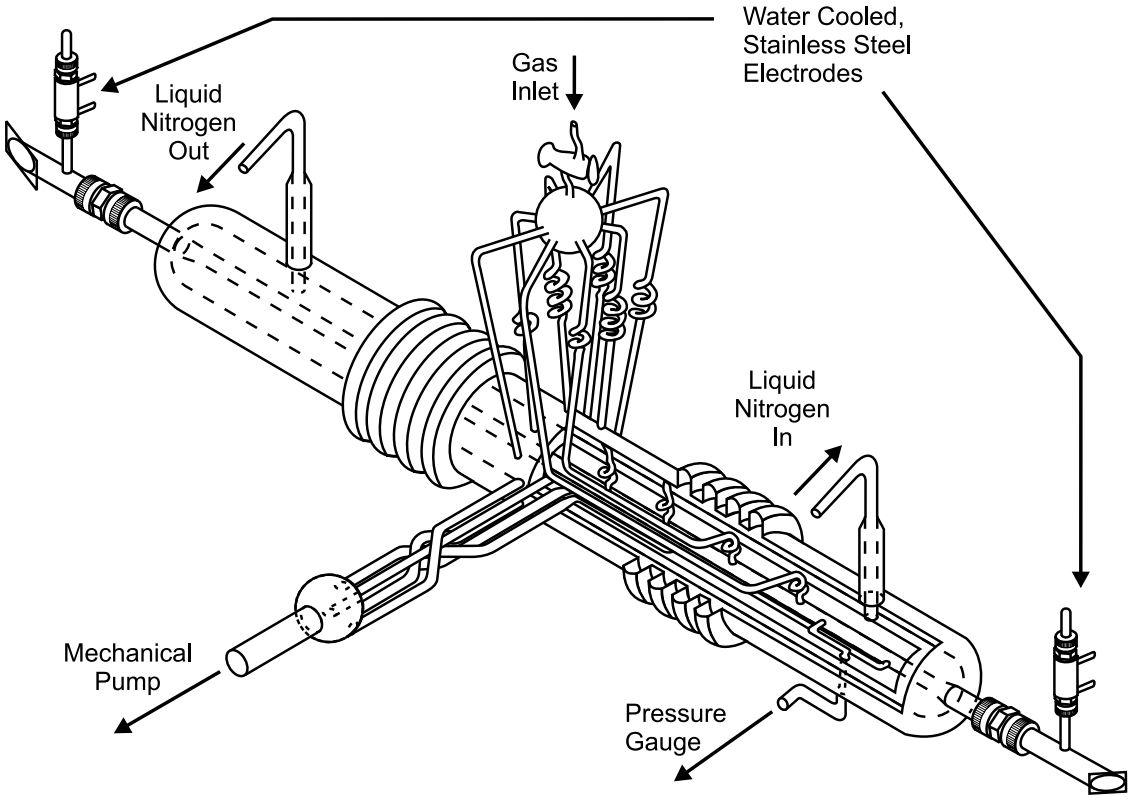

Figure 3.1 Plasma cell used in production of H_3^+. (Courtesy of Mike Lindsay)

current (~ 30 A), low voltage (~ 75 V) signal is then fed into a step-up transformer (Quality Transformer, step-up of 100). The resulting signal has a voltage of several kilovolts, and a current of approximately 310 mA (rms).

This discharge current corresponds to a current density (I/A) of ~ 120 mA cm^{-2}. From the current density, we can estimate the electron number density, using the formula [32]

$$n_e = \frac{(I/A)}{ev_e}$$

where v_e is the drift velocity of the electrons. Given the tube diameter $R = 1.8$ cm and the pressure $p = 0.5$ Torr, the electron drift velocity is approximately $v_e \sim 1 \times 10^7$ cm s^{-1} [33, Fig. 61 and 126]. Thus, the electron density is about 7.5×10^{10} cm^{-3}. Since H_3^+ is known from mass spectroscopic studies to be the dominant cation in hydrogen plasmas, we can conclude (from charge neutrality) that the H_3^+ number density has a similar value.

We keep the inner discharge tube surrounded by liquid nitrogen in order to reduce the temperature of the plasma — this is desirable so that the H_3^+ population will be concentrated in fewer rotational levels, resulting in stronger absorptions for lines arising from each level. With this method, we are able to reduce the rotational temperature of the discharge to around 400 K (in the pure H_2 plasma). The vibrational temperature in these discharges has been observed [34, e.g.] to be somewhat higher due to the relatively inefficient collisional coupling between vibration and either rotation or translation [35]. The electron temperature can be measured using a Langmuir probe, or estimated [33, Fig. 129] from the rate of ionization needed to maintain the plasma, and is of order a few electron volts for our conditions.

3.1.2 Modulation techniques

In any experiment, it is desirable to make "on" and "off" measurements in rapid succession, in order to minimize the inevitable noise and baseline drifts. When working with lasers, the primary source of such noise is the intensity noise of the laser, which is severe at low frequencies (especially at DC) but modest at higher frequencies. A power spectrum of our Titanium:Sapphire laser is shown in Figure 3.2. In order to

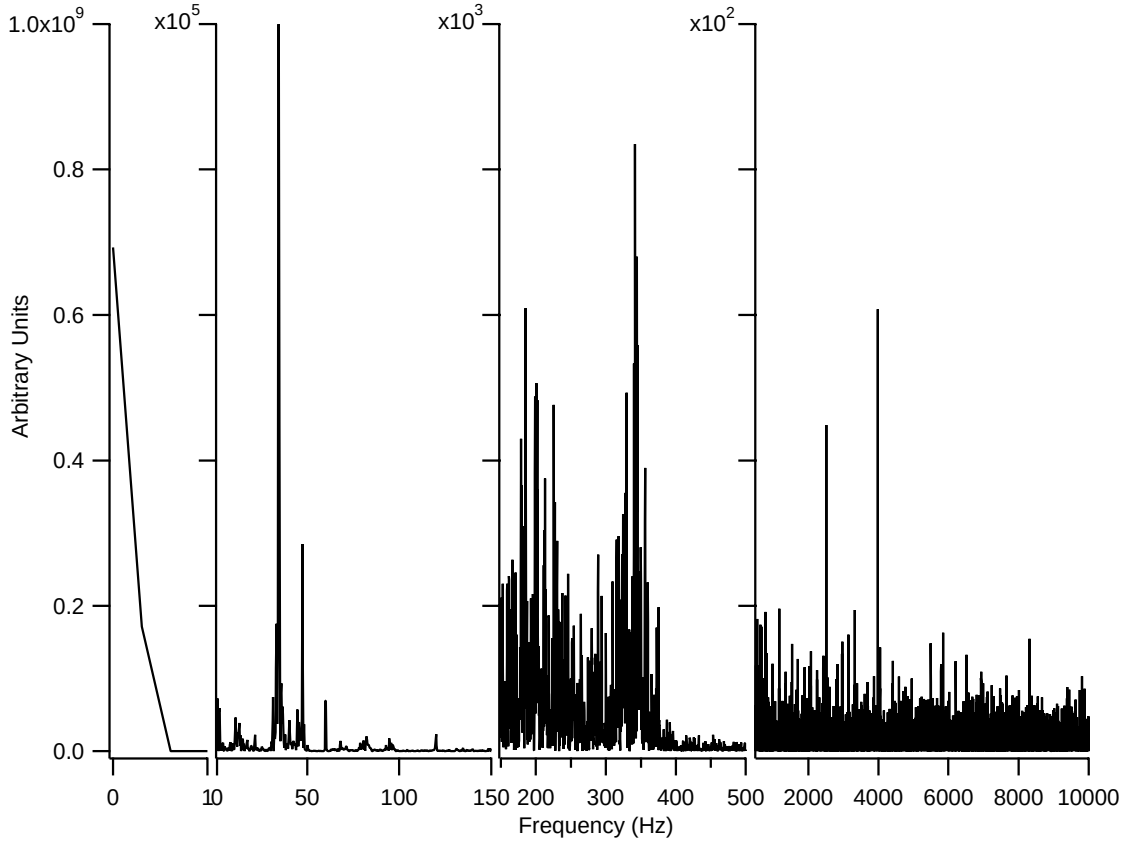

Figure 3.2 Power spectrum of Titanium:Sapphire laser.

obtain the high sensitivity needed to detect weak H_3^+ transitions (or generally, any molecular ion transitions), we need to place the experimental signal of interest at a frequency above the laser noise.

Such a "modulation" is achieved quite naturally by exploiting the AC nature of the plasma. Molecular ions are pulled back and forth along the axis of the plasma tube as the potential alternates. This leads to a periodic Doppler shift of the laser frequency as perceived by the molecular ions — this technique is known as velocity modulation [36]. When the laser is tuned to the red of the rest frequency of a transition, absorption occurs on one half-cycle of the plasma, whereas if the laser is tuned to the blue, the absorption occurs on the other half-cycle.

This effective frequency modulation of the absorption signal (measured by a photodiode, for example) can then be "demodulated" in a phase-sensitive detector (PSD).

The PSD essentially multiplies the experimental signal by the reference signal (in this case, the plasma voltage) and takes the time average of the resulting product. The demodulated signal of a velocity modulated line appears as a derivative shape.

The velocity modulation technique is especially useful because it not only places the experimental signal at high frequency (above the laser noise), but it also performs a discrimination between different types of molecules. Positive and negative ions can be discriminated, as they will appear with opposite phase (since their velocities will be opposite in a given potential). Neutral species such as the reagent molecules or free radicals formed in the plasma, which have concentrations several orders of magnitude higher than the ions, do not feel the pull of the potential, and are not velocity modulated.

Neutrals whose concentration are affected by the discharge can, however, be detected by demodulating at twice the plasma frequency (so-called "$2f$" or concentration modulation). While the product of the neutral absorption with the $1f$ plasma frequency has zero time-average (and hence is not seen with $1f$ demodulation), the product with the $2f$ reference (given an appropriate choice of relative phase) does have a non-zero time-average. Because the velocity of the neutral is not affected, a scan of the laser in frequency will yield a simple Gaussian lineshape (positive or negative in direction, depending on the choice of the phase of the $2f$ reference signal).

3.1.3 Multipassing

In order to increase the depth of absorption (to detect absorptions that are intrinsically very weak), we can either increase the concentration of ions in the lower level of a transition or increase the absorption path length. We already do our best to increase the concentration by cooling the discharge with liquid nitrogen and by using the optimum plasma chemical conditions. While the length of a positive column discharge can, in principle, be made arbitarily long, we are already using a cell greater than 1 meter in length. Longer cells are not only technically difficult for glassblowers to construct, but also are more difficult to work with because of the divergence of the laser beam and the higher voltage needed to maintain the plasma.

We therefore prefer to increase the path length by passing the laser beam through the discharge cell multiple times. The usual techniques for multipassing, White [37] and Herriott [38] cells, allow many passes, but require passing the beam back and forth through the cell. Such an arrangement would wash out the velocity modulation signals, and therefore cannot be used in our experiments.

We use a modified White cell configuration (see Figure 3.3), where the laser beam repeatedly passes through the discharge cell *in the same direction*. The laser beam is focused, using a lens with a long ($f \sim 1$ m) focal length, into the entrance of the White cell. It then passes through the discharge cell, hits a folding mirror, and then hits one of the "half-moon" mirrors. This concave mirror has a 2.4-m radius of curvature, so that the beam will be refocused at the entrance mirror. From the half-moon mirror, the beam hits another folding mirror (the angle of incidence on the concave mirror is minimized to prevent elongation of the beam), then two more folding mirrors (with their separation set to ensure the total distance travelled by the beam between the half-moon and the entrance mirror is 2.4 m), and finally the entrance mirror (again, minimizing the angle of incidence). The entrance mirror (which also has a 2.4-m radius of curvature) is then adjusted so that the reflected beam (now the second pass) strikes the second half-moon mirror. The second half-moon mirror is then adjusted to achieve the appropriate spot pattern on the entrance mirror (inset of Figure 3.3). A more detailed description of the alignment procedure is given in [39, Appendix A].

The White cell configuration shown in Figure 3.3 is only useful for $\sim$4 passes through the cell, because for higher numbers of passes the bottom beams (2 and 4 in the figure inset) tend to partially fall off of the entrance mirror. Mike Lindsay recently developed a new entrance mirror design (see Figure 3.4) which alleviates this problem. With this mirror design, we can achieve 10 or more passes with the Titanium:Sapphire laser.

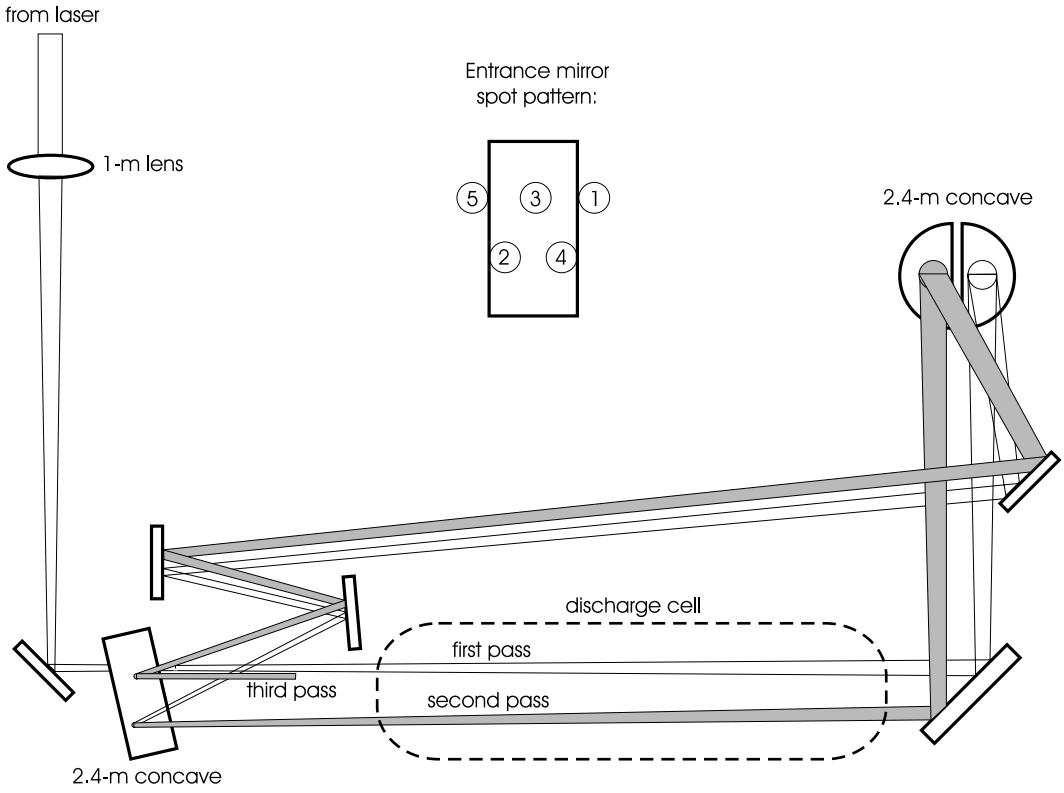

Figure 3.3 Unidirectional multipass cell.

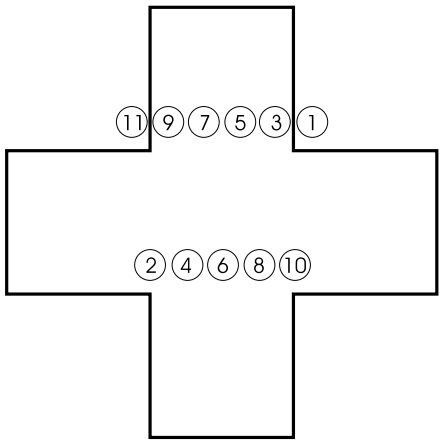

Figure 3.4 Spot pattern for unidirectional multipassing with "cross" entrance mirror.

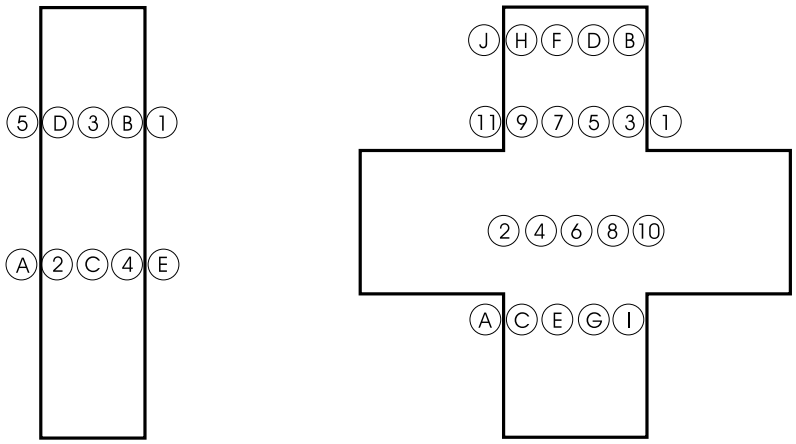

Figure 3.5 Spot patterns for double unidirectional multipassing.

3.1.4 Autobalancing

In order to further reduce noise (for example, residual laser noise at the plasma frequency, or noise induced by the plasma itself) and increase sensitivity, it is useful to use a subtraction scheme. Fortunately, the modified White cells will accept a laser beam travelling in the opposite direction to that shown in Figure 3.3 (the required spot patterns are shown in Figure 3.5). Since the second beam travels in the opposite direction, it experiences the molecular absorptions 180° out of phase with respect to the first beam. When the voltages from photodiodes sensing the two beams are subtracted, the velocity modulated signal is not subtracted, but instead doubled. However, common mode noise (from the laser or the plasma) is subtracted.

Inevitably, the DC levels of the power in the two beams will vary in time and over the course of a frequency scan, due to various processes such as étaloning in the beam-splitter and vibrations in optical elements. In order to effect optimum cancellation of common mode noise, the DC levels of the two beams should be balanced. This has traditionally been accomplished manually by continuously adjusting an attenuator in one beam, but is more effectively performed by an electronic circuit. We use a New Focus 2017 Nirvana dual-beam photoreceiver, which contains an autobalancing circuit designed by Phil Hobbs of IBM [40]. By using this subtraction scheme, we achieve a noise reduction (in the demodulated output) of better than a factor of ten.

3.2 Combination Band Spectroscopy of $\nu_1 + 2\nu_2$ and $2\nu_1 + \nu_2$

3.2.1 Introduction

Since the $\nu_2 \leftarrow 0$ rotation-vibration band of H_3^+ was first detected in the laboratory[2], work has continued to spectroscopically probe higher energy levels using hot bands ($2\nu_2 \leftarrow \nu_2$, $\nu_1 + \nu_2 \leftarrow \nu_1$, etc.), overtone bands ($2\nu_2 \leftarrow 0$ and $3\nu_2 \leftarrow 0$), and forbidden bands ($\nu_1 + \nu_2 \leftarrow \nu_2$ and $\nu_1 \leftarrow 0$). Spectroscopy of high energy levels of H_3^+ provides new data for comparison with theoretical predictions and also extends the list of transitions available for astronomical spectroscopy of hot plasmas (such as Jupiter's ionosphere). For more details on previous laboratory work, readers are referred to a recent review[30].

In this section we report our recent laboratory observation of the $\nu_1 + 2\nu_2^2 \leftarrow 0$ (the superscript refers to $|\ell|$) and $2\nu_1 + \nu_2 \leftarrow 0$ combination bands of H_3^+ near 1.25 μm using a tunable diode laser. These bands reach higher vibrational levels than any previous work, and therefore provide a new test of rovibrational calculations. This work sets the stage for the detection of the $5\nu_2 \leftarrow 0$ overtone band, which probes the theoretically challenging area above the barrier to linearity.

3.2.2 Experimental Setup

Diode laser

The radiation source used in this experiment is a custom-made New Focus 6200 series external-cavity tunable diode laser (serial number LO016). A schematic of the laser cavity is given in Figure 3.6. The essential feature of this laser is that the semiconductor diode laser forms only part of the laser cavity (traditionally the front and rear facets of the diode form the cavity). This is accomplished by placing an anti-reflection (AR) coating on the front facet of the diode, to prevent the front facet from becoming an "end mirror." The rear facet of the diode is coated with a high-reflection (HR) coating.

The beam from the diode is sent through a collimating lens, and then towards a

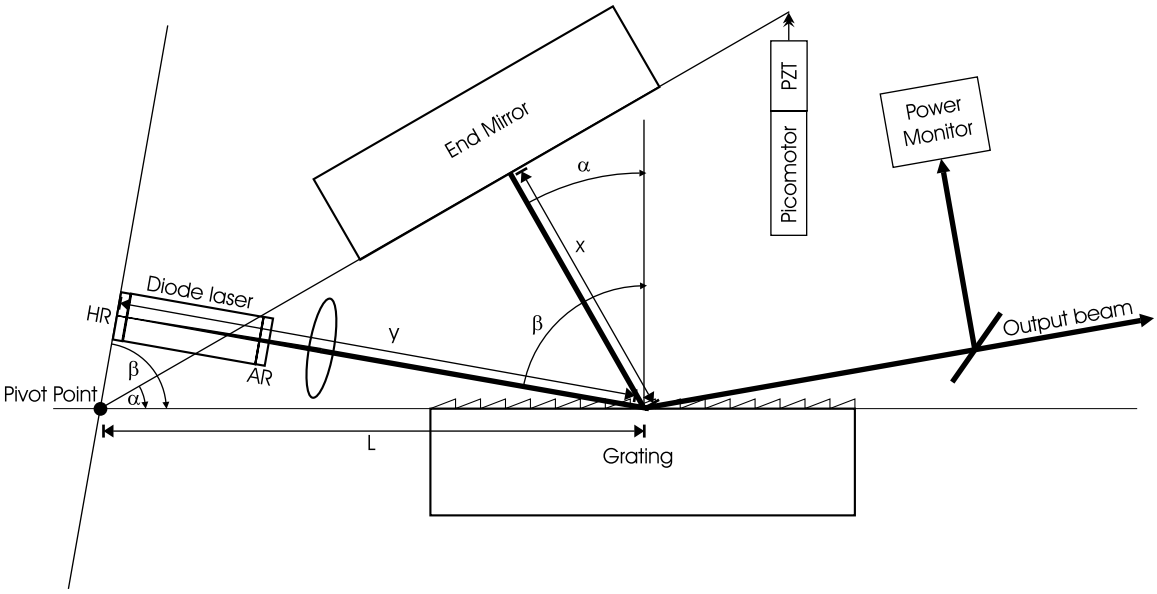

Figure 3.6 Schematic of diode laser cavity.

grating at grazing incidence. Part of the beam is reflected from the grating (forming the output beam), and part of the beam is diffracted towards a high reflecting end mirror. Different wavelengths of light will diffract from the grating at various angles, but only the wavelength which heads toward the end mirror at normal incidence will be reflected back into the diode laser. This wavelength will survive many round trips through the cavity, and therefore will be the lasing wavelength. The value of this wavelength can be determined from the grating equation to be $\lambda = \Lambda(\sin\alpha + \sin\beta)$, where Λ is the groove spacing of the grating, and α and β are the diffracted and incident angles of the beam referenced to the grating normal.

In the New Focus cavity design, the diode laser is fixed with respect to the grating (thus fixing β) but the end mirror is rotated with respect to the grating. The pivot point of the end mirror (the intersection of the axis of the grating surface and the axis of the rear facet of the diode) is chosen such that the angle the end mirror forms with respect to the grating is exactly α. With this design, the distance the beam travels between the diode and grating is $y = L\sin\beta$ and the distance the beam travels between the grating and end mirror is $x = L\sin\alpha$. Thus, the total cavity

length is $x + y = L(\sin\alpha + \sin\beta)$. The number of waves in the cavity is simply $N = (x + y)/\lambda = L/\Lambda$ — a quantity independent of the wavelength! Therefore, the wavelength can be tuned continuously (by rotating the end mirror) over the entire tuning range of the diode laser without inducing a mode hop (a change of N). Single mode operation is ensured because the grating acts as a spectral filter which is narrow ($\sim$ 1 GHz) compared to the longitudinal mode spacing ($c/2L \sim 3.5$ GHz).

In practice, the end mirror angle is set by a combination of a picomotor screw and a piezoelectric transducer (PZT). The picomotor screw permits coarse tuning of the laser frequency, with a precision of a few GHz. The PZT then allows for fine laser tuning within a range of 60 GHz. The laser provides an approximate wavelength reading (with a precision of 0.1 nm but accuracy more like 1 nm) by using an angle sensor to measure α. The laser also provides an approximate power reading by diverting a small portion of the output beam to an internal power meter.

The gain curve of the laser is determined by the intrinsic characteristics of the semiconductor diode as well as the optical properties of the cavity. When the laser was first received from New Focus, it had a tuning range of 7633–8183 cm^{-1}, with a maximum power of $\sim$ 8 mW. However, the AR coating on the front facet of the diode degrades over time, such that at the time of the experiment the useful tuning range was only 7780–8168 cm^{-1}, and continuous tuning was only possible between 7850–8168 cm^{-1}.

A good deal of the loss of tuning range seems to be due to adsorbed water in the AR coating, in part due to the high humidity conditions in our laboratory (New Focus confirms that this is a problem in humid climates). We attempted to remove the adsorbed water by pumping the entire laser head down to high vacuum, but this process did not lead to much increased tuning range. However, we did observe that when the laser was left off for long periods of time (several months), the tuning range was restored when the laser was first turned on again. We suspect the source of this problem is that the diode is kept at a lower temperature than the cavity by the laser controller, which leads to condensation on the diode during operation. This problem could probably be alleviated by leaving the laser dormant for a long period, then pumping it out to high vacuum to remove water elsewhere in the cavity, then sealing

the laser head in an environment (e.g. dry nitrogen) where water cannot reach the diode. Such a procedure is recommended if the laser is brought back into routine operation.

The diode laser is operated through a control box, which is connected to the laser head through an umbilical cord. The control box allows the user to easily set the coarse wavelength (with the picomotor), the PZT voltage (for precision wavelength setting), the temperature of the diode, and the diode current (which controls the output power). The control box allows coarse (picomotor) scans, but does not provide any functionality for high resolution spectroscopy.

Computer interface

The shortcomings of the laser control box necessitated external control of the laser — for this reason, the diode laser spectrometer was the first spectrometer in the Oka Ion Factory^{TM} to be brought completely under computer control. The first key component of the computer interface is control of the laser control box, which is achieved through an RS-232 interface. Using LabWindows (from National Instruments), the front panel of the laser control box was duplicated on the computer to allow the user to set the wavelength, diode temperature, etc. through the computer interface (see Figure 3.7).

A National Instruments (Lab PC+) data acquisition (DAQ) card is used to facilitate both control of the laser and acquisition of experimental signals. The Lab PC+ card has eight 12-bit analog-to-digital converters (ADCs) as well as two 12-bit digital-to-analog converters (DACs). The DACs are used to control the picomotor and the PZT inside the laser, to allow complete control of the laser frequency.

The picomotor signal (fed to the "wavelength input" on the rear of the control box) must be varied between -19.51 and -0.49 volts to nominally vary the laser frequency from 8200.7 cm^{-1} to 7656.4 cm^{-1} (although the entire range could not be used, as described earlier). Because the DAC provides only a ± 5 volt output, the DAC voltage is added to a stable external power supply (Power Designs Model 1570) which provides a -20, -10, or 0 V offset. The PZT signal (fed to the "frequency modulation" input on the rear of the control box) has a range of ± 3 volts, and can therefore be controlled

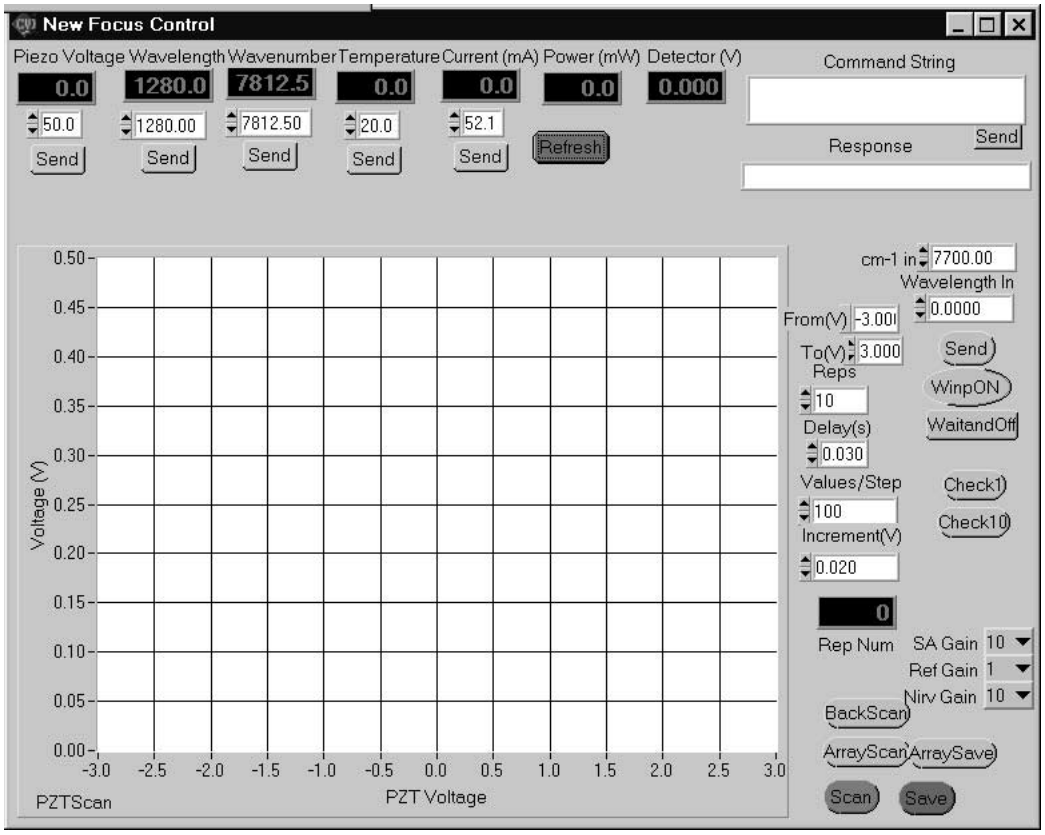

Figure 3.7 LabWindows user interface.

directly by the DAC.

The experimental signals (the output of the PSD, fed by the Nirvana autobalancing photoreceiver, as well as the calibration signals described below) are directly sampled by the ADCs.

The complete computer control of the spectrometer enables not only fast repetitive scanning (as described in the next section), but also allows several useful diagnostic procedures. These include a signal monitor (essentially a very slow oscilloscope, which can be used during optical alignment), a signal histogram tool (which allows for quantitative noise measurements), and a fast Fourier transform capability (which allows measurements of the frequency spectrum of noise).

Scanning protocol

The New Focus diode laser was found to suffer from a square-wave type noise in its optical power, which was random and uncontrollable. [This noise is thought to be due to optical feedback into the cavity, and could in principle be eliminated by placing an optical diode at the exit of the laser.] Because square waves have Fourier components at all frequencies (including the demodulation frequency used in the experiment), this noise is not eliminated by the phase sensitive detector. The square-wave noise is sporadic, which means that in the course of a slow scan there are large baseline excursions, which limit the sensitivity of the experiment to H_3^+ signals.

Because slow scans were not useful in eliminating this noise, we decided to perform rapid repetitive scanning under computer control. This technique has the advantage that spurious (low-frequency) noise tends to contaminate all wavelength "bins" in the spectrum with equal probability (and thus the noise tends to average out), rather than causing "spikes" in the spectrum.

The scanning protocol is as follows:

Repeat:

    Set PZT at 0%

    Wait several τ

    Repeat:

Take N readings of experimental signals & average
Add these values into array[PZT]
Step the PZT
Wait 1 τ
until PZT = 100%
Display array to screen
until you've scanned M times
Divide array by M

In this protocol, "array" represents the array of experimental data, with the PZT voltage as the index, N represents the number of samples to be taken at each PZT voltage, M represents the number of repetitions of the scan, and τ is the time constant of the PSD. In practice, the user selects M and N to optimize the signal-to-noise of observed transitions — M and N must be traded off because they both increase the time it takes to scan the full PZT range (60 GHz). Typical values (with a PZT step size of 200 MHz) are N=100, M=40, and τ=30 ms. With these parameters, each 2 cm^{-1} (60 GHz) segment takes about six minutes to record. When greater sensitivity is needed, M and N are increased, and scans of over one hour can be obtained.

Calibration

Because the internal wavelength meter (angle sensor) of the diode laser is not sufficiently accurate or precise, it is necessary to obtain an independent calibration of the absolute frequency of the laser. This is done by sending a portion of the output beam through a cell of NH_3. The cell used is 2 m in length and contains about 11 Torr of NH_3 (this pressure was chosen so that the pressure broadening would not exceed the Doppler broadening). Because of the weakness of the NH_3 transitions in this frequency range, it is necessary to pass the laser beam through the cell eight times to increase the absorption path length. The beam is then sent to a New Focus 2011 photoreceiver, the output of which is sent into the ADC of the DAQ card. The NH_3 spectrum is obtained simultaneously with the H_3^+ spectrum in order to allow an accurate frequency calibration.

Because the NH_3 lines are often sparse, and because the scanning of the PZT is not completely linear in frequency, it is desirable to have a relative frequency calibration as well as the absolute calibration from the NH_3. For this purpose, a portion of the beam is sent into a TecOptics SA-2 spectrum analyzer (étalon) with a free spectral range of 2 GHz. The transmission signal from this étalon is then sent into the DAQ card, so that a transmission spectrum is also obtained simultaneously with the H_3^+ spectrum. The resulting frequency "ticks," together with the NH_3 reference lines, allow both relative and absolute frequency calibration.

This straightforward calibration scheme is complicated by the fact that the calibration signals (reference gas and étalon) are measured directly, while the experimental signal (H_3^+) is measured through a PSD with a characteristic time constant. Because we are stepping the laser frequency at a rate comparable to the PSD time constant, there is a lag in the observed demodulated spectrum compared to the calibration signals. Consequently, there is a frequency shift between the observed H_3^+ signals and the frequency scale determined by the calibration signals.

This frequency shift was measured with two independent methods. This first method was to alter the scanning protocol to wait longer before stepping the PZT. While this could not be done for all of the scans (because it is too slow), it was done for one strong H_3^+ line. The delay before stepping the PZT was gradually increased until the H_3^+ line no longer shifted in frequency with increasing delay time. This required waiting about 10 τ between PZT steps. The resulting frequency shift (between waiting 1 τ and 10 τ) was then interpreted as the frequency error in all of our measurements.

The second method for determining the frequency error was the measurement of a known spectral line in the plasma. The only suitable species was the hydrogen atom, which could be measured using concentration modulation (demodulating at $2f$). The Paschen β line was measured, and the observed frequency was indeed shifted from the known rest frequency of the line.

The two methods agreed within the measurement uncertainties, and a constant frequency shift of 0.017 cm^{-1} was adopted. By varying the sensitivity of the PSD, we found that this shift was independent of the measured height of a line, which gave us

increased confidence that this was indeed a systematic shift.

3.2.3 Results

The entire frequency range between 7850–8168 cm^{-1} was scanned by overlapping individual 2 cm^{-1} scans. This scanning was performed with both a pure hydrogen discharge ($P_{H_2} \sim 500$ mTorr) and with a helium-dominated discharge ($P_{He} \sim 10$ Torr and $P_{H_2} \sim 500$ mTorr). In addition, individual 2 cm^{-1} scans were made at the frequencies in the range 7785–7850 cm^{-1} where strong lines were expected from the variational calculations of J. K. G. Watson [41]. The spectra containing H_3^+ transitions are shown in Appendix C.

The experiment yielded thirty ro-vibrational transitions of H_3^+ as well as over 200 transitions between Rydberg states of H_2 (denoted H_2^*). A table of the Rydberg transitions and their intensities can be obtained from the EPAPS archive [42]. The Rydberg transitions generally appeared with the phase of negative ions, because H_2^* is formed by impact with electrons [43]. About 10% of the Rydberg lines, however, appeared with the same phase as positive ions. This is interpreted [44] as being due to stimulated emission of transitions between triplet states of H_2^* — the dissociative character of the lower state leads to the necessary population inversion.

Because some Rydberg transitions appear with the same phase as the H_3^+ transitions, the phase alone is not enough to discriminate between H_3^+ and H_2^*. However, the addition of He (10 Torr) as a buffer gas decreases the intensity of the H_2^* lines by about a factor of thirty while not significantly affecting the intensity of the H_3^+ lines, as demonstrated in Figure 3.8. This decrease can be largely attributed to the factor of twenty increase in gas pressure, which provides more collisions to quench the H_2^*. Because of the very low proton affinity of He (1.85 eV) compared to that of H_2 (4.39 eV), the amount of H_3^+ is not reduced by the addition of He to the discharge. By scanning each spectral region in both a pure hydrogen discharge as well as a helium-dominated discharge, we are able to unambiguously identify the H_3^+ lines.

The observed H_3^+ transitions and their assignments are listed in Table 3.1. Twenty-six of the assignments could be made by a simple comparison with Watson's calcu-

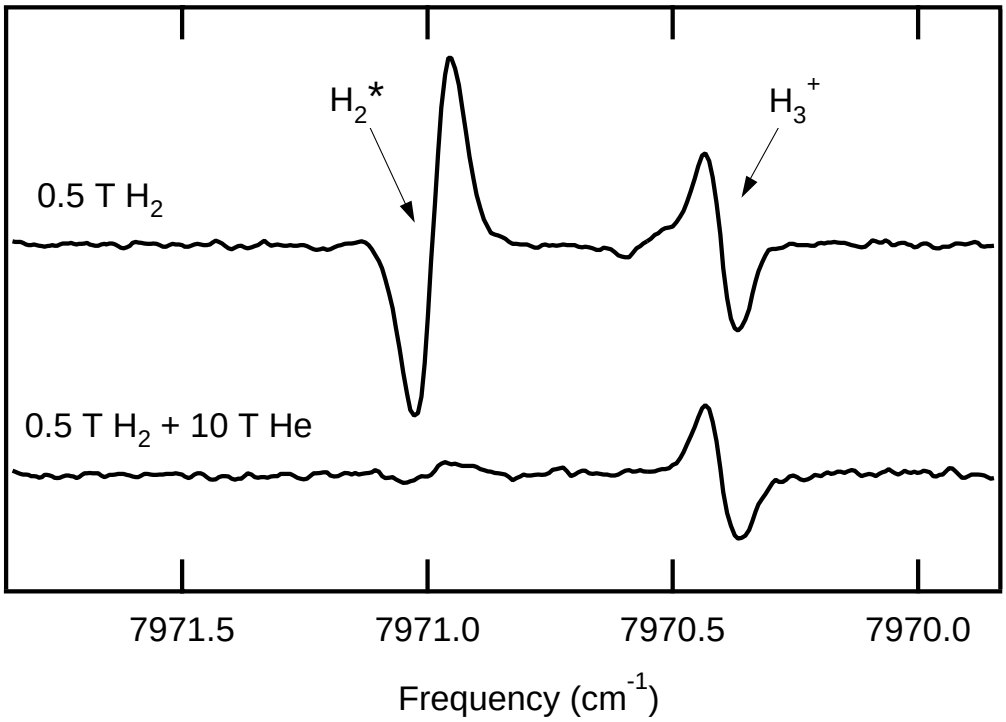

Figure 3.8 Effect of He on H_2^* and H_3^+ [$^tR(1,0)$] absorption lines.

lations. However, there were two pairs of lines (7785.233 and 7785.701; 8162.653 and 8163.129) which were too close in frequency to assign solely by comparison with the calculated frequencies. The first pair of lines was assigned based on the temperature dependence of the observed intensities: the lower frequency line became more intense in the helium-dominated (hotter) discharge and therefore arises from the (J=3,K=0) level in the ground state, rather than (J=1,K=0). The second pair was assigned based on combination differences: the higher frequency line of the pair shares the same upper state as the line at 7905.717 cm^{-1}.

Table 3.1 also shows the uncertainties in the experimental frequencies, which have been estimated by comparing the frequencies obtained in different scans and by considering the proximity of NH_3 reference lines. Also listed in Table 3.1 are the values of J and K in the ground state, along with the values of J and the expectation value of the approximate quantum number G in the upper state. These values are taken from the calculations of J. K. G. Watson [41].

Based on these assignments, twenty-eight of the thirty H_3^+ lines belong to the $\nu_1 + 2\nu_2^2 \leftarrow 0$ band, while two are high-J P-branch lines of the $2\nu_1 + \nu_2 \leftarrow 0$ band, which has its band center [45] near 8487 cm^{-1}. The strongest line in the $\nu_1 + 2\nu_2^2 \leftarrow 0$ band (7970.413 cm^{-1}) was detected with a signal to noise ratio of nearly one hundred. Considering that this band is approximately 270 times less intense than the fundamental band [26], which is a few percent deep in absorption under similar conditions, we estimate that our sensitivity (minimum detectable absorption) is of order $\Delta I/I \sim 3 \times 10^{-6}$. Our sensitivity was hampered by the persistent square-wave shaped noise in the intensity of the diode laser mentioned earlier, which may have been due to optical feedback. This noise appeared most prominently when the multiple path optical arrangement was used. Because of the square-wave nature of the noise, it was not completely filtered out by the phase sensitive detection and thus contributed to noise in our baseline.

The experimentally determined energy levels, based on our observed transitions and the previously determined [46] ground state energy levels, are listed in Table 3.2. In this table, we have listed the value of G for the member of the $|J, G\rangle$ basis set which makes the dominant contribution to the energy level. An energy level diagram

Frequency[a]	Assignment	Band	J'	$\langle G' \rangle^b$	J''	K''
7785.233 (10)	${}^tQ(3,0)$	$\nu_1 + 2\nu_2^2 \leftarrow 0$	3	3.0	3	0
7785.701 (10)	${}^tQ(1,0)$	$\nu_1 + 2\nu_2^2 \leftarrow 0$	1	3.0	1	0
7789.878 (10)	${}^tR(3,3)$	$\nu_1 + 2\nu_2^2 \leftarrow 0$	4	5.9	3	3
7805.893 (10)	${}^nP(1,1)$	$\nu_1 + 2\nu_2^2 \leftarrow 0$	0	2.0	1	1
7820.239 (10)	${}^nP(2,2)$	$\nu_1 + 2\nu_2^2 \leftarrow 0$	1	1.0	2	2
7822.375 (10)	${}^tR(2,2)$	$\nu_1 + 2\nu_2^2 \leftarrow 0$	3	5.0	2	2
7826.739 (10)	${}^nP(3,3)$	$\nu_1 + 2\nu_2^2 \leftarrow 0$	2	0.0	3	3
7833.249 (20)	${}^nP(4,4)^l$	$\nu_1 + 2\nu_2^2 \leftarrow 0$	3	1.1	4	4
7850.959 (10)	${}^tR(1,1)$	$\nu_1 + 2\nu_2^2 \leftarrow 0$	2	4.0	1	1
7880.921 (10)	${}^tR(4,3)$	$\nu_1 + 2\nu_2^2 \leftarrow 0$	5	5.9	4	3
7894.711 (10)	${}^nQ(1,1)$	$\nu_1 + 2\nu_2^2 \leftarrow 0$	1	2.0	1	1
7898.371 (10)	${}^nQ(2,1)$	$\nu_1 + 2\nu_2^2 \leftarrow 0$	2	2.0	2	1
7905.717 (10)	${}^nQ(3,1)$	$\nu_1 + 2\nu_2^2 \leftarrow 0$	3	2.0	3	1
7912.047 (10)	${}^tR(3,2)$	$\nu_1 + 2\nu_2^2 \leftarrow 0$	4	4.9	3	2
7939.619 (10)	${}^tR(2,1)$	$\nu_1 + 2\nu_2^2 \leftarrow 0$	3	4.0	2	1
7970.413 (10)	${}^tR(1,0)$	$\nu_1 + 2\nu_2^2 \leftarrow 0$	2	3.0	1	0
7998.890 (10)	${}^nQ(2,2)$	$\nu_1 + 2\nu_2^2 \leftarrow 0$	2	1.0	2	2
8005.582 (30)	${}^tR(4,2)$	$\nu_1 + 2\nu_2^2 \leftarrow 0$	5	4.8	4	2
8007.410 (10)	${}^nQ(3,2)^u$	$\nu_1 + 2\nu_2^2 \leftarrow 0$	3	1.0	3	2
8022.012 (20)	${}^nQ(4,2)^u$	$\nu_1 + 2\nu_2^2 \leftarrow 0$	4	1.0	4	2
8027.840 (20)	${}^tR(3,1)$	$\nu_1 + 2\nu_2^2 \leftarrow 0$	4	3.5	3	1
8037.673 (10)	${}^nR(3,1)^l$	$\nu_1 + 2\nu_2^2 \leftarrow 0$	4	2.4	3	1
8053.382 (10)	$P(6,6)$	$2\nu_1 + \nu_2 \leftarrow 0$	5	5.5	6	6
8071.617 (10)	${}^nR(1,1)$	$\nu_1 + 2\nu_2^2 \leftarrow 0$	2	2.0	1	1
8089.406 (10)	${}^nQ(4,3)$	$\nu_1 + 2\nu_2^2 \leftarrow 0$	4	0.1	4	3
8110.069 (10)	${}^nQ(3,3)$	$\nu_1 + 2\nu_2^2 \leftarrow 0$	3	0.0	3	3
8123.128 (10)	$P(5,5)$	$2\nu_1 + \nu_2 \leftarrow 0$	4	4.8	5	5
8128.280 (10)	${}^tR(4,1)$	$\nu_1 + 2\nu_2^2 \leftarrow 0$	5	3.4	4	1
8162.653 (10)	${}^tR(3,0)$	$\nu_1 + 2\nu_2^2 \leftarrow 0$	4	2.9	3	0
8163.129 (10)	${}^nR(2,1)$	$\nu_1 + 2\nu_2^2 \leftarrow 0$	3	2.0	2	1

[a] The uncertainty in the last decimal places is listed in parentheses.
[b] The expectation value of the approximate quantum number G in the upper state, from the calculations of J. K. G. Watson [41].

Table 3.1 Observed frequencies and assignments.

of the $\nu_1 + 2\nu_2^2$ state is given in Figure 3.9, where the observed levels are denoted by thick lines. The observed transitions provide nearly complete coverage up to J=4, along with three levels of J=5.

3.2.4 Analysis

The primary motivation for this work was to provide experimental data on the $\nu_1 + 2\nu_2^2 \leftarrow 0$ band for comparison with theoretical calculations. In this section, we briefly discuss several sets of variational calculations performed in recent years and compare them to our observed spectra. A more detailed comparison of recent theoretical calculations with all observed spectral lines of H_3^+ is performed in Appendix D.

We have compared our experimental H_3^+ frequencies with several sets of variational calculations. For each transition we compute the difference of the observed and calculated frequencies (o-c). The average of the (o-c) values for all of the lines can be interpreted simply as an offset in the band origin, perhaps due to omission of various (adiabatic and/or non-adiabatic) corrections to the Born-Oppenheimer approximation and, to a lesser extent, relativistic corrections. The standard deviation σ(o-c) of the (o-c) values gives an indication of the accuracy of the calculation of the rovibrational energies (given some vibrational offset), and should be regarded as the primary figure of merit. The values of (o-c) for each line and for each calculation are tabulated in Table 3.3, along with the average (o-c) and σ(o-c) for each calculation.

The earliest work we have considered in our comparison is that of Wolniewicz and Hinze [49]. These authors calculated rotation-vibration term values up to J=4 using the Meyer-Botschwina-Burton [8] scaled *ab initio* potential and hyperspherical coordinates. The upper states of 19 of our observed transitions were listed in their table. Their average (o-c) was -0.25 cm^{-1}, which was less than the standard deviation σ(o-c) = 0.30 cm^{-1}.

In 1996, J. K. G. Watson [41] provided us with theoretical predictions for the frequency range of this experiment. These calculations are an updated version of those discussed by Majewski et al. [52] and use a "spectroscopically adjusted" adaptation of the MBB [8] potential in which the potential constants have been adjusted to achieve

v_1	v_2	ℓ	J	G [a]	u/l [b]	E
1	2	2	0	2		7870.018
1	2	2	1	3		7872.664
1	2	2	2	4		7915.084
1	2	2	1	2		7958.836
1	2	2	1	1		7989.541
1	2	2	3	5		7991.677
1	2	2	2	3		8057.376
1	2	2	4	6		8105.230
1	2	2	2	2		8135.736
1	2	2	2	0		8142.091
1	2	2	2	1		8168.192
1	2	2	3	4		8176.978
1	2	2	3	3		8302.114
1	2	2	3	1	l	8335.291
1	2	2	4	5		8340.068
1	2	2	3	2		8400.488
1	2	2	3	0		8425.421
1	2	2	3	1	u	8435.431
1	2	2	4	4		8522.611
1	2	2	4	2	l	8532.444
1	2	2	5	6		8539.638
1	2	2	4	3		8679.534
1	2	2	4	0		8748.123
1	2	2	5	5		8774.053
1	2	2	4	1	u	8790.483
1	2	2	5	4		8961.857
2	1	1	4	5		8852.148
2	1	1	5	6		9049.257

[a] The value of G for the member of the $|J, G\rangle$ basis set which makes the dominant contribution to the energy level.
[b] Label for upper and lower states of doublets.

Table 3.2 Experimentally determined energy levels.

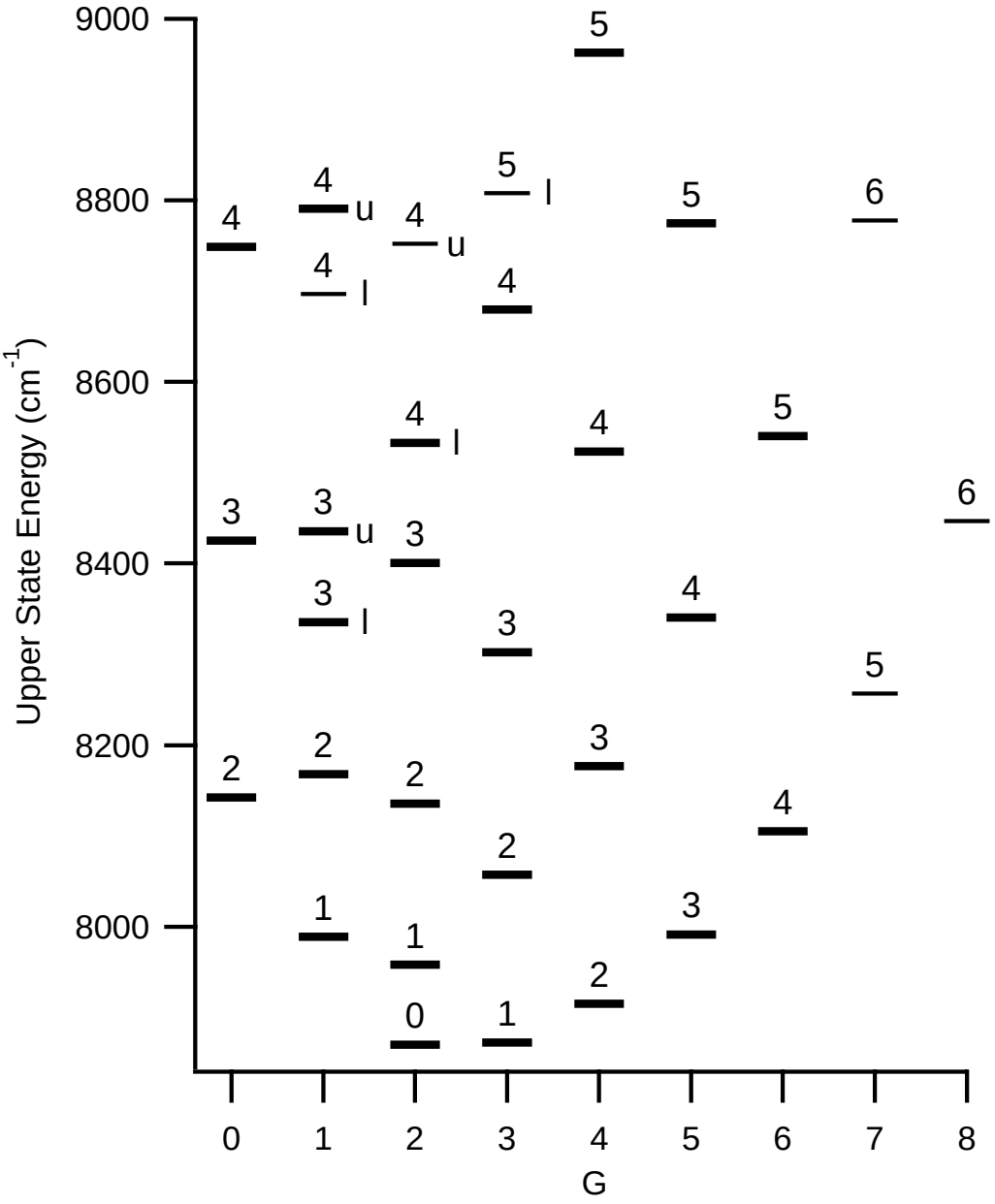

Figure 3.9 Energy level diagram of the $\nu_1 + 2\nu_2^2$ state of H_3^+. Experimentally determined energy levels are denoted by thick lines. The values of J are indicated above the energy levels, and the u and l labels are to the right of the appropriate levels.

Transition	Observed (cm^{-1})	(o-c)[a]							
		Adjusted Potentials			*Ab initio* Potentials				
		W96	N96	D97a	WH94	D97b	P99	J00a	J00b
$^tQ(3,0)$	7785.233	-0.032	-0.297	-0.295	-0.347	-0.714	0.571	0.507	0.138
$^tQ(1,0)$	7785.701	0.361	-0.309	-0.307	-0.326	-0.721	0.528	0.490	0.122
$^tR(3,3)$	7789.878	-0.147	-0.282	-0.233		-0.715	0.541	0.495	0.085
$^nP(1,1)$	7805.893	0.043	-0.647	-0.645	-0.465	-1.038		0.175	-0.221
$^nP(2,2)$	7820.239	0.259	-0.351	-0.356	0.043	-0.738	0.569	0.488	0.116
$^tR(2,2)$	7822.375	0.125	-0.265	-0.251		-0.708		0.513	0.105
$^nP(3,3)$	7826.739	0.060	-0.381	-0.377	0.269	-0.741	0.635	0.494	0.160
$^nP(4,4)^l$	7833.249	-0.195	-0.421	-0.421	0.293	-0.745	0.693	0.497	0.189
$^tR(1,1)$	7850.959	0.283	-0.291	-0.284		-0.719	0.514	0.510	0.103
$^tR(4,3)$	7880.921	-0.522	-0.259	-0.214		-0.711		0.535	0.092
$^nQ(1,1)$	7894.711	0.333	-0.339	-0.335	-0.186	-0.737	0.527	0.510	0.154
$^nQ(2,1)$	7898.371	0.183	-0.329	-0.329	-0.266	-0.735	0.525	0.511	0.079
$^nQ(3,1)$	7905.717	-0.174	-0.313	-0.310	-0.378	-0.725	0.542	0.531	0.172
$^tR(3,2)$	7912.047	-0.148	-0.243	-0.242		-0.714	-0.241	0.541	0.099
$^tR(2,1)$	7939.619	0.120	-0.271	-0.268		-0.713	0.532	0.547	0.135
$^tR(1,0)$	7970.413	0.288	-0.287	-0.285	-0.455	-0.717	0.506	0.549	0.112
$^nQ(2,2)$	7998.890	0.136	-0.350	-0.346	-0.050	-0.729	0.568	0.552	0.198
$^tR(4,2)$	8005.582	-0.858	-0.248					0.581	0.105
$^nQ(3,2)^u$	8007.410	-0.218	-0.350	-0.344	-0.260	-0.729		0.559	0.020
$^nQ(4,2)^u$	8022.012	-0.681	-0.318	-0.318	-0.426	-0.694	0.608	0.605	0.343
$^tR(3,1)$	8027.840	-0.497	-0.250	-0.244	-0.812	-0.698	0.550	0.602	0.015
$^nR(3,1)^l$	8037.673	-0.518	-0.337	-0.335		-0.754	0.538	0.551	0.153
$P(6,6)$	8053.382	-1.428	-0.528						
$^nR(1,1)$	8071.617	0.203	-0.313	-0.316	-0.247	-0.720	0.538	0.579	0.085
$^nQ(4,3)$	8089.406	-0.876	-0.344	-0.344	0.034	-0.724	0.665	0.596	0.168
$^nQ(3,3)$	8110.069	-0.133	-0.381	-0.384	-0.079	-0.725	0.600	0.596	0.144
$P(5,5)$	8123.128	-0.857	-0.492					0.372	0.259
$^tR(4,1)$	8128.280	-1.051	-0.270					0.604	0.007
$^tR(3,0)$	8162.653	-0.666	-0.257	-0.261	-0.780	-0.722	0.483	0.609	0.101
$^nR(2,1)$	8163.129	-0.166	-0.311	-0.310	-0.369	-0.721	0.542	0.612	0.158
Average (o-c)		-0.226	-0.334	-0.321	-0.253	-0.735	0.524	0.528	0.116
σ(o-c)		0.468	0.089	0.083	0.295	0.063	0.178	0.086	0.095
σ(o-c) [no J=0]		0.482	0.069	0.052	0.306	0.014	—	0.052	0.070

[a] Author key: W96 = Watson [41], N96 = Neale, Miller, & Tennyson [47], D97a = Dinelli et al. (adjusted potential) [48], WH94 = Wolniewicz & Hinze [49], D97b = Dinelli et al. (*ab initio*) [48], P99 = Polyansky & Tennyson [50], J00a = Jaquet (*ab initio*) [51], J00b = Jaquet (*ab initio* + non-adiabatic) [51].

Table 3.3 Comparison with variational calculations.

a better fit between experiment and the variational calculations. These calculations were essential for conducting the experiment, as the frequencies and relative intensities were completely reliable. No lines were observed in our region which were not predicted by Watson's calculations, and we observed all of the lines Watson predicted, given our sensitivity. We relied heavily on these calculations in determining where to focus our efforts outside of the continuous tuning range of the laser. A further advantage of Watson's calculations is that they provide the expectation values of the approximate quantum numbers v_1, v_2, ℓ, and G, which make it easy to assign the energy levels and determine when the levels are strongly mixed. The average (o-c) was -0.23 cm^{-1}, which again was less than σ(o-c) = 0.47 cm^{-1}.

We also compared our data to the exhaustive linelist of Neale, Miller, and Tennyson 1996 (NMT) [47], which was developed in part to facilitate opacity calculations of cool stars and the outer planets. These variational calculations are based on the spectroscopically adjusted potential of Dinelli et al. [53]. Their linelist is somewhat difficult to use, as it only provides the value of J and the energy for the upper and lower levels of each transition. In some cases, even the spin modification (ortho or para) is not listed. For these reasons, their linelist can only be interpreted by comparing the energies and J to those in other calculations which give more information about the levels. Their calculations included all 30 of our observed transitions, along with 37,400 others in this wavenumber range. Despite these reservations, the calculated frequencies of NMT are quite good: their average (o-c) was -0.33 cm^{-1}, and their σ(o-c) was only 0.09 cm^{-1}.

In 1997, Dinelli et al. [48] published a list of term values calculated in three different ways. The first used the DVR3D program suite on a spectroscopically adjusted potential [53] and is equivalent to the calculations of NMT, the second used the TRIATOM suite on the same potential, and the third used the TRIATOM suite on the *ab initio* potential surface of Röhse et al. [25] augmented by *ab initio* non-Born-Oppenheimer adiabatic corrections [54]. Their list of term values contains some labelling errors, but is fairly comprehensive up to near 9000 cm^{-1}. Twenty-six of our observed lines could be calculated from their TRIATOM lists. The TRIATOM calculations on the spectroscopically adjusted potential gave an average (o-c) of -0.32

cm^{-1} and a σ(o-c) of 0.08 cm^{-1}. Their TRIATOM *ab initio* calculations gave a larger band origin offset [average (o-c) = -0.74 cm^{-1}] but a better standard deviation [σ(o-c) = 0.06 cm^{-1}].

In 1999, Polyansky and Tennyson [50] published a new list of energy levels using the improved *ab initio* potential of Cencek et al. [55], which includes electronic relativistic and adiabatic corrections. Polyansky and Tennyson also introduced nonadiabatic corrections in these calculations. Only 22 of our observed lines could be calculated from their list, and the fit was less satisfactory than the *ab initio* work of Dinelli et al. [48] The average (o-c) was 0.52 cm^{-1}, and the σ(o-c) was 0.18 cm^{-1}.

Very recently, Jaquet [51] has performed similar calculations based on the Cencek et al. [55] *ab initio* potential. Additionally, he calculated intensities using the dipole moment of Röhse et al. [25], and these were found to be completely consistent with the experimental measurements. His calculations reproduced 29 of the 30 observed lines, with an average (o-c) of 0.53 cm^{-1} and a σ(o-c) of 0.09 cm^{-1}. In subsequent calculations, Jaquet included non-adiabatic corrections as discussed in [56]. These corrections substantially reduced the band origin offset to an average (o-c) of 0.12 cm^{-1}, without changing the standard deviation.

By far the greatest deviation between the experimental and theoretical frequencies is for the ${}^{n}P(1,1)$ line observed at 7805.893 cm^{-1}. This transition is the only one going into J=0 in the $\nu_1 + 2\nu_2^2$ state. Jaquet [51] has suggested that this deviation may be due to the fact that the non-adiabatic correction should be smaller for the J=0 level. Calculations without non-adiabatic corrections will not reproduce this effect, and perhaps even the calculations with non-adiabatic corrections are not fully taking this into account. If the J=0 line is excluded from the comparison with the theoretical predictions, the standard deviations of NMT, Dinelli et al., and Jaquet improve significantly. In fact, the *ab initio* calculation of Dinelli et al. [48] has a σ(o-c) of only 0.014 cm^{-1} when J=0 is excluded — this is comparable to the experimental accuracy.

3.2.5 Conclusions

Variational calculations of H_3^+ transitions using *ab initio* potential energy surfaces [as well as non-Born-Oppenhemier corrections] are beginning to approach experimental accuracy, especially when allowance is made for an offset in the band origin and the $J = 0$ level. Improvements in the treatment of non-adiabatic effects will likely lead to even better agreement in the future.

The next frontier of H_3^+ spectroscopy lies at even higher energies (≥ 10000 cm^{-1}), where H_3^+ has enough energy to sample linear geometries in the course of its vibrational motion. This energy regime is particularly difficult theoretically — few of the ro-vibrational variational calculations performed in this range to date include the correct boundary conditions for linear geometries. All of the vibrational states which have been spectroscopically probed to date (ν_2, ν_1, $2\nu_2^0$, $2\nu_2^2$, $\nu_1 + \nu_2$, $3\nu_2^1$, $\nu_1 + 2\nu_2^2$, and $2\nu_1 + \nu_2$) have been well below the barrier to linearity.

However, the detection of the $\nu_1 + 2\nu_2^2 \leftarrow 0$ band with high signal-to-noise suggests that this barrier may soon be broken. The $5\nu_2^1 \leftarrow 0$ band is expected to lie near 10900 cm^{-1} ($\sim$920 nm) and should be only about a factor of twenty weaker than $\nu_1 + 2\nu_2^2 \leftarrow 0$. With the much higher power and lower noise of the Titanium:Sapphire laser (compared to diode lasers), the detection of the $5\nu_2^1 \leftarrow 0$ band may be within reach.

3.3 Spectroscopy of H_3^+ above the Barrier to Linearity

3.3.1 Introduction

In the pursuit of reaching ever higher energy vibrational states of H_3^+, overtone and combination bands starting from the vibrational ground state have two distinct advantages: the lack of spectral confusion and the high population of the lower state. This is in stark contrast to the case of hot bands, which tend to pile up in the same spectral region, making assignments difficult — in addition, excited vibrational states are less populated than the vibrational ground state.

However, the disadvantage to overtone spectroscopy is the small transition dipole

moment, which decreases with increasing vibrational excitation of the upper state. The $3\nu_2^1 \leftarrow 0$ band is 175 times weaker than the fundamental, the $4\nu_2^2 \leftarrow 0$ band 900 times weaker, and the $5\nu_2^1 \leftarrow 0$ band 4600 times weaker!

Since all of the infrared-active triply excited vibrational states ($3\nu_2^1$, $\nu_1 + 2\nu_2^2$, and $2\nu_1 + \nu_2$) have been studied, the next logical step is to search for the $4\nu_2^2 \leftarrow 0$ band. Unfortunately, the band center of this third overtone lies around 1100 nm, right on the long wavelength edge of the tuning curve of the long wavelength optics set of our Titanium:Sapphire laser. Consequently, we have decided to skip to the fourth overtone, $5\nu_2^1 \leftarrow 0$. While this band is about five times weaker than $4\nu_2^2 \leftarrow 0$, the laser will have higher power and will be considerably more stable.

In this section, I begin with some background about high energy H_3^+ and the theory of operation of the Titanium:Sapphire laser spectrometer. I then briefly discuss the calibration of our system using electronic transitions of N_2^+, and then describe our detection of the first "visible" spectrum of H_3^+, the $5\nu_2^1 \leftarrow 0$ overtone band.

3.3.2 H_3^+ and the Barrier to Linearity

Figure 3.10 shows a one-dimensional slice of the H_3^+ potential energy surface, similar to Figure 2.3, but with an expanded scale. In this picture, the horizontal axis is the angle between two H–H bonds, in units of π radians, and the energy is with respect to the zero point energy. The barrier to linearity, which occurs at $\theta/\pi = 1$, lies near 10,000 cm^{-1}. Also plotted in the potential are the vibrationless ($J = 0$) energy levels calculated by Alijah and Schiffels [57]. Below the barrier to linearity, the vibrational motion samples only one "half" of the potential surface (although rotational motion enables the molecule to move to the other side). Above the barrier, however, the molecule has enough energy to execute vibrational motions through the linear configuration and into the other half of the potential. This "opening up" of the potential contributes to the closer spacing of the energy levels.[1]

The ability of H_3^+ to sample linear configurations also poses serious problems for

[1]The energy level spacing is also decreasing with increasing energy due to the degeneracy of the multi-dimensional potential (e.g. there are nine states with $\Sigma v = 4$: $4\nu_1$, $3\nu_1 + \nu_2$, $2\nu_1 + 2\nu_2^0$, $2\nu_1 + 2\nu_2^2$, $\nu_1 + 3\nu_2^1$, $\nu_1 + 3\nu_2^3$, $4\nu_2^0$, $4\nu_2^2$, and $4\nu_2^4$).

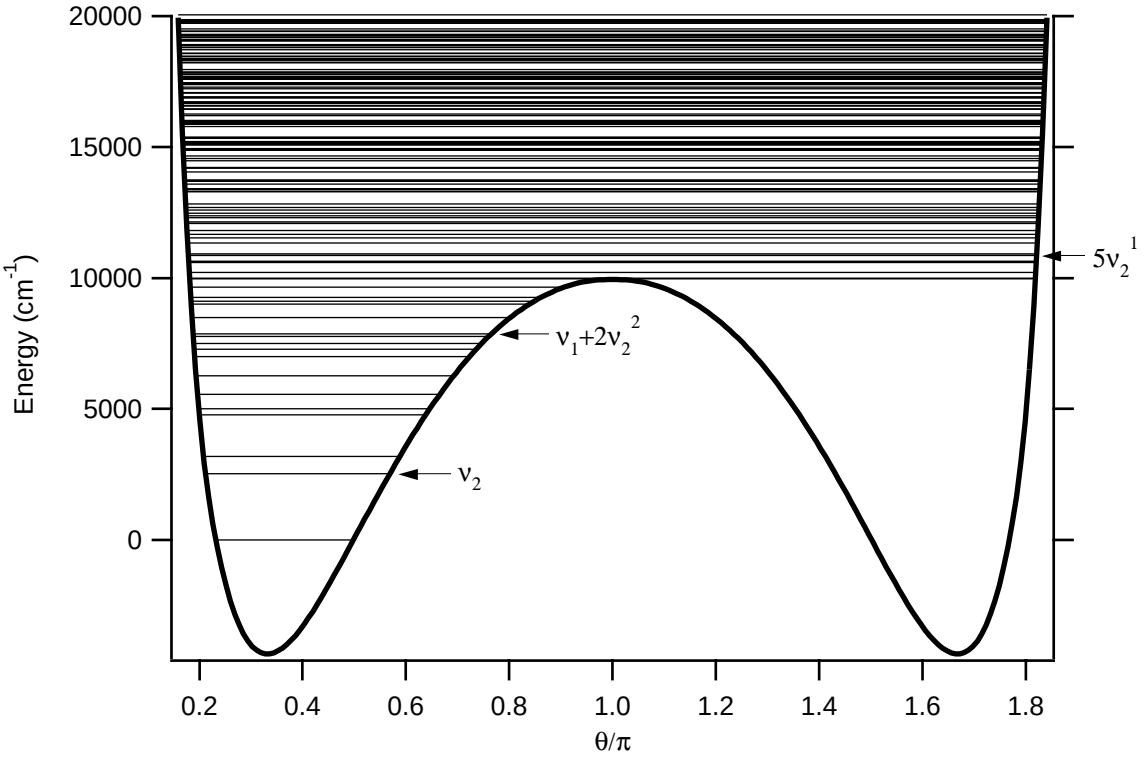

Figure 3.10 Potential energy surface of H_3^+, along with calculated vibrationless ($J = 0$) energy levels.

theoretical calculations of ro-vibrational energy levels, because there is a singularity in the kinetic energy operator at linearity.[2] Such a singularity will necessarily cause problems in numerically calculating matrix elements of the Hamiltonian involving wavefunctions that have non-zero amplitude at linear geometries, which is the case for energies near and above the linearity barrier.

If one is primarily interested in energies well below the barrier, one can circumvent this problem by placing an artificial wall in the potential at linear geometries, which in effect forces the wavefunctions to vanish at linearity (such an approach has been adopted by Watson [59, 60]). However, as Watson points out, these calculations should not be very good near or above the linearity barrier.

The proper way to address this singularity is to use a basis set for which the integrals (over the singular term in the Hamiltonian) can be calculated analytically. The most comprehensive calculations involving such an approach have been performed by Tennyson and co-workers [47, e.g.]. They use Jacobi (or scattering) coordinates, in which one H–H bond length is taken as r, the distance from the center of that bond to the third atom is taken as R, and the angle[3] between the r and R vectors is θ. In this framework, the singularity arises at $R \rightarrow 0$, due to a kinetic energy term proportional to $l(l+1)R^{-2}$, which implies that the wavefunctions must satisfy the boundary condition[4] $\Psi \sim R^l$ as $R \rightarrow 0$ (in this case, l is effectively K_a for a quasi-linear asymmetric top).

This boundary condition is not satisfied by the more (computationally) convenient Morse oscillators, so Tennyson and co-workers resort to spherical oscillator-like functions [61] which handle the singularity but lead to difficulties in convergence. Consequently, the calculations of Neale, Miller, and Tennyson (NMT) [47] are valid above the linearity barrier, but are generally not converged at high values of J (as

[2]The process of transforming the $3N$ coordinates of a molecule with N nuclei into 3 rotational coordinates, 3 translational coordinates, and $(3N-6)$ internal coordinates will always introduce singularities into the Hamiltonian [58]. In this case, we are concerned with the singularity at $\theta = \pi$.

[3]Note that this angle is different from the θ used in Figure 3.10.

[4]This can be compared to the general case of motion in a centrally symmetric field, as discussed by Landau and Lifshitz [16, §32].

suggested by [48] and verified by comparison with experiment in Appendix D).

A more elegant approach to handling the singularity, which has only recently come into widespread use for calculating H_3^+ ro-vibrational energy levels, involves the use of hyperspherical coordinates. When the Hamiltonian is written in these coordinates [62, e.g.], the singularity is contained within the square of the grand angular momentum $\hat{L}^2$ operator. The eigenfunctions of $\hat{L}^2$ (hyperspherical harmonics), with the appropriate choice of coefficients, can then be used as the (angular) basis set for the variational calculations, and the singularity will be handled naturally.

Such calculations using hyperspherical coordinates and hyperspherical harmonics have been performed by Wolniewicz & Hinze [49] and Alijah, Hinze, & Wolniewicz [63]. This approach is currently being extended to higher J and higher energies (Alijah & Schiffels, in preparation) and is also being implemented by Watson [62] — it seems likely that this approach may prove more useful than using spherical oscillators in Jacobi coordinates.

3.3.3 Theory of Operation of Titanium:Sapphire laser

The details of the alignment and operation of the Coherent 899 Titanium:Sapphire laser are provided in the Coherent manuals as well in Rob Dickson's thesis [64] — consequently, in this section I will simply sketch the principles of operation of the laser.

The heart of the laser is a sapphire (Al_2O_3) crystal which has been doped ($\sim$0.1% by weight) with titanium oxide (Ti_2O_3). The titanium ions (Ti^{3+}) have an electron configuration of KL$3s^2 3p^6 3d^1$, and the quintuply degenerate d orbital is split by the O_h crystal field into a doubly degenerate (e_g) upper level and a triply degenerate (t_{2g}) lower level. This system operates as a four-level laser: the pump radiation (provided by a multiline Ar^+ laser) raises population from the ground vibrational state of t_{2g} into various excited vibrational states of e_g, which quickly relax to the e_g vibrational ground state (this provides the necessary population in the upper level of the lasing transition). Lasing can then occur into a vibrationally excited state of t_{2g}, which is rapidly depopulated by vibrational relaxation down to the ground state, where it can

be repumped by the Ar^+ laser. This laser system is widely tunable because the lower level of the lasing transition is actually a continuous band of vibronic levels of the t_{2g} state. The resulting gain curve of the crystal stretches from approximately 675 to 1100 nm.

The laser utilizes a ring-type cavity, with unidirectional lasing imposed by an optical diode. The optical diode consists of a Faraday rotator and a matched optically active quartz plate: a beam propagating in one direction experiences a polarization rotation of an angle $-\alpha$ by the rotator and $+\alpha$ by the quartz plate (and is therefore unchanged), whereas a beam in the other direction is rotated by $+\alpha$ by each element. The latter beam experiences losses in the various Brewster surfaces in the cavity, and is therefore suppressed. The ring cavity is preferred to a standing-wave cavity because the nodes of the laser radiation field are not stationary in the crystal, thus making more efficient and uniform use of the gain medium.

A schematic of the optical cavity is shown in Figure 3.11. The argon laser pump beam is brought in through a periscope and focused into the crystal. The cavity is formed by the upper fold mirror (upper left of diagram), the output coupler (right hand side), the lower fold mirror (left hand side), and the intermediate fold mirror (through which the pump beam enters). The lower fold mirror is mounted on a piezoelectric transducer (PZT), so that the cavity length can be controlled. Near the output coupler is placed a galvanometer-mounted Brewster plate, which can be turned to change the optical length of the cavity by larger amounts.

Three different optics sets (short wave, medium wave, and long wave) can be used in the laser cavity. These optics sets have dielectric coatings which alter the effective gain curve of the laser. Within the gain curve, the lasing wavelength is selected through the use of a birefringent filter (BRF) and two etalons (not shown in the figure). The three-plate BRF provides a bandpass that is broad, but yet considerably narrower than the entire gain curve of the crystal. A "thin" etalon (with a free spectral range of 225 GHz) is mounted on a galvanometer, so it can be angle-tuned. The "thick" etalon (with FSR = 10 GHz) actually consists of two Littrow prisms mounted on PZTs, so that the "thickness" can be varied, which permits the longitudinal mode to be scanned.

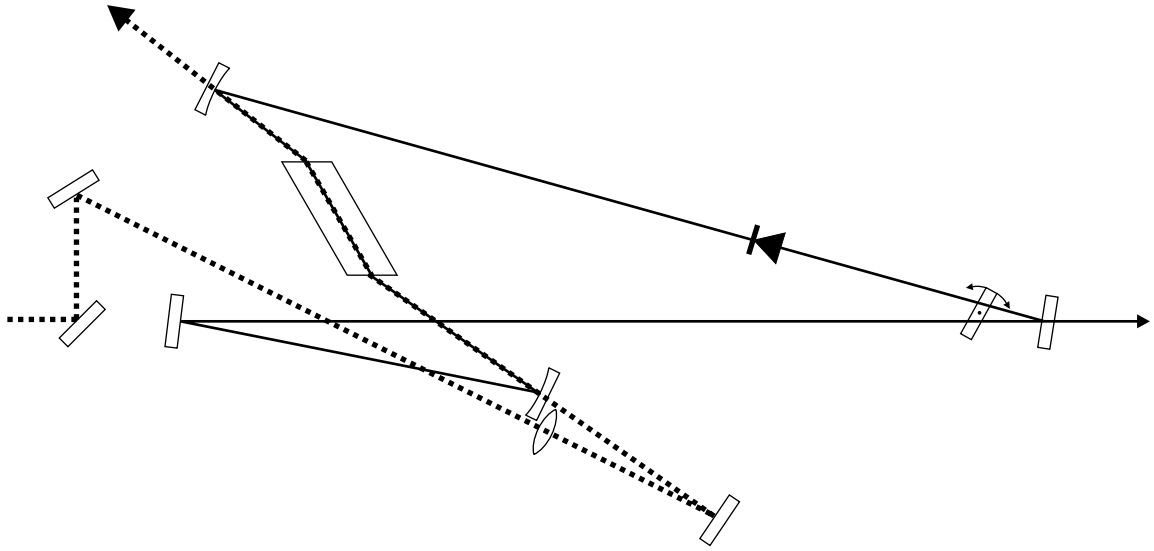

Figure 3.11 Schematic of Ti:Sapphire cavity. Pump laser beam is indicated by the thick dotted line.

The selected wavelength is stablized by locking the laser to a temperature-stabilized reference cavity, through which a small portion of the output beam is sent. Any changes in the lasing wavelength are translated into an error signal in the reference cavity. The laser control box then feeds the high frequency component of the error signal to the PZTs on the lower fold mirror (the "tweeter") and feeds the low frequency component to the galvanometer-mounted Brewster plate (the "woofer").

Scanning of small frequency ranges ($\lesssim$20–25 GHz) is accomplished by simply rotating the Brewster plate so as to change the cavity length (the etalons are optimized during the scan by a feed-forward scheme). When the laser is in wavelength-stablized ("locked") mode, it is scanned by turning a galvanometer-mounted Brewster plate in the reference cavity — since the laser is actively stabilized to the reference cavity, the laser frequency will follow.

To scan longer frequency ranges, a computer control system called AutoScan is employed. This system takes a series of partially overlapping 10 GHz scans using the method described above, and pieces them together based on frequency information from an integrated wavemeter. With this system, it is in principle possible to scan the entire frequency range of the optics set in use.

The integrated wavemeter can be in error when it has not been perfectly and painstakingly aligned, so we generally use a secondary method to check the frequency calibration. The primary and secondary reflections of the laser beam off a glass beamsplitter are sent into an external etalon (to provide frequency "ticks") and a heated iodine cell. The scans can then be calibrated with the use of the iodine atlas [65].

3.3.4 Checking the system with N_2^+

Because the Oka group Titanium:Sapphire laser has not been actively used for over five years, and because the laser had been moved into a different lab, a complete realignment of the system was necessary. Before proceeding directly to the search for the weak $5\nu_2 \leftarrow 0$ band of H_3^+, it seemed prudent to start off with stronger transitions at a similar wavelength. For this purpose, we have selected the $v = 2 \leftarrow 0$ band of the $A^2\Pi_u \leftarrow X^2\Sigma_g^+$ Meinel system of N_2^+, near 800 nm. This band is convenient, as it is near the peak of the tuning curve of the midwave optics set of the Ti:Sapphire laser. Also, recent experience with the Oka group dye laser spectrometer has shown that electronic transitions of N_2^+ can be easily detected even in "pure" He plasmas (N_2 is a common impurity in He gas). This band has also been recently studied by laser optogalvanic spectroscopy [66], so that accurate frequencies are available.

Because the AutoScan software only allows a single scan of a given frequency range, it yields relatively poor sensitivity when searching for ion signals. We were able to see the strong $Q_{11}(8)$ line of the N_2^+ band, but with a signal-to-noise of only a few. Consequently, we abandoned the AutoScan and adapted my custom scanning software for the diode laser (described in Section 3.2) to the Coherent laser. Very few modifications were necessary, as we could use the PZT drive signal to serve as the external ramp signal for the Coherent control box. We did find it necessary to gradually step the ramp voltage back from +5 V to −5 V (rather than changing it discontinuously) in order to prevent mode hops from occuring when the control box loses lock.

A spectrum of a portion of the N_2^+ band is shown in Figure 3.12. The upper

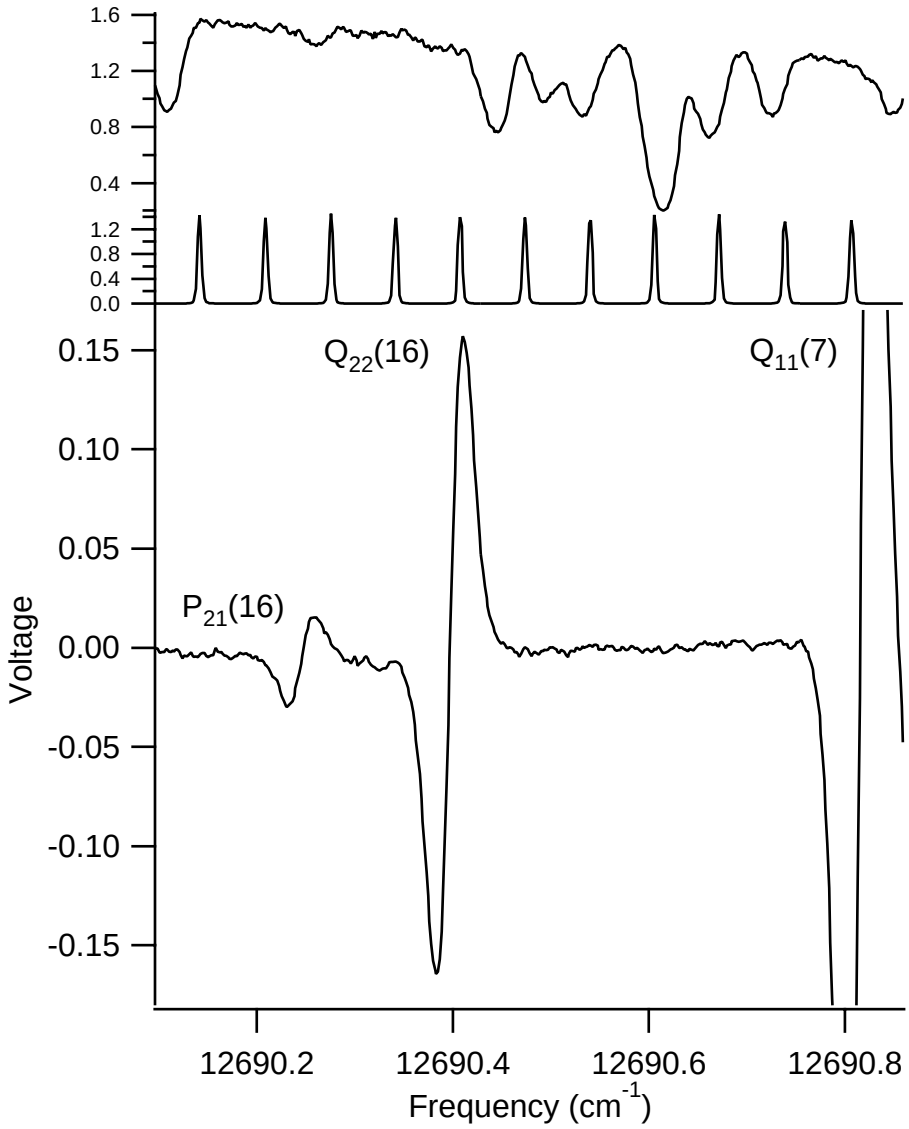

Figure 3.12 Spectrum of a portion of the $v = 2 \leftarrow 0$ band of the $A^2\Pi_u \leftarrow X^2\Sigma_g^+$ Meinel system of N_2^+, in a liquid-nitrogen cooled, "pure" helium discharge.

trace shows the spectrum of a hot (∼600 °C) I_2 cell, the middle trace shows the transmission peaks of an etalon, and the lower trace is our experimental signal from the phase sensitive detector (PSD). This spectrum was obtained by averaging together 40 quick scans of this region, with a total integration time of about 6 minutes. A liquid-nitrogen cooled "pure" helium discharge (with N_2 present as an impurity), with pressure of about 3 Torr, was used to obtain this spectrum. The smallest line, $P_{21}(16)$, is part of a weak satellite branch. From the observed signal height and the sensitivity setting of the PSD, we estimate that this line corresponds to a fractional absorption ($\Delta I/I$) of $\sim 4 \times 10^{-5}$. Since the line is observed with a signal-to-noise ratio of a few tens, we estimate our sensitivity to be $\sim 10^{-6}$, in this 6 minute integration time. Comparing averages of different numbers of scans, we find that the signal-to-noise ratio does improve roughly as the square root of the integration time, so we should be able to see much weaker lines by integrating longer.

3.3.5 Preliminary Results: $5\nu_2 \leftarrow 0$

Figure 3.13 shows a simulated absorption spectrum of H_3^+ near the band center of the $5\nu_2 \leftarrow 0$ band, based on the theoretical calculations of NMT [47]. Also plotted are the tuning curves (from the Coherent manual) of the midwave optics set (dashed line) and the longwave optics set (dotted line) of the Titanium:Sapphire laser.

In addition to NMT, Watson [41] and Alijah [57] have performed calculations of energy levels in this region. The energy levels calculated by Alijah and NMT are generally in very good agreement ($\lesssim 1$ cm^{-1}), whereas Watson's energy levels show much worse agreement (~ 20 cm^{-1}) — this situation is not surprising, given the considerations of Section 3.3.2.

By relating NMT's energy levels to Alijah's energy levels (based strictly on energy agreement), and by relating Alijah's quantum numbers to those of Watson (who has calculated expectation values of v_1, v_2, ℓ, and G), we have assigned some of the stronger lines in Figure 3.13. This region includes not only the $5\nu_2^1 \leftarrow 0$ band, but also strong lines of $2\nu_1 + 2\nu_2^2 \leftarrow 0$, $\nu_1 + 4\nu_2^4 \leftarrow 0$, and $5\nu_2^5 \leftarrow 0$. The last band would be particularly interesting to observe as it has $\Delta\ell = 5$, and therefore has a $\Delta G = \pm 6$

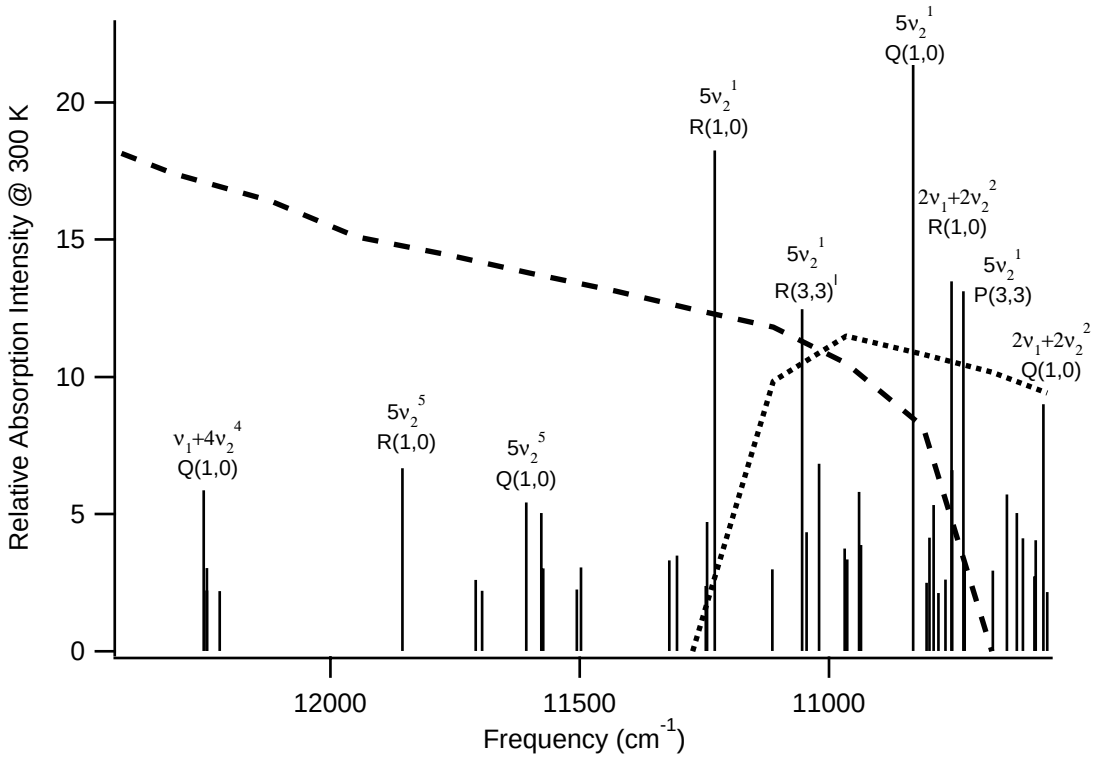

Figure 3.13 Simulated absorption spectrum of H_3^+, including the $5\nu_2 \leftarrow 0$ bands.

selection rule!

We have begun our search with the strongest line easily accessible with the mid-wave optics set (which is easier to work with), the $5\nu_2^1 \leftarrow 0$ $R(1,0)$ line. Based on the fact that this band is 4600 times weaker than the fundamental band, and that the fundamental band is of order a few percent deep under similar conditions, we anticipated that the strongest line of $5\nu_2^1 \leftarrow 0$ would have a fractional absorption $\sim 10^{-5}$ [in fact, the intensity of the observed $R(1,0)$ line is very close to this expected value].

The result of our observation is shown in Figure 3.14. The upper of the two experimental traces shows the spectrum obtained in a pure hydrogen (0.5 Torr) discharge. This spectrum consists of an average of 100 individual scans of this frequency range, with a total integration time of about 30 minutes. A line with the phase of a positive ion is evident on the left side, and a line with the phase of a negative ion is on the right. Both lines are considerably broader than those of N_2^+, which suggests that they are due to hydrogenic species (the Doppler linewidth scales as $1/\sqrt{m}$). While it would appear that the left line is H_3^+ and the right line is a H_2 Rydberg (denoted H_2^*), the left line could possibly be a Rydberg line in emission.

The usual test to discriminate against Rydbergs (as discussed in Section 3.2) is to increase the pressure in the plasma to collisionally quench the Rydbergs. The lower trace of Figure 3.14 shows a spectrum obtained in a 0.5 Torr H_2 plus 7 Torr He discharge (also with a 30 minute integration time). The right-hand line has vanished (or at least has been reduced by a factor of 15, as expected from the pressure increase), while the left-hand line is still fairly strong, indicating that it is due to H_3^+ and not a Rydberg. The fact that the H_3^+ line is weaker in the helium discharge can be interpreted as a temperature effect, as the helium discharge is considerably hotter and the (1,0) level of H_3^+ will be less populated. Such a decrease is consistent with our experience from the $\nu_1 + 2\nu_2^2 \leftarrow 0$ band (Section 3.2).

The observed frequency of the $5\nu_2^1 \leftarrow 0$ $R(1,0)$ line is 11228.61 cm^{-1}, with an uncertainty of roughly 0.03 cm^{-1}. This compares quite favorably with NMT's [47] calculation of 11228.84 cm^{-1} and Alijah's [57] prediction of 11228.43 cm^{-1}. As expected, Watson's calculation (with the artificial wall in the potential) [41] is not very

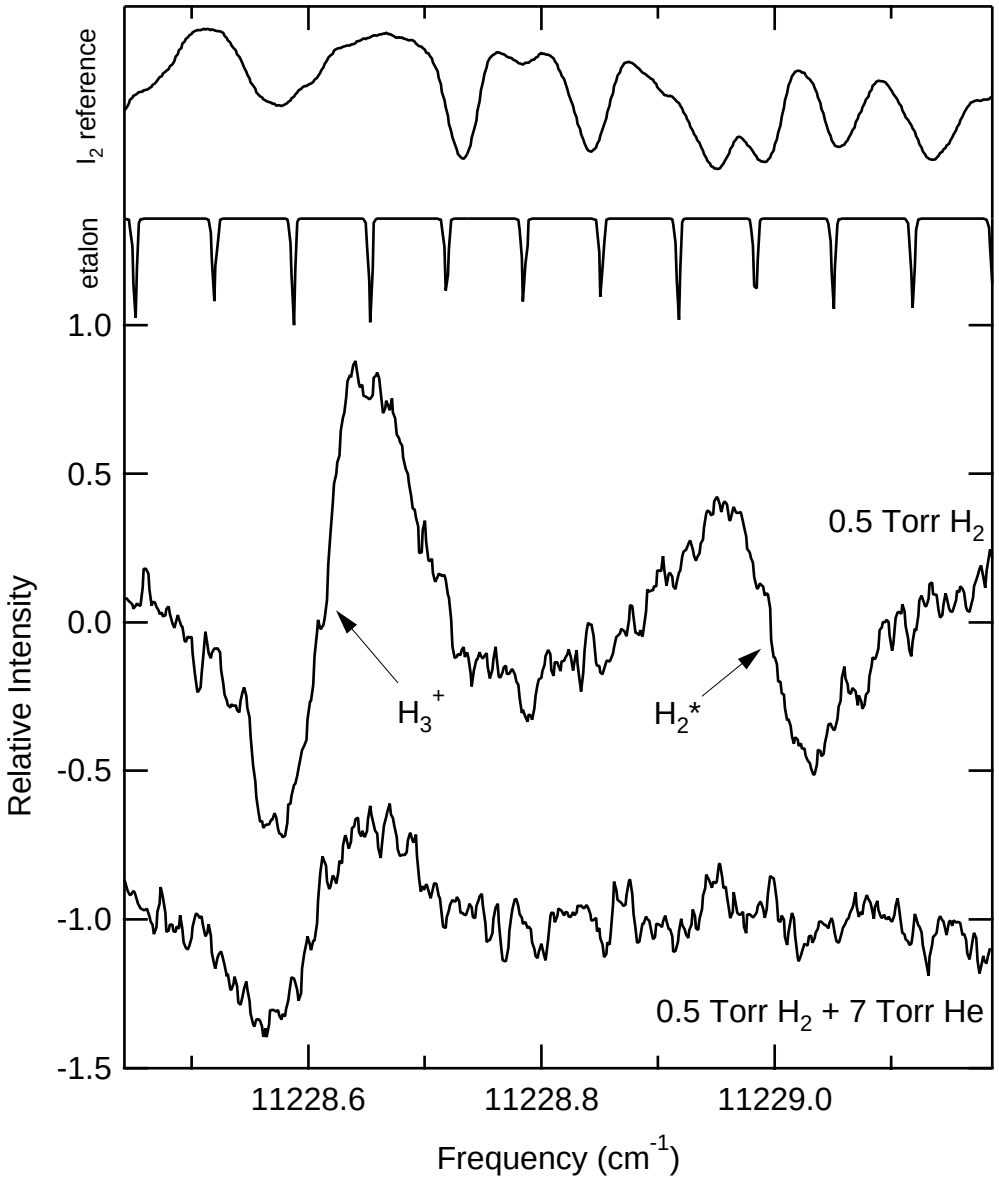

Figure 3.14 Spectrum of the $R(1,0)$ line of the $5\nu_2^1 \leftarrow 0$ band of H_3^+, near 890 nm.

close: 11255.24 cm^{-1}.

3.3.6 Future prospects

We are continuing the search for other lines in this region, using both the midwave and longwave optics sets. With our present sensitivity (and perhaps slightly longer integration times), we expect to be able to detect at least 15 lines or so. Our next primary target is the $R(1,0)$ line of the $5\nu_2^5 \leftarrow 0$ band, with its $\Delta G = \pm 6$ selection rule.

The detection of at least several lines of H_3^+ above the barrier to linearity will provide a crucial test of the validity of various computational approaches. Quite apart from the linearity issue, this work probes energy levels far higher than those previously studied, and will provide a new benchmark for evaluating different potentials, variational techniques, and non-Born-Oppenheimer corrections.

If the sensitivity of our spectrometer can be improved by an order of magnitude (for instance, by introducing frequency modulation with heterodyne detection), it should be possible to extend this work to higher overtone bands, such as $6\nu_2^2 \leftarrow 0$, $7\nu_2^1 \leftarrow 0$, and possibly beyond. If even higher sensitivity can be achieved (for example, by extending the absorption path length using a cavity), it may be possible to extend the spectroscopy of H_3^+ into the range of the dye laser. If overtone or combination bands can be observed near $\sim$17,500 cm^{-1} ($\sim$575 nm), this will represent the halfway point to the energies probed by the near-dissociation spectroscopy of H_3^+ by Carrington and co-workers, recently reviewed in [67]. If their spectroscopy can be performed using a dye laser starting from the energy levels that are the upper levels of our work, as recently suggested by McNab, it might be possible to unify these two regimes of H_3^+ spectroscopy and finally assign the enigmatic near-dissociation spectra.

CHAPTER 4
ASTRONOMICAL OBSERVATIONS OF H_3^+

4.1 The Interstellar Environment

In the canonical picture of the interstellar medium of our galaxy (McKee & Ostriker, [68]), about 70–80% of space is filled with hot ($T \sim 500{,}000$ K), low-density ($n \sim 3 \times 10^{-3}$ cm^{-3}) gas, which essentially consists of many merged supernova remnants. Embedded within the hot gas are relatively cold (~ 80 K) denser ($n \sim 40$ cm^{-3}) clouds, with a filling fraction of about 2–4%. The warm ($T \sim 8000$ K) extended envelopes around these cool clouds fill about 20% of the volume, but contain far less mass. The average number density of the interstellar medium is thus about 1 cm^{-3} (for a comparison of various densities, see Table 4.1). The molecules in the galaxy are predominantly confined to the "cold neutral medium," and it is this 2–4% of the galaxy (which contains $\sim 95\%$ of the mass!) that we now turn our attention to.

The elemental abundances in the interstellar medium are shown pictorially in Figure 4.1. The two most abundant nuclei (hydrogen at ~92% and helium at ~8%) were formed in the early stages of the Big Bang, while the other abundant nuclei (total number fraction ~0.1%) were formed as a result of stellar nucleosynthesis. Most of the heavier elements are not present in the gas phase, but rather as "dust grains," with radii less than about 1 μm. These dust grains extinguish visible light from background stars, more so at the blue end of the spectrum than at the red end. The color excess[1] E_{B-V} is proportional to the amount of dust along the line of sight, and has been shown (at least at low values) to correlate well with the total amount of gas along the line of sight [70].

The interstellar medium is also pervaded by high energy bare nuclei (mostly protons) called "cosmic rays." These particles are able to penetrate deep into the densest concentrations of gas and provide an ionization source when radiation is not present.

[1] B and V are the apparent magnitudes of a star when measured through standard (blue and visible) bandpass filters. The color excess E_{B-V} is defined as the difference between the intrinsic "color" $(B-V)_0$ of a star and its observed color $(B-V)$. Astronomical magnitudes are measured on an inverse logarithmic scale, so that the magnitude $= -2.5 \log(\text{Flux}) + C$, where C is a constant.

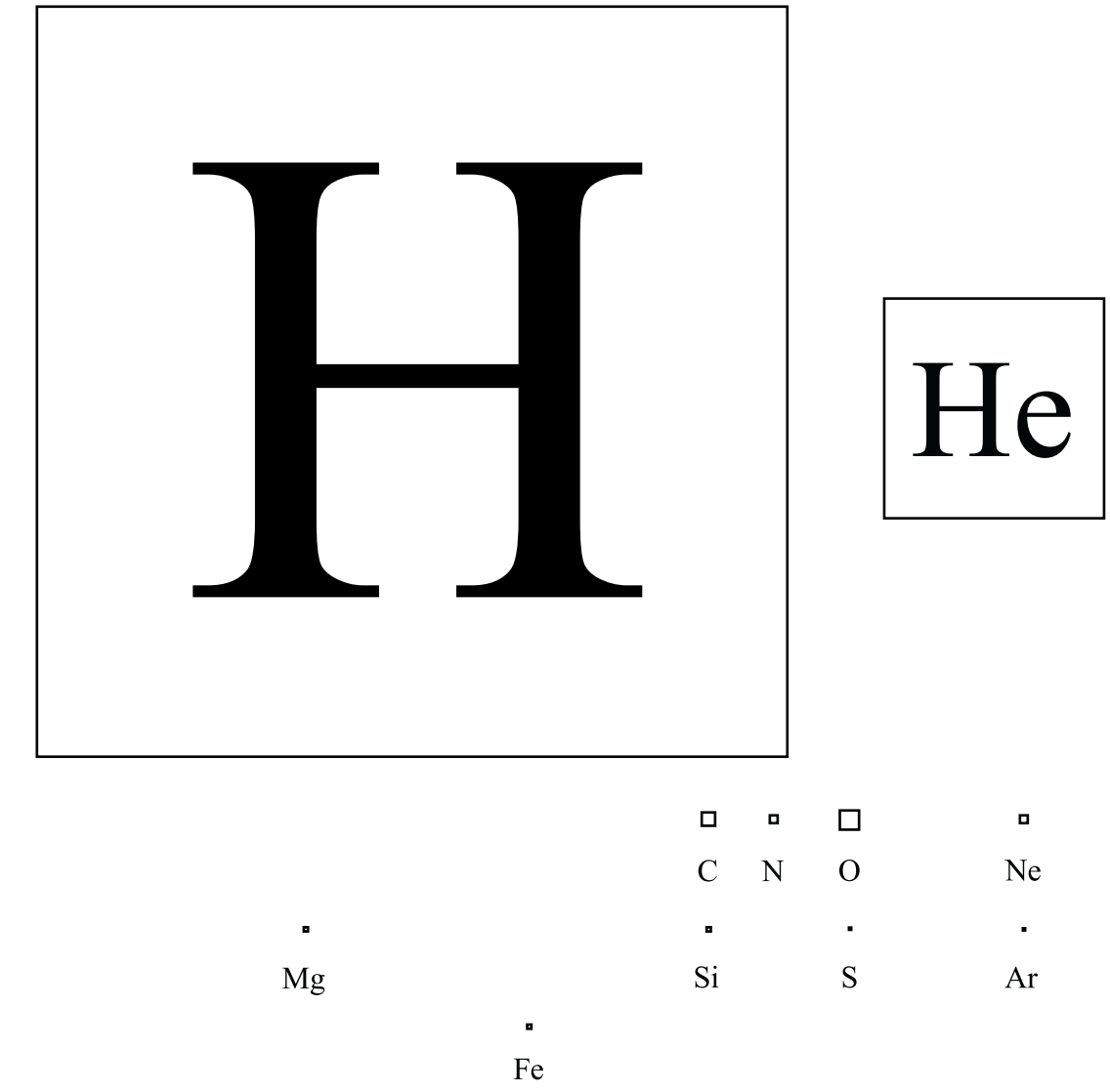

Figure 4.1 “The Astronomer’s Periodic Table”.

Object	Density (cm^{-3})
Intergalactic medium[a]	6×10^{-11}
Critical density[b]	6×10^{-6}
Intercloud medium	3×10^{-3}
Interplanetary medium	10^{1}
Diffuse cloud	10^{2}
Dense cloud	10^{4}
Low Earth Orbit	10^{8}
High vacuum (10^{-6} Torr)	10^{10}
Earth's atmosphere	10^{19}
Earth	10^{23}
Center of Sun	10^{26}
White dwarf	10^{29}
Neutron star	10^{38}

[a] From Gunn & Peterson [69].
[b] For the universe to be closed by hydrogen atoms.

Table 4.1 Number densities of various regimes.

Cosmic rays ensure that all of the interstellar medium is at least a weakly-ionized plasma.

4.1.1 Dense Molecular Clouds

Within the cold neutral medium, there is a wide range of cloud conditions. The densest clouds are gravitationally bound, with densities of order 10^4–10^6 cm^{-3} and temperatures ~ 10 Kelvin. These clouds are completely opaque to visible light (though they are fairly transparent to infrared and longer wavelengths), and they often appear as "holes" in the sky (see Figure 4.2). They have total hydrogen column densities[2] of order $N_H \sim 10^{23}$ cm^{-2}, which correspond to color excesses of $E_{B-V} \sim 20$. These unusually dense concentrations of gas are undergoing gravitational collapse to form young stars and planetary systems.

Dense clouds are often referred to as "molecular clouds" because the large amount of dust protects the molecules inside the cloud from photodissociation. Nearly all hydrogen is in molecular form (H_2), and the vast majority of carbon is in the form of CO. In fact, mapping of the emission from CO and other molecules at millimeter

[2]The column density N is the number of particles in a 1 cm^2 column from the source to the observer. It can also be thought of as the average number density times the effective path length.

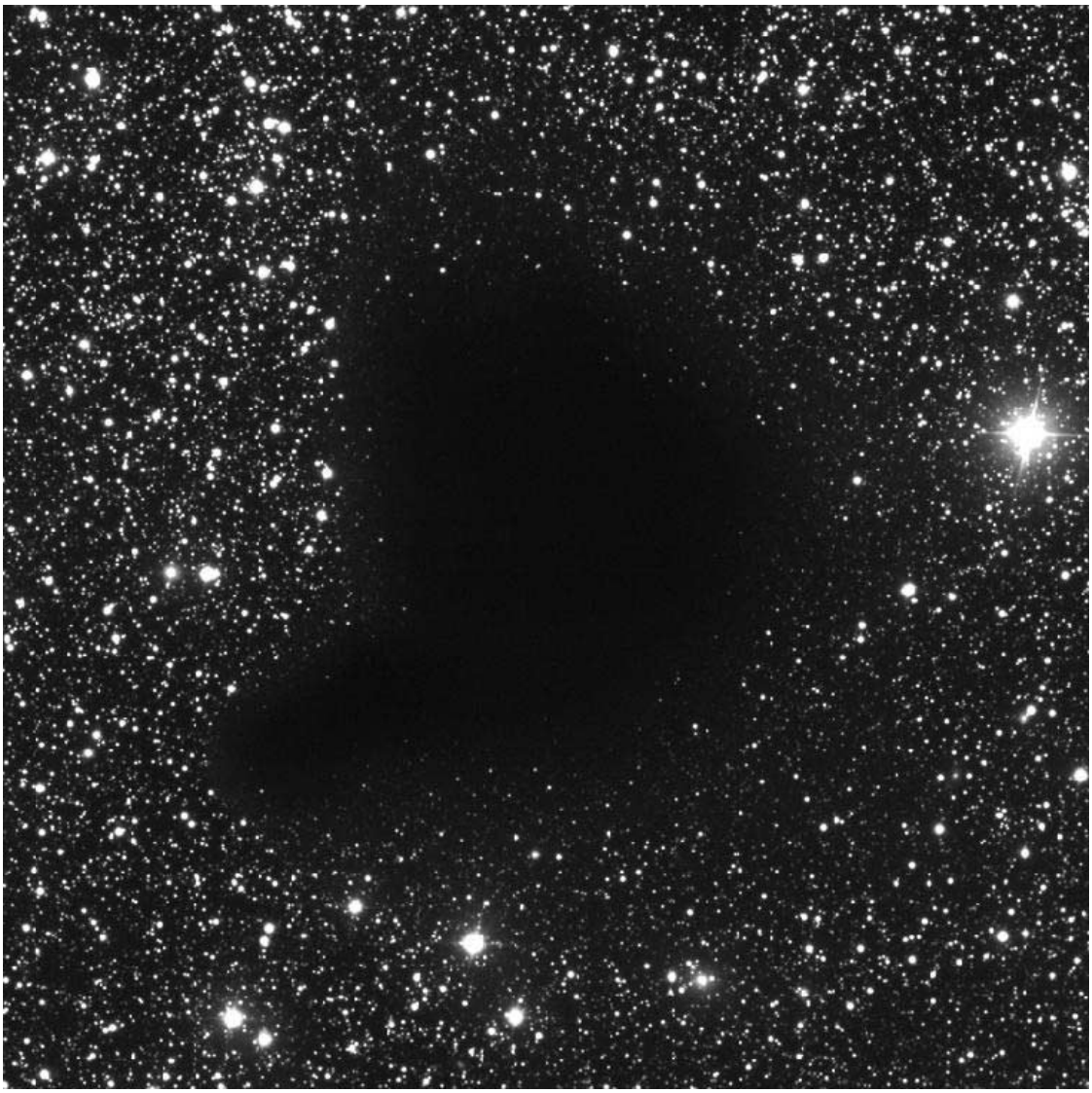

Figure 4.2 The dark cloud Barnard 68 (courtesy European Space Observatory).

wavelengths is a useful tool for studying the morphology of these clouds.

At the low temperatures of dense clouds, the most effective chemical reactions are those that are exothermic and have little or no activation energy barrier. These conditions are satisfied by ion-neutral reactions, as first suggested by Herbst & Klemperer [12] and Watson [13]. The initial source of the ions is the cosmic-ray ionization of H_2 to form H_2^+ [71], followed by the reaction

$$H_2 + H_2^+ \rightarrow H_3^+ + H \tag{4.1}$$

which was first pointed out to astronomers by Martin, McDaniel, & Meeks [11] in 1961. Because H_2 has a lower proton affinity than almost all atoms and molecules (with the notable exceptions of N, O_2 and He), it acts as the "universal protonator":

$$H_3^+ + X \rightarrow H_2 + XH^+ \tag{4.2}$$

The positive ion XH^+ thus produced can then engage in other ion-neutral reactions with neutral species. A simplified picture of the resulting network of chemical reactions is shown in Figure 4.3. This scheme of H_3^+-induced ion-neutral chemistry has now been incorporated into many successful models of dense cloud chemistry [72, e.g.].

4.1.2 Diffuse Clouds

At the other extreme from molecular clouds are the so-called "diffuse" clouds. These clouds have densities of $\sim$ 20–1000 cm^{-3}, and somewhat higher kinetic temperatures than dense clouds. Diffuse clouds typically have color excesses less than about 0.5 magnitudes, corresponding to hydrogen column densities of $\sim 10^{21}$ cm^{-2}. Diffuse clouds are considerably more common than dense clouds — about 10% of stars within 250 pc[3] of the Sun have $E_{B-V} > 0.056$ [73, p. 156].

In diffuse clouds, hydrogen is observed in a mixture of atomic and molecular form,

[3]One parsec (pc) is defined as the distance at which one astronomical unit (AU) has a parallax of one arcsecond. Numerically, 1 pc $\cong 3 \times 10^{18}$ cm.

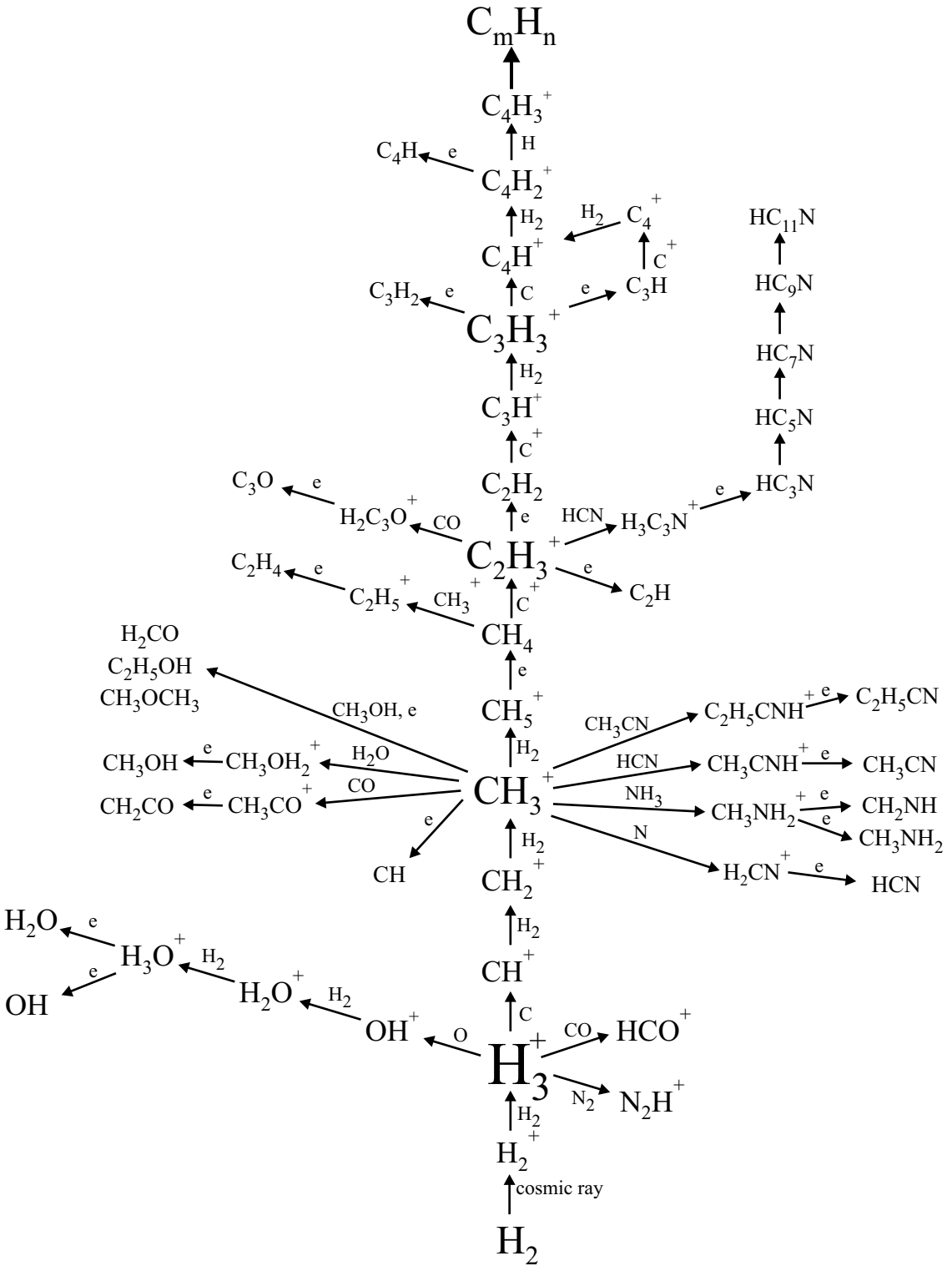

Figure 4.3 Network of ion-neutral chemistry.

due to the competing processes of H_2 formation on dust grains and photodissociation of H_2 by the ultraviolet radiation field (which penetrates through $E_{B-V} \sim 0.1$ of dust). The fraction of hydrogen nuclei in molecular form, $f(H_2) \equiv 2n(H_2)/[n(H) + 2n(H_2)]$ ranges from almost zero for the smallest color excesses up to $\sim 2/3$ for $E_{B-V} \sim 0.5$. Because the small column of dust does not effectively block ultraviolet radiation, atomic carbon is mostly ionized to C^+ (also called C II). While diffuse clouds can be studied using the H I line at 21 cm, they are more often studied via their visible and ultraviolet absorption lines against the continua of background stars.

The chemistry of diffuse clouds is qualitatively different from that of dense clouds, because of the high visible and ultraviolet radiation field and because chemical processes are slower due to the lower density. The high ionization fraction ($\sim 10^{-4}$) caused by the photoionization of atomic carbon leads to a quenching of ion-neutral chemistry through dissociative recombination. In particular, simple chemical models show that the H_3^+ abundance should be two to three orders of magnitude lower in diffuse clouds, due to electron recombination. The chemical models of diffuse clouds like ζ Oph [74] do not produce significant quantities of any polyatomic molecules — in fact, until recently the only molecules observed by visible and ultraviolet spectroscopy were diatomics (H_2, CO, CN, CH, CH^+, C_2, NH, and OH).

However, since the beginning there have been portents of problems with the chemical models. As one example, there is still no explanation for the observed high column density of CH^+, which is formed only by endothermic ($C^+ + H_2 \rightarrow CH^+ + H$) or slow ($C^+ + H_2 \rightarrow CH_2^+$ or $C^+ + H \rightarrow CH^+$) reactions, but is rapidly destroyed by reaction with H, H_2 or electrons. Another obvious problem is our complete lack of knowledge about the origin of the Diffuse Interstellar Bands, a ubiquitous series of over 200 absorption lines, which are presumably caused by gas-phase molecules.

4.1.3 "Translucent" Clouds

Many stars have color excesses in between the diffuse cloud ($E_{B-V} < 0.5$) and dense cloud ($E_{B-V} > 20$) extremes. In particular, the stars HD 183143, Cygnus OB2 12, and Cygnus OB2 5 (discussed in section 4.3) have color excesses between 1 and 4.

Because these sources are faint in the ultraviolet, it has not yet been possible to obtain direct evidence of the fraction of molecular hydrogen, or the ionization stage of carbon. Consequently, it is unclear whether these lines of sight represent a pile-up of diffuse clouds like ζ Oph, or clouds that are have intermediate properties — often called "translucent" clouds. It is conceivable that most of the hydrogen may be in the form of H_2, but that the carbon is neither ionized to C^+ nor converted into CO. An observational program is now underway using the Far Ultraviolet Explorer Satellite (FUSE) to study H_2 and other species in the ultraviolet spectra of a sample of high color excess sources [75]. Hopefully this study will shed some light on the ambiguous status of these "translucent" clouds.

4.2 Observations of H_3^+ in Dense Molecular Clouds

4.2.1 H_3^+ Chemistry

As mentioned earlier, H_3^+ is formed in a two-step process: first molecular hydrogen is ionized by a cosmic ray ($H_2 \rightarrow H_2^+ + e$), then the H_2^+ undergoes an ion-neutral reaction with H_2 to form H_3^+. The rate of cosmic ray ionization, ζ, is generally taken to be $\sim 3 \times 10^{-17}$ s^{-1}, so the typical H_2 molecule is only ionized once every 10^9 years. The ion-neutral reaction has been measured [76] to have a Langevin rate constant of $k \sim 2 \times 10^{-9}$ cm^3 s^{-1}. The rate of ion-neutral reaction for a given H_2^+ is therefore $kn(H_2) \sim 2 \times 10^{-4}$ s^{-1} for a dense cloud with $n(H_2) = 10^5$ cm^{-3}, so that the average H_2^+ is converted to H_3^+ within about one hour. Clearly, the cosmic ray ionization is the rate limiting step, and we can therefore take the rate of H_3^+ formation to be $\zeta n(H_2)$.

The destruction of H_3^+ is dominated by ion-neutral reactions with atoms and molecules, which represent the first step of the network of interstellar chemistry. Table 4.2 shows the seven species most important in the destruction of H_3^+. The dominant destroyer of H_3^+ is the CO molecule, with a Langevin rate constant of 1.8×10^{-9} cm^3 s^{-1} [77]. The second most important species is the O atom, which generally has comparable abundance but has a smaller rate constant, measured to be

Species	Min. Abundance[a] $n/n(H_2)$	Max. Abundance[a] $n/n(H_2)$	Rate Constant cm^3s^{-1}	Min. Rate $s^{-1}/n(H_2)$	Max. Rate $s^{-1}/n(H_2)$
CO	1.45 (-4)	1.46 (-4)	1.8 (-9)[b]	2.6 (-13)	2.6 (-13)
O	8.64 (-5)	1.51 (-4)	8.0 (-10)[c]	6.9 (-14)	1.2 (-13)
e^-	1.89 (-8)	2.31 (-7)	1.8 (-7)[d]	3.4 (-15)	4.2 (-14)
N_2	5.86 (-6)	1.92 (-5)	1.8 (-9)[b]	1.1 (-14)	3.5 (-14)
O_2	2.68 (-5)	5.92 (-5)	2.7 (-10)[e]	7.2 (-15)	1.6 (-14)
H_2O	3.59 (-7)	2.32 (-6)	5.9 (-9)[b]	2.1 (-15)	1.4 (-14)
CO_2	1.41 (-7)	9.45 (-7)	2.0 (-9)[b]	2.8 (-16)	1.9 (-15)

[a]Minimum and maximum abundances are taken from the steady state abundances of the "new standard model" of Lee, Bettens, and Herbst [72], for hydrogen number densities of 10^3–10^5 cm^{-3} and temperatures of 10–50 K.
[b]Anicich & Huntress 1986 [77]
[c]Fehsenfeld 1976 [78]
[d]Amano 1988 [80]; Sundström *et al.* (1994) [81] give 4.6×10^{-6} $T^{-0.65}$
[e]Adams & Smith 1984 [82]

Table 4.2 Species important in the destruction of H_3^+.

$(0.8 \pm 0.4) \times 10^{-9}$ cm^3 s^{-1} by Fehsenfeld [78] and $(1.2 \pm 0.48) \times 10^{-9}$ by Millgan and McEwan [79]. If we neglect the contribution ($\sim 30\%$) of the O atom, we can write the destruction rate of H_3^+ as simply $k\ n(H_3^+)\ n(CO)$.

To calculate the number density of H_3^+, we make the steady state approximation — we assume that the rates of H_3^+ production and destruction are equal. Therefore $\zeta n(H_2) = kn(H_3^+)n(CO)$, and we can solve for $n(H_3^+)$:

$$n(H_3^+) = \frac{\zeta}{k} \frac{n(H_2)}{n(CO)} \tag{4.3}$$

This equation shows us that the number density of H_3^+ is simply a ratio of two constants (ζ/k) times the H_2/CO ratio. However, the H_2/CO ratio is constant over a wide variety of cloud conditions [72] — because essentially all of the carbon is converted into CO (and all hydrogen is in the form of H_2), the H_2/CO ratio is related simply to the H/C abudance ratio. Thus we reach the surprising result that the H_3^+ number density is independent of the overall density of the cloud! It is this property of H_3^+ that makes it a particularly powerful probe of the physical conditions of dense clouds. Plugging in the values $\zeta \sim 3 \times 10^{-17}$ s^{-1}, $k \sim 2 \times 10^{-9}$ cm^3 s^{-1}, and

$CO/H_2 \sim 1.5 \times 10^{-4}$ [72], we obtain

$$n(H_3^+) \sim 1 \times 10^{-4} \text{ cm}^{-3} \tag{4.4}$$

The validity of the steady state approximation can be evaluated by considering the timescales for formation and production of H_3^+. The order of magnitude of the formation timescale can be estimated by assuming we start out with no H_3^+ and that the destruction process is turned off. Then H_3^+ is formed at a constant rate of $\zeta\ n(H_2)$. The formation timescale is then roughly

$$\tau_f \sim \frac{n(H_3^+)_{ss}}{\zeta n(H_2)} \sim \frac{10^{-4}}{(3 \times 10^{-17})(10^5)} \sim 3 \times 10^7 \text{ s} \sim 1 \text{ yr}$$

The characteristic timescale for the decay of an overabundance of H_3^+ (assuming the formation mechanism is turned off) is roughly

$$\tau_d \sim [k\ n(CO)]^{-1} \sim [(2 \times 10^{-9})(15)]^{-1} \sim 3 \times 10^7 \text{ s} \sim 1 \text{ yr}$$

Because both the formation and destruction timescales are rapid compared to the lifetime of the cloud ($\sim 10^6$ yr), the steady state approximation is an extremely good one.

At the low temperatures (less than ~50 K) of interstellar clouds, only the lowest two rotational levels of H_3^+ — (J,K)=(1,1) and (1,0) — are populated. The *ortho* (1,0) and *para* (1,1) states of H_3^+ are not interconverted by any radiative pathway. However, because H_2 is abundant and because the Langevin rate constant is large, they will be efficiently equilibrated by the "proton-hop" $H_3^+ + \tilde{H}_2 \rightarrow H_2 + \tilde{H}_2H^+$ and "proton-exchange" $H_3^+ + \tilde{H}_2 \rightarrow H_2\tilde{H}^+ + H\tilde{H}$ reactions, where the tildes represent the protons originally in H_2. The difference in energy between (1,0) and (1,1) is 22.84 cm^{-1} (32.9 K), so in thermal equilibrium at interstellar temperatures, the statistical weight factor 4/2 in favor of (1,0) nearly offsets the Boltzmann factor $e^{-\Delta E/kT}$, leaving (1,0) with only a slight deficit in population compared with (1,1).

Label	Upper state	Lower state	ν (cm^{-1})	λ (Å)	$\|\mu\|^2$ (D^2)
$P(1,1)$	(0,1)	(1,1)	2457.290	40695.24	0.0086
$Q(1,0)$	(1,0)	(1,0)	2529.724	39530.00	0.0254
$Q(1,1)$	(1,1)	(1,1)	2545.418	39286.28	0.0128
$R(1,1)^l$	$(2,1)^l$	(1,1)	2691.444	37154.78	0.0140
$R(1,0)$	(2,0)	(1,0)	2725.898	36685.16	0.0259
$R(1,1)^u$	$(2,1)^u$	(1,1)	2726.219	36680.84	0.0158

Table 4.3 Lines of the H_3^+ $\nu_2 \leftarrow 0$ band suitable for interstellar absorption studies.

4.2.2 Detection Method

Because the (1,0) and (1,1) levels are nearly equally populated, there are six possible transitions in the $\nu_2 \leftarrow 0$ band that can be observed in absorption, as listed in Table 4.3. The transition frequencies in the table are taken from the compilation of Section D, while the dipole moments are from Watson [41]. It is particularly fortunate for astronomers that the $J = 0$ level is forbidden by the Pauli principle, or else there would only be one transition available!

For practical purposes, the $R(1,0)$ and $R(1,1)^u$ transitions are most convenient because they can be observed together in a single integration, providing information on both *ortho* and *para* H_3^+. An energy level diagram showing these transitions is given in Figure 4.4. Because $R(1,0)$ is inherently a bit stronger than $R(1,1)^u$, and because the (1,0) level is slightly less populated, the two absorption lines are observed with nearly equal strength.

The primary disadvantage of these transitions is that they lie near two atmospheric HDO (monodeuterated water) lines at 36681.6 Å and 36688.1 Å. Because the water vapor content of the atmosphere varies on short timescales, these lines are difficult to remove from the spectrum when substantial amounts of water are present [the atmospheric CH_4 line at 36675.3 Å, which is considerably stronger, is farther from the H_3^+ transitions and also tends to ratio out more cleanly]. Under such conditions (such as when observing from Kitt Peak) we rely on the $R(1,1)^l$ line, which is not affected by atmospheric water (but does lie near some relatively weak CH_4 lines).

For our studies of H_3^+ in dense clouds, we have used two spectrometers: the CGS4 (Cooled Grating Spectrometer 4) spectrometer at the United Kingdom Infrared Telescope (UKIRT) [83] and the Phoenix spectrometer at Kitt Peak National Observa-

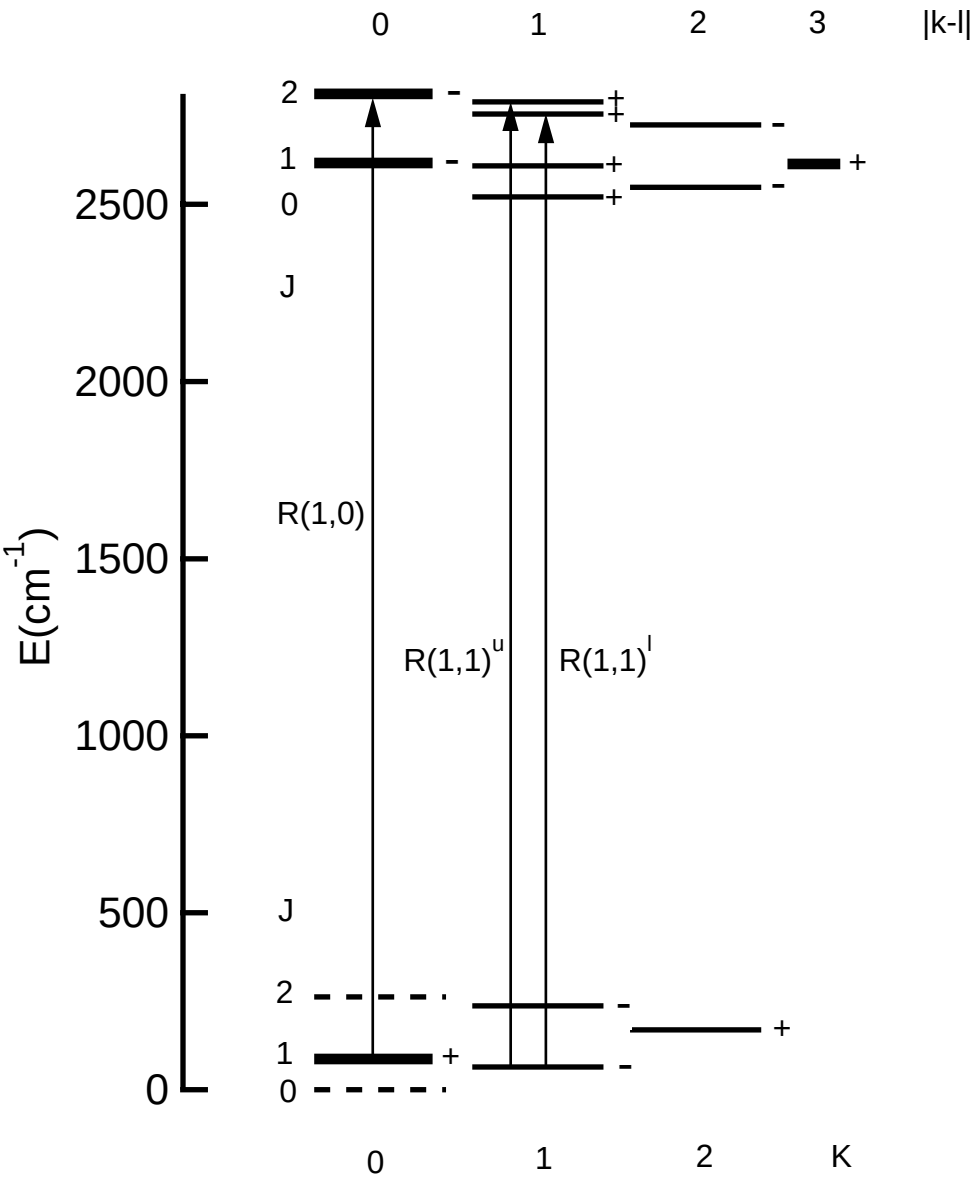

Figure 4.4 Energy level diagram of H_3^+, showing transitions observed in dense clouds.

tory [84]. Both of these instruments are cryogenically cooled echelle spectrometers mounted on four-meter class telescopes. The radiation from the target star, after being collected by the telescope, is sent through a long slit, diffracted off the echelle grating, and collected by an Indium-Antimonide (InSb) two-dimensional array detector. On the array, one axis is wavelength and the other is a direction on the sky (along the slit). The "spectral image" from the array is then processed to extract a one-dimesional spectrum of the star. In our work, young hot stars embedded in (or behind) the dense clouds serve as the continuum source, and we search for H_3^+ absorption lines caused by intervening gas.

Because these obscured stars are invisible at optical wavelengths, it is somewhat tricky to keep the source centered on the narrow slit. In practice, a nearby visible star is used to guide the telescope, with a fixed offset determined by imaging the obscured star on the array (in the case of Phoenix) or by maximizing the intensity of the observed spectrum (in the case of CGS4).

Since the sky is bright at these wavelengths due to thermal emission from the atmosphere (at 3.6 μm, the sky is roughly 5th magnitude per square arcsecond!), we must take short exposures to avoid saturating the array. In order to effectively remove the sky emission, we nod the star along the slit and subtract, thus yielding a "positive" and "negative" spectrum of the star along two different lines on the array.

To remove the many atmospheric absorption lines in the spectrum (due to gases such as HDO, CH_4, etc.), we also obtain spectra of unreddened stars with similar airmasses[4]. We can then ratio the spectrum of the obscured star to that of the unreddened star to obtain a spectrum relatively free of atmospheric absorption. For further details of the data processing procedure, see Section 4.4.

4.2.3 Observations

Interstellar H_3^+ was first detected by Tom Geballe and Takeshi Oka in 1996 at UKIRT [14]. They obtained spectra of the dense clouds AFGL 2136 and W33A on 29 April and 15 July 1996, but published only the 15 July data. The $R(1,1)^u$–$R(1,0)$ "dou-

[4]The airmass is the column of the atmosphere the stellar radiation passes through, and is usually taken as the secant of the zenith angle.

blet" was marginally detected in both sources, with a signal-to-noise ratio of a few. However, when I re-reduced the April spectra, the lines were apparent (though also at low signal-to-noise). Between the two spectra, the component of the Earth's orbital motion along the line of sight had changed, causing a Doppler shift in the H_3^+ lines which confirms their interstellar origin (see Figure 4.5).

In order to followup on the initial detections, we undertook a study of a small sample of dense cloud sources, using both CGS4 at UKIRT (in collaboration with Tom Geballe) and Phoenix at Kitt Peak (in collaboration with Ken Hinkle). We obtained detections of H_3^+ in four additional sources (Mon R2 IRS 3, AFGL 961E, AFGL 490, and AFGL 2591), as shown in Figures 4.6 and 4.7. We also derived upper limits of the H_3^+ column density in nine sources (Orion BN, NGC 2024 IRS 2, Mon R2 IRS 2, AFGL 989, Elias 29, M17 IRS 1, W3 IRS 5, S140 IRS 1, and LkHα 101) where we were not able to detect H_3^+. For further details on the survey, see Appendix A.4 [85].

4.2.4 Analysis

For each absorption line of H_3^+, we measure the area of the line (called the equivalent width), $W_\lambda \equiv \int(1 - \frac{I}{I_0})d\lambda$. From the equivalent width, we can derive the column density of absorbers in the lower level of the transition (assuming the line is optically thin) from the standard equation $W_\lambda = (8\pi^3\lambda/3hc)N_{level}|\mu|^2$. Because only the (1,0) and (1,1) levels of H_3^+ are populated at the temperatures of interstellar clouds, we can measure the column densities N_{ortho} and N_{para} and take the total H_3^+ column density to be $N(H_3^+) = N_{ortho} + N_{para}$.

The observed column densities of H_3^+ allow estimates of the three most important physical parameters of dense clouds: the absorption path length, the cloud number density, and the kinetic temperature. The effective absorption path length can be estimated by dividing the observed column density by the H_3^+ number density calculated from the chemical model:

$$L \sim \frac{N(H_3^+)}{n(H_3^+)} \sim N(H_3^+)\frac{k}{\zeta}\frac{n(CO)}{n(H_2)} \sim N(H_3^+) \times (10^4 \text{ cm}^3) \tag{4.5}$$

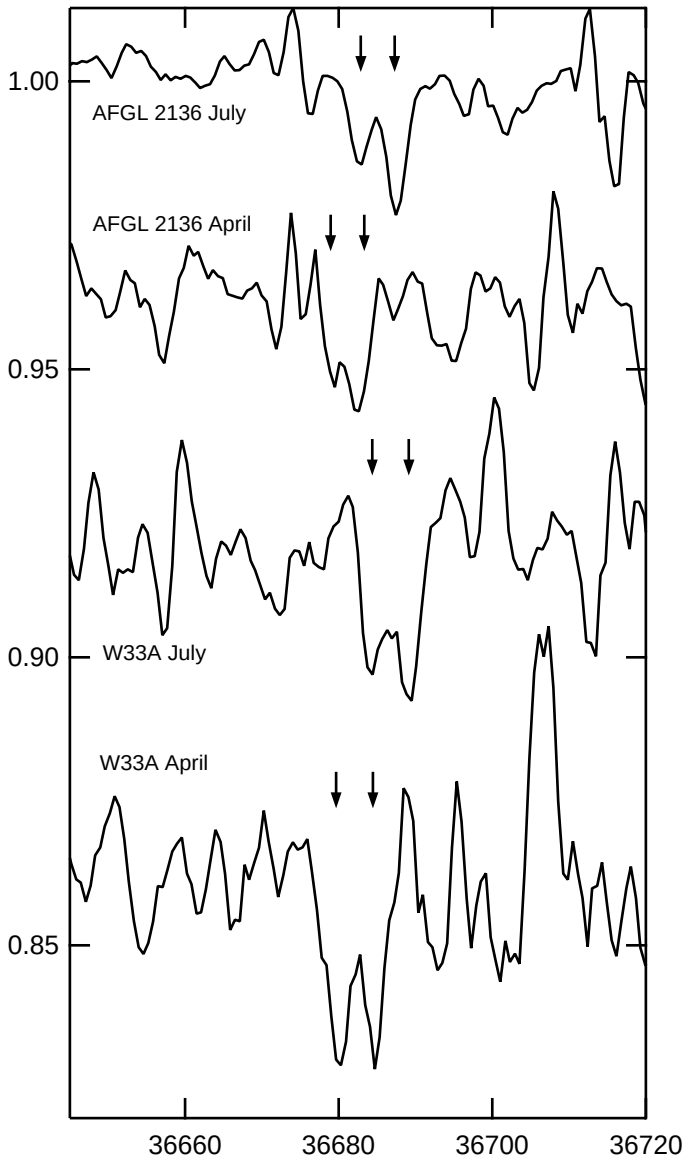

Figure 4.5 Spectra of the $R(1,1)^u$–$R(1,0)$ doublet of H_3^+ toward AFGL 2136 and W33A, obtained with UKIRT (the horizontal scale is wavelength in Ångstroms).

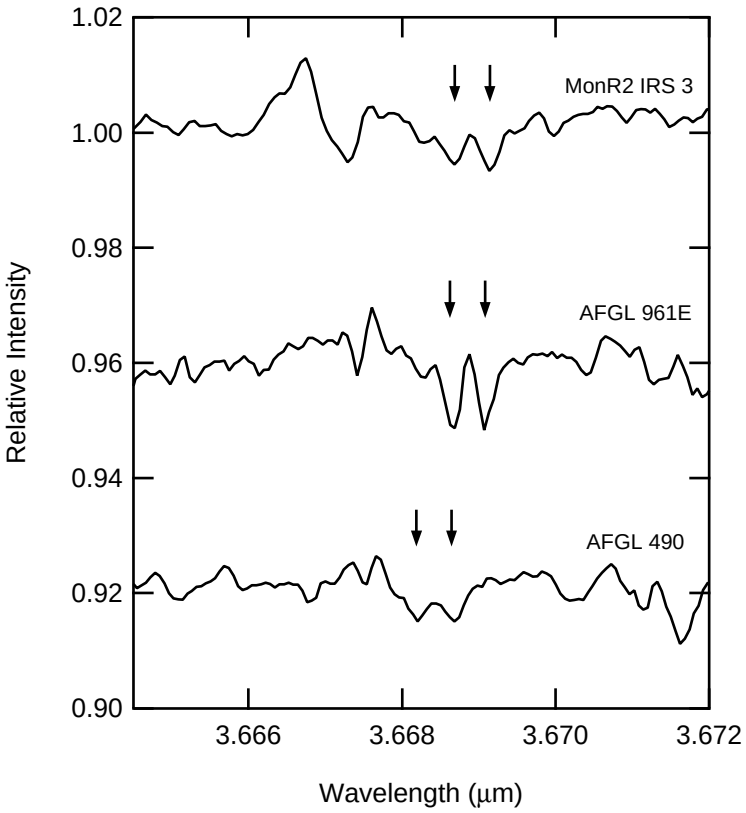

Figure 4.6 Spectra of the $R(1,1)^u$–$R(1,0)$ doublet of H_3^+ toward MonR2 IRS 3, AFGL 961E, and AFGL 490, obtained with UKIRT.

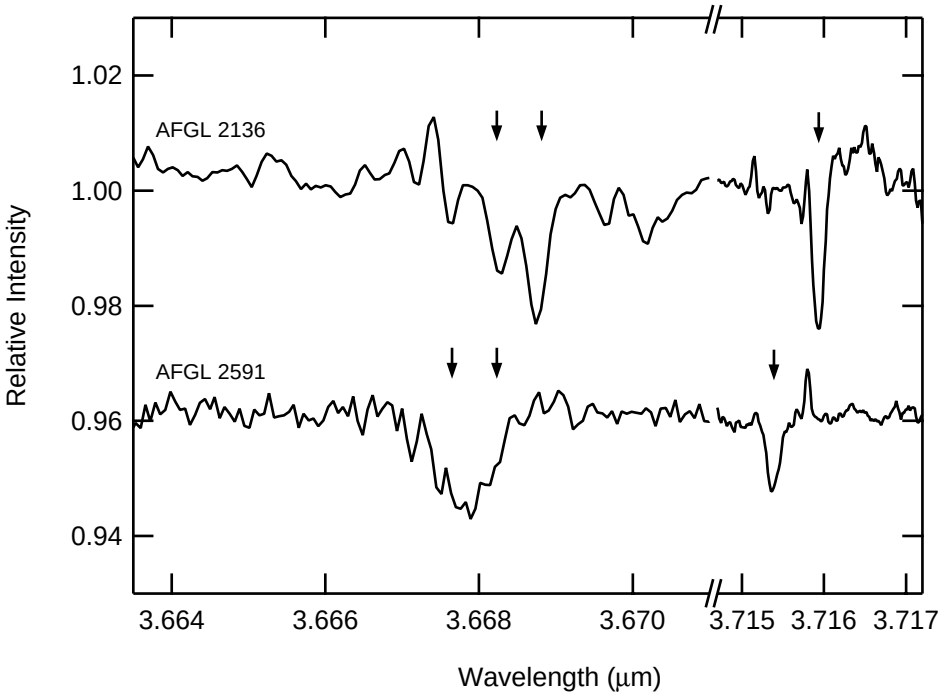

Figure 4.7 Spectra of the $R(1,1)^u$–$R(1,0)$ doublet (left, from UKIRT) and the $R(1,1)^l$ line (right, from Kitt Peak) of H_3^+ toward AFGL 2136 and AFGL 2591.

In units of parsecs, the effective path length is then $N(H_3^+)$ (in cm^{-2}) divided by 3×10^{14}. Thus, a column density of 3×10^{14} cm^{-2} corresponds to a length of one parsec.[5]

If an estimate of the hydrogen column density $N(H_2)$ is available, we can infer the average number density of the cloud, as $\langle n(H_2) \rangle = N(H_2)/L$. Direct determination of $N(H_2)$ is difficult in dense clouds because the ultraviolet spectrum of H_2 is obscured by the dust, and the rotation-vibration (quadrupole) infrared spectrum of H_2 is very weak. To date, the infrared absorption spectrum of H_2 has only been measured in the three dense cloud sources NGC 2024 IRS 2, AFGL 2591, and AFGL 490 [86, 87, 88]. In lieu of a direct determination of $N(H_2)$, we generally use a surrogate such as CO (assuming a constant H_2/CO ratio [72]) or the optical depth of the silicate feature at 9.7 μm (assuming a constant gas-to-dust ratio [89]).

Finally, the kinetic temperature of the gas can be estimated by the *ortho*:*para* ratio of H_3^+. For this, we use a standard Boltzmann expression:

$$\frac{N_{ortho}}{N_{para}} = \frac{g_{ortho}}{g_{para}} e^{-\Delta E/kT} = 2e^{-32.87/T} \tag{4.6}$$

where g is the spin statistical weight (4 or 2), and ΔE is the energy separation between the (1,0) and (1,1) levels.

The results of our analysis are listed in Table 4.4. The derived physical parameters (path lengths ~ 1 pc, average densities $\sim 5 \times 10^4$ cm^{-3}, and temperatures ~ 35 K) all agree with the canonical values of dense clouds. In this respect, these results confirm the general picture of dense cloud H_3^+ chemistry.

4.2.5 Recent Developments

Since the publication of our paper on dense cloud H_3^+ [85], there have been some exciting developments. A number of our H_3^+ non-detections have turned into detections, thanks to higher signal-to-noise observations. Craig Kulesa and John Black have

[5] It should be noted that these length determinations (and all subsequent estimates) depend on the assumed value of $\zeta \sim 3 \times 10^{-17}$ s^{-1}. It would be more rigorous to say that we have obtained an estimate of the quantity ζL.

Object	$N_o(H_3^+)$ 10^{14} cm^{-2}	$N_p(H_3^+)$[a] 10^{14} cm^{-2}	$N_{tot}(H_3^+)$ 10^{14} cm^{-2}	ζL cm s^{-1}	L pc	$\tau_{9.7}$ [b]	N_H [c] 10^{22} cm^{-2}	N(CO) 10^{19} cm^{-2}	$N(H_2)$[d] 10^{22} cm^{-2}	$\langle n(H_2)\rangle$ 10^4 cm^{-3}	T K
AFGL 2136	1.9	1.9	3.8	110	1.3	5.07	18	3.2[f]	22	6	47
W33A	2.3	2.9	5.2	150	1.7	7.84	28	3.9[f]	27	5	36
MonR2 IRS 3	0.6	0.8	1.4	41	0.5	2[e]	7	1.1[g]	7.6	5	31
AFGL 961E	0.6	1.1	1.7	49	0.6	2.11	7.5	0.4[g]	2.8	2	25
AFGL 490	0.4	0.7	1.1	32	0.4	2.77	9.8	1.1[h]	7.6	6	26
AFGL 2591[i]	1.0	1.2	2.2	64	0.7	4.14	15	1.9[f]	13	6	38

[a]For AFGL 2136 and AFGL 2591, where both the R(1,1)^u and R(1,1)^l *para*-H_3^+ lines were observed, the R(1,1)^l values have been used because they have a lower $\sigma(N)$.
[b]Silicate optical depths at 9.7 μm from Willner *et al.* 1982 [90] except as noted.
[c]Hydrogen column derived from $A_V/\tau_{9.7} = 18.6$ (Roche & Aitken 1994 [91]) and $N_H/A_V = 1.9 \times 10^{21}$ (Bohlin, Savage, & Drake 1978 [70]).
[d]Hydrogen column derived from $n(CO)/n(H_2) \sim 1.5 \times 10^{-4}$ from Lee, Bettens, & Herbst 1996 [72].
[e]Beckwith *et al.* 1976 [92].
[f]Mitchell *et al.* 1990 [93].
[g]McCall *et al.* 1999 [85].
[h]Mitchell *et al.* 1995 [94], assuming $^{12}CO/^{13}CO = 89$.
[i]Estimates for AFGL 2591 have large systematic uncertainties due to the short integration time and telluric interference, as discussed in the text.

Table 4.4 Estimated dense cloud parameters.

confirmed our H_3^+ detections in AFGL 2591 and AFGL 490, and have also reported [87] detecting H_3^+ in NGC 2024 IRS 2 with a column density of 9.5×10^{12} cm^{-2}, using the Phoenix spectrometer at Kitt Peak. Additionally, Tom Geballe (private communication) has detected weak H_3^+ lines in AFGL 989, with a column density of $\sim 6 \times 10^{13}$ cm^{-2}, using CGS4 at UKIRT. We suspect that all of our non-detections will eventually turn into detections, with higher sensitivity observations.

Another interesting development has been the progress in theoretical modelling of dense clouds. Our treatment described above assumes that the H_3^+ exists in a cloud of constant density, which is certainly not an accurate physical picture. Using maps of the submillimeter continuum, as well as line spectra of CO, CS, and H_2CO, van der Tak *et al.* [95] have constructed detailed self-consistent models of the temperature and density structure of several of the dense cloud sources in our sample. When they use these models to predict [96] the observed H_3^+ column densities, they come up short by as much as a factor of 7. They suggest that this implies that a substantial fraction of the observed H_3^+ lies outside of the region of their models. They point out that the observed H_3^+ radial velocities are consistent with radio spectra of CO and CS, so that the H_3^+ is likely associated with the dense clouds — however, they also find a rough correlation between the observed H_3^+ column density and the distance from the Earth, which suggests that intervening clouds could play a role. Hopefully, this discrepancy between the models and the observations will be reconciled soon!

4.3 Observations of H_3^+ in Diffuse Clouds

The following section is being submitted to the *Astrophysical Journal*, with co-authors K. H. Hinkle (National Optical Astronomy Observatories), T. R. Geballe (Gemini Observatory), G. H. Moriarty-Schieven (Joint Astronomy Centre), N. J. Evans II (University of Texas at Austin), K. Kawaguchi (Okayama University), S. Takano (Nobeyama Radio Observatory), V. V. Smith (University of Texas at El Paso), and T. Oka (University of Chicago).

4.3.1 Introduction

The H_3^+ molecular ion has long been considered to play an important role in the chemistry of dense molecular clouds, as it initiates the network of ion-neutral reactions [12, 13] that is responsible for the wealth of molecules observed by infrared and radioastronomers. However, H_3^+ has not been considered to be an important species in diffuse clouds, because it is thought to be destroyed rapidly by dissociative recombination with the abundant electrons.

The detection of H_3^+ in the diffuse interstellar medium toward the Galactic Center [97] and toward the visible star Cygnus OB2 12 [98] with similar column densities to those of dense clouds [85] was therefore quite surprising. These observational results imply either a very long pathlength (hundreds of parsecs) of absorbing material, or a serious problem with the standard model of diffuse cloud chemistry. Various attempts have been made to explain the abundance of H_3^+ toward Cygnus OB2 12 while preserving the standard model of the chemistry, either by adjusting all parameters to optimize H_3^+ [99] or by postulating an additional H_2 ionization source peculiar to the neighborhood of the Cygnus OB2 association [88].

We have conducted a small survey of twelve diffuse cloud sources with the aim of determining whether the sightline toward Cygnus OB2 12 is unique, or whether high column densities of H_3^+ are common in diffuse clouds. As a result of this survey, we have secure detections of H_3^+ in four diffuse cloud sources (Cygnus OB2 12, Cygnus OB2 5, HD 183143, and HD 20041), tentative detections toward three Wolf-Rayet stars (WR 104, WR 118, and WR 121), and upper limits toward five stars (HD 194279, HD 168607, P Cygni, χ^2 Ori, and ζ Ophiuchi). For Cygnus OB2 12 and 5 and HD 181343, we have also obtained infrared and radio spectra of CO, as well as high-resolution visible spectra of relevant atoms and molecules.

These results demonstrate the ubiquity of H_3^+ in diffuse clouds, and suggest that there is a "global" problem with the current models. In this respect, H_3^+ represents the third major problem in diffuse cloud chemistry, following the Diffuse Interstellar Bands and CH^+.

4.3.2 Observations and Data Reduction

A summary of the observations is provided in Table 4.5. The $R(1,1)^l$ line of H_3^+ (for a description of the new standard notation for H_3^+, see Section 2.9) at 3.715 μm was observed using the Phoenix spectrometer on the Mayall 4-meter telescope at Kitt Peak National Observatory (KPNO). The H_3^+ observations were performed in three runs (July 1998, June 2000, and March 2001). Phoenix was also used to study the fundamental (v=1-0) and overtone (v=2-0) bands of CO, in June 1997, July 1999, and June 2000. The CGS4 facility spectrometer on the United Kingdom Infrared Telescope (UKIRT) was used in July 2000 to study the $R(1,0)$–$R(1,1)^u$ doublet of H_3^+. The data were reduced using the same procedure outlined in [85], which is described in more detail in Section 4.4. The wavelength calibration was achieved using telluric absorption lines, and is estimated to be accurate to roughly 2 km/s. The resolving power of the Phoenix spectrometer was roughly 40,000 until 1998, and approximately 60,000 during 1999–2001. The CGS4 spectrometer was used with the long camera, yielding a resolving power of 40,000.

High resolution visible spectra of atoms and molecules of interest were obtained using the Coudé spectrometer on the Smith 2.7-m telescope at McDonald Observatory. A total of three echelle settings were used. The first covered the K I line at 7699 Å and the CN A-X v=2-0 $R_2(0)$ line at 7875 Å. The second covered the C_2 A-X v=2-0 band near 8760 Å. These two echelle settings were used with the F1E2 configuration and the 0.2" slit, which yielded a resolving power of about 200,000. The third echelle setting covered Ca I at 4227 Å, Ca II at 3934 Å, CH at 4300 Å, CH^+ at 4232 Å, and CN B-X v=0-0 near 3874 Å. This setting was used with the F1E1 configuration and the 0.6" slit, to yield a resolving power of approximately 120,000. The McDonald data were reduced using standard IRAF routines (CCDPROC and DOECSLIT). Wavelength calibration was achieved using comparison spectra of a Th-Ar lamp, and is estimated to be good to about 0.01 Å in all cases.

Rotational spectra of CO in the Cygnus OB2 association were obtained at the Nobeyama Radio Observatory (NRO) for J=1-0, and the Caltech Submillimeter Observatory (CSO) for J=2-1 and 3-2. In both cases, position switching was used, with

Date (UT)	Observatory	Species	Transition	Object	Standard	Time (min)
Jun 25, 1997	KPNO	CO	v=2-0	HD 183143	α Lyr	60
Jul 3, 1998	KPNO	H_3^+	$R(1,1)^l$	Cyg OB2 12	α Cyg	30
Jul 3, 1998	KPNO	H_3^+	$R(1,1)^l$	Cyg OB2 5	α Cyg	164
Jul 4, 1998	KPNO	H_3^+	$R(1,1)^l$	WR 104	α Lyr	35
Jul 4, 1998	KPNO	H_3^+	$R(1,1)^l$	WR 121	α Lyr	112
Jul 4, 1998	KPNO	H_3^+	$R(1,1)^l$	WR 118	α Cyg	46
Jul 4, 1998	KPNO	H_3^+	$R(1,1)^l$	HD 194279	α Cyg	92
Jul 4, 1999	KPNO	CO	v=2-0	Cyg OB2 12	α Cyg	4
Jul 5, 1999	KPNO	CO	v=1-0	Cyg OB2 12	α Lyr	4
Jul 5, 1999	KPNO	CO	v=1-0	Cyg OB2 5	α Lyr	8
Jun 25, 2000	KPNO	H_3^+	$R(1,1)^l$	Cyg OB2 12	α Cyg	60
Jun 25, 2000	KPNO	H_3^+	$R(1,1)^l$	HD 183143	α Lyr	84
Jun 25, 2000	KPNO	H_3^+	$R(1,1)^l$	P Cygni	α Lyr	78
Jun 26, 2000	KPNO	H_3^+	$R(1,1)^l$	ζ Oph	α Lyr	48
Jun 26, 2000	KPNO	CO	v=1-0	Cyg OB2 12	α Lyr	36
Jun 26, 2000	KPNO	CO	v=1-0	Cyg OB2 5	α Lyr	90
Mar 13, 2001	KPNO	H_3^+	$R(1,1)^l$	HD 20041	α CMa	100
Mar 13, 2001	KPNO	H_3^+	$R(1,1)^l$	χ^2 Ori	α CMa	60
Jul 6, 2000	UKIRT	H_3^+	$R(1,0)$,$R(1,1)^u$	HD 183143	α Lyr	29
Jul 6, 2000	UKIRT	H_3^+	$R(1,0)$,$R(1,1)^u$	Cyg OB2 5	α Cyg	43
Jul 7, 2000	UKIRT	H_3^+	$R(1,0)$,$R(1,1)^u$	HD 168607	π Sgr	25
Sep 12, 2000	McDonald	K I CN	$^2P - ^2S$ A-X v=2-0	Cyg OB2 12	α Cyg	60
Sep 12, 2000	McDonald	"	"	Cyg OB2 5	α Cyg	60
Sep 12, 2000	McDonald	"	"	HD 183143	α Cyg	60
Sep 12, 2000	McDonald	C_2	A-X v=2-0	Cyg OB2 12	α Cep	60
Sep 12, 2000	McDonald	C_2	A-X v=2-0	Cyg OB2 5	α Cep	60
Sep 12, 2000	McDonald	C_2	A-X v=2-0	HD 183143	α Cep	60
Sep 14, 2000	McDonald	Ca I Ca II CH CH^+ CN	$^1P - ^1S$ $^2P - ^2S$ A-X v=0-0 A-X v=0-0 B-X v=0-0	Cyg OB2 5	α Cyg	200
Sep 14, 2000	McDonald	"	"	HD 183143	α Cyg	100
Jul 28, 1999	CSO	^{12}CO	J=2-1	Cyg OB2 12	30' S	14
Jul 28, 1999	CSO	^{12}CO	J=2-1	Cyg OB2 5	30' S	14
Jul 28-29, 1999	CSO	^{13}CO	J=2-1	Cyg OB2 12	30' S	32
Jul 28-29, 1999	CSO	^{13}CO	J=2-1	Cyg OB2 5	30' S	32
Jul 28, 1999	CSO	^{13}CO	J=3-2	Cyg OB2 12	30' S	20
Jul 28, 1999	CSO	^{13}CO	J=3-2	Cyg OB2 5	30' S	20
Apr 9, 2000	NRO	^{12}CO	J=1-0	Cyg OB2 12	(l=81,b=3)	18
Apr 9, 2000	NRO	^{13}CO	J=1-0	Cyg OB2 12	(l=81,b=3)	37
Apr 11, 2000	NRO	^{12}CO	J=1-0	Cyg OB2 "A"	(l=81,b=3)	10
Apr 11, 2000	NRO	^{12}CO	J=1-0	Cyg OB2 "B"	(l=81,b=3)	10
Apr 11, 2000	NRO	^{12}CO	J=1-0	Cyg OB2 "C"	(l=81,b=3)	15
Apr 11, 2000	NRO	^{12}CO	J=1-0	Cyg OB2 "D"	(l=81,b=3)	10
Apr 14, 2000	NRO	^{12}CO	J=1-0	Cyg OB2 5	(l=81,b=3)	13
Oct 13, 2000	JCMT	^{12}CO	J=2-1	HD 183143	(8 MHz)	60
Oct 13, 2000	JCMT	^{12}CO	J=2-1	HD 183143	(16 MHz)	60
Dec 14, 2000	NRO	^{12}CO	J=1-0	HD 183143	(3 MHz)	12
Dec 14, 2000	NRO	^{12}CO	J=1-0	HD 183143	(6 MHz)	13
Dec 15, 2000	NRO	^{12}CO	J=1-0	HD 183143	(4 MHz)	31
Dec 15, 2000	NRO	^{12}CO	J=1-0	HD 183143	(9 MHz)	45

Table 4.5 Log of observations.

an "off" position of 30' south for the CSO spectra and (l=81,b=3) for the NRO spectra. CO spectra toward HD 183143 were also obtained at the James Clerk Maxwell Telescope (JCMT) for J=2-1, and at NRO for J=1-0, using frequency switching. In all cases, data were reduced using the standard procedures.

4.3.3 Results

H_3^+ Spectra

In our 1998 observing run at Kitt Peak, we detected H_3^+ for the first time toward Cygnus OB2 5, which lies approximately 6' (3 pc at 1.7 kpc) away from Cygnus OB2 12. Although the H_3^+ $R(1,1)^l$ line was unfortunately Doppler shifted under the telluric CH_4 feature near 37152 Å, we are confident that the detection is secure, because the other CH_4 line (near 37158 Å) ratios out very well and because we observed a similar H_3^+ feature in Cygnus OB2 12 at the same velocity with an equivalent width consistent with our earlier observations [98]. However, the fact that the H_3^+ line lies underneath the telluric line makes us hesitant to rely on the observed velocity structure (or lack thereof). Our Kitt Peak H_3^+ observations are summarized in Figure 4.8.

Our 1998 run also yielded probable detections of H_3^+ toward the Wolf-Rayet stars WR 121, WR 104, and WR 118. We consider these features as tentative detections because they have not yet been confirmed using the $R(1,0)$–$R(1,1)^u$ doublet from UKIRT, and because we are not aware of any other high resolution spectroscopy of these sightlines which could confirm the radial velocities of the features. The source WR 118 is unusual in that it apparently shows two H_3^+ features, which have similar (though not the same) spacing as the two telluric CH_4 lines. Consequently, the scaling and ratioing by the standard star was performed by choosing parameters which minimized the residual of CH_4 lines elsewhere in the spectrum (not shown in the figure). It is worth noting that the inferred velocities of the peaks ($\sim$+5 and +48 km/s) would occur at heliocentric distances of $\sim$0.5 and 3 kpc, respectively, assuming a flat Galactic rotation curve with $v_c = 220$ km/s, $R_0 = 8$ kpc, and $l = 21°.80$. These distances do not exceed the estimated distance to the source ($m - M = 14$, or $d \sim$ 6.3 kpc) obtained from the observed V magnitude of 22, the visual extinction $A_V =$

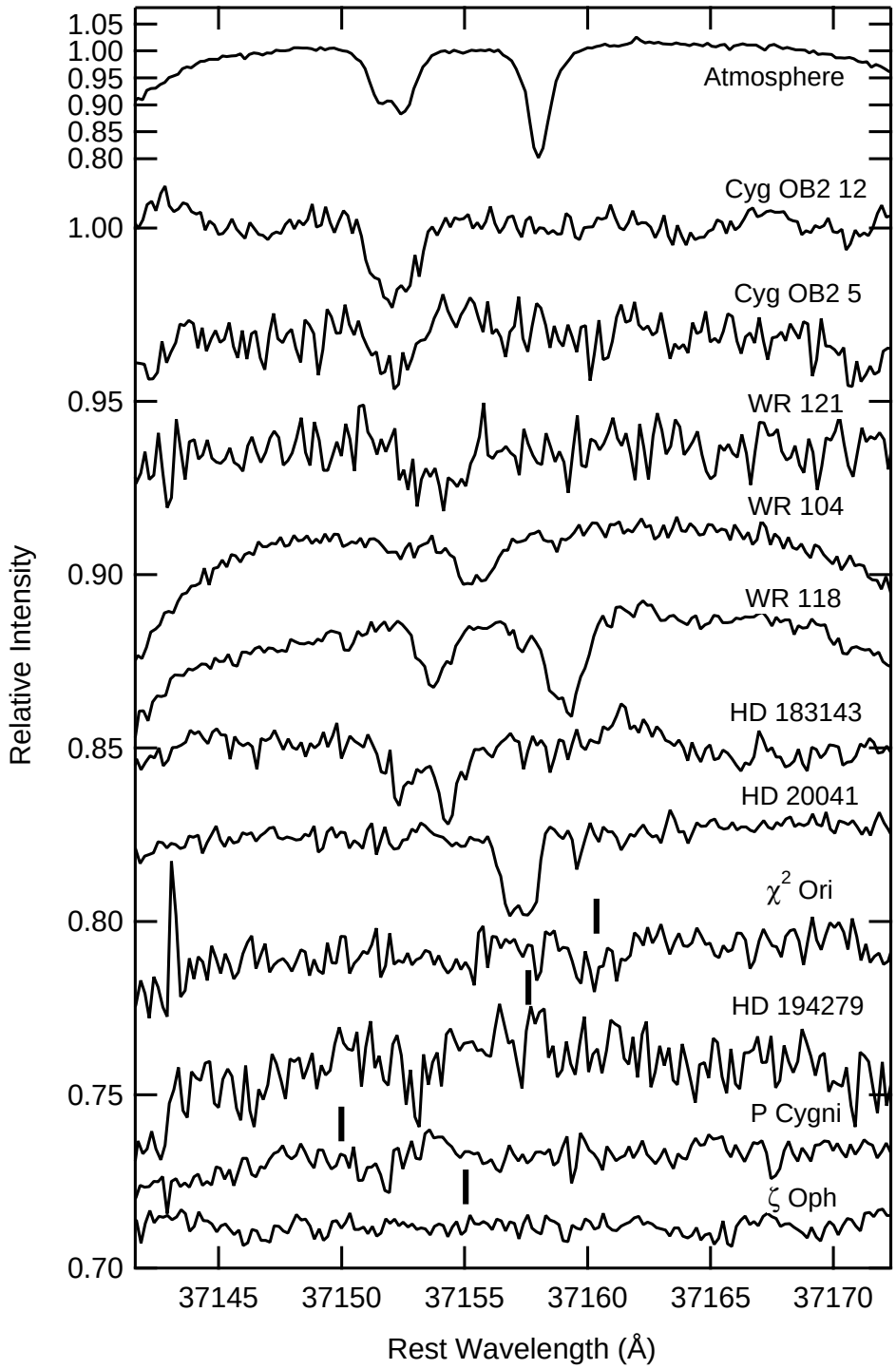

Figure 4.8 Spectra of the H_3^+ $R(1,1)^l$ line observed with Phoenix at Kitt Peak. The vertical bars denote the expected positions of H_3^+ in the sources where the line was not detected.

12.8 from [100], and the absolute magnitude M_V = -4.8 for WC 10 stars [101].

Finally, our 1998 Kitt Peak run yielded a non-detection toward HD 194279, toward which CH is observed with a heliocentric velocity of -11.8 km/s (G. Galazutdinov, private communication). This source, along with the Wolf-Rayet stars, was chosen for study because the 3.4 μm aliphatic carbon feature (a signature of diffuse clouds) had been detected by Pendleton et al. [102].

Our June 2000 run at Kitt Peak yielded the first detection of H_3^+ toward a more traditional diffuse cloud source, HD 183143. Two components of H_3^+ were seen, in agreement with the visible spectra of other molecules (see below), although the blue component was somewhat affected by the telluric CH_4 line. During this run, we also obtained non-detections toward P Cygni (which has an LSR velocity of CH^+ of -9 km/s [103]) and toward ζ Oph (which has an LSR velocity of CO of -0.79 km/s [104]). Our March 2001 run at Kitt Peak yielded a detection of H_3^+ toward the least reddened star to date, HD 20041. We also obtained an upper limit of H_3^+ absorption towards χ^2 Ori.

Our run at UKIRT in July 2000 (see Figure 4.9) confirmed the detections of H_3^+ toward Cygnus OB2 5 and HD 183143. In the case of HD 183143, the two-component velocity structure is very clear. For both the Cygnus OB2 5 and HD 183143 observations, instrumental artifacts were present in the "negative" spectrum — these features changed in intensity (and sometimes disappeared) depending on exactly which rows of the array were extracted, while the H_3^+ features were consistently present. We also obtained a non-detection toward HD 168607 (which has a heliocentric CH velocity of 22 km/s [105]).

A table of the observed H_3^+ line parameters is given in Table 4.6.

CO towards the Cygnus OB2 Association

A brief look at the high resolution infrared spectrum of CO toward Cygnus OB2 12 and Cygnus OB2 5 was obtained during test and engineering time with Phoenix at Kitt Peak in July 1999. Followup observations with longer integration time in June 2000 yielded higher signal-to-noise spectra, displayed in Figure 4.10. The observations

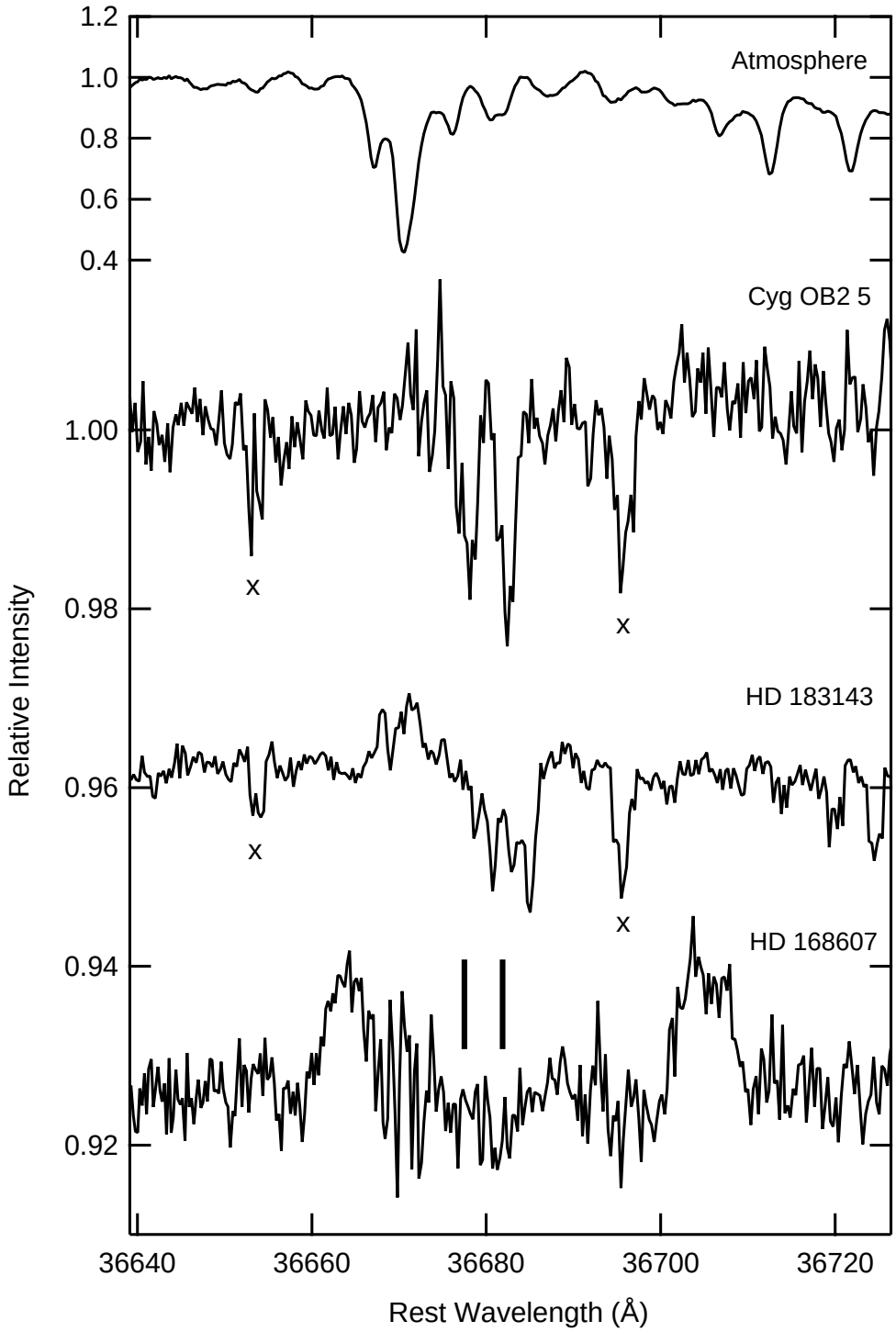

Figure 4.9 Spectra of the H_3^+ $R(1,0)$–$R(1,1)^u$ doublet of H_3^+ observed with CGS4 at UKIRT. The vertical bars denote the expected position of the doublet in HD 168607, and the crosses label instrumental artifacts.

Object	Line	v_{LSR} (km/s)	FWHM (km/s)	W_λ (Å)	$\sigma(W_\lambda)^a$ (Å)	$N(H_3^+)$ (10^{14} cm^{-2})	$\sigma(N)^a$ (10^{14} cm^{-2})
Cyg OB2 12	$R(1,1)^l$	7.0	14.6	0.044	0.002	2.02	0.09
Cyg OB2 5	$R(1,1)^l$	7.3	11.5	0.022	0.003	0.99	0.15
	$R(1,1)^u$	5.6	15.2	0.035	0.004	1.43	0.16
	$R(1,0)$	5.8	15.4	0.048	0.004	1.21	0.10
WR 121	$R(1,1)^l$	9.7	17.8	0.024	0.004	1.12	0.20
WR 104	$R(1,1)^l$	10.9	15.1	0.028	0.002	1.27	0.07
WR 118	$R(1,1)^l$	4.8	9.5	0.019	0.001	0.89	0.06
		47.6	12.3	0.041	0.002	1.88	0.07
HD 183143	$R(1,1)^l$	8.3[d]	10.5	0.020	0.002	0.94	0.08
		23.6	8.4	0.024	0.002	1.10	0.07
	$R(1,1)^u$	7.1	12.2	0.012	0.001	0.50	0.05
		23.4	9.9	0.017	0.001	0.70	0.05
	$R(1,0)$	5.6	14.0	0.022	0.001	0.54	0.03
		22.1	11.0	0.023	0.001	0.59	0.03
HD 20041	$R(1,1)^l$	-0.5	11.5	0.038	0.002	1.74	0.09
HD 194279	$R(1,1)^l$	—	10[b]	—	0.005	—	0.21[c]
P Cygni	$R(1,1)^l$	—	10[b]	—	0.002	—	0.10[c]
ζ Oph	$R(1,1)^l$	—	10[b]	—	0.001	—	0.06[c]
HD 168607	$R(1,1)^u$	—	10[b]	—	0.003	—	0.13[c]
	$R(1,0)$	—	10[b]	—	0.003	—	0.07[c]
χ^2 Ori	$R(1,1)^l$	—	10[b]	—	0.003	—	0.12[c]

[a] Statistical uncertainties (1σ) are listed. Systematic errors (for instance, due to ratioing of telluric lines) are difficult to estimate and may be larger.
[b] Adopted FWHM for purposes of computing upper limits.
[c] The firm upper limit for $N(H_3^+)$ should be considered to be 3σ.
[d] Affected by telluric line.

Table 4.6 H_3^+ Line Parameters.

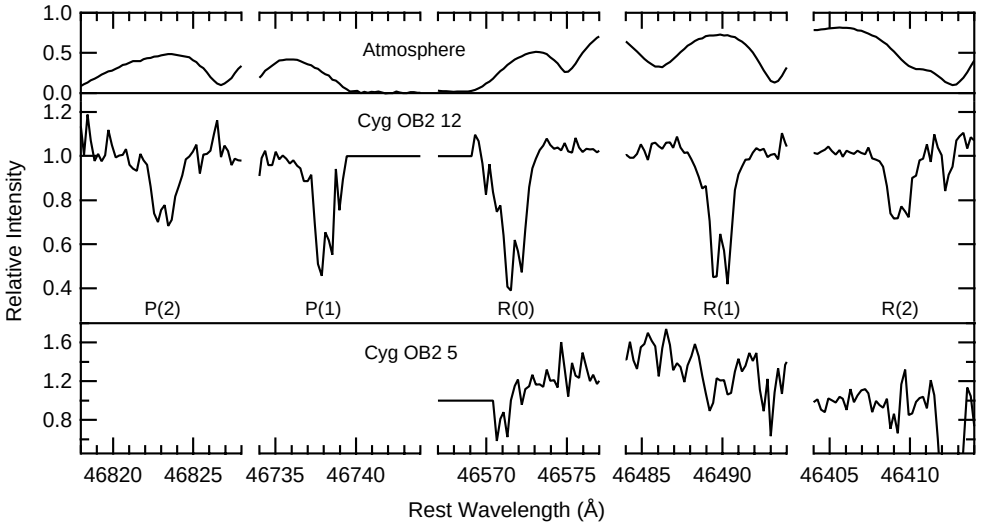

Figure 4.10 Infrared v=1-0 CO spectra obtained with Phoenix at Kitt Peak.

of Cygnus OB2 12 clearly show the two closely-spaced (~ 5 km/s) velocity components reported in the mm-wave spectrum from JCMT [97]. The infrared lines suggest a CO excitation temperature of $\sim$10 K toward Cygnus OB2 12, but this should not be taken as an indication of the kinetic temperature of the gas [97].

The signal-to-noise ratio of the Cygnus OB2 12 spectrum is clearly not high enough to reliably measure the equivalent widths of the individual components, particularly because of the contamination of the telluric lines. However, we can estimate the column density of CO by assuming that the equivalent widths of the two components have the same ratio as the integrated areas of the components in the ^{13}CO emission spectrum, and by adopting the b-values of the ^{13}CO in estimating the saturation corrections. This analysis was performed with the high-quality ^{13}CO spectrum obtained at CSO (shown in Figure 4.11). We assume that the 7 km/s peak carries 0.39 of the equivalent width (and has b=0.75 km/s), and that the 12 km/s peak carries 0.61 of the equivalent width (and has b=0.88 km/s). With these assumptions we estimate a total CO column density of $\sim 1.4 \times 10^{17}$ cm^{-2} in front of Cygnus OB2 12.

This estimate is considerably higher than the estimate of 3×10^{16} cm^{-2} given in [97], but still much lower than the total column density of carbon ($\sim 2.5 \times 10^{18}$ cm^{-2})

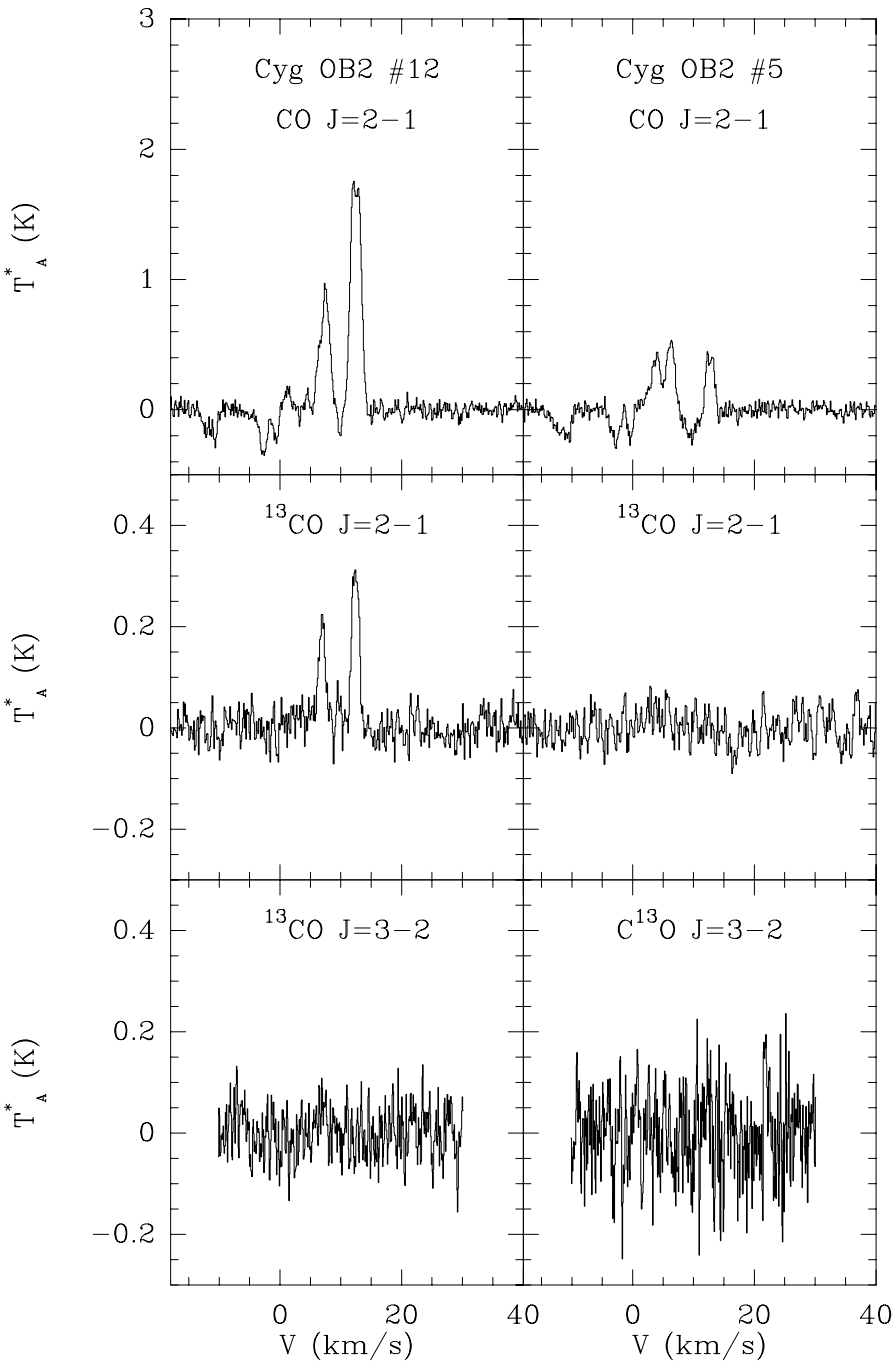

Figure 4.11 CO spectra obtained at CSO.

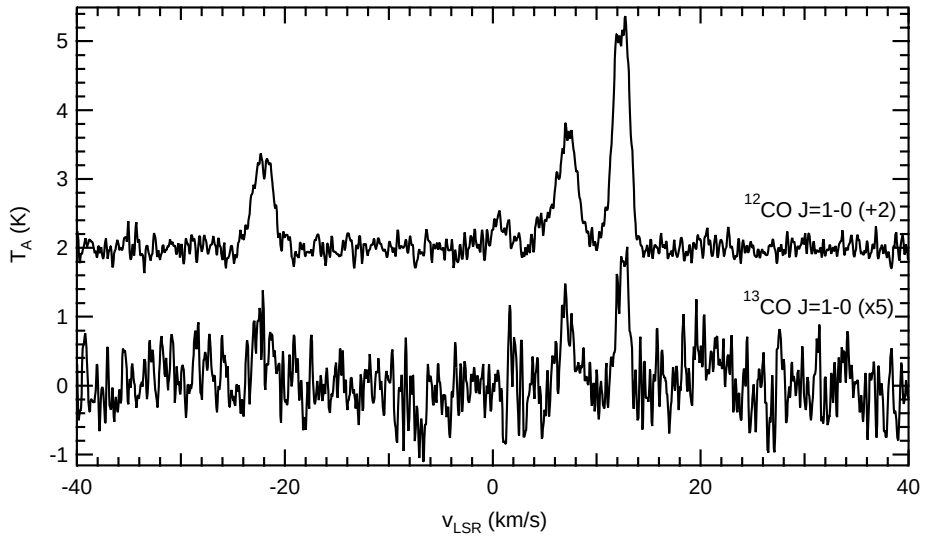

Figure 4.12 CO J=1-0 spectra of Cygnus OB2 12 obtained at NRO.

inferred from the color excess. An independent estimate of the column density can be obtained by assuming the ^{13}CO emission lines are optically thin. Using the NRO data for J=1-0 (see Figure 4.12) and the CSO data for J=2-1 and (an upper limit for) J=3-2, we estimate a total column density of $\sim 8 \times 10^{16}$ cm^{-2} (assuming T$_{ex} \sim$ 10 K).

While these methods are somewhat uncertain, we have obtained an upper limit on the CO column density based on our failure to detect the v=2-0 overtone with Phoenix. The upper limit on the v=2-0 features yield an upper limit (3σ) of N(CO) $\lesssim 3 \times 10^{17}$ cm^{-2}. This suggests that at most about 10% of the carbon along the line of sight to Cygnus OB2 12 can be in the form of CO, and that this sightline does not consist of dense clouds.

The line of sight toward Cygnus OB2 5 appears to have considerably less CO than that toward Cygnus OB2 12, based both on the marginal detections in the infrared spectrum (Figure 4.10) as well as the CSO ^{13}CO spectra (Figure 4.11). Therefore we expect that this sightline is also dominated by diffuse cloud material, although because of the low signal-to-noise of the infrared spectrum it is difficult to estimate the CO column density.

In order to probe the spatial extent of the CO gas in the Cygnus OB2 association, we have obtained ^{12}CO J=1-0 spectra at four other locations in the association, labelled A through D in Table 4.5 and Figure 4.13, which also shows the spectra toward Cygnus OB2 12 and 5.

CO towards HD 183143

Since our detection of H_3^+ toward HD 183143, we have not had an opportunity to obtain a spectrum of the infrared v=1-0 fundamental band of CO in this direction. However, a previously obtained Phoenix spectrum of the v=2-0 overtone band (from June 1997) provides an upper limit of $\sim 10^{17}$ cm^{-2}. To check for the presence of CO in this sightline, we have obtained rotational spectra of the J=2-1 line (at JCMT) and the J=1-0 line (at NRO). The JCMT results (frequency-switched at 8 MHz and 16 MHz) are shown in Figure 4.14. While the J=2-1 spectrum of Cygnus OB2 12 showed nearly 2 K of emission at the H_3^+ velocity, the spectrum of HD 183143 shows no emission at the correct velocites in excess of $\sim$ 0.1 K. The NRO results are shown in Figure 4.15, and provide an upper limit of $\sim$ 0.2 K for the J=1-0 emission at the observed H_3^+ velocities. The closest reasonable velocity component is at +25 km/s, and is only about 0.5 K. In contrast, Cygnus OB2 12 shows 3 K of emission. Overall, these results demonstrate that there is very little CO associated with the H_3^+ toward HD 183143.

C_2 Spectra

The C_2 A-X v=2-0 band was clearly detected toward Cygnus OB2 12 at McDonald, as shown in Figure 4.16. Each line appears as a clear doublet with a separation comparable to that of the CO, except for the $Q(8)$ line which is blended with $P(4)$. The equivalent widths were measured separately for the two velocity components, except for the $Q(8) + P(4)$ blend, for which only the total equivalent width could be measured. The contribution of $P(4)$ was estimated from the strength of $Q(4)$, which permitted an estimate of the $Q(8)$ equivalent width for the sum of the two velocity components. The $Q(10)$ line was contaminated by a telluric absorption line, and the

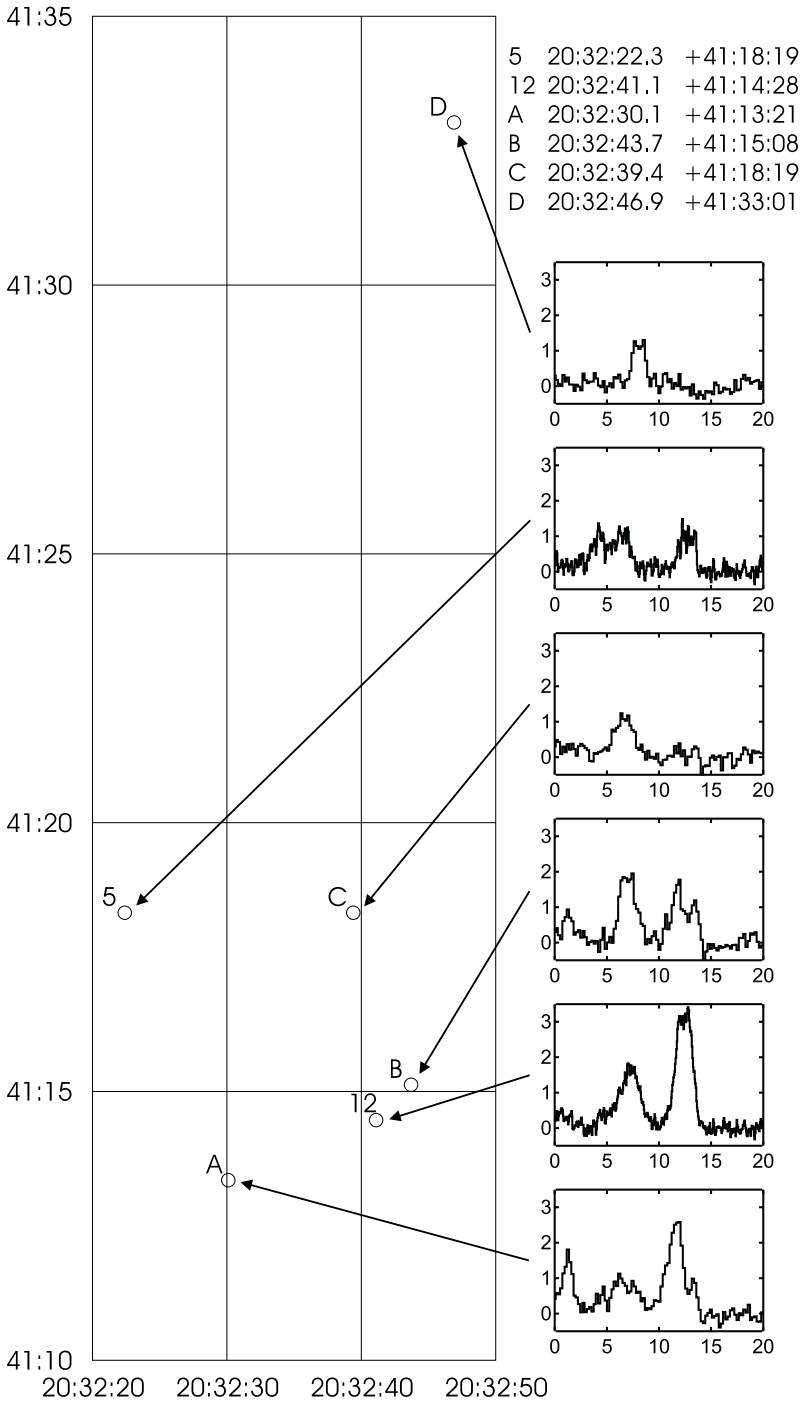

Figure 4.13 CO J=1-0 "map" of the Cygnus OB2 association obtained at NRO. Spectra have T_A^* (K) as vertical axis, v_{LSR} (km/s) as horizontal axis. All coordinates are J2000.

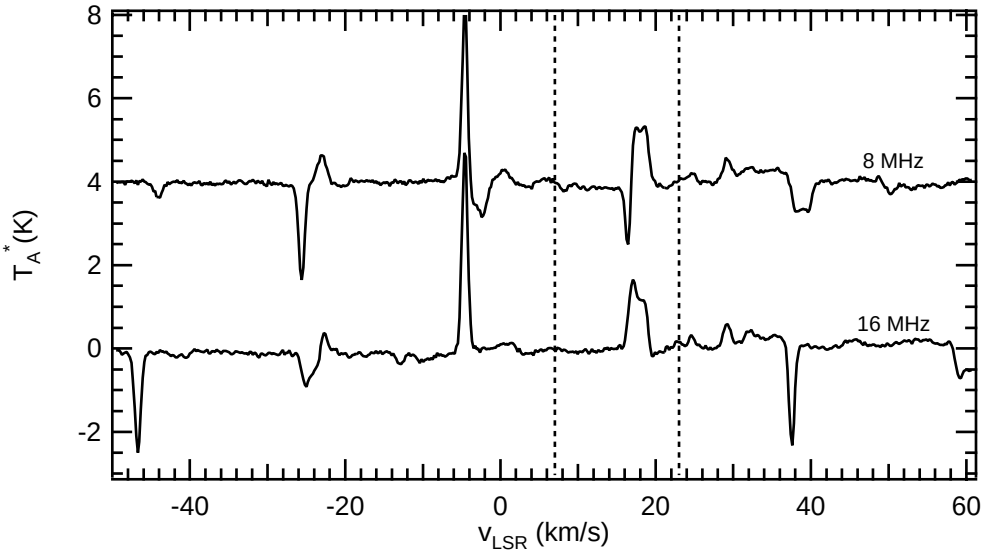

Figure 4.14 ^{12}CO J=2-1 frequency switched spectra toward HD 183143, obtained at JCMT. The velocities of the H_3^+ lines are marked with vertical dashed lines.

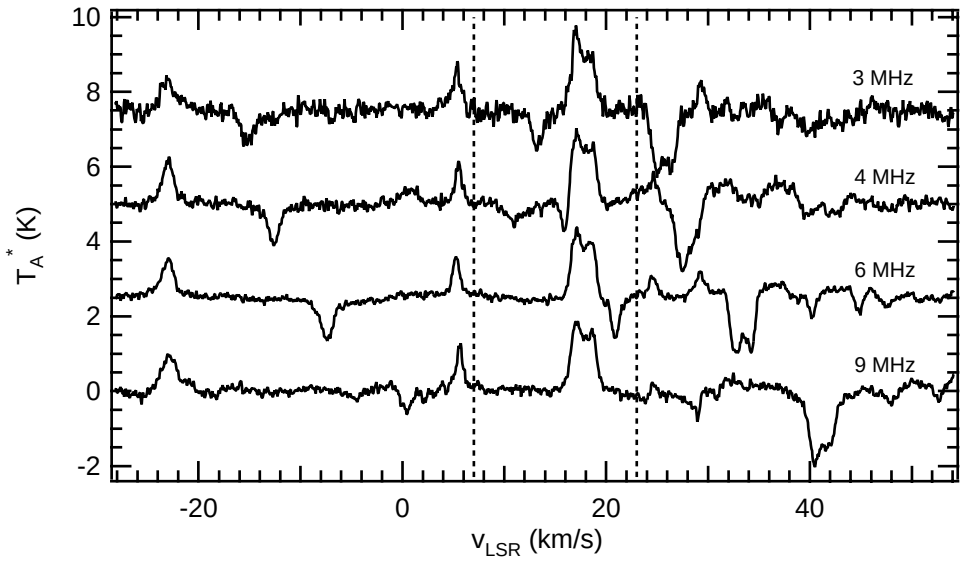

Figure 4.15 ^{12}CO J=1-0 frequency switched spectra toward HD 183143, obtained at Nobeyama. The velocities of the H_3^+ lines are marked with vertical dashed lines.

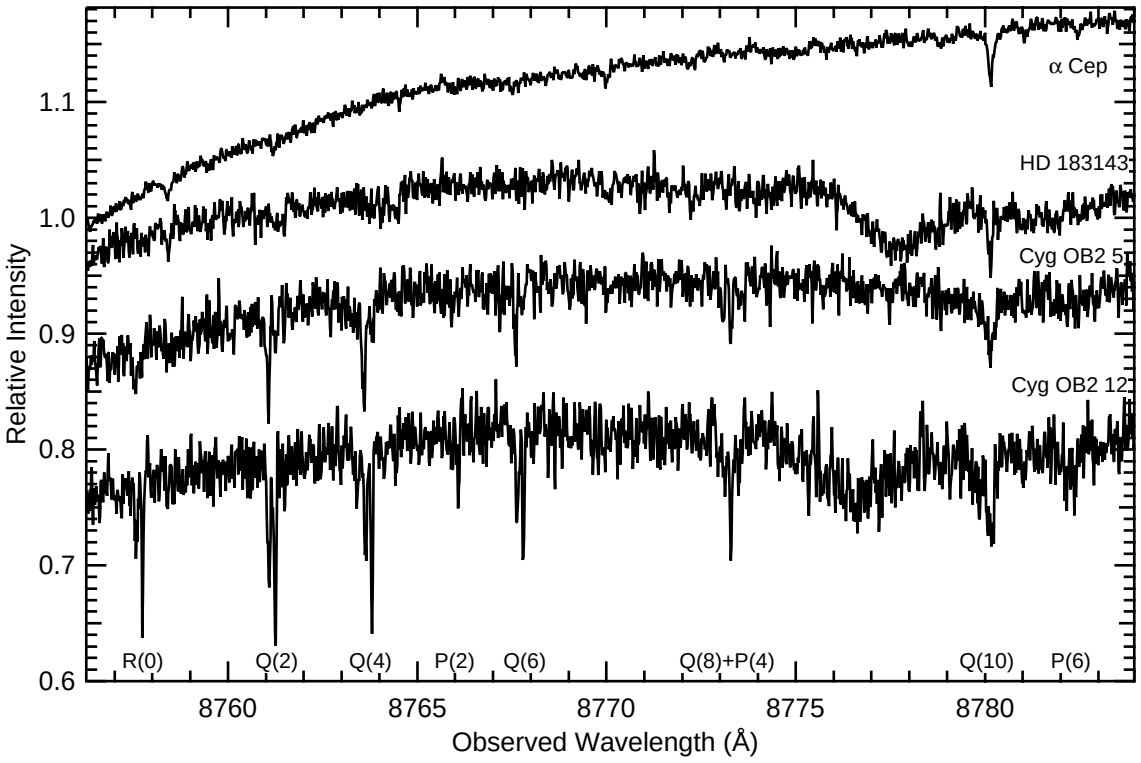

Figure 4.16 Spectra of the A-X v=2-0 band of C_2 obtained at McDonald.

spectra were ratioed by that of α Cep in order to remove the contribution of the telluric line. The derived C_2 line parameters (for each component separately, as well as for the total profile) for Cygnus OB2 12 are listed in Table 4.7. Column densities have been determined assuming the lines are optically thin.

Using the method of van Dishoeck and Black [106], and assuming the scaling factor for the radiation field $I = 1$ and the C_2–H_2 collisional cross-section $\sigma_0 = 2 \times 10^{-16}$ cm^2, we can estimate the number density n of collision partners, as well as the kinetic temperature T. For the 7 km/s component, we obtain a best fit value of (n,T)=(220 cm^{-3}, 40 K), and for the 12 km/s component we obtain (210 cm^{-3}, 30 K). Using the total column densities rather than those of the individual components yields (200 cm^{-3}, 30 K). These values are fairly well constrained by the observational data — it is exceedingly unlikely (i.e. it requires more than a 3σ error in at least one of

Line	$W_\lambda^{1\ a}$ (mÅ)	$N(J)^1$ (10^{12} cm^{-2})	v_{LSR}^1 (km/s)	$FWHM^1$ (km/s)	$W_\lambda^{2\ a}$ (mÅ)	$N(J)^2$ (10^{12} cm^{-2})	v_{LSR}^2 (km/s)	$FWHM^2$ (km/s)	$W_\lambda^{tot\ a}$ (mÅ)	$N(J)^{tot}$ (10^{12} cm^{-2})
$R(0)$	4.96 ± 0.60	4.38 ± 0.53	6.7	2.8	6.87 ± 0.46	6.06 ± 0.41	12.6	1.7	11.83 ± 0.76	10.4 ± 0.7
$Q(2)$	9.91 ± 0.83	17.5 ± 1.5	6.7	3.1	10.67 ± 0.70	18.8 ± 1.2	12.4	2.2	20.58 ± 1.09	36.3 ± 1.9
$Q(4)$	8.97 ± 0.75	15.8 ± 1.3	6.6	3.2	9.65 ± 0.59	17.0 ± 1.0	12.3	2.0	18.62 ± 0.95	32.8 ± 1.7
$P(2)$	2.05 ± 0.60	—	6.8	2.0	3.38 ± 0.55	—	12.6	1.7	5.43 ± 0.81	—
$Q(6)$	7.40 ± 0.66	13.0 ± 1.2	6.6	3.1	7.33 ± 0.53	12.9 ± 0.9	12.2	2.0	14.73 ± 0.85	25.9 ± 1.5
$\left\{ \begin{matrix} Q(8) \\ P(4) \end{matrix} \right\}$	—	—	—	—	—	—	—	—	19 ± 2^b	—
$P(4)^c$	—	—	—	—	—	—	—	—	6 ± 0.3	—
$Q(8)^d$	—	—	—	—	—	—	—	—	13 ± 2^b	22.3 ± 5.2
$Q(10)$	3.9 ± 0.6	6.6 ± 1.2	$(6.7)^e$	$(3)^e$	3.0 ± 0.5	5.3 ± 1.5	$(12.5)^e$	$(2.1)^e$	6.9 ± 0.8	11.9 ± 2.0

[a] Statistical uncertainties (1σ) are listed unless otherwise noted. Systematic errors are difficult to estimate and may be larger.
[b] Estimate of systematic uncertainty.
[c] Estimated from $Q(4)$.
[d] Blend equivalent width minus $P(4)$ estimate.
[e] Values constrained in the fit to the ratioed spectrum.

Table 4.7 C_2 Line Parameters (components labelled as 1 and 2) for Cygnus OB2 12.

Line	W_λ [a] (mÅ)	N(J) (10^{12} cm^{-2})
$R(0)$	6.6 ± 0.8	5.8 ± 0.7
$Q(2)$	10.7 ± 1.0	18.9 ± 1.8
$Q(4)$	13.5 ± 1.0	23.8 ± 1.8
$Q(6)$	8.0 ± 1.2	14.1 ± 2.1
$\left\{ \begin{matrix} Q(8) \\ P(4) \end{matrix} \right\}$	11 ± 3[b]	—
$P(4)$[c]	4.5 ± 0.3	—
$Q(8)$[d]	7 ± 3[b]	12.3 ± 5.3
$Q(10)$[e]	1.5 ± 0.5	2.6 ± 0.9

[a] Statistical uncertainties (1σ) are listed unless otherwise noted. Systematic errors are difficult to estimate and may be larger.
[b] Estimate of systematic uncertainty.
[c] Estimated from $Q(4)$.
[d] Blend equivalent width minus $P(4)$ estimate.
[e] Marginal feature; values very uncertain.

Table 4.8 C_2 Line Parameters for Cygnus OB2 5.

the measurements) that the density is outside the range 150–600 cm^{-3} or that the temperature is outside the range 25–55 K.

The spectrum of Cygnus OB2 5 also shows a hint of the doublet structure, but the signal-to-noise of the spectrum is not sufficient to reliably measure the equivalent widths of the individual components. Therefore we have measured only the total equivalent widths, which are reported in Table 4.8. An analysis of the rotational excitation (while very uncertain) suggests that the density exceeds 800 cm^{-3} and that the temperature lies in the range 60–90 K. According to Gredel & Münch [107], chemical models predict a sudden decrease in C_2 abundance at densities above $10^{3.5}$ cm^{-3}. Taken with our (uncertain) results, this suggests that the density in the region where C_2 is found is in the range 800–3000 cm^{-3}.

In agreement with the results of Gredel [105], we saw absolutely no trace of C_2 towards HD 183143. Assuming the $Q(2)$ line would have a width of $\sim$ 5 km/s, the 3σ limit on the equivalent width is about 1.7 mÅ, which corresponds to a column density of N(J=2) $\lesssim 3 \times 10^{12}$ cm^{-2} (comparable to Gredel's upper limit), which is more than ten times less than that of Cygnus OB2 12!

Object	Species	Line	v_{LSR} (km/s)	FWHM (km/s)	W_λ [a] (mÅ)	N [a] (10^{12} cm^{-2})
Cyg OB2 5	CH	4300	5.6	6.0	26.5 ± 0.7	44.0 ± 1.2 [b]
			12.7	3.4	7.1 ± 0.5	9.2 ± 0.6 [b]
HD 183143	CH	4300	7.7	7.7	12.3 ± 0.7	17.0 ± 1.0 [b]
			23.6	4.9	18.6 ± 0.6	27.7 ± 0.9 [b]
Cyg OB2 5	CH^+	4232	2.6	5.0	11.2 ± 0.6	12.8 ± 0.7
			7.6	4.1	7.1 ± 0.6	8.1 ± 0.7
			13.3	8.9	11.8 ± 0.8	13.5 ± 0.9
HD 183143	CH^+	4232	9.0	4.9	18.3 ± 0.5	21.0 ± 0.6
			24.8	4.5	22.1 ± 0.5	25.3 ± 0.6
Cyg OB2 12	CN	A-X $R_2(0)$	6.8	1.1	1.3 ± 0.4	1.6 ± 0.5
			12.4	1.7	4.3 ± 0.6	5.2 ± 0.7
Cyg OB2 5	CN	A-X $R_2(0)$	5.6	2.0	1.2 ± 0.3	1.5 ± 0.4
			13.7	1.7	1.4 ± 0.3	1.7 ± 0.4
		B-X R(0)	5.6	3.9	4.1[c]	0.9[c]
			12.1	3.9	2.8[c]	0.6[c]
HD 183143	CN	B-X R(0)	25.2	2.5	5.6 ± 0.4	1.3 ± 0.1
		B-X R(1)	24.1	1.5	1.2 ± 0.2	0.4 ± 0.1

[a] Statistical uncertainties (1σ) are listed unless otherwise noted. Systematic errors are difficult to estimate and may be larger.
[b] Estimated using the CH curve of growth of van Dishoeck & Black [108], assuming b=1 km/s. All other column densities computed assuming the lines are optically thin.
[c] These values are extremely uncertain due to the low flux of Cygnus OB2 5 at violet wavelengths.

Table 4.9 Line Parameters for CH, CH^+, and CN.

Other Visible Spectra

The results of our high resolution visible spectroscopy are shown in Figure 4.17 (HD 183143), Figure 4.18 (Cygnus OB2 5), and Figure 4.19 (Cygnus OB2 12). These figures are plotted in velocity (with respect to the local standard of rest), and also display the infrared measurements of H_3^+ and CO.

CH appears as a doublet in Cygnus OB2 5, with velocities consistent with the infrared CO measurements. CH also appears as a doublet in HD 183143, with remarkably similar velocity structure to the H_3^+. The blue wavelength (4300 Å) of the CH transition made it inaccessible in the case of Cygnus OB 12 (which is very heavily reddened), but it may be possible to detect the line with a larger telescope such as the Hobby-Eberly Telescope. The line parameters of CH (as well as CH^+ and CN) are listed in Table 4.9. The CH column densities have been derived using the curve of growth of van Dishoeck & Black [108], assuming b=1 km/s.

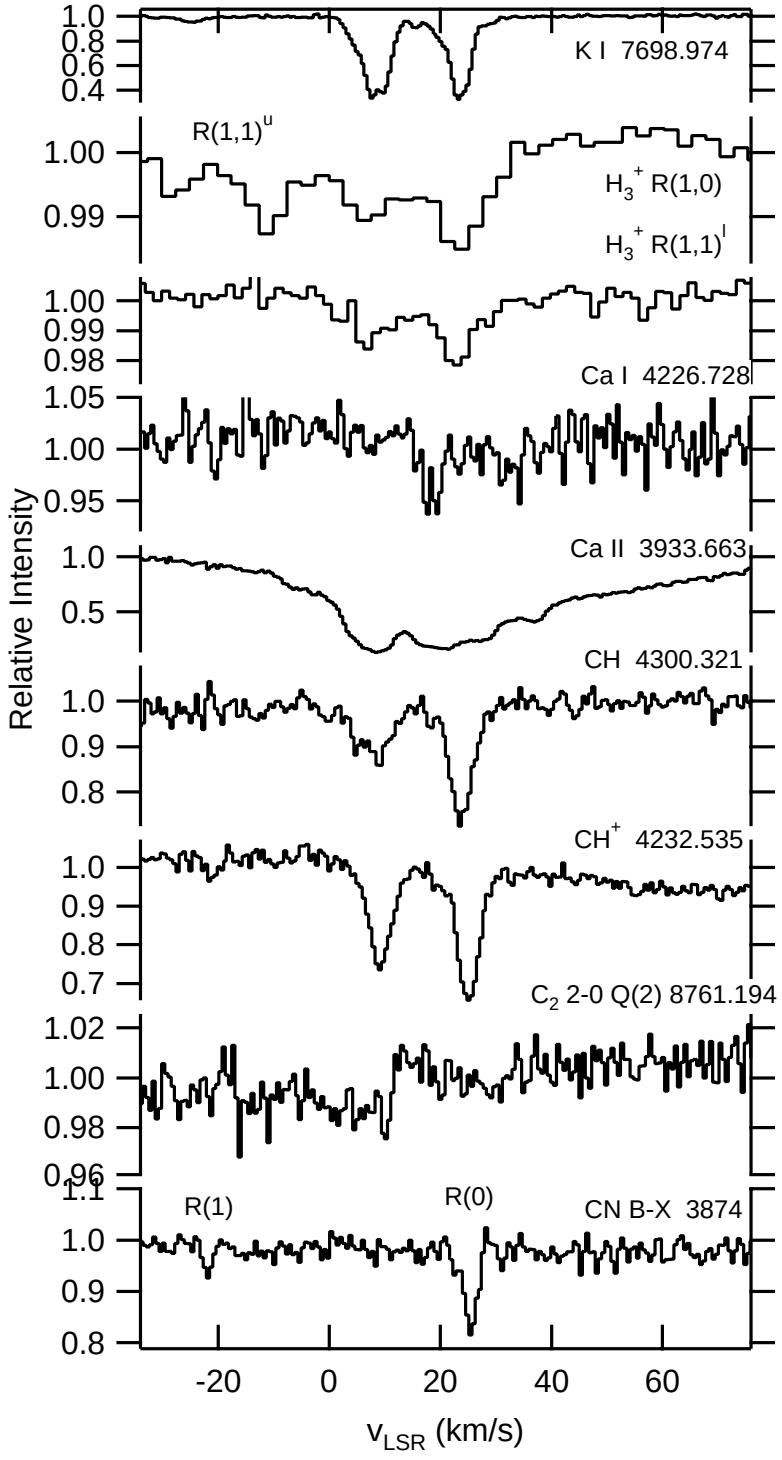

Figure 4.17 Summary of spectra of HD 183143, in velocity space.

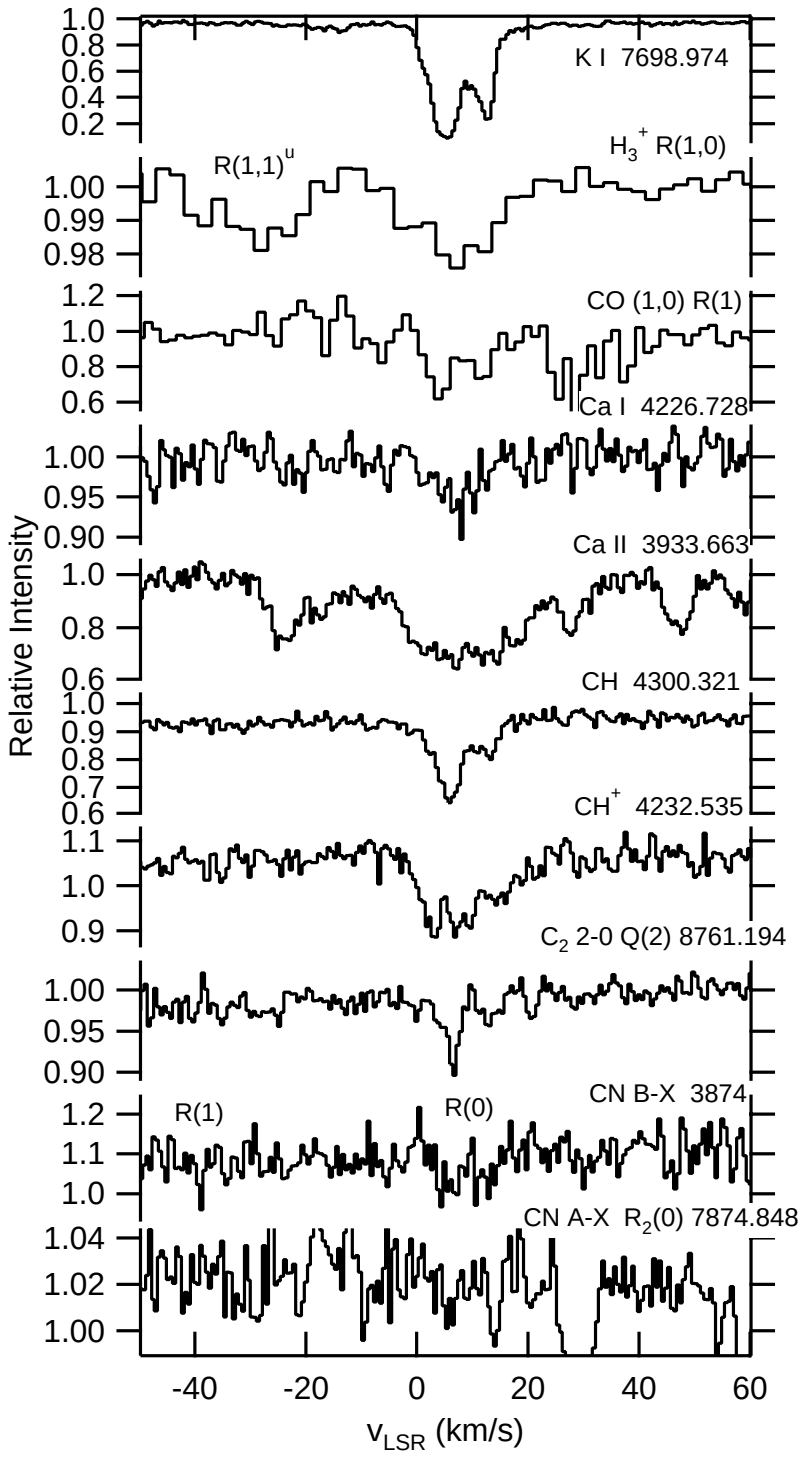

Figure 4.18 Summary of spectra of Cyg OB2 5, in velocity space.

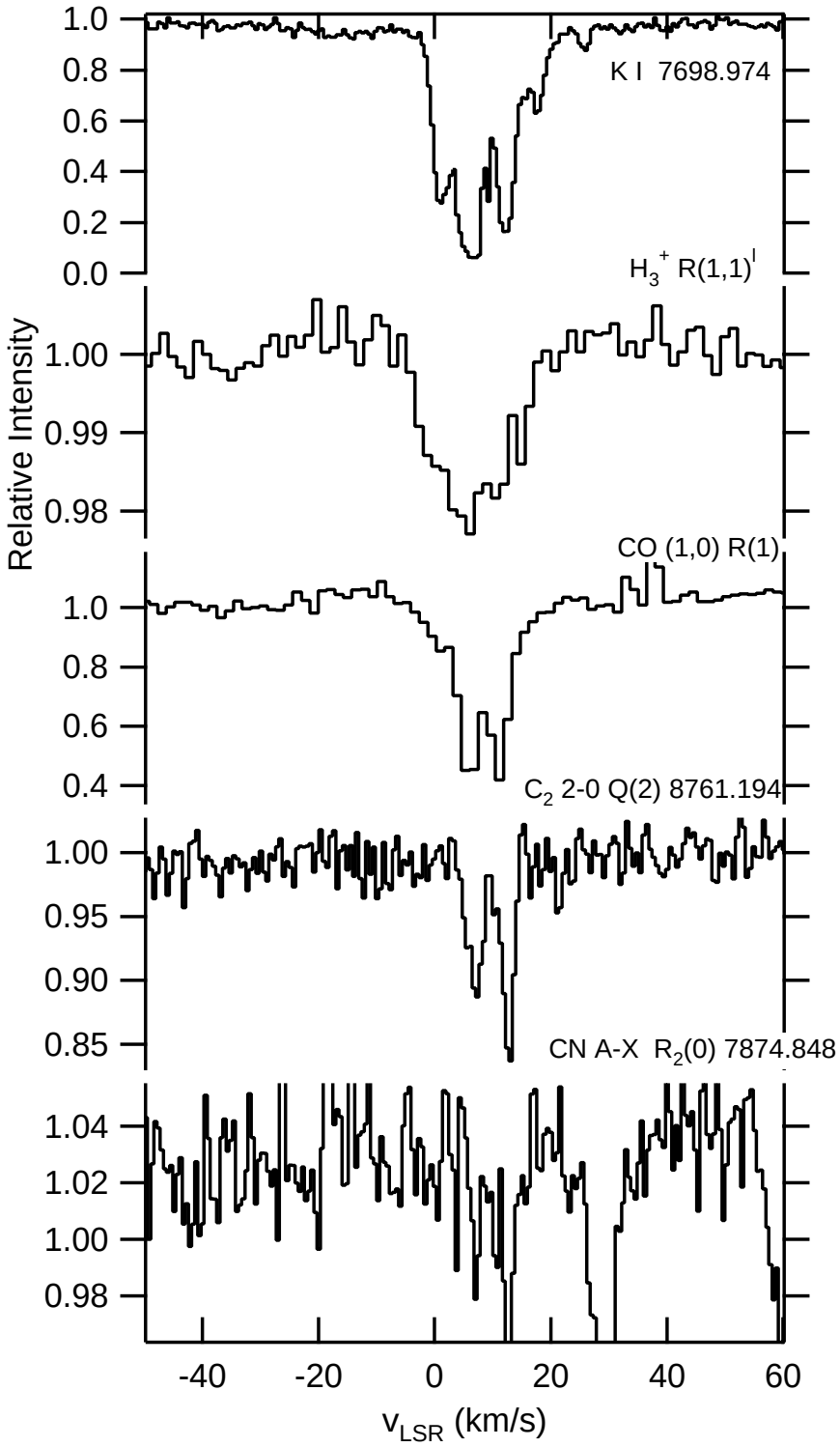

Figure 4.19 Summary of spectra of Cyg OB2 12, in velocity space.

It is interesting to compare the observed CH column densities with those which would be predicted from the empirical relation between H_2 and CH [109]:

$$N(H_2) = 2.1 \times 10^7 N(CH) + 2.2 \times 10^{20} cm^{-2}$$

For HD 183143, E(B-V)=1.2, so $N_H \sim 7 \times 10^{21}$ (assuming the standard gas-to-dust conversion factor [70]), and (if $f \equiv 2N(H_2)/[N(H)+2N(H_2)] = 2/3$) $N(H_2) \sim 2.3 \times 10^{21}$ cm^{-2}. From the empirical relation, one would then predict $N(CH) \sim 1.0 \times 10^{14}$, roughly twice the observed value. For Cygnus OB2 5, with E(B-V) = 2.1, we estimate $N(H_2) \sim 4 \times 10^{21}$ and therefore $N(CH) \sim 1.8 \times 10^{14}$ cm^{-2}, over three times the observed value. Assuming our choice of b-value is not too large, this suggests that these two sources may be somewhat different chemically from the usual diffuse cloud sources used to develop the empirical relation. However, this discrepancy may not indicate a drastic departure in chemical conditions, as other sources with lower color excess have been observed with similar departures from the empirical relations [110].

Another interesting molecule is CN: it is observed (marginally) as a doublet in both Cygnus OB2 12 (A-X) and in Cygnus OB2 5 (A-X and B-X). However, only one component (at $v_{LSR} \sim 25$ km/s) is observed toward HD 183143 — whereas H_3^+ and CH have two velocity components! The R(1) line is also detected toward HD 183143, and the population of the $J = 0$ and $J = 1$ levels are consistent with the temperature of the cosmic microwave background.

Finally, it is worth noting that, at least in the case of Cygnus OB2 12 (Figure 4.19), the velocity profile of H_3^+ is more similar to that of K I than to C_2, CN, or CO. This could be because these diatomic molecules are concentrated in the denser regions of the sightline, whereas H_3^+ (and K I) may exist over a larger path length.

4.3.4 Discussion

Model of H_3^+ Chemistry in Diffuse Clouds

The formation of H_3^+, in dense or diffuse clouds, begins with the (cosmic ray induced) ionization of H_2 to form H_2^+. The generally assumed rate of ionization is $\zeta \sim 3 \times 10^{-17}$

s^{-1}, so that the average H_2 gets ionized roughly once every 10^9 years. Once ionized, the H_2^+ quickly reacts with another H_2 to form H_3^+ and an H atom. This ion-neutral reaction proceeds with the Langevin rate constant of 2×10^{-9} cm^3 s^{-1}, so that in a medium of H_2 density 100 cm^{-3}, the average H_2^+ must wait about 2 months to react to form H_3^+. Clearly the initial ionization is the rate-limiting step, so we can say that H_3^+ is formed at a rate of ζ n(H_2).

The destruction of H_3^+ is very different in diffuse clouds, compared to dense clouds. In dense clouds, the dominant destruction path is an ion-neutral reaction with CO, with a rate constant of $\sim 2 \times 10^{-9}$ cm^3 s^{-1}. In diffuse clouds, electrons are very abundant (due to photoionization of C), so dissociative recombination dominates, with a rate constant of $k_e = 4.6 \times 10^{-6}\ T_e^{-0.65}$ cm^3 s^{-1} [81].

Although the electrons produced by photoionization are probably formed at a high temperature (photons are available at energies up to 13.6 eV, and the ionization potential of C is only 11.3 eV), they will be quickly thermalized by collisions with H_2. Such collisions will occur with a Langevin rate constant (which scales as $\mu^{-1/2}$, where μ is the reduced mass) of $\sim 8 \times 10^{-8}$ cm^3 s^{-1} — in a medium with n(H_2) = 100 cm^{-3}, an electron experiences such a collision about once per day. The lifetime of the electron is limited by radiative recombination with C^+ ions, which occurs with a rate constant of $\alpha \sim 2 \times 10^{-11}$ cm^3 s^{-1} [111] at the low temperatures ($\sim$30 K) of diffuse clouds. If n(C^+) = 10^{-2} cm^{-3}, the average electron lifetime is about 10^5 years. Evidently the electrons will be very quickly thermalized to the kinetic temperatures of the clouds, the H_3^+ electron recombination rate constant will be $k_e \sim 5 \times 10^{-7}$ cm^3 s^{-1}, and the destruction rate of H_3^+ can be given as $k_e\ n(H_3^+)\ n(e)$.

To calculate the number density of H_3^+ [98, 97], we make the steady-state approximation that the rates of formation and destruction are equal. Thus,

$$\zeta n(H_2) = k_e n(H_3^+) n(e)$$

which can be rearranged to give

$$n(H_3^+) = \frac{\zeta}{k_e} \frac{n(H_2)}{n(e)}$$

The chemistry of H_3^+ is unique in the sense that the number density of H_3^+ is not dependent upon the number density of the cloud, but only on the ratio of the number densities of molecular hydrogen and electrons (as well as the ratio of two constants ζ/k_e). We can further simplify the above equation by considering f, the fraction of protons in H_2, writing $n(H_2) = \frac{f}{2}[2n(H_2) + n(H)] = \frac{f}{2}n(\Sigma H)$. Since most electrons are formed from the ionization of carbon, we can also write $n(e) = (1-\alpha)n(\Sigma C)$, where α is the fraction of carbon in un-ionized (neutral or molecular) form. Finally, the gas-phase ratio of carbon atoms to hydrogen atoms is usually defined as $z_C \equiv n(\Sigma C)/n(\Sigma H)$. Putting this all together, we find

$$n(H_3^+) = \frac{\zeta}{k_e}\ \frac{f}{2}\ \frac{1}{1-\alpha}\ \frac{1}{z_C} \tag{4.7}$$

Adopting the values $\zeta = 3 \times 10^{-17}$ s^{-1}, $k_e = 5 \times 10^{-7}$ cm^3 s^{-1}, $f = 2/3$, $\alpha \sim 0$, and $z_C = 1.4 \times 10^{-4}$ [112, 113], we obtain

$$n(H_3^+) = 1.4 \times 10^{-7}\ \text{cm}^{-3} \tag{4.8}$$

The validity of the steady-state approximation can be checked by comparing the timescale needed to reach steady-state with other relevant timescales. The timescale needed to achieve steady-state is approximately the steady state number density of H_3^+ divided by the formation rate, or $\frac{n(H_3^+)}{\zeta n(H_2)}$, which for n($H_2$) = 100 cm^{-3} is about one year — clearly much shorter than other relevant timescales!

Inferred Cloud Parameters

One cloud parameter can be determined from the H_3^+ observations independent of the chemical model — the kinetic temperature of the gas. This is possible because the *ortho* ($J = 1$,$K = 0$) and *para* ($J = 1$,$K = 1$) levels of H_3^+ are efficiently thermalized together through proton hop and proton exchange reactions with H_2 [114]. These reactions occur with the Langevin rate constant of 2×10^{-9} cm^3 s^{-1}, so that the average H_3^+ experiences such a reaction about every two months (assuming $n(H_2) =$ 100 cm^{-3}). The lifetime of the average H_3^+ can be estimated from the dissociative

recombination rate k_e and the number density of electrons $n(e) \sim 10^{-2}$ cm^{-3} to be about 4.5 years, considerably longer than the thermalization timescale. Therefore, we can use the Boltzmann expression

$$\frac{N_{ortho}}{N_{para}} = \frac{g_{ortho}}{g_{para}} e^{-\frac{\Delta E}{kT}} = 2e^{-\frac{32.87}{T}}$$

to estimate the kinetic temperature from the observed *ortho:para* ratio (in this equation, the g values are the statistical weights). For Cygnus OB2 12, we obtain T=27 K [98]; for Cygnus OB2 5, 47 K; and for HD 183143, 31 K.

Given our calculated number density of H_3^+ from the chemical model, we can now estimate the path length of absorption, using the relation $L = N(H_3^+)/n(H_3^+)$. Once the path length has been calculated, we can then estimate the average number density along the path length as $\langle n \rangle = [N(H_2) + N(H)]/L$, where $N(H_2)$ and $N(H)$ can be estimated from the color excess and an assumed value of f (2/3). The results of this analysis are given in Table 4.10.

In most cases, the derived pathlengths are a substantial fraction of the estimated distance to the star, which seems difficult to accept. In addition, the derived average number densities (for the sources in which H_3^+ was detected) are in the range 1–5 cm^{-3}, which seems unreasonably low. These densities are nearly two orders lower than than the densities typically derived from the rotational excitation of C_2. In addition, these densities are so low that a substantial fraction of H_2 should be photodissociated, meaning that our value of $f = 2/3$ should be lowered, which would in turn make the H_3^+ number density even smaller, the path lengths even longer, and the average density even lower.

It seems clear that there is a serious problem with the model, and that $n(H_3^+)$ must be larger (probably by at least one order of magnitude) than we have calculated. In the next subsection, we explore possible solutions to this problem.

Object	$N(H_3^+)$ (10^{14} cm^{-2})	L (pc)	d (pc)	E(B-V) (mag)	$N(H_2) + N(H)$ (10^{21} cm^{-2})	$\langle n \rangle$ (cm^{-3})
Cyg OB2 12	3.8[a]	905	1700[b]	3.35[c]	12.95	4.8
Cyg OB2 5	2.6[d]	629	1700[b]	1.99[c]	7.69	4.1
HD 183143	2.3[d]	552	1000[e]	1.28[f]	4.95	3.0
HD 20041	3.5[g]	833	1400[e]	0.70[h]	2.71	1.1
WR 121	2.2[g]	524	1690[i]	1.68[j]	6.50	4.1
WR 104	2.5[g]	595	1300[i]	2.10[j]	8.12	4.5
WR 118	5.5[g]	1310	6300[i]	4.13[j]	15.97	4.1
HD 194279	<1.2[g]	<286	1100[e]	1.22[f]	4.72	>5.5
HD 168607	<0.6	<143	1100[e]	1.61[f]	6.23	>14.5
P Cygni	<0.6[g]	<143	1800[k]	0.63[k]	2.44	>5.7
χ^2 Ori	<0.7[g]	<171	1000[e]	0.44[l]	1.70	>3.3
ζ Oph	<0.4[g]	<86	140[m]	0.32[f]	1.24	>4.8

[a] From McCall *et al.* [98].
[b] Torres-Dodgen, Carroll, & Tapia [115].
[c] From Schulte [116].
[d] The UKIRT observations of $R(1,0)$ and $R(1,1)^u$ are adopted for these sources.
[e] Our estimate (spectroscopic parallax).
[f] From Snow, York, & Welty [117].
[g] Total H_3^+ column density estimated to be twice that of *para*-H_3^+.
[h] Racine [118].
[i] Smith, Shara, & Moffat [101].
[j] From Pendleton *et al.* [102], assuming $R_V = A_V$ / E(B-V) = 3.1.
[k] From Lamers *et al.* [119].
[l] From the intrinsic color of Wegner [120].
[m] From Hipparcos catalog [121].

Table 4.10 Inferred Cloud Parameters.

Possible Solutions

The equation for the number density of H_3^+

$$n(H_3^+) = \frac{\zeta}{k_e} \frac{f}{2} \frac{1}{1-\alpha} \frac{1}{z_C} \tag{4.9}$$

contains five parameters: the H_2 ionization rate (ζ), the dissociative recombination rate (k_e), the fraction of protons in molecular form (f), the fraction of carbon atoms that are not ionized (α), and the gas phase carbon fraction (z_C). We now consider each one of these parameters in more detail.

The fraction of protons in molecular form (f) has been assumed to have the value 2/3, which is the largest value found in the studies of molecular and atomic hydrogen by Copernicus, IUE, and FUSE. The maximum value of f is 1, so even making this adjustment (as is done in the model of Cecchi-Pestellini & Dalgarno [99]) will only increase $n(H_3^+)$ by a factor of 1.5 — hardly enough to fix the problem.

The gas phase carbon fraction (z_C) has been taken to be 1.4×10^{-4} based on ultraviolet observations of classical diffuse clouds [112, 113]. Lowering this value (for instance, by assuming that a larger fraction of the carbon is depleted onto grains) would reduce the number density of electrons and therefore increase the number density of H_3^+. However, there is no astronomical evidence to support the magnitude of depletion necessary to mitigate the H_3^+ problem.

The fraction of carbon that is not ionized (α) has been assumed to be near zero. It is conceivable that a substantial fraction of the carbon could be in the form of neutral C atoms (rather than C^+), and there is no observational evidence (in these particular sightlines) that requires most of the carbon to be ionized. However, chemical models of translucent clouds (see, for example, Figure 9 of van Dishoeck & Black [122]) suggest that when the optical depth has increased to the point where $n(C)=n(C^+)$, over 10% of the carbon atoms are already in the form of CO. Taken along with our observations of a low column density of CO in these sightlines, this suggests that α must be less than 0.5, and thus could contribute at most a factor of 2 towards increasing the H_3^+ column density. The lack of a substantial change in the C^+ abundance is also supported by our observations of CH, which is not much less abundant than usual in

diffuse clouds — since CH is produced from C^+, this also suggests that α must not be too large.

Along the same lines, one might speculate about the possibility of an "electron sink" in these sightlines, so that C could still be ionized but the free electron abundance would be low. The best candidate mechanism for removing electrons from the gas is probably attachment to grains or large molecules (e.g., [123]). However, because the number density of large molecules or grains is orders of magnitude lower than the number density of electrons (since these molecules or grains form from elements with cosmic abundance less than or equal to that of carbon, and each molecule or grain contains many atoms), this process could not effect the removal of a significant fraction of the electrons from the gas phase.

The H_2 ionization rate (ζ) has been assumed to be 3×10^{-17} s^{-1}, but this value is not terribly well constrained. Cecchi-Pestellini and Dalgarno [99] assume 6×10^{-17} in order to increase the H_3^+ number density, and values as high as $\sim 2 \times 10^{-16}$ have been derived from analysis of the chemistry leading to OH in diffuse clouds [74]. [However, we should view constraints based on chemical models with some skepticism, especially since these same models are unable to account for the observed CH^+ column densities by more than an order of magnitude!] While the flux of high energy ($\gtrsim$ 100 MeV) cosmic rays can be constrained by observations in the interplanetary medium, the flux of lower energy cosmic rays is essentially unconstrained, due to the influence of the heliopause. If the cosmic ray spectrum is assumed not to roll off too rapidly below 100 MeV, it is conceivable that ζ might be as high as 10^{-15} s^{-1} [124]. A large flux of low energy cosmic rays might increase the H_3^+ number density in diffuse clouds while not seriously affecting the situation in dense clouds, into which the low energy cosmic rays could not penetrate.

Other sources of H_2 ionization have also been suggested. Black [88] has suggested that X-rays from the luminous stars in the Cygnus OB2 association could increase the effective ζ and therefore $n(H_3^+)$. While this suggestion might solve the problem for the sightlines toward Cygnus OB2, our observations of high $N(H_3^+)$ toward HD 183143 and HD 20041 imply that a more general solution is needed. Black [88] has also suggested that ultraviolet photoionization of H_2 might contribute. However,

photoionization of H_2 requires photons with energies above 15.4 eV, which will ionize H atoms. While Black suggests that such photons could escape the H II region near the Cygnus OB2 giants, it seems unlikely that they could penetrate the boundaries of diffuse clouds, where H atoms are abundant. Furthermore, the detection of H_3^+ toward HD 183143 and HD 20041 again suggests that the sightlines toward the Cygnus OB2 association are not unique.

The last parameter in the equation for the H_3^+ number density is the dissociative recombination rate (k_e). In this work, we have adopted the value of $k_e = 4.6 \times 10^{-6}\ T_e^{-0.65}$ cm^3 s^{-1} derived from storage ring experiments [81]. However, the value of this constant has been the matter of great controversy over the past two decades — other experimental techniques currently yield a value of k_e that is about one order of magnitude lower (for a review of the field, see [125]). It has been suggested that the discrepancy might be due to stray fields present in the storage ring experiments, and that the recombination rate under interstellar conditions could be quite low. To make matters worse, attempts to theoretically calculate the recombination rate yield rates more than an order of magnitude smaller than the smallest values obtained in experiments [126], but it should be noted that the theory of this recombination process is not yet mature. Given the present uncertainty in the true value of k_e, it is possible that the problem of diffuse cloud H_3^+ may be solved on this front.

Observational Tests

The resolution of the mystery of diffuse cloud H_3^+ will most likely come from further observational work. First we must determine with certainty whether the unexpectedly high number density of H_3^+ is a "local" problem (i.e., due to special conditions in these particular sightlines, or this class of sightlines), or if it is a "global" problem. The present observational situation is summarized in Figure 4.20, which plots the observed H_3^+ column density (or the upper limit, denoted by a bar to zero) versus the color excess E(B-V). In addition to the present observations, the detection of H_3^+ toward the Galactic Center source GC IRS 3 [97] has been added (the H_3^+ column density plotted is that of the narrow component attributed to diffuse clouds [97], and the

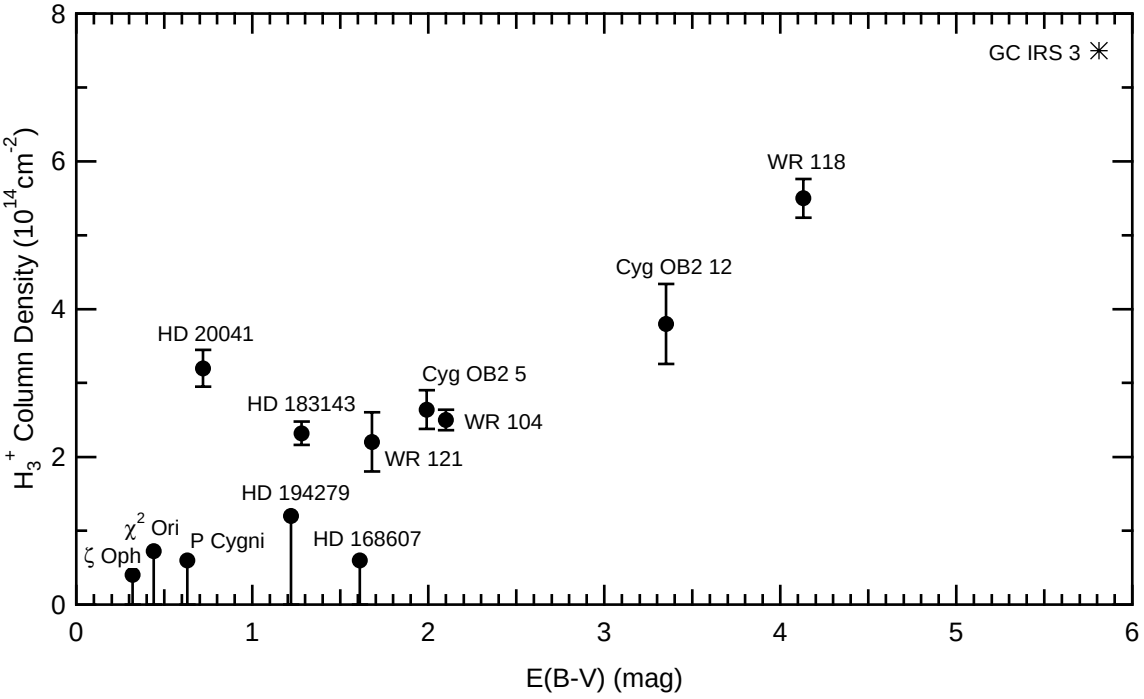

Figure 4.20 H_3^+ Column Density versus color excess.

adopted color excess is that attributed to diffuse clouds [127]). Keeping in mind that

$$N(\mathrm{H}_3^+) \sim n(\mathrm{H}_3^+)\ L \propto n(\mathrm{H}_3^+)\ \frac{E(B-V)}{\langle n_{\mathrm{H}} \rangle} \tag{4.10}$$

the plot is not inconsistent with a constant $n(\mathrm{H}_3^+)$ and small variations (of a factor of a few) in the average density $\langle n_{\mathrm{H}} \rangle$. Therefore at this stage there is no strong evidence that the "local" parameters (f, α, and z_{C}) are any different in the detection sources than they are in the non-detections such as ζ Oph.

However, this inference needs to be tested directly by observations. This can be achieved by detecting H_3^+ along a line of sight with lower E(B-V) which can be studied by FUSE and HST. Once the column densities of H_3^+, H I, H_2, C I, C II, CO, and CH are obtained for a single sightline, the influence of the "local" parameters will be directly determined.

Assuming that these parameters are found to have their canonical values, we will

be left with the ratio ζ/k_e. Absent a speedy resolution from the experimenters or theorists in the field of dissociative recombination, further insight into these two constants can perhaps best be obtained through an observational survey of H_3^+ in more heavily reddened lines of sight. The rate of H_3^+ destruction is controlled by $n(e)/n_{\rm H}$ (which depends on the optical depth in the ultraviolet), whereas the rate of H_3^+ formation is controlled by ζ (which, with a given incident cosmic ray spectrum, depends on the stopping power of the gas as a function of cosmic ray energy). Therefore, a detailed study of the diffuse-to-dense cloud transition, along with chemical models, could constrain the values of ζ and k_e. The highly-reddened, early-type subset of the Stephenson catalog recently compiled by Rawlings, Adamson, and Whittet [128] may serve as a good starting point for such a study.

4.3.5 Conclusions

The H_3^+ molecular ion has now been definitely detected in at least four (and perhaps as many as seven) diffuse cloud lines of sight, suggesting that its unexpectedly high abundance is not due to the peculiarities of a particular region (the Cygnus OB2 association), but rather a general feature of the diffuse interstellar medium. H_3^+ is observed in clouds with and without CO, C_2, and CN, confirming that the chemistry that leads to H_3^+ is completely decoupled from that which is responsible for these heavier diatomics. The most likely explanation for the high H_3^+ abundance is a larger than expected ζ/k_e ratio — due either to a larger flux of low-energy cosmic rays or to a lower value of k_e in interstellar conditions. The possibility of a lower than expected electron density has not been completely ruled out, and should be directly tested by finding H_3^+ in a less reddened source.

4.3.6 Acknowledgements

The authors wish to acknowledge helpful discussions with D. G. York and L. M. Hobbs. We are grateful to the staffs of the various observatories we have used, as well as to the respective telescope allocation committees. This work has made use of the NASA Astrophysics Data Service, as well as the SIMBAD database at the Centre

de Données astronomiques de Strasbourg. The University of Chicago portion of this work has been supported by NSF grant PHYS-9722691 and NASA grant NAG5-4070. B.J.M. has been supported by the Fannie and John Hertz Foundation, and wishes to acknowledge a Sigma Xi Grant-in-Aid of Research and NOAO for travel support.

4.4 Data Reduction Techniques

This section is intended to serve as a handbook for the data reduction techniques developed[6] for the processing of H_3^+ spectra obtained with the CGS4 (at UKIRT) and Phoenix spectrometers. The techniques used for reducing cross-dispersed echelle spectra (e.g. the Coudé at McDonald) are more complicated, and beyond the scope of this section. This section assumes that the reader is familiar with the IRAF (the Image Reduction and Analysis Facility, written by the National Optical Astronomy Observatory) and Igor (the spectral analysis package from Wavemetrics) environments.

The data reduction process can be roughly separated into four steps: preparing calibration files for the InSb array, calibrating and removing sky emission from the raw images obtained, extracting one-dimensional spectra from the processed images, and processing of the resulting one-dimensional spectra. Each of these four steps is covered separately in the following subsections.

In the case of CGS4 data, the first two steps are performed automatically at the telescope, and the "data reducer" can skip forward to subsection 4.4.3(b).

4.4.1 Preparing calibration files

The InSb array in the Phoenix spectrometer essentially consists of 256×1024 different infrared detectors, each with its own offset and gain. The "flat-fielding" process is designed to calibrate the individual responses of the detectors, thus placing each detector on the same scale.

At the telescope (usually while it is still light outside), the user obtains a series of "darks" and "flats." The darks are exposures in which the array is read out without being exposed to any light, and provide the offset of each pixel. The flats are exposures of a uniform white-light source, and are used to measure the pixel-to-pixel sensitivity variations.

I have written a custom IRAF routine called `pxflats`, which interactively guides

[6]The custom IRAF routines, the custom Igor package, and a demo version of Igor are available at http://fermi.uchicago.edu/~bjmccall/datareduction

the user through the flat-fielding process. The `pxflats` routine asks for the image names of the flat and dark exposures, reports the image statistics and allows the user to exclude any deviant exposures, and combines the flats and the darks. The average dark is then subtracted from the average flat, and the resulting image is normalized to an average of one. The user is given the option of replacing small values in the processed flat in order to prevent division by zero when later using the flat to calibrate the astronomical images.

The `pxflats` routine also permits the user to create a "bad pixel map," which identifies the pixels whose responses are non-linear or otherwise unacceptable. This technique requires two sets of flat fields with different exposure times (usually a factor of two). This bad pixel map can later be used to exclude the bad pixels, to prevent spikes from appearing in the reduced spectra.

4.4.2 Processing the image files

The processing of the raw image files is performed by another custom IRAF routine called `pxextract` (this routine also handles the extraction of one-dimensional spectra, as discussed in the next subsection).

The first step in `pxextract` is to identify pairs of images to subtract (in order to remove sky emission). During the observation, the target star is nodded back and forth along the slit, so that spectra at two different positions on the array are obtained. The `pxextract` routine subtracts adjacent images and asks for user approval[7].

Each difference image is then divided by the processed flat field. Finally, the bad pixel map (if available) is applied — the value of each bad pixel is replaced by the average of the adjacent pixels. If a bad pixel map is not applied, the user will have to "despike" each extracted spectrum later (see subsection 4.4.4).

[7] In some cases, especially with early Phoenix data, the grating could move between exposures, making some "difference" images unusable. Additionally, when ABBA (rather than ABAB) beam switching is used, the user must select the appropriate difference images.

4.4.3 Extracting one-dimensional spectra

(a) Phoenix spectra

The `pxextract` routine next runs the built-in `apall` routine, which interactively guides the user through the process of extracting one-dimensional spectra.

The first step in `apall` is the selection of the "aperture" which will be used. A cross-sectional cut of the image is shown (perpendicular to the dispersion axis), and the user specifies which pixels contain the spectrum. The lower (left) boundary of the aperture is set by placing the cursor in the desired position and pressing the `l` key, and the upper (right) boundary is set with the `u` key. In order to zoom in on the peak which represents the stellar flux, the user can use the `w` (window) key, place the cursor in the lower left of the region they wish to enlarge and press `e`, then place the cursor in the upper right of the region and press `e` again. After the aperture has been defined, the user presses `q` to continue.

The next step is the tracing of the aperture along the spectrum. The user is shown the aperture positions at various points along the dispersion axis, as well as a fit to the positions. To increase the order of the fit (for example, to third order), the user enters `:o 3 <return>`. To set the sample area of the fit, the user places the cursor on the left side of the region to be fit and presses `s`, then places the cursor on the right and presses `s` again. To refit, the user presses `f`. When satisfied with the fit, the user presses `q`.

The user is then shown the extracted spectrum, and should press `q` to continue. The `pxextract` routine then calls `apall` again for the next difference image, and the process repeats until all have been extracted. Finally, `pxextract` converts the extracted spectra into text (ASCII) format. The resulting ASCII files should then be transfered by FTP to a Windows machine.

(b) CGS4 spectra

For CGS4 spectra, the process is similar, except that all of the various difference spectra have been coadded at the telescope, so one need only extract the "positive"

and the "negative" spectra of a single image. First, however, the "rg" image must be converted into FITS format. At the UNIX command line, the user types `figaro`, and then `wdfits rg<num> <name>.fits`, where the CGS4 image file is `rg<num>.sdf` and `<name>` is the desired name of the output file.

Next, the user runs IRAF and enters `apall <name>`. The user then follows the same procedure as described above for defining the aperture, tracing the aperture, and reviewing the extracted spectrum. Next, the user needs to multiply the image by -1 by entering `imarith <name> * -1 n<name>`. Then the user can extract the negative spectrum by executing `apall n<name>`. Finally, the user converts the extracted spectra into ASCII format by entering `wspectext <name>.ms <name>p.txt` and `wspectext n<name>.ms <name>n.txt`. The two resulting text files can then be transfered to a Windows machine using FTP.

4.4.4 Processing the spectra

The processing of the one-dimensional spectra is by far the most subtle step of the data reduction process, when searching for small ($\sim$1%) absorption lines such as those of H_3^+. Many possible mis-steps can wipe out or distort these features, so the data reduction is a bit of an art. Because of the difficulty in performing this process within the IRAF environment, I have designed an Igor "experiment" which allows more interactive tweaking. This Igor package does not prescribe a particular data reduction path, but rather provides a set of useful tools, which can be used in different sequences depending on the nature of the data. A screen capture of the Igor package is shown in Figure 4.21 for reference. In this section, I outline the sequence of data reduction that I have found most effective for CGS4 data and for Phoenix data.

CGS4 spectra

Loading data The first step in the reduction is loading in a spectrum of interest using the LoadOneWave button (located on the Calibration panel). The user then presses Display to display the spectrum. At this point, one notices the "hairy"

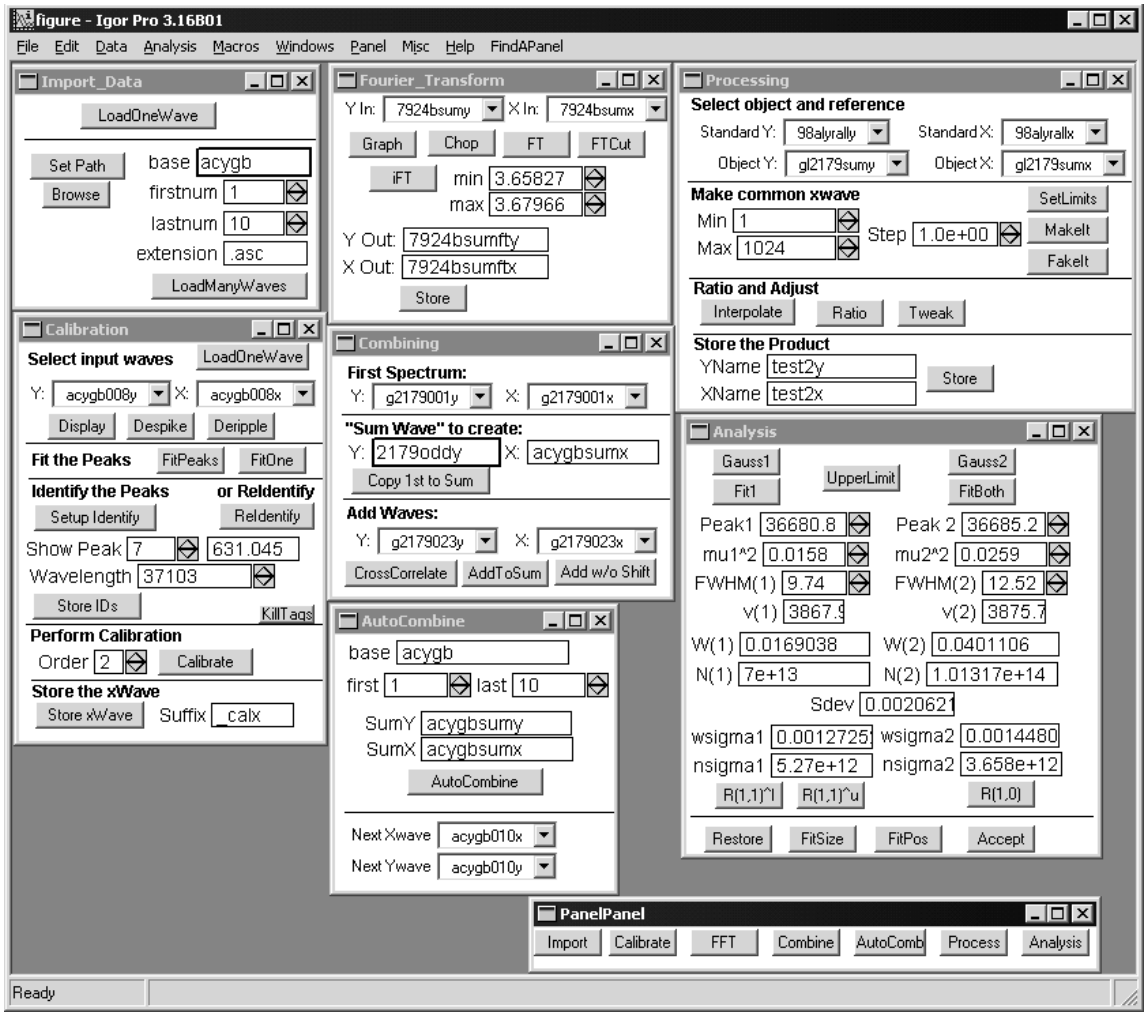

Figure 4.21 A screen capture of the Igor data reduction package.

appearance of the spectrum — this is due to the fact that the CGS4 array is mechanically stepped three times during the exposure, leading to a steady ripple with a period of three pixels. The user can remove this ripple by pressing the Deripple button. The user then repeats this process for all spectra.

Combining spectra The positive and negative spectra are next coadded using the Combining panel. The positive spectrum is selected as the "First Spectrum," then a name is entered for the "Sum Wave" to create. The user then presses Copy 1st to Sum to display the positive spectrum. The negative spectrum is then selected under "Add Waves," and then the user presses CrossCorrelate to align the spectra. If satisfied with the shift, the user presses AddToSum to coadd the spectra. If the user wishes to coadd without a shift, he can press Add w/o Shift.

Fourier transform The CGS4 spectra suffer from an excessive fringing pattern caused by étaloning in the circular variable filter (CVF) used for order sorting (Phoenix spectra do not suffer this problem because we have purchased a custom filter for this purpose). The amplitude of this fringing pattern far exceeds the size of the H_3^+ absorption lines, and even makes wavelength calibration difficult. Consequently, it is important to remove the fringing pattern. This is accomplished easily using the Fourier Transform panel. The user selects the "Y In" and "X In" waves, and presses the Graph button to display the raw (coadded) spectrum. The user then selects the region of the spectrum to be Fourier transformed using the cursors (the round cursor must go on the left side) — one should select as much of the spectrum as possible, avoiding only the very edges of the spectrum.

The user then presses the Chop button, which truncates the spectrum to the desired region and applies a Hanning filter to prevent ringing in the Fourier transform. The user presses the FT button, and a new window pops up, displaying the squared modulus of the Fourier transform of the spectrum. Usually the peak due to the fringing will be easily seen, although in some cases the user may need to rescale the window to find the peak. The user then surrounds the offending peak with the cursors (staying as close as possible to the peak), and presses the FTCut button, which

interpolates across the offending peak in both the real and imaginary components of the Fourier transform.

Next, the user presses the iFT button to perform the inverse Fourier transform, and the resulting Fourier-filtered spectrum is displayed atop the original spectrum (at the same time, the window displaying the power spectrum is dismissed). If the results are acceptable, the user enters a new name in the "Y Out" and "X Out" boxes and presses Store to save the new spectrum.

This Fourier filtering process should be performed for the coadded spectrum of the object and again for the coadded spectrum of the standard star.

Ratioing The ratioing of the object and standard star spectra (to remove atmospheric absorption lines) is performed using the Processing panel. The user first selects the standard and object Y and X waves at the top of the panel. The user then presses the SetLimits button, which displays the minimum and maximum values common to both X waves in the corresponding boxes. The average X wave step size is also placed in the "Step" box. If desired, the user can modify these values, which are used to create a common wavelength wave which both the object and standard spectrum will be interpolated onto. To make this standard wavelength wave, the user presses the MakeIt button (if the user prefers to keep the X wave of the standard star, he can press the FakeIt button instead).

The user then presses the Interpolate, Ratio, and Tweak buttons in that order. The system then displays a new window, showing the object and standard[8] spectra at the top, and their ratio at the bottom. The user then selects the region of interest with the cursors. An example of the tweaking window is shown in Figure 4.22.

Now the user can interactively tweak the standard star spectrum to best match the atmospheric lines observed in the object spectrum. The first parameter is the Scale value, which scales the standard spectrum according to Beer's Law, to increase or decrease the depth of atmospheric absorptions. The second parameter is the Shift value, which allows the user to compensate for a slight wavelength shift between the

[8]Actually, the standard spectrum displayed is that which has been scaled and shifted by the user-tweaked parameters.

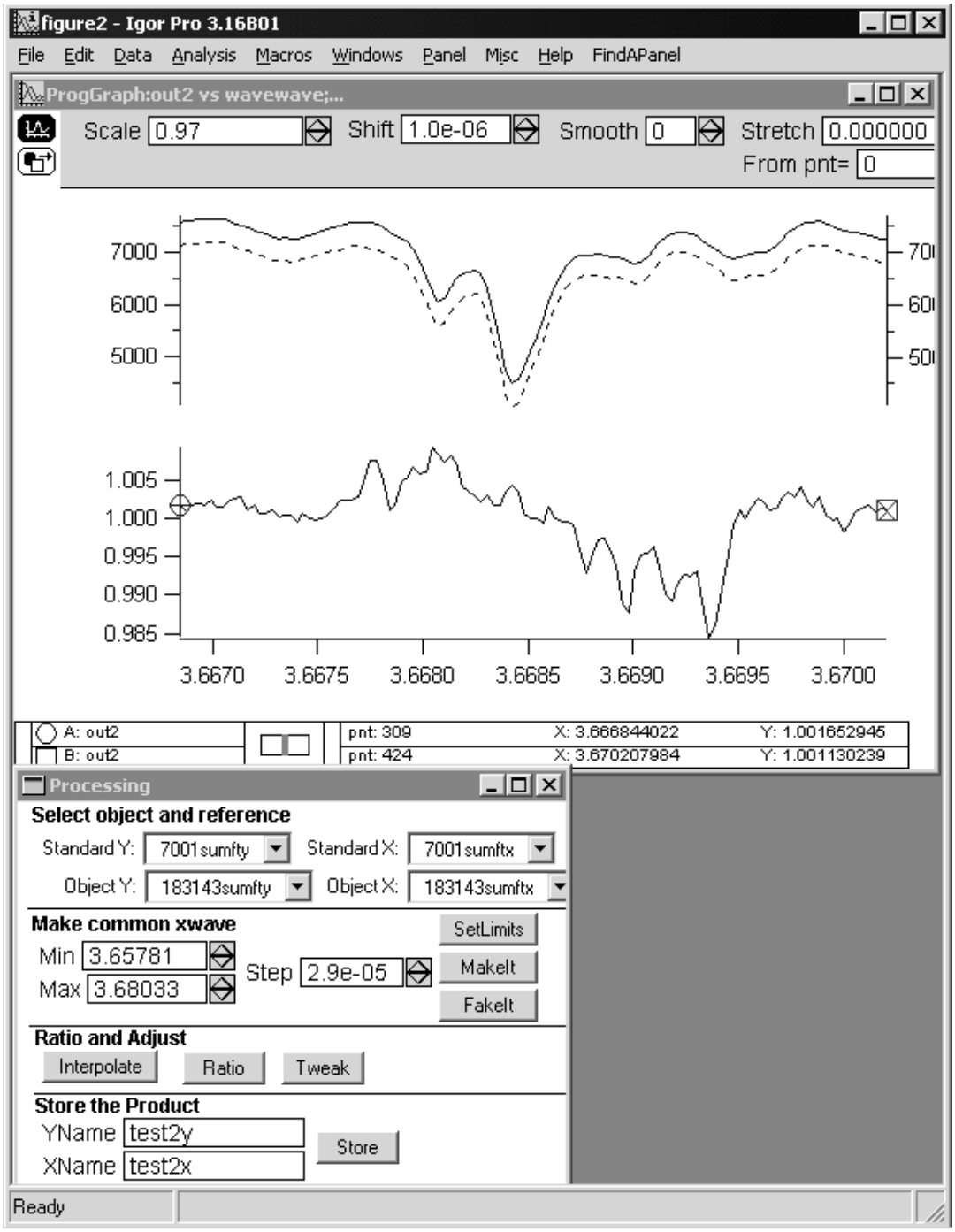

Figure 4.22 A screen capture of the tweaking window in the Igor data reduction package. The (tweaked) standard spectrum is dashed in this reproduction, for clarity.

object and standard spectra (such a shift leads to an apparent first derivative lineshape when the Scale parameter is optimized). In the rare cases when a constant shift is not sufficient, the Stretch parameter can also be used to apply a linear transformation of the wavelength). Using these parameters (generally the Scale first to form a good first derivative shape and then the Shift to make the derivative shape vanish) the user minimizes the residuals of the atmospheric lines. If desired, a Smooth parameter is also provided to boxcar average the spectrum (this is useful if the spectrum is particularly noisy).

When the user is satisfied, he enters a new "YName" and "XName," and presses the Store button to save the ratioed spectrum. The tweaking window is left open to allow further adjustments if needed.

Wavelength calibration The next step is the wavelength calibration, which is accomplished in the Calibration panel. First, the user selects the coadded *object* spectrum in the Y and X boxes. The user then presses Display to show the spectrum. The user selects the region to be used for calibration with the cursors (again, the round cursor must be on the left). The user then presses the FitPeaks button, which will find all of the atmospheric absorption features.

If a spectrum has previously been calibrated at this wavelength setting, the user can simply press ReIdentify, otherwise the rest of this paragraph should be followed. First the user presses Setup Identify, which initializes the calibration process. The user then increases or decreases the "Show Peak" box, which will highlight the different peaks in the spectrum. When the user has found a well-fit peak that corresponds to a known atmospheric absorption line[9] , he enters the rest wavelength in the "Wavelength" box and presses return. The user then adjusts the "Show Peak" box again, and continues in this way until all good peaks are identified. The user then presses Store IDs for use in later re-identification.

The user then selects the order of the polynomial to be used for the wavelength solution (usually 2) in the "Order" box, and presses the Calibrate button. The user

[9]The Hinkle atlas of the atmospheric spectrum [129] is available online from the CDS at ftp://cdsarc.u-strasbg.fr/pub/cats/J/PASP/107/1042/

then selects a suffix to be added to the name of the X wave (usually `_calx` is used, but it must end in `x`), and presses Store xWave to save the result of the calibration.

Once the coadded object spectrum has been calibrated in this manner, the ratioed object spectrum can now be easily calibrated by selecting it in the Y and X boxes, and then pressing Calibrate and Store xWave.

Analysis The final step is analyzing the ratioed spectrum to derive the parameters of the observed absorption lines (or upper limits). This task is performed using the Analysis panel. First, the wavelength calibrated ratioed spectrum should be displayed in a window (e.g. using the Display function of the Calibration panel).

For a single absorption peak, the user enters the rest wavelength in "Peak 1" and the squared transition dipole moment $|\mu|^2$ in the "mu1^2" box. The user then places the cursors just inside the peak, and presses Gauss1 (this performs a fit to get the rough parameters of the feature). The user then places the cursors outside the peak, with some baseline in between, and presses Fit1. This fits both the peak and the baseline and calculates the line parameters. These parameters include the full-width at half-maximum (FWHM), the radial velocity (v), the equivalent width (W), and the column density (N). The uncertainties in the equivalent width and column density are also calculated, based on the residuals in the fit. All of these parameters are displayed in the corresponding boxes under Peak1.

For two nearby peaks, e.g. the $R(1,1)^u$–$R(1,0)$ doublet of H_3^+, the single peak fit often fails. In this case, the user first enters the rest wavelengths and dipole moments of both transitions. The user next places the cursors inside the first peak and presses Gauss1, and then places the cursors inside the second peak and presses Gauss2. The user then places the cursors outside both peaks, with some baseline in between, and presses FitBoth. This simultaneously fits the baseline and both peaks, and returns all of the appropriate line parameters in the corresponding boxes.

In the rare case where four peaks must be fit simultaneously (e.g. the H_3^+ doublet in HD 183143), one can access a special panel called FourGauss from the FindAPanel menu. The process is a simple extension of the two peak fit, although it is recommended that the peak positions be constrained (by checking the box) for the first

press of the FitFour button. If the resulting fit is not totally satisfactory, the user can unconstrain the peak positions and then press FitFour again to vary all parameters.

To calculate an upper limit, the user simply places the cursors around the area where the line(s) would be expected. The user enters the wavelengths and transition dipoles, and also sets the expected full-widths at half-maximum (FWHM). The user then presses the UpperLimit button, which then returns the 1σ limits in the equivalent widths and column densities in the appropriate boxes. Note that the assumption of the expected FWHM affects the derived limits.

For ease of use with H_3^+ data, buttons are provided to automatically bring up the rest wavelengths (in Å) and transition dipoles (from Watson [41]) for the $R(1,0)$, $R(1,1)^u$, and $R(1,1)^l$ transitions.

Phoenix spectra

Loading data Because the Phoenix images are not coadded automatically like the CGS4 images, the user must load in many more spectra. This process is automated with the Import Data panel. The user can select a path to the data, browse that directory, and then enter the base filename, the starting spectrum number, and the ending spectrum number. The user then simply presses LoadManyWaves, and the corresponding spectra are loaded in.

If a bad pixel map was not used in the image processing stage, the user may need to manually remove spikes in the spectra. This can be done interactively by selecting each spectrum as the Y and X input waves in the Calibration panel, and then pressing the Display and Despike buttons. The computer then identifies all possibly suspicious features, highlights each feature for the user, and asks if it should be deleted. At the end of the process, the user can either abandon or save the changes to the spectrum.

Combining spectra Combining many spectra has been automated with the Auto-Combine panel. The values of the base filename and first and last spectrum numbers are retained from the Import Data panel. If these values are still correct, the user can simply type in a new name for "SumY" and "Sum X" and then press the AutoCom-

bine button. The computer performs a cross-correlation to align each spectrum and automatically sums them. The process is displayed for the user, and in case there is a problem the addition can be performed manually using the Combining panel.

Remaining analysis Fourier filtering is not necessary with Phoenix spectra when a custom (wedged) order-sorting filter has been employed for the observations. If this has not been done, the Fourier filtering technique described for the CGS4 spectra can be performed.

The remaining steps of the data reduction (ratioing, wavelength calibration, and analysis) are the same as in the case of the CGS4 spectra.

APPENDIX A
ASTRONOMY PUBLICATIONS

A.1 "Detection of H_3^+ in the Diffuse Interstellar Medium Toward Cygnus OB2 No. 12"

Reprinted from *Science* 279, 1910 (1998).

Detection of H_3^+ in the Diffuse Interstellar Medium Toward Cygnus OB2 No. 12

B. J. McCall,* T. R. Geballe, K. H. Hinkle, T. Oka

The molecular ion H_3^+ is considered the cornerstone of interstellar chemistry because it initiates the reactions responsible for the production of many larger molecules. Recently discovered in dense molecular clouds, H_3^+ has now been observed in the diffuse interstellar medium toward Cygnus OB2 No. 12. Analysis of H_3^+ chemistry suggests that the high H_3^+ column density (3.8×10^{14} per square centimeter) is due not to a high H_3^+ concentration but to a long absorption path. This and other work demonstrate the ubiquity of H_3^+ and its potential as a probe of the physical and chemical conditions in the interstellar medium.

The molecular ion H_3^+ is generally considered a fundamental molecule of interstellar chemistry, as it reacts efficiently with almost any neutral atom or molecule to initiate a network of ion-neutral reactions. It was suggested in the 1970s (*1*) that this network of reactions is responsible for producing molecules such as OH, CO, and H_2O, which not only serve as important astronomical probes but also play important roles in processes such as star formation.

The recent discovery of interstellar H_3^+ in dense molecular clouds toward the young stellar objects GL2136 and W33A (*2*), which are deeply embedded within the clouds, has provided direct observational evidence supporting the ion-neutral reaction scheme for the chemical evolution of molecular clouds. Subsequent observations have revealed the presence of abundant H_3^+ in many other dense clouds (*3*). Because of the simplicity of the H_3^+ chemistry, these observations provide direct estimates of the most fundamental properties of the clouds: number density, column length, and temperature.

In the course of carrying out this survey, we observed strong and broad H_3^+ absorption lines in the direction of the galactic center source GC IRS 3 (*4*). This finding suggested that H_3^+ is abundant not only in gravitationally bound dense clouds with high density ($n \sim 10^3$ to 10^5 cm^{-3}) but also in unbound diffuse clouds with low density ($\sim$10 to 10^3 cm^{-3}). To test this possibility, Cygnus OB2 No. 12 was observed, as this source is believed to be obscured largely by diffuse low-density clouds containing little molecular material (*5*). We report here the detection of a large amount of H_3^+ in the diffuse clouds in the direction of Cygnus OB2 No. 12.

Cygnus OB2 No. 12 (or VI Cygni 12) is the 12th member of the Cygnus OB2 association of young stars and was discovered in 1954 (*6*). This association is estimated to be 1.7 kpc (*7*) from Earth or about one-fifth of the distance to the center of the galaxy. The star Cygnus OB2 No. 12 suffers the largest extinction of any of the members of the association, $A_v \sim 10$, indicating that it has the largest column of absorbing material along its line of sight (*8*). On the basis of its extinction, distance, spectral type (B5), and luminosity class (Ie), the star Cygnus OB2 No. 12 is one of the most luminous stars in the galaxy (absolute visual magnitude ~ -10), more than a million times brighter than our sun (*9*).

Although Cygnus OB2 No. 12 suffers higher extinction than other members of its association, it is generally accepted that all the extinction occurs in a spatially patchy distribution of the interstellar dust (*5*). The absence of the 3.08-μm water ice absorption feature, associated with dense molecular clouds, and the presence of a 3.4-μm hydrocarbon feature (*5*), associated with diffuse interstellar gas, indicate that no dense molecular clouds occur along the line of sight. The identification of the gas with a circumstellar shell is rejected on the basis of a lack of excess infrared emission and the unusually strong stellar wind ($\sim$1400 km s^{-1}) of Cygnus OB2 No. 12 (*10*).

We detected two closely spaced lines of H_3^+ near 3.67 μm toward Cygnus OB2 No. 12 on 11 July 1997, using the CGS4 spectrometer at the United Kingdom Infrared Telescope (UKIRT) (*11*). A third line near 3.71 μm was detected on 17 September 1997 with the use of the Phoenix infrared spectrometer on the 4.0-m Mayall telescope of the Kitt Peak National Observatory (KPNO) (*12*). To further constrain the chemistry of the line of sight toward Cygnus OB2 No. 12, we also obtained spectra of CO (*13*).

The reduced H_3^+ spectra are shown in Fig. 1. The left portion of the figure, taken with CGS4, shows absorption of the $R(1,1)^+$ line of *para*-(*p*-)H_3^+ and the R(1,0) line of *ortho*-(*o*-)H_3^+. The right portion, obtained with Phoenix, shows absorption of the $R(1,1)^-$ line of *p*-H_3^+. The reduced CO absorption spectrum from CGS4 is relatively weak (Fig. 2). In dense molecular cloud sources, the fundamental CO lines are often saturated, so the relatively weak absorption toward Cygnus OB2 No. 12 suggests that the relative abundance of CO is much lower than in dense molecular clouds.

The amount of H_3^+ toward Cygnus OB2 No. 12 can be expressed as the column density $N(H_3^+)$, which can be defined as the integral of the H_3^+ number density (in molecules per cubic centimeter) along the line of sight $N \equiv \int [H_3^+] d\ell$. The equivalent width (or area) of an absorption line, $W_\lambda \equiv \int (1 - \frac{I}{I_0}) d\lambda$, taken from the spectrum can be related to the column density of the level N_{level} (for an optically thin line) by the standard equation $W_\lambda = (8\pi^3\lambda/3hc)\, N_{level} |\mu|^2$. In these formulas, $|\mu|^2$ is the square of the transition dipole moment (a measure of the inherent strength of the transition) (*14*), λ and I are the wavelength and intensity of the radiation, respectively, h is Planck's con-

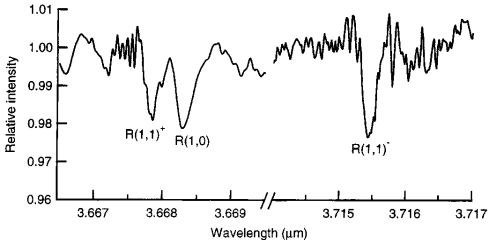

Fig. 1. Reduced spectra of Cygnus OB2 No. 12 in two wavelength intervals near 3.7 μm. The spectra were divided by spectra of the comparison star α Cygni and were wavelength calibrated with the use of atmospheric absorption lines. The left side contains two absorption lines of H_3^+ arising from the ground *para* and *ortho* states. The right side shows a single absorption from the ground *para* state. The high-frequency noise near 3.6675 μm is due to the removal of a strong CH_4 atmospheric line. Because the two spectra were obtained on different dates, they show different observed Doppler shifts.

B. J. McCall and T. Oka, Department of Astronomy and Astrophysics, Department of Chemistry, and the Enrico Fermi Institute, University of Chicago, Chicago, IL 60637, USA.
T. R. Geballe, Joint Astronomy Centre, University Park, Hilo, HI 96720, USA.
K. H. Hinkle, National Optical Astronomy Observatories, Tucson, AZ 85726, USA.
*To whom correspondence should be addressed.

stant, and c is the speed of light.

Because the two p-H_3^+ lines $R(1,1)^+$ and $R(1,1)^-$ arise from the same energy level, the column densities N derived from the two should agree. The large discrepancy (Table 1) is most likely due to the effect of a strong (~45% deep) terrestrial line of CH_4 at 3.6675 μm, which was nearly coincident with the $R(1,1)^+$ line at the time of measurement. For the remainder of this discussion, we adopt a value for the H_3^+ column density of $N(H_3^+) = N_{ortho} + N_{para} = 3.8 \times 10^{14}$ cm^{-2}. From the CO spectrum (Fig. 2) we estimate a value of $N(CO) = 2 \times 10^{16}$ cm^{-2} (*15*).

To interpret the observed column densities of H_3^+ and CO, we developed a model of the H_3^+ chemistry of the interstellar medium (*16*). Using this model, we can extract $[H_3^+]$, L (the effective path length of the absorption), and $[\Sigma H]$ (the total number density of H atoms).

The molecular ion H_3^+ is formed by a two-step process: cosmic-ray ionization of H_2 to form H_2^+ and reaction of H_2^+ with H_2 to form H_3^+. Because the second step is faster than the first by many orders of magnitude, the formation rate of H_3^+ can be expressed as $\zeta[H_2]$, where ζ is the cosmic-ray ionization rate. There are two primary destruction paths for H_3^+: recombination with an electron and ion-neutral reaction with a neutral atom or molecule. The rate due to the former reaction is $k_e[e^-][H_3^+]$, where k_e is the rate constant for electron recombination and $[e^-]$ is the number density of electrons. The dominant ion-neutral destruction path for H_3^+ is assumed to be reaction with CO, with a rate of $k_{CO}[CO][H_3^+]$, where k_{CO} is the rate constant. If we assume a steady state, the rates of H_3^+ formation and destruction are equal, so that

$$\zeta[H_2] = k_e[e^-][H_3^+] + k_{CO}[CO][H_3^+] \quad (1)$$

Because not all of the number densities in this equation can be obtained by observations, some assumptions must be made to reduce the number of unknowns in this equation. First, we assume that all electrons in diffuse clouds come from ionization of atomic C to form C^+ (*17*), so that $[e^-] = [C^+]$. Second, we assume that all C is in the form of either C^+ or CO, so that $[\Sigma C] = [C^+]+[CO]$, where $[\Sigma C]$ denotes the total concentration of gaseous C atoms in any form (*18*). Third, we assume that nearly all H is in the form of H or H_2, so that $[\Sigma H] = [H] + 2[H_2]$.

To understand the meaning of Eq. 1, we introduce a parameter that represents the fraction of H in molecular form, $f \equiv 2[H_2]/[\Sigma H]$, or $[H_2] = (f/2)[\Sigma H]$. We also introduce a parameter that represents the fraction of C in molecular form $\alpha \equiv [CO]/[\Sigma C]$, so that $[CO] = \alpha[\Sigma C]$ and $[C^+] = (1-\alpha)[\Sigma C]$. Substituting these relations into Eq. 1 and solving for $[H_3^+]$ yields

$$[H_3^+] = \zeta\left(\frac{f}{2}\right)\left(\frac{[\Sigma H]}{[\Sigma C]}\right)\left(\frac{1}{k_e(1-\alpha) + k_{CO}\alpha}\right) \quad (2)$$

Note that the number density of H_3^+ does not depend on the absolute number density of the gas.

With the observed value of $N(H_3^+)$, one can determine the effective path length L of the absorption using the approximate relation $N(H_3^+) = [H_3^+]L$, which implies

$$L = \frac{N(H_3^+)}{[H_3^+]} = \left[\frac{2N(H_3^+)}{f\zeta}\right]\left(\frac{[\Sigma C]}{[\Sigma H]}\right) \cdot [k_e(1-\alpha) + k_{CO}\alpha] \quad (3)$$

Table 1. Observed H_3^+ lines and column densities derived from each line. Statistical uncertainties (3σ) are given in parentheses, but systematic errors are difficult to estimate and may be larger. Also listed are the Doppler velocities with respect to the local standard of rest v_{LSR} and the observed linewidths Δv (full width at half maximum). The uncertainty in the equivalent width (and column density) of the $R(1,1)^+$ line is large as a result of the effects of a nearly overlapping telluric CH_4 line. Rest wavelengths are from (*27*).

Transition	Rest wavelength (μm)	$\|\mu\|^2$ (D^2)	W_λ (μm)	N_{level} (cm^{-2})	Δv (km s^{-1})	v_{LSR} (km s^{-1})
$R(1,1)^+$	3.668084	0.0158	$3.9(9) \times 10^{-6}$	$1.6(4) \times 10^{14}$	17(5)	8(5)
R(1,0)	3.668516	0.0259	$5.4(9) \times 10^{-6}$	$1.4(2) \times 10^{14}$	22(5)	11(5)
$R(1,1)^-$	3.715478	0.0140	$5.2(7) \times 10^{-6}$	$2.4(3) \times 10^{14}$	16(3)	8(3)

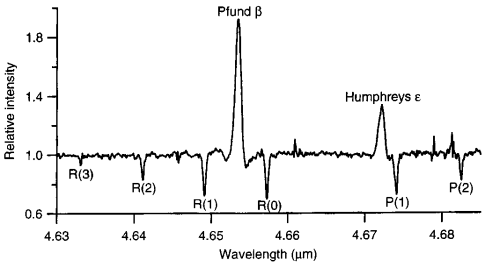

Fig. 2. Spectrum from 4.63 to 4.68 μm of Cygnus OB2 No. 12, showing R- and P-branch absorption lines of CO in the interstellar medium and emission lines of atomic H from the stellar atmosphere (Pfund β and Humphreys ε). The spectrum was divided by a spectrum of the comparison star γ Cygni and was wavelength calibrated with the use of atmospheric absorption lines.

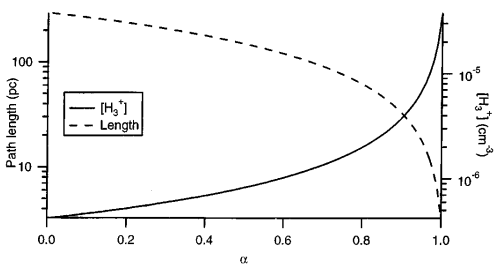

Fig. 3. Model results for the H_3^+ number density $[H_3^+]$ and the effective absorption path length L for Cygnus OB2 No. 12.

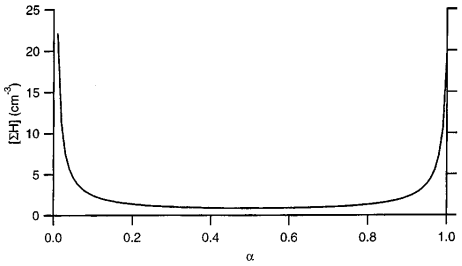

Fig. 4. Model results for the total number density of H atoms $[\Sigma H]$ for Cygnus OB No. 12.

To obtain an expression for the number density [ΣH], the definition of α can be rewritten as α = ([CO]/[ΣH])([ΣH]/[ΣC]). Substituting the approximate relation [CO]/[ΣH] ≅ N(CO)/N(ΣH) into this and solving for N(ΣH) gives

$$N(\Sigma H) = \frac{N(CO)}{\alpha}\left(\frac{[\Sigma H]}{[\Sigma C]}\right) \qquad (4)$$

Equations 3 and 4 can be combined to derive an expression for the number density of the cloud

$$[\Sigma H] \cong \frac{N(\Sigma H)}{L} = \left[\frac{f\zeta N(CO)}{2\alpha N(H_3^+)}\right]\left(\frac{[\Sigma H]}{[\Sigma C]}\right)^2 \cdot \left[\frac{1}{k_e(1-\alpha) + k_{CO}\alpha}\right] \qquad (5)$$

To determine [H_3^+], L, and [ΣH], we used $\zeta \sim 3 \times 10^{-17}$ s^{-1} (*19*), $f \sim 0.5$ (*20*), [ΣH]/[ΣC] ~ 10^4 (*21*), $k_e \sim 1.8 \times 10^{-7}$ cm^3 s^{-1} (*22*), and $k_{CO} \sim 2.0 \times 10^{-9}$ cm^3 s^{-1} (*23*). For $N(H_3^+)$ and N(CO) we used our adopted observational values. The parameter α is difficult to estimate, and we leave it as a free parameter.

The resulting values of [H_3^+] and L for Cygnus OB2 No. 12 as a function of α (Fig. 3) show that, as α increases (more C is in molecular form) from 0 to 1, [H_3^+] increases from 4×10^{-7} to 4×10^{-5} cm^{-3} and L decreases from ~300 to ~3 pc. The limit α = 0 corresponds to the case where H_3^+ destruction is dominated by electron recombination (very diffuse clouds), and the limit α = 1 corresponds to the case where H_3^+ destruction is dominated by reaction with CO (very dense clouds).

The key parameter in these estimates (α) has not been determined, but, on the basis of observations and theoretical models of diffuse clouds (*17*), we infer that it is less than 0.1. From Fig. 3 we estimate [H_3^+] ~4×10^{-7} cm^{-3} and L ~300 pc. Unlike [H_3^+] and L, [ΣH] changes a lot for α < 0.1 (Fig. 4). From the visual extinction we can estimate N(ΣH), assuming the standard gas-to-dust ratio (*24*). If all of the extinction arises from the region where H_3^+ is observed (*25*), we estimate N(ΣH) ~ 2×10^{22} cm^{-2}. The calculated L ~ 300 pc then implies [ΣH] ~ 20 cm^{-3}.

Because H_3^+ undergoes constant chemical reactions with H_2 at a Langevin rate (*26*) and because there are no radiative transitions between *o*-H_3^+ and *p*-H_3^+, H_3^+ is in thermal equilibrium with H_2 in the cloud. By measuring the column densities of *o*- and *p*-H_3^+, one can estimate the kinetic temperature of the cloud. In thermal equilibrium, the ratio of the two states is given by the Boltzmann expression

$$\frac{N_{ortho}}{N_{para}} = \frac{g_{ortho}}{g_{para}} e^{-\frac{\Delta E}{kT}} = 2e^{-\frac{32.87}{T}} \qquad (6)$$

where the g values are the statistical weights of the *o*- and *p*-H_3^+ states, ΔE is the energy difference between them, k is the Boltzmann constant, and T is temperature. Using the data in Table 1, we obtain an estimate of the cloud temperature of 27 K. This temperature is higher than the excitation temperature derived from the CO spectrum (Fig. 2), which is 10 K. This difference in temperatures may be reasonable because spontaneous emission will lower the excitation temperature of CO in diffuse clouds, where the collisional pumping to higher rotational states is slow as a result of the low number density.

These observations indicate that $N(H_3^+)$ in the diffuse clouds toward Cygnus OB2 No. 12 (3.8×10^{14} cm^{-2}) is comparable to that of the dense clouds toward the young stellar objects GL2136 (4.0×10^{14} cm^{-2}) and W33A (6.0×10^{14} cm^{-2}) (*2*). This is not because of a higher number density [H_3^+] but because of a large effective path length L toward Cygnus OB2 No. 12, which may cross many diffuse clouds. Although large column densities of H_3^+ have been predicted in diffuse clouds (*17*), these calculations were based on a value of the H_3^+ electron recombination rate that has since been shown to be more than three orders of magnitude too low (*22*). This detection and analysis extend the diagnostic powers of H_3^+ to a new class of objects that are chemically quite different from dense molecular clouds and may allow us to gain further insight into the physical and chemical conditions of diffuse interstellar clouds.

REFERENCES AND NOTES

1. E. Herbst and W. Klemperer, *Astrophys. J.* **185**, 505 (1973); W. D. Watson, *ibid.* **183**, L17 (1973); *ibid.* **188**, 35 (1974).
2. T. R. Geballe and T. Oka, *Nature* **384**, 334 (1996).
3. B. J. McCall, T. R. Geballe, K. H. Hinkle, T. Oka, in preparation.
4. T. R. Geballe, B. J. McCall, K. H. Hinkle, T. Oka, in preparation.
5. A. J. Adamson, D. C. B. Whittet, W. W. Duley, *Mon. Not. R. Astron. Soc.* **243**, 400 (1990); D. C. B. Whittet *et al.*, *Astrophys. J.* **490**, 729 (1997).
6. W. W. Morgan, H. L. Johnson, N. G. Roman, *Publ. Astron. Soc. Pac.* **66**, 85 (1954).
7. A. V. Torres-Dodgen, M. Tapia, M. Carroll, *Mon. Not. R. Astron. Soc.* **249**, 1 (1991). One parsec (1 pc) is ~3.1×10^{18} cm.
8. S. Sharpless, *Publ. Astron. Soc. Pac.* **69**, 239 (1957). The quantity A_v is the number of magnitudes by which a star would be brighter if there were no interstellar absorption. Magnitude is defined as −2.5 log (brightness), so −2.5 magnitudes corresponds to one power of ten in brightness.
9. P. Massey and A. B. Thompson, *Astron. J.* **101**, 1408 (1991).
10. P. Persi and M. Ferrari-Toniolo, *Astron. Astrophys.* **111**, L7 (1982); J. H. Bieging, D. C. Abbott, E. B. Churchwell, *Astrophys. J.* **340**, 518 (1989).
11. The UKIRT is operated by the Joint Astronomy Centre on behalf of the U.K. Particle Physics and Astronomy Research Council. CGS4 is a grating spectrometer for the region from 1 to 5 μm, currently incorporating a 256 by 256 InSb array. For details on the CGS4 spectrometer, see C. M. Mountain, D. J. Robertson, T. J. Lee, R. Wade, *Proc. Soc. Photo.-Opt. Instrum. Eng.* **1235**, 25 (1990).
12. The KPNO, a division of the National Optical Astronomy Observatories, is operated by the Association of Universities for Research in Astronomy, Inc., under cooperative agreement with the National Science Foundation. For details on the Phoenix spectrometer, see K. H. Hinkle *et al.*, *Proc. Soc. Photo.-Opt. Instrum. Eng.*, in press.
13. We observed the fundamental band of ^{12}CO near 4.66 μm in absorption on 1 August 1997 using CGS4 at UKIRT and also on 16 September 1997 using Phoenix on the 2.1-m telescope at KPNO. Millimeter-wave spectra of ^{12}CO (J = 2→1) and ^{13}CO (J = 2→1) were also obtained at the James Clerk Maxwell Telescope (JCMT) on 5 August 1997 and 13 November 1997, respectively. The JCMT is operated by the Joint Astronomy Centre on behalf of the U.K. Particle Physics and Astronomy Research Council, the Netherlands Organisation for Scientific Research, and the National Research Council of Canada. We obtained the CO measurements at the JCMT using the heterodyne receiver A2.
14. The values of $|\mu|^2$ were provided to us by J. K. G. Watson.
15. This adopted value assumes that the CO lines are unsaturated and that the populations of the $J > 2$ levels are negligible. The measured equivalent widths are R(2) = 7.0×10^{-5} μm, R(1) = 1.3×10^{-4} μm, R(0) = 1.4×10^{-4} μm, P(1) = 1.3×10^{-4} μm, and P(2) = 7.2×10^{-5} μm. These values are uncertain by perhaps a factor of 2 because the atmospheric CO lines were nearly overlapping the interstellar CO lines at the time of measurement, causing the atmospheric correction to be quite imprecise. The line widths are ~20 to 30 km s^{-1}. The Doppler velocity with respect to the local standard of rest v_{LSR} (~15 km s^{-1}) of the CO lines is in rough agreement with the H_3^+ data, although the systematic uncertainty due to atmospheric interference is difficult to estimate.
16. Many models of H_3^+ chemistry in the interstellar medium have been discussed in the literature. See, for example, S. Lepp, A. Dalgarno, A. Sternberg, *Astrophys. J.* **321**, 383 (1987), and J. H. Black, E. F. van Dishoeck, S. P. Willner, R. C. Woods, *ibid.* **358**, 459 (1990).
17. E. F. van Dishoeck and J. H. Black, *Astrophys. J. Suppl. Ser.* **62**, 109 (1986).
18. In diffuse clouds, models (*17*) indicate that atomic C is another abundant form of carbon. However, [C] can be included in [CO] in these expressions, as it has a similar Langevin rate constant for reaction with H_3^+, so it behaves just like CO with respect to H_3^+ chemistry.
19. The adopted value of ζ varies in the literature. We have adopted an average of the value $\zeta = 1 \times 10^{-17}$ s^{-1} used in model calculations of dense clouds [H.-H. Lee, R. P. A. Bettens, E. Herbst, *Astron. Astrophys. Suppl. Ser.* **119**, 111 (1996)] and the value $\zeta = 5 \times 10^{-17}$ s^{-1} used for diffuse clouds (*17*). We expect that further H_3^+ observations will lead to a better estimate of this important parameter.
20. A. E. Glassgold and W. D. Langer, *Astrophys. J.* **193**, 73 (1974).
21. J. A. Cardelli, D. M. Meyer, M. Jura, B. D. Savage, *ibid.* **467**, 334 (1996).
22. T. Amano, *ibid.* **329**, L121 (1988).
23. V. G. Anicich and W. T. Huntress Jr., *Astrophys. J. Suppl. Ser.* **62**, 553 (1986).
24. The standard gas-to-dust ratio can be expressed as N(ΣH)/E(B-V) ~ 5.8×10^{21} [R. C. Bohlin, B. D. Savage, J. F. Drake, *Astrophys. J.* **224**, 132 (1978)], and $R \equiv A_v/E$(B-V) = 3.09 [G. H. Rieke and M. J. Lebofsky, *Astrophys. J.* **288**, 618 (1985)]. The optical depth of the silicate feature at 9.7 μm [G. H. Rieke, *Astrophys. J.* **193**, L81 (1974)] may also constrain the column density of H.
25. This assumption is supported by the currently available spectral data on Cygnus OB2 No. 12. The C_2 observations of R. Gredel and G. Münch [*Astron.*

Astrophys. **285**, 640 (1994)] show that at least 90% of the C_2 along this line of sight has v_{LSR} between ~6 and 15 km s^{-1}, whereas there is only a small component at $v_{LSR} \sim 30$ km s^{-1}. In addition, the K I spectroscopy of F. H. Chaffee Jr. and R. E. White [*Astrophys. J. Suppl. Ser.* **50**, 169 (1982)] shows evidence of K I absorption only near the observed velocity of H_3^+.

26. D. Uy, M. Cordonnier, T. Oka, *Phys. Rev. Lett.* **78**, 3844 (1997).
27. T. Oka, *Philos. Trans. R. Soc. London Ser. A* **303**, 543 (1981).
28. We thank G. Sandell and R. P. Tilanus for obtaining the JCMT CO spectra; E. Herbst, L. M. Hobbs, T. P. Snow, P. Thaddeus, and E. F. van Dishoeck for helpful conversations and correspondences; and J. H. Black for assistance in interpreting the C_2 data and for many other helpful comments. B.J.M. is supported by the Fannie and John Hertz Foundation. The University of Chicago portion of this work was supported by NSF grant PHYS-9722691 and NASA grant NAG5-4234.

15 December 1997; accepted 5 February 1998

A.2 "H_3^+ in Dense and Diffuse Clouds"

Reprinted from *Faraday Discussions* 109, 267 (1998).

Faraday Discuss., 1998, **109**, 267–280

H_3^+ in dense and diffuse clouds

Benjamin J. McCall,[a]* Kenneth H. Hinkle,[b] Thomas R. Geballe[c] and Takeshi Oka[a]

[a] *Department of Astronomy and Astrophysics, Department of Chemistry, and the Enrico Fermi Institute, The University of Chicago, Chicago, IL 60637, USA*
[b] *National Optical Astronomy Observatories, Tucson, AZ 85726, USA*
[c] *Joint Astronomy Centre, University Park, Hilo, HI 96720, USA*

Interstellar H_3^+ has been detected in dense as well as diffuse clouds using three 3.7 μm infrared spectral lines of the v_2 fundamental band. Column densities of H_3^+ from (1.7–5.5) × 10^{14} cm^{-2} have been measured in dense clouds in absorption against the infrared continua of the deeply embedded young stellar objects GL2136, W33A, MonR2 IRS 3, GL961E, and GL2591. Strong and broad H_3^+ absorptions have been detected in dense and diffuse clouds towards GC IRS 3 and GCS3-2 in the region of the galactic center. A large column density of H_3^+, comparable to that of a dense cloud, has been detected towards the visible star Cygnus OB2 No. 12, which has a line of sight that crosses mostly diffuse clouds. The H_3^+ chemistry of dense and diffuse clouds are discussed using a very simple model. Some future projects and problems are discussed.

1 Background

Protonated hydrogen, H_3^+, is the simplest stable polyatomic molecule, and was discovered in 1911 by J. J. Thompson.[1] It is the most abundant ion in hydrogen plasmas, as initially discovered by A. J. Dempster.[2] In 1925, Hogness and Lunn[3] introduced the celebrated ion–neutral reaction

$$H_2^+ + H_2 \rightarrow H_3^+ + H \quad \text{(I)}$$

as the primary mechanism for H_3^+ production. By the 1930s, the predominance of H_3^+ among cations in hydrogen plasmas was well established experimentally,[4] and the systematic theoretical studies by Eyring, Hirschfelder and others had explained the large cross-section[5] and high exothermicity[6] of reaction (I). Readers are referred to a review[7] for more details of early works.

1.1 Interstellar H_3^+

The 1961 paper by Martin *et al.*[8] seems to be the first to suggest that H_3^+ should be abundant in interstellar space. In 1970, Stecher and Williams[9] discussed the production and destruction rates of interstellar H_3^+. The first numerical estimate of the interstellar H_3^+ concentration was reported by Solomon and Werner,[10] who also took the decisive step of introducing the cosmic ray as the major agent of ionization. Their estimate of the H_3^+ fraction $X(H_3^+) \equiv [H_3^+]/[\Sigma H] \approx 10^{-6}$ (where $[\Sigma H]$ denotes the total number density of hydrogen atoms), can be contrasted to the value 10^{-8} derived in this paper. de

Jong[11] did similar calculations and obtained $X(H_3^+) \approx 0.4\text{–}1.0 \times 10^{-6}$. Reaction (I) was also used by Glassgold and Langer[12] as the mechanism for cosmic ray heating of molecular clouds and by Watson[13] in his theory of isotope fractionation in interstellar HD.

In 1973, the science of interstellar H_3^+ acquired a new dimension, when Watson[14] and Herbst and Klemperer[15] independently proposed a network of ion–neutral reactions as the mechanism to generate the wide variety of simple molecules that had been observed in interstellar space by radioastronomers.[16] This idea, which was perhaps influenced by the millimeter wave detection of X-ogen by Buhl and Snyder[17] and its subsequent identification as HCO^+ by Klemperer,[18] revealed that H_3^+ plays a central role in interstellar chemistry. Because of the relatively low proton affinity of H_2 (4.5 eV), H_3^+ protonates practically all atoms and molecules through the general reaction

$$H_3^+ + X \rightarrow HX^+ + H_2 \qquad \text{(II)}$$

(He, Ne, Ar, N and O_2 are notable exceptions). After protonation, the HX^+ combines with other species through the reaction

$$HX^+ + Y \rightarrow XY^+ + H \qquad \text{(III)}$$

and initiates a network of chemical reactions. The detailed numerical model calculation of such networks in the classic paper by Herbst and Klemperer[15] explained many of the observed results. Their success triggered an avalanche of papers and reviews on interstellar chemistry based on the ion–neutral reaction scheme. While they are too numerous to cite, many important papers can be traced from the references given in three works that were essential in the preparation of this discussion: the paper by de Jong *et al.*[19] on H_3^+ chemistry, the chemical model calculation for diffuse clouds by van Dishoeck and Black,[20] and the model for dense clouds by Lee *et al.*[21]

1.2 The search for H_3^+

> 'It is likely that H_3^+ is present in the interstellar medium, since H_2^+ ions must be formed from the H_2 molecules present in the interstellar medium either by light absorption beyond 805 Å or by cosmic rays and since each H_2^+ ion will, upon collision with a neutral H_2 molecule, immediately form H_3^+ according to reaction (I). However, the possibility of detecting H_3^+ in interstellar space depends on the discovery of a spectrum of this molecule in the laboratory.'
>
> Gerhard Herzberg, 1967[22]

Herzberg thus attempted together with J. W. C. Johns to observe the infrared ν_2 fundamental band of H_3^+ in emission. Since H_3^+ does not have well-bound electronic excited states,[7] no ultraviolet or visible spectrum is expected. Its symmetric equilateral triangle structure also forbids a conventional rotational spectrum. Therefore, the infrared active degenerate ν_2 band is the most straightforward way to detect interstellar H_3^+.

There were other proposals based on radioastronomy, which is by far the most sensitive method of detecting interstellar molecules. Salpeter and Malone[23] pointed out the possibility of detecting H_3^+ using its radio recombination lines, which are slightly shifted from the H^+ recombination lines due to the difference in reduced mass. The recombination lines of He^+ and C^+ were well known. An emission line feature was noted between the $85\alpha H^+$ and $85\alpha He^+$ in NGC2024[24] but its frequency was not quite right.[25] The detection of H_3^+ using this technique is probably very difficult because of the low abundance of H_3^+ in H II regions, where recombination lines are strong.

Another proposal[26] was to detect the deuterated species H_2D^+. The deuteration shift of the center of gravity from the center of charge produces an effective dipole moment of 0.6 D and makes the rotational spectrum active in the radio and far-infrared region. The abundance of H_2D^+ is much higher than expected from the natural abun-

dance of deuterium because of the efficient isotope fractionation, first explained by Watson.[13, 27] A detection of H_2D^+ emission at 372 GHz was reported[28] in NGC2264 but was later negated.[29] A more recent detection of an H_2D^+ signal by Boreiko and Betz[30] in absorption at 1370 GHz in IRc2 has a better signal-to-noise ratio, though its authenticity has yet to be confirmed. The search for interstellar H_3^+ using its centrifugal distortion spectrum[31] was noted[32] and advocated by Draine and Woods[33] for studies of high temperature objects such as the X-ray heated clouds NGC6240.

The most straightforward way of searching for H_3^+ became possible in 1980 when its infrared v_2 band spectrum was discovered in the laboratory.[34] An immediate attempt to detect H_3^+ in the Becklin–Neugebauer (BN) source in Orion using the FTIR spectrometer at the 4 m Mayall Telescope of the Kitt Peak National Observatory (KPNO) was unsuccessful.[35] A search by two of the authors (T.R.G. and T.O.) was continued using a Fabry–Perot interferometer and a generation of cooled grating spectrometers (CGS) at the UK Infrared Telescope (UKIRT) on Mauna Kea, during which negative results for several sources were published.[36] The search was also attempted by many other groups and some of them published their inconclusive results.[37–40]

From 1988 to 1994, our observational work was diverted to studying H_3^+ in planetary ionospheres following the discovery of strong H_3^+ emission in the auroral regions of Jupiter, Saturn and Uranus,[41] as well as the Comet SL-9 impact on Jupiter. During this time the resolution, sensitivity and reliability of observational infrared spectrometers improved dramatically—a major factor in this development was the use of infrared detector arrays. In 1994, an infrared absorption line of H_2 in NGC2024 was detected at the NASA Infrared Telescope Facility (IRTF).[42] This detection suggested that the sensitivity of IRTF's CSHELL spectrometer had reached the point necessary for H_3^+ detection, since it was known[35] that the ratio of the intensities of the H_3^+ dipole transition and the H_2 quadrupole transition ($\approx 10^9$) just about cancelled the abundance ratio of H_3^+ to H_2 ($\approx 10^{-9}$). Our applications for observing time using CSHELL on IRTF were rejected for three consecutive terms, and interstellar H_3^+ was instead detected by the CGS4 spectrometer at UKIRT, in 1996. Since then our observations have progressed, yielding positive detections in dense clouds, diffuse clouds, and in the region of the galactic center.

2 The H_3^+ spectrum

Since the details of the v_2 fundamental band vibration–rotation spectrum were given in a recent Faraday Discussion,[43] here we simply note two characteristics of the H_3^+ spectrum: the vibrational frequency and the rotational level structure. Both of these characteristics have important consequences for the observation of interstellar H_3^+.

2.1 Vibrational frequency

When a proton is added to an H_2 molecule, the extra charge pushes the two protons away and the equilibrium interproton distance increases from 0.74 Å to 0.87 Å. The vibrational frequency is reduced from 4161.2 cm^{-1} to $v_1 = 3178.3$ cm^{-1} [44] and $v_2 = 2521.3$ cm^{-1}.[45] The infrared active v_2 band is located in a region free from spectral lines of ordinary molecules made from atoms with high cosmic abundance. The hydrogen stretching vibrations of C—H, N—H and O—H bonds are all much higher in frequency and even the high J P-branch lines of light molecules, such as CH_4, NH_3 and H_2O, do not reach the 4 μm region. The hydrogen bending vibrations are all too low in frequency and their R-branches do not reach this region. The stretching vibrations of heavier elements such as C═O, C≡N and C≡C are the closest to this region, but their rotational structures do not extend much in frequency because of their larger moments of inertia. Fig. 1, which was adapted from Genzel's review,[46,47] shows the unique position

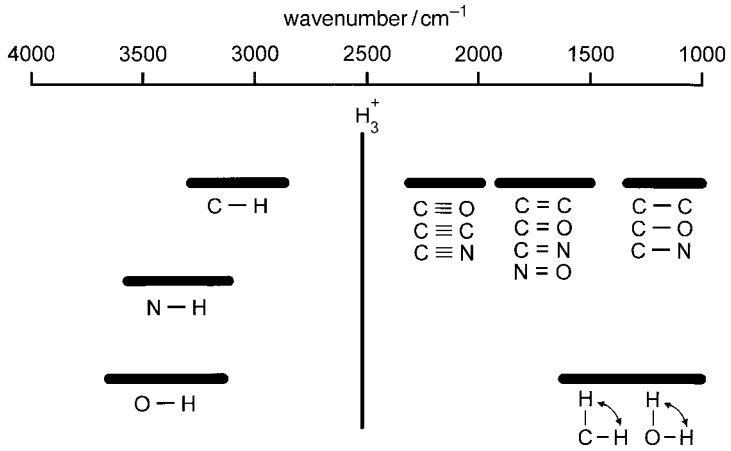

Fig. 1 Position of the v_2 band of H_3^+ compared with other common molecular vibrations. Note that H_3^+ is relatively free of interference from spectral lines of ordinary molecules made from atoms with high cosmic abundance. This figure is adapted from Genzel's review.[46,47]

of the H_3^+ v_2 band. This freedom from the spectra of other molecules is the reason for the extremely pure H_3^+ emission spectrum of Jupiter reported by Maillard *et al.*[48] More importantly for observations of interstellar H_3^+, this favored location of the band origin makes our ground-based observation relatively unhindered by interference with molecules in the terrestrial atmosphere (L window). The only spectral lines that interfere with our observations are deuterium stretching vibrations, notably of HDO, and overtone and combination bands, notably of the $v_2 + v_4$ band of CH_4, which are of course orders of magnitude weaker than the fundamental bands. Had the v_2 band appeared in the 3 μm region, it would have been next to impossible to detect interstellar H_3^+ from ground-based observatories.

2.2 Rotational level structure

Because of its small mass, H_3^+ has large rotational constants[45] $B = 43.56$ cm^{-1} and $C = 20.61$ cm^{-1}, and only the lowest few levels are significantly populated in molecular clouds with temperatures of 10–100 K. The structure of the lowest rotational levels is shown in Fig. 2, where the energy scale is expressed in temperature (Kelvin). J is the rotational angular momentum quantum number and K is its projection onto the C_3 symmetry axis. A special characteristic of this rotational structure is that the lowest level with $J = K = 0$ (shown in Fig. 2 with a broken line) is not allowed by the Pauli exclusion principle. According to Dirac's statement of the Pauli principle,[49,50] the total wavefunction must change sign when two protons are interchanged but must remain invariant when the three protons are cyclicly permuted. The wavefunction of the lowest rotational level is simply a constant and these conditions cannot be simultaneously satisfied, whether this rotational wavefunction is combined with the *ortho* nuclear spin function (in which all proton spins are parallel, $I = \frac{3}{2}$, and the first condition is not satisfied) or with the *para* nuclear spin function (in which one proton spin is antiparallel, $I = \frac{1}{2}$, and the second condition is not satisfied).

This leaves the $J = 1$, $K = 1$ level of *para*-H_3^+ as the lowest ground rotational level. This and the next lowest level with $J = 1$, $K = 0$ of *ortho*-H_3^+, which is higher than the ground level by 32.9 K, are the only levels that are significantly populated for temperatures of 5–50 K. These two levels contain nearly equal populations of molecules,

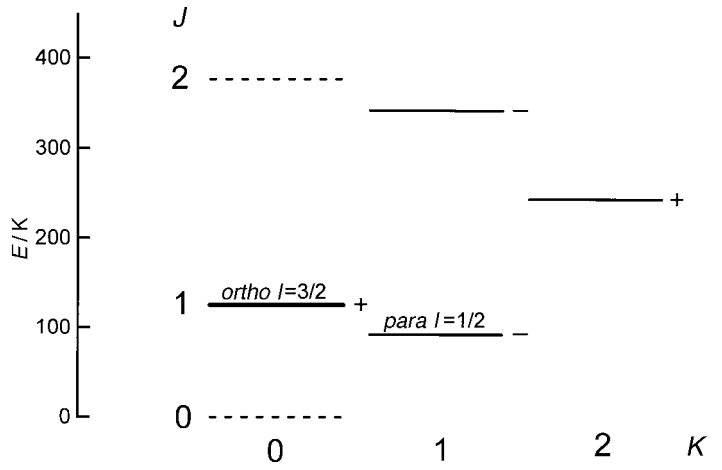

Fig. 2 Structure of the lowest rotational levels of H_3^+. Broken lines represent forbidden levels, the bold line indicates a level with the *ortho* ($I = \frac{3}{2}$) spin modification, the thin lines indicate levels with the *para* ($I = \frac{1}{2}$) spin modifications. The (+) and (−) signs indicate the parity of the levels. The transitions studied in interstellar space arise from the $J = 1$ levels.

since the higher spin statistical weight of *ortho*-H_3^+ ($g_I = 2I + 1 = 4$) than that of *para*-H_3^+ ($g_I = 2$) is approximately compensated for by the Boltzmann factor $\exp(-32.9/T)$. We thus have six spectral lines of comparable intensities at 30 K as shown in Fig. 3, two from *ortho*-H_3^+ [R(1,0) and Q(1,0)] and four from *para*-H_3^+ [$R(1,1)^+$, $R(1,1)^-$, Q(1,1) and P(1,1)]. The existence of six lines makes the observation flexible—we may choose lines that are freest from the telluric interference depending on the weather and the Doppler shift of the night. Two of the spectral lines, $R(1,1)^+$ of *para*-H_3^+ and R(1,0) of

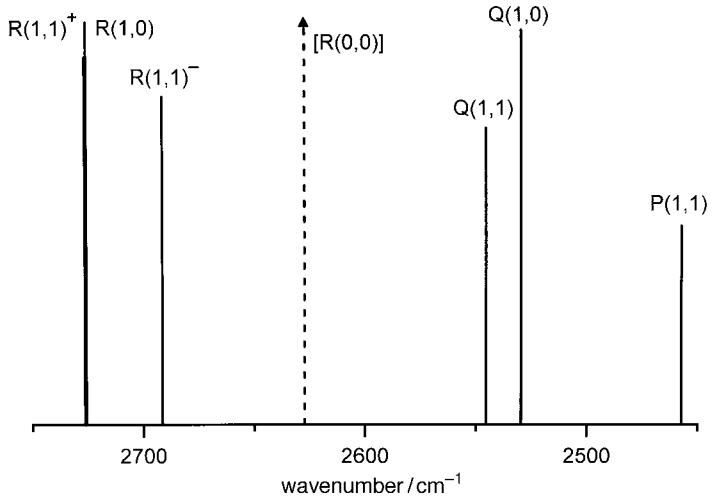

Fig. 3 Six available spectral lines of the ν_2 band of H_3^+. Note that $R(1,1)^+$ and R(1,0) form a doublet with spacing of 0.321 cm^{-1}, which is particularly useful for astronomical observations. The broken line marks the hypothetical position of the transition arising from the forbidden level $J = K = 0$. This line would have an intensity four times that of the other strongest lines if it were allowed. These intensities are calculated for an assumed temperature of 30 K.

ortho-H_3^+, are separated by only 0.321 cm^{-1} and are particularly useful for the measurement of temperature and for confirmation of detections.

Had the lowest $J = K = 0$ level been allowed, the spectrum of H_3^+ would be like an atomic spectrum, since most of the molecules would be in the lowest level, and the R(0,0) line would be the only strong line, at the position shown with a broken arrow in Fig. 3.

3 Observed results

Observations of interstellar H_3^+ have so far been conducted using three infrared spectrometers: the CGS4 at UKIRT with spectral resolution $R \approx 20\,000$, the Phoenix spectrometer at KPNO with $R \approx 60\,000$, and the CSHELL at NASA IRTF with $R \approx 20\,000$. All of them have produced positive results. Interstellar H_3^+ has been found in gravitationally bound dense clouds with high density ($[\Sigma H] \approx 10^3$–10^5 cm^{-3}) as well as in unbound diffuse clouds with low density (10–10^3 cm^{-3}).

3.1 H_3^+ in dense clouds

The first spectra of interstellar H_3^+ were detected towards the young stellar objects (YSOs) GL2136 and W33A, which are deeply embedded in dense molecular clouds.[51] These spectra were obtained with CGS4 at UKIRT on the nights of April 25, June 10 and July 15, 1996. These YSOs were chosen because of their infrared brightness and because of their large column densities of foreground gas. In addition, it was thought advantageous[52] to use carbon depleted clouds where H_3^+ is destroyed less by the proton hop reaction (II). Strong absorptions of solid CO frozen on dust grains have been reported[53,54] although the depletions might not be large.[55]

The R(1,0)–R(1,1)$^+$ doublet of H_3^+ mentioned earlier was used for the detection. The observed signal to noise ratios of the absorption lines were by no means great, but the Doppler shift of the doublet lines due to the earth's orbital motion from April 25 to July 15 convinced us that the signals were genuine (see Fig. 4).

Subsequent observations revealed interstellar H_3^+ in dense clouds towards three other YSOs: MonR2 IRS 3 and GL961E (February 11–14, 1997, at UKIRT), and

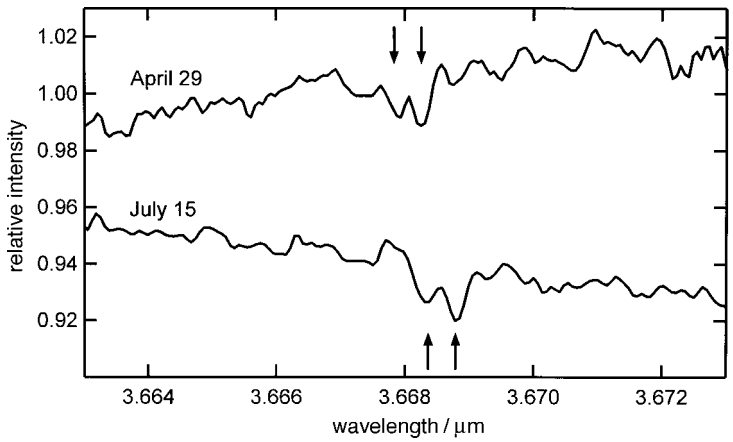

Fig. 4 Spectra of the R(1,0)–R(1,1)$^+$ doublet of H_3^+ obtained with the CGS4 spectrometer at UKIRT along the line of sight to GL2136. The upper trace was obtained on 29 April, 1996, while the lower trace was obtained on 15 July, 1996. The observed Doppler shift of the doublet (marked with arrows) between the two dates matches that expected from the Earth's orbital motion, providing convincing evidence that the doublet is genuine.

GL2591 (July 11–12, 1997, at UKIRT). The observed equivalent widths W_v yield the H_3^+ column densities using the standard formula

$$W_v \equiv \int [\Delta I(v)/I(v)]\, dv = (8\pi^3 v/3hc) N |\boldsymbol{\mu}|^2 \quad (1)$$

where $|\boldsymbol{\mu}|^2$ is the square of the transition dipole moment. The spectral lines of *ortho*-H_3^+ and *para*-H_3^+ give their column densities N_o and N_p separately, and their sum gives the total H_3^+ column density $N(H_3^+)$. The ratio of N_o and N_p gives the temperature of the clouds using the standard formula

$$\frac{N_o}{N_p} = \frac{g_o}{g_p} e^{(-\Delta E/kT)} = 2\, e^{(-32.9/T)} \quad (2)$$

These results are summarized in Table 1. We have also studied the infrared sources GL490, GL989, LkHα 101, MonR2 IRS 2, M17 IRS 1, S140 IRS 1, W3 IRS 5, Elias 29, NGC2024 IRS 2 and BN. So far, our data reduction has not provided evidence of column densities at the level of *ca.* 2–3 × 10^{14} cm^{-2}, but careful reprocessing of these spectra continues. The lack of strong H_3^+ absorption towards NGC2024 IRS 2 and BN was particularly surprising in view of the large column density of H_2 reported in the former[42] and the observed richness of molecules in the latter. We believe that these non-detections are not due to the absence of H_3^+ in the clouds but are simply due to the short column length of the clouds in front of the source (see the discussion in Section 4.1). More details of our study of dense clouds will be published elsewhere.[56]

3.2 H_3^+ in diffuse clouds

During our survey of H_3^+ in dense clouds, we observed strong and broad H_3^+ absorption signals in the direction of the infrared sources GC IRS 3 and GCS3-2 (July 11–12, UKIRT), in the region near the galactic center. These sources are thought to be 8 kpc away and their lines of sight may cross several clouds, both dense and diffuse. Indeed McFadzean *et al.*[57] reported observational evidence for two components in the extinction: the 3.0 μm ice absorption (a signature of dense clouds) and the 3.4 μm hydrocarbon absorption (a signature of diffuse clouds). More details of our galactic center observations will be published separately.[58]

The galactic center results led us to try Cygnus OB2 No. 12, a visible star with high extinction discovered in 1954.[59] It is generally believed that this star is obscured largely by diffuse, low density clouds containing little molecular material.[60] We clearly observed

Table 1 Positions and derived column densities and temperatures for H_3^+ sources

infrared source	position		$N(H_3^+)/(10^{14}\ cm^{-2})^a$	T/K
	α (1950)	δ (1950)		
dense clouds				
GL2136	18 : 19 : 36.6	−13 : 31 : 40	3.6 ± 0.6	35 ± 4
W33A	18 : 11 : 44.2	−17 : 52 : 56	5.5 ± 1.9	30 ± 6
MonR2 IRS 3	06 : 05 : 21.8	−06 : 22 : 26	2.1 ± 0.7	24 ± 4
GL961E	06 : 31 : 59.1	+04 : 15 : 10	1.7 ± 0.7	24 ± 5
GL2591	20 : 27 : 35.8	+40 : 01 : 14	2.0 ± 1.0[b]	
diffuse clouds				
Cyg OB2 No. 12	20 : 30 : 53.4	+ 41 : 03 : 52	3.8 ± 0.5	20 ± 4

[a] Statistical uncertainties (3σ) are quoted in parentheses but systematic errors are difficult to estimate and might be larger. [b] Estimated systematic uncertainty is given for GL2591, as this spectrum is not yet fully reduced.

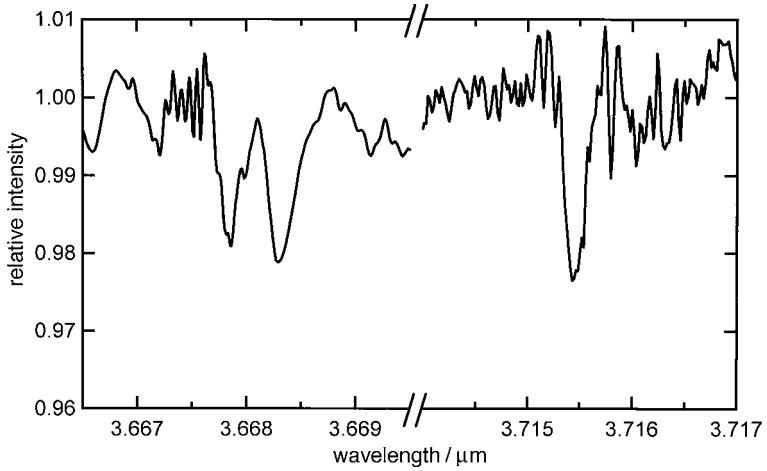

Fig. 5 Spectra of the line of sight towards the visible star Cygnus OB2 No. 12. The left trace, showing the R(1,0)–R(1,1)$^+$ doublet of H_3^+, was obtained with CGS4 at UKIRT on 11 July, 1997. The right trace, showing the R(1,1)$^-$ line of H_3^+, was obtained with the new Phoenix spectrometer at KPNO on 17 September, 1997. The high frequency interference in the CGS4 spectrum near 3.6675 μm is due to the removal of a telluric CH_4 absorption line.

the H_3^+ R(1,0)–R,(1,1)$^+$ doublet (July 11–12, UKIRT) and the R(1,1)$^-$ singlet (September 15–17, KPNO).[61] Because of the high humidity in Arizona in September, strong and wide telluric HDO lines (ν_2 band $1_{10} \leftarrow 1_{11}$ and $4_{22} \leftarrow 4_{23}$) made the observation of the doublet impossible, but the singlet (which has only CH_4 lines nearby) was clearly observed. The observed spectrum is shown in Fig. 5. Using the observed equivalent widths of the lines and eqn. (1), we obtain the remarkable result that the column density of H_3^+ in the direction of Cygnus OB2 No. 12 is $(3.8 \pm 0.5) \times 10^{14}$ cm^{-2}, comparable to that of the dense clouds listed in Table 1. van Dishoeck and Black[20,62] reported their extensive chemical model calculation in diffuse clouds and predicted high column densities of H_3^+, but their calculation was based on an extremely small electron recombination rate constant, which has since been demonstrated to be too low by more than three orders of magnitude.[63] Calculations given in the next section show that the large column density of H_3^+ in the diffuse clouds towards Cygnus OB2 No. 12 is due not to a high number density of H_3^+ but simply to a long column length. Our calculation is much cruder than that of van Dishoeck and Black but is essentially the same as far as the H_3^+ chemistry is concerned, except that a revised recombination rate is used.

4 H_3^+ chemistry

A very attractive aspect of H_3^+ as a molecular astronomical probe is its simple chemistry. The simplicity of the chemistry allows us to make relatively simple and reliable arguments about the H_3^+ number densities and other astrophysical quantities. In the following, we give a crude order of magnitude discussion of its chemistry; more detailed chemical model calculations such as those given by Lee *et al.*[21] and by van Dishoeck and Black[20] are of course desirable for more accurate discussions.

4.1 H_3^+ chemistry in dense clouds

In cold dense clouds, which are protected from star radiation, H_3^+ is produced almost exclusively from the cosmic ray (CR) ionization of H_2 to H_2^+,

$$H_2 \xrightarrow{CR} H_2^+ + e^- \qquad \text{(IV)}$$

followed by the ion–neutral reaction (I). Reaction (I) is many orders of magnitude more rapid than reaction (IV) and the production rate is governed by the rate of reaction (IV), *i.e.*, $\zeta[H_2]$. The cosmic ray ionization rate $\zeta \approx 10^{-17}$ s^{-1} and H_2 number density $[H_2] \approx 10^4$ cm^{-3} yield an H_3^+ production rate of *ca.* 10^{-13} cm^{-3} s^{-1}.

H_3^+ is destroyed predominantly by the proton hop reaction (II). Equating the production and destruction rates, we have the steady-state equation

$$\zeta[H_2] = \sum_x k_x[H_3^+][X] \tag{3}$$

where k_x is the rate constant for reaction (II). Since CO is the most abundant molecule in dense clouds, we neglect the terms of the other atoms and molecules in eqn. (3) and obtain the H_3^+ number density

$$[H_3^+] = \frac{\zeta}{k_{CO}} \frac{[H_2]}{[CO]} \tag{4}$$

Since the ratio $[H_2]/[CO] \approx 10^4$ is approximately constant over a wide variety of molecular parameters,[21] this shows that $[H_3^+]$ is constant. Using the Langevin rate[64] $k_{CO} \approx 10^{-9}$ cm^3 s^{-1} we obtain $[H_3^+] \approx 10^{-4}$ cm^{-3}. The observed H_3^+ column density of 3×10^{-14} cm^{-2} (see Table 1) gives a typical effective column length of ≈ 1 pc.

The most serious omission in this discussion is the neglect of X terms other than CO from eqn. (3). In the model calculations of Lee *et al.*,[21] the abundance of O is predicted to be comparable to that of CO. Inclusion of the O term will reduce the $[H_3^+]$ by *ca.* 30% since the rate constant k_O is about 1/2.5 of k_{CO}.[64] The neglect of the electron term $X = e^-$ in eqn. (3) also has to be addressed since the recombination rate constant k_e is larger than k_{CO} by more than two orders of magnitude (see Section 4.2). However, the model calculations of Lee *et al.*[21] show that this correction is significant only in clouds with high metallicity, where the electron concentration is increased by the ionization of alkali and alkaline-earth metals with low work functions. The lack of accurate measurements of k_O (and for that matter even of k_{CO}) is also a source of error and more laboratory studies are awaited.

However, all these corrections will be small compared to the large uncertainty in ζ. We hope that our H_3^+ measurements will help further constrain this important parameter.

4.2 H_3^+ chemistry in diffuse clouds

In diffuse clouds where the number density is low (10–10^3 cm^{-3}) and visible light passes through, cosmic ray ionization followed by reaction (I) is again the primary mechanism for H_3^+ production. Photoionization of H_2 is not effective because the cloud contains abundant atomic H atoms whose ionization potential (13.6 eV) is lower than that of H_2 (15.4 eV).

The main destruction mechanism of H_3^+ in diffuse clouds is expected to be electron recombination, because of the high number density of electrons created by photoionization of carbon (the carbon atom has the lowest ionization potential, 11.3 eV, of any abundant species). We assume for simplicity that all carbon atoms which are not depleted onto dust grains are ionized and that all electrons come from the ionization of carbon atoms, *i.e.*, $[e^-] = [C^+] = [\Sigma C]$, where $[\Sigma C]$ denotes the total number density of carbon atoms. The solution of the steady state equation is then

$$[H_3^+] = \frac{\zeta}{k_e} \frac{[H_2]}{[e^-]} \tag{5}$$

indicating that the H_3^+ number density is constant also in diffuse clouds. Using $k_e \approx 10^{-7}$ cm^3 s^{-1} [63] and $[H_2]/[e^-] \approx [H_2]/[\Sigma C] \approx 10^4$ we obtain an H_3^+ number

density of $[H_3^+] \approx 10^{-6}$ cm^{-3}, smaller than that of dense clouds by two orders of magnitude. Thus the same H_3^+ column density as in dense clouds (3×10^{14} cm^{-2}) implies an effective path length (L) that is longer by two orders of magnitude, $L \sim 100$ pc. This path length is very likely composed of several diffuse clouds rather than a single cloud.

There is a major uncertainty in the above estimates, apart from that of ζ. Unlike other k_x with Langevin rates, which are independent of temperature,[65,66] k_e varies significantly at low temperature. If we use $k_e = 4.6 \times 10^{-6}/T^{0.65}$ cm^3 s^{-1}, as determined from the storage ring experiment of Sundström *et al.*,[67] and assume $T \approx 30$ K, k_e is closer to 10^{-6} cm^3 s^{-1} and $L \approx 1$ kpc. In addition, we have not considered direct photodissociation of H_3^+. This is thought to be slow[68] but more theoretical and experimental studies are certainly needed.

4.3 Intermediate case

The above two analyses for the extreme cases can be generalized to the intermediate case where the destruction rates of H_3^+ by CO and by electrons are comparable. We assume that all carbon atoms in the gas phase are either in the form of C^+ or CO, that is, $[\Sigma C] = [C^+] + [CO]$, where $[\Sigma C]$ denotes the total number density of carbon atoms in any gaseous form. Other carbon species (atomic C, CO_2, CH_4, *etc.*) can be included in [CO] since they all have Langevin rates for the proton hop reaction (II). We have

$$[H_3^+] = \zeta \frac{f}{2} \frac{[\Sigma H]}{[\Sigma C]} \left[\frac{1}{k_e(1-\alpha) + k_{CO}\alpha} \right] \tag{6}$$

where f is the fraction of hydrogen atoms in molecular form $f \equiv 2[H_2]/[\Sigma H]$ and α is the fraction of carbon atoms in molecular form, $\alpha \equiv [CO]/[\Sigma C]$. For derivation of this formula and further discussions of the total number density $[\Sigma H]$ and path length L of the cloud, see McCall *et al.*[61]

5 Future prospects

Our observations have established that interstellar H_3^+ exists with sufficient abundance to be observable from ground-based observatories both in dense and diffuse clouds. In fact, we find it easier to observe H_3^+ absorption lines than H_2 infrared absorption lines. Perhaps H_3^+ is not only a powerful probe for the study of plasma activities of astronomical objects, but also a most convenient probe for the detection of hydrogenic molecular species. In the spirit of this conference, we speculate in this section on some possible developments in the immediate future.

5.1 Future observations

From ground-based observatories, H_3^+ will be found in many other sources. For dense clouds the observations will give information of the depth of the embedded YSO and for diffuse clouds they will give the dimension of the clouds. For a source like the Quintuplet near the galactic center where many infrared sources are positioned within a narrow angle of sight, some type of 'mapping' such as radioastronomers do might be possible. This will be most efficiently done when the Phoenix spectrometer is moved to the Cerro Tololo Interamerican Observatory next year (1999). The expected advent of larger telescopes with high-resolution infrared spectrometers, such as Gemini and Subaru, and the installation of a high-resolution spectrometer at Keck will allow us to observe much fainter infrared sources. H_3^+ will be observed in a great many more

objects with higher spectral resolution. We may not have to wait many years before H_3^+ is observed in extragalactic objects.

5.2 H_3^+ emission

Observing the infrared spectrum of H_3^+ in emission is an interesting possibility. One remembers the strong and pure H_3^+ emission lines observed in planetary ionospheres.[7] The strongest H_2 quadrupole emission line $S_1(1)$ (with a spontaneous emission lifetime of 7×10^6 s [69]) is observed with large signal to noise ratios in planetary nebulae,[70] extragalactic superluminous objects,[71] and many other objects, even using low resolution spectrometers. In order to evaluate the prospects for detecting H_3^+ emission we make a rough estimate of the ratio of intensities for H_3^+ emission, $I_{H_3^+}$, and H_2 emission, I_{H_2}:

$$\frac{I_{H_3^+}}{I_{H_2}} = \frac{[H_3^+]}{[H_2]} \frac{k_{H_3^+}}{k_{H_2}} \tag{7}$$

where $k_{H_3^+}$ and k_{H_2} are rate constants for collisional pumping from $v = 0$ to $v = 1$. We estimate that the abundance of H_3^+ should be roughly $[H_3^+]/[H_2] \approx 10^{-8}$, which one would think would make the ratio small. However, we must consider the differences in the vibrational pumping mechanisms. The collisional excitation of H_2 by H_2

$$H_2 + H_2 \rightarrow H_2^* + H_2 \tag{V}$$

is performed by a weak physical interaction, in which the translational energy of H_2 must be converted to vibrational energy (V–T transfer) during the short time of the encounter. Resonant V–V transfer cannot contribute, since the number of H_2^* remains the same in the 'reaction' $H_2^* + H_2 \rightarrow H_2 + H_2^*$.

On the other hand, the excitation of H_3^+ is performed by a strong chemical interaction

$$H_3^+ + H_2 \rightarrow H_3^{+*} + H_2 \tag{VI}$$

where asterisks signify vibrational excitation. In this case, the molecules attract each other by the Langevin force, form an activated complex $(H_5^+)^*$, and then dissociate into H_3^{+*} and H_2. This reaction is known to have a Langevin rate from a deuterium experiment[64] and a recent experiment of spin modification.[72] The branching ratio of reaction (VI) to form H_3^+ or H_3^{+*} is not known but we assume that it is not much different from 1 : 1. Then using the approximate equality between the Langevin rate and the rate of rotational energy transfer (R–R),[73] and the rule of thumb[74] $k_{V-T}/k_{R-R} \approx 10^{-5}$, we obtain $k_{H_3^+}/k_{H_2} \approx 10^5$. If we use experimental and theoretical $v' = 1 \rightarrow 0$ de-excitation rates[75] and the principle of detailed balancing, we find that $k_{H_3^+}/k_{H_2} \approx 10^5$–$10^6$ for $T = 2000$–1000 K.

Thus we obtain an estimate of $I_{H_3^+}/I_{H_2} \approx 10^{-3}$–$10^{-2}$. This is a minimum value and will be larger for a molecular cloud with a density higher than the critical density.[76] In such a high-density environment, the H_3^+ intensity will be increased due to the faster collisional pumping (as H_3^+ has a spontaneous emission time of only ≈ 10 ms[77]), but the H_2 intensity will be limited by the slower rate of spontaneous emission.

Even if $I_{H_3^+}/I_{H_2} \approx 10^{-3}$, the detection of H_3^+ emission is a realistic prospect in view of the extremely high observed signal to noise ratios of H_2 emission ($\gtrsim 1000$ at low resolution).

5.3 H_3^+ as an interstellar agent

Interstellar H_3^+ not only plays the central role of the protonator to initiate a network of chain reactions, but also performs other essential functions of interstellar chemistry. For

example, it will mediate conversion of *ortho*-H_2 to *para*-H_2 through the proton hop reaction

$$H_3^+ + \tilde{H}_2 \rightarrow H_2 + \tilde{H}_2H^+ \quad \text{(VII)}$$

and proton exchange reaction

$$H_3^+ + \tilde{H}_2 \rightarrow H_2\tilde{H}^+ + H\tilde{H} \quad \text{(VIII)}$$

This scrambling of protons will thermalize spin modifications. The actual efficiency of this mechanism should be calculated using the nuclear modification branching ratios theoretically predicted by Quack[78] and recently experimentally demonstrated.[72] These processes must be much more efficient than the mechanism proposed earlier[79]

$$H^+ + o\text{-}H_2 \rightarrow H^+ + p\text{-}H_2 \quad \text{(IX)}$$

both because of the higher abundance of H_3^+ and the higher rate constant of reactions (VII) and (VIII) than (IX).

Klemperer and Miller[80] have recently proposed that the strong CO Cameron band emission ($a\,^3\Pi \rightarrow X\,^1\Sigma^+$) from 1850–2600 Å observed in the Red Rectangle nebula[81,82] might be due to a chemical pumping of CO by H_3^+ through the reactions

$$H_3^+ + CO \rightarrow HCO^+ + H_2 \quad \text{(X)}$$

and

$$HCO^+ + e^- \rightarrow CO^* + H \quad \text{(XI)}$$

where the asterisk signifies CO in the $a\,^3\Pi$ excited state. In diffuse clouds where $[e^-] \gg [CO]$, the second reaction is much faster than the first and the rate for CO* excitation is $k_{CO}[H_3^+][CO] \approx 10^{-26}$ cm^{-3} s^{-1} (here again we neglect the branching ratio between CO and CO*). Glinski *et al.*[81] proposes the direct electron pumping

$$CO + e^-* \rightarrow CO^* + e^- \quad \text{(XII)}$$

to be the main mechanism where e^-* signifies electrons at high energy $\approx$ 8–12 eV. The rate of this process is $k[CO][e^-*]$ where the rate constant of excitation k is $\approx 10^{-8}$ cm^3 s^{-1}. Thus the relative efficiency of the H_3^+ pumping of Klemperer and Miller and the electron pumping of Glinski *et al.* depends on the relative magnitudes of $[H_3^+]$ and $10[e^-*]$. It is quite probable that H_3^+ is the agent for the emission, especially for the rotationally cold emission core.

We have profited from discussions with W. Klemperer and K. Takayanagi. B.J.M. is supported by the Fannie and John Hertz Foundation. The University of Chicago portion of this work has been supported by NSF grant PHYS-9722691 and NASA grant NAG5-4070.

References

1 J. J. Thompson, *Philos. Mag.*, 1911, **21**, 225.
2 A. J. Dempster, *Philos. Mag.*, 1916, **31**, 438.
3 T. R. Hogness and E. G. Lunn, *Phys. Rev.*, 1925, **26**, 44.
4 H. D. Smyth, *Rev. Mod. Phys.*, 1931, **3**, 347.
5 H. Eyring, J. O. Hirschfelder and H. S. Taylor, *J. Chem. Phys.*, 1936, **4**, 479.
6 J. O. Hirschfelder, *J. Chem. Phys.*, 1938, **6**, 795.
7 T. Oka, in *Molecular Ions: Spectroscopy, Structure and Chemistry*, ed. T. A. Miller and V. E. Bondybey, North Holland, New York, 1983, p. 73.
8 D. W. Martin, E. W. McDaniel and M. L. Meeks, *Astrophys. J.*, 1961, **134**, 1012.
9 T. P. Stecher and D. A. Williams, *Astrophys. Lett.*, 1970, **7**, 59.
10 P. M. Solomon and M. W. Werner, *Astrophys. J.*, 1971, **165**, 41.

11 T. de Jong, *Astron. Astrophys.*, 1972, **20**, 263. We assume that his Case (A) is closer to reality than Case (B).
12 A. E. Glassgold and W. D. Langer, *Astrophys. J.*, 1973, **179**, L147.
13 W. D. Watson, *Astrophys. J.*, 1973, **182**, L73.
14 W. D. Watson, *Astrophys. J.*, 1973, **183**, L17.
15 E. Herbst and W. Klemperer, *Astrophys. J.*, 1973, **185**, 505.
16 D. M. Rank, C. H. Townes and W. J. Welch, *Science*, 1971, **174**, 1083.
17 D. Buhl and L. E. Snyder, *Nature* (*London*), 1970, **228**, 267.
18 W. Klemperer, *Nature* (*London*), 1970, **227**, 1230.
19 T. de Jong, A. Dalgarno and W. Boland, *Astron. Astrophys.*, 1980, **91**, 68.
20 E. F. van Dishoeck and J. H. Black, *Astrophys. J. Suppl.*, 1986, **62**, 109.
21 H.-H. Lee, R. P. A. Bettens and E. Herbst, *Astron. Astrophys. Suppl.*, 1996, **119**, 111.
22 G. Herzberg, *Trans. R. Soc. Can.*, 1967, **V**, 3.
23 E. E. Salpeter and R. C. Malone, *Astrophys. J.*, 1971, **167**, 27.
24 J. M. MacLeod, L. H. Doherty and L. A. Higgs, *Astron. Astrophys.*, 1975, **42**, 195.
25 T. Oka, personal communication.
26 A. Dalgarno, E. Herbst, S. Novick and W. Klemperer, *Astrophys. J.*, 1973, **183**, L131.
27 W. D. Watson, *Rev. Mod. Phys.*, 1976, **48**, 513.
28 T. G. Phillips, G. A. Blake, J. Keene, R. C. Woods and E. Churchwell, *Astrophys. J.*, 1985, **294**, L45.
29 E. F. van Dishoeck, T. G. Phillips, J. Keene and G. A. Blake, *Astron. Astrophys.*, 1992, **261**, L13.
30 R. T. Boreiko and A. L. Betz, *Astrophys. J.*, 1993, **405**, L39.
31 J. K. G. Watson, *J. Mol. Spectrosc.*, 1971, **40**, 536.
32 F.-S. Pan and T. Oka, *Astrophys. J.*, 1986, **305**, 518.
33 B. T. Draine and D. T. Woods, *Astrophys. J.*, 1990, **363**, 464.
34 T. Oka, *Phys. Rev. Lett.*, 1980, **45**, 531.
35 T. Oka, *Philos. Trans. R. Soc. London, A*, 1981, **303**, 543.
36 T. R. Geballe and T. Oka, *Astrophys. J.*, 1989, **342**, 855.
37 P. G. Burton, E. von Nagy-Felsobuki and G. Doherty, *Chem. Phys. Lett.*, 1984, **104**, 323.
38 J. H. Black, E. F. van Dishoeck, S. P. Willner and R. C. Woods, *Astrophys. J.*, 1990, **358**, 459.
39 J. Tennyson, S. Miller and H. Schild, *J. Chem. Soc., Faraday Trans.*, 1993, **89**, 2155.
40 J. P. Maillard, *Spectrochim. Acta, Part A*, 1995, **51**, 1105.
41 See for review, T. Oka, *Rev. Mod. Phys.*, 1992, **64**, 1141.
42 J. H. Lacy, R. Knacke, T. R. Geballe and A. T. Tokunaga, *Astrophys. J.*, 1994, **428**, L69.
43 T. Oka and M.-F. Jagod, *J. Chem. Soc., Faraday Trans.*, 1993, **89**, 2147.
44 W. Ketterle, M.-P. Messmer and H. Walther, *Europhys. Lett.*, 1989, **8**, 333.
45 J. K. G. Watson, S. C. Foster, A. R. W. McKellar, P. Bernath, T. Amano, F.-S. Pan, M. W. Crofton, A. J. Altman and T. Oka, *Can. J. Phys.*, 1984, **62**, 1875.
46 R. Genzel, in *The Galactic Interstellar Medium*, ed. D. Pfenniger and P. Bartholdi, Springer-Verlag, Berlin, 1992, p. 275.
47 L. J. Allamandola, in *Galactic and Extragalactic Infrared Spectroscopy*, ed. M. F. Kessler and J. P. Phillips, Reidel, Dordrecht, 1984, p. 5.
48 J.-P. Maillard, P. Drossart, J. K. G. Watson, S. J. Kim and J. Caldwell, *Astrophys. J.*, 1990, **363**, L37.
49 P. A. M. Dirac, *Proc. R. Soc. London, A*, 1926, **112**, 661.
50 For a pedagogical explanation of the relation between the Pauli principle and relativity, see S. Tomonaga, *The Story of Spin*, Univ Chicago Press, Chicago, IL, 1998.
51 T. R. Geballe and T. Oka, *Nature* (*London*), 1996, **384**, 334.
52 S. Lepp, A. Dalgarno and A. Sternberg, *Astrophys. J.*, 1987, **321**, 383.
53 T. R. Geballe, F. Baas, J. M. Greenberg and W. Schutte, *Astron. Astrophys.*, 1985, **146**, L6.
54 W. A. Schutte, P. A. Gerakines, T. R. Geballe, E. F. van Dishoeck and J. M. Greenberg, *Astron. Astrophys.*, 1996, **309**, 633.
55 G. F. Mitchell, J.-P. Maillard, M. Allen, R. Beer and K. Belcourt, *Astrophys. J.*, 1990, **363**, 554.
56 B. J. McCall, T. R. Geballe, K. H. Hinkle and T. Oka, manuscript in preparation.
57 A. D. McFadzean, D. C. B. Whittet, A. J. Longmore, M. F. Bode and A. J. Adamson, *Mon. Not. R. Astron. Soc.*, 1989, **241**, 873.
58 T. R. Geballe, B. J. McCall, K. H. Hinkle and T. Oka, manuscript in preparation.
59 W. W. Morgan, H. L. Johnson and N. G. Roman, *Publ. Astron. Soc. Pac.*, 1954, **66**, 85.
60 D. C. B. Whittet, A. C. A. Boogert, P. A. Gerakines, W. Schutte, A. G. G. M. Tielens, Th. de Graauw, T. Prusti, E. F. van Dishoeck, P. R. Wesselius and C. M. Wright, *Astrophys. J.*, 1997, **490**, 729.
61 B. J. McCall, T. R. Geballe, K. H. Hinkle and T. Oka, *Science*, 1998, **279**, 1910.
62 J. H. Black, in *IAU Symp. 120 Astrochemistry*, ed. M. S. Vardya and S. P. Tarafdar, Dordrecht, Reidel, 1987, p. 217.
63 T. Amano, *Astrophys. J.*, 1988, **329**, L121.
64 V. G. Anicich and W. T. Huntress, Jr., *Astrophys. J. Suppl.*, 1986, **62**, 553.
65 J. C. Maxwell, *Philos. Trans. R. Soc.*, 1879, **170**, 231.

66 M. P. Langevin, *Ann. Chim. Phys*., 1905, **5**, 245.
67 G. Sundström, J. R. Mowat, H. Danared, S. Datz, L. Broström, A. Filevich, A. Källberg, S. Mannervik, K. G. Rensfelt, P. Sigray, M. af Ugglas and M. Larsson, *Science*, 1994, **263**, 785.
68 E. F. van Dishoeck, in *IAU Symp. 120, Astrochemistry*, ed. M. S. Vardya and S. P. Trafdar, Dordrecht, Reidel, 1986, p. 51.
69 J. H. Black and A. Dalgarno, *Astrophys. J*., 1976, **203**, 132.
70 See for example, H. A. Thronson, Jr., *Astrophys. J*., 1981, **248**, 984.
71 See for example, T. R. Geballe, *Can. J. Phys*., 1994, **72**, 782.
72 D. Uy, M. Cordonnier and T. Oka, *Phys. Rev. Lett*., 1997, **78**, 3844.
73 T. Oka, *Adv. Atom. Mol. Phys*., 1973, **9**, 127.
74 W. H. Flygare, *Acc. Chem. Res*., 1968, **1**, 121.
75 M. Cacciatore, M. Capitelli and G. D. Billing, *Chem. Phys. Lett*., 1989, **157**, 305.
76 J. M. Shull and D. J. Hollenbach, *Astrophys. J*., 1978, **220**, 525.
77 G. D. Carney and R. N. Porter, *J. Chem. Phys*., 1976, **65**, 3547.
78 M. Quack, *Mol. Phys*., 1977, **34**, 477.
79 A. Dalgarno, J. H. Black and J. C. Weisheit, *Astrophys. Lett*., 1973, **14**, 77.
80 W. Klemperer and A. Miller, personal communication.
81 R. J. Glinski, J. A. Nuth, M. D. Reese and M. L. Sitko, *Astrophys. J*., 1996, **467**, L109.
82 R. J. Glinski, J. T. Lauroesch, M. D. Reese and M. L. Sitko, *Astrophys. J*., 1997, **490**, 826.

Paper 8/00655E; *Received* 23*rd January*, 1998

A.3 "Detection of H_3^+ in the Diffuse Interstellar Medium: The Galactic Center and Cygnus OB2 Number 12"

Reprinted from *Astrophysical Journal* 510, 251 (1999).

THE ASTROPHYSICAL JOURNAL, 510:251–257, 1999 January 1

DETECTION OF H_3^+ IN THE DIFFUSE INTERSTELLAR MEDIUM: THE GALACTIC CENTER AND CYGNUS OB2 NUMBER 12

T. R. GEBALLE
Joint Astronomy Centre, Hilo, HI 96720; t.geballe@jach.hawaii.edu
B. J. MCCALL
Department of Astronomy and Astrophysics, Department of Chemistry, and Enrico Fermi Institute, University of Chicago, Chicago, IL 60637
K. H. HINKLE
National Optical Astronomy Observatories,[1] Tucson, AZ 85726
AND
T. OKA
Department of Astronomy and Astrophysics, Department of Chemistry, and Enrico Fermi Institute, University of Chicago, Chicago, IL 60637
Received 1998 June 29; accepted 1998 August 4

ABSTRACT

Absorption lines of H_3^+ have been detected in the spectra of two infrared sources in the Galactic center and also toward the heavily reddened star Cygnus OB2 No. 12, whose line of sight is believed to include only diffuse interstellar gas. The absorptions toward the Galactic center sources (IRS 3 and GCS 3-2) probably are due to H_3^+ both in diffuse gas and in molecular clouds. The ratios of H_3^+ line equivalent width to extinction toward these three sources are much greater than those toward dense clouds where H_3^+ has been detected previously. Analysis of the spectra coupled with a simple model for the abundance of H_3^+ in the diffuse interstellar medium implies that the observed H_3^+ is present at low densities along long path lengths. These are the first detections of H_3^+ in the diffuse interstellar medium.

Subject headings: Galaxy: center — infrared: ISM: lines and bands — ISM: clouds — ISM: molecules — molecular processes — stars: individual (Cygnus OB2 No. 12)

1. INTRODUCTION

The triatomic molecular ion H_3^+ is widely regarded as a cornerstone of chemistry in the gaseous interstellar medium. Ion-molecule reactions involving it are the starting point of reaction chains that lead to the production of many of the molecules that have been detected in dense molecular clouds (Herbst & Klemperer 1973; Watson 1973). H_3^+ does not have a conventional pure rotational spectrum, and astronomical searches for it had to await the measurement of its fundamental vibration-rotation band in the laboratory (Oka 1980) and the advent of sensitive high-resolution infrared array spectrometers for astronomy.

The first detections of H_3^+ outside the solar system, via two absorption lines near 3.67 μm, were reported in two dense molecular cloud cores along the lines of sight to the embedded young stellar objects W33A and GL 2136 (Geballe & Oka 1996). Since then a small survey at this wavelength has resulted in the detection of H_3^+ in several additional molecular clouds containing bright embedded young stellar objects (McCall, Geballe, & Oka 1999). In all of these cases the observed line strengths, which are very small, are consistent with the expected abundance of H_3^+ as determined by its predicted rates of production (following ionization of H_2 by cosmic rays) and destruction (by its reactions with other molecules, principally CO).

In the course of carrying out the above survey, we observed the Galactic center nuclear source IRS 3 (Becklin et al. 1978) and detected the 3.67 μm H_3^+ doublet in absorption. The absorption is unusually strong compared to those that have been measured in dense clouds, with a ratio of equivalent width to total extinction an order of magnitude larger than what is typical for dense clouds. We also detected absorption by H_3^+ with similar strength in the Galactic center "quintuplet" source GCS 3-2 (Nagata et al. 1990) located a quarter of a degree from the nucleus, which implies that the IRS 3 result is not anomalous.

The long lines of sight to the infrared sources in the Galactic center include molecular clouds near the Galactic center and in intervening spiral arms (Geballe, Baas, & Wade 1989), as well as considerable diffuse interstellar material, evidenced by the presence of a strong 3.4 μm absorption feature (Butchart et al. 1986; Okuda at al. 1990; Pendleton et al. 1994; Whittet et al. 1997). In order to better understand the origin of the large column density of H_3^+ toward the Galactic center, we obtained a spectrum near 3.67 μm of the heavily reddened star Cygnus OB2 No. 12, which is believed to be obscured almost entirely by diffuse, low-density material (and toward which the 3.4 μm absorption feature also is present; Adamson, Whittet, & Duley 1990; Pendleton et al. 1994). The H_3^+ doublet was detected in absorption there as well, and its equivalent width, while not approaching that of the Galactic center sources, is comparable to that seen toward sources embedded in dense molecular clouds despite the much lower extinction.

These observations clearly demonstrate that H_3^+ exists in detectable quantities in the diffuse interstellar medium as well as in molecular clouds. Much of the H_3^+ seen toward the Galactic center and Cygnus OB2 No. 12 thus exists in an environment completely different from that of the dense clouds studied to date. Few, if any, polyatomic molecules have been reported in diffuse clouds. In the following sections we describe these new observations and several follow-up measurements in more detail and discuss the physical conditions and processes affecting the abundance of H_3^+ in the diffuse interstellar medium.

[1] Operated by the Association of Universities for Research in Astronomy, Inc., under cooperative agreement with the National Science Foundation.

2. OBSERVATIONS AND DATA REDUCTION

A log of the observations is provided in Table 1. The first detections of absorption by H_3^+ in the Galactic center sources IRS 3 and GCS 3-2, and in Cygnus OB2 No. 12, were of the $R(1, 0)$ and $R(1, 1)^+$ ortho-para doublet at 3.67 μm (see Oka & Jagod 1993 for an explanation of the spectroscopic notation). They were obtained on UT 1997 July 11 at the 3.8 m United Kingdom Infrared Telescope (UKIRT) on Mauna Kea with the facility spectrometer CGS4, and its echelle was used, which provided a resolution of 15 km s^{-1}. The observing techniques were standard and similar to those described in Geballe & Oka (1996). The identification of the rather broad 3.67 μm absorption in the Galactic center as owing to H_3^+ was supported by detection of a broad isolated line of H_3^+ at 3.953 μm.

A spectrum of the 3.715 μm $R(1, 1)^-$ line of H_3^+ was obtained toward Cygnus OB2 No. 12 on 1997 September 5 using the echelle spectrometer, Phoenix, at the 4.0 m Mayall Telescope on Kitt Peak. The resolution achieved by Phoenix was approximately 9 km s^{-1}, somewhat higher than that by CGS4. To test for molecular material along the line of sight to Cygnus OB2 No. 12, CGS4 was used again on 1997 August 2 to obtain a spectrum of $v = 1$–0 lines of the fundamental vibration rotation band of CO near 4.65 μm at a resolution of 20 km s^{-1}. Several narrow absorption lines from low-lying J levels were detected. Finally, spectra of the pure rotational $J = 2$–1 emission lines of ^{12}CO and ^{13}CO in the direction of the star were secured on 1997 August 5 and November 13 at the James Clerk Maxwell Telescope (JCMT) on Mauna Kea using the heterodyne receiver A2. A background sky position 30′ north of the star was used for the ^{13}CO spectrum, and a combination of sky positions was used for the ^{12}CO spectrum.

Each of the spectra obtained with CGS4 was sampled every $\frac{1}{3}$ resolution element; those obtained by Phoenix were sampled every 0.18 resolution element. Data reduction consisted of small wavelength shifts of the spectra to bring atmospheric features in the source and calibration star spectra into coincidence, dividing the spectra of the sources by those of the comparison stars (adjusted for air mass using Beer's law), and wavelength calibration (using telluric absorption lines). The comparison stars are expected to be featureless in the wavelength regions observed except for the presence of the H I Pfβ line at 4.654 μm. Wavelength calibration is accurate to ± 3 km s^{-1} for the CGS4 spectra, and ± 2 km s^{-1} for the Phoenix spectra.

Two of the three H_3^+ lines observed near 3.7 μm are clear of strong telluric absorption lines; however, the shorter wavelength component of the 3.67 μm doublet is in near coincidence with a strong telluric absorption of methane centered at 3.6675 μm. Two telluric lines of HDO lie just longward in wavelength of the methane feature. For the Galactic center sources, which have broad absorption profiles, the wavelengths of these telluric lines lie within the blended H_3^+ profile. On the date that the doublet was measured toward Cygnus OB2 No. 12, the methane absorption coincided with the short-wavelength edge of the $R(1, 1)^+$ (shorter wavelength) line. Care was taken to observe each source and its calibration star close to the same air mass, and in fact the air masses of the pairs of observations were equal to within 4% in the case of the Galactic center, and to within 2% in the case of Cygnus OB2 No. 12 (for both the H_3^+ and the CO spectra). Nevertheless, proper correction of the methane line is problematic. In both the Galactic center and Cygnus 3.67 μm spectra it is likely that the divided spectra are distorted near the $R(1, 1)^+$ line. Consequently, the parameters derived from this line have relatively large uncertainties. At Kitt Peak, measurement of the doublet was virtually impossible because of the much stronger telluric absorption lines, and hence the single line at 3.715 μm was observed.

3. RESULTS

The observed H_3^+ lines originate from the lowest lying ortho and para states of the molecular ion. The $R(1, 1)$ absorptions are from the ground $(J, K) = (1, 1)$ para state, and the $R(1, 0)$ absorptions are from the lowest ortho level 33 K above the ground state. The lowest lying $J = 2$ level (2, 2) is 151 K above ground. Because of this and the low temperatures of dark clouds and the interiors of diffuse clouds (van Dishoeck 1990), $J = 1$ levels are the only ones significantly populated in interstellar clouds (Oka & Jagod 1993). Although no radiative transitions are permitted between ortho and para states of H_3^+ (Pan & Oka 1986), collisions of H_3^+ with H_2 exchange protons and thereby maintain the relative populations of the two types of H_3^+ in thermal equilibrium (Uy, Cordonnier, & Oka 1997).

3.1. *Galactic Center Sources*

Figure 1 shows the spectrum of the Galactic center nuclear source IRS 3 and the quintuplet source GCS 3-2 near the 3.67 μm H_3^+ doublet. A broad absorption, which extends over at least 0.003 μm (250 km s^{-1}) is seen in each spectrum. The rest wavelengths of the components of the doublet are separated by only 0.00043 μm (35 km s^{-1}). Thus toward these objects a significant part of the line absorption extends over a wide range of velocities, and the individual profiles of the lines in the doublet considerably overlap one

TABLE 1

LOG OF OBSERVATIONS

UT Date (1997)	Telescope	Instrument	Object	Molecule	Wavelength/Frequency	Integration Time (minutes)	Standard Star	Resolution (km s^{-1})
Jul 11	UKIRT	CGS4	GC IRS 3	H_3^+	3.668 μm	29	HR 6486	15
			GCS 3-2	H_3^+	3.668 μm	7	HR 6486	15
			GC IRS 3	H_3^+	3.953 μm	16	HR 6486	16
			Cyg OB2 12	H_3^+	3.668 μm	10	HR 7924	15
Aug 2	UKIRT	CGS4	Cyg OB2 12	CO	4.65 μm	3	HR 7924	20
Aug 5	JCMT	A2	Cyg OB2 12	^{12}CO	230 GHz	4	...	0.3
Sep 5	Mayall	Phoenix	Cyg OB2 12	H_3^+	3.715 μm	60	HR 7924	9
Nov 13.....	JCMT	A2	Cyg OB2 12	^{13}CO	220 GHz	30	...	0.3

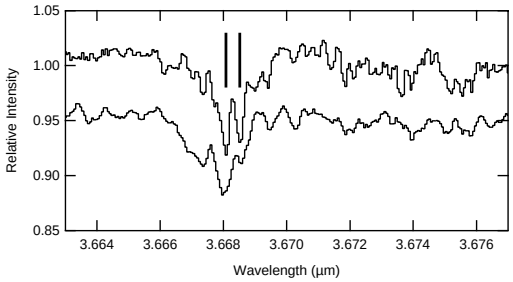

FIG. 1.—Spectrum of the Galactic nuclear source IRS 3 (*upper line*) and the "quintuplet" source GCS 3-2 (*lower line*, shifted down by 0.05 units), near the $R(1, 1)^+$ and $R(1, 0)$ doublet of H_3^+. The rest wavelengths of the lines are indicated by vertical bars. The noise levels are indicated by the point-to-point variations.

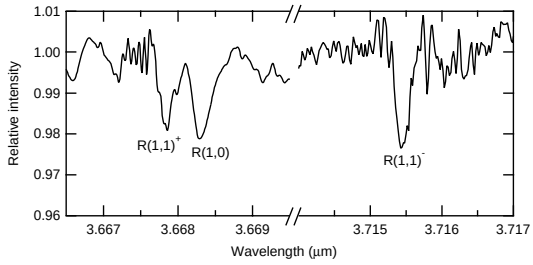

FIG. 2.—Spectrum of Cygnus OB2 No. 12 in two wavelength intervals near 3.7 μm. Lines of H_3^+ are indicated. The high-frequency noise near 3.6675 μm is a result of the correction for a strong telluric CH_4 line.

another. A narrow doublet is observed toward IRS 3 at $v_{LSR} = 0$ km s^{-1} with the correct (4.3 Å) spacing, and it also may be present toward GCS 3-2, but it is less obvious there. The measured equivalent widths of the observed lines toward both Galactic center sources are given in Table 2. The equivalent width toward IRS 3 has been separated into a broad component and a narrow component (the latter defined as absorption below 0.97, which corresponds to the $v_{LSR} = 0$ component). Also listed in Table 2 are the estimated column densities of H_3^+ that were obtained using the standard formula for an optically thin line, $W_\lambda = (8\pi^3\lambda/3hc)N|\mu|^2$, where N is the column density in the lower state of the transition and μ is the dipole moment of the transition (values have been provided by J. K. G. Watson and are listed by Geballe & Oka 1996).

In view of the detection of H_3^+ toward Cygnus OB2 No. 12, the H_3^+ absorptions toward the Galactic center sources are expected to include both diffuse and dark cloud components, each of which should contribute to the overall line profile. Infrared absorption lines of the fundamental vibration-rotation band of carbon monoxide previously have been observed toward both IRS 3 and GCS 3-2 (Geballe et al. 1989; Okuda et al. 1990). The velocity profiles of these CO lines are complex and contain a number of discrete components, several of which are identified with specific dense clouds known from radio and millimeter spectral mapping. In the case of IRS 3, the CO absorption lines, which are heavily saturated at low-J levels, have strong components at $v_{LSR} = 0$ km s^{-1}, similar to H_3^+. Their centroids, however, are at $v_{LSR} \sim 30$ km s^{-1}, and weak blue-shifted absorption extending to -150 km s^{-1} is present (Geballe et al. 1989). For GCS 3-2, strong absorption by CO is centered roughly at -70 km s^{-1}. The observed H_3^+ profiles and source-to-source differences are crudely similar to those of the CO observations. This suggests that some of the H_3^+ observed toward the Galactic center indeed is found in molecular clouds.

3.2. *Cygnus OB2 No. 12*

The spectral lines of H_3^+ toward Cygnus OB2 No. 12 (initially reported by McCall et al. 1998) are shown in Figure 2. Parameters derived from each line in Figure 2 are listed in Table 3. In contrast to the Galactic center, the components of the 3.67 μm doublet are well resolved from one another, and no broad component is observed. The individual lines of the doublet were partially resolved by CGS4, and the $R(1, 1)^-$ transition was more fully resolved by Phoenix. Each $R(1, 1)$ line arises from the lowest lying para level and hence should yield the same column density; however, as pointed out above, possible noncancellation of the telluric CH_4 line leads to large uncertainties in the column density and velocity width derived for the $R(1, 1)^+$ line. Hence we rely on the measurement of the $R(1, 1)^-$ line to determine the column density of para-H_3^+. We calculate a total H_3^+ column density of 3.8×10^{14} cm^{-2} toward Cygnus OB2 No. 12 and derive an intrinsic line width of ~ 14 km s^{-1} (FWHM).

The infrared spectrum of CO toward Cygnus OB2 No. 12, which also was presented by McCall et al. (1998), is

TABLE 2

H_3^+ LINE PARAMETERS TOWARD THE GALACTIC CENTER

Source	Line(s)	λ (μm)	W_λ (10^{-6} μm)[a]	$N_{level}(H_3^+)$ (10^{14} cm^{-2})[a]	Level
Narrow component:[b]					
GC IRS 3	$R(1, 1)^+$	3.66808	12(4)	5.1(1.7)	para
GC IRS 3	$R(1, 0)$	3.66852	9(4)	2.4(1.1)	ortho
Broad component:[c]					
GC IRS 3	$R(1, 1)^+ + R(1, 0)$	3.668	53(12)	17.5(3.9)	Total
GCS 3-2.....	$R(1, 1)^+ + R(1, 0)$	3.668	83(8)	27.7(2.4)	Total

[a] Statistical uncertainties (3 σ) are given in parentheses. Systematic errors are difficult to estimate and may be larger.

[b] The narrow component at $v_{LSR} \approx 0$, defined as the absorption below 0.97.

[c] Column densities for broad components are estimated assuming equal amounts of para- and ortho-H_3^+ and using an average value of $|\mu|^2 = 0.0209$ D^2.

TABLE 3

H_3^+ Line Parameters toward Cygnus OB2 No. 12

Line	λ (μm)	W_λ (10^{-6} μm)[a]	N_{level} (10^{14} cm^{-2})[a]	v_{LSR} (km s^{-1})[a]	FWHM$_{obs}$ (km s^{-1})[a]	FWHM$_{deconv}$ (km s^{-1})
$R(1, 1)^+$	3.66808	3.9(9)	1.6(4)	8(5)	17(5)	8
$R(1, 0)$	3.66852	5.4(9)	1.4(2)	11(5)	22(5)	16
$R(1, 1)^-$	3.71548	5.2(7)	2.4(3)	8(3)	16(3)	13

[a] Statistical uncertainties (3 σ) are given in parentheses.

shown in Figure 3, and the millimeter-wave spectra of the $J = 2$–1 lines of ^{12}CO and ^{13}CO are shown in Figure 4. Six narrow absorption lines of ^{12}CO can be seen in the infrared spectrum. Of these, the weaker ones are unresolved and therefore have widths much less than the resolution of 20 km s^{-1}. The stronger lines appear to be partially resolved, although their profiles may be contaminated by incomplete removal of telluric CO lines. If they are composed of a few very narrow components, the stronger lines may be saturated. The CO absorption profiles are centered at $v_{LSR} \sim 15 \pm 4$ km s^{-1}. The millimeter CO spectra, obtained at a much higher spectral resolution but with an angular resolution of 21″, much lower than the pencil beam of the infrared absorption spectra, show narrow emission lines at three velocities, -21, 7, and 12 km s^{-1}. This suggests that the CO absorption lines are produced largely by the 7 and 12 km s^{-1} clouds.

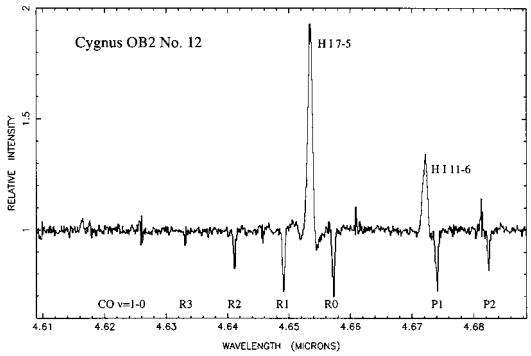

FIG. 3.—Spectrum of Cygnus OB2 No. 12 near 4.65 μm, which shows absorption lines of ^{12}CO and emission lines of atomic hydrogen.

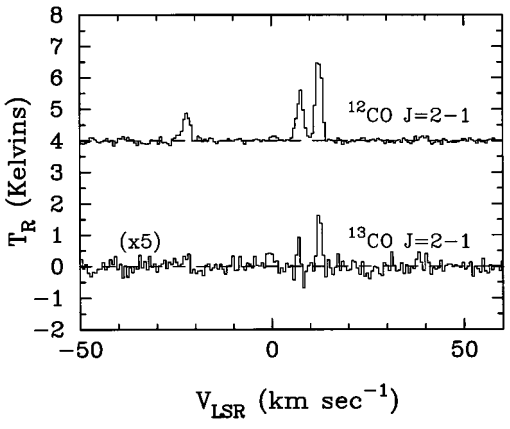

FIG. 4.—Spectra of pure rotational 2–1 lines of ^{12}CO and ^{13}CO. The original data have been binned into 0.6 km s^{-1} intervals, and a 4 K offset has been given to the ^{12}CO spectrum. The vertical axis is detected antenna temperature corrected for the telescope efficiency.

Additional information on the molecular gas along the line of sight to Cygnus OB2 No. 12 is available from high-resolution near-infrared spectra of C_2 obtained by Gredel & Münch (1994). Their spectra reveal four absorption components at LSR velocities of 7, 12, 15, and 31 km s^{-1}, with the last of these very weak compared to the first three. As in the case of the infrared CO lines, absorption at -21 km s^{-1} was not detected and therefore the -21 km s^{-1} cloud seen in emission in the millimeter-wave spectra either does not fill the millimeter beam or lies beyond Cygnus OB2 No. 12.

As pointed out earlier, the relative populations of ortho- and para-H_3^+ are in LTE. The mean temperature of the H_3^+ may be derived from the column densities of the lowest lying ortho and para levels, according to the formula

$$N_{ortho}/N_{para} = (g_{ortho}/g_{para})e^{-32.87/T} . \quad (1)$$

Using the measured column densities derived from the $R(1, 0)$ and $R(1, 1)^-$ lines (Table 3), we estimate the mean temperature of the H_3^+ to be $\sim$30 K. Gas temperatures of 35 and 50 K were derived from the C_2 spectra of Souza & Lutz (1977) and Gredel & Münch (1994), respectively. Assuming LTE, the relative strengths of the infrared CO lines (see Table 4) suggest a temperature of 5–10 K; however, the gas temperatures derived from C_2 are more realistic than those from CO because the long radiative relaxation time of C_2 guarantees that C_2 level populations are governed by collisions. Indeed the difference in these derived temperatures indicates that the rotational levels of

TABLE 4

CO Infrared Lines toward Cygnus OB2 No. 12

Line	λ_{obs} (μm)	W_λ (10^{-6} μm)[a]	v_{LSR} (km s^{-1})[a]
$R(3)$.....	4.63308	19(4)	13(4)
$R(2)$.....	4.64112	62(6)	19(4)
$R(1)$.....	4.64913	121(7)	15(4)
$R(0)$.....	4.65727	134(7)	12(4)
$P(1)$.....	4.67401	132(7)	18(4)
$P(2)$.....	4.68243	69(6)	13(4)

[a] Statistical uncertainties (3 σ) are given in parentheses. Systematic errors due to incomplete cancellation of telluric CO lines are difficult to estimate and may be larger.

CO are not in LTE, which is not surprising for diffuse clouds. From strengths of the absorption lines of CO we estimate a total column density of CO of 3×10^{16} cm^{-2} toward Cygnus OB2 No. 12.

4. DISCUSSION

4.1. *Abundances of H_3^+ in Molecular Clouds and Diffuse Clouds*

In interstellar clouds most H_3^+ is thought to be formed following cosmic-ray ionization of H_2 via the rapid reaction of the newly formed H_2^+ with H_2 (Martin, McDaniel, & Meeks 1961). It is destroyed by recombination with free electrons or via reactions with any number of neutral atoms or molecules. In diffuse clouds the former destruction process should dominate; in dark molecular clouds, it is reactions with neutrals and molecules (in particular with CO) that are dominant. McCall et al. (1998) have given a general treatment for determining the density of H_3^+ where both of the destructive processes are included. Here we separate the two cases of dark and diffuse clouds, which allows simple approximate expressions for the density of H_3^+ to be derived for both. We then apply these to the observations in hand: those of Cygnus OB2 No. 12 where only the diffuse component is present, and those of the Galactic center in which both environments exist along the line of sight.

The analysis for molecular clouds has been given elsewhere (see, e.g., Geballe & Oka 1989, 1996). To summarize, the concentration of H_3^+, derived from the approximate equation equating its rates of creation and destruction, is

$$n(H_3^+) = (\zeta/k_{CO})n(H_2)/n(CO) , \quad (2)$$

where ζ is the cosmic-ray ionization rate per H_2 molecule, and k_{CO} is the reaction rate constant of H_3^+ with CO. This simple equation arises because the proton hop from H_3^+ to CO dominates the destruction of H_3^+. To evaluate the equation we use $\zeta = 3 \times 10^{-17}$ s^{-1}, which is an average of recently used values (van Dishoeck & Black 1986; Lee, Bettens, & Herbst 1996), and $k_{CO} = 2 \times 10^{-9}$ cm^3 s^{-1} (Anicich & Huntress 1986), and the result from Lee, Bettens, & Herbst (1996) that in dark clouds with gas phase $C/H = 7.3 \times 10^{-5}$, $n(CO)/n(H_2) = 1.5 \times 10^{-4}$ is constant over a wide range of conditions. [Note that Lacy et al. 1994 have measured $N(CO)/N(H_2) = 2.8 \times 10^{-4}$ in one cloud, with a large uncertainty.] Then $n(H_3^+) \sim 1 \times 10^{-4}$ cm^{-3} is independent of cloud density, and from the measured H_3^+ column density one can estimate the distance through the dark cloud to the source. An interesting consequence of this result is that the column density of H_3^+ is simply proportional to the column length of the cloud rather than the column density of all molecules in the cloud. For example, for two molecular clouds of equal masses but one with twice the linear dimensions of the other [i.e., with 8 times lower density $n(H_2)$], $N(H_3^+)$ in the larger cloud is twice as high even though the column density $N(H_2)$ is 4 times less.

In diffuse clouds H_3^+ is formed in the same way as in dense clouds, but its destruction is dominated by recombination with electrons (van Dishoeck & Black 1986). Thus, the steady state rate equation for H_3^+ is

$$\zeta n(H_2) = k_e n(e) n(H_3^+) . \quad (3)$$

Both atomic and molecular hydrogen are abundant in diffuse clouds, and very little H is ionized; thus $n(H_2)$ may be expressed as $(f/2)n(\Sigma H)$, where f is the fraction of hydrogen in molecular form, $f = 2n(H_2)/[n(H) + 2n(H_2)]$, and $n(\Sigma H) = n(H) + 2n(H_2)$ is the density of H atoms in atomic and molecular form. Essentially all of the electrons in the diffuse interstellar medium are from carbon, which is almost fully singly ionized, and hence $n(e)$ may be expressed as $z_C n(\Sigma H)$, where z_C is the fractional abundance of *free* carbon. We thus obtain

$$n(H_3^+) = \zeta f/(2k_e z_C) . \quad (4)$$

To estimate $n(H_3^+)$ we use the same value for ζ as we used for dark clouds. If H_2-dissociating UV radiation is shielded from the regions where H_3^+ is observed (which requires boundary column densities of $\sim 10^{20}$ cm^{-2}; Glassgold & Langer 1974), $f \sim \frac{1}{2}$ (see also van Dishoeck & Black 1986). Cardelli et al. (1996) and Sofia et al. (1997) have measured z_C to be 1.4×10^{-4} in diffuse clouds.

The final parameter needed to estimate $n(H_3^+)$ is the rate constant k_e for electron recombination of H_3^+. Experimental values of this constant have varied widely, but recent results seem to be converging to a value of $k_e \sim 10^{-7}$ cm^3 s^{-1} at room temperature. Using Amano's (1988) value of 1.8×10^{-7}, we obtain $n(H_3^+) \sim 3 \times 10^{-7}$ cm^{-3}. Using the expression derived from storage ring experiments, $k_e = 4.6 \times 10^{-6}\ T^{-0.65}$ cm^3 s^{-1} (Sundström et al. 1994), and using an assumed electron temperature of 30 K, we obtain $n(H_3^+) \sim 1 \times 10^{-7}$ cm^{-3}. The uncertainty in k_e, along with that of ζ, is the greatest uncertainty in the determination of $n(H_3^+)$. Further experimental and theoretical results for k_e are eagerly awaited.

Thus under the above conditions, the volume density of H_3^+ in diffuse clouds also is approximately independent of cloud density, but its value is roughly 3 orders of magnitude less than in dark clouds. Only if the path length through diffuse clouds is vastly greater than that through an individual dark cloud can the column density of H_3^+ be comparable to its value through the dark cloud.

4.2. H_3^+ *toward Cygnus OB2 No. 12*

From the visual extinction of 10.2 magnitudes to Cygnus OB2 No. 12 (Humphreys 1978), its distance of 1.7 kpc (Torres-Dodgen, Tapia, & Carroll 1991) and the standard gas-to-dust conversion factor (Bohlin, Savage, & Drake 1978), the column density of hydrogen atoms, $N(\Sigma H) = N(H) + 2N(H_2)$, along the line of sight is roughly 2×10^{22} cm^{-2}. The analysis of the infrared CO absorption lines indicates that along the line of sight $N(CO)/N(\Sigma H) \sim 1.5 \times 10^{-6}$, which is much less than C/H. Thus at most a few percent of the carbon is in molecular form. This is consistent with the clouds in front of Cygnus OB2 No. 12 being diffuse.

Using the measured value of $N(H_3^+)$ and the values of $n(H_3^+)$ calculated in § 4.1, the length of the absorbing column of H_3^+ is roughly $L = N(H_3^+)/n(H_3^+) \sim 400$–$1200$ pc. This path length seems unreasonably large (although it does not exceed the total distance to the star). The mean gas density over the path would be $N(\Sigma H)/L \sim 10$ cm^{-3}. Carbon monoxide at such low densities is virtually completely confined to the lowest rotational level (Zuckerman & Palmer 1974) and could not produce the observed CO and ^{13}CO $J = 2$–1 line emission. The derived path length also is not in agreement with observations of rotational lines of CH (E. F. van Dishoeck 1997, private communication) and the near-infrared spectra of C_2 (Souza

& Lutz 1977; Gredel & Münch 1994). Those observations suggest that the bulk of the intervening molecular material exists in clouds with typical densities of a few hundred cm^{-3}. The total gas column density then implies that these clouds have an aggregate length of ~ 30 pc. If the H_3^+ at densities of $(1\text{–}3) \times 10^{-7}$ cm^{-3} were confined to such diffuse clouds it would have a column density more than an order of magnitude less than observed. Taken together these results suggest that most of the H_3^+ is found where the other molecules do not exist. It is, of course, possible that the H_3^+ does not trace the presence of other molecules, but there is no a priori reason to assume that it should not.

On the other hand, if the observed H_3^+ is confined solely to clouds containing CH and C_2 along a path length of ~ 30 pc, the density of H_3^+ in them is $\sim 4 \times 10^{-6}$ cm^{-3}. This is more than an order of magnitude higher than the estimated density of H_3^+ in diffuse clouds (see § 4.1). This density would imply either that the value of ζ/k_e is at least 1 order of magnitude larger than that used here (suggesting that one or both of these assumed constants needs to be revised), or that one or more processes in addition to the interaction of cosmic rays with H_2 governs the production of H_3^+ in diffuse clouds.

Galactic rotation along the line of sight to Cygnus OB2 No. 12 produces a range of radial velocities of approximately 3.3 km s^{-1}, assuming a flat rotation curve with $v_c = 220$ km s^{-1}, $R_0 = 8$ kpc, and $l = 80.^\circ 10$. The velocity dispersion of the interstellar medium ($\sigma \sim 6.6$ km s^{-1}, which implies FWHM = 15.6 km s^{-1}; Welty, Hobbs, & Kulkarni 1994) is considerably greater than this. The presence of H_3^+ along a large fraction of the line of sight to Cygnus OB2 No. 12 thus is not ruled out by the observed line width and is consistent with typical velocity dispersions observed in the interstellar medium. If the path length over which H_3^+ absorption occurs is indeed very long compared to those of other molecular absorption lines, the profiles of H_3^+ lines should differ from those of the other molecules, probably in the sense of being more complex. Higher resolution spectroscopy of the H_3^+ infrared absorption lines will test this possibility and will facilitate important comparisons with the C_2 near-infrared and CO radio spectra, both of which show a few well-defined velocity components.

4.3. H_3^+ *toward the Galactic Center*

The total column density of H_3^+ observed toward the Galactic center source IRS 3 is 25×10^{14} cm^{-2}, nearly an order of magnitude greater than those found in dense cloud cores (Geballe & Oka 1996; McCall, Geballe, & Oka 1999) and along the line of sight to Cygnus OB2 No. 12. The visual extinction toward the nuclear sources in the Galactic center is approximately 27 mag (Wade et al. 1987). Various lines of evidence suggest that roughly one-third of the extinction occurs in molecular clouds and that two-thirds arises in diffuse gas (see, e.g., Whittet et al. 1997). However, there is no a priori reason that the division of H_3^+ column density between the diffuse and molecular clouds should be the same as the division of visual extinctions. Neither can it be assumed that the column density of H_3^+ in the diffuse gas toward the Galactic center may be determined by scaling $N(H_3^+)$ toward Cygnus OB2 No. 12 by the ratio of visual extinctions in diffuse gas or by the ratio of optical depths of the 3.4 μm absorption feature.

It is likely that toward the Galactic center substantial column densities of H_3^+ are found in both dark and diffuse environments. For illustrative purposes we assume that the sharp H_3^+ doublet is due to diffuse gas in the bulk of the Galaxy. This assumption seems reasonable since gas on circular orbits at $l = 0^\circ$ should appear near $v_{LSR} \sim 0$, which is where the doublet is seen. We assume that the remainder of the H_3^+ line profile occurs in denser gas nearer the Galactic center and presumably in noncircular orbits.

For the diffuse gas we employ the H_3^+ density estimates derived in § 4.1. For $N(H_3^+) \sim 7.5 \times 10^{14}$ cm^{-2} (Table 2), the H_3^+ absorption toward IRS 3 extends over $\sim 0.8\text{–}2.5$ kpc. While this is a surprisingly extended path length, it is not completely unrealistic in view of the much larger distance to the Galactic center than toward Cygnus OB2; however, as also pointed out for Cygnus OB2 No. 12, if k_e is lower or ζ higher than our assumptions in § 4.1, the derived path length would decrease proportionately.

In molecular clouds, the number density of H_3^+ is roughly 3 orders of magnitude greater, and for a column density of $\sim 17.5 \times 10^{14}$ cm^{-2} we deduce a path length of ~ 6 pc. From the extinction produced by the molecular clouds (5–10 mag; see Whittet et al. 1997), the standard gas-to-dust ratio (Bohlin et al. 1978), and the above path length, a mean gas density of ~ 1000 cm^{-3} is derived. This is considerably less than the densities in the cloud cores in which H_3^+ has been detected. The difference is not surprising, however, because the line of sight to the Galactic center, which is known to pass through a number of massive clouds near the center as well as spiral arms, does not pass through or even very close to any cloud cores (see, e.g., Federman & Evans 1981).

Here we have discussed only the source IRS 3. These conclusions should in general also apply to the quintuplet source GCS 3-2, although in the case of this source it is difficult to separate the diffuse and dense cloud contributions to the H_3^+ profile.

5. CONCLUSIONS

H_3^+ has been detected in the diffuse interstellar medium toward two sources in the Galactic center and toward the highly reddened star Cygnus OB2 No. 12. The column density of H_3^+ observed toward the Galactic center is nearly an order of magnitude greater than that toward the dense cloud cores where interstellar H_3^+ has been found. Despite the relatively low extinction toward Cygnus OB2 No. 12, the column density of H_3^+ in front of it is comparable to those found toward cloud cores. Using the best values currently available for the rates of cosmic-ray ionization of H_2 in diffuse clouds and dissociative recombination of H_3^+, the density of H_3^+ in the diffuse interstellar medium is roughly 3 orders of magnitude less than in dark clouds, which implies that toward both the Galactic center and Cygnus OB2 No. 12 the observed H_3^+ exists along very long path lengths. Measurements of H_3^+ toward Cygnus OB2 No. 12 at higher spectral resolution coupled with more accurate values of the above two rates are required to understand the physical relation between H_3^+ and the other molecules observed along this line of sight.

These detections open the way for organized study of the diffuse interstellar medium via infrared spectroscopy. Both CO and H_3^+ are demonstrated here to have detectable infrared signatures for modest amounts of extinction by diffuse gas within the Galaxy. It is likely that soon there will be detections of these features in the diffuse interstellar media of external galaxies.

We thank the staff of the Joint Astronomy Centre for the support of these measurements. We particularly thank G. Sandell and R. P. Tilanus for securing and reducing the JCMT spectra, and E. F. van Dishoeck, L. M. Hobbs, N. J. Evans, and the referee, J. H. Lacy, for helpful discussions, comments, and information. The United Kingdom Infrared Telescope is operated by the Joint Astronomy Centre on behalf of the U.K. Particle Physics and Astronomy Research Council. The James Clerk Maxwell Telescope is operated by the Joint Astronomy Centre on behalf of the Particle Physics and Astronomy Research Council of the United Kingdom, the Netherlands Organization for Scientific Research, and the National Research Council of Canada. B. J. McCall is supported by the Fannie and John Hertz Foundation. The University of Chicago portion of this work has been supported by NSF grant PHYS-9722691 and NASA grant NAG 5-4234.

REFERENCES

Adamson, A. J., Whittet, D. C. B., & Duley, W. W. 1990, MNRAS, 243, 400
Amano, T. 1988, ApJ, 329, L121
Anicich, V. G., & Huntress, W. T., Jr. 1986, ApJS, 62, 553
Becklin, E. E., Matthews, K., Neugebauer, G., & Willner, S. P. 1978, ApJ, 219, 121
Bohlin, R. C., Savage, B. D., & Drake, J. F. 1978, ApJ, 224, 132
Butchart, I., McFadzean, A. D., Whittet, D. C. B., Geballe, T. R., & Greenberg, J. M. 1986, A&A, 154, L5
Cardelli, J. A., Meyer, D. M., Jura, M., & Savage, B. D. 1996, ApJ, 467, 334
Federman, S. R., & Evans, N. J., II. 1981, ApJ, 248, 113
Geballe, T. R., Baas, F., & Wade, R. 1989, A&A, 208, 255
Geballe, T. R., & Oka, T. 1989, ApJ, 342, 855
———. 1996, Nature, 384, 334
Glassgold, A. E., & Langer, W. D. 1974, ApJ, 193, 73
Gredel, R., & Münch, G. 1994, A&A, 285, 640
Herbst, E., & Klemperer, W. 1973, ApJ, 185, 505
Humphreys, R. M. 1978, ApJS, 38, 309
Lacy, J. H., Knacke, R., Geballe, T. R., & Tokunaga, A. T. 1994, ApJ, 428, L69
Lee, H.-H., Bettens, R. P. A., & Herbst, E. 1996, A&AS, 119, 111
Martin, D. W., McDaniel, E. W., & Meeks, M. L. 1961, ApJ, 134, 1012
McCall, B. J., Geballe, T. R., Hinkle, K. H., & Oka, T. 1998, Science, 279, 1910
McCall, B. J., Geballe, T. R., & Oka, T. 1999, in preparation
Nagata, T., Woodward, C. E., Shure, M., Pipher, J. L., & Okuda, H. 1990, ApJ, 351, 83
Oka, T. 1980, Phys. Rev. Lett., 45, 531
Oka, T., & Jagod, M.-F. 1993, J. Chem. Soc. Faraday Trans., 89, 2147
Okuda, H., et al. 1990, ApJ, 351, 89
Pan, F.-S., & Oka, T. 1986, ApJ, 305, 518
Pendleton, Y. J., Sandford, S. A., Allamandola, L. J., Tielens, A. G. G. M., & Sellgren, K. 1994, ApJ, 437, 683
Sofia, U. J., Cardelli, J. A., Guerin, K. P., & Meyer, D. M. 1997, ApJ, 482, L105
Souza, S. P., & Lutz, B. L. 1977, ApJ, 216, L49
Sundström, G., et al. 1994, Science, 263, 785
Torres-Dodgen, A. V., Tapia, M., & Carroll, M. 1991, MNRAS, 249, 1
Uy, D., Cordonnier, M., & Oka, T. 1997, Phys. Rev. Lett., 78, 3844
van Dishoeck, E. F. 1990, in Molecular Astrophysics, ed. T. W. Hartquist (Cambridge: Cambridge Univ. Press), 55
van Dishoeck, E. F., & Black, J. H. 1986, ApJS, 62, 109
Wade, R., Geballe, T. R., Krisciunas, K., Gatley, I., & Bird, M. C. 1987, ApJ, 320, 570
Watson, W. D. 1973, ApJ, 183, L17
Welty, D. E., Hobbs, L. M., & Kulkarni, V. P. 1994, ApJ, 436, 152
Whittet, D. C. B., et al. 1997, ApJ, 490, 729
Zuckerman, B., & Palmer, P. 1974, ARA&A, 12, 279

A.4 "Observation of H_3^+ in Dense Molecular Clouds"

Reprinted from *Astrophysical Journal* 522, 338 (1999).

THE ASTROPHYSICAL JOURNAL, 522:338–348, 1999 September 1

OBSERVATIONS OF H_3^+ IN DENSE MOLECULAR CLOUDS

B. J. McCALL
Department of Astronomy and Astrophysics, Department of Chemistry, and the Enrico Fermi Institute, University of Chicago, Chicago, IL 60637; bjmccall@uchicago.edu
T. R. GEBALLE[1]
Joint Astronomy Centre, Hilo, HI 96720
K. H. HINKLE
National Optical Astronomy Observatories,[2] Tucson, AZ 85726
AND
T. OKA
Department of Astronomy and Astrophysics, Department of Chemistry, and the Enrico Fermi Institute, University of Chicago, Chicago, IL 60637
Received 1998 December 21; accepted 1999 April 13

ABSTRACT

H_3^+ has been detected using infrared absorption spectroscopy along the lines of sight to six infrared sources in dense molecular clouds: AFGL 2136, W33A, Mon R2 IRS 3, AFGL 961E, AFGL 2591, and AFGL 490. Upper limits to the column densities of H_3^+ are reported for an additional nine sources. The column densities of CO toward Mon R2 IRS 3 and AFGL 961E have been determined from observations of the first-overtone lines of CO. For the six sources toward which H_3^+ was detected, a simple model of H_3^+ chemistry has been used together with column densities of H_2 derived from infrared CO measurements to estimate column lengths, mean number densities, and temperatures of molecular clouds. The derived column lengths are on the order of a parsec, the number densities are 10^4–10^5 cm^{-3}, and the temperatures are $\sim$25–50 K.

Subject headings: infrared: ISM: lines and bands — ISM: clouds — ISM: molecules — molecular processes

1. INTRODUCTION

The H_3^+ molecular ion plays the pivotal role in the gas-phase chemistry of the interstellar medium, as it initiates a chain of ion-neutral reactions that produce many of the chemical species detected by radio and infrared astronomers (Herbst & Klemperer 1973; Watson 1973). H_3^+ does not have a well-bound electronic excited state and therefore does not have a sharp electronic spectrum. Also, the symmetry of the equilateral triangle configuration of H_3^+ forbids a conventional rotational spectrum. Consequently, the detection of this important ion in the interstellar medium was not possible until the infrared spectrum was measured in the laboratory (Oka 1980) and until high-resolution array spectrometers enabled high-sensitivity spectroscopy in the infrared.

The first detection of H_3^+ in the interstellar medium came in 1996 in dense molecular clouds along the line of sight to the embedded young stellar objects AFGL 2136 and W33A (Geballe & Oka 1996). Subsequently, H_3^+ has been detected in the diffuse interstellar medium toward the visible star Cygnus OB2 No. 12 and toward two Galactic center sources whose lines of sight include both diffuse and dense clouds (McCall et al. 1998a; Geballe et al. 1999).

The H_3^+ ion serves as an important probe of molecular clouds because of a unique feature of its chemistry—the number density of H_3^+ is approximately independent of the total number density in the dense cloud environment. A simple model of H_3^+ formation and destruction can be used to estimate its number density, and the observed column density then provides an estimate of the effective path length through the cloud. This effective path length, coupled with the observed column density of CO and an assumed H_2:CO ratio, allows an estimate of the absolute number density of the cloud. Additionally, when transitions of both ortho- and para-H_3^+ are observed, the observed ortho-to-para ratio can be used to estimate the temperature of the cloud. Unlike in neutral species, the spin modifications in ionic species are thermalized quickly because of rapid Langevin reactions with H_2 (McCall et al. 1998b).

In this work we report the results of a small survey of young stellar objects embedded in dense molecular clouds. H_3^+ was detected in six of the clouds (toward AFGL 2136, W33A, Mon R2 IRS 3, AFGL 961E, AFGL 2591, and AFGL 490) but was not detected in nine others (toward Orion BN, NGC 2024 IRS 2, Mon R2 IRS 2, AFGL 989, Elias 29, M17 IRS 1, W3 IRS 5, S140 IRS 1, and LkHα 101). In two of the clouds that showed H_3^+ absorption (Mon R2 IRS 3 and AFGL 961E), the CO column density had not been reported, so the first overtone of CO was observed.

2. OBSERVATIONS AND DATA REDUCTION

A summary of the observations is provided as Table 1. This table incorporates the initial observations of H_3^+ in 1996 as reported earlier (Geballe & Oka 1996). The $R(1, 0)$ and $R(1, 1)^+$ ortho-para doublet of H_3^+ near 3.67 μm was studied at the 3.8 m United Kingdom Infrared Telescope (UKIRT) on Mauna Kea with the facility spectrometer CGS4 (Mountain et al. 1990), using its echelle at a resolution of 15 km s^{-1}. The UKIRT observations were performed on UT 1996 April 29, 1996 July 15, 1997 February 12-15, and 1997 July 11. The $R(1, 1)^-$ line of para-H_3^+ near 3.71 μm was studied at the 4.0 m Mayall Telescope on

[1] Present address: Gemini Observatory, 670 North A'ohoku Place, Hilo, HI 96720.
[2] Operated by the Association of Universities for Research in Astronomy, Inc. under cooperative agreement with the National Science Foundation.

TABLE 1

LOG OF OBSERVATIONS

Object	UT Date (yy mm dd)	Telescope	Instrument	Molecule	λ (μm)	Integration Time (minute)	Standard
AFGL 2136	960429[a]	UKIRT	CGS4	H_3^+	3.668	5	BS 6378
	960715[a]	UKIRT	CGS4	H_3^+	3.668	7	BS 6378
	970918	Mayall	Phoenix	H_3^+	3.715	78	BS 7001
W33A	960429[a]	UKIRT	CGS4	H_3^+	3.668	7	BS 6378
	960715[a]	UKIRT	CGS4	H_3^+	3.668	14	BS 6378
	970711	UKIRT	CGS4	H_3^+	3.668	33	BS 6378
Mon R2 IRS 3	970213	UKIRT	CGS4	H_3^+	3.668	10	BS 2421
	970214	UKIRT	CGS4	H_3^+	3.668	13	BS 1713
	970215	UKIRT	CGS4	H_3^+	3.668	13	BS 1713
	980102	IRTF	CSHELL	CO	2.343	60	BS 3982
	980103	IRTF	CSHELL	CO	2.337	60	BS 3982
AFGL 961E	970212	UKIRT	CGS4	H_3^+	3.668	16	BS 2421
	970213	UKIRT	CGS4	H_3^+	3.668	44	BS 2421
	970214	UKIRT	CGS4	H_3^+	3.668	36	BS 2421
	980102	IRTF	CSHELL	CO	2.343	50	BS 3982
	980103	IRTF	CSHELL	CO	2.337	70	BS 3982
AFGL 2591	970711	UKIRT	CGS4	H_3^+	3.668	6	BS 7924
	970918	Mayall	Phoenix	H_3^+	3.715	23	BS 7001
AFGL 490	970212	UKIRT	CGS4	H_3^+	3.668	16	BS 1040
	970214	UKIRT	CGS4	H_3^+	3.668	13	BS 0936
	970215	UKIRT	CGS4	H_3^+	3.668	13	BS 0936
Orion BN	970212	UKIRT	CGS4	H_3^+	3.668	12	BS 1899
	970215	UKIRT	CGS4	H_3^+	3.668	5	BS 1713
NGC 2024 IRS 2	970212	UKIRT	CGS4	H_3^+	3.668	7	BS 2421
	970213	UKIRT	CGS4	H_3^+	3.668	12	BS 1713
	970215	UKIRT	CGS4	H_3^+	3.668	10	BS 1713
Mon R2 IRS 2	970212	UKIRT	CGS4	H_3^+	3.668	11	BS 2421
	970213	UKIRT	CGS4	H_3^+	3.668	10	BS 1713
	970214	UKIRT	CGS4	H_3^+	3.668	16	BS 1790
AFGL 989	970212	UKIRT	CGS4	H_3^+	3.668	9	BS 2421
	970215	UKIRT	CGS4	H_3^+	3.668	7	BS 2421
Elias 29	970711	UKIRT	CGS4	H_3^+	3.668	16	BS 5953
M17 IRS 1	970711	UKIRT	CGS4	H_3^+	3.668	19	BS 7340
W3 IRS 5	970917	Mayall	Phoenix	H_3^+	3.715	54	BS 2491
S140 IRS 1	970918	Mayall	Phoenix	H_3^+	3.715	57	BS 1713
LkHα 101	970918	Mayall	Phoenix	H_3^+	3.715	18	BS 1713

[a] First reported by Geballe & Oka 1996.

Kitt Peak, using the echelle spectrometer Phoenix (Hinkle et al. 1998), which afforded a resolution of 9 km s^{-1}. The Kitt Peak observations were made on UT 1997 September 17–18. Finally, the $R(0)$–$R(5)$ lines of the first overtone of ^{12}CO near 2.34 μm were studied at the 3.0 m NASA Infrared Telescope Facility (IRTF) on Mauna Kea, using the facility spectrometer CSHELL (Tokunaga, Toomey, & Carr 1990), with a nominal resolution of 15 km s^{-1}. The CO observations were made on UT 1998 January 2–3. The spectra obtained with CGS4 and CSHELL were sampled every one-third resolution element, and those obtained with Phoenix were sampled every 0.18 resolution element.

Standard stars were observed as a part of each observation in order to correct for telluric absorptions. The standard stars used for each source are listed in Table 1. These stars are expected to be featureless in the wavelength regions observed.

Each object (or standard star) was observed alternately at two different beam positions. Each set of exposures was then subtracted in order to remove sky background. The subtracted exposures were then flat-fielded, and bad pixel masks were applied. One-dimensional spectra were then extracted from the resultant images. All extracted spectra for each object (or standard) were then shifted in wavelength when necessary to bring features into coincidence, and then they were summed. The summed spectrum for each object was then divided by a summed spectrum of a standard star, which had been shifted in wavelength and adjusted using Beer's law in order to effect optimum cancellation of telluric absorption lines. Residual interference fringes in the ratio of these spectra were then removed from the resultant spectra using Fourier-transform techniques, and finally the reduced spectrum was wavelength calibrated based on the telluric lines originally present in the spectrum. The wavelength calibration is estimated to be accurate to ± 3 km s^{-1} for the CGS4 and CSHELL spectra and ± 2 km s^{-1} for the Phoenix spectra. A more detailed description of the data reduction technique and the software tools developed for processing these data will be given elsewhere (McCall 1999).

The lines observed are relatively clear of strong telluric absorption lines, with the exception of the $R(1, 1)^+$ line of H_3^+ (with rest wavelength 3.6681 μm), which is quite close to a strong telluric absorption of methane centered at 3.6675 μm. When Doppler shifts are unfavorable, the $R(1, 1)^+$ line can be affected by this methane feature, resulting in rela-

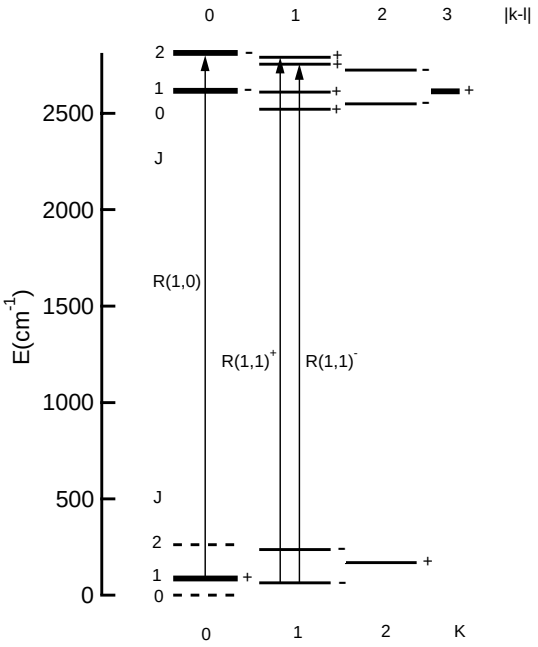

FIG. 1.—Energy-level diagram for the ground state (*below*) and ν_2 state (*above*) of H_3^+. The three transitions studied in this work are depicted with vertical arrows. Heavy lines refer to ortho-H_3^+ levels, thin lines refer to para-H_3^+ levels, and dashed lines indicate levels forbidden by the Pauli principle. The plus and minus signs beside the levels indicate the parities of the levels, while the plus and minus signs as superscripts to $R(1, 1)$ simply give the ordering of the levels. In the upper state, the quantum number K is replaced by the quantity $|k - l|$, where l is the quantum number for vibrational angular momentum ($l = \pm 1$ for the ν_2 state).

tively large systematic uncertainties in the parameters derived in these cases. Additionally, there are two telluric lines of HDO that lie slightly longer in wavelength than the methane feature. These lines preclude the measurement of the $R(1, 0)$ and $R(1, 1)^+$ lines at Kitt Peak in the summer months, when substantial quantities of water vapor are present.

The H_3^+ rotation-vibration transitions studied are members of the fundamental band of the ν_2 degenerate bending mode. An energy-level diagram for the ground state and the ν_2 state of H_3^+ is shown in Figure 1, which also shows the three transitions observed. The energy levels of H_3^+ in the vibrational ground state can be described in terms of the quantum numbers I (total nuclear spin), J (rotational angular momentum), and K (projection of the rotational angular momentum along the symmetry axis). The $R(1, 1)^+$ and $R(1, 1)^-$ transitions arise from the lowest allowed level of H_3^+, the $(J, K) = (1, 1)$ level, which has the para ($I = 1/2$) spin modification. The $R(1, 0)$ transition arises from the second lowest level, the $(J, K) = (1, 0)$ level, which has the ortho ($I = 3/2$) spin modification and lies 32.87 K higher. The next higher level, $(J, K) = (2, 2)$, lies 151 K above the (1, 1) level and is therefore expected to have negligible population at the low temperatures of molecular clouds. For more details on the spectroscopic notation, see Oka & Jagod (1993).

3. RESULTS

3.1. H_3^+ *Detections*

The parameters of the observed H_3^+ lines are listed in Table 2. In the case of the $R(1, 1)^-$ line, the equivalent widths W_λ were derived from Gaussian fits to the observed features. In the case of the $R(1, 1)^+$-$R(1, 0)$ doublet, the W_λ were derived from fits to two Gaussians. In the latter fit, all parameters were left free to vary, except in some cases the FWHM was constrained in order to obtain a reasonable fit. The $\sigma(W_\lambda)$ listed in Table 2 is the 1 σ statistical uncertainty, which was calculated from the standard deviation of a straight-line fit to the residuals of the Gaussian fits and the square root of the number of pixels contributing to the feature. The column density for the lower level of each transition, $N_{\rm level}$, was calculated from the standard formula for an optically thin line, $W_\lambda = (8\pi^3\lambda/3hc)N_{\rm level}|\mu|^2$, where $|\mu|^2$ is the square of the transition dipole moment, provided to us by J. K. G. Watson (1992, private communication). Also listed are the corresponding uncertainties in the equivalent width and column density, the observed velocity $v_{\rm obs}$, the

TABLE 2

H_3^+ LINE PARAMETERS[a]

Object	Line	λ (Å)	W_λ (Å)	$\sigma(W_\lambda)$ (Å)	$\|\mu\|^2$ (D^2)	$N_{\rm level}(H_3^+)$ (10^{14} cm^{-2})	$\sigma(N)$ (10^{14} cm^{-2})	$v_{\rm obs}$ (km s^{-1})	$v_{\rm LSR}$ (km s^{-1})	FWHM (km s^{-1})
AFGL 2136	$R(1, 1)^+$	36680.84	0.049	0.009	0.0158	2.0	0.38	15.8	21.5	21.8
	$R(1, 0)$	36685.16	0.075	0.009	0.0259	1.9	0.23	18.9	24.6	21.9
	$R(1, 1)^-$	37154.78	0.041	0.003	0.0140	1.9	0.14	36.7	21.9	11.2
W33A	$R(1, 1)$	36680.84	0.069	0.019	0.0158	2.9	0.79	30.8	34.3	20[b]
	$R(1, 0)^+$	36685.16	0.091	0.019	0.0259	2.3	0.48	31.0	34.5	20[b]
Mon R2 IRS 3.....	$R(1, 1)^+$	36680.84	0.020	0.006	0.0158	0.83	0.26	47.1	7.6	20[b]
	$R(1, 0)$	36685.16	0.023	0.006	0.0259	0.58	0.16	50.9	11.4	20[b]
AFGL 961E.....	$R(1, 1)^+$	36680.84	0.028	0.008	0.0158	1.2	0.35	47.5	10.2	14.8
	$R(1, 0)$	36685.16	0.024	0.008	0.0259	0.60	0.21	46.7	9.4	14.4
AFGL 490	$R(1, 1)^+$	36680.84	0.016	0.010	0.0158	0.66	0.39	10.3	−11.4	19.9
	$R(1, 0)$	36685.16	0.015	0.009	0.0259	0.37	0.22	12.4	−9.4	17.2
AFGL 2591	$R(1, 1)^+$	36680.84	0.051	0.004	0.0158	2.1	0.18	−27.9	−1.2	20[b]
	$R(1, 0)$	36685.16	0.039	0.004	0.0259	0.98	0.11	−35.4	−8.8	20[b]
	$R(1, 1)^-$	37154.78	0.025	0.002	0.0140	1.2	0.07	−7.6	1.2	14.7

[a] Statistical uncertainties (1 σ) are listed. Systematic errors are difficult to estimate and may be larger.
[b] For these objects the FWHM was constrained to the listed value in order to effect a reasonable fit.

TABLE 3

COMPARISON OF v_{LSR} OF H_3^+ AND CO

Object	H_3^+ v_{LSR}[a] (km s^{-1})	Infrared CO v_{LSR} (km s^{-1})	Millimeter CO v_{LSR} (km s^{-1})
AFGL 2136	22.7	26.5 ± 2.8[b]	27.2[c]
W33A	34.4	32.6 ± 1.7[b]	36[d]
Mon R2 IRS 3.....	9.5	9.7[e]	10.7[f]
AFGL 961E.....	9.8	12.4[e]	12.5[g]
AFGL 2591[h]	−2.9	− 10.7 ± 0.4[b]	−6[i]
AFGL 490	−10.4	−13.5[i]	−13.5[j]

[a] Average v_{LSR} of observed lines. The estimated uncertainty is ±3 km s^{-1}.
[b] Mitchell et al. 1990.
[c] Dinger et al. 1979.
[d] Goldsmith & Mao 1983.
[e] This work.
[f] Maddalena et al. 1986.
[g] Schneider et al. 1998.
[h] The H_3^+ v_{LSR} for AFGL 2591 is uncertain and may be bluer owing to telluric interference, as discussed in the text.
[i] Bally & Lada 1983.
[j] Mitchell et al. 1995.

derived velocity with respect to the local standard of rest v_{LSR}, and the FWHM.

Table 3 compares the LSR velocities derived from our H_3^+ measurements with those derived from infrared and millimeter CO measurements. The agreement between the H_3^+ and CO velocities, along with the correct observed separations of the $R(1, 1)^+$-$R(1, 0)$ doublet, is strong evidence of the reality of the H_3^+ features.

As was previously reported (Geballe & Oka 1996), the lines of sight toward AFGL 2136 and W33A were observed at 3.67 μm at UKIRT on the nights of UT 1996 April 29 and 1996 July 15. The data from these observations have recently been reprocessed, and the H_3^+ ortho-para doublet is clearly visible in both data sets, taken 77 days apart (Fig. 2). The H_3^+ lines show the expected change in observed wavelength due to the Earth's orbital motion over this time, providing strong evidence that the individual detections are genuine.

Figure 3 shows the reduced spectra of the H_3^+ doublet in the lines of sight toward Mon R2 IRS 3, AFGL 961E, and AFGL 490. The case of AFGL 490 might be considered a marginal detection because of the low signal-to-noise ratio, but the correct separation of the observed doublet suggests that the detection is probably secure. The equivalent widths of the H_3^+ absorptions in each of these objects are less than half of those toward W33A and AFGL 2136.

Figure 4 shows the reduced spectra of AFGL 2136 and AFGL 2591. In both cases, the $R(1, 1)^+$-$R(1, 0)$ doublet was observed using CGS4 at UKIRT (the spectrum of AFGL 2136 shown is from 1996 July 15) and the $R(1, 1)^-$ line was observed using Phoenix at Kitt Peak. In the case of AFGL 2136, both spectra are of good quality and the column densities of para-H_3^+ derived from the $R(1, 1)^+$ and $R(1, 1)^-$ lines are in good agreement. In the case of AFGL 2591, the doublet in the UKIRT spectrum is unresolved owing to an unfavorable Doppler shift into the region of the telluric lines and the short integration time. However, coupled with the observation of the $R(1, 1)^-$ line at Kitt Peak, the detection appears secure. The fact that the $R(1, 1)^-$ line was also unfavorably Doppler-shifted into the shoulder of a telluric line at 3.7152 μm may have effectively redshifted the center of the observed line by partially obscuring the blue side of

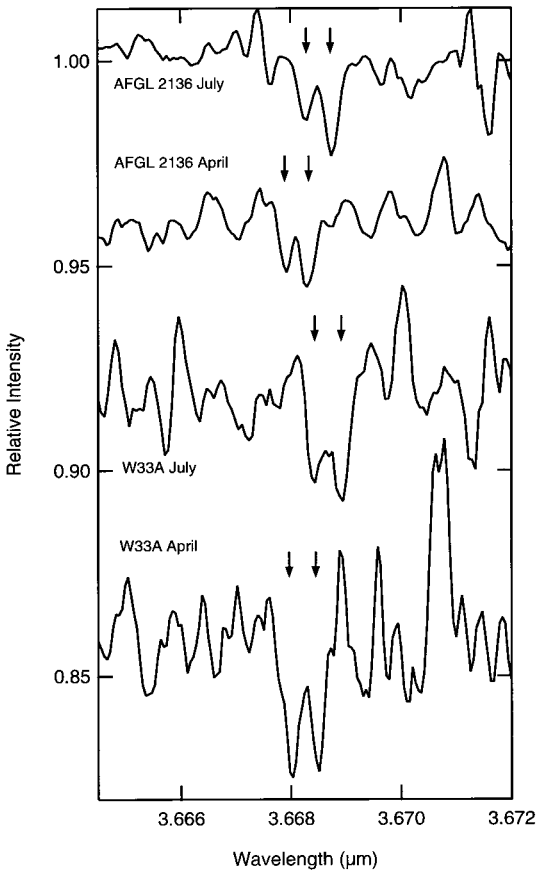

FIG. 2.—Spectra of the $R(1, 1)^+$-$R(1, 0)$ doublet of H_3^+ toward AFGL 2136 and W33A, obtained with UKIRT in 1996 July and April. The arrows indicate the H_3^+ lines. In Figs. 2–6 the lower traces are shifted downward from unity, and the spectra have been smoothed to reduce pixel-to-pixel variations for clarity.

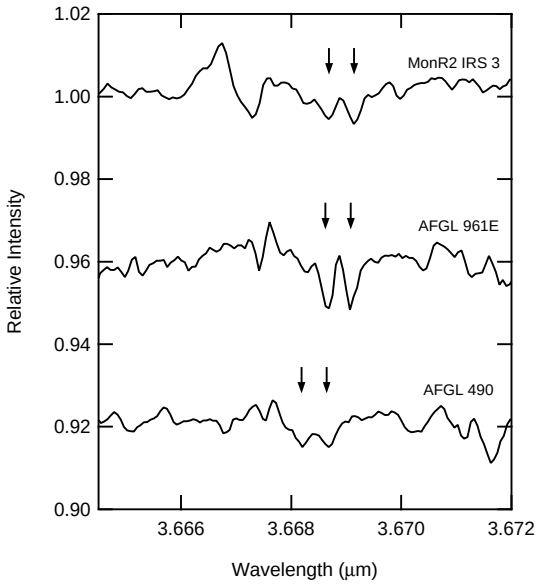

FIG. 3.—Spectra of the $R(1, 1)^+$-$R(1, 0)$ doublet of H_3^+ toward Mon R2 IRS 3, AFGL 961E, and AFGL 490, obtained with UKIRT. The arrows indicate the H_3^+ lines.

the line, so that the true v_{LSR} may be more negative than our analysis reveals.

3.2. H_3^+ *Upper Limits*

Table 4 summarizes our nondetections of H_3^+ in the dense clouds along the lines of sight to Orion BN, NGC 2024 IRS 2, Mon R2 IRS 2, AFGL 989, Elias 29, M17 IRS 1, W3 IRS 5, S140 IRS 1, and LkHα 101. The 1 σ deviations of the baseline, computed for an assumed line width of 20 km s^{-1} for the first six objects (observed with CGS4) and 15 km s^{-1} for the last three objects (observed with Phoenix), are listed in the table. The firm upper limits for these nondetections should be considered 3 σ. The CGS4 spectra are shown in Figure 5, and the Phoenix spectra are shown in Figure 6. In the spectra of Mon R2 IRS 2 and NGC 2024 IRS 2, the $R(1, 1)^+$-$R(1, 0)$ doublets appear to be present near the expected positions, but the signal-to-noise ratios are too low to consider these as firm detections. We recently learned that Kulesa & Black (1999) detected H_3^+ with rea-

TABLE 4

H_3^+ NONDETECTIONS[a]

Object	Line	$\sigma(W_\lambda)$ (Å)	$\sigma(N_{level})$ (10^{14} cm^{-2})
Orion BN	$R(1, 1)^+$	0.012	0.51
	$R(1, 0)$	0.012	0.31
NGC 2024 IRS 2	$R(1, 1)^+$	0.0071	0.29
	$R(1, 0)$	0.0071	0.18
Mon R2 IRS 2	$R(1, 1)^+$	0.010	0.42
	$R(1, 0)$	0.010	0.26
AFGL 989	$R(1, 1)^+$	0.0057	0.24
	$R(1, 0)$	0.0057	0.15
Elias 29	$R(1, 1)^+$	0.012	0.50
	$R(1, 0)$	0.012	0.31
M17 IRS 1	$R(1, 1)^+$	0.054	2.2
	$R(1, 0)$	0.054	1.4
W3 IRS 5	$R(1, 1)^-$	0.0038	0.18
S140 IRS 1	$R(1, 1)^-$	0.0020	0.091
LkHα 101	$R(1, 1)^-$	0.0049	0.23

[a] The firm upper limits for these nondetections should be considered 3 σ. Upper limits have been derived using an assumed FWHM of 20 km s^{-1} for all UKIRT spectra and 15 km s^{-1} for KPNO spectra (the last three entries).

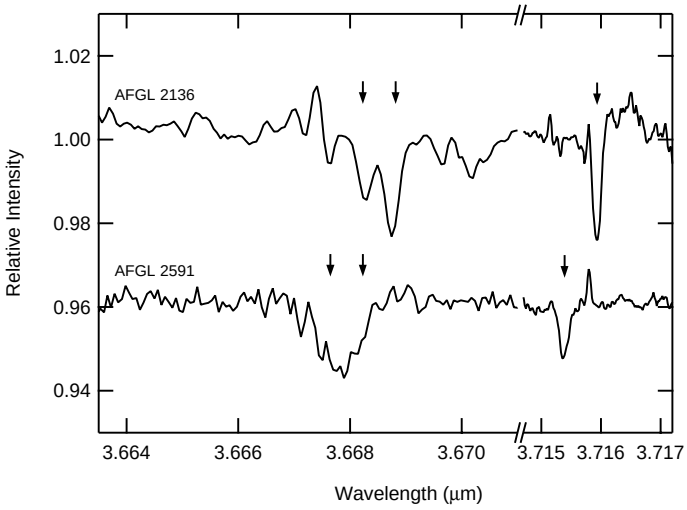

FIG. 4.—Spectra of the $R(1, 1)^+$-$R(1, 0)$ doublet of H_3^+ obtained with UKIRT (*left*) and the $R(1, 1)^-$ line of H_3^+ obtained at Kitt Peak (*right*), toward AFGL 2136 (1996 July 15) and AFGL 2591. The arrows indicate the H_3^+ lines.

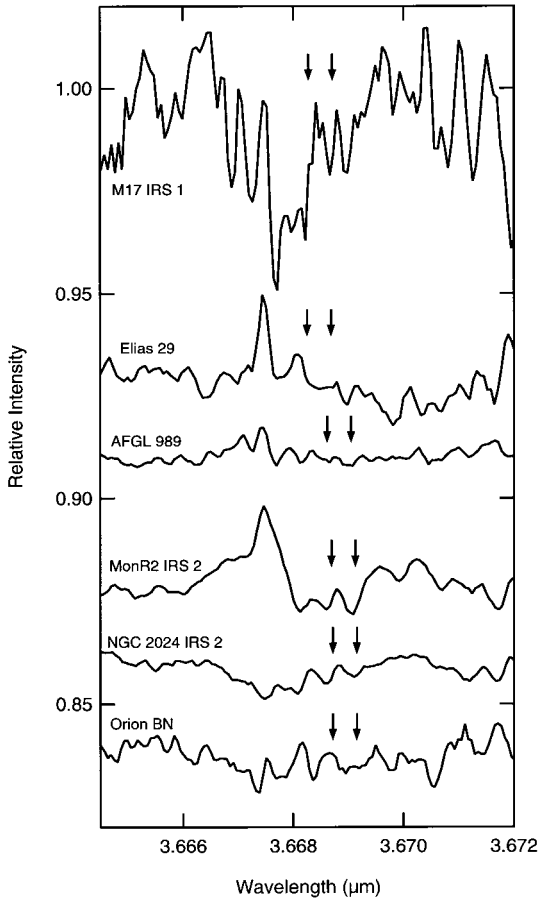

FIG. 5.—Nondetections of the $R(1, 1)^+$-$R(1, 0)$ doublet of H_3^+ toward six dense cloud sources from UKIRT data. The arrows indicate the expected positions of the H_3^+ lines.

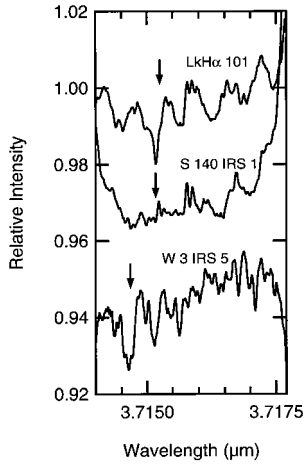

FIG. 6.—Nondetections of the $R(1, 1)^-$ line of H_3^+ toward three dense cloud sources from Kitt Peak. The arrows indicate the expected positions of the H_3^+ line.

sonable signal-to-noise ratio in NGC 2024 IRS 2 at Kitt Peak using long integrations.

3.3. CO *Detections*

Table 5 summarizes our observations of CO toward AFGL 961E and Mon R2 IRS 3. In both cases the first six lines of the *R*-branch were observed with good signal-to-noise ratios. The observed spectra are shown in Figure 7. The transition dipole moments were calculated from *f*-values obtained from the ab initio calculations of Huré & Roueff (1996). The nonlinearity of the absorption was taken into account in calculating the column densities. Figure 8 shows the Boltzmann plots for these two sources. For Mon R2 IRS 3, a straight-line fit yields an excitation temperature of 80 K. For AFGL 961E, the fit yields $T_{ex} = 6$ K and $J = 1$–5 yields $T_{ex} = 39$ K. The rotational distribution of

TABLE 5

CO LINE PARAMETERS.[a]

Object	Line	λ (Å)	W_λ (Å)	$\sigma(W_\lambda)$ (Å)	$\lvert\mu\rvert^2$ (10^{-5} D^2)	N_{level} (10^{17} cm^{-2})	$\sigma(N)$ (10^{17} cm^{-2})	v_{obs} (km s^{-1})	v_{LSR} (km s^{-1})	FWHM (km s^{-1})
AFGL 961E.....	*R*(0)	23453.05	0.220	0.005	4.28	5.37	0.20	29.5	11.9	12.1
	R(1)	23432.69	0.176	0.004	2.87	6.23	0.15	29.7	12.1	10.7
	R(2)	23412.75	0.249	0.005	2.60	9.83	0.33	30.6	13.0	12.8
	R(3)	23393.23	0.241	0.010	2.49	10.1	0.51	29.4	11.3	14.4
	R(4)	23374.13	0.146	0.006	2.43	6.84	0.53	28.7	10.5	11.5
	R(5)	23355.44	0.102	0.008	2.40	4.62	0.36	33.8	15.7	11.5
Mon R2 IRS 3.....	*R*(0)	23453.05	0.249	0.007	4.28	7.69	0.23	28.6	6.0	14.6
	R(1)	23432.69	0.300	0.005	2.87	14.8	0.46	32.6	10.0	13.0
	R(2)	23412.75	0.423	0.006	2.60	28.9	0.90	33.7	11.1	15.2
	R(3)	23393.23	0.429	0.006	2.49	30.8	1.07	33.8	10.8	14.9
	R(4)	23374.13	0.401	0.005	2.43	28.0	0.82	31.4	8.3	15.1
	R(5)	23355.44	0.385	0.007	2.40	27.0	0.97	35.1	12.1	15.7

[a] Statistical uncertainties (1 σ) are listed. Systematic errors due to incomplete cancellation of telluric CO lines are difficult to estimate and probably larger.

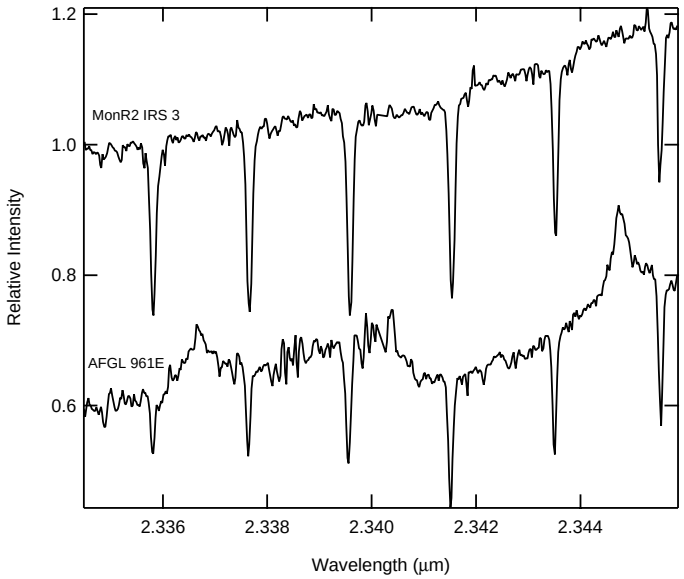

FIG. 7.—^{12}CO first overtone spectra of Mon R2 IRS 3 and AFGL 961E obtained at IRTF. The emission features in the AFGL 961E spectrum are Pfund series lines from high n (30, 31, and 32). The spectrum of AFGL 961E has been shifted downward for clarity.

CO in molecular clouds has been discussed by Mitchell et al. (1990). We estimate total CO column densities of 1.9×10^{19} cm^{-2} for Mon R2 IRS 3 and 0.5×10^{19} cm^{-2} for AFGL 961E.

4. DISCUSSION

4.1. H_3^+ *Chemistry in Molecular Clouds*

4.1.1. H_3^+ *Formation*

In the interstellar medium, as in the laboratory, H_3^+ is formed in a two-step reaction sequence: the ionization of H_2 to form H_2^+, followed by the Langevin reaction $H_2^+ + H_2 \rightarrow H_3^+ + H$. Since the Langevin reaction is quite fast (rate constant $k \sim 2 \times 10^{-9}$ cm^3 s^{-1}; Bowers, Elleman, & King 1969), the rate of formation of H_3^+ is completely determined by the rate of H_2 ionization.

The process generally assumed to dominate the ionization of H_2 is bombardment by cosmic-ray protons with energies near 100 MeV (Herbst & Klemperer 1973). At these energies, protons can travel through an H_2 column of $\sim 10^{24}$ cm^{-2}, which is more than the column densities of typical dense clouds. As a result, the rate of cosmic-ray ionization should be relatively constant and has been estimated (Herbst & Klemperer 1973) to be $\zeta \sim 10^{-17}$ s^{-1}. The order of magnitude of this result has been confirmed by observations of HCO^+ and DCO^+ (Plume et al. 1998). Recently used values of ζ average around 3×10^{-17} s^{-1} (van Dishoeck & Black 1986; Lee, Bettens, & Herbst 1996), so we adopt this value.

Ionization of H_2 by ultraviolet photons should not be a significant source of H_2^+ in dense clouds because photons with sufficient energy (15.4 eV) will not penetrate the clouds

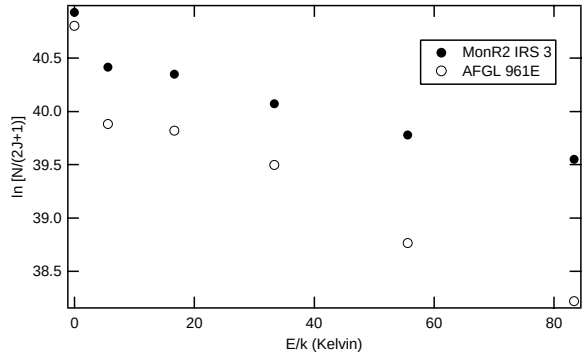

FIG. 8.—Boltzmann plots for the ^{12}CO overtone observations of Mon R2 IRS 3 and AFGL 961E

even if they escape the H II regions around their sources. The ionization of H_2 by X-rays has also been suggested as an efficient process leading to H_3^+ formation (Draine & Woods 1990; Black 1998). However, this mechanism could operate only in unusual environments near strong X-ray sources, such as active galactic nuclei, and is probably not important in most dense clouds in our Galaxy.

Thus, for the remainder of the discussion in this paper, we adopt the usual assumption that H_2^+ production is dominated by cosmic-ray ionization and therefore that the H_3^+ production rate is $\zeta n(H_2)$, where $\zeta \sim 3 \times 10^{-17}$ s^{-1}.

4.1.2. H_3^+ *Destruction*

The destruction of H_3^+ in dense clouds is dominated by chemical reactions that lead (after subsequent reactions) to more complicated molecules. Reactions of H_3^+ with hydrogen species (H_2 or H) do not cause a net loss of H_3^+, and the reaction with He (the next most abundant element) to form HeH^+ is endothermic by 2.6 eV and cannot occur at the low temperatures of dense clouds.

The next most abundant elements are C and O, and we expect that the destruction of H_3^+ should be dominated by species containing these elements. In dense clouds, over 99% of gas-phase carbon atoms are in the form of CO, and of the O atoms that are not in CO, the majority exist as free atoms according to the extensive chemical model calculation by Lee et al. (1996). Since the reaction rate of H_3^+ with O is slower than that with CO, the destruction of H_3^+ is dominated by reaction with CO.

Table 6 shows the eight species that most efficiently destroy H_3^+ in dense clouds. In this table we have listed, for each species, the maximum and minimum abundances in steady state from the "new standard model" of Lee et al. (1996) for hydrogen densities from 10^3–10^5 cm^{-3} and temperatures from 10–50 K. Also listed are the measured rate constants with H_3^+ and the minimum and maximum expected rates of H_3^+ destruction. The electron is one noteworthy entry—electron recombination, which in diffuse clouds is the primary destruction path of H_3^+, is seen not to play a major role in the dense cloud environment because of the lower electron abundance.

In the following discussion we will consider only H_3^+ destruction by CO for reasons of simplicity. Clearly a rigorous quantitative model must take into account the contribution (~20%–30% of the total destruction) of atomic oxygen. However, since the cosmic-ray ionization rate ζ is uncertain to a factor on the order of a few, the neglect of oxygen in this model is not a serious omission. In our discussions here we take the rate of H_3^+ destruction to be given by the simple expression $k_{CO}\, n(CO) n(H_3^+)$.

4.1.3. H_3^+ *Abundance*

To estimate the abundance of H_3^+ in dense clouds, we make the assumption of a steady state and equate the rates of formation and destruction. From §§ 4.1.1 and 4.1.2, this gives $\zeta n(H_2) = k_{CO}\, n(CO) n(H_3^+)$. This equation can be rearranged to yield the number density of H_3^+:

$$n(H_3^+) = \frac{\zeta}{k_{CO}} \frac{n(H_2)}{n(CO)} . \quad (1)$$

In order to obtain a numerical estimate, we substitute $\zeta \sim 3 \times 10^{-17}$ s^{-1}, $k_{CO} = 2 \times 10^{-9}$ cm^3 s^{-1}, and $n(CO)/n(H_2) \sim 1.5 \times 10^{-4}$ (Lee et al. 1996). This yields a value of $n(H_3^+) \sim 1 \times 10^{-4}$ cm^{-3}. As mentioned earlier, H_3^+ (unlike most molecules) has a constant number density in molecular clouds independent of total H_2 number density; because of this, measurements of H_3^+ column density can be of distinct value in determining cloud parameters.

4.1.4. *Ortho-to-Para Ratio*

The ratio of ortho- to para-H_3^+ in dense clouds is expected to reflect the kinetic temperature of the background (H_2) gas. This is because ortho- and para-H_3^+ are not linked by any radiative transitions but are linked by ion-neutral reactions with H_2 that proceed at the Langevin rate ($k \sim 2 \times 10^{-9}$ cm^3 s^{-1}). The proton hop reaction

$$H_3^+ + \tilde{H}_2 \rightarrow H_2 + \tilde{H}_2 H^+ \quad (2)$$

and the proton exchange reaction

$$H_3^+ + \tilde{H}_2 \rightarrow H_2 \tilde{H}^+ + H\tilde{H} \quad (3)$$

scramble protons between H_2 and H_3^+ and thereby thermalize the spin temperature of H_3^+ to the kinetic temperature of H_2 (Uy, Cordonnier, & Oka 1997). In the above reactions, the tildes indicate the protons from the reactant H_2.

4.2. *Estimates of Cloud Parameters*

Because the number density of H_3^+ is independent of the total H_2 number density, the observed column density of H_3^+ directly yields an estimate of the effective column length of absorption. This corresponds physically to the length of the portion of the cloud that lies along the line of sight to

TABLE 6

SPECIES IMPORTANT IN THE DESTRUCTION OF H_3^+

Species	Minimum Abundance $[n/n(H_2)]$	Maximum Abundance $[n/n(H_2)]$	Rate Constant (cm^{3}s^{-1})	Minimum Rate $[s^{-1}/n(H_2)]$	Maximum Rate $[s^{-1}/n(H_2)]$
CO	1.45 (−4)	1.46 (−4)	1.8 (−9)[a]	2.6 (−13)	2.6 (−13)
O	8.64 (−5)	1.51 (−4)	8.0 (−10)[b]	6.9 (−14)	1.2 (−13)
e^-	1.89 (−8)	2.31 (−7)	1.8 (−7)[c]	3.4 (−15)	4.2 (−14)
N_2	5.86 (−6)	1.92 (−5)	1.8 (−9)[a]	1.1 (−14)	3.5 (−14)
O_2	2.68 (−5)	5.92 (−5)	2.7 (−10)[d]	7.2 (−15)	1.6 (−14)
H_2O	3.59 (−7)	2.32 (−6)	5.9 (−9)[a]	2.1 (−15)	1.4 (−14)
N	4.34 (−6)	3.08 (−5)	4.5 (−10)[e]	2.0 (−15)	1.4 (−14)
CO_2	1.41 (−7)	9.45 (−7)	2.0 (−9)[a]	2.8 (−16)	1.9 (−15)

[a] Anicich & Huntress 1986.
[b] Fehsenfeld 1976.
[c] Amano 1988; Sundström et al. 1994 give a temperature dependent rate constant of $4.6 \times 10^{-6}\, T^{-0.65}$ cm^3 s^{-1}.
[d] Adams & Smith 1984.
[e] Scott et al. 1997.

TABLE 7

ESTIMATED CLOUD PARAMETERS

Object	$N_\sigma(H_3^+)$ (10^{14} cm^{-2})	$N_\beta(H_3^+)$[a] (10^{14} cm^{-2})	$N_{tot}(H_3^+)$ (10^{14} cm^{-2})	ζL (cm s^{-1})	L (parsec)	$\tau_{9.7}$[b]	N_H[c] (10^{22} cm^{-2})	N(CO) (10^{19} cm^{-2})	$N(H_2)$[d] (10^{22} cm^{-2})	$\langle n(H_2)\rangle$ (10^4 cm^{-3})	T (K)
AFGL 2136	1.9	1.9	3.8	110	1.3	5.07	18	3.2[f]	22	6	47
W33A	2.3	2.9	5.2	150	1.7	7.84	28	3.9[f]	27	5	36
Mon R2 IRS 3.....	0.6	0.8	1.4	41	0.5	2[e]	7	1.9[g]	1.3	9	31
AFGL 961E.....	0.6	1.1	1.7	49	0.6	2.11	7.5	0.5[g]	3.2	2	25
AFGL 490	0.4	0.7	1.1	32	0.4	2.77	9.8	1.1[h]	7.6	6	26
AFGL 2591[i]	1.0	1.2	2.2	64	0.7	4.14	15	1.9[f]	13	6	38

[a] For AFGL 2136 and AFGL 2591, where both the $R(1, 1)^+$ and $R(1, 1)^-$ para-H_3^+ lines were observed, the $R(1, 1)^-$ values have been used because they have a lower $\sigma(N)$.
[b] Silicate optical depths at 9.7 μm from Willner et al. 1982, except as noted.
[c] Hydrogen column derived from $A_V/\tau_{9.7} = 18.6$ (Roche & Aitken 1994) and $N_H/A_V = 1.9 \times 10^{21}$ cm^{-2} mag^{-1} (Bohlin, Savage, & Drake 1978).
[d] Hydrogen column derived from $n(CO)/n(H_2) \sim 1.5 \times 10^{-4}$ from Lee et al. 1996.
[e] Beckwith et al. 1976.
[f] Mitchell et al. 1990.
[g] This work.
[h] Mitchell et al. 1995, assuming $^{12}CO/^{13}CO = 89$.
[i] Estimates for AFGL 2591 have large systematic uncertainties due to the short integration time and telluric interference, as discussed in the text.

the infrared source. We estimate this length from the following approximate relation

$$L \sim \frac{N(H_3^+)}{n(H_3^+)}, \quad (4)$$

where $n(H_3^+)$ has been estimated to be $\sim 1 \times 10^{-4}$ cm^{-3}. The resulting lengths are on the order of a parsec, consistent with the usual dimensions of molecular clouds.

Given the effective column length of a cloud, we estimate the absolute number density of H_2, assuming that the majority of the H_2 along the line of sight is contained in the molecular cloud where the H_3^+ absorption is seen. The column density of H_2 is estimated from the observed column density of CO using $n(CO)/n(H_2) \sim 1.5 \times 10^{-4}$ from the model calculations of Lee et al. (1996). For comparison, in Table 7 we have also estimated N_H from the silicate optical depth as prescribed by Tielens et al. (1991). We note that the estimated values of N_H and $2N(H_2)$ are quite similar, within a factor of a few. Given an estimate of $N(H_2)$, we estimate the mean hydrogen number density

$$\langle n(H_2) \rangle \sim \frac{N(H_2)}{L} \sim \frac{N(H_2)}{N(H_3^+)}\, n(H_3^+)\,. \quad (5)$$

Finally, the observed H_3^+ ortho-to-para ratio allows us to estimate the kinetic temperature of the cloud using the standard Boltzmann formula,

$$\frac{N_{ortho}}{N_{para}} = \frac{g_{ortho}}{g_{para}}\, e^{-\Delta E/kT} = 2e^{-32.87/T}, \quad (6)$$

where the g values are the statistical weights of the ortho- and para-H_3^+ states and ΔE is the energy difference between them.

The estimated column lengths, H_2 number densities, and kinetic temperatures for the sources where H_3^+ has been detected are listed in Table 7. These values pertain only to the portions of the clouds in front of the infrared sources. Note that the derived values of L are inversely proportional to the assumed value of ζ and the values of $\langle n(H_2) \rangle$ are proportional to ζ, so both are uncertain to a factor on the order of a few.

Measurements of H_3^+, along with an assumed H_2:CO ratio, directly provide an accurate value of the quantity ζL but cannot constrain ζ or L independently. Better estimates of either ζ or L, along with improved determinations of the H_2:CO ratio using infrared spectroscopy (e.g., Lacy et al. 1994), will allow more accurate estimates of $\langle n(H_2) \rangle$. As extensive models of molecular clouds (from core to edge) are developed from radio and millimeter observations, it will be of considerable interest to compare these models with the estimates of $\langle n(H_2) \rangle$ from H_3^+ observations.

5. CONCLUSIONS

The fundamental molecular ion H_3^+ has now been detected along many lines of sight in the interstellar medium. In addition to the initial detections in the dense molecular clouds toward AFGL 2136 and W33A, H_3^+ has also been detected toward the dense cloud sources Mon R2 IRS 3, AFGL 961E, AFGL 2591, and AFGL 490 with column densities ~ 1–2×10^{14} cm^{-2}.

The nondetections reported here should not be taken as due to the absence of H_3^+ but rather as due to a lack of sensitivity in the observations. In many cases, the established upper limits to H_3^+ are higher than observed H_3^+ column densities in other sources, so that H_3^+ may be detectable in these clouds using longer integrations or more sensitive spectrometers. In the cases where the upper limits are very low (e.g., S140 IRS 1), it is likely that H_3^+ is still present, but that the absorption path length is too short to permit detection at current levels of sensitivity.

The simplicity of interstellar H_3^+ chemistry enables estimates of the effective path lengths, the hydrogen number densities, and the kinetic temperatures of the gas in these dense clouds. The fact that the resulting estimates are consistent with the canonical values for dense clouds represents an important confirmation of the theory of H_3^+ chemistry in this environment. The observation of H_3^+ in several dense molecular clouds, along with the recent detections of H_3^+ in the diffuse interstellar medium and toward the Galactic center, confirms the expected ubiquity of H_3^+ and demonstrates its promise as a powerful probe of the interstellar medium.

We thank the staffs of the Joint Astronomy Centre, the United Kingdom Infrared Telescope, and the Kitt Peak National Observatory for the support of these measurements. Some of the observations reported here were made during UKIRT Service observing. UKIRT is operated by the Joint Astronomy Centre on behalf of the U.K. Particle Physics and Astronomy Research Council. B. J. McCall is supported by the Fannie and John Hertz Foundation. The University of Chicago portion of this work has been supported by NSF grant PHYS-9722691 and NASA grant NAG5-4070.

REFERENCES

Adams, N. G., & Smith, D. 1984, Chem. Phys. Lett., 105, 604
Amano, T. 1988, ApJ, 329, L121
Anicich, V. G., & Huntress, W. T., Jr., 1986, ApJS, 62, 553
Bally, J., & Lada, C. J. 1983, ApJ, 265, 824
Beckwith, S., Evans, N. J., II, Becklin, E. E., & Neugebauer, G. 1976, ApJ, 208, 390
Black, J. H. 1998, Faraday Discuss., 109, 257
Bohlin, R. C., Savage, B. D., & Drake, J. F. 1978, ApJ, 224, 132
Bowers, M. T., Elleman, D. D., & King, J., Jr. 1969, J. Chem. Phys., 50, 4787
Dinger, A., Dickinson, D. F., Gottlieb, C. A., & Gottlieb, E. W. 1979, PASP, 91, 830
Draine, B. T., & Woods, D. T. 1990, ApJ, 363, 464
Fehsenfeld, F. C. 1976, ApJ, 209, 638
Geballe, T. R., McCall, B. J., Hinkle, K. H., & Oka, T. 1999, ApJ, 510, 251
Geballe, T. R., & Oka, T. 1996, Nature, 384, 334
Goldsmith, P. F., & Mao, X.-J. 1983, ApJ, 265, 791
Herbst, E., & Klemperer, W. 1973, ApJ, 185, 505
Hinkle, K. H., Cuberly, R., Gaughan, N., Heynssens, J., Joyce, R., Ridgway, S. T., Schmitt, P., & Simmons, J. E. 1998, Proc. SPIE, 3354, 810
Huré, J. M., & Roueff, J. M. 1996, A&AS, 117, 561
Kulesa, C., & Black, J. H. 1999, in preparation
Lacy, J. H., Knacke, R., Geballe, T. R., & Tokunaga, A. T. 1994, ApJ, 428, L69
Lee, H.-H., Bettens, R. P. A., & Herbst, E. 1996, A&AS, 119, 111
Maddalena, R. J., Morris, M., Moscowitz, J., & Thaddeus, P. 1986, ApJ, 303, 375
McCall, B. J. 1999, in preparation
McCall, B. J., Geballe, T. R., Hinkle, K. H., & Oka, T. 1998a, Science, 279, 1910
McCall, B. J., Hinkle, K. H., Geballe, T. R., & Oka, T. 1998b, Faraday Discuss., 109, 267
Mitchell, G. F., Lee, S. W., Maillard, J.-P., Matthews, H., Hasegawa, T. I., & Harris, A. I. 1995, ApJ, 438, 794
Mitchell, G. F., Maillard, J.-P., Allen, M., Beer, R., & Belcourt, K. 1990, ApJ, 363, 554
Mountain, C. M., Robertson, D. J., Lee, T. J., & Wade, R. 1990, Proc. SPIE, 1235, 25
Oka, T. 1980, Phys. Rev. Lett., 45, 531
Oka, T., & Jagod, M.-F. 1993, J. Chem. Soc. Faraday Trans., 89, 2147

Plume, R., Bergin, E. A., Williams, J. P., & Myers, P. C. 1998, Faraday Discuss., 109, 47
Roche, P. F., & Aitken, D. K. 1984, MNRAS, 208, 481
Schneider, N., Stutzki, J., Winnewisser, G., & Block, D. 1998, A&A, 335, 1049
Scott, G. B. I., Fairley, D. A., Freeman, C. G., & McEwan, M. J. 1997, Chem. Phys. Lett., 269, 88
Sundström, G., et al. 1994, Science, 263, 785
Tielens, A. G. G. M., Tokunaga, A. T., Geballe, T. R., & Baas, F. 1991, ApJ, 381, 181
Tokunaga, A. T., Toomey, D. W., & Carr, J. S. 1990, Proc. SPIE, 1235, 131
Uy, D., Cordonnier, M., & Oka, T. 1997, Phys. Rev. Lett., 78, 3844
van Dishoeck, E. F., & Black, J. H. 1986, ApJS, 62 109
Watson, W. D. 1973, ApJ, 183, L17
Willner, S. P., et al. 1982, ApJ, 253, 174

A.5 "Observations of Diffuse Interstellar Bands Attributed to C_7^-"

Reprinted from *Astrophysical Journal* 531, 329 (2000).

THE ASTROPHYSICAL JOURNAL, 531:329–335, 2000 March 1

OBSERVATIONS OF DIFFUSE INTERSTELLAR BANDS[1] ATTRIBUTED TO C_7^-

B. J. McCALL, D. G. YORK, AND T. OKA
Department of Astronomy and Astrophysics and the Enrico Fermi Institute, University of Chicago, 5735 South Ellis Avenue, Chicago, IL 60637; bjmccall@uchicago.edu

Received 1999 July 26; accepted 1999 October 15

ABSTRACT

Recent advances in laboratory gas-phase spectroscopy of large molecules and their ions permit a direct comparison between the diffuse interstellar bands (DIBs) and proposed carriers. On the basis of gas-phase data, Tulej et al. recently suggested that five $A^2\Pi_u \leftarrow X^2\Pi_g$ electronic transitions of the linear carbon-chain anion C_7^- match with DIBs. We have obtained high-resolution visible spectra of four reddened stars (HD 46711, HD 50064, HD 183143, and Cyg OB2 12) to make a detailed comparison with the C_7^- laboratory data. Our data show that three of the C_7^- bands (0_0^0 at 6270.2 Å, 3_0^1 at 6064.0 Å, and $1_0^2 3_0^1$ at 4963.0 Å) are in good agreement with DIBs in wavelength and relative intensity. A fourth band (1_0^1 at 5612.8 Å) also agrees in intensity but is apparently off by 2 Å in wavelength. All other laboratory bands of C_7^- are not expected to be detectable in astronomical spectra with the current level of sensitivity. The gas-phase spectrum of C_7^- agrees with the DIBs better than that of any previously proposed molecule. However, the question of whether C_7^- is a DIB carrier cannot be definitively answered until (1) better laboratory measurements confirm, refute, or explain the wavelength discrepancy for the 1_0^1 band and/or (2) better astronomical spectra reveal the presence or absence of other C_7^- bands.

Subject headings: ISM: molecules — line: identification — methods: laboratory — molecular data

1. INTRODUCTION

The diffuse interstellar bands, a series of absorption features in the visible spectra of reddened stars, have defied explanation for over half a century. It is now generally accepted that the diffuse interstellar bands (DIBs) are most likely due to free molecules in the gas phase (Herbig 1995), but so far there has been no definitive match between a subset of the diffuse bands and the gas-phase spectrum of any individual molecule.

One class of molecules that has been proposed to explain the diffuse bands is carbon-chain molecules. As pointed out by Douglas (1977) and Smith, Snow, & York (1977), rapid internal conversion of electronic energy into vibrational energy in these molecules can explain the "diffuse" character of their spectral lines and also protect the molecules from photodissociation caused by ultraviolet radiation from stars. This explanation has the advantage that diffuse-band carriers need not be destroyed by the absorption (unlike the case of predissociation broadening) and thus do not require replacement by some rapid chemical process. Carbon-chain molecules are also attractive because of the high cosmic abundance of carbon and because they are similar to molecules observed by radio astronomers in dense clouds, such as the cyanopolyacetylenes (Avery et al. 1976). The production and chemical stability of carbon-chain molecules (particularly C_7^-) has been recently examined by Ruffle et al. (1999).

To test potential diffuse-band carriers effectively, gas-phase laboratory spectra are essential. Spectra recorded in rare-gas matrices are far easier to obtain but are subject to unpredictable wavelength shifts that make comparison with astronomical spectra impractical. It has recently become possible, using the technique of resonance-enhanced two-color photodetachment, to obtain relatively sharp gas-phase spectra of carbon-chain anions. Based on such spectra, Tulej et al. (1998) pointed out that five spectral lines of the C_7^- anion coincide (within 2 Å) with diffuse bands tabulated by Jenniskens & Désert (1994).

Because most of the diffuse bands attributed to C_7^- had a low signal-to-noise ratio in the data of Jenniskens & Désert (1994), it was necessary to improve the astronomical measurements to test the assignment of these lines to C_7^-.

2. OBSERVATIONS AND DATA REDUCTION

High-resolution visible spectra of four reddened and two unreddened stars were obtained using the Astrophysical Research Consortium Echelle Spectrometer (ARCES). ARCES was commissioned from 1999 January to March and is now in routine use on the 3.5 m telescope at Apache Point Observatory. The instrument is mounted at the Nasmyth focus, from which it receives an f/10 beam from the telescope. The slit plane holds either a 1.″6 × 1.″6 or a 1.″6 × 3.″2 slit. The main optics path is orthogonal to the local zenith, with the collimator fed by a folding flat just behind the slit. A Bausch and Lomb 31.6 line mm^{-1} replica grating provides the high dispersion, and a pair of UBK7 prisms provides the cross-dispersion. The collimator defines an 8 inch beam which, after dispersion, feeds a 14 inch Schmidt camera. The detector is a Tektronix 2048 × 2048 CCD with 24 μm pixels.

The use of prismatic cross-dispersion allows efficient use of the CCD area so that complete spectral coverage is achieved from just shortward of 3400 Å to just longward of 10,200 Å. Each order is fully captured, so that a virtually blazeless echellogram can be obtained for each object by adding all redundant coverage of a given spectral interval. The resolving power is 37,500 (8 km s^{-1}), the read noise is 7 electrons $pixel^{-1}$, and the radiation rate is 0.013 $pixel^{-1}$ hr^{-1}. The half-peak counts are achieved at 4600 and 8200 Å for an unreddened F0 subdwarf star. The spectrograph

[1] Based on observations obtained with the Apache Point Observatory 3.5 m telescope, which is owned and operated by the Astrophysical Research Consortium.

design efficiency is 9% at $\lambda < 4100$ Å and 3% at 3500 Å. While we cannot confirm the efficiency until further tests are made on the telescope throughput, we believe that we are at or near the design goal. The instrument design principles of such spectrographs are given by Schroeder (1987), and the ARCES instrument is fully described by York et al. (2000).

The reddened stars HD 46711 and HD 50064 were chosen for their large color excesses, for their favorable placement in the late winter, and because it should be possible to observe H_2 in their spectra with the *Far-Ultraviolet Spectroscopic Explorer* (*FUSE*) ultraviolet spectrometer (Moos, Sembach, & Bianchi 1998). The star HD 183143 was observed because it is one of the stars used in the catalog of Jenniskens & Désert (1994) and because of its long history in the field (Herbig 1995). The star Cyg OB2 12 was selected because of its unusually large color excess and because the molecular ion H_3^+ has recently been observed in this source (McCall et al. 1998). The comparatively unreddened stars HD 164353 and HD 186994 were chosen because of their spectral types and favorable placement in the summer. We have not attempted telluric correction for any of the spectra, and any telluric interference can be judged from the spectra of these unreddened comparison stars.

Table 1 lists the stars and their spectral type and luminosity classes, V-band magnitudes, color excesses, stellar velocities with respect to the local standard of rest, stellar line widths, and interstellar LSR velocities and full widths. Also listed are the dates of observation and exposure times.

The data reduction started with the standard IRAF routines CCDPROC and DOECSLIT, which processed the CCD frames, extracted each order of the echelle, and (air) wavelength-calibrated the orders based on comparison exposures of a Th-Ar lamp. It was recently discovered that because of the large pixel scale of the CCD and the close spacing of the orders, the APTRACE routine introduces an unpredictable fringing (aliasing) into the spectra, which reduces the effective signal-to-noise ratio. Attempts are under way to modify the APTRACE procedure to prevent this effect, but they have not yet been successful. This problem does not change our conclusions about the relatively sharp lines we have observed, but its resolution may enable the detection of weaker and broader lines in our data.

After each order was extracted and wavelength-calibrated by IRAF, it was transferred into IGOR PRO (version 3.14), a commercial graphing and analysis program produced by Wavemetrics. Within the IGOR environment, the orders were coadded in wavelength space to form a single array of data for each exposure. All exposures from a single night were then coadded, with small wavelength shifts used to align telluric absorption lines when necessary because of wavelength calibration errors.

The same extraction and coadding routine was performed on flat-field exposures of a tungsten filament housed in a quartz envelope. The large-scale spectral profile of each resulting flat-field spectrum was then removed by dividing out a 13th order polynomial fit to the spectrum. This afforded a normalized spectrum, which contained only information on pixel-to-pixel sensitivity variations. Each coadded stellar spectrum was then divided by this normalized flat field. In the case of HD 46711, the resulting flat-fielded spectra for each night were coadded after aligning the interstellar K I line at 7699 Å. Finally, each flat-fielded spectrum was divided by a 13th order polynomial fit to provide a flat continuum for analysis.

3. RESULTS AND DISCUSSION

3.1. *Laboratory Spectrum of* C_7^-

The spectrum of C_7^- observed in the laboratory can be separated into two electronic transitions, the $A^2\Pi_u \leftarrow X^2\Pi_g$ system and the $B^2\Pi_u \leftarrow X^2\Pi_g$ system. The latter system lies to higher energy and is intrinsically broadened by internal conversion. While the intensities of the two systems are comparable, the large width of the $B \leftarrow X$ lines make their astronomical detection extremely difficult. All of the lines observed in the laboratory and expected in interstellar space originate in the ground vibrational level of the ground (X) electronic state.

TABLE 1

STELLAR DATA AND OBSERVING LOG

Star	Type[a]	V[a] (mag)	E_{B-V}[b] (mag)	v^*[c] (km s^{-1})	Δv^*[d] (km s^{-1})	v_{IS}[e] (km s^{-1})	Δv_{IS}[e] (km s^{-1})	UT Date (1999)	Integration Time (minutes)
Reddened Stars									
HD 46711	B3 II	9.1	1.05	23	84	8	19	Feb 01	30
								Feb 03	60
								Feb 07	50
								Feb 20	60
								Feb 22	60
HD 50064	B6 Ia	8.2	0.85	61	88	18	40	Feb 22	60
Cyg OB2 No. 12.....	B5 Iab	12.5	3.2	25	70	7	19	May 31	60
HD 183143	B7 Ia	6.9	1.28	34	69	7	23	Jun 10	35
Unreddened Stars									
HD 164353	B5 Ib	4.0	0.12	13	69	2	13	Jun 10	6
HD 186994	B0 III	7.5	0.19	−52	231	2	17	Jun 10	30

[a] From the SIMBAD Astronomical Database.
[b] From Snow, York, & Welty 1977.
[c] Determined from He D_3 lines in our spectra.
[d] FWHM of He I λ7065.
[e] Determined from K I λ7699.

The $A \leftarrow X$ system consists of a progression of vibrational bands, starting with the origin band at 6270.2 Å, which is the strongest band and corresponds to transitions from the ground vibrational state of the X electronic state to the ground vibrational state of the A (first excited) electronic state. In all of the laboratory spectra obtained to date, the resolution is not sufficiently high to resolve the rotational structure of the bands.

In addition to the strong origin band, the $A \leftarrow X$ system shows a progression of weaker bands, which represent transitions into vibrationally excited states of the A electronic state. These transitions are described by the vibrational mode that is excited, the number of quanta of this mode in the lower state (always 0), and the number of quanta in the upper state. We utilize the standard notation introduced by J. K. G. Watson (Brand et al. 1983), in which, for example, 3_0^1 represents a transition into the state in the A electronic state where the ν_3 mode is singly excited. The bands reported by Tulej et al. (1998), in addition to the origin band (0_0^0), are 3_0^1 at 6064.0 Å, 2_0^1 at 5747.6 Å, 1_0^1 at 5612.8 Å, $1_0^1 3_0^1$ (a combination band, which happens to be a doublet) at 5456.7 and 5449.6 Å, 1_0^2 (also a doublet) at 5095.7 and 5089.5 Å, and $1_0^2 3_0^1$ at 4963.0 Å.

Because of the nature of the experimental technique, the intensities of the gas-phase lines obtained with the resonance-enhanced two-color photodetachment technique are unreliable as a result of power-broadening and saturation effects. Therefore, the intensities of the neon-matrix absorptions must be used in comparison with astronomical spectra. For this purpose, we have remeasured the relative intensities of the C_7^- bands from original spectra provided by J. P. Maier (1999, private communication), and these intensities are listed in Table 2. Because of contamination in the spectrum given by Forney et al. (1997), our intensities differ slightly from, and should be considered more accurate than, those listed in Tulej et al. (1998).

It should be emphasized that the C_7^- lines are just above the level of sensitivity of the gas-phase techniques. The difficulties in the experiment are illustrated by the differences in the three traces provided by M. Tulej, M. Pachkov, and J. P. Maier (1999, private communication) in Figure 1. According to the experimenters, the width and shape of the absorption features are extremely dependent on experimental conditions, and one must not try to overinterpret the details of the spectra. The lack of repeatability in the current state-of-the-art laboratory measurements makes detailed comparisons with astronomical spectra challenging.

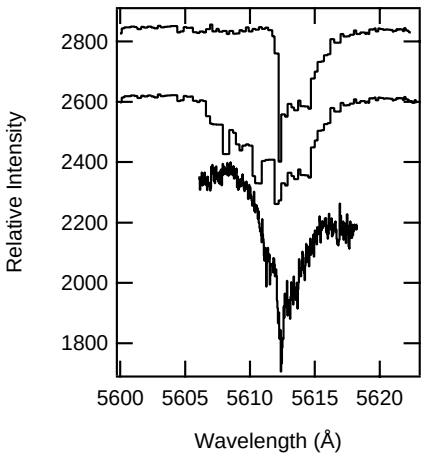

FIG. 1.—*Top to bottom*: Three traces of the 1_0^1 band of C_7^- from the gas-phase experiments of M. Tulej, M. Pachkov, and J. P. Maier (1999, private communication): trace from Tulej et al. (1998), trace from Fig. 5, and trace from a more recent experiment with higher instrumental resolution.

3.2. *Diffuse Band Spectra*

Spectra of the λ6270 diffuse band, along with the laboratory trace of the C_7^- origin band, are shown in Figure 2. Also shown, for comparison, is a simulation of the diffuse-band catalog of Jenniskens & Désert (1994). This line (with FWHM $\sim$1.2 Å) is clearly observed in all four reddened stars and is only slightly present in the "unreddened" [$E(B-V) = 0.12$] star HD 164353. There is good wavelength agreement between the astronomical lines and the sharp feature in the laboratory data.

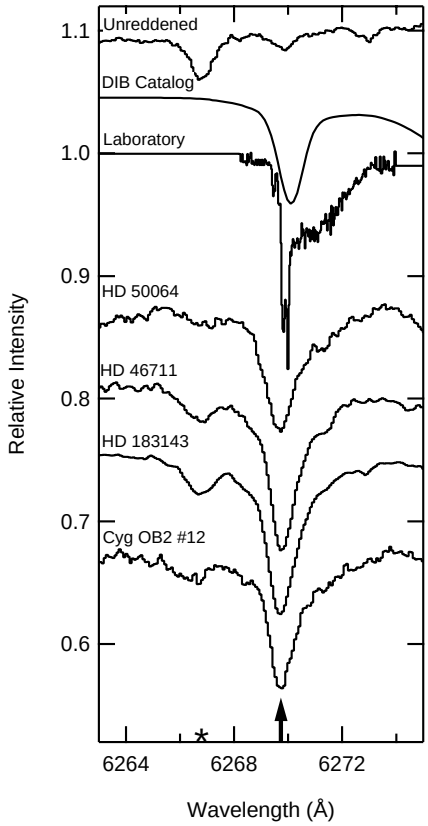

FIG. 2.—Origin (0_0^0) band of C_7^- and the diffuse band at 6270 Å attributed to it. Trace labeled "DIB catalog" is derived from the catalog of Jenniskens & Désert (1994). Stellar spectra have been shifted from unity for clarity and have been adjusted to rest air–wavelengths using the K I line at 7699 Å. The top trace is the (relatively) unreddened star HD 164353. The position of the diffuse band is marked with an arrow along the bottom axis, and the asterisk indicates a stellar line.

TABLE 2

LINE INTENSITIES

	$\lambda 6270/0_0^0$		$\lambda 6065/3_0^1$		$\lambda 5610/1_0^1$		$\lambda 4964/1_0^2 3_0^1$	
SOURCE	W_λ	$\sigma(W_\lambda)$	W_λ	$\sigma(W_\lambda)$	W_λ	$\sigma(W_\lambda)$	W_λ	$\sigma(W_\lambda)$
Laboratory.....	1	0.2	0.16	0.03	0.22	0.04	0.12[a]	0.02
HD 50064	152	22	16	6	24	10	23[b]	4
HD 46711	180	16	19	6	20	10	26[b]	6
HD 183143.....	190	23	15	3	24	10	22	3
Cyg OB2 12.....	174	26	13	6	20	10	...[c]	...

NOTE.—Intensities for astronomical spectra are listed as equivalent widths W_λ in mÅ. Their uncertainties $\sigma(W_\lambda)$ are rough estimates based on the uncertain placement of the continuum. Laboratory (matrix) line intensities have been remeasured from the original spectra. They are in arbitrary units and have uncertainties of 20% (Tulej et al. 1998).

[a] The $1_0^2 3_0^1$ line lies on the shoulder of the 0_0^0 $B \leftarrow X$ transition, and thus it is difficult to estimate its intensity. The value listed should be considered a lower limit.

[b] The equivalent width measurement of $\lambda 4964$ toward these sources is complicated by an instrumental artifact (seen in Fig. 4). The W_λ listed here were measured from the unflattened spectra, and corrections for the artifact have been attempted. This artifact did not affect HD 183143 because of the different Doppler shift.

[c] The $\lambda 4964$ line was marginally detected toward Cyg OB2 12 but with a very low signal-to-noise ratio due to the high reddening of the object.

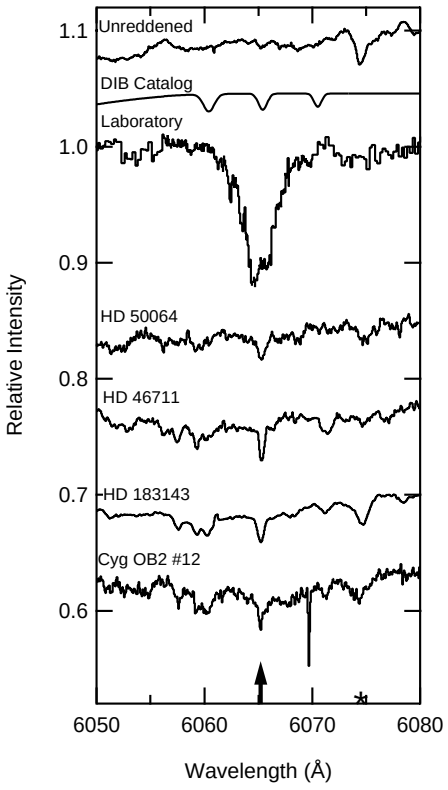

FIG. 3.—Same as Fig. 2, but for the 3_0^1 band of C_7^- and the diffuse band near 6065 Å. Note that the wavelength scale in this and the following figures is different from Fig. 2.

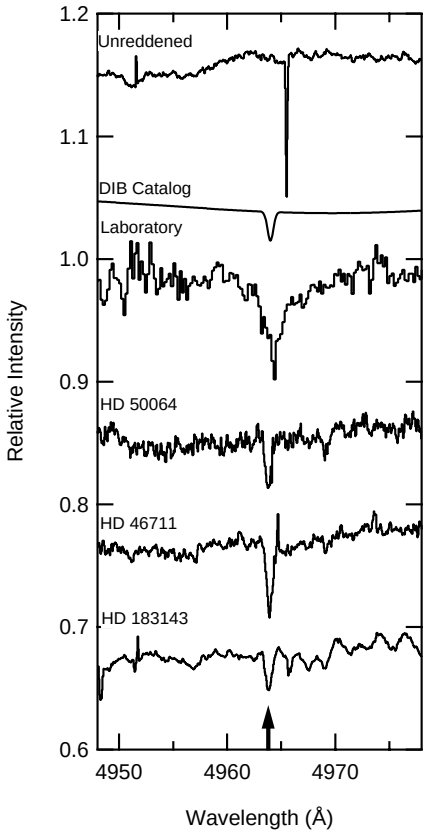

FIG. 4.—Same as Fig. 3, but for the $1_0^2 3_0^1$ band of C_7^- and the diffuse band near 4964 Å. Cyg OB2 12 is not shown because of its low signal-to-noise ratio at blue wavelengths.

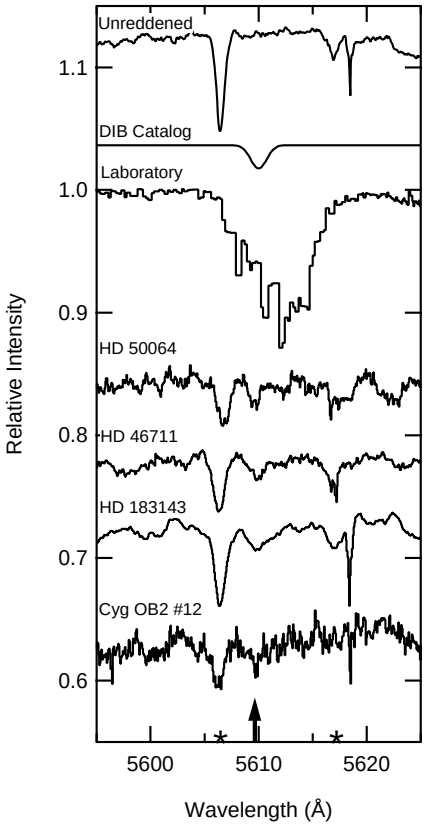

FIG. 5.—Same as Fig. 3, but for the 1_0^1 band of C_7^- and the diffuse band near 5610 Å.

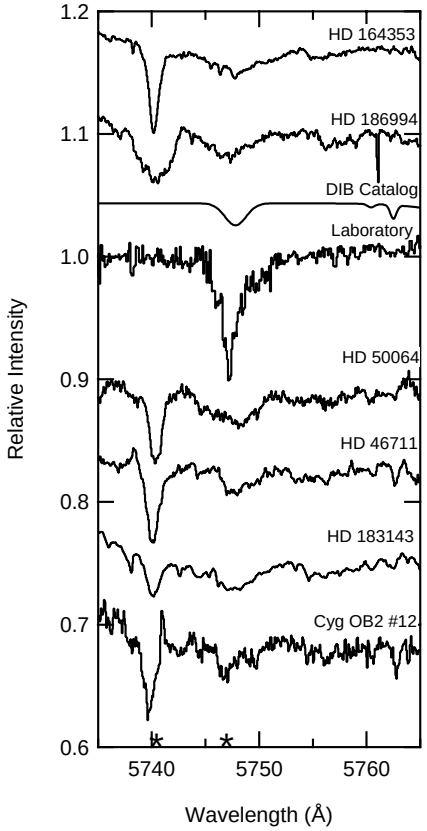

FIG. 6.—Same as Fig. 3, but for the 2_0^1 band of C_7^-. The spectra of the two unreddened stars HD 164353 and HD 186994 are very similar to those of the reddened stars near the position of the laboratory line, so it is difficult to confirm the presence (or absence) of a weak diffuse band corresponding to the 2_0^1 band.

Figure 3 shows the spectra of λ6065, attributed to the C_7^- 3_0^1 band (note that the wavelength scale in this and the following figures differs from that of Fig. 2). The line is very sharp (FWHM $\sim$0.7 Å), is present in all four reddened stars, and shows good wavelength agreement with the laboratory data. The two nearby "probable" diffuse bands of Jenniskens & Désert (1994) are difficult to pick out.

Figure 4 shows the diffuse band near 4964 Å, which is attributed to the $1_0^2 3_0^1$ combination band of C_7^-. This feature, like λ6065, is quite sharp (FWHM $\sim$ 0.7 Å) and clearly present in HD 50064, HD 46711, and HD 183143. The feature is also marginally present in Cyg OB2 12, which has very low flux at such blue wavelengths because of its extinction.

Figure 5 shows our spectra of the λ5610 diffuse band, attributed to the 1_0^1 band of C_7^-. The astronomical line (FWHM $\sim$ 1 Å) falls within the envelope of the laboratory data shown, but there is some uncertainty as to the intensity distribution of the laboratory line (see Fig. 1). The diffuse band is approximately 2 Å away from the maximum of the laboratory peak. This wavelength discrepancy must be explained or resolved by further experiments to conclusively assign this diffuse band to C_7^-.

Figure 6 shows the position of the 2_0^1 band of C_7^-, at 5747.6 Å. Jenniskens & Désert (1994) claim a "certain" diffuse band at 5747.8 Å, but their identification may be confused by the presence of stellar lines at this position. As is evident in Figure 6, the spectra of the unreddened stars HD 164353 and HD 186994 are very similar to those of the reddened stars at the position of the 2_0^1 band. Because of this, and the intrinsic weakness of the transition (its laboratory intensity is 0.05, compared with the origin band), it is difficult to confirm or refute the existence of a diffuse band at this position, which would correspond to the 2_0^1 C_7^- band.

The two doublets corresponding to the $1_0^1 3_0^1$ and 1_0^2 bands of C_7^- were not detected in the astronomical spectra. From the matrix spectra (in which the doublets are not resolved), we estimate total intensities of 0.04 and 0.09, respectively, for these two bands. Because of their low intensity, these bands are not detectable given the current signal-to-noise ratio of the observations.

Neither were the $B \leftarrow X$ bands of C_7^- detected. These bands are intrinsically broadened by internal conversion and have FWHM $\sim$ 20 Å, about 20 times that of the $A \leftarrow X$ bands. Since the integrated laboratory intensity of the strongest $B \leftarrow X$ band is no greater than that of the $A \leftarrow X$

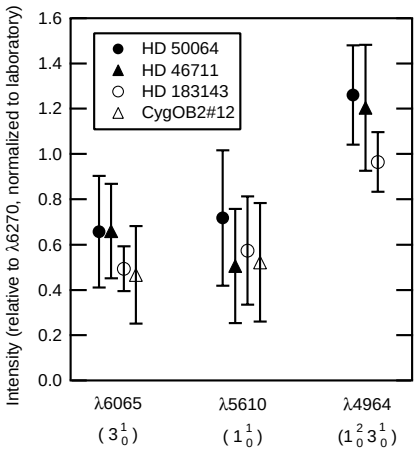

FIG. 7.—Equivalent widths of the diffuse bands attributed to C_7^-, relative to λ6270 (the origin band), and normalized to the intensities of the laboratory matrix data. The error bars represent 1 σ uncertainties as listed in Table 2.

origin band at 6270 Å, these very broad lines will be difficult to detect in astronomical spectra. The present sensitivity and problems with flat-fielding completely exclude the possibility of detecting these bands in our spectra.

The equivalent widths of the observed diffuse bands, along with the estimated uncertainties, are listed in Table 2. If the four diffuse bands (λλ6270, 6065, 5610, and 4964) are to be assigned to C_7^-, their relative intensities should remain constant from star to star, and should also agree with laboratory matrix data within the corresponding uncertainties. This agreement can be judged from Figure 7, in which the intensities of the three weaker bands relative to λ6270, normalized to the matrix intensities, are plotted. Deviations of all data points for a particular band from unity would indicate disagreement with the laboratory matrix data, while scatter between the data points for a given band would indicate that the diffuse bands do not share a common carrier. Not accounted for in Figure 7 are the uncertainties in the equivalent widths of λ6270, which could cause systematic shifts in the data points for an individual star (e.g., to lower all the closed circles). Given the uncertainties in the measurements, the intensity information does not seem to exclude the possibility that all four bands can be attributed to C_7^-.

The final consideration in comparing diffuse bands to the laboratory data is the line widths. Although it is difficult to accurately measure the line widths of the diffuse bands, they all have FWHM near 0.7–1.2 Å. Because the temperature distribution is not well known in the laboratory experiments or in the astronomical sources and because the molecular constants (spin-orbit coupling and rotational constant in the ground and excited states) are unknown, it is quite possible that the interstellar line widths might be different from the laboratory line widths.

In the cases of the 1_0^1, 3_0^1, and $1_0^2 3_0^1$ bands, the astronomical line width is smaller than the laboratory line width, which poses no problem in the assignment. In the case of the origin band, however, there is an apparent discrepancy:

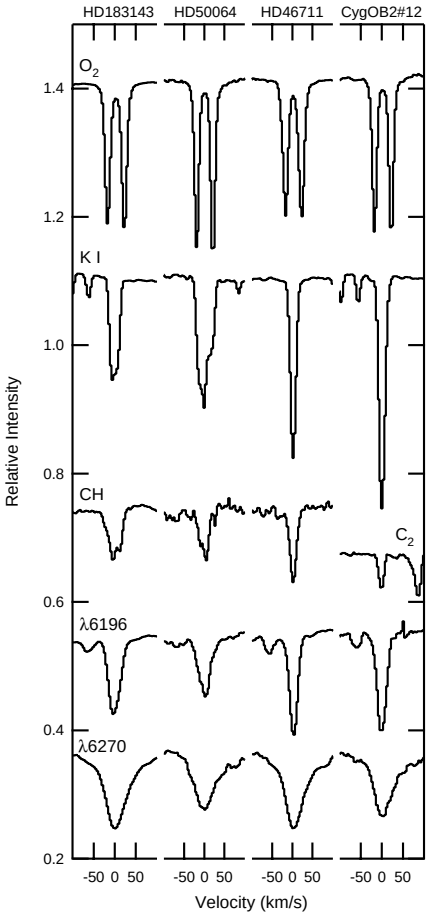

FIG. 8.—Profiles of telluric O_2, interstellar K I, CH and C_2, and the narrow diffuse band at 6196 Å, compared with the λ6270 diffuse band, attributed to the origin band of C_7^-. The λ6270 band is clearly broader than can be explained by the velocity distribution of the atomic or molecular interstellar gas. The O_2 and K I lines have been divided by 2 for clarity.

the profile of the λ6270 diffuse band does not show the sharp peak (presumably the *R*-heads) that is present in the laboratory data (see Fig. 2). If the assignment to C_7^- is correct, this implies that either this sharp peak is not present at the temperature of the diffuse interstellar medium, or the peak has been "smeared out" by the velocity distribution of the gas.

Figure 8 demonstrates that the width of λ6270 cannot be explained by the velocity distribution of either the atomic or molecular gas. The λ6270 diffuse band in all four sources is significantly broader than the lines of K I, CH (in the cases of HD 46711, HD 50064, and HD 183143), C_2 (in Cyg OB2 12), and the narrow diffuse band λ6196. The question of whether the observed profile of λ6270 can be explained by temperature differences is key to the assignment of these diffuse bands to C_7^- and may remain unanswered until better laboratory data become available.

It is interesting to note from Tables 1 and 2 that the diffuse bands attributed to C_7^- do not behave linearly with reddening. Most notably, these bands are weaker in the spectrum of Cyg OB2 12 than in HD 183143, although the former star has more than twice the reddening. The relative deficiency of diffuse band strength per unit color excess toward Cyg OB2 12 has been known for some time (e.g., Bromage 1971; Wampler 1966). We plan to explore the relationships between various molecules by extending observations of H_3^+ to stars of lower reddening (especially HD 183143) and extending observations of H_2 to higher reddenings (with *FUSE*), typically up to $E(B-V) \sim 1$.

4. CONCLUSIONS

Diffuse bands lying near four gas-phase laboratory bands of the C_7^- anion have been confirmed with high-resolution spectra of four highly reddened stars. The signal-to-noise ratio of the lines in these spectra is considerably better than in the diffuse-band catalog of Jenniskens & Désert (1994). The remaining laboratory lines of C_7^- are not expected to be detectable in our spectra because of stellar line confusion (2_0^1), their intrinsic weakness ($1_0^1 3_0^1$ and 1_0^2), or their intrinsic breadth (the $B \leftarrow X$ transitions).

The match in both wavelength and intensity is far better than has ever been attained by any proposed carrier; however, there remain two serious problems with the assignment of these four diffuse bands to C_7^-. First, the diffuse band corresponding to 1_0^1 may be off by as much as 2 Å from the laboratory gas-phase data. Second, the profile of the λ6270 diffuse band differs substantially from that of the laboratory spectrum of the C_7^- origin band.

Better laboratory measurements are needed to confirm the wavelengths and intensity distributions of the C_7^- bands and, ideally, to resolve the bands rotationally. Rotational resolution would provide the information about the rotational constants and spin-orbit splitting necessary to predict the appearance of the spectrum at different temperatures and would thus enable a more meaningful comparison with astronomical spectra. With this data in hand, it would be possible either to explain the apparent discrepancies between the laboratory and astronomical spectra or to state definitively that the discrepancies rule out the assignment of these diffuse bands to C_7^-.

Further observational work may also be of assistance. Longer integration times and refinements in the flat-fielding procedure should lead to higher signal-to-noise ratios and may eventually enable an observational test of the presence or absence of the two doublets ($1_0^1 3_0^1$ and 1_0^2) of the $A \leftarrow X$ system or even of the very broad lines of the $B \leftarrow X$ system.

The probability of four lines accidentally showing such good wavelength and intensity agreement with diffuse bands is perhaps less than 1 in 10^6, which strongly suggests that C_7^- is the carrier of these diffuse bands. However, the observed wavelength discrepancies and the profile of λ6270 are difficult to explain given our current understanding of the C_7^- molecule.

The referee has pointed out that Galazutdinov, Krelowski, & Musaev have also conducted diffuse-band observations specifically to check the possibility of C_7^- as a diffuse-band carrier and have reached a more pessimistic conclusion.

The authors wish to thank J. P. Maier, M. Tulej, and M. Pachkov for providing their laboratory data to enable a direct comparison with astronomical spectra; D. Duncan, L. M. Hobbs, C. Mallouris, and C. Rockosi for their assistance with the observations; and C. M. Lindsay and J. Thorburn for helpful discussions about data reduction and analysis. We are particularly grateful to R. Hildebrand for his extensive effort to deliver the echelle spectrograph in time for the 1999 January observing session. B. J. M. is supported by the Fannie and John Hertz Foundation. This work was supported by NSF grant PHYS-9722691 and NASA grant NAG5-4070.

REFERENCES

Avery, L. W., Broten, N. W., Macleod, J. M., Oka, T., & Kroto, H. W. 1976, ApJ, 205, L173
Brand, J. C. D., et al. 1983, J. Mol. Spectrosc., 99, 482
Bromage, G. E. 1971, Nature, 230, 172
Douglas, A. E. 1977, Nature, 269, 130
Forney, D., Grutter, M., Freivogel, P., & Maier, J. P. 1997, J. Phys. Chem. A, 101, 5292
Herbig, G. H. 1995, ARA&A, 33, 19
Jenniskens, P., & Désert, F.-X. 1994, A&AS, 106, 39
McCall, B. J., Geballe, T. R., Hinkle, K. H., & Oka, T. 1998, Science, 279, 1910
Moos, H. W., Sembach, K. R., & Bianchi, L. 1988, in ASP Conf. Ser. 148, Origins, ed. C. E. Woodward, J. M. Shull, & H. A. Thronson, Jr. (San Francisco: ASP), 304
Ruffle, D. P., Bettens, R. P. A., Terzieva, R., & Herbst, E. 1999, ApJ, 523, 678
Schroeder, D. J. 1987, Astronomical Optics (New York: Academic Press)
Smith, W. H., Snow, T. P., Jr., & York, D. G. 1977, ApJ, 218, 124
Snow, T. P., Jr., York, D. G., & Welty, D. E. 1977, AJ, 82, 113
Tulej, M., Kirkwood, D. A., Pachkov, M., & Maier, J. P. 1998, ApJ, 506, L69
Wampler, E. J. 1966, ApJ, 144, 921
York, D. G., et al. 2000, in preparation

APPENDIX B
LABORATORY PUBLICATIONS

B.1 "Combination band spectroscopy of H_3^+"

Reprinted from *Journal of Chemical Physics*, 113, 3104 (2000).

JOURNAL OF CHEMICAL PHYSICS VOLUME 113, NUMBER 8 22 AUGUST 2000

Combination band spectroscopy of H_3^+

Benjamin J. McCall[a] and Takeshi Oka
Department of Chemistry, Department of Astronomy & Astrophysics, and the Enrico Fermi Institute, University of Chicago, Chicago, Illinois 60637

(Received 9 May 2000; accepted 25 May 2000)

Thirty rovibrational transitions of H_3^+ have been observed near 1.25 μm using a tunable diode laser and a positive column discharge. In addition to the H_3^+ transitions, over 200 transitions between Rydberg states of H_2 were observed—these could be discriminated against by using a discharge dominated by He, which apparently collisionally quenches the Rydberg states of H_2 without affecting H_3^+. Twenty-eight of the H_3^+ transitions have been assigned to the $\nu_1+2\nu_2^2\leftarrow 0$ band, and provide experimentally determined energy levels for most of the levels up to $J=4$ in the $\nu_1+2\nu_2^2$ state. The remaining two H_3^+ transitions have been assigned to the $2\nu_1+\nu_2\leftarrow 0$ band. These bands represent a crucial test of *ab initio* calculations, as they reach higher vibrational levels of H_3^+ than any yet observed. We have compared our experimental results with recent variational calculations by several groups. © *2000 American Institute of Physics.* [S0021-9606(00)02132-2]

I. INTRODUCTION

H_3^+, the simplest stable polyatomic molecule, plays important roles in laboratory, theoretical, and astronomical spectroscopy. In the laboratory, H_3^+ is the primary positive charge carrier in hydrogen plasmas. The intense spectrum of H_3^+ has been used as a diagnostic of these plasmas, in order to measure the radial distribution of charge,[1] the rate of electron recombination,[2] and the rate of destruction of ions by ambipolar diffusion.[3] For theoreticians, H_3^+ serves as a benchmark for rovibrational calculations of polyatomic molecules[4–6]—indeed, *ab initio* theory is now approaching spectroscopic accuracy for this ion. Finally, H_3^+ plays a major role in astronomical plasmas, where its rovibrational spectrum serves as an important remote probe for studying the ionospheres of the outer planets[7,8] as well as dense[9–11] and diffuse[11–13] interstellar clouds.

These applications depend on accurate laboratory measurements of H_3^+ transition frequencies. Since the $\nu_2\leftarrow 0$ rotation–vibration band of H_3^+ was first detected in the laboratory,[14] work has continued to spectroscopically probe higher energy levels using hot bands, overtone bands, and forbidden bands. Spectroscopy of high energy levels of H_3^+ provides new data for comparison with theoretical predictions and also extends the list of transitions available for astronomical spectroscopy of hot plasmas (such as Jupiter's ionosphere). For more details on previous laboratory work, readers are referred to a recent review.[15]

In this paper we report our recent laboratory observation of the $\nu_1+2\nu_2^2\leftarrow 0$ (the superscript refers to $|l|$, as defined in the following) and $2\nu_1+\nu_2\leftarrow 0$ combination bands of H_3^+ near 1.25 μm using a tunable diode laser. These bands reach higher vibrational levels than any previous work, and therefore provide a new test of rovibrational calculations. This work sets the stage for the detection of the $5\nu_2\leftarrow 0$ overtone band, which probes the theoretically challenging area above the barrier to linearity.

[a]Electronic mail: bjmccall@uchicago.edu

II. THEORY AND NOTATION

The quantum numbers F (total angular momentum) and $\pm$ (parity) are rigorously good quantum numbers due to the isotropy and inversion symmetry of free space. Neglecting the very small nuclear spin–rotation interaction, we can write $F=I+J$ and consider I (total nuclear spin angular momentum) and J (angular momentum of nuclear and electronic motion) to be good quantum numbers. The electric dipole selection rules for these quantum numbers are $\Delta J=0$ or ± 1, $\Delta I=0$, and $+\leftrightarrow -$.

There are other quantum numbers that are approximately good at low energies. These include v_1 and v_2 (the number of quanta in the symmetric ν_1 stretching and the degenerate ν_2 mode) as well as $|l|$, the vibrational angular momentum of the ν_2 mode (the signed quantity l, which is not a good quantum number, runs from $v_2, v_2-2, \ldots, -v_2$). These three approximate quantum numbers $(v_1, v_2, |l|)$ collectively specify the vibrational state of H_3^+. We can also consider the quantity k, the (signed) component of J along the molecular symmetry axis.

The symmetry of H_3^+ is best considered using the S_3^* permutation-inversion group, which is isomorphic to the D_{3h} point group. The symmetry properties of the rovibrational wave functions with respect to the $(123)=C_3$ and $E^*=\sigma_h$ operations can be shown[16] to be

$$(123)|J,k,l\rangle=\exp\left[\frac{2\pi i}{3}(k-l)\right]|J,k,l\rangle \tag{1}$$

and

$$E^*|J,k,l\rangle=(-1)^k|J,k,l\rangle. \tag{2}$$

Based on Eq. (1), it is convenient to introduce the quantum number $g\equiv k-l$, which can be thought of physically as the component of J along the symmetry axis which is due to

rotation. The quantum number g is connected to the spin modification of H_3^+ ($g=3n$ is *ortho* [$I=3/2$] and $g=3n\pm1$ is *para* [$I=1/2$]) by the Pauli principle, which requires that the total (spin and rovibrational) wave function be antisymmetric with respect to the interchange of two protons (12) and symmetric with respect to cyclic permutation of all three protons (123). This requirement is equivalent to the requirement that the total wave function belong to the A_2 representation. A further consequence of the Pauli principle is that certain rovibrational levels (e.g., $J=$even, $G=0$ in the ground vibrational state) do not exist. Equation (2) shows that the parity is $+$ when k is even, and $-$ when k is odd.

Because the space-fixed electric dipole moment is invariant to (123) but changes sign with E^*,[17] it follows that the electric dipole selection rules for H_3^+ are

$$\Delta g \equiv \Delta(k-l)=3n \quad (n \text{ integer}) \quad \text{and} \quad \Delta k=\text{odd}, \tag{3}$$

which are closely related to the original selection rules $\Delta I=0$, and $+\leftrightarrow-$.

For vibrational bands with $\Delta l=\pm1$ (e.g., $\nu_2\leftarrow0$), the selection rules (3) imply that $\Delta g=0$ and $\Delta k=\pm1$. For bands with $\Delta l=\pm2$ (e.g., $\nu_1+2\nu_2^2\leftarrow0$), the selection rules imply that $\Delta g=\mp3$ and $\Delta k=\mp1$. Bands with $\Delta l=0$ (e.g., $\nu_1+2\nu_2^0\leftarrow0$) are ''forbidden'' because they require $\Delta k=\pm3$ (and therefore $\Delta g=\pm3$) to satisfy Eq. (3) — however, some transitions in such ''forbidden'' bands can still be weakly observed due to intensity borrowing from ''allowed'' bands.

Since the energy is independent of the sign of g, the unsigned $G\equiv|g|$ is more often used. For vibrational bands with $l\neq0$, certain (J,G) levels are doubled, because there are two sets of k and l which give the same G. This occurs for $J>|l|$ and for $J-|l|\geqslant G\geqslant1$. In such cases it is convenient to label the upper and lower levels of each doublet as u and l (for ''upper'' and ''lower''). The labels u and l, respectively, replace the $+$ and $-$ labels previously used in the literature and correspond to $U=|l|$ and $-|l|$ (the U label was introduced by Watson[16] for $|l|=1$ and extended to $|l|>1$ by Miller and Tennyson[18]).

With this labeling, a new shorthand notation has recently been introduced[15] to describe rovibrational transitions of H_3^+. This notation consists of the vibrational band including $|l|$ as a superscript when $|l|\neq1$ (e.g., $\nu_1+2\nu_2^2\leftarrow0$) and an extension of the usual nomenclature $\{P|Q|R\}(J,G)$, where P, Q, and R as usual refer to $\Delta J=-1$, 0, and $+1$, respectively, and J and G refer to the lower state of the transition. If the upper level of the transition belongs to a doublet, then the appropriate u or l is appended as a superscript after the (J,G). Similarly, if the lower level belongs to a doublet, a u or l subscript is appended. For $\Delta g=\pm3$ bands, a superscript n or t is prepended to indicate $\Delta G=-3$ or $+3$, respectively. Note that for $G''=1$ and 2, the n transitions formally appear as $\Delta G=+1$ and -1, respectively. For $G''=0$ there are only t transitions.

Although they were not encountered in this work, transitions with $\Delta g=\pm3m$ ($m>1$) which can be observed due to intensity borrowing are denoted with a signed value of $|\Delta g|$ as a superscript in the place of n or t. In analogy with n and t, the sign is taken to be that of ΔG, except that the sign is always taken to be $-$ when G ''wraps around zero'' (e.g., $g=+4\leftarrow-2$).

III. EXPERIMENT

The experiment employed a custom-built external-cavity tunable diode laser from New Focus. When manufactured, the laser had a nominal tuning range of 7633–8183 cm^{-1}, but due to degradation of the antireflection coating on the front facet of the diode, it only had a useful tuning range of ~7780–8168 cm^{-1} at the time of the observations. The effect of this degradation is most pronounced on the low frequency side of the tuning range, such that it is only possible to continuously tune the laser from about 7850 to 8168 cm^{-1}. At the center of its tuning range, the laser produces approximately 8 mW of radiation.

The H_3^+ was produced inside a liquid-nitrogen cooled discharge cell with an inner diameter of 18 mm and a length of approximately 1 m.[15] The reagent gas (~500 mTorr of H_2 and optionally ~10 Torr of He) flowed into the cell through multiple inlets, and was pumped out through multiple outlets by a mechanical pump. The plasma was produced by a several kilovolt, 18 kHz ac potential applied across two electrodes, one on each side of the cell. This potential was produced by a step-up transformer driven by a Techron 7780 power amplifier (4 kW peak output), which was fed by a sine-wave generator. The discharge current was approximately 310 mA rms, which corresponds to a current density of ~120 mA cm^{-2}. The use of an alternating current discharge allowed the velocity modulation technique[19] to be used to increase the sensitivity.

The output of the diode laser was split into two beams, which were sent through the discharge cell in opposite directions. Each beam was passed through the cell four times (with the same directionality each time) in order to increase the absorption path length without sacrificing the velocity modulation. The two beams were then directed into the two detectors of an autobalancing photoreceiver (New Focus Nirvana), which electronically balanced the signals from the two detectors in order to effect optimum cancellation of common-mode noise. The output of the photoreceiver was sent to a phase sensitive detector, which used the discharge sine-wave generator as the reference. The phase sensitive detector output was then digitized by a personal computer.

The diode laser was tuned by changing the angle of the cavity end mirror with respect to the grating. Coarse tuning was accomplished by a motor-turned screw, while fine tuning was effected by a piezoelectric transducer (PZT). The voltage on the PZT was controlled via a digital–analog converter in the PC, which enabled computer-controlled scanning of a 2 cm^{-1} range. The computer control of both tuning and data acquisition enabled multiple scans of each 2 cm^{-1} frequency range to be averaged together in order to reduce low frequency noise and produce a flatter baseline.

Each 2 cm^{-1} range was divided into 300 frequency steps (200 MHz each). While the bandwidth of the laser was far lower ($<$ 5 MHz), this interval was chosen as a tradeoff between spectral resolution and integration time. During each scan of the 2 cm^{-1} range, the computer instructed the

laser to move from one frequency step to the next. At each step, the computer averaged 100 samples of each experimental input, moved the laser to the next frequency step, and waited 30 ms before taking any more data. This delay time was chosen to be equal to the phase sensitive detector time constant. At the end of the 2 cm^{-1} range, the laser was instructed to return to the first frequency point and the computer waited for 1 s for the laser to stabilize.

Each scan of the 2 cm^{-1} range took approximately 10 s. The laser was extremely stable and reproducible in frequency, such that hundreds of scans could be averaged together when necessary to increase the signal-to-noise ratio. This corresponded to repeated scanning of the same frequency range for over 1 h.

Frequency calibration was achieved by simultaneously measuring the H_3^+ spectrum, an absorption spectrum of NH_3, and the transmission of a 2 GHz etalon. The etalon ticks were used for relative frequency calibration, and the NH_3 wave numbers of Guelachvilli[20] were used for absolute calibration. Observation of the Paschen β line of atomic hydrogen showed that there was a slight (0.017 cm^{-1}) shift between the modulated absorption lines and the direct absorption lines of NH_3, most likely caused by the time constant of the phase sensitive detector. This shift was found to be independent of the intensity of the absorption line, so this shift was adopted as a constant correction to our observed wave numbers.

IV. RESULTS

The entire frequency range between 7850 and 8168 cm^{-1} was scanned by overlapping individual 2 cm^{-1} scans. This scanning was performed with both a pure hydrogen discharge ($P_{H_2} \sim 500$ mTorr) and with a helium-dominated discharge ($P_{He} \sim 10$ Torr and $P_{H_2} \sim 500$ mTorr). In addition, individual 2 cm^{-1} scans were made at the frequencies in the range 7785–7850 cm^{-1} where strong lines were expected from the variational calculations of Watson.[21]

The experiment yielded 30 rovibrational transitions of H_3^+ as well as over 200 transitions between Rydberg states of H_2 (denoted H_2^*). A table of the Rydberg transitions and their intensities can be obtained from the EPAPS archive.[22] The Rydberg transitions generally appeared with the phase of negative ions, because H_2^* is formed by impact with electrons.[23] About 10% of the Rydberg lines, however, appeared with the same phase as positive ions. This is interpreted[24] as being due to stimulated emission of transitions between triplet states of H_2^* — the dissociative character of the lower state leads to the necessary population inversion.

Because some Rydberg transitions appear with the same phase as the H_3^+ transitions, the phase alone is not enough to discriminate between H_3^+ and H_2^*. However, the addition of He (10 Torr) as a buffer gas decreases the intensity of the H_2^* lines by about a factor of 30 while not significantly affecting the intensity of the H_3^+ lines, as demonstrated in Fig. 1. This decrease can be largely attributed to the factor of 20 increase in gas pressure, which provides more collisions to quench the H_2^*. Because of the very low proton affinity of He (1.85 eV) compared to that of H_2 (4.39 eV), the amount of H_3^+ is not reduced by the addition of He to the discharge. By scanning each spectral region in both a pure hydrogen discharge as well as a helium-dominated discharge, we are able to unambiguously identify the H_3^+ lines.

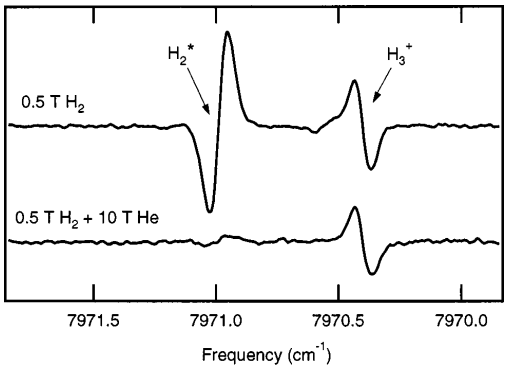

FIG. 1. Effect of He on H_2^* and H_3^+ [$^tR(1,0)$] absorption lines.

The observed H_3^+ transitions and their assignments are listed in Table I. Twenty-six of the assignments could be made by a simple comparison with Watson's calculations.

TABLE I. Observed frequencies and assignments.

Frequency[a]	Assignment	Band	J'	$\langle G' \rangle$[b]	J''	K''
7785.233 (10)	$^tQ(3,0)$	$\nu_1+2\nu_2^2 \leftarrow 0$	3	3.0	3	0
7785.701 (10)	$^tQ(1,0)$	$\nu_1+2\nu_2^2 \leftarrow 0$	1	3.0	1	0
7789.878 (10)	$^tR(3,3)$	$\nu_1+2\nu_2^2 \leftarrow 0$	4	5.9	3	3
7805.893 (10)	$^nP(1,1)$	$\nu_1+2\nu_2^2 \leftarrow 0$	0	2.0	1	1
7820.239 (10)	$^nP(2,2)$	$\nu_1+2\nu_2^2 \leftarrow 0$	1	1.0	2	2
7822.375 (10)	$^tR(2,2)$	$\nu_1+2\nu_2^2 \leftarrow 0$	3	5.0	2	2
7826.739 (10)	$^nP(3,3)$	$\nu_1+2\nu_2^2 \leftarrow 0$	2	0.0	3	3
7833.249 (20)	$^nP(4,4)^l$	$\nu_1+2\nu_2^2 \leftarrow 0$	3	1.1	4	4
7850.959 (10)	$^tR(1,1)$	$\nu_1+2\nu_2^2 \leftarrow 0$	2	4.0	1	1
7880.921 (10)	$^tR(4,3)$	$\nu_1+2\nu_2^2 \leftarrow 0$	5	5.9	4	3
7894.711 (10)	$^nQ(1,1)$	$\nu_1+2\nu_2^2 \leftarrow 0$	1	2.0	1	1
7898.371 (10)	$^nQ(2,1)$	$\nu_1+2\nu_2^2 \leftarrow 0$	2	2.0	2	1
7905.717 (10)	$^nQ(3,1)$	$\nu_1+2\nu_2^2 \leftarrow 0$	3	2.0	3	1
7912.047 (10)	$^tR(3,2)$	$\nu_1+2\nu_2^2 \leftarrow 0$	4	4.9	3	2
7939.619 (10)	$^tR(2,1)$	$\nu_1+2\nu_2^2 \leftarrow 0$	3	4.0	2	1
7970.413 (10)	$^tR(1,0)$	$\nu_1+2\nu_2^2 \leftarrow 0$	2	3.0	1	0
7998.890 (10)	$^nQ(2,2)$	$\nu_1+2\nu_2^2 \leftarrow 0$	2	1.0	2	2
8005.582 (30)	$^tR(4,2)$	$\nu_1+2\nu_2^2 \leftarrow 0$	5	4.8	4	2
8007.410 (10)	$^nQ(3,2)^u$	$\nu_1+2\nu_2^2 \leftarrow 0$	3	1.0	3	2
8022.012 (20)	$^nQ(4,2)^u$	$\nu_1+2\nu_2^2 \leftarrow 0$	4	1.0	4	2
8027.840 (20)	$^tR(3,1)$	$\nu_1+2\nu_2^2 \leftarrow 0$	4	3.5	3	1
8037.673 (10)	$^nR(3,1)^l$	$\nu_1+2\nu_2^2 \leftarrow 0$	4	2.4	3	1
8053.382 (10)	$P(6,6)$	$2\nu_1+\nu_2 \leftarrow 0$	5	5.5	6	6
8071.617 (10)	$^nR(1,1)$	$\nu_1+2\nu_2^2 \leftarrow 0$	2	2.0	1	1
8089.406 (10)	$^nQ(4,3)$	$\nu_1+2\nu_2^2 \leftarrow 0$	4	0.1	4	3
8110.069 (10)	$^nQ(3,3)$	$\nu_1+2\nu_2^2 \leftarrow 0$	3	0.0	3	3
8123.128 (10)	$P(5,5)$	$2\nu_1+\nu_2 \leftarrow 0$	4	4.8	5	5
8128.280 (10)	$^tR(4,1)$	$\nu_1+2\nu_2^2 \leftarrow 0$	5	3.4	4	1
8162.653 (10)	$^tR(3,0)$	$\nu_1+2\nu_2^2 \leftarrow 0$	4	2.9	3	0
8163.129 (10)	$^nR(2,1)$	$\nu_1+2\nu_2^2 \leftarrow 0$	3	2.0	2	1

[a]The uncertainty in the last decimal places is listed in parentheses.
[b]The expectation value of the approximate quantum number G in the upper state, from the calculations of Watson (Ref. 21).

However, there were two pairs of lines (7785.233 and 7785.701; 8162.653 and 8163.129) which were too close in frequency to assign solely by comparison with the calculated frequencies. The first pair of lines was assigned based on the temperature dependence of the observed intensities: the lower frequency line became more intense in the helium-dominated (hotter) discharge and therefore arises from the $(J=3, K=0)$ level in the ground state, rather than $(J=1, K=0)$. The second pair was assigned based on combination differences: the higher frequency line of the pair shares the same upper state as the line at 7905.717 cm^{-1}.

Table I also shows the uncertainties in the experimental frequencies, which have been estimated by comparing the frequencies obtained in different scans and by considering the proximity of NH_3 reference lines. Also listed in Table I are the values of J and K in the ground state, along with the values of J and the expectation value of the approximate quantum number G in the upper state. These values are taken from the calculations of Watson.[21]

Based on these assignments, 28 of the 30 H_3^+ lines belong to the $\nu_1+2\nu_2^2\leftarrow 0$ band, while two are high-J P-branch lines of the $2\nu_1+\nu_2\leftarrow 0$ band, which has its band center[25] near 8487 cm^{-1}. The strongest line in the $\nu_1+2\nu_2^2\leftarrow 0$ band (7970.413 cm^{-1}) was detected with a signal-to-noise ratio of nearly 100. Considering that this band is approximately 270 times less intense than the fundamental band,[26] which is a few percent deep in absorption under similar conditions, we estimate that our sensitivity (minimum detectable absorption) is of order $\Delta I/I\sim 3\times 10^{-6}$. Our sensitivity was hampered by a persistent square-wave shaped noise in the intensity of the diode laser, which may have been due to optical feedback. This noise appeared most prominently when the multiple path optical arrangement was used. Because of the square-wave nature of the noise, it was not completely filtered out by the phase sensitive detection and thus contributed to noise in our baseline.

The experimentally determined energy levels, based on our observed transitions and the previously determined[27] ground state energy levels, are listed in Table II. In this table, we have listed the value of G for the member of the $|J,G\rangle$ basis set which makes the dominant contribution to the energy level. An energy level diagram of the $\nu_1+2\nu_2^2$ state is given in Fig. 2, where the observed levels are denoted by thick lines. The observed transitions provide nearly complete coverage up to $J=4$, along with three levels of $J=5$.

TABLE II. Experimentally determined energy levels.

v_1	v_2	l	J	G[a]	u/l[b]	E
1	2	2	0	2		7870.018
1	2	2	1	3		7872.664
1	2	2	2	4		7915.084
1	2	2	1	2		7958.836
1	2	2	1	1		7989.541
1	2	2	3	5		7991.677
1	2	2	2	3		8057.376
1	2	2	4	6		8105.230
1	2	2	2	2		8135.736
1	2	2	2	0		8142.091
1	2	2	2	1		8168.192
1	2	2	3	4		8176.978
1	2	2	3	3		8302.114
1	2	2	3	1	l	8335.291
1	2	2	4	5		8340.068
1	2	2	3	2		8400.488
1	2	2	3	0		8425.421
1	2	2	3	1	u	8435.431
1	2	2	4	4		8522.611
1	2	2	4	2	l	8532.444
1	2	2	5	6		8539.638
1	2	2	4	3		8679.534
1	2	2	4	0		8748.123
1	2	2	5	5		8774.053
1	2	2	4	1	u	8790.483
1	2	2	5	4		8961.857
2	1	1	4	5		8852.148
2	1	1	5	6		9049.257

[a]The value of G for the member of the $|J,G\rangle$ basis set which makes the dominant contribution to the energy level.
[b]Label for upper and lower states of doublets.

V. ANALYSIS

The primary motivation for this work was to provide experimental data on the $\nu_1+2\nu_2^2\leftarrow 0$ band for comparison with theoretical calculations. In this section, we briefly discuss several sets of variational calculations performed in recent years and compare them to our observed spectra. We also examine some previously observed lines that have been assigned to transitions involving the $\nu_1+2\nu_2^2$ state.

A. Comparison with variational calculations

We have compared our experimental H_3^+ frequencies with several sets of variational calculations. For each transition we compute the difference of the observed and calculated frequencies [observed−calculated (o−c)]. The average of the (o−c) values for all of the lines can be interpreted simply as an offset in the band origin, perhaps due to omission of various (adiabatic and/or nonadiabatic) corrections to the Born–Oppenheimer approximation and, to a lesser extent, relativistic corrections. The standard deviation σ(o−c) of the (o−c) values gives an indication of the accuracy of the calculation of the rovibrational energies (given some vibrational offset), and should be regarded as the primary figure of merit. The values of (o−c) for each line and for each calculation are tabulated in Table III, along with the average (o−c) and σ(o−c) for each calculation.

The earliest work we have considered in our comparison is that of Wolniewicz and Hinze (1994).[28] These authors calculated rotation-vibration term values up to $J=4$ using the Meyer-Botschwina–Burton (MBB)[29] *ab initio* potential and hyperspherical coordinates. The upper states of 19 of our observed transitions were listed in their table. Their average (o−c) was -0.25 cm^{-1}, which was less than the standard deviation σ(o−c)=0.30 cm^{-1}.

In 1996, Watson[21] provided us with theoretical predictions for the frequency range of this experiment. These calculations are an updated version of those discussed by Majewski *et al.*[30] and use a ''spectroscopically adjusted'' adaptation of the MBB[29] potential in which the potential constants have been adjusted to achieve a better fit between experiment and the variational calculations. These calculations were essential for conducting the experiment, as the

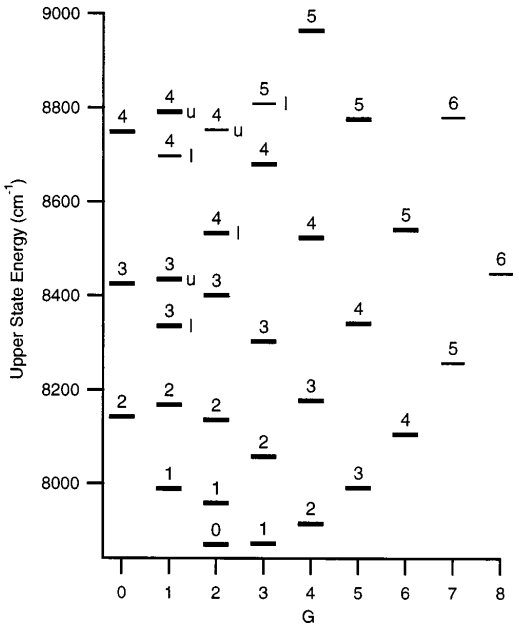

FIG. 2. Energy level diagram of the $\nu_1+2\nu_2^2$ state of H_3^+. Experimentally determined energy levels are denoted by thick lines. The values of J are indicated above the energy levels, and the u and l labels are to the right of the appropriate levels.

frequencies and relative intensities were completely reliable. No lines were observed in our region which were not predicted by Watson's calculations, and we observed all of the lines Watson predicted, given our sensitivity. We relied heavily on these calculations in determining where to focus our efforts outside of the continuous tuning range of the laser. A further advantage of Watson's calculations is that they provide the expectation values of the approximate quantum numbers v_1, v_2, l, and G, which make it easy to assign the energy levels and determine when the levels are strongly mixed. The average (o−c) was -0.23 cm^{-1}, which again was less than σ(o−c) = 0.47 cm^{-1}.

We also compared our data to the exhaustive line list of Neale, Miller, and Tennyson (1996) (NMT),[31] which was developed in part to facilitate opacity calculations of cool stars and the outer planets. These variational calculations are based on the spectroscopically adjusted potential of Dinelli, Polyansky, and Tennyson.[32] Their line list is somewhat difficult to use, as it only provides the value of J and the energy for the upper and lower levels of each transition. In some cases, even the spin modification (*ortho* or *para*) is not listed. For these reasons, their line list can only be interpreted by comparing the energies and J to those in other calculations which give more information about the levels. Their calculations included all 30 of our observed transitions, along with 37 400 others in this wave number range. Despite these reservations, the calculated frequencies of NMT are quite good: their average (o−c) was -0.33 cm^{-1}, and their σ(o−c) was only 0.09 cm^{-1}.

In 1997, Dinelli *et al.*[33] published a list of term values calculated in three different ways. They first used the DVR3D program suite on a spectroscopically adjusted potential[32] which is equivalent to the calculations of NMT. Second, they used the TRIATOM suite on the same potential. Third, they used the TRIATOM suite on the *ab initio* potential surface of Röhse *et al.*[34] augmented by *ab initio* non-Born–Oppenheimer adiabatic corrections.[35] Their list of term values contains some labeling errors, but is fairly comprehensive up to near 9000 cm^{-1}. Twenty-six of our observed lines could be calculated from their TRIATOM lists. The TRIATOM calculations on the spectroscopically adjusted potential gave an average (o−c) of -0.32 cm^{-1} and a σ(o−c) of 0.08 cm^{-1}. Their TRIATOM *ab initio* calculations gave a larger band origin offset [average (o−c)=-0.74 cm^{-1}] but a better standard deviation [σ(o−c)=0.06 cm^{-1}].

In 1999, Polyansky and Tennyson[5] published a new list of energy levels using the improved *ab initio* potential of Cencek *et al.*,[36] which includes electronic relativistic and adiabatic corrections. Polyansky and Tennyson also introduced nonadiabatic corrections in these calculations. Only 22 of our observed lines could be calculated from their list, and the fit was less satisfactory than the *ab initio* work of Dinelli *et al.*[33] The average (o−c) was 0.52 cm^{-1}, and the σ(o−c) was 0.18 cm^{-1}.

Very recently, Jaquet[37] has performed similar calculations based on the Cencek *et al.*[36] *ab initio* potential. Additionally, he calculated intensities using the dipole moment of Röhse *et al.*,[34] and these were found to be completely consistent with the experimental measurements. His calculations reproduced 29 of the 30 observed lines, with an average (o−c) of 0.53 cm^{-1} and a σ(o−c) of 0.09 cm^{-1}. In subsequent calculations, Jaquet included nonadiabatic corrections as discussed in Ref. 38. These corrections substantially reduced the band origin offset to an average (o−c) of 0.12 cm^{-1}, without changing the standard deviation.

By far the greatest deviation between the experimental and theoretical frequencies is for the $^nP(1,1)$ line observed at 7805.893 cm^{-1}. This transition is the only one going into $J=0$ in the $\nu_1+2\nu_2^2$ state. Jaquet[37] has suggested that this deviation may be due to the fact that the nonadiabatic correction should be smaller for the $J=0$ level. Calculations without nonadiabatic corrections will not reproduce this effect, and perhaps even the calculations with nonadiabatic corrections are not fully taking this into account. If the $J=0$ line is excluded from the comparison with the theoretical predictions, the standard deviations of NMT, Dinelli *et al.*, and Jaquet improve significantly. In fact, the *ab initio* calculation of Dinelli *et al.*[33] has a σ(o−c) of only 0.014 cm^{-1} when $J=0$ is excluded — this is comparable to the experimental accuracy.

B. Other assignments

With the energy levels of the $\nu_1+2\nu_2^2$ levels now experimentally determined, it is possible to evaluate some previously observed lines which have been assigned by other authors to transitions involving $\nu_1+2\nu_2^2$.

The transition $^tP(5,3)_l$ in the $\nu_1+2\nu_2^2 \leftarrow 2\nu_2^2$ band has

TABLE III. Comparison with variational calculations.

Transition	Observed (cm^{-1})	(o−c) Adjusted Potentials W96[a]	N96[b]	D97a[c]	*Ab initio* Potentials WH94[d]	D97b[e]	P99[f]	J00a[g]	J00b[h]
$^tQ(3,0)$	7785.233	−0.032	−0.297	−0.295	−0.347	−0.714	0.571	0.507	0.138
$^tQ(1,0)$	7785.701	0.361	−0.309	−0.307	−0.326	−0.721	0.528	0.490	0.122
$^tR(3,3)$	7789.878	−0.147	−0.282	−0.233		−0.715	0.541	0.495	0.085
$^nP(1,1)$	7805.893	0.043	−0.647	−0.645	−0.465	−1.038		0.175	−0.221
$^nP(2,2)$	7820.239	0.259	−0.351	−0.356	0.043	−0.738	0.569	0.488	0.116
$^tR(2,2)$	7822.375	0.125	−0.265	−0.251		−0.708		0.513	0.105
$^nP(3,3)$	7826.739	0.060	−0.381	−0.377	0.269	−0.741	0.635	0.494	0.160
$^nP(4,4)^l$	7833.249	−0.195	−0.421	−0.421	0.293	−0.745	0.693	0.497	0.189
$^tR(1,1)$	7850.959	0.283	−0.291	−0.284		−0.719	0.514	0.510	0.103
$^tR(4,3)$	7880.921	−0.522	−0.259	−0.214		−0.711		0.535	0.092
$^nQ(1,1)$	7894.711	0.333	−0.339	−0.335	−0.186	−0.737	0.527	0.510	0.154
$^nQ(2,1)$	7898.371	0.183	−0.329	−0.329	−0.266	−0.735	0.525	0.511	0.079
$^nQ(3,1)$	7905.717	−0.174	−0.313	−0.310	−0.378	−0.725	0.542	0.531	0.172
$^tR(3,2)$	7912.047	−0.148	−0.243	−0.242		−0.714	−0.241	0.541	0.099
$^tR(2,1)$	7939.619	0.120	−0.271	−0.268		−0.713	0.532	0.547	0.135
$^tR(1,0)$	7970.413	0.288	−0.287	−0.285	−0.455	−0.717	0.506	0.549	0.112
$^nQ(2,2)$	7998.890	0.136	−0.350	−0.346	−0.050	−0.729	0.568	0.552	0.198
$^tR(4,2)$	8005.582	−0.858	−0.248					0.581	0.105
$^nQ(3,2)^u$	8007.410	−0.218	−0.350	−0.344	−0.260	−0.729		0.559	0.020
$^nQ(4,2)^u$	8022.012	−0.681	−0.318	−0.318	−0.426	−0.694	0.608	0.605	0.343
$^tR(3,1)$	8027.840	−0.497	−0.250	−0.244	−0.812	−0.698	0.550	0.602	0.015
$^nR(3,1)^l$	8037.673	−0.518	−0.337	−0.335		−0.754	0.538	0.551	0.153
$P(6,6)$	8053.382	−1.428	−0.528						
$^nR(1,1)$	8071.617	0.203	−0.313	−0.316	−0.247	−0.720	0.538	0.579	0.085
$^nQ(4,3)$	8089.406	−0.876	−0.344	−0.344	0.034	−0.724	0.665	0.596	0.168
$^nQ(3,3)$	8110.069	−0.133	−0.381	−0.384	−0.079	−0.725	0.600	0.596	0.144
$P(5,5)$	8123.128	−0.857	−0.492					0.372	0.259
$^tR(4,1)$	8128.280	−1.051	−0.270					0.604	0.007
$^tR(3,0)$	8162.653	−0.666	−0.257	−0.261	−0.780	−0.722	0.483	0.609	0.101
$^nR(2,1)$	8163.129	−0.166	−0.311	−0.310	−0.369	−0.721	0.542	0.612	0.158
Average (o−c)		−0.226	−0.334	−0.321	−0.253	−0.735	0.524	0.528	0.116
σ(o−c)		0.468	0.089	0.083	0.295	0.063	0.178	0.086	0.095
σ(o−c) [no $J=0$]		0.482	0.069	0.052	0.306	0.014	—	0.052	0.070

[a]Reference 21.
[b]Reference 31.
[c]Reference 33 (adjusted potential).
[d]Reference 28.
[e]Reference 33 (*ab initio*).
[f]Reference 5.
[g]Reference 37 (*ab initio*).
[h]Reference 37 (*ab initio* + nonadiabatic).

been assigned by Majewski *et al.*[30] to an observed line at 2134.241 cm^{-1}, but has also been assigned by Dinelli *et al.*[33] to an observed line at 2134.607 cm^{-1}. Based on the energy of the ($J=4$, $G=6$) level of $\nu_1+2\nu_2^2$ from this work and the energy of the lower level determined by Xu, Gabrys, and Oka,[27] we calculate that this transition should occur at 2134.000 cm^{-1}. This casts doubt on both assignments, but particularly on that of Dinelli *et al.*

Dinelli *et al.* have also assigned an observed line at 2403.350 cm^{-1} to the $Q(2,3)$ transition of the $\nu_1+2\nu_2^2 \leftarrow \nu_1+\nu_2$ band. Based on our experimental energy of the ($J=2$, $G=3$) level of $\nu_1+2\nu_2^2$ and the previously determined energy of the lower level,[39] we calculate that this transition should occur at 2403.367 cm^{-1}. Given the experimental uncertainties, this assignment cannot be excluded. In addition, Dinelli *et al.* assigned an observed line at 2648.105 cm^{-1} to the $R(2,3)$ transition of the same band. We calculate that this transition should occur at 2648.105 cm^{-1}, which confirms the assignment.

VI. CONCLUSIONS

Variational calculations of H_3^+ transitions using *ab initio* potential energy surfaces [as well as non-Born–Oppenhemier corrections] are beginning to approach experimental accuracy, especially when allowance is made for an offset in the band origin and the $J=0$ level. Improvements in the treatment of nonadiabatic effects will likely lead to even better agreement in the future.

The next frontier of H_3^+ spectroscopy lies at even higher energies ($\gtrsim$10000 cm^{-1}), where H_3^+ has enough energy to sample linear geometries in the course of its vibrational mo-

tion. This energy regime is particularly difficult theoretically — none of the rovibrational variational calculations performed in this range to date include the correct boundary conditions for linear geometries. All of the vibrational states which have been spectroscopically probed to date (ν_2, ν_1, $2\nu_2^0$, $2\nu_2^2$, $\nu_1+\nu_2$, $3\nu_2^1$, $\nu_1+2\nu_2^2$, and $2\nu_1+\nu_2$) have been well below the barrier to linearity.

However, the detection of the $\nu_1+2\nu_2^2\leftarrow 0$ band with high signal to noise suggests that this barrier may soon be broken. The $5\nu_2^1\leftarrow 0$ band is expected to lie near 10 900 cm^{-1} ($\sim$920 nm) and should be only about a factor of 20 weaker than $\nu_1+2\nu_2^2\leftarrow 0$. With the much higher power and lower noise of the titanium:sapphire laser (compared to diode lasers), the detection of the $5\nu_2^1\leftarrow 0$ band may be within reach.

ACKNOWLEDGMENTS

We thank J. K. G. Watson and R. Jaquet for sending us the results of their calculations in advance of publication, as well as for many helpful discussions. We also thank G. Guelachvilli, who kindly provided the NH_3 frequency standard list that made this work possible. We would also like to acknowledge T. Huet and C. M. Lindsay for their assistance in the laboratory. This work was supported by NSF Grant No. PHYS-9722691 and NASA Grant No. NAG5-4070. B. J. M. is supported by the Fannie and John Hertz Foundation.

[1] F.-S. Pan and T. Oka, Phys. Rev. A **36**, 2297 (1987).
[2] T. Amano, Astrophys. J. **320**, L121 (1988).
[3] C. M. Lindsay, E. T. White, and T. Oka, Chem. Phys. Lett. (submitted).
[4] R. Jaquet, W. Cencek, W. Kutzelnigg, and J. Rychlewski, J. Chem. Phys. **108**, 2837 (1998).
[5] O. L. Polyansky and J. Tennyson, J. Chem. Phys. **110**, 5056 (1999).
[6] J. K. G. Watson, Chem. Phys. **190**, 291 (1995).
[7] J. Connerney, Philos. Trans. R. Soc. London, Ser. A (in press).
[8] S. Miller *et al.*, Philos. Trans. R. Soc. London, Ser. A (in press).
[9] T. R. Geballe and T. Oka, Nature (London) **384**, 334 (1996).
[10] B. J. McCall, T. R. Geballe, K. H. Hinkle, and T. Oka, Astrophys. J. **522**, 338 (1999).
[11] B. J. McCall, K. H. Hinkle, T. R. Geballe, and T. Oka, Faraday Discuss. **109**, 267 (1998).
[12] B. J. McCall, T. R. Geballe, K. H. Hinkle, and T. Oka, Science **279**, 1910 (1998).
[13] T. R. Geballe, B. J. McCall, K. H. Hinkle, and T. Oka, Astrophys. J. **510**, 251 (1999).
[14] T. Oka, Phys. Rev. Lett. **45**, 531 (1980).
[15] B. J. McCall, Philos. Trans. R. Soc. London, Ser. A (in press).
[16] J. K. G. Watson, J. Mol. Spectrosc. **103**, 350 (1984).
[17] J. T. Hougen, J. Chem. Phys. **37**, 1433 (1962).
[18] S. Miller and J. Tennyson, J. Mol. Spectrosc. **128**, 530 (1988).
[19] C. S. Gudeman, M. H. Begemann, J. Pfaff, and R. J. Saykally, Phys. Rev. Lett. **50**, 727 (1983).
[20] G. Guelachvilli (private communication).
[21] J. K. G. Watson (private communication).
[22] See EPAPS Document No. E-JCPSA6-113-021032 for a file containing the frequencies and intensities of the observed Rydberg transitions. This document may be retrieved via the EPAPS homepage (http://www.aip.org/pubservs/epaps.html) or from ftp.aip.org in the directory /epaps/. See the EPAPS homepage for more information. The table is also available on the author's web site (at http://h3plus.uchicago.edu/data/rydbergs.html).
[23] D. Uy, Ph.D. thesis, University of Chicago, 1998.
[24] D. Uy, C. M. Gabrys, T. Oka, B. J. Cotterell, R. J. Strickland, and Ch. Jungen (unpublished).
[25] B. M. Dinelli, S. Miller, and J. Tennyson, J. Mol. Spectrosc. **163**, 71 (1994).
[26] B. M. Dinelli, S. Miller, and J. Tennyson, J. Mol. Spectrosc. **153**, 718 (1992).
[27] L.-W. Xu, C. Gabrys, and T. Oka, J. Chem. Phys. **93**, 6210 (1990).
[28] L. Wolniewicz and J. Hinze, J. Chem. Phys. **101**, 9817 (1994).
[29] W. Meyer, P. Botschwina, and P. Burton, J. Chem. Phys. **84**, 891 (1986).
[30] W. A. Majewski, A. R. W. McKellar, D. Sadovskiĭ, and J. K. G. Watson, Can. J. Phys. **72**, 1016 (1994).
[31] L. Neale, S. Miller, and J. Tennyson, Astrophys. J. **464**, 516 (1996).
[32] B. M. Dinelli, O. L. Polyansky, and J. Tennyson, J. Chem. Phys. **103**, 10433 (1995).
[33] B. M. Dinelli, L. Neale, O. L. Polyansky, and J. Tennyson, J. Mol. Spectrosc. **181**, 142 (1997).
[34] R. Röhse, W. Kutzelnigg, R. Jaquet, and W. Klopper, J. Chem. Phys. **101**, 2231 (1994).
[35] B. M. Dinelli, C. B. Le Sueur, J. Tennyson, and R. D. Amos, Chem. Phys. Lett. **232**, 295 (1995).
[36] W. Cencek, J. Rychlewski, R. Jaquet, and W. Kutzelnigg, J. Chem. Phys. **108**, 2831 (1998).
[37] R. Jaquet (private communication).
[38] R. Jaquet, Chem. Phys. Lett. **302**, 27 (1999).
[39] L.-W. Xu, M. Rösslein, C. M. Gabrys, and T. Oka, J. Mol. Spectrosc. **153**, 726 (1992).

B.2 "Laboratory Spectroscopy of H_3^+"

Reprinted from *Philosophical Transactions of the Royal Society*, A358, 2385 (2000).

10.1098/rsta.2000.0655

THE ROYAL SOCIETY

Laboratory spectroscopy of H_3^+

By Benjamin J. McCall

Department of Chemistry and Department of Astronomy and Astrophysics, University of Chicago, Chicago, IL 60637, USA

The experimental determination of the low-lying rovibrational energy levels of H_3^+ using high-resolution, high-sensitivity infrared laser spectroscopy has confirmed this ion's equilateral triangle equilibrium geometry, provided direct information on its quantum mechanical characteristics, and enabled its extensive study in planetary ionospheres and in the interstellar medium.

Since the discovery of the $\nu_2 \leftarrow 0$ fundamental band, the laboratory spectroscopy of H_3^+ has been pushed to higher energies through the study of vibrational hot bands, overtones, forbidden bands and combination bands. We review the 20 years of laboratory spectroscopy of this important ion, discuss our recent work on the $\nu_1 + 2\nu_2^2 \leftarrow 0$ and $2\nu_1 + \nu_2 \leftarrow 0$ bands, and examine the prospects for the future of H_3^+ spectroscopy.

Keywords: infrared spectroscopy; molecular ions, H_3^+; plasma spectroscopy

1. Introduction

Ever since H_3^+ was first identified in the laboratory by Thomson (1911), it has played a central role in the study of laboratory plasmas. Indeed, it is by far the most abundant ion in pure hydrogen discharges, owing to its stability and its efficient production from hydrogen. H_3^+ is also important in astrophysical plasmas (which are dominated by hydrogen) such as planetary ionospheres and the interstellar medium, where it serves as the cornerstone of ion–molecule chemistry.

H_3^+ is also of fundamental theoretical interest, because it is the simplest polyatomic molecule (consisting of only three protons and two electrons) and also possesses a high symmetry (D_{3h}) because of its equilateral triangle equilibrium geometry. While theoretical calculations are essential in predicting and understanding the structure of molecules such as H_3^+, experiment (in particular high-resolution spectroscopy) ultimately provides the decisive test of theory, and also provides the information necessary for the refinement of the calculations.

The immediate product of laboratory spectroscopy of H_3^+ is the determination of accurate transition frequencies, which are important to both astronomers and theoreticians. These frequencies have enabled astronomers to detect H_3^+ in the interstellar medium and in the atmospheres of Jupiter, Saturn, and Uranus, and also to use H_3^+ as a remote probe for studying these astrophysical plasmas. For theoreticians, these H_3^+ transition frequencies have determined the molecular structure and constants, allowed the refinement of *ab initio* potential surfaces, and permitted a direct comparison with the results of variational calculations. Ultimately, a complete theoretical understanding of the observed spectra of H_3^+ (the simplest polyatomic) should lead to improved calculations for more complicated polyatomic molecules.

2. Laboratory production of H_3^+

From a chemical perspective, the production of H_3^+ is quite straightforward. All that is necessary is H_2 and a source of ionization. In the laboratory, the ionization is provided by electron impact in a plasma:

$$H_2 + e^- \rightarrow H_2^+ + 2e^- . \tag{2.1}$$

The production of H_3^+ then proceeds rapidly through the reaction

$$H_2^+ + H_2 \rightarrow H_3^+ + H, \tag{2.2}$$

which proceeds with the Langevin rate coefficient of 2×10^{-9} cm^3 s^{-1} (Bowers *et al.* 1969).

Experimentally, however, it is necessary to design a vessel to contain the plasma and optimize the conditions to produce the maximum amount of H_3^+. Two primary types of vessels have been used for the production of H_3^+: the hollow cathode cell (which exploits the negative glow region of the plasma); and the positive column cell (which exploits the positive column glow). Here I will focus on the positive column cell, which has been used most extensively for laser absorption spectroscopy of H_3^+.

A diagram of one of the discharge cells used to produce H_3^+ is shown in figure 1. The central bore of the cell (which contains the plasma) is *ca.* 1 m in length and 18 mm in diameter. The reagent gas is continuously flowed in through multiple inlets and pumped out through several outlets. This continuous flow of fresh reagent gas is essential when studying carbocations, but less important for H_3^+. To either end of the central bore is attached a fixture that contains both a Brewster window (to pass the laser radiation) and an electrode (which drives the plasma). Just outside of the central bore is a concentric volume, which contains the coolant (in this case liquid nitrogen). The outermost jacket is evacuated to provide thermal insulation for the liquid nitrogen.

The reagent gas used to produce H_3^+ is pure H_2 at a pressure of *ca.* 500–800 mTorr. In certain situations, it is preferable to add *ca.* 5–10 Torr of He as a buffer gas. Typically, a voltage of *ca.* 6 kV is applied across the electrodes, and a current density of *ca.* 60 mA cm^{-2} flows through the cell. Interestingly, these discharge conditions combined with a multiple-reflection cell lead to column densities (that is, concentration times absorption path length) of order 10^{14} cm^{-2}, comparable with those found in the interstellar medium!

Thermodynamically, the plasma discharge is a non-equilibrium system, but can be characterized to a first approximation by three different temperatures: the electron temperature (T_e), the vibrational temperature (T_v), and the rotational temperature (T_r). (The translational temperature is found to be closely coupled with the rotational temperature.) In the case of the positive column discharge, T_e is of the order of 10 000 K. T_v and T_r depend on the reagent gas used and the cooling method employed. For liquid-nitrogen-cooled cells, Bawendi *et al.* (1990) have spectroscopically measured $T_v \sim 600$ K and $T_r \sim 300$ K for pure-H_2 discharges and $T_v \sim 1000$ K and $T_r \sim 400$ K for H_2/He discharges. For a water-cooled cell, Uy *et al.* (1994) have measured $T_r \sim 1000$ K for a H_2/He discharge.

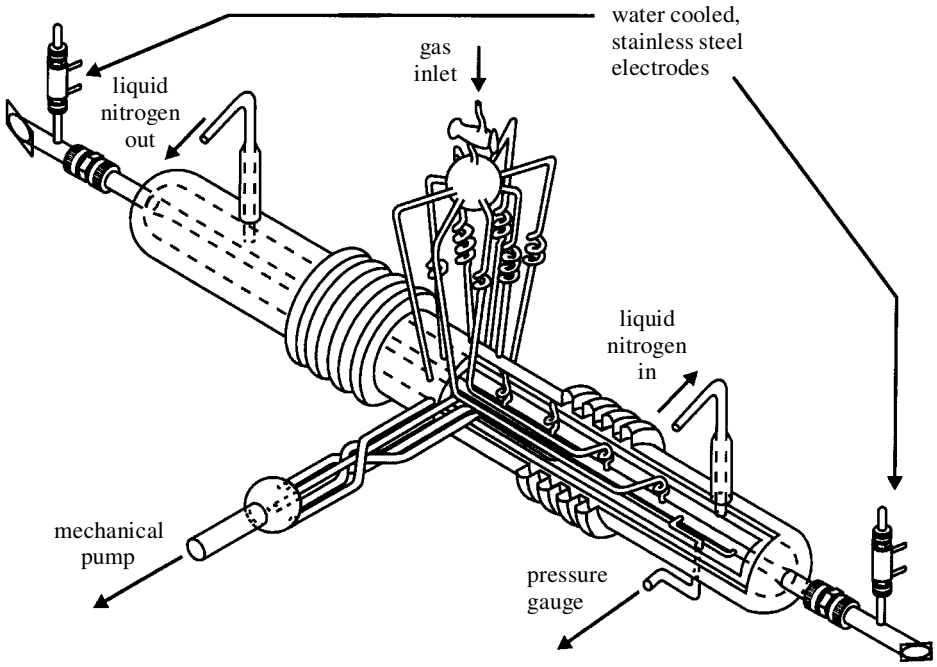

Figure 1. Liquid-nitrogen-cooled discharge cell used for producing H_3^+ (illustration by C. M. Lindsay).

3. Spectroscopy of H_3^+

(*a*) *Electronic spectroscopy*

For many molecules, electronic spectroscopy is a powerful probe of molecular structure both in the laboratory and in astronomical objects. However, this is not the case for H_3^+, which does not possess a stable electronic excited state. It is thought that H_3^+ has an excited triplet state (Friedrich & Alijah 2000) that lies above the dissociation energy to $H_2 + H^+$, but this would be difficult to probe spectroscopically.

(*b*) *Rotational spectroscopy*

Another important tool for the study of most molecules is rotational spectroscopy. This tool is particularly useful in detecting interstellar molecules because of the high sensitivity of radioastronomy.

The equilateral triangle geometry of H_3^+ suggests that this ion does not possess a permanent dipole moment, which is necessary for a rotational spectrum. However, centrifugal distortion caused by the rotation of the molecule can produce a small dipole moment, which leads to a weak 'forbidden' rotational spectrum (Watson 1971). The forbidden rotational spectrum of H_3^+ has been calculated by Pan & Oka (1986) to be several orders of magnitude weaker than typical allowed rotational spectra. It is worth noting that because of the small nuclear masses and large anharmonicity of H_3^+, even this weak spectrum is two to three orders of magnitude stronger than the forbidden rotational spectra of other molecules such as NH_3 and CH_4.

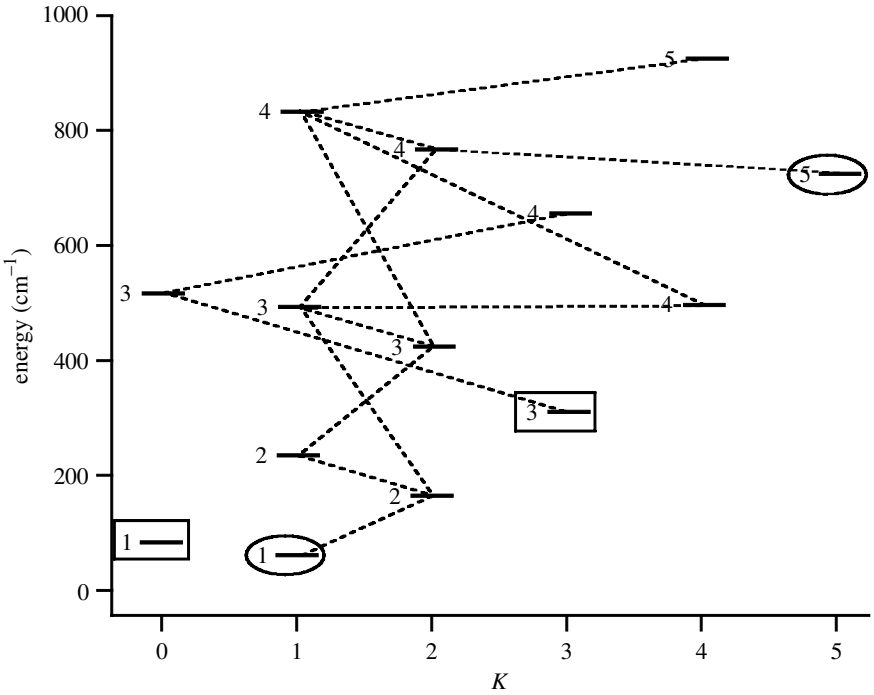

Figure 2. Energy-level diagram of the ground vibrational state of H_3^+. The numbers to the left of the levels are the values of J. The broken lines indicate the forbidden rotational transitions. The radiatively stable states are indicated by rectangles (ortho) and ovals (para).

These forbidden rotational transitions play an important role in the relaxation of H_3^+ in the interstellar medium, where their spontaneous emission times are shorter than the collision time-scale.

The rotational energy-level structure of the ground vibrational state of H_3^+ is shown in figure 2. The quantum numbers which describe the ground state are J, the angular momentum of the nuclear motion, and $K = |k|$, the magnitude of the projection of J onto the symmetry axis of the molecule. The structure is that of an oblate symmetric top, with the exception that the (J even, $K = 0$) levels are forbidden by the Pauli principle. One particular consequence of this is that the usual ground state (0,0) does not exist, leaving (1,1) as the lowest state.

Since H_3^+ consists of three protons (each with nuclear spin $I = \frac{1}{2}$), it possesses two spin modifications: ortho-H_3^+, in which all three spins are aligned and $I = \frac{3}{2}$; and para-H_3^+, in which one spin is antiparallel and $I = \frac{1}{2}$. Due to symmetry requirements on the total wave function, ortho-H_3^+ exists only with $K = 3n$ and para-H_3^+ exists only with $K = 3n \pm 1$, where n is an integer. The ortho and para spin modifications of H_3^+ are not connected by radiative transitions. The parity of the rotational levels is given by $(-1)^K$.

The selection rules for the forbidden rotational spectrum are $\Delta J = 0, \pm 1$ and $\Delta k = 3$. These transitions are indicated in figure 2 as dashed lines. It is interesting to note that the levels (1,0), (3,3) and (5,5) are not connected to any lower states by rotational transitions; thus, they are radiatively stable. The rotational spectrum of H_3^+ spans over two decades in frequency, from *ca.* 7 to 1000 cm^{-1}. At the low

temperatures of the interstellar medium, the strongest transition (in absorption or emission) would be (2,2)–(1,1) at 105.177 cm^{-1}.

(*c*) *Vibrational spectroscopy*

H_3^+ has two vibrational modes: the totally symmetric stretch ν_1 and the doubly degenerate stretch ν_2. The ν_2 mode possesses vibrational angular momentum, which is denoted by the quantum number ℓ_2. If v_2 is the number of quanta in the ν_2 mode, then $\ell_2 = v_2, v_2 - 2, \ldots, -v_2$. Because of an effect known as 'ℓ-resonance', rovibrational levels with different values of k and ℓ_2 but with the same value of $|k - \ell_2|$ are severely mixed. The result of this is that k and ℓ_2 are individually no longer good quantum numbers in vibrational states with $v_2 \neq 0$; instead, we define a new quantum number $g \equiv k - \ell_2$ that physically represents the part of the projection of J that is due to rotation. The connection with spin modification in $v_2 \neq 0$ states is through $G \equiv |g|$: ortho-H_3^+ must have $G = 3n$ and para-H_3^+ must have $G = 3n \pm 1$. Because $G = K$ in the vibrational ground state, it is convenient to use G rather than K in all states.

Theoretical calculations of the vibrational energy structure of H_3^+ are based on the potential energy surface, which describes the 'electronic energy' of the molecule as a function of the nuclear coordinates. Figure 3 shows a one-dimensional version of the potential energy surface of R¨ohse*et al.* (1994). This surface has been generated by forcing two of the H–H bonds to be of equal length, but allowing that length to vary for each value of θ (the angle between these two H–H bonds) in order to find the minimum energy for that value of θ. For small values of θ, the potential surface rises sharply, corresponding to the Coulomb repulsion between the two protons being brought close together. For $\theta \rightarrow \pi$, the potential surface rises but then flattens out; this is known as the 'barrier to linearity' because at $\theta = \pi$, H_3^+ becomes a linear molecule.

Also plotted in figure 3 are the theoretical rotationless ($J = 0$) vibrational states of H_3^+, from the calculations of J. K. G. Watson (1999, personal communication). Note that the ground state ($v_1 = v_2 = 0$) lies 4364 cm^{-1} above the bottom of the potential; this is the zero point vibrational energy of H_3^+. States with $v_2 > 1$ have multiple substates corresponding to the different values of $|l_2|$. For clarity, the states have been separated horizontally based on their values of v_1.

Five types of vibrational transitions can be studied. The *fundamental* band $\nu_2 \leftarrow 0$ is by far the strongest band, and was the first to be studied in the laboratory (Oka 1980). *Overtone* bands are transitions of the type $n\nu_2 \leftarrow 0$, representing multiple excitations of the ν_2 mode. *Hot* bands are transitions starting from vibrationally excited states, such as $2\nu_2 \leftarrow \nu_2$ and $\nu_1 + \nu_2 \leftarrow \nu_1$. *Forbidden* bands are transitions which involve only excitations of the infrared-inactive ν_1 mode, such as $\nu_1 \leftarrow 0$ and $\nu_1 + \nu_2 \leftarrow \nu_2$. Finally, *combination* bands are transitions from the ground state to states which are excited in both ν_1 and ν_2, such as $\nu_1 + 2\nu_2 \leftarrow 0$ and $2\nu_1 + \nu_2 \leftarrow 0$.

Figure 4 shows the band centres and intensities of the strongest vibrational bands, at an assumed temperature of 600 K. The values of the band origins as well as their intensities are calculated from the predictions of Dinelli *et al.* (1992). Hot bands are labelled with arrows, and the superscripts above ν_2 are the values of $|\ell_2|$ ($|\ell_2| = 1$ is omitted in the ν_2 state for brevity). Also shown, at the top of the figure, are the different tunable radiation sources available for H_3^+ spectroscopy, and their

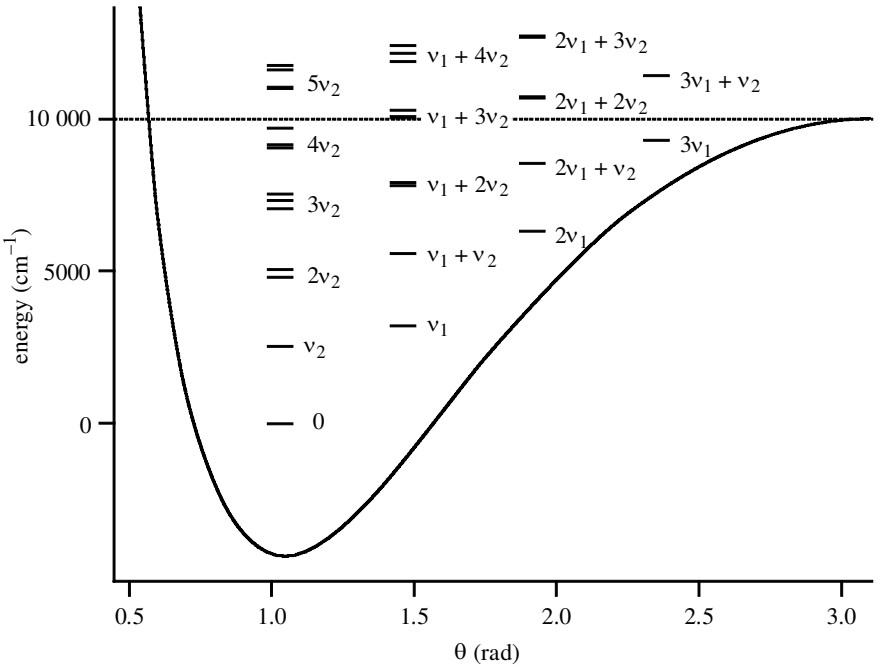

Figure 3. A one-dimensional representation of the potential surface of H_3^+, where two H–H bond lengths are required to be equal, and the angle between them (θ) is varied. Also shown are the calculated vibrational energy levels ($J = 0$) from the calculations of J. K. G. Watson and the barrier to linearity (dotted line).

approximate power (on the right axis). The bars at the bottom of the diagram show the spectral ranges which have been continuously scanned with laser spectroscopy (tall light-grey bars) and Fourier transform infrared (FTIR) spectroscopy (medium dark-grey bars). Also indicated (short bar) is the region where work is in progress using laser spectroscopy.

4. The $\nu_2 \leftarrow 0$ fundamental band

The ν_2 fundamental band is by far the strongest spectral signature of H_3^+. Using a cell such as the one shown in figure 1, and a multiple-reflection system that allows eight passes through the cell, the strongest lines of the fundamental are of the order of 5% deep. The strongest lines in this band can therefore be observed using direct absorption spectroscopy (both in the laboratory and in the interstellar medium). Consequently, this was the first band of H_3^+ to be observed and has been studied in more detail than any other band.

The $\nu_2 \leftarrow 0$ band of H_3^+ was first observed 20 years ago by Oka (1980). Because H_3^+ is such a light molecule, it has very large rotational constants ($B \sim 44\,\mathrm{cm}^{-1}$), and its spectrum is spread out over a wide frequency range. After a search of over two years, Oka (1980) scanned 500 cm^{-1} and was rewarded with only 15 lines! Oka knew approximately what frequency range to scan, thanks to the *ab initio* calculations of Carney & Porter (1976). While the search for this spectrum was lengthy, the assignment was completed by Watson overnight.

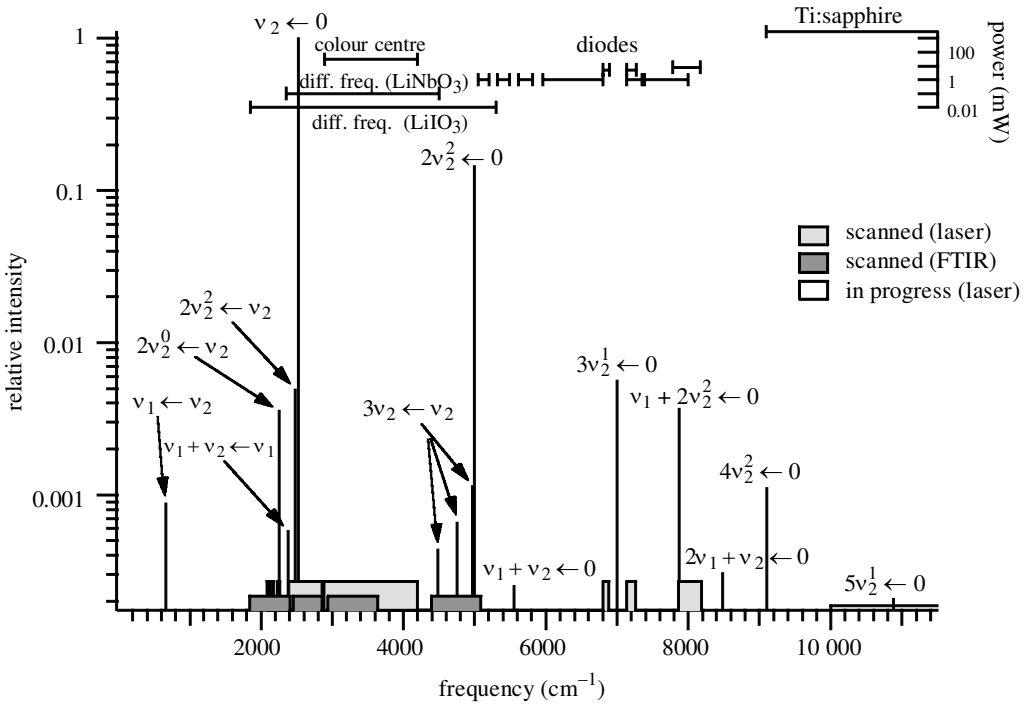

Figure 4. Vibrational band centres of H_3^+ and their relative intensities (note logarithmic scale) in absorption at 600 K. See text for explanation.

Within a year, the number of observed transitions had been doubled to 30 (Oka 1981). In another three years the number had risen to 46 (Watson *et al.* 1984), and the next three years saw a rise to 113 (Majewski *et al.* 1987) using FTIR emission spectroscopy. By this time, transitions starting from J as high as 9 had been observed. In 1990, Nakanaga *et al.* (1990) reported the first FTIR absorption spectrum of H_3^+. Uy *et al.* (1994) extended the spectroscopy of the fundamental band up to $J = 15$ using a water-cooled discharge, and found 38 new lines. Majewski *et al.* (1994) found an additional 55 lines of the fundamental band using FTIR emission spectroscopy. Recent work has been performed by Joo *et al.* (2000), who found the lowest frequency line to date at 1546.901 cm^{-1}, and by Lindsay *et al.* (2000*a*), who observed new lines in the region 3000–3600 cm^{-1}. Also of note is the recent work of McKellar & Watson (1998), who presented the first wide-band spectrum of the fundamental band of H_3^+, using FTIR absorption spectroscopy.

The observed spectrum of the $\nu_2 \leftarrow 0$ fundamental of H_3^+ is shown in figure 5. Since laboratory intensities are not as reliable (for technical reasons) as theoretical intensities, the intensities in the figure have been computed based on a temperature of 400 K from the theoretical calculations of Watson (1992, personal communication).

This observed spectrum immediately yields both qualitative and quantitative information about the structure of H_3^+. Qualitatively, the lack of an $R(0)$ line shows that this molecule possesses three equivalent fermions with spin $\frac{1}{2}$ (as discussed above, the (0,0) state is forbidden by the Pauli principle), and therefore has an equilateral triangle equilibrium structure. Furthermore, the intensity variations represent the 2:1 statistical weights of ortho:para H_3^+. The spacing between the sub-branches

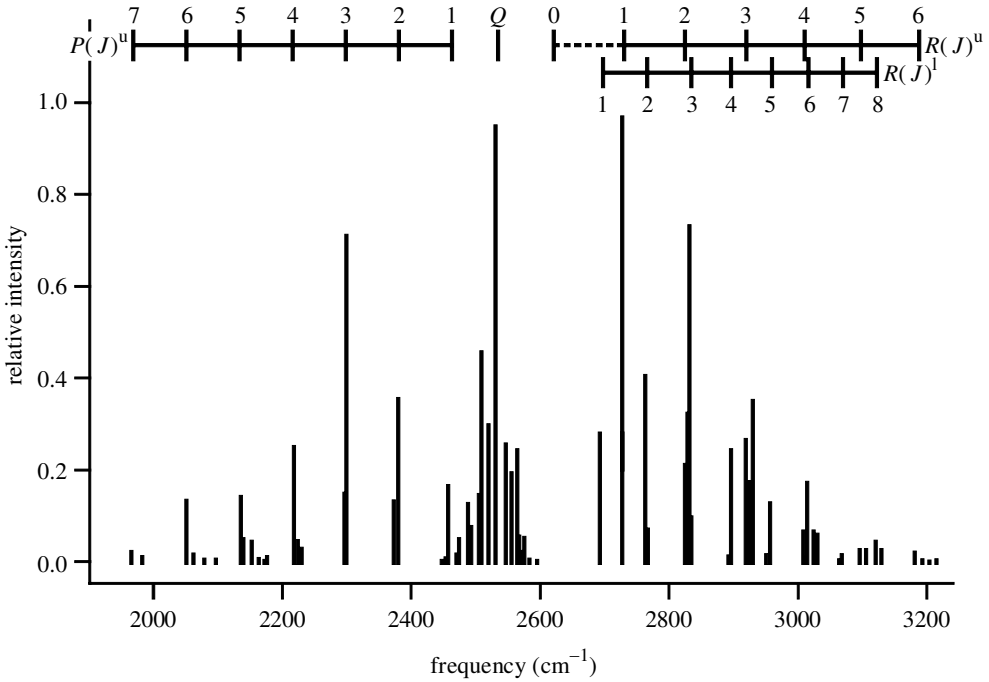

Figure 5. The observed spectrum of the ν_2 fundamental of H_3^+. The intensities are theoretical, assuming a temperature of 400 K. The branches and sub-branches are noted along the top; note in particular the absence of an $R(0)$ line, proof that all three protons are equivalent.

(most easily seen in the P-branch) illustrates the large rotational constants. Quantitatively, the frequencies of the observed transitions can be fitted to those predicted by an effective Hamiltonian in order to compute not only the rotational constants, but also higher-order terms in the perturbation treatment. The observation of this band also fixes the energy of the ν_2 level (2521 cm^{-1}).

The $\nu_2 \leftarrow 0$ fundamental band has proven to be an exceptionally useful probe of H_3^+, both in the laboratory and in space. In the laboratory, it has been used as a spectroscopic probe in studying the H_3^+ electron recombination rate (Amano 1988), the spin conversion of H_3^+ in chemical reactions (Uy *et al.* 1997), and the rate of ambipolar diffusion in plasmas (Lindsay *et al.* 2000*b*). Astronomically, it has served as a remote probe of the ionospheres of the giant planets (Connerney, this issue; Miller, this issue), and has also enabled the direct confirmation of the ion–molecule scheme of interstellar chemistry (Geballe, this issue; Herbst, this issue).

5. A digression on notation

The notation used for labelling H_3^+ transitions deserves some explanation. While different notations have been used to describe H_3^+ transitions, there has not yet been one consistent notation that can be used for all types of transitions (fundamental, hot bands, etc.). Here, we introduce a new standard, which is more flexible than those previously used and can be used to label all of the lines likely to observed astronomically, as well as the vast majority of lines observed in the laboratory.

The limitations of this notation are that one must specify the vibrational band including $|\ell_2|$ (e.g. $\nu_1 + 2\nu_2^2 \leftarrow 0$) and that it assumes that G is an approximately good quantum number. In cases where the quantum numbers v_1, v_2, $|\ell_2|$ and G become so badly mixed that it is not possible to identify the dominant contribution to the mixing, this notation will fail. One must then resort to a full description of the rigorous quantum numbers (see § 10 and table 1). Fortunately, such badly mixed cases correspond to weak transitions, so these problems should not concern astronomers or laboratory spectroscopists studying relatively strong lines.

The new preferred notation for H_3^+ rovibrational transitions is:

$$^{[\mathrm{n}|\mathrm{t}]}\{P \mid Q \mid R\}(J,G)^{[\mathrm{u}|\mathrm{l}]}_{[\mathrm{u}|\mathrm{l}]}. \tag{5.1}$$

As is usual in spectroscopy, $\{P \mid Q \mid R\}$ represents $\Delta J = \{-1 \mid 0 \mid +1\}$, and (J, G) are the values of these quantum numbers in the lower state (G is preferred to K because the latter is not a good quantum number when $\ell_2 \neq 0$). The [u | l] is used to discriminate between the two levels of an ℓ-resonance pair (states with the same $G = |k - \ell_2|$ but different k and ℓ_2). If the transition originates from such a pair in the lower state, a subscript 'u' or 'l' is used to represent the upper or lower energy member of the pair. Similarly, if the transition ends in such a pair in the upper state, a superscript 'u' or 'l' is used. The labels + and − were previously used for this purpose, but these were often confused with parity. Finally, the superscripted n or t before the $\{P \mid Q \mid R\}$ is used for transitions (such as the first overtone) where $\Delta g = \mp 3$. For $\Delta g = 0$ transitions, neither n nor t is used.

6. The hot bands: $2\nu_2 \leftarrow \nu_2$ and $\nu_1 + \nu_2 \leftarrow \nu_1$

As mentioned above, hot bands are transitions starting from vibrationally excited states. At a temperature of 600 K (see figure 4), the hot bands are a few hundred times weaker than the fundamental. However, the addition of helium to a hydrogen discharge has been found to increase the vibrational temperature T_v to *ca.* 1000 K. At these temperatures, the hot bands are observed to be only about 50 times weaker than the fundamental. Using a helium-dominated liquid-nitrogen-cooled discharge, Bawendi *et al.* (1990) were able to observe 72 lines of the $2\nu_2^2 \leftarrow \nu_2$ band, 14 lines of the $2\nu_2^0 \leftarrow \nu_2$ band, and 21 lines of the $\nu_1 + \nu_2 \leftarrow \nu_1$ band.

While the $\nu_2 \leftarrow 0$ fundamental band could be understood using a perturbation approach, this was not the case for the hot bands. Because of the small nuclear masses and the highly anharmonic potential of H_3^+, different rovibrational states are badly mixed and the traditional perturbation approach does not work well. In assigning the hot bands, the variational calculations developed by Sutcliffe (1983) and applied to H_3^+ by Miller & Tennyson (1988, 1989) were essential. As Bawendi *et al.* (1990) stated,

> probably the best strategy for this molecule is to provide the *ab initio* theorists with our experimentally determined energy levels so that they can further adjust... their potentials and accurately predict new rovibrational transitions.

The hot band transitions have also found their place in astronomy. The temperature of Jupiter's ionosphere (*ca.* 1000 K) is sufficiently high that the emission of

hot bands is observable. The simultaneous observation of both fundamental and hot band transitions provides an accurate 'thermometer' of this hot astronomical plasma. During the collision of comet Shoemaker–Levy 9 with Jupiter in 1994, Jupiter's ionosphere was significantly heated, and a strong hot band transition was observed alongside transitions of the fundamental (Dinelli *et al.* 1997).

7. The overtone bands: $2\nu_2 \leftarrow 0$ and $3\nu_2 \leftarrow 0$

In ordinary molecules, the first overtone band ($2\nu_2 \leftarrow 0$) is orders of magnitude weaker than the fundamental. In the case of H_3^+, because of the small masses and large anharmonicity in the potential surface, the first overtone is only about a factor of 7 times weaker.

In hindsight, the first overtone band was initially detected in emission at the time of the early observations of the ν_2 band (Majewski *et al.* 1987). However, as this spectrum also contained many emission lines of H_2 and neutral H_3, an assignment of the H_3^+ lines was not possible. In 1987–1988, a series of unidentified emission lines from the ionosphere of Jupiter was observed (Trafton *et al.* 1989; Drossart *et al.* 1989). After a month's work, Watson was able to assign these lines (and from there, many of the laboratory lines) to the $2\nu_2$ band of H_3^+. His assignment was aided by the laboratory observations of the $2\nu_2^2 \leftarrow \nu_2$ hot band (Bawendi *et al.* 1990), and indirectly by the variational calculations of Miller & Tennyson (1989) used to assign the hot band spectrum. In the end, 47 transitions of the first overtone band were assigned (Majewski *et al.* 1989). Subsequently, 27 of these lines (as well as seven new lines) were observed in absorption using a difference frequency laser spectrometer (Xu *et al.* 1990), yielding more accurate transition frequencies.

The second overtone band of H_3^+ is approximately 200 times weaker than the fundamental band. Using tunable diode lasers, 15 transitions of this band have been observed (Lee *et al.* 1991; Ventrudo *et al.* 1994). These transitions were assigned based on the variational calculations of Miller & Tennyson (1988, 1989), which were accurate to within a few cm^{-1}.

8. Absolute energy levels

The fundamental band and the hot bands obey the selection rule $\Delta G = 0$ because they involve a single excitation of the ν_2 mode. Using these transitions, it is therefore only possible to experimentally determine the relative energies of different rovibrational states with the same value of G. However, with the observation of the first overtone (which obeys the selection rule $\Delta G = \pm 3$), it was possible to fix the separations between levels with different G values for all ortho-H_3^+ energy levels and for all para-H_3^+ levels. Although ortho- and para-H_3^+ are not radiatively coupled, their relative energies can be fixed by fitting the energies of the ground state (J, K) levels to the symmetric rotor energy formula. In this way, experiments now yield absolute H_3^+ energy levels completely independent of theoretical predictions.

9. The forbidden bands: $\nu_1 \leftarrow 0$ and $\nu_1 + \nu_2 \leftarrow \nu_2$

The transition $\nu_1 \leftarrow 0$ is forbidden in the sense that it involves only excitation of the infrared-inactive ν_1 mode. Such a transition is especially forbidden not only because

Table 1. *Observed transitions of the* $\nu_1 + 2\nu_2^2$ *and* $2\nu_1 + \nu_2^1$ *bands of* H_3^+*, along with the quantum numbers and expectation values of the upper and lower states from the calculations of J. K. G. Watson*

(Single prime denotes the upper state of the transition, double prime denotes the lower state.)

symbol	observed	calculated	J'	$\langle G' \rangle$	$\pm'$	o/p′	n'	$\langle v_1' \rangle$	$\langle v_2' \rangle$	$\langle l_2' \rangle$	J''	k''
$^{t}Q(3,0)$	7785.233	7785.2642	3	3.0	−	o	12	1.0	2.0	−2.0	3	0
$^{t}Q(1,0)$	7785.701	7785.3404	1	3.0	−	o	5	1.0	2.0	−2.0	1	0
$^{t}R(3,3)$	7789.878	7790.0248	4	5.9	+	o	9	1.0	2.0	−2.0	3	3
$^{n}P(1,1)$	7805.893	7805.8506	0	2.0	+	p	5	1.0	2.0	2.0	1	1
$^{n}P(2,2)$	7820.239	7819.9804	1	1.0	−	p	12	1.0	2.0	2.0	2	2
$^{t}R(2,2)$	7822.375	7822.2495	3	5.0	−	p	18	1.0	2.0	−2.0	2	2
$^{n}P(3,3)$	7826.739	7826.6791	2	0.0	+	o	6	1.0	2.0	2.0	3	3
$^{n}P(4,4)^{l}$	7833.249	7833.4442	3	1.1	−	p	21	1.0	2.0	1.8	4	4
$^{t}R(1,1)$	7850.959	7850.6766	2	4.0	+	p	15	1.0	2.0	−2.0	1	1
$^{t}R(4,3)$	7880.921	7881.4428	5	5.9	+	o	13	1.0	2.0	−2.0	4	3
$^{n}Q(1,1)$	7894.711	7894.3784	1	2.0	+	p	5	1.0	2.0	2.0	1	1
$^{n}Q(2,1)$	7898.371	7898.1873	2	2.0	+	p	17	1.0	2.0	2.0	2	1
$^{n}Q(3,1)$	7905.717	7905.8910	3	2.0	+	p	17	1.0	2.0	1.9	3	1
$^{t}R(3,2)$	7912.047	7912.1958	4	4.9	−	p	18	1.0	2.0	−2.0	3	2
$^{t}R(2,1)$	7939.619	7939.4988	3	4.0	+	p	15	1.0	2.0	−2.0	2	1
$^{t}R(1,0)$	7970.413	7970.1244	2	3.0	−	o	5	1.0	2.0	−2.0	1	0
$^{n}Q(2,2)$	7998.890	7998.7540	2	1.0	−	p	12	1.0	2.0	2.0	2	2
$^{t}R(4,2)$	8005.582	8006.4406	5	4.8	−	p	30	1.0	2.0	−1.9	4	2
$^{n}Q(3,2)^{u}$	8007.410	8007.6278	3	1.0	−	p	22	1.0	2.0	1.9	3	2
$^{n}Q(4,2)^{u}$	8022.012	8022.6927	4	1.0	−	p	22	1.0	2.0	1.7	4	2
$^{t}R(3,1)$	8027.840	8028.3370	4	3.5	+	p	26	1.0	2.0	−1.8	3	1
$^{n}R(3,1)^{l}$	8037.673	8038.1911	4	2.4	+	p	27	0.9	2.1	1.7	3	1
$P(6,6)$	8053.382	8054.8101	5	5.5	−	o	17	1.8	1.2	−1.2	6	6
$^{n}R(1,1)$	8071.617	8071.4139	2	2.0	+	p	17	1.0	2.0	2.0	1	1
$^{n}Q(4,3)$	8089.406	8090.2817	4	0.1	+	o	11	1.0	2.0	2.0	4	3
$^{n}Q(3,3)$	8110.069	8110.2024	3	0.0	+	o	11	1.0	2.0	1.8	3	3
$P(5,5)$	8123.128	8123.9852	4	4.8	+	p	30	1.9	1.1	−1.1	5	5
$^{t}R(4,1)$	8128.280	8129.3311	5	3.4	+	p	27	0.9	2.1	−1.8	4	1
$^{t}R(3,0)$	8162.653	8163.3190	4	2.9	−	o	12	1.0	2.0	−1.9	3	0
$^{n}R(2,1)$	8163.129	8163.2943	3	2.0	+	p	17	1.0	2.0	1.9	2	1

this $A_1 \leftarrow A_1$ transition is vibrationally forbidden, but also because there is no Coriolis coupling between the ν_1 and ν_2 states. The first mixing term is due to the effect of a vibration–rotation interaction known as 'Birss resonance' (Majewski *et al.* 1987). This mixing term is $\kappa^4 \sim 10^{-4}$ smaller than the vibrational energy and the mixing is only effective (and, hence, the transitions only observable) when there is an 'accidental' degeneracy between a state in ν_1 and a state in ν_2 with the same value of J and with G different by 3. Such a degeneracy only occurs for fairly high J, where the variation in rotational energy with G can compensate for the difference in vibrational energy (656.9 cm^{-1}). Nine such weak transitions into states with $J = 5$–7 were observed by Xu *et al.* (1992). This work determined the energy of the ν_1 level

to be 3178 cm^{-1}, in agreement with the value derived from the Rydberg spectrum of H_3 (Ketterle *et al.* 1989).

The $\nu_1 + \nu_2 \leftarrow \nu_2$ band is less forbidden, because the anharmonicity of the H_3^+ potential energy surface suffices to mix the $\nu_1 + \nu_2$ state with other vibrational states such as $2\nu_2^2$ and $3\nu_2^1$. The resulting mixing with the upper states of allowed hot band transitions leads to intensity borrowing, which makes the $\nu_1+\nu_2 \leftarrow \nu_2$ band observable, though still weak. Nevertheless, Xu *et al.* (1992) were able to observe 21 lines in this band.

10. Combination bands: $\nu_1 + 2\nu_2 \leftarrow 0$ and $2\nu_1 + \nu_2 \leftarrow 0$

The $\nu_1+2\nu_2$ and $2\nu_1+\nu_2$ vibrational states are among the highest energy states below the barrier to linearity (see figure 3). The combination bands from the vibrational ground state into these states are weaker than any allowed bands previously observed (see figure 4). The spectroscopy of these combination bands is very exciting because it represents the best test yet of theoretical calculations of H_3^+.

A tunable external cavity diode laser spectrometer was assembled specifically for the study of these bands. This diode laser has a nominal tuning range of 7633–8183 cm^{-1}, but due to degradation of the anti-reflection coating on the front facet of the diode, it only has a useful tuning range of *ca.* 7780–8168 cm^{-1}. The effect of this degradation is most severe on the low-frequency side, such that continuous scanning is only possible between *ca.* 7850 and *ca.* 8168 cm^{-1}.

Using the liquid-nitrogen-cooled discharge in figure 1, we continuously scanned both a pure hydrogen discharge ($P_{H_2} \sim 500$ mTorr) and a helium-dominated discharge ($P_{He} \sim 10$ Torr, $P_{H_2} \sim 500$ mTorr) from 7850 to 8168 cm^{-1}. Additionally, narrow (2 cm^{-1}) scans were made at the frequencies in the range of 7785–7850 cm^{-1} where H_3^+ lines were expected from theoretical calculations. In the course of this scanning we observed 30 transitions of H_3^+ and over 200 transitions between Rydberg states of H_2. The latter were easily discriminated against because of their greatly reduced intensity when helium was added to the discharge. A stick diagram of the observed H_3^+ spectrum is shown in figure 6, where the stronger lines have been labelled in accordance with the convention of expression (5.1). The intensities in figure 6, and the majority of our assignments, are taken directly from the calculations of J. K. G. Watson (1996, personal communication). Of the 30 H_3^+ transitions, two belong to the high-J portion of the P-branch of the $2\nu_1 + \nu_2 \leftarrow 0$ band, while the rest all belong to the $\nu_1 + 2\nu_2^2 \leftarrow 0$ band.

Table 1 includes the observed transitions and the calculated frequencies from Watson (1996, personal communication). In most cases, the observed frequencies are accurate to *ca.* 0.01 cm^{-1}. Also listed, from Watson's calculations, are the quantum numbers of the upper (primed) and lower (double-primed) states of each transition. Note that at these high energies, the quantities G and $|\ell_2|$ are no longer good quantum numbers; as a result, the expectation values of these quantities are given. This is also true, though to a lesser extent, of the quantities v_1 and v_2 (the number of quanta in each vibrational mode).

At these high energies, the only rigorous quantum numbers are J (the angular momentum of nuclear motion), the spin modification (ortho or para, listed as o/p in the table), and the parity ($\pm$). The quantity n in the table is not a quantum number, but simply a label giving the energy ordering of the states with the same $(J, \pm, \mathrm{o/p})$.

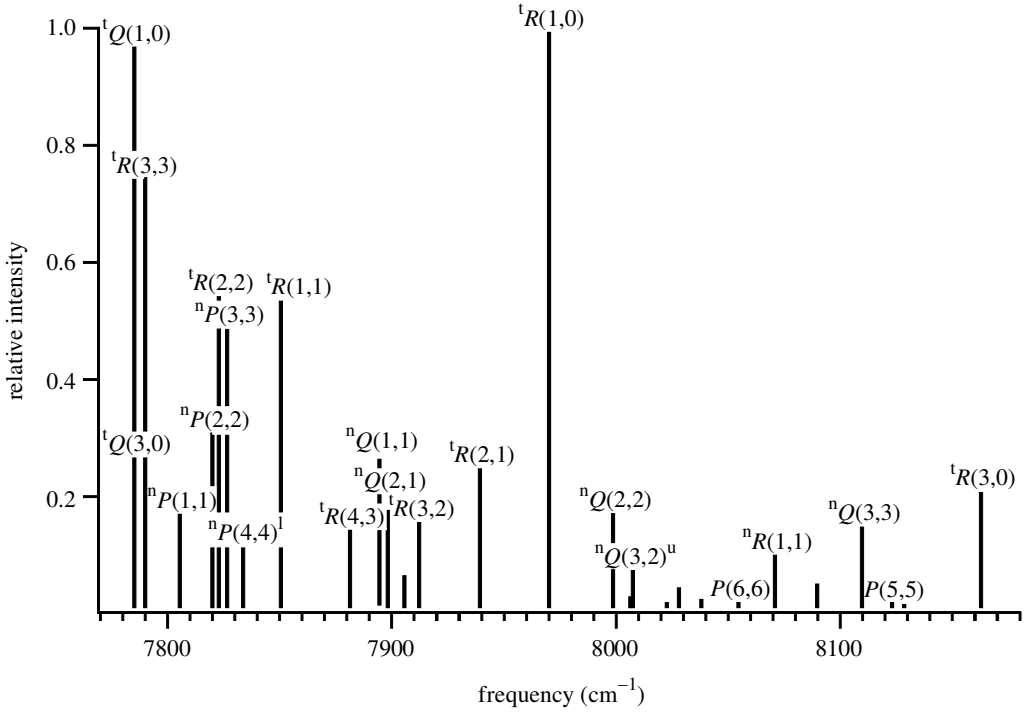

Figure 6. The observed spectrum of the $\nu_1 + 2\nu_2^2$ band of H_3^+, recently obtained using a tunable diode laser. The stronger lines are labelled as described in equation (5.1). The two weakest labelled lines belong to the $2\nu_1 + \nu_2^1$ band.

The failure of the traditional quantum numbers of H_3^+ is illustrated in figure 7, which shows the energy-level structure of the $\nu_1 + 2\nu_2^2$ vibrational state. The horizontal axis is the expectation value of G, and it is easily seen that the levels do not lie along vertical lines. Below each level the expectation value of ℓ_2 is listed, which should be ± 2, but is, in most cases, non-integral due to mixing.

The $\nu_1 + 2\nu_2^2 \leftarrow 0$ band is particularly amenable to astronomical observation, as it lies in a transparent spectral region of the atmosphere known as the J-band. While detection of this band in absorption in the interstellar medium is probably not feasible (since it is about 300 times weaker than the fundamental band), it may serve as a particularly useful probe of the emission from hot astronomical plasmas. At a vibrational temperature of 1000 K, this band is 25 000 times weaker than the fundamental, but by 1500 K this deficit is only 1700, at 2000 K it is down to only a factor of 450. Given the strong emission that has been observed from Jupiter's ionosphere, it is hoped that this band may serve as a thermometer for this type of environment.

11. Future prospects

In many ways, we have reached a milestone in the laboratory spectroscopy of H_3^+. With the exceptions of $2\nu_1$, $3\nu_1$, and $4\nu_2$, every vibrational state below the barrier to linearity has been studied in the laboratory. While the spectroscopy of these states

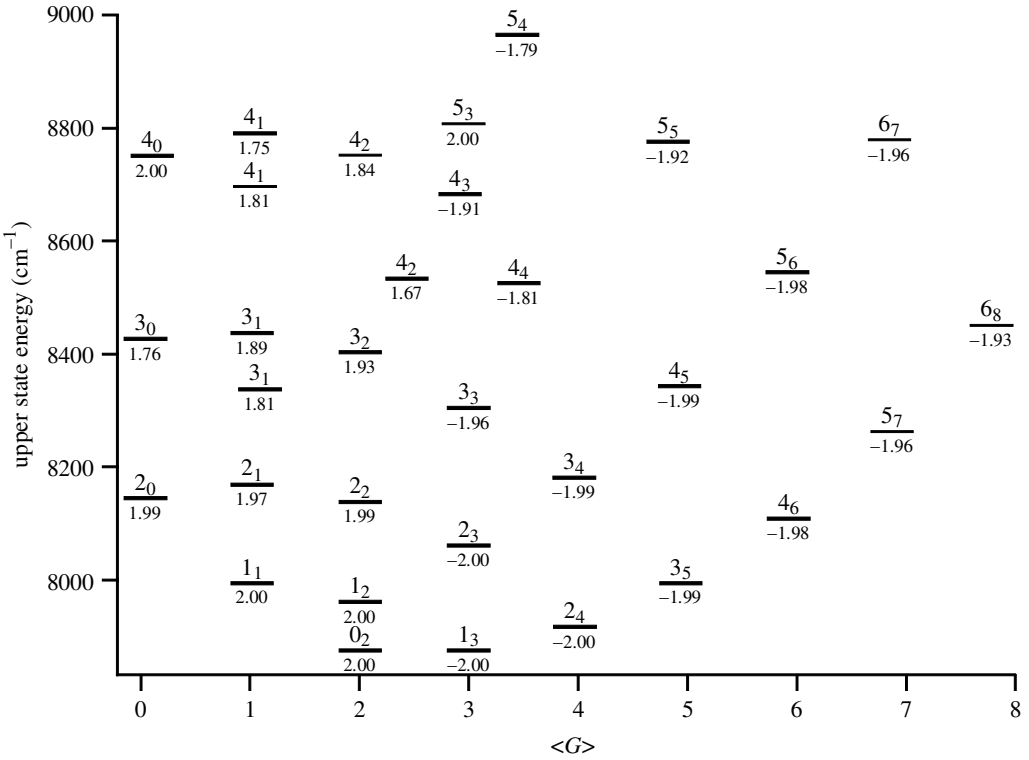

Figure 7. Energy-level diagram of the $\nu_1 + 2\nu_2^2$ vibrational state of H_3^+. The numbers above the levels are J_{G^*}, where G^* is the unmixed value of G. The numbers below the levels are the expectation value of $|\ell_2|$. Observed levels are indicated with heavy lines.

(and all of their $|\ell_2|$ substates) is by no means complete, we have established most of the band origins and filled in the rotational structure of many of the bands. State-of-the-art variational calculations based on spectroscopically adjusted potentials (e.g. J. K. G. Watson 1996, personal communication) now yield amazingly accurate predictions of both transition frequencies and intensities.

We are now entering a new era as we begin to probe the theoretically challenging region near and above the barrier to linearity. With our titanium:sapphire laser, we are preparing to attack $5\nu_2^1$, and perhaps even higher vibrational states. While these high overtones are very weak, they are well within reach given our current sensitivity. We expect that the breakdown of the G, $|\ell_2|$, and even v_1 and v_2 quantum numbers, which is already evident in our combination band spectra, will become even worse as we move to higher energies. Eventually, the energy-level diagrams may no longer even qualitatively resemble the ones in figures 2 and 7, but may be completely chaotic.

At the same time, theoreticians are rising to the challenge of predicting these high-energy vibrational states. Watson (this issue) is incorporating hyperspherical coordinates, which promise to alleviate the problems associated with linearity. On another front, Cencek *et al.* (1998) and Polyansky & Tennyson (1999) are working to incorporate relativistic and non-adiabatic effects into the rovibrational calculations.

Starting from $4\nu_2 \leftarrow 0$ (*ca.* 9000 cm^{-1}), the titanium:sapphire and ring-dye lasers provide continuous spectral coverage and ample power (watts) out to *ca.* 20 000 cm^{-1}.

With the introduction of new noise-reduction (e.g. heterodyne detection) and signal-enhancement (e.g. cavity) techniques, we may be able to continue the spectroscopy of H_3^+ out to $10\nu_2$ or even farther.

I acknowledge the assistance of T. Oka, who introduced me to this most remarkable molecular ion and has offered his insight and encouragement. I also thank J. K. G. Watson for helpful conversations and for providing the results of his calculations before publication. Finally, I thank the Fannie and John Hertz Foundation for their financial support. This work was also supported by NSF grant PHYS-9722691 and NASA grant NAG5-4070.

References

Amano, T. 1988 Is the dissociative recombination of H_3^+ really slow? A new spectroscopic measurement of the rate constant. *Astrophys. J.* **329**, L121–L124.

Bawendi, M. G., Rehfuss, B. D. & Oka, T. 1990 Laboratory observation of hot bands of H_3^+. *J. Chem. Phys.* **93**, 6200–6209.

Bowers, M. T., Elleman, D. D. & King Jr, J. 1969 Analysis of the ion–molecule reactions in gaseous H_2, D_2, and HD by ion cyclotron resonance techniques. *J. Chem. Phys.* **50**, 4787–4804.

Carney, G. D. & Porter, R. N. 1976 H_3^+: *ab initio* calculation of the vibration spectrum. *J. Chem. Phys.* **65**, 3547–3565.

Cencek, W., Rychlewski, J., Jaquet, R. & Kutzelnigg, W. 1998 Sub-micro-Hartree accuracy potential energy surface for H_3^+ including adiabatic and relativistic effects. I. Calculation of the potential points. *J. Chem. Phys.* **108**, 2831–2836.

Dinelli, B. M., Miller, S. & Tennyson, J. 1992 Bands of H_3^+ up to $4\nu_2$: rovibrational transitions from first principles calculations. *J. Mol. Spectrosc.* **153**, 718–725.

Dinelli, B. M., Miller, S., Achilleos, N., Lam, H. A., Cahill, M., Tennyson, J., Jacod, M.-F., Oka, T., Hilico, J.-C. & Geballe, T. R. 1997 UKIRT observations of the impact and consequences of Comet Shoemaker–Levy 9 on Jupiter. *Icarus* **126**, 107–125.

Drossart, P. (and 11 others) 1989 Detection of H_3^+ on Jupiter. *Nature* **340**, 539–541.

Friedrich, O. & Alijah, A. 2000 Triplet H_3^+. Exhibit, this meeting.

Joo, S.-W., Kühnemann, F., Jagod, M.-F. & Oka, T. 2000 Diode laser spectroscopy of the high J $P(12,12)^{\mathrm{u}}$ transition of H_3^+. Exhibit, this meeting.

Ketterle, W., Messmer, H.-P. & Walther, H. 1989 The ν_1 vibration of H_3^+ and autoionizing Rydberg states of H_3. *Europhys. Lett.* **8**, 333–338.

Lee, S. S., Ventrudo, B. F., Cassidy, D. T., Oka, T., Miller, S. & Tennyson, J. 1991 Observation of the $3\nu_2 \leftarrow 0$ overtone band of H_3^+. *J. Mol. Spectrosc.* **145**, 222–224.

Lindsay, C. M., Rade, R. M. & Oka, T. 2000*a* Survey of H_3^+ transitions between 3000 cm^{-1} and 4200 cm^{-1}. Exhibit, this meeting.

Lindsay, C. M., White, E. T. & Oka, T. 2000*b* Measurement of the H_3^+ destruction rate due to ambipolar diffusion in an AC positive column discharge. *Chem. Phys. Lett.* (In the press.)

McKellar, A. R. W. & Watson, J. K. G. 1998 The infrared spectrum of H_3^+ revealed. *J. Mol. Spectrosc.* **191**, 215–217.

Majewski, W. A., Marshall, M. D., McKellar, A. R. W., Johns, J. W. C. & Watson, J. K. G. 1987 Higher rotational lines in the ν_2 fundamental of the H_3^+ molecular ion. *J. Mol. Spectrosc.* **122**, 341–355.

Majewski, W. A., Feldman, P. A., Watson, J. K. G., Miller, S. & Tennyson, J. 1989 Laboratory observation of the $2\nu_2$ band of the H_3^+ molecular ion. *Astrophys. J.* **347**, L51–L54.

Majewski, W. A., McKellar, A. R. W., Sadovskiĭ, D. & Watson, J. K. G. 1994 New observations and analysis of the infrared vibration–rotation spectrum of H_3^+. *Can. J. Phys.* **72**, 1016–1027.

Miller, S. & Tennyson, J. 1988 Overtone bands of H_3^+: first principle calculations. *J. Mol. Spectrosc.* **128**, 530–539.

Miller, S. & Tennyson, J. 1989 Hot band transition frequencies and line strengths in H_3^+: first principles calculations. *J. Mol. Spectrosc.* **136**, 223–240.

Nakanaga, T., Ito, F., Sugawara, K., Takeo, H. & Matsumura, C. 1990 Observation of infrared absorption spectra of molecular ions, H_3^+ and HN_2^+, by FTIR spectroscopy. *Chem. Phys. Lett.* **169**, 269–273.

Oka, T. 1980 Observation of the infrared spectrum of H_3^+. *Phys. Rev. Lett.* **45**, 531–534.

Oka, T. 1981 A search for interstellar H_3^+. *Phil. Trans. R. Soc. Lond.* A **303**, 543–549.

Pan, F.-S. & Oka, T. 1986 Calculated forbidden rotational spectra of H_3^+. *Astrophys. J.* **305**, 518–525.

Polyansky, O. L. & Tennyson, J. 1999 *Ab initio* calculation of the rotation–vibration energy levels of H_3^+ and its isotopomers to spectroscopic accuracy. *J. Chem. Phys.* **110**, 5056–5064.

R¨ohse,R., Kutzelnigg, W., Jaquet, R. & Klopper, W. 1994 Potential energy surface of the H_3^+ ground state in the neighborhood of the minimum with micro-Hartree accuracy and vibrational frequencies derived from it. *J. Chem. Phys.* **101**, 2231–2243.

Sutcliffe, B. T. 1983 A comment on a recent proposal for the calculation of vibrational energies in the general triatomic molecule. *Mol. Phys.* **48**, 561–566.

Thomson, J. J. 1911 Rays of positive electricity. *Phil. Mag.* **21**, 225–249.

Trafton, L., Lester, D. F. & Thompson, K. L. 1989 Unidentified emission lines in Jupiter's northern and southern 2 micron aurorae. *Astrophys. J.* **343**, L73–L76.

Uy, D., Gabrys, C. M., Jagod, M.-F. & Oka, T. 1994 Spectral lines and distribution of H_3^+ in high rotational levels. *J. Chem. Phys.* **100**, 6267–6274.

Uy, D., Cordonnier, M. & Oka, T. 1997 Observation of ortho–para H_3^+ selection rules in plasma chemistry. *Phys. Rev. Lett.* **78**, 3844–3847.

Ventrudo, B. F., Cassidy, D. T., Guo, Z. Y., Joo, S., Lee, S. S. & Oka, T. 1994 Near infrared $3\nu_2$ overtone band of H_3^+. *J. Chem. Phys.* **100**, 6263–6266.

Watson, J. K. G. 1971 Forbidden rotational spectra of polyatomic molecules. *J. Mol. Spectrosc.* **40**, 536–544.

Watson, J. K. G., Foster, S. C., McKellar, A. R. W., Bernath, P., Amano, T., Pan, F. S., Crofton, M. W., Altman, R. S. & Oka, T. 1984 The infrared spectrum of the ν_2 fundamental band of the H_3^+ molecular ion. *Can. J. Phys.* **62**, 1875–1885.

Xu, L.-W., Gabrys, C. & Oka, T. 1990 Observation of the $2\nu_2(\ell = 2) \leftarrow 0$ overtone band of H_3^+. *J. Chem. Phys.* **93**, 6210–6215.

Xu, L.-W., R¨osslein,M., Gabrys, C. M. & Oka, T. 1992 Observation of infrared forbidden transitions of H_3^+. *J. Mol. Spectrosc.* **153**, 726–737.

Discussion

G. Duxbury (*Department of Physics and Applied Physics, University of Strathclyde, UK*). In his paper, McCall demonstrated the range of laser spectrometric techniques which have been used successfully to map the mid- and near-infrared spectra of H_3^+. It has also been suggested that the far-infrared transitions induced by vibration–rotation mixing may also be detectable. It is the purpose of this comment to show that a new class of lasers, quantum cascade (or QC) lasers, have the potential to fill in many of the holes in the currently available tuning range of tunable lasers, in particular at the long-wavelength end of the infrared spectrum.

Quantum cascade lasers were first demonstrated by Faist *et al.* (1994), and are based upon electrons making transitions between energy levels created by quantum confinement. This confinement is in quantum wells created in semiconductors which

are based on gallium arsenide. Since the wavelength depends upon the quantum well structure and not upon the band gap of the parent semiconductor, the wavelengths of QC lasers may be tailored to operate over most of the region from 3 to 17 μm. These sources have much higher output power levels of between 10 and 20 milliwatts (Faist *et al.* 1994; Normand *et al.* 1999). They are much more compact and with lower power consumption than ion or YAG laser pumped difference frequency or F-centre lasers. They have also been shown to be excellent spectroscopic sources, with sufficient sensitivity to detect the ^{13}C and D content of methane (Kosterev *et al.* 1999), and have been shown to be frequency stabilized with a kilohertz linewidth (Williams *et al.* 1999).

The performance that has already been demonstrated (see Kosterev *et al.* 1999; Williams *et al.* 1999) shows that these lasers have the potential to be used not only to study the longer-wavelength transitions of ions such as H_3^+, but also other ions such as H_3O^+ and H_2O^+, which are interesting in the ion–molecule reactions. Williams *et al.* (1999) have also pointed out that these lasers have the potential to be part of a highly sensitive infrared heterodyne spectrometer, such as those currently based on CO_2 lasers.

Additional references

Faist, J., Capasso, F., Sivco, D. L., Sirtori, C., Hutchinson, A. L. & Cho, A. Y. 1994 *Science* **264**, 553.

Kosterev, A. A., Curl, R. F., Tittel, F. K., Gmachl, C., Capasso, F., Sivco, D. L., Baillargeon, J. N., Hutchinson, A. L. & Cho, A. Y. 1999 *Optics Lett.* **24**, 1762.

Normand, E., Duxbury, G., Langford, N. J., Farmer, C. & Ironside, C. N. 1999 In *16th Colloquium on High Resolution Molecular Spectroscopy, Dijon, 6–10 September 1999*, poster 4.

Williams, R. M. (and 10 others) 1999 *Optics Lett.* **24**, 1844.

APPENDIX C
LABORATORY SPECTRA OF H_3^+

The Combination Bands $\nu_1 + 2\nu_2 \leftarrow 0$ and $2\nu_1 + \nu_2 \leftarrow 0$

In each panel, the upper trace is a spectrum of an NH_3 reference cell, the second trace is an étalon, and the third trace is the velocity modulated spectrum of the He/H_2 plasma. When a fourth trace is present, it is a spectrum of a pure H_2 plasma — the H_3^+ transitions are then easily identified as those which do not decrease too much in intensity when going from a pure H_2 to a He/H_2 plasma.

The bottom scale in all cases is frequency (cm^{-1}). The scale for the reference trace gives an indication of the total laser power, and the scale on the experimental traces permits an estimate of the strength of the absorption.

For reference, the lines are tabulated on page 184 in Appendix B.1.

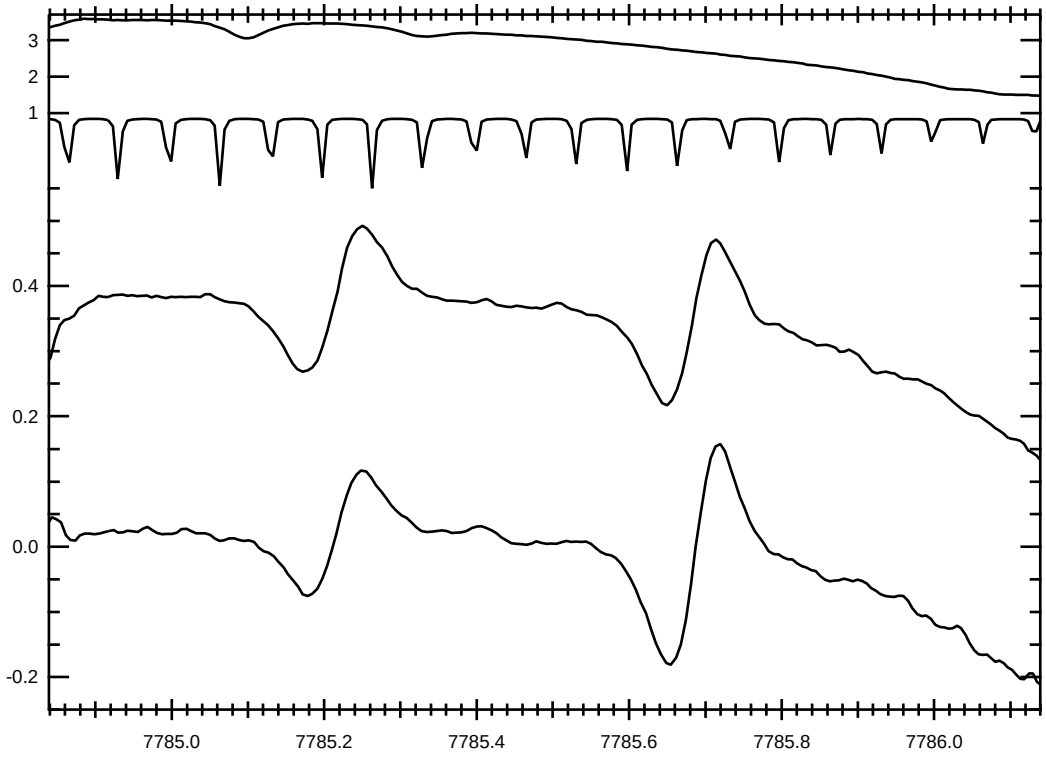
3
2
1
0.4
0.2
0.0
-0.2
7785.0
7785.2
7785.4
7785.6
7785.8
7786.0

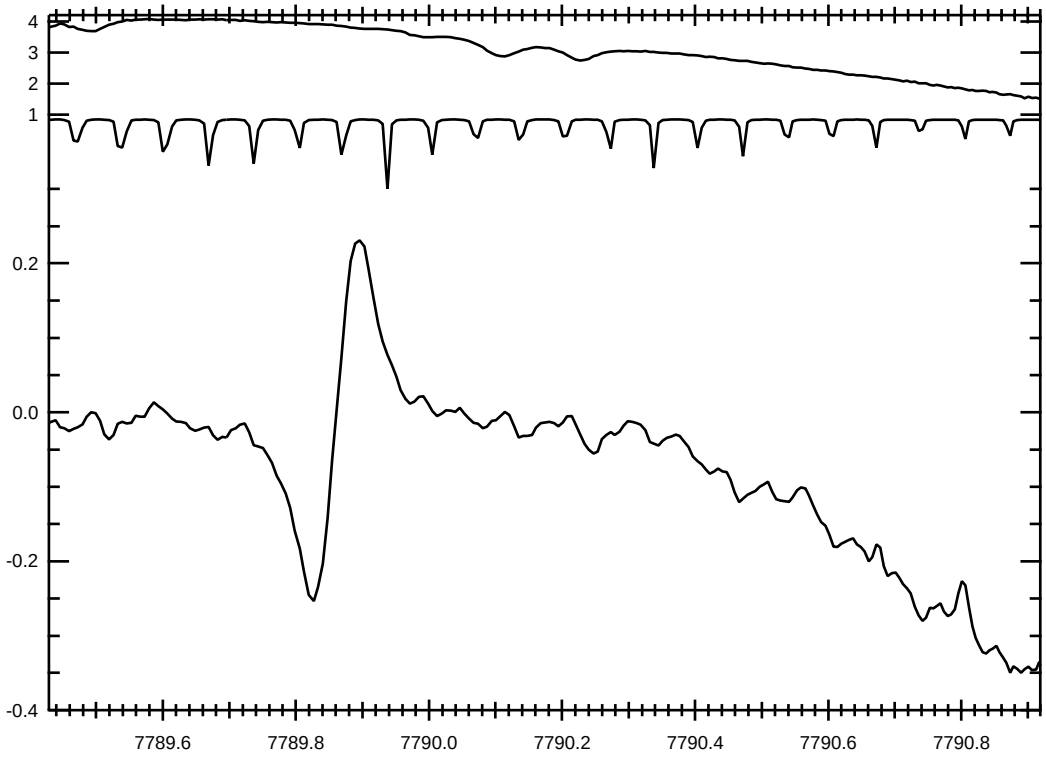
4
3
2
1
0.2
0.0
-0.2
-0.4
7789.6
7789.8
7790.0
7790.2
7790.4
7790.6
7790.8

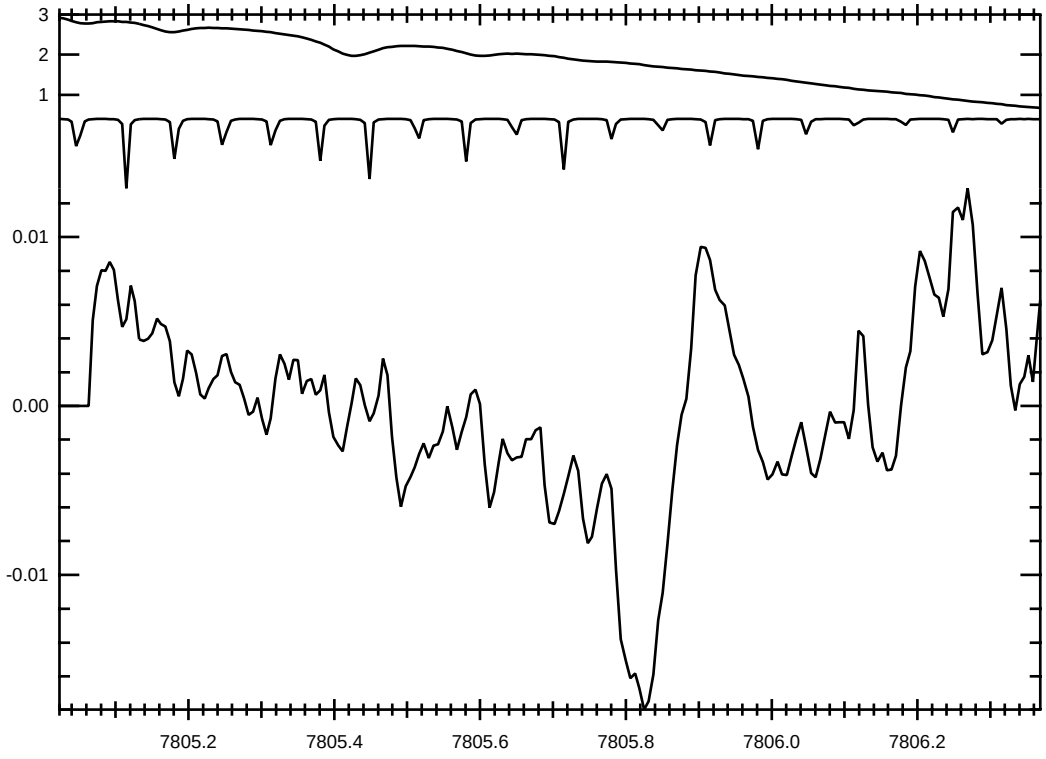
3
2
1
0.01
0.00
-0.01
7805.2
7805.4
7805.6
7805.8
7806.0
7806.2

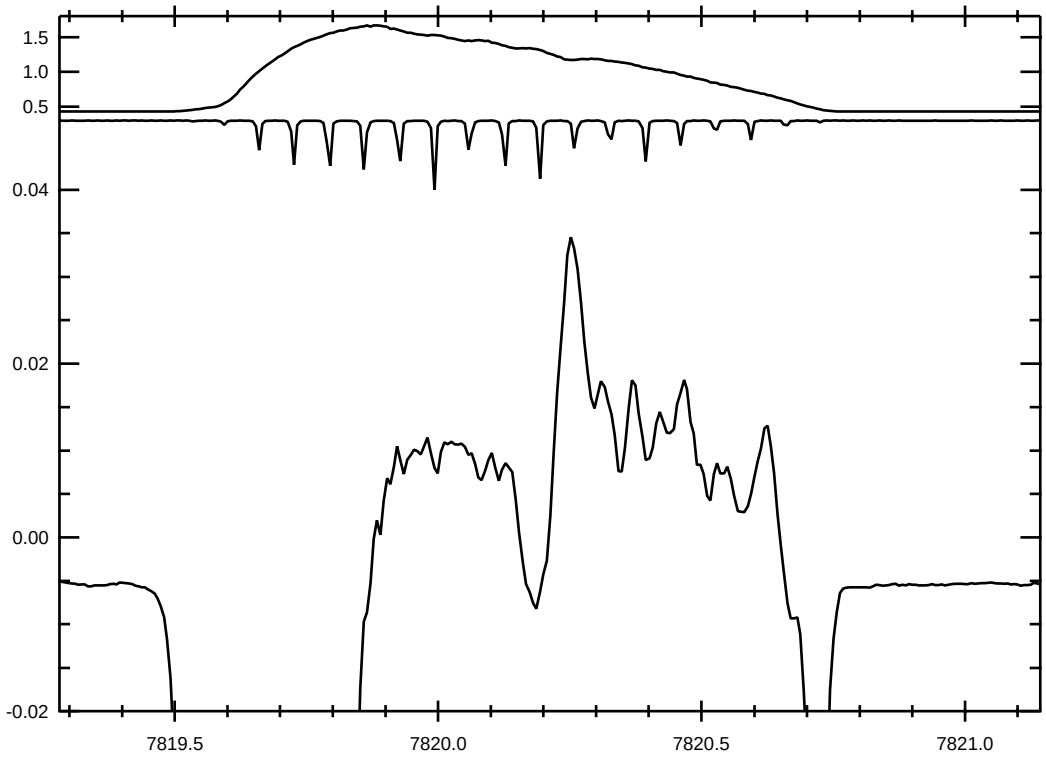
1.5
1.0
0.5
0.04
0.02
0.00
-0.02
7819.5
7820.0
7820.5
7821.0

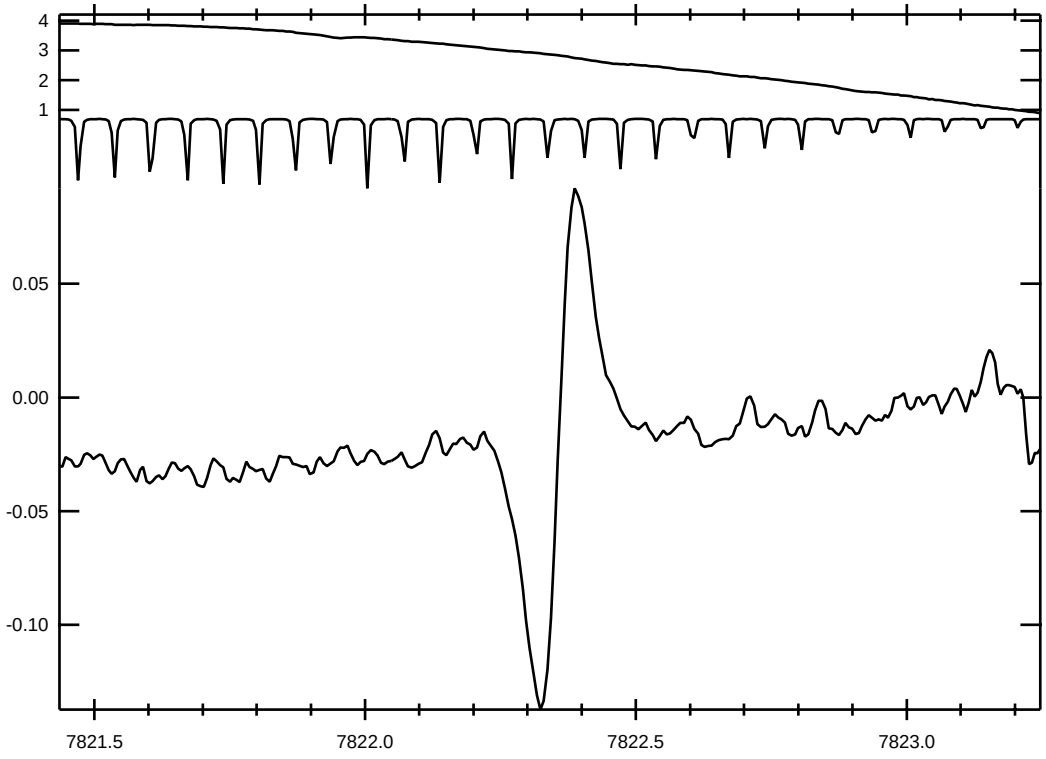
4
3
2
1
0.05
0.00
-0.05
-0.10
7821.5
7822.0
7822.5
7823.0

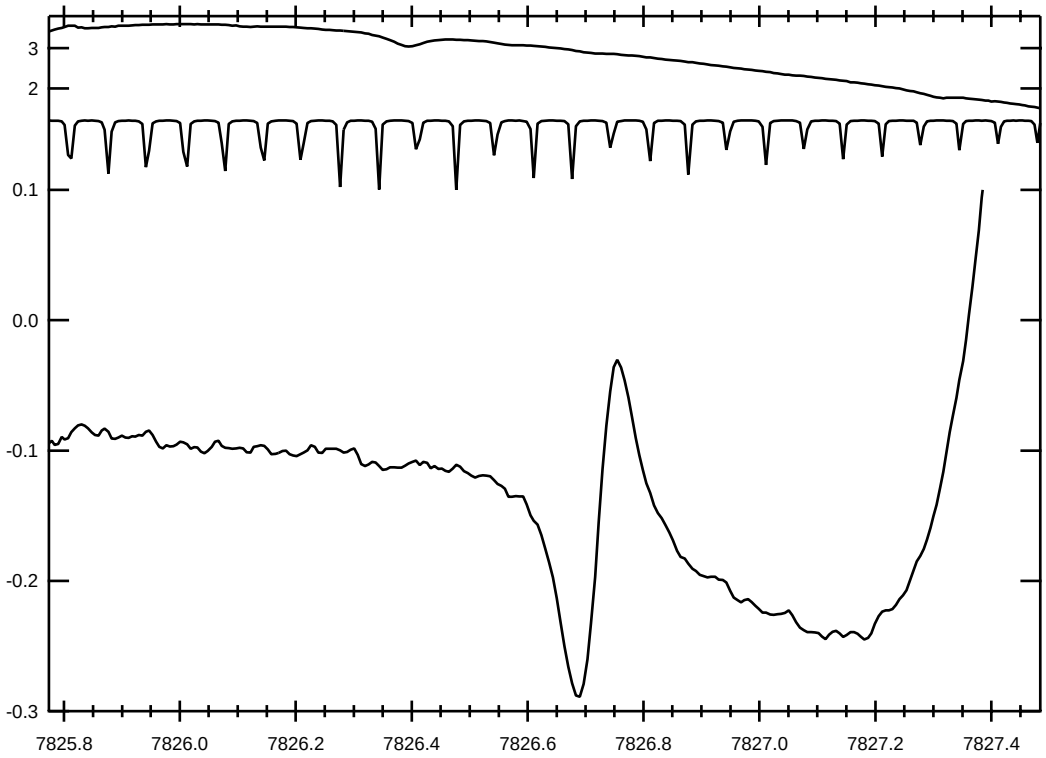
3
2
0.1
0.0
-0.1
-0.2
-0.3
7825.8
7826.0
7826.2
7826.4
7826.6
7826.8
7827.0
7827.2
7827.4

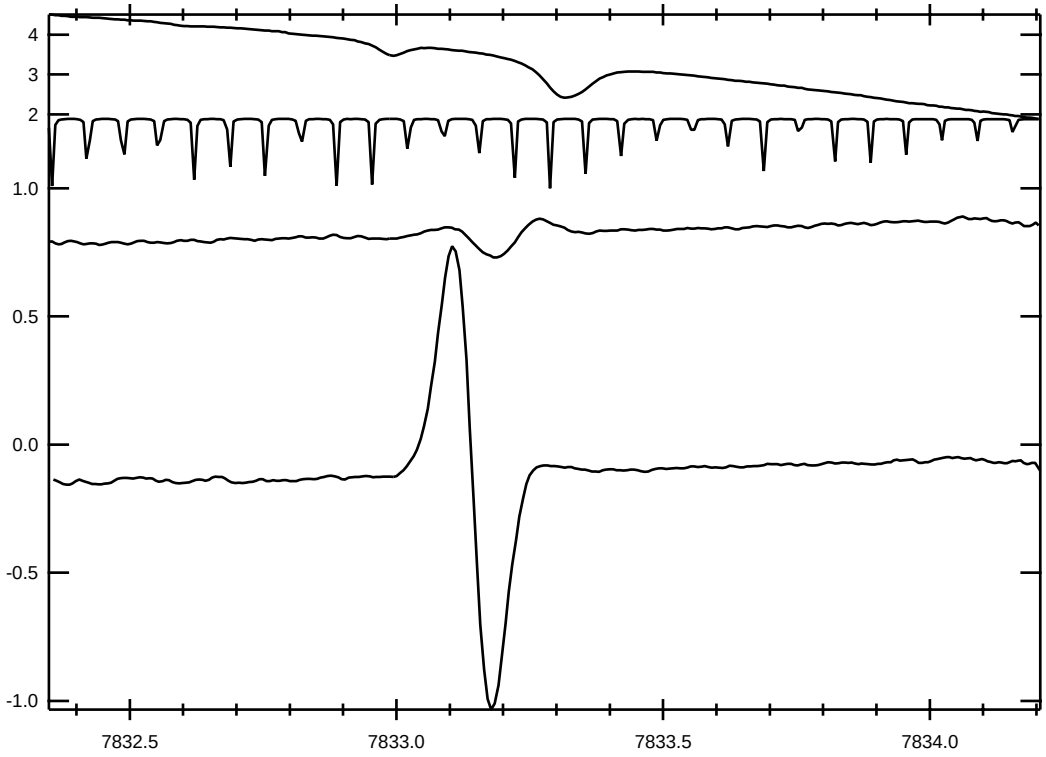
4
3
2
1.0
0.5
0.0
-0.5
-1.0
7832.5
7833.0
7833.5
7834.0

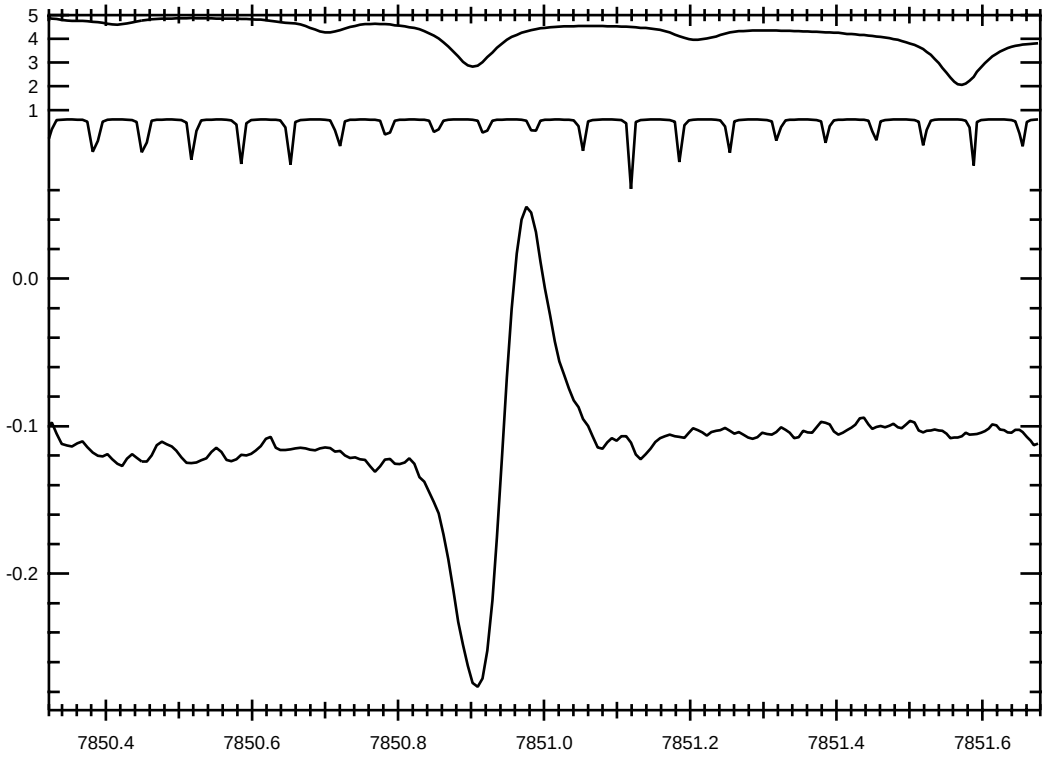
5
4
3
2
1
0.0
-0.1
-0.2
7850.4
7850.6
7850.8
7851.0
7851.2
7851.4
7851.6

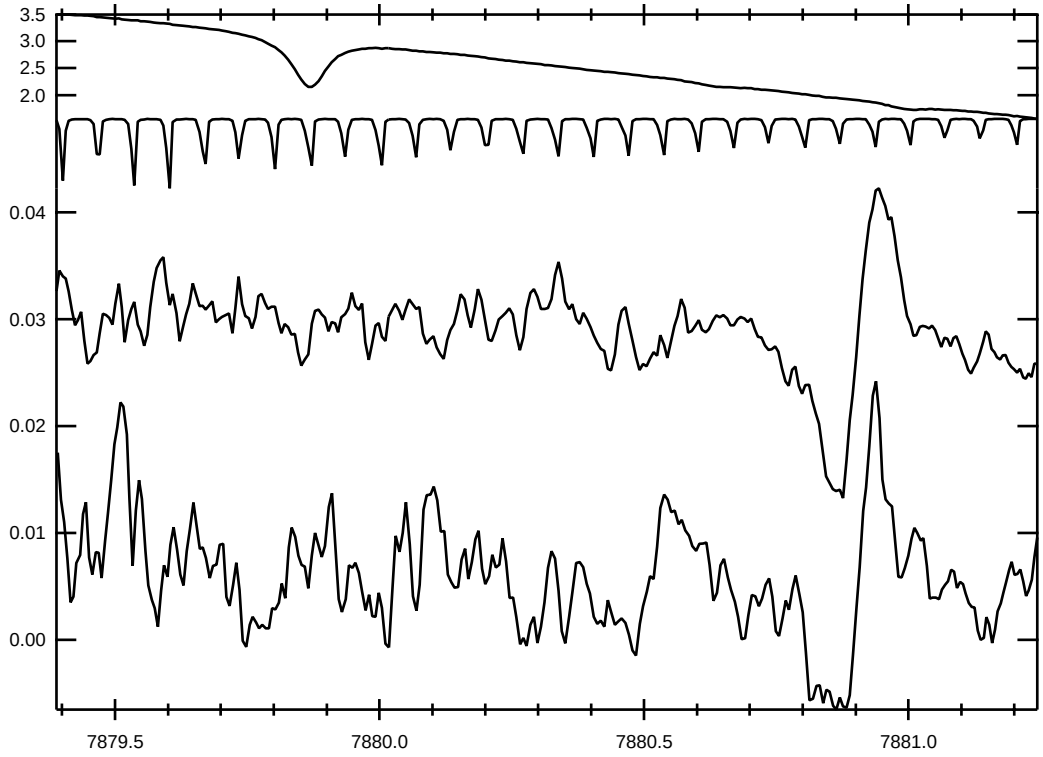
3.5
3.0
2.5
2.0
0.04
0.03
0.02
0.01
0.00
7879.5
7880.0
7880.5
7881.0

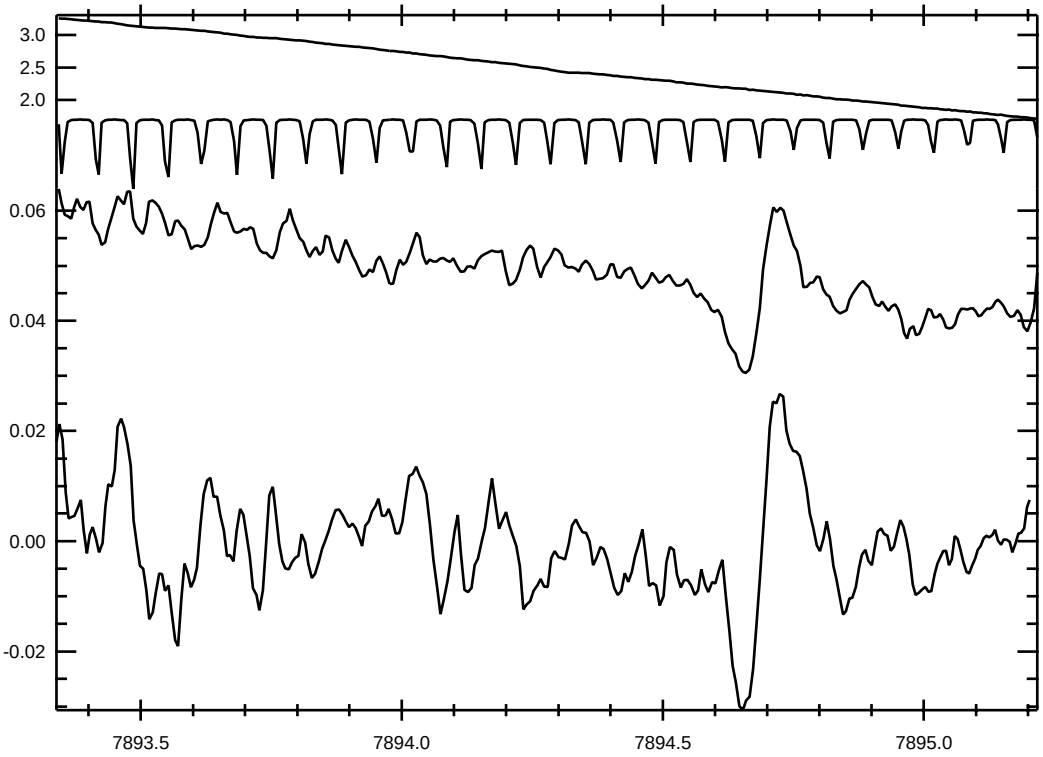
3.0
2.5
2.0
0.06
0.04
0.02
0.00
-0.02
7893.5
7894.0
7894.5
7895.0

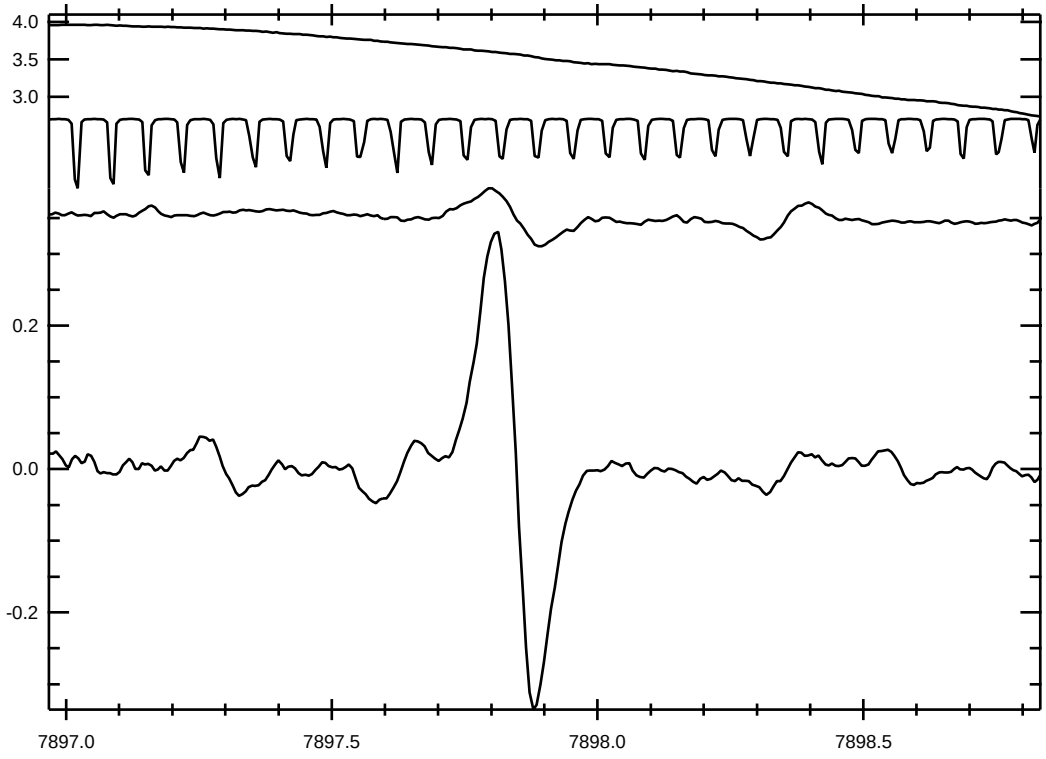
4.0
3.5
3.0
0.2
0.0
-0.2
7897.0
7897.5
7898.0
7898.5

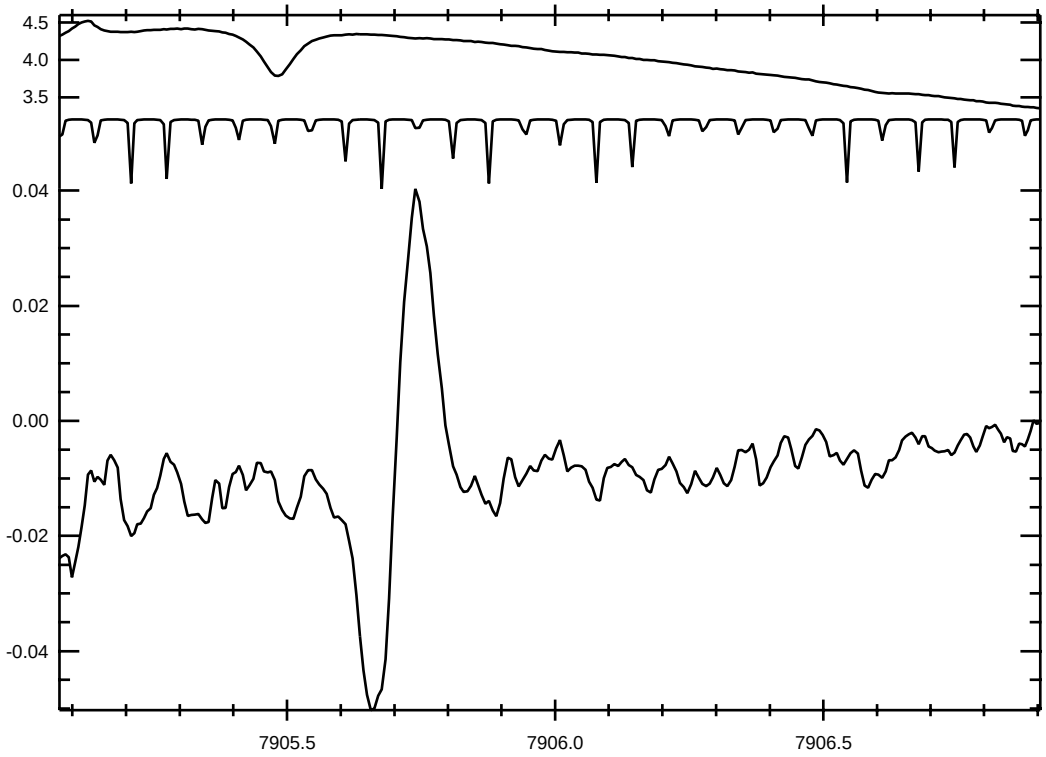
4.5
4.0
3.5
0.04
0.02
0.00
-0.02
-0.04
7905.5
7906.0
7906.5

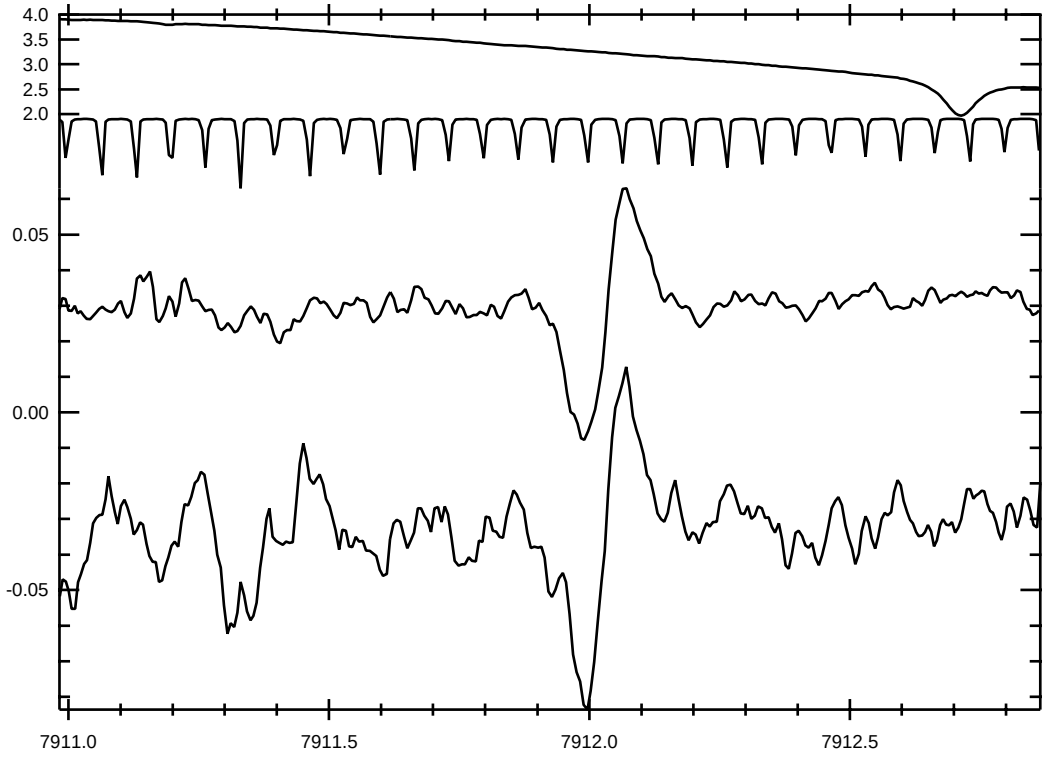
4.0
3.5
3.0
2.5
2.0
0.05
0.00
-0.05
7911.0
7911.5
7912.0
7912.5

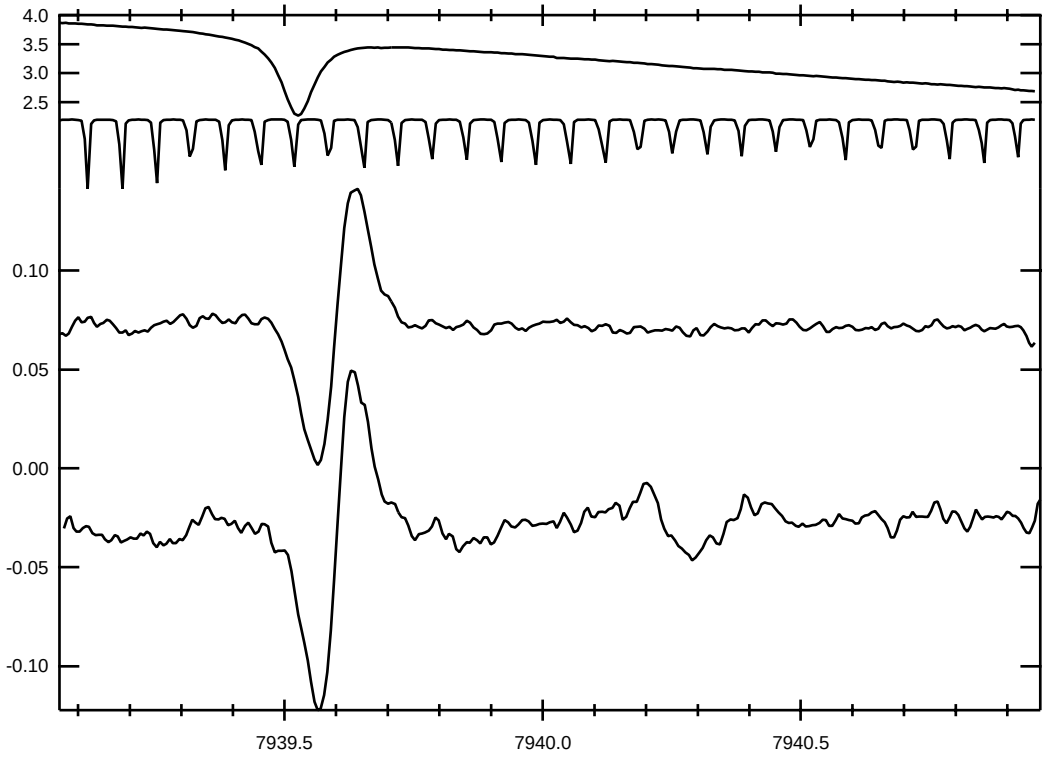
4.0
3.5
3.0
2.5
0.10
0.05
0.00
-0.05
-0.10
7939.5
7940.0
7940.5

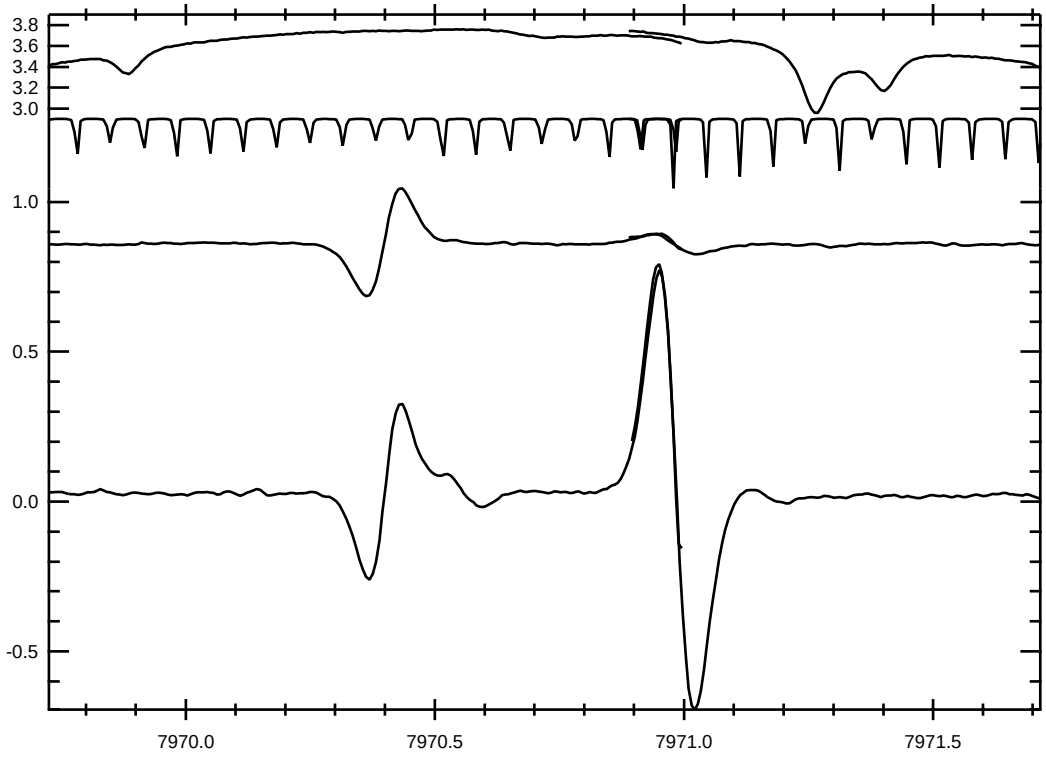
3.8
3.6
3.4
3.2
3.0
1.0
0.5
0.0
-0.5
7970.0
7970.5
7971.0
7971.5

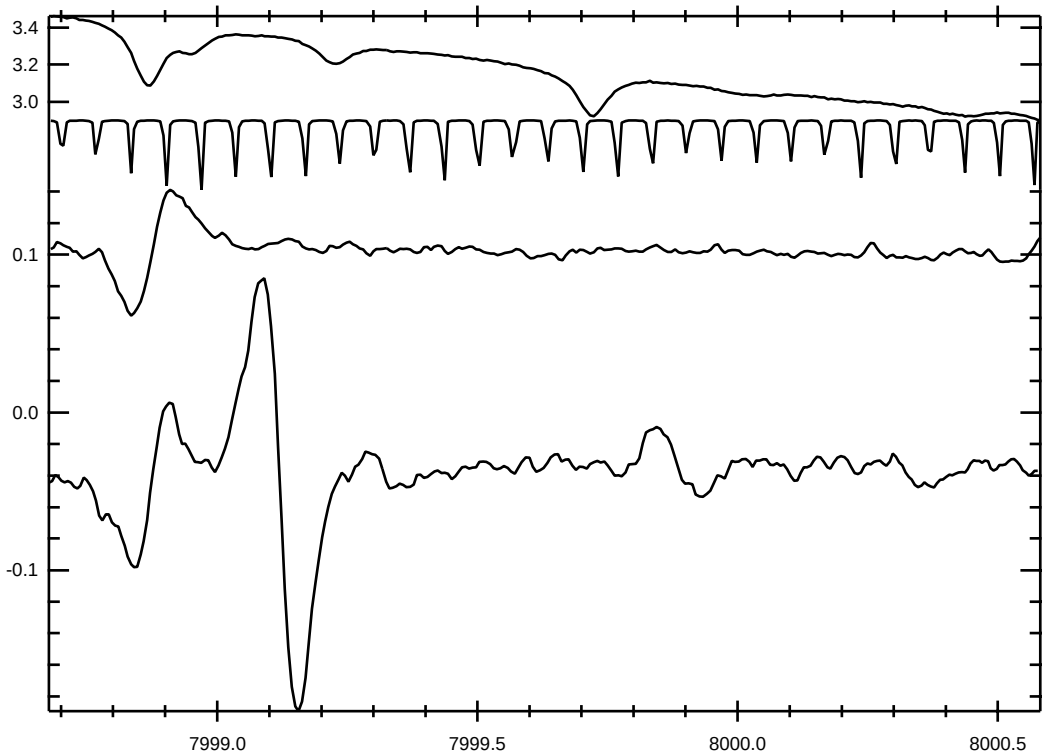
3.4
3.2
3.0
0.1
0.0
-0.1
7999.0
7999.5
8000.0
8000.5

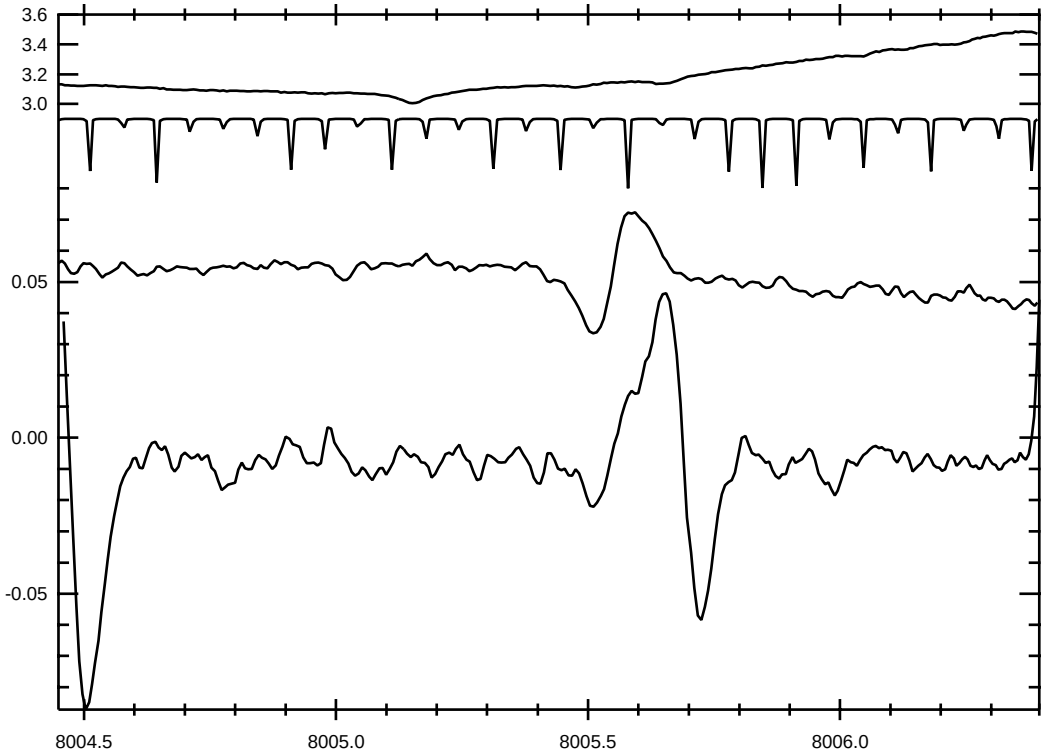
3.6
3.4
3.2
3.0
0.05
0.00
-0.05
8004.5
8005.0
8005.5
8006.0

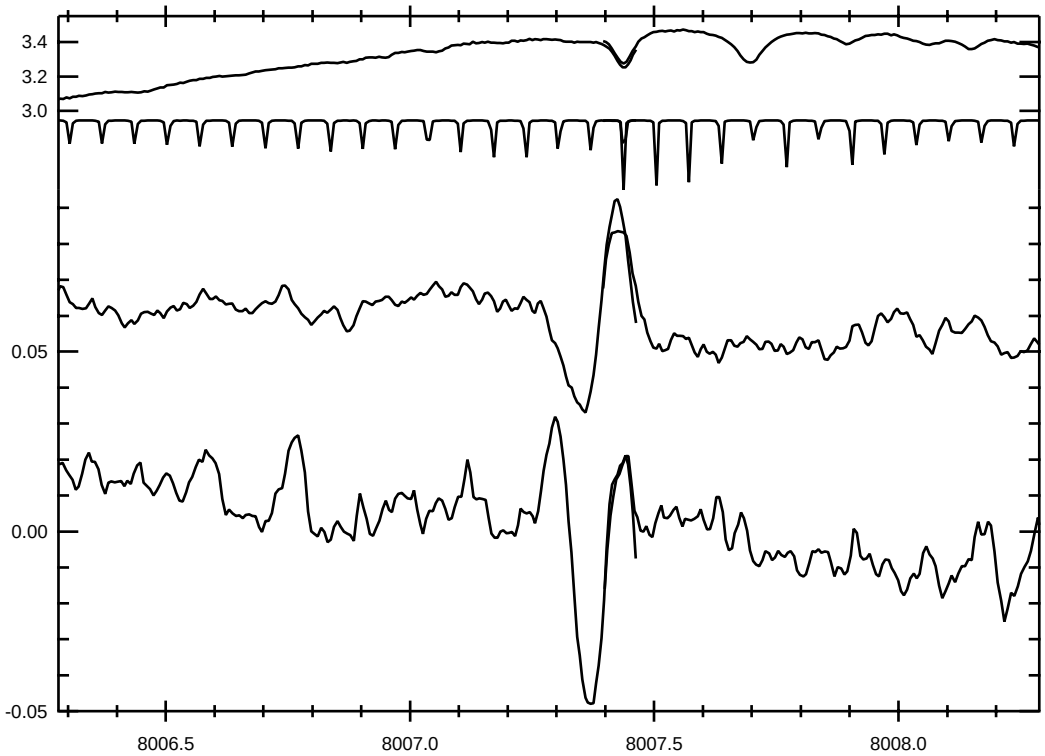
3.4
3.2
3.0
0.05
0.00
-0.05
8006.5
8007.0
8007.5
8008.0

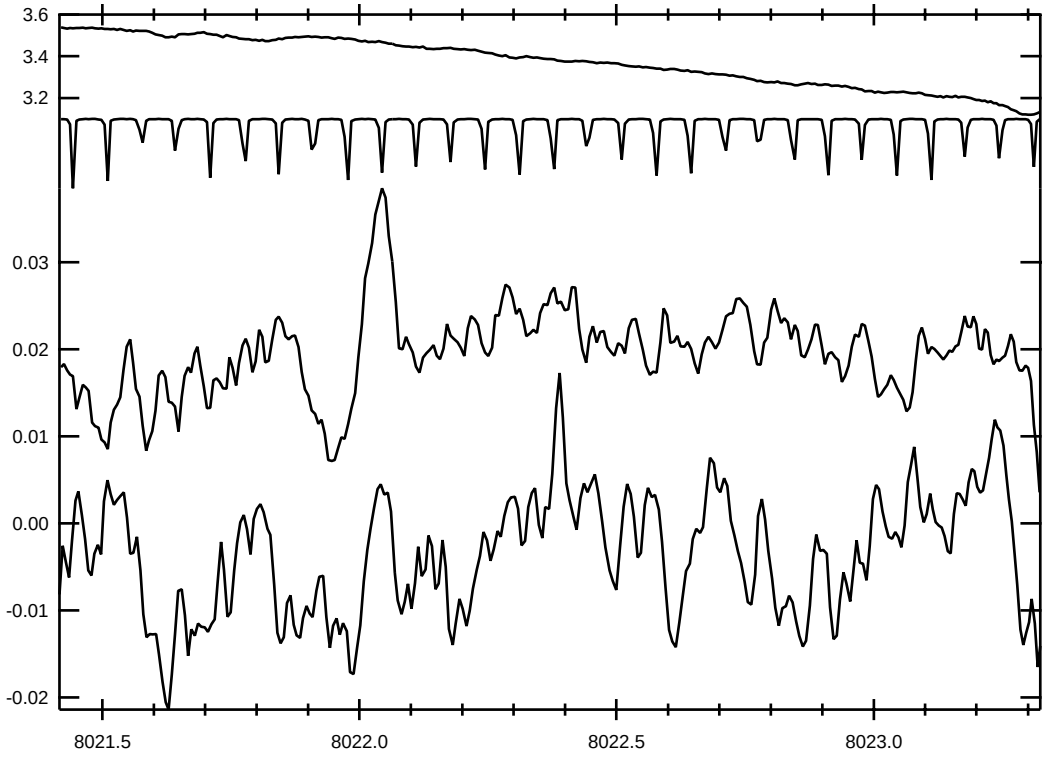
3.6
3.4
3.2
0.03
0.02
0.01
0.00
-0.01
-0.02
8021.5
8022.0
8022.5
8023.0

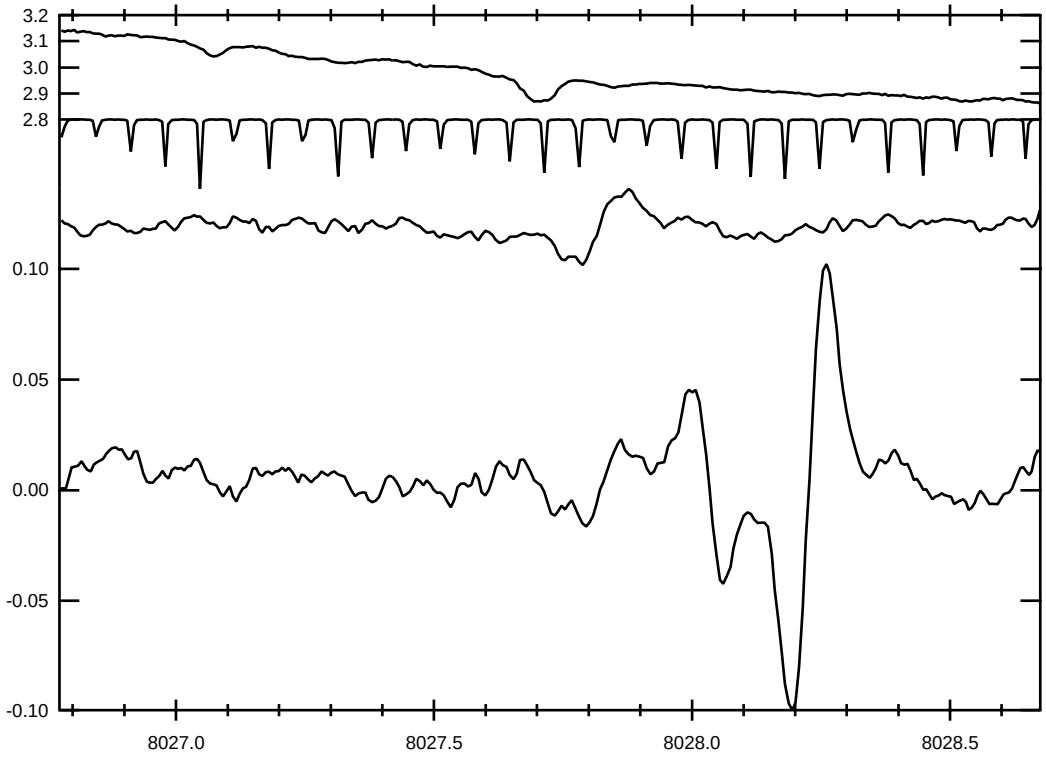
3.2
3.1
3.0
2.9
2.8
0.10
0.05
0.00
-0.05
-0.10
8027.0
8027.5
8028.0
8028.5

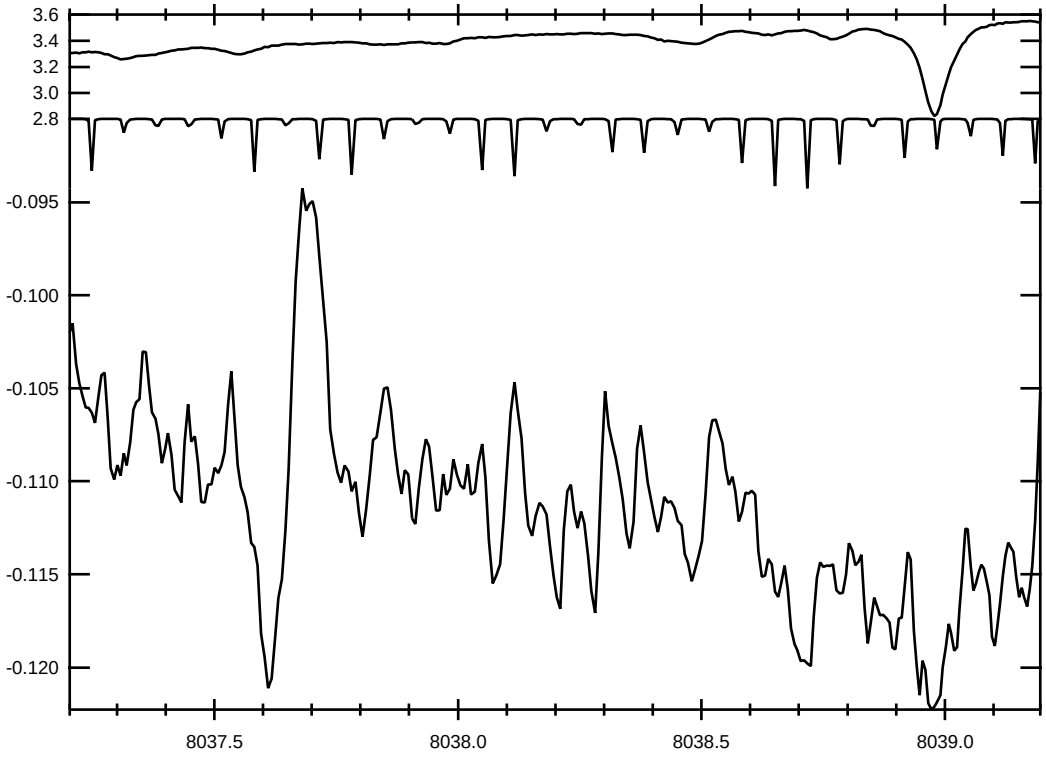
3.6
3.4
3.2
3.0
2.8
-0.095
-0.100
-0.105
-0.110
-0.115
-0.120
8037.5
8038.0
8038.5
8039.0

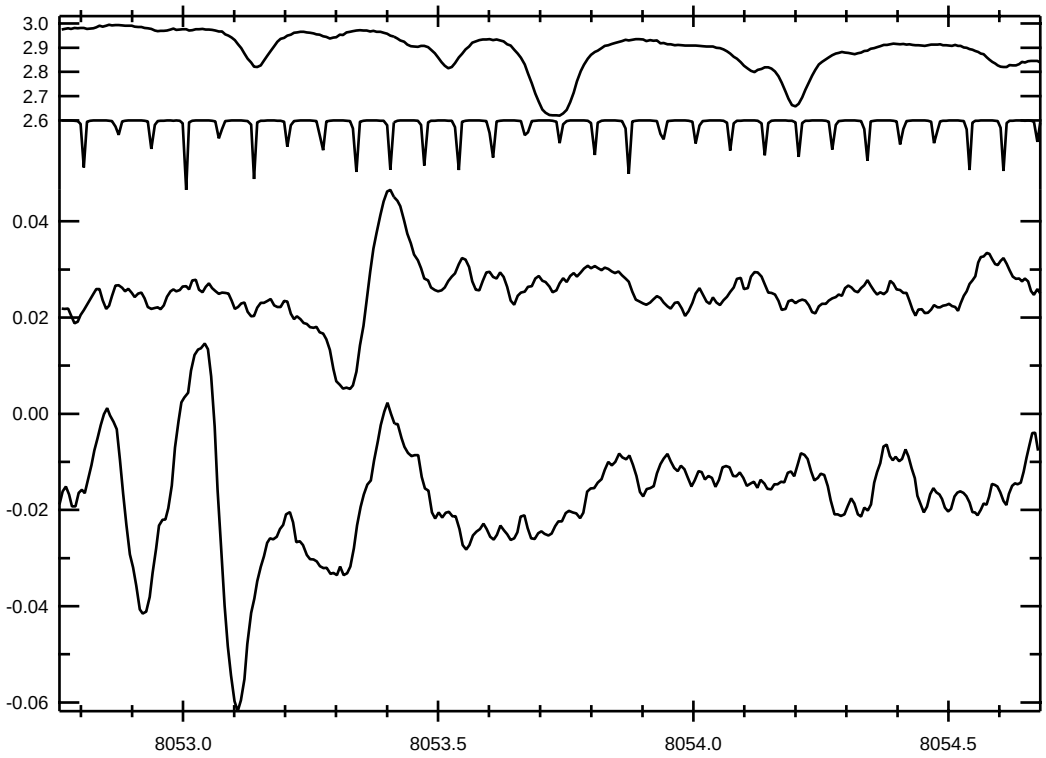
3.0
2.9
2.8
2.7
2.6
0.04
0.02
0.00
-0.02
-0.04
-0.06
8053.0
8053.5
8054.0
8054.5

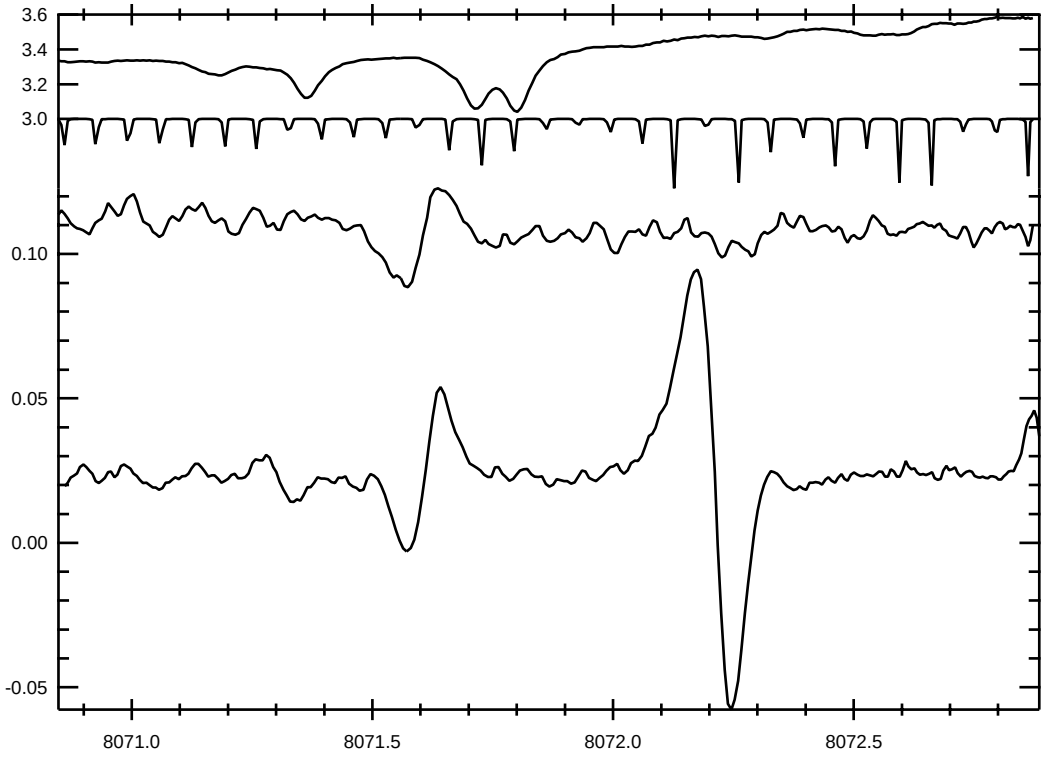
3.6
3.4
3.2
3.0
0.10
0.05
0.00
-0.05
8071.0
8071.5
8072.0
8072.5

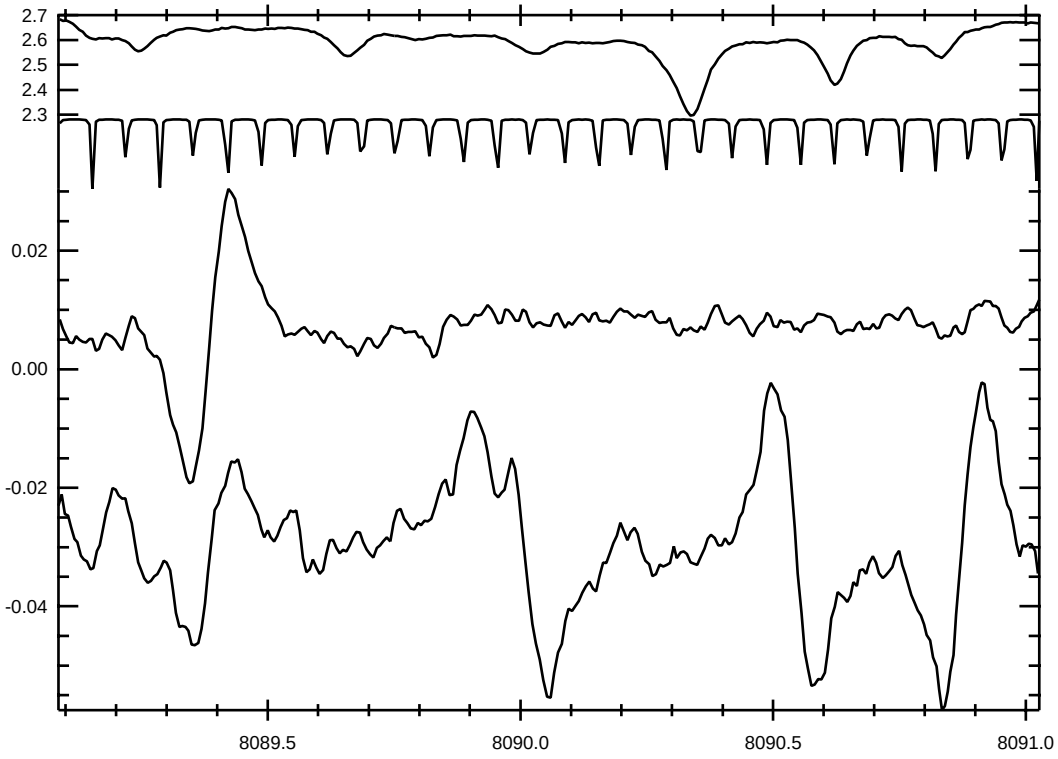
2.7
2.6
2.5
2.4
2.3
0.02
0.00
-0.02
-0.04
8089.5
8090.0
8090.5
8091.0

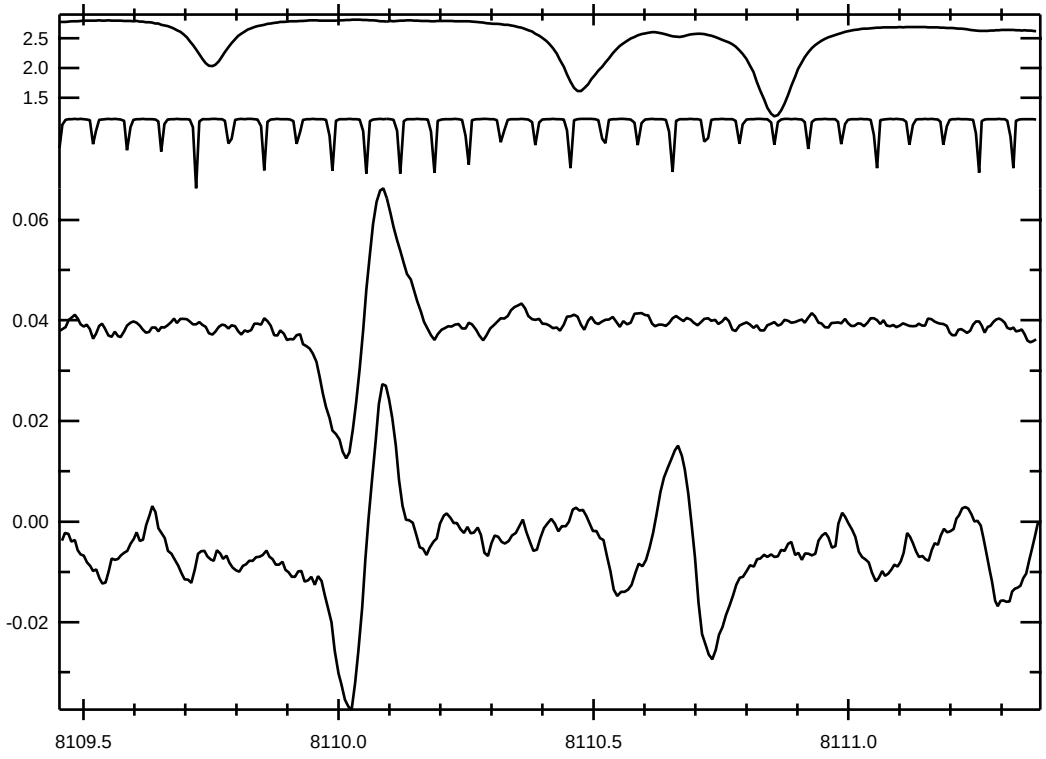
2.5
2.0
1.5
0.06
0.04
0.02
0.00
-0.02
8109.5
8110.0
8110.5
8111.0

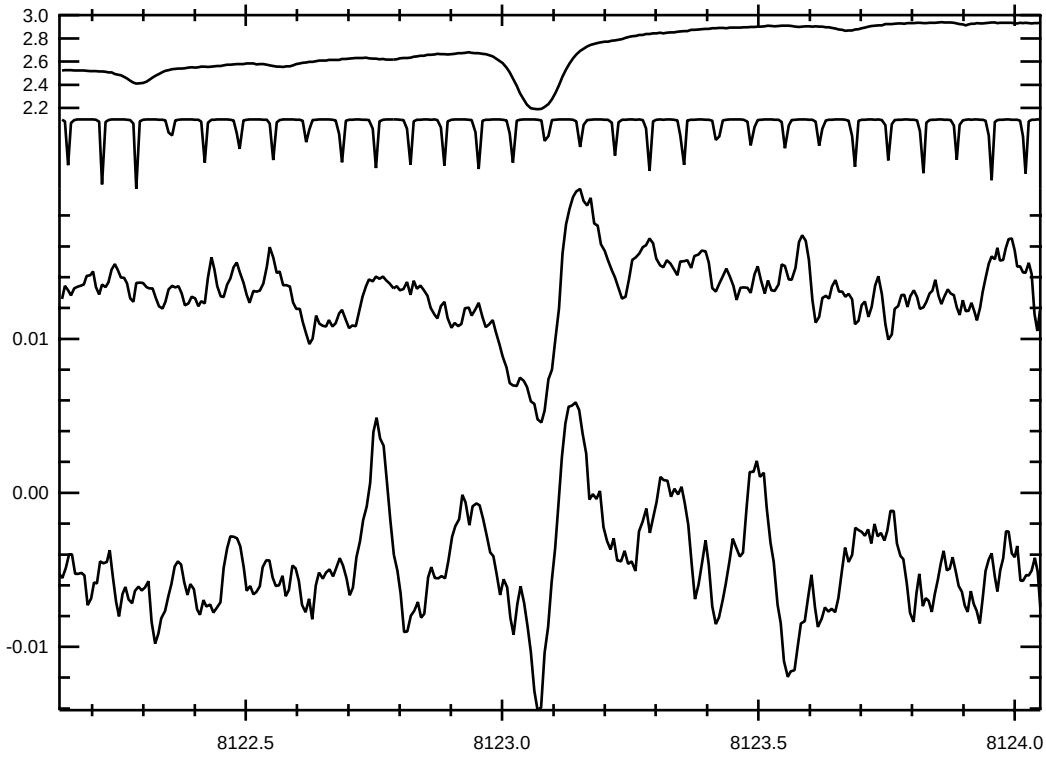
3.0
2.8
2.6
2.4
2.2
0.01
0.00
-0.01
8122.5
8123.0
8123.5
8124.0

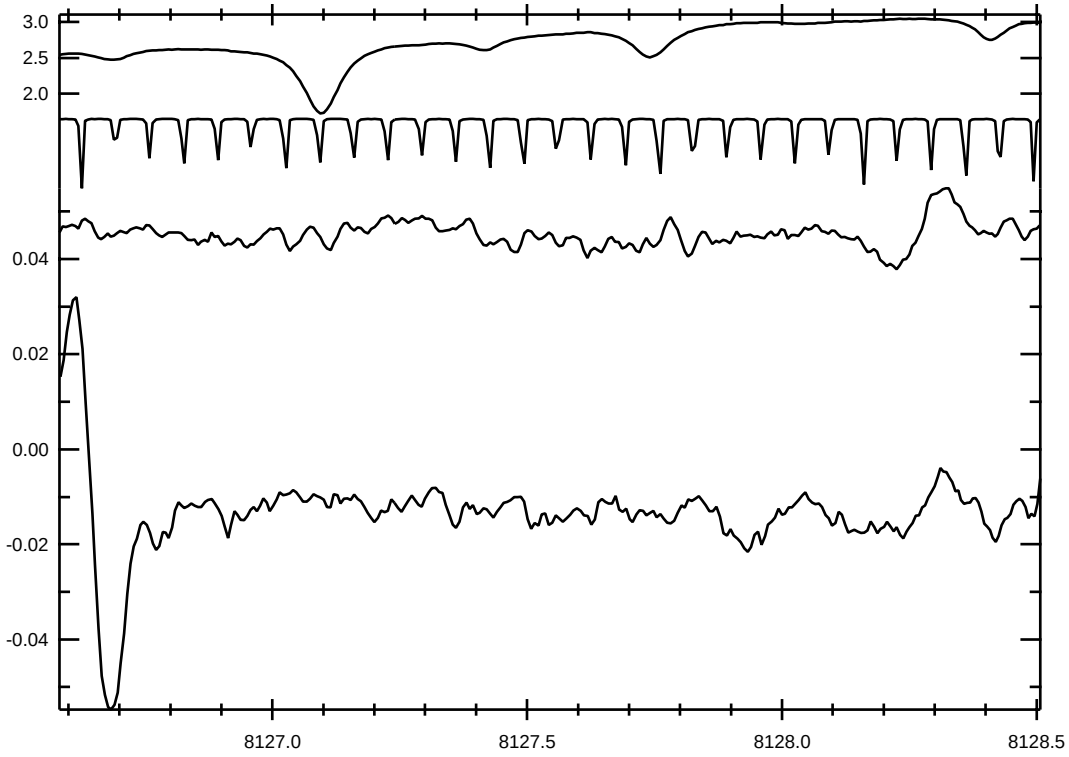
3.0
2.5
2.0
0.04
0.02
0.00
-0.02
-0.04
8127.0
8127.5
8128.0
8128.5

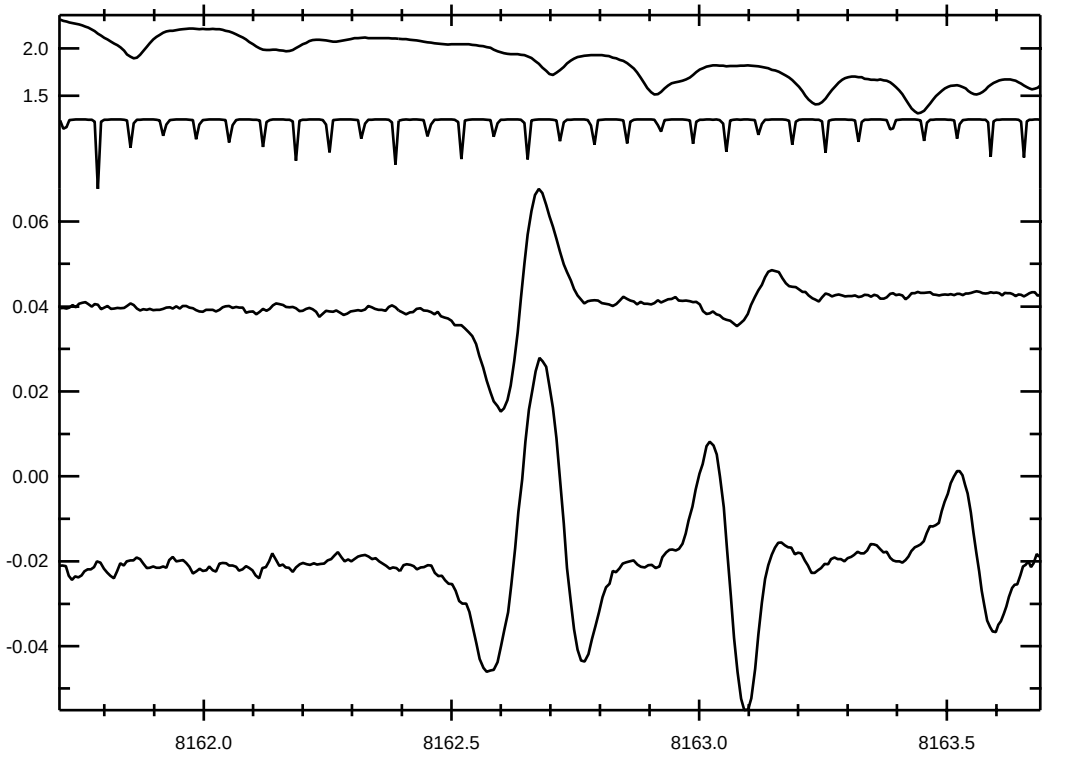
2.0
1.5
0.06
0.04
0.02
0.00
-0.02
-0.04
8162.0
8162.5
8163.0
8163.5

APPENDIX D
COMPREHENSIVE EVALUATION AND COMPILATION OF H_3^+ SPECTROSCOPY

The following preprint is the result of a collaboration between myself and Mike Lindsay, and has been submitted to the *Journal of Molecular Spectroscopy*.

Comprehensive Evaluation and Compilation of H_3^+ Spectroscopy

C. Michael Lindsay and Benjamin J. McCall

Department of Chemistry, Department of Astronomy & Astrophysics, and the Enrico Fermi Institute, The University of Chicago, Chicago, IL 60637

Since the initial detection of its infrared spectrum in 1980, there have been 17 laboratory studies of the H_3^+ spectrum, reporting 895 transitions from a variety of fundamental, overtone, combination, and hot bands. The results of these two decades of labor, however, are difficult to utilize. There is no comprehensive list of the observed H_3^+ transitions, and the literature contains errors in frequency measurement and assignment due to the inherent difficulty of the measurements and the complexity of the spectrum. This paper resolves these problems while assembling all of the data into a single source. We have reviewed all reported transitions of H_3^+ for reliability in frequency measurement and have reassigned them based on comparison with recent theoretical calculations. We have also developed a complete labeling scheme for all energy levels below 9000 cm^{-1}, which alleviates the confusion in assigning H_3^+ transitions that results from the difficulty of labeling the ro-vibrational energy levels of a molecule with such strong mixing. Our comprehensive linelist was used to produce a set of 526 experimentally determined energy levels, which facilitates a direct comparison with theoretical calculations and the prediction of the "forbidden" pure rotation spectrum of H_3^+.

I. INTRODUCTION

H_3^+ plays important roles in many varied fields (*1*), including interstellar chemistry, the study of planetary ionospheres, and theoretical calculations of ro-vibrational energy levels of polyatomic molecules. The detailed study of H_3^+ in these fields has only been possible because of the observation of infrared transitions of H_3^+ in laboratory discharges.

The laboratory detection (*2*) of the fundamental band $\nu_2 \leftarrow 0$ of H_3^+ opened the door to the detailed study of H_3^+ in astronomical sources. In dense interstellar clouds, spectra of H_3^+ have not only confirmed the general picture of ion-neutral chemistry, but also enabled measurements of the physical conditions in the clouds (*3, 4*). In diffuse clouds, H_3^+ has been observed (*5*) to be far more abundant than predicted by chemical models. H_3^+ has also been observed in emission from several planetary ionospheres (*6–9*) and has been used to image the plasma activity of the Jovian ionosphere (*10*).

The continued lab work on other vibrational bands of H_3^+ has enabled a detailed comparison with theoretical predictions of ro-vibrational energy levels from variational calculations. The variational approach is particularly well suited to H_3^+ because this simple system (consisting of only three protons and two electons) is amenable to detailed calculations.

Both astronomical spectroscopy and theoretical calculations of H_3^+ have advanced to the point where the quality of the existing laboratory database may soon hinder their progress. The state-of-the-art infrared spectrometers on large telescopes (*11*) have now achieved resolving powers of $R \approx 75,000$ (corresponding to a resolution of ≈ 0.03 cm^{-1} at 4 μm). Soon, this resolution may approach the precision of the existing laboratory data, and the ability of astronomers to accurately measure Doppler shifts (which measure the velocities of molecular clouds and the motions of planetary ionospheres) will be impeded. On the computational side, *ab initio* calculations have produced highly accurate potential energy surfaces for H_3^+ which take into account adiabatic and non-adiabatic corrections to the Born-Oppenheimer approximation, as well as relativistic corrections (*12–14*). Variational calculations of energy levels using these potentials are said to have an accuracy of a few hundredths of a wavenumber (*15*). Increasingly accurate laboratory frequencies (as well as reliable assignments of spectral lines) are essential to evaluate the quality of the newest theoretical calculations.

In order to provide transition frequencies of H_3^+ to theorists and astronomers, 17 laboratory spectroscopic studies (*2, 16–31*) have been performed over the past two decades, resulting in the observation of over 800 different transitions. These experiments have probed a wide range of rotational and vibrational states in both emission and absorption using several different experimental techniques. The job of the laboratory spectroscopists has been a difficult one — many of the observations have been performed at the limits of the sensitivity, making the frequency measurements difficult. The assignment of H_3^+ transitions also poses a formidable task, due to the strong mixing between ro-vibrational levels. Despite the best efforts of the spec-

troscopists, the literature still contains errors in frequencies as well as assignments.

Because the precision of theoretical and astronomical work is approaching that of the laboratory work, it is now important to correct these problems and produce a convenient and reliable collection of the laboratory data. In this work, we have re-assigned all of the observed transitions, scrutinized the frequency measurements, and compiled a comprehensive list of transitions. Using this linelist, we have also calculated a set of experimentally determined energy levels for direct comparison with theory. This paper is intended to provide a convenient summary of H_3^+ laboratory spectroscopy and replaces the outdated lists of Kao *et al.* (*32*), Majewski *et al.* (*27*), and Dinelli *et al.* (*33*).

II. BACKGROUND

II.1. Theoretical background

The quantum numbers, symmetry restrictions, energy level structure, and selection rules for H_3^+ have been discussed in detail elsewhere (*34,35*). Here we provide a brief discussion of the basic concepts needed to understand the ro-vibrational spectroscopy of the ground electronic state of H_3^+.

II.1.1. Quantum Numbers

The total angular momentum (F) and the parity ($\pm$) are the only completely rigorous quantum numbers of any molecule, as a consequence of the isotropy and inversion symmetry of free space. For H_3^+, the total angular momentum F is the vector sum of the total nuclear spin angular momentum I and the angular momentum associated with the motion of the nuclei J. H_3^+ contains three spin 1/2 protons, so I is either 1/2 (referred to as *para*) or 3/2 (*ortho*). Because the interaction between the nuclear spin and nuclear motion is extremely weak, I and J can be considered good quantum numbers, along with $\pm$.

In addition to these good quantum numbers, there are several approximately good quantum numbers which help us understand the behavior of H_3^+ at low energies. These include v_1 and v_2, which specify the number of quanta in the ν_1 and ν_2 vibrational modes, as well as the vibrational angular momentum ℓ (associated with the degenerate ν_2 mode) which takes values of v_2, v_2-2, ..., $-v_2+2$, or $-v_2$.

For most molecules, the projection of J onto the molecular symmetry axis (k) is a good quantum number. In H_3^+, however, there is a near degeneracy for levels with the same $|k-\ell|$ as a result of the form of the Coriolis interaction and the values of the B and C rotational constants.[1] These levels mix strongly by the ℓ-resonance term, and it becomes useful to define a new quantum number $g \equiv k-\ell$ (*37*), which can be thought of as the portion of the projection of J on the molecular axis that is due to the rotation of the molecular frame. Because the energy does not depend on the the sign of g, $G \equiv |g|$ is usually used. G is a reasonably good quantum number at low energies.

II.1.2. Symmetry Restrictions and Energy Level Structure

The Pauli principle requires the total wavefunction to be antisymmetric with respect to (12) permutation of any two protons and symmetric upon cyclic permutation (123) of all three protons (*i.e.* the total wavefunction must belong to the A_2 representation). This requirement imposes a relationship between the nuclear spin modification and the quantum number G: when $I=3/2$, only $G=3n$ levels (and when $I=1/2$, only $G=3n\pm1$ levels) have the proper symmetry. Additionally, certain $G=0$ levels (most notably the $J=$ even and $G=0$ in the ground vibrational state) do not satisfy the symmetry requirement and therefore do not exist.

The energy level structure of H_3^+ is similar to that of a normal oblate symmetric top (when plotted versus G rather than k) except that certain levels come in pairs. These pairs are due to the two ways of forming the same G with different values of k and ℓ. Energy level diagrams for the ground and $v_2=2, \ell=2$ vibrational states are plotted in Figure 1.

II.1.3. Selection Rules

We first consider the electric dipole selection rules for the good quantum numbers I, J, and $\pm$. Because the dipole operator $\hat{\mu}$ does not operate on the nuclear spin wavefunctions, the nuclear spin must not change during a radiative transition, and thus the selection rule for I is $\Delta I=0$. The total angular momentum F must obey the "triangle rule" for angular momentum addition [as $\hat{\mu}$ is a tensor of rank one and transforms as the spherical harmonics $Y_{1,0}$ and $Y_{1,\pm1}$ (*38*)], and thus $\Delta F=0$ or ±1, and $0 \nleftrightarrow 0$. Since $\Delta I=0$, the "triangle rule" also applies to J: $\Delta J=0$ or ±1, and $0 \nleftrightarrow 0$. The selection rule for the parity can be obtained by considering that the matrix elements of the dipole operator, $\langle\psi_f|\hat{\mu}|\psi_i\rangle$, must be totally symmetric. Since $\hat{\mu}$ changes sign with the inversion operation ($\vec{r} \rightarrow -\vec{r}$), the parity of the initial and final wavefunctions must be different ($+ \leftrightarrow -$).

The selection rule for g can be found by examining the symmetry of the wavefunctions (*34*) with respect to the cyclic permutation (123):

$$(123)|J,k,\ell\rangle = e^{\frac{2\pi i}{3}(k-\ell)}|J,k,\ell\rangle \qquad [1]$$

Combining this with the required invariance of the transition dipole moment matrix elements with respect to (123), we see that

$$(123)\langle J',k',\ell'|\hat{\mu}|J'',k'',\ell''\rangle = e^{\frac{2\pi i}{3}\{(k''-\ell'')-(k'-\ell')\}}\langle J',k',\ell'|\hat{\mu}|J'',k'',\ell''\rangle \qquad [2]$$

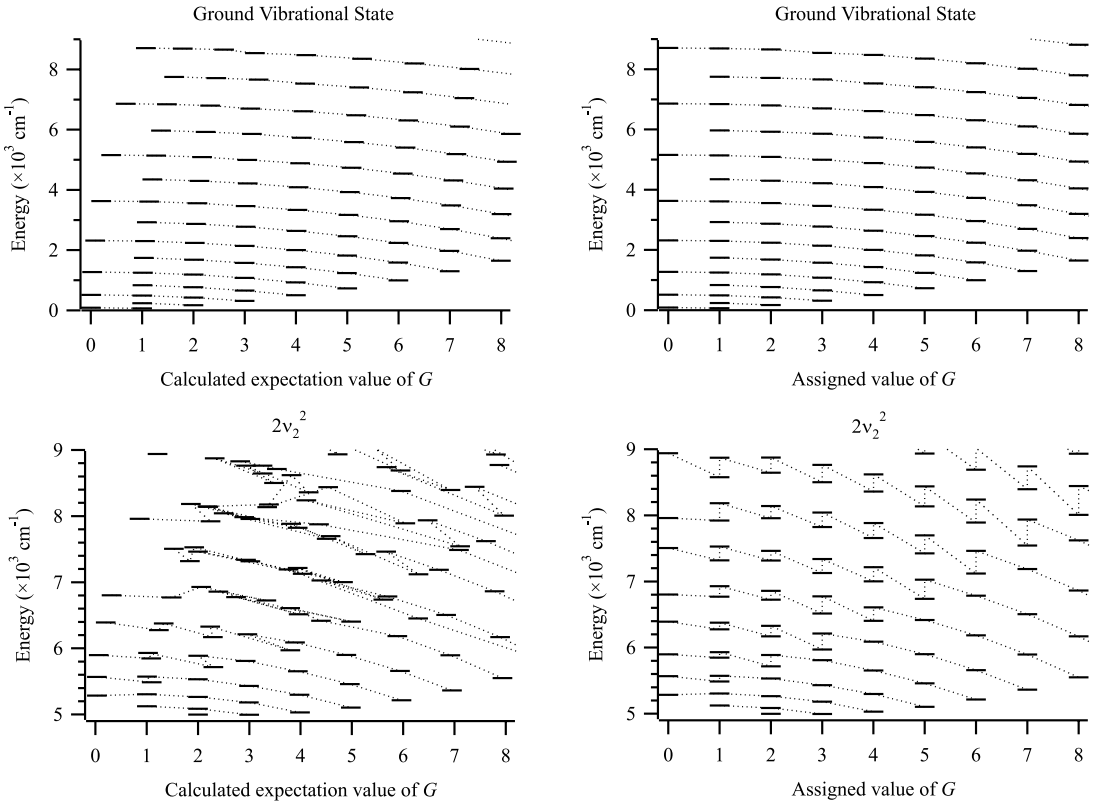

FIG. 1. Energy level diagrams of H_3^+ for the ground vibrational state (top two plots) and the $\nu_2 = 2, \ell = 2$ vibrational state (lower plots). [Dashed lines connect levels with the same J.] On the two left plots, Watson's calculated energy levels are plotted against the expectation values of G (see Section 3.1 for comments on this calculation). On the right plots, the same energy levels are plotted versus our assigned values of G, presented in Table 3. Before relabeling, the levels in the ground state look much like a classic oblate symmetric top with a small distortion in G at higher energy. The excited vibrational states are highly perturbed, and this mixing is the reason for many of the mislabeled transitions the literature. Once the G values are assigned, the energy level diagram looks relatively well behaved. Similar figures for every vibrational state below 9000 cm^{-1} are available online (*39*).

which is only invariant when $\Delta g = (k''-\ell'')-(k'-\ell') = 3n$.

The possible selection rules for k (the projection of J) can be derived from the "triangle rule" to be $\Delta k = 0$ or ± 1. Because the parity is linked to k by the symmetry of the wavefunctions (*34*) with respect to the inversion (E^*) operation

$$E^*|J,k,\ell\rangle = (-1)^k|J,k,\ell\rangle \qquad [3]$$

and because the parity selection rule is $+ \leftrightarrow -$, Δk must be odd, restricting its selection rule to $\Delta k = \pm 1$.

The selection rule for ℓ depends on those of g and k:

$$\begin{aligned} \Delta g = g' - g'' = (k' - \ell') - (k'' - \ell'') = \Delta k - \Delta \ell \\ \Delta \ell = \Delta k - \Delta g = (\pm 1) - (\pm 3n) \\ \Delta \ell \neq 3n. \end{aligned} \qquad [4]$$

For transitions with $\Delta\ell = \pm 1$ (*e.g.*, the $\Delta\nu_2 = 1$ fundamental and hot bands) Δg must be 0, and for transitions with $\Delta\ell = \pm 2$ ($\Delta v_2 = 2$ overtone bands) Δg must be ± 3.

It should be kept in mind that the selection rules for g, k, and ℓ are not rigorous, because these quantum numbers are not rigorous. For example, the $\Delta k = \pm 1$ selection rule can break down due to mixing, but $\Delta k =$ odd is maintained because it is based on the parity, which is a rigorously good quantum number.

Finally, we consider the selection rules (which are only approximate) for the vibrational quantum numbers. The ν_1 normal mode is totally symmetric and therefore has the selection rule[2] $\Delta v_1 = 0$. For the symmetry allowed ν_2 mode, the selection rule $\Delta v_2 = \pm 1$ holds in the approximation of using harmonic oscillator wavefunctions and only the first order term in the Taylor series expansion of $\hat{\mu}$. Because the H_3^+ potential and dipole operator are very

anharmonic, this is a poor approximation, and transitions with $\Delta v_2 > 1$ have reasonable intensity.

II.1.4. Effects of Mixing

Levels with the same good quantum numbers [J, I, and $\pm$] can mix with one another. The strength of the mixing is inversely proportional to the energy separation between the two unmixed levels, so that strong mixing is increasingly common at higher energies where the levels tend to be more closely spaced. When mixing occurs, the energy levels are shifted from the oblate symmetric top energy pattern and the approximate quantum numbers break down. The mixed states can no longer be described by single integral values of g, ν_1, ν_2, and ℓ, but can be described by their expectation values, which are linear combinations of the quantum numbers of the unmixed values. The extent of the mixing can be visualized by plotting the energy versus the expectation values of the quantum numbers (see Figures 1 and 2). When the energy levels are not significantly mixed, the expectation values of their quantum numbers will be nearly integral.

The selection rules for mixed levels incorporate the selection rules of each of the levels involved in the mixing. A consequence of this mixing is the appearance of additional lines in the spectrum — forbidden transitions effectively borrow intensity from allowed ones. One example of these forbidden transitions is the pure rotational transitions, which obey the selection rule $\Delta\ell = 0$. These transitions are weak, but should be observable experimentally (see Section 4.1). Each transition's intensity will depend on the magnitude of mixing, and must be treated on a line by line basis. The topic of ro-vibrational level mixing and the breakdown of the approximate quantum numbers is discussed further in Section 3.1.

II.2. Previous laboratory work

Many infrared absorption and emission studies of H_3^+ have been performed in the laboratory over the last two decades to characterize the ro-vibrational spectrum and energy levels of H_3^+ (see (*40*) for a recent review). These works were considered in our analysis and in this section we briefly summarize each of them (see Table 1). It should be noted that the predissociation spectrum of H_3^+ has also been measured in the laboratory (*41–43*) and is the subject of a recent review (*44*). This subject, however, lies outside the scope of this paper.

The infrared spectrum of H_3^+ was initially sought after by Herzberg in the mid 1960's when it became clear that H_3^+ did not possess a stable excited electronic state (*45*). In the course of this work he observed a group of emission lines near 3600 cm^{-1} in hydrogen hollow cathode discharges. These were eventually identified by Watson as emission lines of neutral H_3 which are produced in excited states after dissociative recombination of H_5^+ with electrons. It wasn't until 1980 that Oka (*2*) observed in absorption the first 15 lines of the ν_2 fundamental of H_3^+ between 2450 and 2950 cm^{-1}. His success was enabled by the development of the broadly tunable difference frequency (DF) spectrometer by Pine (*46*) and the use of the long positive column discharge by Woods (*47*). In his search he scanned roughly 500 cm^{-1}, a feat only possible with the DF laser. To increase the sensitivity, he frequency modulated the radiation and achieved a signal-to-noise ratio of ~ 30 for the strongest H_3^+ lines. In the first studies, a liquid nitrogen cooled positive column discharge was used to produce H_3^+ in a pure hydrogen discharge.

In the year that followed, Oka (*16*) was able to extend his observations to higher J levels (to a total of 30 lines) by studying a warmer, ice-cooled discharge. By 1984, the frequency coverage was expanded by making adjustments to the DF laser and by using diode lasers. Two major advances in sensitivity also occured. It was found that modulating the discharge current (concentration modulation (*48*)) or applying an AC field across a positive column discharge (velocity modulation (*49*)) could substantially improve the sensitivity. The combination of these improvements enabled Watson, Oka, and coworkers (*17*) to observe an additional 16 $\nu_2 \leftarrow 0$ transitions, bringing the total up to 46.

All of the observed lines up to this point were from levels with $J \leq 5$, and it was expected that large perturbations would occur at higher J between the ν_1 and ν_2 states. With this in mind, Majewski *et al.* (*18*) in Ottawa constructed a high pressure hollow cathode discharge coupled to a Fourier transform infrared (FTIR) spectrometer to observe the emission of H_3^+ in a hydrogen discharge. With an ingeniously designed hollow cathode discharge and a pressure discrimination method, this technique turned out to be very effective, nearly tripling the number of observed lines and probing levels up to $J' = 10$. Many perturbations were indeed observed, and they provided a new test for theoretical calculations. Many additional emission features were recorded around 2 μm. At the time, the authors could not rule out the possibility that the 2 μm lines were due to Rydberg H_2 or H_3 neutral transitions, and consequently the lines were not reported.

In 1987 Trafton *et al.* (*6*) and in 1988 Drossart *et al.* (*7*) stumbled upon a rich set of unidentified emission features at 2 μm while observing H_2 emission in Jupiter. This prompted the Ottawa group to revisit the 2 μm lines observed with the FTIR emission apparatus, and after a month, Watson assigned many of the FTIR and Jovian features to the $2\nu_2^2 \leftarrow 0$ band of H_3^+. The new-found confidence in these assignments was based upon the latest *ab initio* calculations of Miller and Tennyson (*50*) as well as the yet-to-be published work on the $2\nu_2^2 \leftarrow \nu_2$ hot band by Bawendi *et al.* in Chicago (see below). Once assigned, 47 lines of the $2\nu_2^2 \leftarrow 0$ band were reported from the FTIR studies (*19*).

TABLE 1
Summary of the laboratory spectroscopic studies of H_3^+.

Label	cm^{-1}	Observed	Assignment	Technique[a]	Reference
Oka80	2460-2800 2450-2900†	15 lines	$\nu_2 \leftarrow 0$	ℓ–N_2 cooled positive column, DF laser, FM detection	T. Oka, *Phys. Rev. Lett.* **45**, 531-534, (1980).
Oka81	2450-3030†	30 lines (15 new)	$\nu_2 \leftarrow 0$	ℓ–N_2 and ice-water cooled positive column, DF laser, FM detection	T. Oka, *Phil. Trans. R. Soc. Lond. A* **303**, 543-549(1981).
Wat84	2210-3030†	46 lines (16 new)	$\nu_2 \leftarrow 0$	ℓ–N_2 cooled positive column, DF and diode lasers, VM and CM detection	J. K. G. Watson, S. C. Foster, A. R. W. McKellar, P. Bernath, T. Amano, F. S. Pan, M. W. Crofton, R. S. Altman, and T. Oka, *Can. J. Phys.* **62**, 1875-1885 (1984).
Maj87	1800-3300	113 lines (67 new)	$\nu_2 \leftrightarrow 0$	Water cooled, high-pressure hollow cathode, FTIR emission, and diode laser absorption	W. A. Majewski, M. D. Marshall, A. R. W. McKellar, J. W. C. Johns, and J. K. G. Watson, *J. Mol. Spectrosc.* **122**, 341-355, (1987).
Maj89	4500-5100	47 new lines	$2\nu_2^2 \rightarrow 0$	Water cooled, high-pressure hollow cathode, FTIR emission	W. A. Majewski, P. A. Feldman, J. K. G. Watson, S. Miller, and J. Tennyson, *Astrophys. J.* **347**, L51-L54, (1989).
Nak90	2400-2800	12 re-measured	$\nu_2 \leftarrow 0$	Water cooled hollow cathode, FTIR absorption	T. Nakanaga, F. Ito, K. Sugawara, H. Takeo, and C. Matsumura, *Chem. Phys. Lett.* **169**, 269-273 (1990).
Baw90	2080-2950†	14 new lines 70 new lines 14 new lines 21 new lines 136 new lines	$\nu_2 \leftarrow 0$ $2\nu_2^2 \leftarrow \nu_2$ $2\nu_2^0 \leftarrow \nu_2$ $\nu_1 + \nu_2 \leftarrow \nu_1$ unassigned	ℓ–N_2 cooled positive column, DF laser, VM detection	M. G. Bawendi, B. D. Rehfuss, and T. Oka, *J. Chem. Phys.* **93**, 6200-6209 (1990).
Xu90	4550-6000†	34 lines (7 new)	$2\nu_2^2 \leftarrow 0$	ℓ–N_2 cooled positive column, DF laser, VM detection	L.-W. Xu, C. M. Gabrys, and T. Oka, *J. Chem. Phys.* **93**, 6210-6215 (1990).
Lee91	6860-6900†	4 new lines	$3\nu_2^1 \leftarrow 0$	ℓ–N_2 cooled positive column, diode laser, VM detection	S. S. Lee, B. F. Ventrudo, D. T. Cassidy, T. Oka, S. Miller, J. Tennyson, *J. Mol. Spectrosc.* **145**, 222-224 (1991).
Xu92	2400-3300†	9 new lines 21 new lines 30 new lines 13 new lines 89 new lines	$\nu_1 \leftarrow 0$ $\nu_1 + \nu_2 \leftarrow \nu_2$ $\nu_2 \leftarrow 0$ $2\nu_2^2 \leftarrow \nu_2$ unassigned	ℓ–N_2 cooled positive column, DF laser, VM detection	L.-W. Xu, M. Rösslein, C. M. Gabrys, and T. Oka, *J. Mol. Spec.* **153**,726-737 (1992).
Ven94	6800-7270†	15 lines (11 new)	$3\nu_2^1 \leftarrow 0$	ℓ–N_2 cooled positive column, diode laser, VM detection	B. Ventrudo, D. T. Cassidy, Z. Y. Guo, S. Joo, S. S. Lee, and T. Oka, *J. Chem. Phys.* **100**, 6263-6266 (1994).
Uy94	2690-3580†	75 lines (37 new)	$\nu_2 \leftarrow 0$	Water cooled positive column, DF laser, VM detection	D. Uy, C. M. Gabrys, M.-F. Jagod, and T. Oka, *J. Chem. Phys* **100**, 6267-6274 (1994).
Maj94	1800-2550 2900-5000	52 new lines 9 new lines 12 new lines 31 new lines 16 new lines 2 new lines 1 new line	$\nu_2 \rightarrow 0$ $2\nu_2^2 \rightarrow 0$ $\nu_1 + \nu_2 \rightarrow \nu_1$ $2\nu_2^2 \rightarrow \nu_2$ $2\nu_2^0 \rightarrow \nu_2$ $3\nu_2^3 \rightarrow \nu_2$ $3\nu_2^3 \rightarrow 2\nu_2^2$	Water cooled, high-pressure hollow cathode, FTIR emission	W. A. Majewski, A. R. W. McKellar, D. Sadovskiĭ, and J. K. G. Watson, *Can. J. Phys.* **72**, 1016-1027 (1994).
McK98	2450-2850	27 re-measured	$\nu_2 \leftarrow 0$	Refrig. methanol cooled hollow cathode, FTIR absorption	A. R. W. McKellar and J. K. G. Watson, *J. Mol. Spectrosc.* **191**, 215-217(1998).
Joo00	~ 1550	1 new line	$\nu_2 \leftarrow 0$	ℓ–N_2 cooled positive column, diode laser, VM detection	S. Joo, F. Kühnemann, M.-F. Jagod, and T. Oka, *The Royal Society Discussion Meeting on Astronomy, Physics and Chemistry of H_3^+*, London, February 9-10, (2000) (poster).
McC01	7850-8170	28 new lines 2 new lines	$\nu_1 + 2\nu_2^2 \leftarrow 0$ $2\nu_1 + \nu_2 \leftarrow 0$	ℓ–N_2 cooled positive column, diode laser, VM detection	B. J. McCall and T. Oka, *J. Chem. Phys.* **113**, 3104-3110 (2000).
Lin01	3000-4200	6 lines (5 new) 22 lines (10 new) 5 lines (4 new) 76 lines (44 new) 4 lines (3 new) 1 new line 25 lines (9 new) 14 lines (7 new) 2 new lines 1 re-measured 3 lines (2 new) 3 lines (1 new) 6 lines (5 new)	$\nu_2 \leftarrow 0$ $\nu_1 \leftarrow 0$ $2\nu_2^0 \leftarrow \nu_2$ $2\nu_2^2 \leftarrow \nu_2$ $2\nu_2^2 \leftarrow \nu_1$ $2\nu_2^0 \leftarrow \nu_1$ $\nu_1 + \nu_2 \leftarrow \nu_2$ $\nu_1 + \nu_2 \leftarrow \nu_1$ $2\nu_1 \leftarrow \nu_1$ $\nu_1 + 2\nu_2^2 \leftarrow \nu_1 + \nu_2$ $3\nu_2^3 \leftarrow 2\nu_2^2$ $3\nu_2^1 \leftarrow 2\nu_2^0$ unassigned	ℓ–N_2 cooled positive column, CCL, VM detection	C. M. Lindsay, R. M. Rade, Jr., and T. Oka, *J. Mol. Spectrosc.* XXX XXX-XXX (2001)**Previous paper**

[a] Abbreviations used in this column are defined as follows: FM = frequency modulation VM = velocity modulation, DF = difference frequency, CM = concentration modulation, and CCL = color center laser.
† Region was not scanned continuously.

Quite apart from the work in Chicago and Ottawa, Nakanaga and coworkers in 1990 successfully performed the first FTIR *absorption* spectroscopy of molecular ions, including 10 fundamental transitions of H_3^+ (*20*). While all of these lines had been observed initially 9 years earlier, this work represented the first accurate measurement of the relative absorption intensities.

After several years of refining their technique of DF laser/velocity modulation spectroscopy of carbocations (*51*) and introducing the helium dominated positive column discharge, the Chicago group revisited H_3^+ with a tremendous increase in sensitivity. The next 5 years brought 7 experiments which substantially increased the number of probed levels. Initially, Bawendi *et al.* (*21*) observed lines of the $2\nu_2^2 \leftarrow \nu_2$, $2\nu_2^0 \leftarrow \nu_2$, and $\nu_1 + \nu_2 \leftarrow \nu_1$ hot bands as well as 14 new fundamental lines and 136 lines which they could not confidently assign. Shortly after, Xu *et al.* (*22*) observed the $2\nu_2^2 \leftarrow 0$ band, though they only observed 7 lines not covered in Majewski's work. Two years later, Xu *et al.* (*24*) reported the $\nu_1 \leftarrow 0$ and $\nu_1 + \nu_2 \leftarrow \nu_2$ forbidden bands, as well as more transitions from the $\nu_2 \leftarrow 0$ and $2\nu_2^2 \leftarrow \nu_2$ bands, and additional unassignable lines. Advances in external cavity near infrared diode lasers enabled the scanning to be extended to higher frequency allowing the second overtone, $3\nu_2^1 \leftarrow 0$, to be observed (*23, 25*). During this period a diode laser was also used to measure the lowest frequency line to date (the $\nu_2 \leftarrow 0$ $P(12,12)$ at 1546.901 cm^{-1}), though this was only reported recently (*29*). Finally, Uy and coworkers (*26*) recorded an H_3^+ spectrum with a water cooled cell and observed highly excited rotational levels of the ν_2 fundamental, up to $J' = 16$.

With the large amount of experimental data made available, Watson (*52, 27*) and, independently, Dinelli, Polyansky, and Tennyson (*53*) produced empirically fitted potentials which were used to calculate more accurate transition frequencies (see Section 4.2 for more details). All of the experimental data available at the time, as well as some newly measured FTIR emission lines (*27*), were collected and included into these calculations. These calculations proved to be essential to the understanding the unassigned lines in Bawendi's and Xu's (1992) data, which were assigned in subsequent papers (*27, 33*).

Four years later, McKellar and Watson recorded a clean broadband absorption spectrum of H_3^+ with an FTIR spectrometer. Their work was similar to that of Nakanaga *et al.* 8 years earlier, but achieved about a factor of 10 improvement in signal-to-noise ratio enabling them to observe 27 lines of the ν_2 fundamental. This beautiful spectrum is published in its entirety in a Letter (*28*).

No new data were reported until the year 2000 when McCall and Oka (*30*) recorded lines from the $\nu_1 + 2\nu_2^2 \leftarrow 0$ and $2\nu_1 + \nu_2 \leftarrow 0$ combination bands using an external cavity diode laser and the velocity modulation/positive column discharge technique. Thirty lines were observed from these two bands, probing the highest vibrational states observed to date.

Most recently, Lindsay and coworkers (*31*) used a computer controlled color center laser (CCL) spectrometer to continuously scan H_3^+ from 3000–4200 cm^{-1}. The improved sensitivity of their spectrometer and the hottest discharge to date enabled them to study very high ro-vibrational levels. A total of 96 new transitions were observed from a variety of hot, overtone, fundamental, and forbidden bands—some probing ro-vibrational levels in the vicinity of the barrier to linearity.

A total of 895 unique transitions of H_3^+ have been reported over the past 21 years, probing every vibrational state below the barrier to linearity (except $3\nu_1$ and $4\nu_2$). Many of these transitions have been recorded multiple times by multiple techniques with multiple sensitivities. This work was only possible with substantial advancements to the sensitivity of the experiments, which improved dramatically over the last 21 years. It is interesting to note that if the sensitivity of the latest studies were applied to the transitions observed by Oka in 1980, the signal-to-noise ratio would be 3000-6000 — a two order of magnitude improvement over the initial spectrum!

III. ANALYSIS AND RESULTS

In this section we explain our efforts to assign approximate quantum numbers to every energy level below 9000 cm^{-1}, evaluate the assignment and quality of every reported laboratory absorption and emission transition, and determine energy levels from the experimental transitions. Most of the results of this work are tabulated here in print, but an electronic version of the complete work (tables and figures) is available online (*39*).

III.1. Labeling of ro-vibrational levels below 9000 cm^{-1}

Much of the confusion in "assigning" transitions in the literature is based upon energy level labeling and not the actual assignment of the transitions. This distinction is important — most of the assignments (that is the identification of an observed transition based on a particular calculated transition between two levels with a similar frequency and intensity) were correctly made, but there has been confusion in the naming of the transition and energy levels which were involved in the transition. Before each transition can be labeled, every energy level must be given a unique label. Below the barrier to linearity, the approximate quantum numbers G, v_1, v_2, and ℓ are reasonably good and can be used to label ro-vibrational energy levels. Many of these levels mix, and the resulting levels have character of two or more levels with different values of the approximate quantum numbers. In most cases this mixing is not complete, and each mixed level can be labeled by the quantum numbers of the dominant unmixed level.

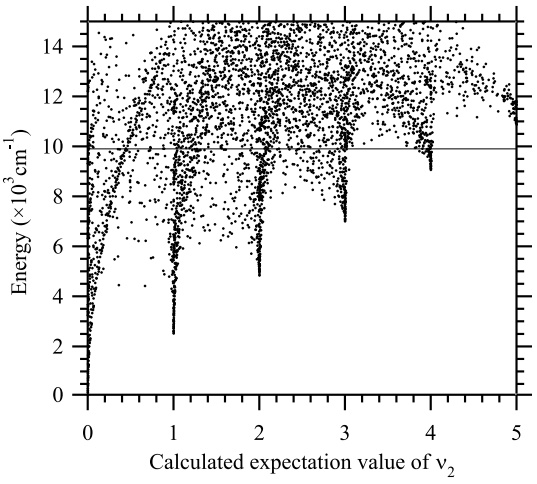

FIG. 2. Ro-vibrational energy of H_3^+ plotted against the expectation value of the approximate quantum number v_2. Energies and expectation values (see Section 3.1 for comments on this calcluation) are from the calculations of Watson (*27, 54*). The solid line is drawn at the barrier to linearity. This plot shows that at lower energies, v_2 describes the system quite well, but at higher energies, the amount of mixing increases to the point where the value of this approximate quantum number has little meaning.

Theoretical calculations of energy levels provide only the quantum numbers J, parity, and (in most cases) I — the assignment of the approximate quantum numbers to each level must be done manually. This task would be nearly impossible without the help of the expectation values calculated by Watson (*54*). Even with the expectation values, this task is not easy. One can appreciate the difficulty in applying labels by examining the energy dependence of various expectation values. In Figure 2 the energy is plotted versus the expectation value of v_2. At energies close to each band origin, the values of $\langle v_2 \rangle$ are very close to integers. As the energy approaches 10,000 cm^{-1} however, many levels have expectation values in between the integer values, as a result of mixing. Likewise, we can look at the expectation values of G (Figure 1). While well behaved in the ground vibrational state (top left), G becomes extremely mixed at higher vibrational states (bottom left). By carefully considering the energy, the expectation values of G, v_1, v_2, and ℓ, and the values of J, I, and parity of all of the levels simultaneously, it is possible to assign integral values of G, v_1, v_2, and ℓ for each energy level (Figure 1 right, top and bottom). We have produced energy level diagrams similar to those in Figure 1 for all vibrational states below 9000 cm^{-1}, and these are available online (*39*). Please note that these calculated expectation values are only approximate and were performed with the intention of forming a qualitative picture of the nature of the energy levels (*54*).

The five quantum numbers J, G, v_1, v_2, and ℓ are not sufficient to uniquely label each level. For levels with $\ell \neq 0$ and $(J - |\ell|) \geq G \geq 1$ there are two ways to form the same G for different values of k. Take as an example a level where $\ell = 1$ and $J = 2$. Since $G \equiv |k - \ell|$, both $k = 0$ and $k = 2$ make $G = 1$. These levels always differ in energy, and we have distinguished them by assigning a "u" and an "l" to the upper and lower energy level, respectively (*30*). In the earliest papers, these levels were designated by "I" or "II" (*2, 16*) or later with "+" or "−". Also used was the U notation initially defined by Watson (*34*) as +1 for "u" levels and −1 for "l" levels of the ν_2 vibrational state. Later, Miller and Tennyson (*50*) extended the notation to arbitrary v_2 by redefining $U = +|\ell|$ for "u" and $U = -|\ell|$ for "l" levels. We have abandoned these other notations due to the confusion with the value of the real quantum numbers ℓ and parity. We instead use the symbol (*40*)

$$(J, G)\{u|l\} \qquad [5]$$

to label individual rotational levels within the vibrational state

$$v_1\nu_1 + v_2\nu_2^{|\ell|} \quad \text{or} \quad v_1 v_2^{|\ell|}. \qquad [6]$$

A small number of levels are so badly mixed that the assignment of their approximate quantum numbers is almost arbitrary. In some cases the expectation value of one quantum number suggests an assignment to one vibrational state, while another suggests a different vibrational state. Table 2 lists all of the badly mixed levels below 9000 cm^{-1}. Above 9000 cm^{-1}, the density of states becomes quite large and severe mixing occurs for many levels with $J \gtrsim 5$. For these levels, it probably isn't useful to assign approximate quantum numbers. It should still be possible, however, to label low J levels with approximate quantum numbers because their density of states is much lower and the mixing will be less complete. At very high energy, even the low J levels will mix and their approximate quantum numbers will eventually fail. When

TABLE 2

Heavily mixed ro-vibrational levels of H_3^+ below 9000 cm^{-1}. Each row corresponds to a set of mixed levels.

$\nu_1 + 2\nu_2^0$ (5,4)	$\nu_1 + 2\nu_2^0$ (5,2)	$\nu_1 + 2\nu_2^2$ (5,2)l	$\nu_1 + 2\nu_2^2$ (5,2)u
$3\nu_2^3$ (6,2)l	$3\nu_2^1$ (6,2)u	$\nu_1 + 2\nu_2^2$ (6,3)	
$2\nu_2^2$ (7,0)	$\nu_1 + \nu_2$ (7,3)l		
$\nu_1 + \nu_2$ (7,3)u	ν_1 (7,6)		
$\nu_1 + \nu_2$ (7,5)l	$2\nu_2^2$ (7,4)u		
ν_1 (8,6)	$\nu_1 + \nu_2$ (8,3)u		
$2\nu_2^0$ (8,2)	$2\nu_2^2$ (8,2)u		
$\nu_1 + \nu_2$ (8,5)l	ν_1 (8,8)		
ν_2 (9,2)u	ν_1 (9,5)		
$2\nu_2^2$ (9,5)l	$2\nu_2^0$ (9,1)		
$2\nu_2^2$ (9,1)u	$\nu_1 + \nu_2$ (9,2)l		
$2\nu_2^0$ (9,3)	$2\nu_2^2$ (9,3)u		
ν_1 (10,5)	ν_2 (10,2)u		
$2\nu_2^0$ (10,2)	$2\nu_2^2$ (10,4)		
$\nu_1 + \nu_2$ (11,9)l	$2\nu_2^2$ (11,6)		
ν_2 (12,6)l	ν_1 (12,9)		

TABLE 3

Energy level labels and experimentally determined energy levels.

Q. N.[a] J	I	P	n	E_{calc} [b] (cm^{-1})	E_{exp} [c] (cm^{-1})	Label[d] Rot.	Vib.
1	$p-1$	64.123		64.121(00)*	(1,1)	00^0
1	$o+1$	86.959		86.960(00)*	(1,0)	00^0
2	$p+1$	169.296		169.295(04)*	(2,2)	00^0
2	$p-1$	237.350		237.356(05)*	(2,1)	00^0
3	$o-1$	315.342		315.349(04)*	(3,3)	00^0
3	$p+1$	428.009		428.018(07)*	(3,2)	00^0
3	$p-1$	494.753		494.775(07)*	(3,1)	00^0
4	$p+1$	502.023		502.032(06)*	(4,4)	00^0
3	$o+1$	516.867		516.873(07)*	(3,0)	00^0
4	$o-1$	658.698		658.720(06)*	(4,3)	00^0
5	$p-1$	728.991		729.022(07)*	(5,5)	00^0
4	$p+2$	768.451		768.476(09)*	(4,2)	00^0
4	$p-1$	833.555		833.583(08)*	(4,1)	00^0
5	$p+1$	928.943		928.965(10)*	(5,4)	00^0
6	$o+1$	995.842		995.884(05)*	(6,6)	00^0
5	$o-1$	1080.453		1080.490(08)*	(5,3)	00^0
5	$p+2$	1187.067		1187.115(10)*	(5,2)	00^0
6	$p-1$	1238.409		1238.462(11)*	(6,5)	00^0
5	$p-2$	1250.267		1250.313(10)*	(5,1)	00^0
5	$o+1$	1271.225		1271.245(10)*	(5,0)	00^0
7	$p-1$	1302.095		1302.141(09)*	(7,7)	00^0
6	$p+1$	1430.667		1430.706(11)*	(6,4)	00^0
6	$o-1$	1577.279		1577.334(09)*	(6,3)	00^0
7	$o+1$	1586.535		1586.594(08)*	(7,6)	00^0
8	$p+1$	1647.199		1647.267(12)	(8,8)	00^0
6	$p+2$	1679.734		1679.805(14)*	(6,2)	00^0
6	$p-2$	1740.834		1740.906(14)*	(6,1)	00^0
7	$p-2$	1818.077		1818.155(13)*	(7,5)	00^0
8	$p-1$	1972.727		1972.800(11)*	(8,7)	00^0
7	$p+1$	2002.387		2002.456(14)*	(7,4)	00^0
9	$o-1$	2030.535		2030.623(13)*	(9,9)	00^0
7	$o-1$	2142.025		2142.094(11)*	(7,3)	00^0
7	$p+2$	2241.910		2241.999(20)*	(7,2)	00^0
8	$o+1$	2242.117		2242.206(10)*	(8,6)	00^0
7	$p-3$	2300.773		2300.879(19)*	(7,1)	00^0
7	$o+2$	2320.309		2320.372(15)	(7,0)	00^0
9	$p+1$	2396.323		2396.426(15)	(9,8)	00^0
10	$p+1$	2451.425			(10,10)	00^0
8	$p-2$	2462.786		2462.889(15)*	(8,5)	00^0
0	$p+1$	2521.416		2521.411(05)*	(0,1)	01^1
1	$p-2$	2548.171		2548.164(11)*	(1,2)	01^1
1	$p+1$	2609.542		2609.541(05)*	(1,1)	01^1
2	$o+1$	2614.279		2614.279(11)*	(2,3)	01^1
1	$o-1$	2616.686		2616.684(05)*	(1,0)	01^1
8	$p+2$	2639.046		2639.135(17)*	(8,4)	00^0
9	$p-1$	2701.980		2702.076(13)*	(9,7)	00^0
3	$p-2$	2719.486		2719.482(12)*	(3,4)	01^1
2	$p-2$	2723.958		2723.962(06)*	(2,2)	01^1
2	$p+2$	2755.565		2755.565(04)*	(2,1)l	01^1
8	$o-1$	2775.568		2775.667(13)*	(8,3)	00^0
2	$p+3$	2790.335		2790.344(04)*	(2,1)u	01^1
2	$o-1$	2812.850		2812.857(05)*	(2,0)	01^1
10	$o-1$	2856.600		2856.725(15)	(10,9)	00^0
4	$p+3$	2863.938		2863.944(12)*	(4,5)	01^1
8	$p+3$	2868.766		2868.892(27)	(8,2)	00^0
3	$o+2$	2876.835		2876.847(06)*	(3,3)	01^1
11	$p-1$	2909.130			(11,11)	00^0
8	$p-3$	2925.302		2925.456(39)	(8,1)	00^0
3	$p-3$	2931.365		2931.366(05)*	(3,2)l	01^1
9	$o+1$	2957.195		2957.306(13)*	(9,6)	00^0
3	$p-4$	2992.421		2992.436(05)*	(3,2)u	01^1
3	$p+2$	3002.888		3002.905(05)*	(3,1)l	01^1
3	$o-2$	3025.943		3025.951(08)*	(3,0)	01^1
5	$o-2$	3047.383		3047.394(11)*	(5,6)	01^1
3	$p+3$	3063.453		3063.478(05)*	(3,1)u	01^1
4	$p-2$	3069.310		3069.317(07)*	(4,4)	01^1
4	$o+1$	3145.267		3145.276(05)*	(4,3)l	01^1
9	$p-2$	3167.221		3167.341(17)*	(9,5)	00^0
10	$p+2$	3196.769		3196.907(19)	(10,8)	00^0
4	$o+2$	3233.351		3233.377(06)*	(4,3)u	01^1
1	$p-3$	3240.678		3240.739(18)*	(1,1)	10^0
4	$p-3$	3260.197		3260.219(07)*	(4,2)l	01^1
1	$o+2$	3263.054		3263.145(16)	(1,0)	10^0
6	$p+3$	3269.582		3269.591(09)*	(6,7)	01^1
5	$p+3$	3300.113		3300.141(08)*	(5,5)	01^1
4	$p+4$	3326.091		3326.118(08)*	(4,1)l	01^1
9	$p+2$	3335.438		3335.559(19)*	(9,4)	00^0
2	$p+4$	3343.086		3343.147(14)*	(2,2)	10^0
4	$p-4$	3351.353		3351.385(08)*	(4,2)u	01^1
11	$p+1$	3352.780			(11,10)	00^0
5	$p-3$	3396.514		3396.519(09)*	(5,4)l	01^1
12	$o+1$	3402.858			(12,12)	00^0
2	$p-3$	3409.771		3409.825(15)*	(2,1)	10^0
4	$p+5$	3423.085		3423.125(08)*	(4,1)u	01^1
4	$o-2$	3447.011		3447.031(09)*	(4,0)	01^1
9	$o-2$	3460.941		3461.058(17)*	(9,3)	00^0
10	$p-1$	3484.646		3484.761(16)*	(10,7)	00^0
3	$o-3$	3485.258		3485.306(12)*	(3,3)	10^0
5	$p-4$	3510.119		3510.142(07)*	(5,4)u	01^1
7	$p-4$	3530.235		3530.252(16)*	(7,8)	01^1
5	$o+2$	3553.304		3553.333(09)*	(5,3)l	01^1
9	$p+3$	3555.305		3555.438(35)	(9,2)	00^0
6	$o-2$	3569.436		3569.467(07)*	(6,6)	01^1
3	$p+4$	3595.694		3595.739(20)	(3,2)	10^0
9	$p-3$	3609.462		3609.643(52)	(9,1)	00^0
9	$o+2$	3627.453		3627.578(19)	(9,0)	00^0
5	$p-5$	3660.307		3660.348(10)*	(5,2)l	01^1
3	$p-5$	3661.043		3661.081(21)	(3,1)	10^0
4	$p+6$	3667.082		3667.126(16)*	(4,4)	10^0
5	$o+3$	3673.918		3673.958(06)*	(5,3)u	01^1
3	$o+3$	3682.683		3682.750(16)	(3,0)	10^0
6	$p+4$	3685.067		3685.094(10)*	(6,5)l	01^1
5	$p+4$	3722.593		3722.636(10)*	(5,1)l	01^1
11	$o-1$	3725.471		3725.625(19)	(11,9)	00^0
10	$o+1$	3726.430		3726.566(16)*	(10,6)	00^0
5	$o-3$	3743.140		3743.168(14)*	(5,0)	01^1
5	$p-6$	3792.977		3793.038(08)*	(5,2)u	01^1
4	$o-3$	3820.769		3820.805(12)*	(4,3)	10^0
6	$p+5$	3825.386		3825.442(07)*	(6,5)u	01^1
8	$o+2$	3828.991		3829.019(13)*	(8,9)	01^1
5	$p+5$	3863.351		3863.417(09)*	(5,1)u	01^1
7	$p+3$	3877.008		3877.036(10)*	(7,7)	01^1
12	$p-1$	3884.031			(12,11)	00^0
6	$p-3$	3884.088		3884.117(10)*	(6,4)l	01^1
5	$p-7$	3888.654		3888.682(08)*	(5,5)	10^0
10	$p-2$	3926.036		3926.180(23)	(10,5)	00^0
4	$p+7$	3928.143			(4,2)	10^0
13	$p-1$	3931.766			(13,13)	00^0
4	$p-5$	3991.803		3991.806(25)	(4,1)	10^0
7	$o-2$	4010.200		4010.245(07)*	(7,6)l	01^1
6	$o+2$	4029.988		4030.048(09)*	(6,3)l	01^1
6	$p-4$	4035.720		4035.770(08)*	(6,4)u	01^1
11	$p+2$	4044.000			(11,8)	00^0
5	$p+6$	4084.701		4084.730(14)*	(5,4)	10^0
10	$p+3$	4086.290		4086.425(25)	(10,4)	00^0
6	$p-5$	4129.260		4129.331(11)*	(6,2)l	01^1
6	$o+3$	4147.034		4147.057(07)*	(6,6)	10^0
9	$p-4$	4165.459		4165.479(17)*	(9,10)	01^1
7	$o-3$	4177.864		4177.920(06)*	(7,6)u	01^1
6	$p+6$	4188.726		4188.806(11)*	(6,1)l	01^1
6	$o+4$	4202.235		4202.300(07)*	(6,3)u	01^1
10	$o-2$	4215.094		4215.251(20)	(10,3)	00^0
8	$p-4$	4222.533		4222.583(11)*	(8,8)	01^1
5	$o-4$	4232.684		4232.694(14)*	(5,3)	10^0
7	$p+4$	4249.902		4249.973(10)*	(7,5)l	01^1
12	$p+1$	4286.946			(12,10)	00^0
10	$p+4$	4296.478			(10,2)	00^0
6	$p-6$	4309.271		4309.368(11)*	(6,2)u	01^1
11	$p-2$	4315.413			(11,7)	00^0
5	$p+7$	4337.019			(5,2)	10^0
10	$p-3$	4348.219		4348.435(64)	(10,1)	00^0
8	$p+4$	4371.260		4371.318(09)*	(8,7)l	01^1
6	$p+7$	4378.282		4378.380(10)*	(6,1)u	01^1
6	$p-7$	4389.279		4389.287(09)	(6,5)	10^0
5	$p-8$	4398.694			(5,1)	10^0
6	$o-3$	4400.982		4401.056(10)*	(6,0)	01^1
5	$o+4$	4419.137			(5,0)	10^0
7	$p-5$	4420.158		4420.218(14)*	(7,4)l	01^1
7	$p+5$	4431.609		4431.693(08)*	(7,5)u	01^1
13	$o+1$	4449.473			(13,12)	00^0
7	$p-6$	4456.873		4456.867(09)*	(7,7)	10^0
14	$p+1$	4494.966			(14,14)	00^0
10	$p+5$	4539.221			(10,11)	01^1
11	$o+1$	4544.240		4544.410(22)	(11,6)	00^0
7	$o+3$	4562.728		4562.825(10)*	(7,3)l	01^1
8	$p+5$	4567.212		4567.277(08)*	(8,7)u	01^1
6	$p+8$	4575.977		4575.987(14)	(6,4)	10^0
9	$o+3$	4605.661		4605.735(33)*	(9,9)	01^1
12	$o-1$	4634.047			(12,9)	00^0
7	$p-7$	4635.928		4636.020(09)*	(7,4)u	01^1
8	$o-2$	4650.861		4650.945(08)*	(8,6)l	01^1
7	$p-8$	4663.773		4663.887(14)*	(7,2)l	01^1
6	$o-4$	4719.294		4719.259(11)	(6,3)	10^0
7	$p+6$	4720.296		4720.421(17)	(7,1)l	01^1
7	$o+4$	4721.787		4721.794(07)	(7,6)	10^0
11	$p-3$	4733.919			(11,5)	00^0
7	$o-4$	4739.173		4739.271(18)	(7,0)	01^1
9	$p-5$	4767.501		4767.585(11)	(9,8)l	01^1
8	$p+6$	4774.975		4774.998(33)	(8,8)	10^0
7	$o+5$	4793.598		4793.695(09)*	(7,3)u	01^1
6	$p+9$	4818.401			(6,2)	10^0
1	$p-4$	4842.455		4842.607(71)	(1,1)	02^0
8	$o-3$	4862.697		4862.793(07)*	(8,6)u	01^1
1	$o+3$	4870.187		4870.309(08)*	(1,0)	02^0
8	$p+7$	4874.318		4874.407(11)*	(8,5)l	01^1
6	$p-8$	4877.837			(6,1)	10^0
13	$p-2$	4879.901			(13,11)	00^0
11	$p+3$	4886.315		4886.494(31)	(11,4)	00^0
7	$p-9$	4891.925		4892.057(14)	(7,2)u	01^1
12	$p+2$	4932.993			(12,8)	00^0
2	$p+5$	4942.656		4942.720(15)	(2,2)	02^0
11	$o-2$	4949.854			(11,12)	01^1
7	$p+7$	4961.582		4961.729(16)	(7,1)u	01^1
7	$p-10$	4962.125		4962.118(11)	(7,5)	10^0
9	$p-6$	4992.888		4992.978(13)	(9,8)u	01^1
1	$o-2$	4994.698		4994.833(08)*	(1,3)	02^2
11	$o-3$	4994.803			(11,3)	00^0
0	$p+2$	4997.920		4998.049(15)	(0,2)	02^2
2	$p-4$	5023.366		5023.458(13)*	(2,1)	02^0
10	$p-4$	5026.026			(10,10)	01^1
8	$p-5$	5028.265		5028.395(12)*	(8,4)l	01^1
2	$p+6$	5032.288		5032.393(07)*	(2,4)	02^2
14	$p-1$	5048.185			(14,13)	00^0
3	$o-4$	5078.915		5078.930(09)*	(3,3)	02^0
9	$p+4$	5086.222		5086.331(10)*	(9,7)l	01^1
11	$p+4$	5087.285			(11,2)	00^0
1	$p+2$	5087.485		5087.617(08)*	(1,2)	02^2
15	$o-1$	5091.529			(15,15)	00^0
3	$p-6$	5105.206		5105.292(10)*	(3,5)	02^2
8	$p+8$	5107.141		5107.271(11)*	(8,5)u	01^1
8	$p-6$	5109.777		5109.740(19)	(8,7)	10^0
1	$p-5$	5125.166		5125.292(06)*	(1,1)	02^2
11	$p-4$	5136.560			(11,1)	00^0
7	$p+8$	5136.682		5136.658(15)	(7,4)	10^0
9	$o-3$	5149.109			(9,9)	10^0
11	$o+2$	5152.963		5153.139(22)	(11,0)	00^0
8	$o+3$	5171.026		5171.168(11)*	(8,3)l	01^1
2	$o-2$	5181.056		5181.184(07)*	(2,3)	02^2
12	$p-2$	5189.071			(12,7)	00^0
10	$o+2$	5198.110		5198.221(11)	(10,9)l	01^1

TABLE 3 (continued)

Q. N.[a]	E_{calc} [b]	E_{exp} [c]	Label[d]		Q. N.[a]	E_{calc} [b]	E_{exp} [c]	Label[d]		Q. N.[a]	E_{calc} [b]	E_{exp} [c]	Label[d]	
$J\ I\ P\ n$	(cm^{-1})	(cm^{-1})	Rot.	Vib.	$J\ I\ P\ n$	(cm^{-1})	(cm^{-1})	Rot.	Vib.	$J\ I\ P\ n$	(cm^{-1})	(cm^{-1})	Rot.	Vib.
3 $p+5$	5210.738	5210.797(12)*	(3,2)	02^0	4 $o-5$	5810.924	5811.003(06)*	(4,3)	02^2	6 $o-5$	6301.641	6301.446(09)*	(6,3)	02^0
4 $o+3$	5215.696	5215.742(08)*	(4,6)	02^2	2 $p+9$	5815.659	5815.854(12)*	(2,1)u	11^1	13 $o+2$	6304.993		(13,6)	00^0
4 $p+8$	5251.799	5251.736(16)	(4,4)	02^0	9 $p-8$	5819.792		(9,7)	10^0	9 $p+10$	6306.607	6306.854(34)	(9,1)u	01^1
13 $p+1$	5253.446		(13,10)	00^0	10 $p-6$	5827.581	5827.721(13)	(10,8)u	01^1	9 $p-12$	6310.290	6310.308(27)	(9,5)	10^0
8 $p-7$	5257.167	5257.344(29)	(8,2)l	01^1	5 $o-5$	5830.536	5830.435(07)*	(5,3)	02^0	7 $o+7$	6312.444	6312.163(08)*	(7,6)	02^0
2 $p+7$	5266.301	5266.427(08)*	(2,2)	02^2	2 $o-3$	5835.140	5835.365(12)*	(2,0)	11^1	1 $p-7$	6323.167		(1,1)	20^0
7 $o-5$	5269.950		(7,3)	10^0	10 $p+7$	5842.601	5842.715(11)*	(10,7)l	01^1	10 $p+10$	6326.372		(10,8)	10^0
3 $p-7$	5282.255	5282.318(11)*	(3,1)	02^0	9 $p+8$	5842.747	5842.897(14)	(9,5)u	01^1	5 $p+12$	6327.871	6327.954(06)*	(5,2)u	02^2
2 $o+2$	5286.801	5286.913(06)*	(2,0)	02^2	4 $p-8$	5846.716	5846.800(08)*	(4,1)l	02^2	9 $p-13$	6333.126	6332.831(16)	(9,11)	02^2
3 $p+6$	5299.131	5299.227(09)*	(3,4)	02^2	12 $o-2$	5856.687		(12,3)	00^0	16 $o-1$	6341.543		(16,15)	00^0
8 $p-8$	5304.760	5304.879(13)*	(8,4)u	01^1	13 $p+2$	5858.836		(13,8)	00^0	4 $p+14$	6342.605	6342.581(23)	(4,1)l	11^1
2 $p-5$	5304.836	5304.960(07)*	(2,1)	02^2	13 $p-3$	5880.157		(13,14)	01^1	1 $o+4$	6345.170		(1,0)	20^0
3 $o+4$	5305.521	5305.584(09)*	(3,0)	02^0	4 $p+12$	5888.230	5888.310(08)*	(4,2)u	02^2	5 $p+13$	6346.262	6346.291(06)*	(5,5)	11^1
8 $p+9$	5312.854	5313.058(40)	(8,1)l	01^1	8 $o-5$	5895.174	5895.122(21)	(8,3)	10^0	11 $o+4$	6359.874	6360.031(18)	(11,9)u	01^1
9 $p+5$	5328.204	5328.318(10)*	(9,7)u	01^1	6 $p-9$	5895.861	5895.803(08)*	(6,7)	02^2	4 $p-12$	6363.351	6363.417(22)	(4,2)u	11^1
9 $o-4$	5341.999	5342.110(09)*	(9,6)l	01^1	4 $o+4$	5896.787	5896.838(08)*	(4,0)	02^2	11 $p-8$	6373.929	6374.075(19)	(11,8)l	01^1
8 $o+4$	5361.226	5361.203(12)	(8,6)	10^0	5 $p-11$	5899.394	5899.405(07)*	(5,5)	02^2	5 $p-14$	6376.427	6376.531(13)*	(5,1)u	02^2
5 $p-9$	5363.833	5363.825(09)*	(5,7)	02^2	14 $p-2$	5900.751		(14,11)	00^0	17 $p-1$	6380.839		(17,17)	00^0
7 $p+9$	5368.025		(7,2)	10^0	9 $p-9$	5908.498	5908.688(37)	(9,2)l	01^1	5 $o+7$	6391.743	6391.860(08)*	(5,0)	02^2
12 $p+3$	5396.949		(12,13)	01^1	3 $o+6$	5909.950	5910.110(06)*	(3,3)	11^1	6 $p+13$	6395.046	6394.877(10)	(6,2)	02^0
12 $o+2$	5406.041		(12,6)	00^0	4 $p+13$	5920.770	5920.863(09)*	(4,5)	11^1	14 $o+2$	6399.234		(14,15)	01^1
7 $p-11$	5424.988		(7,1)	10^0	12 $p+5$	5922.883		(12,2)	00^0	10 $p-7$	6400.921	6401.106(27)	(10,4)l	01^1
3 $o-5$	5431.017	5431.122(06)*	(3,3)	02^2	4 $p-9$	5931.782	5931.881(06)*	(4,1)u	02^2	6 $p+14$	6403.624	6403.513(08)*	(6,4)l	02^2
4 $o-4$	5434.341	5434.331(12)	(4,3)	02^0	5 $p+9$	5939.804	5939.707(12)	(5,2)	02^0	5 $p-15$	6410.567	6410.544(19)	(5,4)l	11^1
7 $o+6$	5443.899		(7,0)	10^0	10 $o-3$	5944.621		(10,9)	10^0	10 $o-5$	6412.156	6412.314(12)	(10,6)u	01^1
10 $o+3$	5454.327	5454.430(11)	(10,9)u	01^1	3 $p-11$	5949.328	5949.443(17)	(3,2)l	11^1	6 $p-11$	6415.774	6415.757(07)*	(6,5)	02^2
4 $p-6$	5460.400	5460.464(24)*	(4,5)	02^2	11 $p-6$	5950.826		(11,10)u	01^1	2 $p+10$	6422.880		(2,2)	20^0
5 $p-10$	5460.611	5460.464(24)	(5,5)	02^0	9 $p+9$	5962.005		(9,1)l	01^1	11 $p+6$	6429.599		(11,10)	10^0
8 $o+5$	5463.022	5463.104(10)*	(8,3)u	01^1	12 $p-4$	5969.587		(12,1)	00^0	4 $p+15$	6430.890	6430.944(23)	(4,1)u	11^1
11 $p+5$	5483.252		(11,11)	01^1	5 $o-6$	5971.155	5971.228(08)*	(5,3)l	02^2	9 $p+11$	6449.215	6449.198(39)	(9,4)	10^0
3 $p-8$	5486.357	5486.457(06)*	(3,1)l	02^2	12 $o-3$	5976.967		(12,12)	01^1	7 $p-13$	6451.317	6451.126(14)*	(7,8)	11^1
9 $p+6$	5487.233	5487.329(18)	(9,8)	10^0	9 $o-6$	5979.029	5979.217(21)	(9,0)	01^1	4 $o-6$	6453.613	6453.690(19)	(4,0)	11^1
14 $o+1$	5502.846		(14,12)	00^0	8 $p+12$	5981.430		(8,2)	10^0	6 $p-12$	6461.276		(6,1)	02^0
8 $p-9$	5532.618	5532.751(20)	(8,2)u	01^1	6 $p-10$	5984.075	5983.896(13)	(6,5)	02^0	13 $p-5$	6476.011		(13,5)	00^0
3 $p+7$	5533.626	5533.730(06)*	(3,2)	02^2	7 $p-12$	5985.536	5985.149(13)	(7,7)	02^0	12 $p+7$	6481.539		(12,11)u	01^1
4 $p+9$	5544.226	5544.213(08)*	(4,2)	02^0	5 $p-12$	6003.275	6003.183(14)	(5,1)	02^0	8 $o-6$	6482.308	6482.118(19)*	(8,9)	02^2
6 $p+10$	5549.695	5549.624(11)*	(6,8)	02^2	11 $p-7$	6003.418		(11,11)	10^0	12 $o+3$	6483.120		(12,12)	10^0
0 $p+3$	5554.029		(0,1)	11^1	3 $p-12$	6015.800	6015.946(17)	(3,2)u	11^1	2 $p-7$	6488.458		(2,1)	20^0
10 $p-5$	5555.295	5555.440(16)	(10,8)l	01^1	5 $o+6$	6023.187	6023.081(17)	(5,0)	02^0	7 $p-14$	6505.291	6505.157(08)*	(7,7)	02^2
10 $p+6$	5558.547		(10,10)	10^0	3 $p+8$	6023.657	6023.757(18)	(3,1)l	11^1	13 $p+3$	6506.815		(13,13)	01^1
9 $p+7$	5565.214	5565.255(12)*	(9,5)l	01^1	9 $p-10$	6031.544	6031.681(15)	(9,4)u	01^1	6 $o-6$	6516.118	6516.152(09)*	(6,3)l	02^2
3 $o+5$	5567.276	5567.389(07)*	(3,0)	02^2	8 $p+13$	6034.410	6034.182(13)*	(8,10)	02^2	5 $p-16$	6529.268	6529.276(11)*	(5,4)u	11^1
3 $p-9$	5573.651	5573.764(05)*	(3,1)u	02^2	8 $p-11$	6035.672		(8,1)	10^0	10 $o+4$	6539.707	6539.950(14)	(10,3)l	01^1
13 $o-1$	5577.736		(13,9)	00^0	3 $o-6$	6047.437	6047.564(19)	(3,0)	11^1	14 $o-1$	6552.138		(14,9)	00^0
1 $p-6$	5584.000	5584.224(10)*	(1,2)	11^1	9 $o+5$	6053.084	6053.096(14)*	(9,6)	10^0	9 $o-7$	6559.077		(9,3)	10^0
12 $p-3$	5585.628		(12,5)	00^0	11 $o+3$	6057.273	6057.448(13)	(11,9)l	01^1	3 $o-7$	6561.242		(3,3)	20^0
8 $p-10$	5604.263	5604.254(22)	(8,5)	10^0	3 $p+9$	6080.829	6080.967(18)	(3,1)u	11^1	5 $o+8$	6568.335	6568.247(10)*	(5,3)l	11^1
8 $p+10$	5606.619	5606.814(20)	(8,1)u	01^1	10 $o-4$	6087.435	6087.522(11)*	(10,6)l	01^1	7 $p-15$	6571.908		(7,5)	02^0
9 $o-5$	5610.185	5610.323(10)*	(9,6)u	01^1	5 $p+10$	6089.800	6089.815(06)*	(5,4)	02^2	15 $o+1$	6574.418		(15,12)	00^0
4 $p-7$	5610.453	5610.451(13)	(4,1)	02^0	13 $p-4$	6100.528		(13,7)	00^0	10 $p-8$	6579.738		(10,7)	10^0
8 $o-4$	5628.911	5629.057(13)	(8,0)	01^1	4 $p-10$	6105.534	6105.639(06)*	(4,4)	11^1	12 $p-5$	6591.347		(12,10)l	01^1
1 $p+3$	5640.267	5640.488(15)*	(1,1)	11^1	5 $o-7$	6129.541	6129.539(07)*	(5,6)	11^1	6 $p+15$	6608.128	6608.127(07)*	(6,4)u	02^2
1 $o-3$	5644.521	5644.739(15)	(1,0)	11^1	6 $p+11$	6141.434	6141.238(13)	(6,4)	02^0	10 $p-9$	6612.267		(10,2)l	01^1
4 $p+10$	5652.415	5652.479(07)*	(4,4)	02^2	10 $p+8$	6145.084	6145.224(14)	(10,7)u	01^1	13 $p+4$	6612.793		(13,4)	00^0
2 $o+3$	5653.801	5654.004(06)*	(2,3)	11^1	15 $p-1$	6154.036		(15,13)	00^0	10 $p+11$	6628.474	6628.649(18)	(10,5)u	01^1
5 $o+5$	5659.211	5659.227(07)*	(5,6)	02^2	4 $o+5$	6158.228	6158.271(15)*	(4,3)l	11^1	6 $o-7$	6639.008	6638.903(05)*	(6,6)	11^1
11 $p-5$	5662.198		(11,10)l	01^1	12 $p+6$	6158.807		(12,11)l	01^1	11 $p+7$	6644.910	6644.997(17)	(11,7)l	01^1
15 $p+1$	5679.206		(15,14)	00^0	5 $p+11$	6169.392	6169.455(08)*	(5,2)l	02^2	6 $p+16$	6650.995	6650.933(10)*	(6,5)l	11^1
9 $p-7$	5689.513	5689.686(14)*	(9,4)l	01^1	7 $p+10$	6170.176	6170.055(11)*	(7,8)	02^2	9 $o-8$	6651.211	6650.536(16)*†	(9,9)	02^0
5 $p+8$	5690.933	5690.831(12)	(5,4)	02^0	9 $o+6$	6175.031	6175.176(14)	(9,3)u	01^1	9 $p+12$	6654.121		(9,2)	10^0
6 $o+5$	5705.301	5705.046(15)	(6,6)	02^0	6 $o+6$	6184.588	6184.537(07)*	(6,6)	02^2	10 $p+12$	6665.886	6666.104(18)	(10,1)l	01^1
4 $p+11$	5716.408	5716.491(08)*	(4,2)l	02^2	5 $o-8$	6213.676	6213.703(06)*	(5,3)u	02^2	10 $o+5$	6669.331	6668.954(16)	(10,12)	02^2
16 $p+1$	5720.486		(16,16)	00^0	9 $p-11$	6225.491	6225.639(27)	(9,2)u	01^1	3 $p+10$	6669.884		(3,2)	20^0
12 $p+4$	5730.235		(12,4)	00^0	10 $p+9$	6226.551	6226.722(20)	(10,5)l	01^1	5 $p-17$	6672.901		(5,2)l	11^1
2 $p-6$	5755.800	5756.002(11)*	(2,2)	11^1	14 $p+2$	6248.125		(14,10)	00^0	7 $p+11$	6674.151	6673.853(14)	(7,4)	02^0
8 $p+11$	5762.544	5762.522(20)	(8,4)	10^0	6 $p+12$	6250.711	6250.710(09)*	(6,7)	11^1	8 $p-12$	6676.055	6675.655(14)	(8,7)	02^0
3 $p-10$	5764.716	5764.879(07)*	(3,4)	11^1	4 $o+6$	6254.620	6254.705(10)*	(4,3)u	11^1	5 $o+9$	6679.239		(5,3)u	11^1
7 $o-6$	5773.241	5773.110(11)*	(7,9)	02^2	4 $p-11$	6276.360	6276.370(22)	(4,2)l	11^1	13 $o-2$	6686.925		(13,12)l	01^1
2 $p+8$	5778.823	5778.995(16)	(2,1)l	11^1	5 $p-13$	6276.694	6276.726(07)*	(5,1)l	02^2	13 $o-3$	6700.977		(13,3)	00^0
9 $o+4$	5809.240	5809.413(12)*	(9,3)l	01^1	8 $p+14$	6300.971	6300.448(19)†	(8,8)	02^0	9 $p-14$	6705.311		(9,1)	10^0

TABLE 3 (continued)

Q. N.[a] J I P n	E_{calc} [b] (cm^{-1})	E_{exp} [c] (cm^{-1})	Label[d] Rot.	Vib.	Q. N.[a] J I P n	E_{calc} [b] (cm^{-1})	E_{exp} [c] (cm^{-1})	Label[d] Rot.	Vib.	Q. N.[a] J I P n	E_{calc} [b] (cm^{-1})	E_{exp} [c] (cm^{-1})	Label[d] Rot.	Vib.
11 $p-9$	6710.274	6710.449(19)	(11,8)u	01^1	1 $o-4$	7082.860		(1,0)	03^1	3 $p+11$	7460.169		(3,1)l	03^1
9 $o+7$	6722.382		(9,0)	10^0	1 $p+4$	7102.718	7103.087(70)*	(1,1)	03^1	7 $p+19$	7462.158	7462.319(12)	(7,2)u	02^2
6 $p+17$	6724.776	6724.704(11)*	(6,2)l	02^2	9 $p-15$	7105.227	7104.956(13)*	(9,10)	11^1	8 $o+9$	7463.737	7463.686(08)*	(8,6)u	02^2
5 $p+14$	6733.406		(5,1)l	11^1	8 $o+8$	7119.292	7119.112(07)*	(8,6)l	02^2	11 $p+12$	7472.560	7472.755(24)	(11,5)u	01^1
3 $p-13$	6734.090		(3,1)	20^0	2 $o+4$	7122.615	7122.646(70)*	(2,3)	03^1	10 $p+17$	7474.940		(10,11)	11^1
7 $p-16$	6736.644	6736.501(11)	(7,5)l	02^2	7 $o-9$	7126.799	7126.714(08)*	(7,3)l	02^2	5 $o+10$	7475.145		(5,0)	20^0
4 $p+16$	6738.201		(4,4)	20^0	6 $p-17$	7137.200		(6,2)l	11^1	8 $p+18$	7478.072		(8,2)	02^0
5 $o-9$	6753.295		(5,0)	11^1	11 $p+10$	7143.390		(11,8)	10^0	9 $o+8$	7487.746		(9,6)	02^0
3 $o+7$	6755.339		(3,0)	20^0	5 $p+16$	7147.109		(5,4)	20^0	0 $o+1$	7492.558	7492.912(13)†	(0,3)	03^3
11 $o-4$	6765.378	6765.479(18)	(11,9)	10^0	13 $p+6$	7156.697		(13,11)l	01^1	12 $p+10$	7494.243		(12,7)l	01^1
8 $o+6$	6766.598	6766.387(12)	(8,9)	11^1	11 $p-11$	7157.738		(11,4)l	01^1	13 $o+4$	7496.871		(13,12)	10^0
6 $p-13$	6768.699	6768.675(14)*	(6,1)l	02^2	6 $o+9$	7184.268	7184.132(24)	(6,3)u	11^1	3 $o-9$	7498.146		(3,0)	03^1
6 $o-8$	6775.243	6775.358(05)*	(6,3)u	02^2	8 $p-14$	7187.096	7186.960(11)	(8,7)	02^2	7 $p-21$	7499.704		(7,7)	20^0
7 $o+8$	6784.144	6784.078(06)*	(7,6)	02^2	10 $p+15$	7191.871		(10,4)	10^0	7 $o+10$	7504.956	7504.928(11)*	(7,0)	02^2
5 $p-18$	6792.527		(5,2)u	11^1	6 $p+20$	7192.784		(6,1)l	11^1	10 $o-8$	7507.678	7507.250(34)	(10,9)	02^0
13 $p+5$	6798.691		(13,2)	00^0	7 $p+15$	7193.350	7193.266(12)	(7,5)l	11^1	2 $p-9$	7514.456		(2,4)	03^3
7 $o-7$	6801.893	6801.634(14)	(7,3)	02^0	2 $p+11$	7208.359	7208.334(70)*	(2,1)l	03^1	4 $p+19$	7514.707		(4,7)	03^3
6 $o+7$	6803.721	6803.674(08)*	(6,0)	02^2	7 $o-10$	7209.275	7209.165(07)*	(7,6)u	11^1	13 $p+7$	7518.884		(13,11)u	01^1
10 $o+6$	6804.407	6804.385(17)	(10,6)	10^0	6 $o+10$	7214.088		(6,6)	20^0	13 $p-8$	7522.856		(13,10)l	01^1
10 $p-10$	6811.587	6811.748(17)	(10,4)u	01^1	7 $p+16$	7215.802	7215.768(09)*	(7,4)u	02^2	3 $p-16$	7525.632		(3,2)u	03^1
14 $p+3$	6816.687		(14,8)	00^0	10 $p-13$	7220.112		(10,11)	02^2	14 $p+5$	7528.745		(14,4)	00^0
16 $p+2$	6831.384		(16,14)	00^0	3 $p-14$	7230.283		(3,4)	03^1	7 $p-22$	7529.091	7529.104(12)*	(7,1)u	02^2
9 $p+13$	6832.272	6832.012(23)*	(9,10)	02^2	12 $p-8$	7231.551		(12,8)l	01^1	17 $o-1$	7532.405		(17,15)	00^0
13 $p-6$	6842.607		(13,1)	00^0	2 $p-8$	7235.508	7235.742(70)*	(2,2)	03^1	8 $p-17$	7533.994		(8,1)	02^0
6 $p+18$	6842.645	6842.628(11)*	(6,5)u	11^1	8 $p-15$	7237.698		(8,8)	11^1	9 $p-17$	7543.585	7543.360(08)	(9,7)l	02^2
13 $o+3$	6857.353		(13,0)	00^0	14 $o+3$	7240.093		(14,6)	00^0	14 $p+6$	7543.859		(14,14)	10^0
6 $p+19$	6858.525	6858.614(10)*	(6,2)u	02^2	8 $p+16$	7245.339	7244.972(17)	(8,4)	02^0	16 $p+3$	7544.997		(16,17)	01^1
5 $p+15$	6859.884	6859.846(27)	(5,1)u	11^1	14 $p+4$	7245.506		(14,13)l	01^1	8 $p+19$	7550.745	7550.536(10)	(8,7)u	11^1
8 $p+15$	6862.974	6862.763(11)*	(8,8)	02^2	11 $o+5$	7255.270		(11,3)l	01^1	4 $o+7$	7551.194	7550.316(17)*	(4,3)l	03^1
7 $p+12$	6863.533	6863.442(14)	(7,7)	11^1	9 $o-9$	7256.963	7256.689(34)*	(9,9)	02^2	15 $o-2$	7552.649		(15,9)	00^0
6 $p-14$	6885.871	6885.838(07)*	(6,4)l	11^1	11 $o-6$	7257.663	7257.845(16)	(11,6)u	01^1	5 $o-11$	7554.025		(5,6)	03^1
11 $o-5$	6889.006	6888.997(16)	(11,6)l	01^1	15 $p+2$	7267.339		(15,10)	00^0	1 $p-10$	7571.716		(1,2)	03^3
4 $o-7$	6889.507		(4,3)	20^0	16 $p-1$	7272.831		(16,13)	00^0	11 $o+6$	7592.288	7592.299(21)	(11,6)	10^0
7 $p+13$	6910.479		(7,2)	02^0	5 $o-10$	7292.388		(5,3)	20^0	7 $o+11$	7596.047	7595.852(11)*	(7,3)l	11^1
12 $p-6$	6924.053		(12,10)u	01^1	6 $p-18$	7295.826		(6,2)u	11^1	3 $p+12$	7597.008		(3,1)u	03^1
6 $p-15$	6929.171	6929.194(10)*	(6,1)u	02^2	2 $p+12$	7301.181	7301.423(50)*	(2,1)u	03^1	4 $p-14$	7598.521		(4,4)	03^1
12 $o+4$	6934.573	6934.696(19)	(12,9)l	01^1	12 $o+5$	7304.749	7304.925(24)	(12,9)u	01^1	12 $o-4$	7607.102	7607.488(24)	(12,6)l	11^1
15 $p-2$	6942.487		(15,11)	00^0	10 $o-7$	7316.361		(10,3)	10^0	7 $p-23$	7618.630	7618.564(17)	(7,4)u	11^1
8 $o+7$	6942.604	6942.162(31)	(8,6)	02^0	7 $p+17$	7317.914	7317.753(12)	(7,2)l	02^2	8 $o-8$	7620.729	7620.408(12)	(8,6)l	11^1
12 $p-7$	6946.958		(12,11)	10^0	7 $p-19$	7318.407	7318.322(15)	(7,1)l	02^2	9 $p+15$	7622.656	7622.455(12)	(9,8)	02^2
5 $p-19$	6953.844		(5,5)	20^0	12 $p+8$	7319.294		(12,10)	10^0	6 $p+22$	7628.078		(6,4)	20^0
15 $p-3$	6954.114		(15,16)	01^1	1 $p-9$	7325.092		(1,4)	03^3	12 $p-9$	7632.355		(12,8)u	01^1
10 $o+7$	6958.960	6959.029(17)	(10,3)u	01^1	2 $o-4$	7327.984	7328.209(18)*	(2,0)	03^1	11 $p-15$	7638.575	7638.738(29)	(11,4)u	01^1
7 $p-17$	6961.325		(7,1)	02^0	7 $o-11$	7340.062	7340.114(08)*	(7,3)u	02^2	5 $p-21$	7639.368		(5,8)	03^3
10 $p-11$	6967.179	6967.296(36)	(10,5)	10^0	9 $p-16$	7349.528	7348.806(13)†	(9,7)	02^0	14 $p+7$	7641.001		(14,13)u	01^1
7 $o-8$	6985.302	6985.098(12)	(7,6)l	11^1	8 $p+17$	7352.822	7352.467(13)	(8,7)l	11^1	11 $o+7$	7645.892		(11,12)	02^2
7 $o+9$	6990.002	6989.796(20)	(7,0)	02^0	11 $p-12$	7357.593		(11,2)l	01^1	9 $o+9$	7651.520	7651.050(13)	(9,9)	11^1
4 $p+17$	6994.960		(4,2)	20^0	6 $p+21$	7361.961		(6,1)u	11^1	8 $p+20$	7656.631	7656.488(15)*	(8,4)l	02^2
13 $p-7$	6996.883		(13,13)	10^0	3 $p-15$	7362.607	7362.203(70)*	(3,2)l	03^1	16 $o+1$	7658.990		(16,12)	00^0
11 $p+8$	6999.062		(11,5)l	01^1	2 $p+13$	7368.759		(2,5)	03^3	3 $p+13$	7659.448		(3,5)	03^3
7 $p+14$	7002.735	7002.630(09)	(7,4)l	02^2	4 $p+18$	7374.555		(4,5)	03^1	14 $o-2$	7662.640		(14,3)	00^0
0 $p+4$	7005.822		(0,1)	03^1	1 $o+5$	7380.868		(1,3)	03^3	7 $p-24$	7667.810		(7,2)l	11^1
11 $p+9$	7008.607	7008.759(17)	(11,7)u	01^1	10 $p+16$	7381.747		(10,2)	10^0	15 $o+2$	7673.607		(15,15)	01^1
7 $p-18$	7027.151	7027.114(09)	(7,5)u	02^2	6 $o-9$	7383.902		(6,0)	11^1	9 $p-18$	7676.894	7676.650(34)	(9,8)u	11^1
17 $p+1$	7034.173		(17,16)	00^0	11 $p-13$	7391.054		(11,7)	10^0	10 $p+18$	7686.921	7686.522(17)	(10,10)	02^2
6 $p-16$	7034.347		(6,4)u	11^1	3 $o+8$	7394.164		(3,3)	03^1	8 $p-18$	7697.713	7697.709(10)	(8,5)u	02^2
10 $p+13$	7035.883	7035.014(19)	(10,10)	02^0	5 $p+17$	7394.743		(5,2)	20^0	4 $p-15$	7701.393		(4,2)l	03^1
11 $p-10$	7043.023		(11,13)	02^2	14 $p-5$	7400.014		(14,5)	00^0	2 $p+14$	7702.893	7702.986(12)*	(2,1)	03^3
6 $o+8$	7043.586	7043.279(17)*	(6,3)l	11^1	8 $o-7$	7401.351		(8,3)	02^0	14 $p+8$	7710.495		(14,2)	00^0
14 $p-3$	7044.849		(14,7)	00^0	11 $p+11$	7405.502		(11,1)l	01^1	7 $p+20$	7717.101		(7,1)l	11^1
13 $o-4$	7045.395		(13,12)u	01^1	3 $o-8$	7418.573	7418.432(13)	(3,6)	03^3	7 $o-12$	7734.043		(7,0)	11^1
1 $p-8$	7046.574	7046.841(70)*	(1,2)	03^1	7 $p+18$	7422.683	7422.591(14)	(7,5)u	11^1	7 $o+12$	7743.316	7742.932(15)	(7,3)u	11^1
10 $p+14$	7055.069	7055.344(53)	(10,1)u	01^1	8 $p-16$	7425.250	7425.161(08)*	(8,5)l	02^2	12 $o-5$	7749.110		(12,9)	10^0
4 $p-13$	7057.420		(4,1)	20^0	11 $o-7$	7427.159	7427.400(24)	(11,0)	01^1	14 $p-6$	7751.221		(14,1)	00^0
18 $o+1$	7071.560		(18,18)	00^0	10 $p-14$	7429.353		(10,1)	10^0	2 $p-10$	7751.596	7751.830(09)*†	(2,2)	03^3
10 $p-12$	7072.371	7072.389(36)	(10,2)u	01^1	7 $p-20$	7436.896	7436.606(12)	(7,4)l	11^1	14 $o-3$	7752.530		(14,12)l	01^1
14 $p-4$	7072.465		(14,14)	01^1	6 $p-19$	7444.159		(6,5)	20^0	11 $p-16$	7754.315		(11,5)	10^0
8 $p-13$	7073.046	7072.703(22)	(8,5)	02^0	12 $p+9$	7454.321		(12,14)	02^2	18 $p-1$	7756.049		(18,17)	00^0
9 $p+14$	7074.515	7074.017(15)	(9,8)	02^0	11 $p-14$	7454.676		(11,11)	02^0	2 $o+5$	7758.547	7758.675(12)†	(2,3)	03^3
10 $o-6$	7080.191	7080.429(15)	(10,0)	01^1	5 $p-20$	7455.136		(5,1)	20^0	11 $o+8$	7766.629	7766.831(25)	(11,3)u	01^1

TABLE 3 (continued)

Q. N.[a] $J\ I\ P\ n$	E_{calc}[b] (cm^{-1})	E_{exp}[c] (cm^{-1})	Label[d] Rot.	Vib.	Q. N.[a] $J\ I\ P\ n$	E_{calc}[b] (cm^{-1})	E_{exp}[c] (cm^{-1})	Label[d] Rot.	Vib.	Q. N.[a] $J\ I\ P\ n$	E_{calc}[b] (cm^{-1})	E_{exp}[c] (cm^{-1})	Label[d] Rot.	Vib.
6 $o-10$	7768.674		(6,3)	20^0	3 $p-19$	8017.654		(3,2)	03^3	6 $p-22$	8275.953		(6,4)l	03^1
6 $p+23$	7769.017		(6,7)	03^1	7 $p-28$	8019.418		(7,8)	03^1	5 $o-13$	8277.627	8277.033(09)*	(5,6)	03^3
5 $p-22$	7769.343	7767.914(70)*	(5,4)l	03^1	6 $p+25$	8020.895		(6,5)l	03^1	13 $o+6$	8281.674		(13,9)u	01^1
4 $p+20$	7773.696		(4,1)l	03^1	4 $o-9$	8031.115	8030.925(13)*	(4,0)	03^1	8 $p-24$	8288.656	8288.481(16)	(8,4)u	11^1
9 $p-19$	7778.214	7777.748(34)	(9,5)	02^0	4 $p+22$	8036.056		(4,5)	03^3	9 $o-12$	8294.533		(9,6)l	11^1
8 $p+21$	7785.048		(8,5)l	11^1	8 $o-11$	8043.282	8043.489(10)	(8,3)u	02^2	9 $p+19$	8296.092		(9,7)u	11^1
4 $o-8$	7786.995	7786.722(09)*	(4,6)	03^3	8 $p-20$	8045.233		(8,4)l	11^1	3 $o-12$	8302.131	8302.108(12)*	(3,3)	12^2
10 $p+19$	7787.226	7786.171(12)	(10,8)	02^0	5 $p-23$	8054.048		(5,4)u	03^1	8 $p+28$	8303.162		(8,1)l	11^1
19 $p-1$	7791.596		(19,19)	00^0	9 $p+17$	8055.975		(9,7)l	11^1	7 $o-13$	8303.281	8300.927(18)†	(7,6)l	03^1
4 $o+8$	7795.070	7794.757(13)	(4,3)u	03^1	2 $o-5$	8057.083	8057.354(21)*	(2,3)	12^2	8 $o+12$	8305.143		(8,9)	03^1
3 $p-17$	7796.561		(3,4)	03^3	11 $o-9$	8058.834		(11,3)	10^0	7 $o-14$	8306.730		(7,3)	20^0
7 $o+13$	7797.199	7796.716(15)†	(7,6)	20^0	8 $p+25$	8071.099		(8,5)u	11^1	16 $p+4$	8306.809		(16,10)	00^0
6 $o+11$	7798.639		(6,9)	03^3	4 $p+23$	8074.027		(4,1)l	03^3	16 $p-3$	8309.933		(16,16)	01^1
15 $p+3$	7801.887		(15,8)	00^0	14 $p-7$	8078.755		(14,13)	10^0	12 $p+15$	8315.622		(12,13)	11^1
12 $p+11$	7808.089		(12,5)l	01^1	5 $p-24$	8090.997		(5,2)l	03^1	4 $p+24$	8332.152		(4,1)u	03^3
8 $o-9$	7822.890	7822.667(08)*	(8,3)l	02^2	10 $o-9$	8092.072	8091.784(33)	(10,9)	02^2	3 $p-21$	8335.467	8335.280(21)	(3,1)l	12^2
5 $p+18$	7831.448		(5,5)	03^1	6 $o-11$	8099.519		(6,6)	03^1	4 $p-18$	8340.205	8340.064(12)	(4,5)	12^2
15 $p-4$	7833.506		(15,14)l	01^1	12 $o+7$	8100.211		(12,3)l	01^1	12 $p+16$	8348.569		(12,5)u	01^1
8 $p+22$	7837.460		(8,8)	20^0	9 $p+18$	8104.543		(9,2)	02^0	15 $p-7$	8352.686		(15,5)	00^0
1 $p-11$	7839.758		(1,1)	12^0	4 $o+9$	8105.366	8105.227(11)	(4,6)	12^2	9 $p+20$	8359.938	8359.769(13)	(9,4)l	02^2
13 $o+5$	7844.719		(13,9)l	01^1	10 $o+8$	8108.521		(10,9)l	11^1	4 $p+25$	8365.683		(4,4)	12^0
11 $p+13$	7846.486		(11,1)u	01^1	10 $p-16$	8109.690		(10,7)	02^0	4 $o+10$	8365.752	8365.478(08)*†	(4,3)	03^3
8 $o-10$	7851.386	7851.267(11)	(8,6)u	11^1	12 $p-11$	8109.750		(12,13)	02^2	4 $p-19$	8366.382	8366.107(13)†	(4,2)	03^3
3 $o+9$	7854.403		(3,3)	03^3	15 $o-3$	8123.151		(15,15)	10^0	8 $o+13$	8370.655		(8,6)	20^0
1 $o+6$	7857.588		(1,0)	12^0	13 $p-11$	8128.161		(13,8)l	01^1	6 $p+26$	8377.251		(6,5)u	03^1
6 $p+24$	7865.379		(6,2)	20^0	2 $p+17$	8135.537	8135.727(11)*	(2,2)	12^2	15 $p+4$	8378.098		(15,13)l	01^1
7 $p-25$	7866.075		(7,2)u	11^1	9 $p-22$	8135.925	8135.743(12)	(9,5)l	02^2	11 $p+17$	8380.507		(11,11)	11^1
3 $o-10$	7866.482	7866.300(07)*	(3,0)	03^3	14 $p+9$	8136.791		(14,11)l	01^1	10 $p-17$	8380.721		(10,5)	02^0
0 $p+5$	7869.974	7870.015(10)†	(0,2)	12^2	5 $o-12$	8138.695	8137.585(71)*	(5,0)	03^1	14 $p+10$	8391.253		(14,16)	02^2
1 $o-5$	7872.300	7872.661(10)	(1,3)	12^2	3 $o-11$	8139.528	8139.068(12)	(3,3)	12^0	13 $p+9$	8391.710		(13,7)l	01^1
9 $p+16$	7875.817		(9,4)	02^0	8 $p+26$	8139.636	8139.751(15)	(8,2)u	02^2	13 $p-12$	8394.156		(13,13)	02^0
11 $o-8$	7878.132		(11,12)	11^1	2 $o+6$	8142.021	8142.088(11)	(2,0)	12^2	10 $p-18$	8395.134	8394.981(14)	(10,7)l	02^2
11 $p-17$	7882.766		(11,2)u	01^1	14 $o-4$	8142.969		(14,12)u	01^1	17 $p-2$	8395.571		(17,13)	00^0
8 $p+23$	7883.920	7883.910(10)	(8,4)u	02^2	8 $p-21$	8143.854		(8,7)	20^0	5 $p-27$	8397.251		(5,2)u	03^1
9 $o+10$	7891.450	7891.333(07)*	(9,6)l	02^2	9 $o+11$	8145.964	8145.790(09)	(9,0)	02^0	3 $p+17$	8400.644	8400.492(12)*	(3,2)	12^2
13 $p-9$	7897.671		(13,11)	10^0	12 $o-6$	8149.413		(12,6)u	01^1	7 $p+23$	8401.355		(7,7)	03^1
13 $o-5$	7903.526		(13,15)	02^2	12 $p-12$	8151.257		(12,2)l	01^1	7 $p+24$	8402.733		(7,2)	20^0
12 $o+6$	7907.409		(12,12)	02^0	11 $p-18$	8152.184		(11,11)	02^2	5 $p+21$	8405.601		(5,1)l	03^3
12 $p+12$	7911.595		(12,7)u	01^1	5 $p+20$	8153.168		(5,1)l	03^1	6 $o+12$	8413.795		(6,3)l	03^1
2 $p+15$	7914.800	7915.081(10)	(2,4)	12^2	11 $p+16$	8160.296		(11,2)	10^0	3 $o+11$	8425.544	8425.436(16)*	(3,0)	12^2
4 $p-16$	7915.419	7915.179(16)	(4,2)u	03^1	4 $p-17$	8167.805		(4,4)	03^3	7 $o+14$	8432.257		(7,9)	03^3
10 $p-15$	7921.531		(10,10)	11^1	2 $p-12$	8168.050	8168.185(11)	(2,1)	12^2	12 $o+8$	8435.511		(12,6)	10^0
8 $p-19$	7921.988	7921.807(17)	(8,1)l	02^2	9 $o-11$	8169.582		(9,9)	20^0	3 $p-22$	8435.637	8435.428(12)	(3,1)u	12^2
6 $p-20$	7923.430		(6,1)	20^0	17 $o-2$	8172.423		(17,18)	01^1	9 $p-24$	8438.879	8438.843(12)	(9,5)u	02^2
13 $p-10$	7927.073		(13,10)u	01^1	9 $p-23$	8176.283	8176.101(12)	(9,1)	02^0	10 $p+21$	8443.972	8443.688(14)	(10,8)u	02^2
7 $p+21$	7931.270		(7,1)u	11^1	3 $p+15$	8176.849	8176.975(11)	(3,4)	12^2	9 $p+21$	8444.698		(9,5)l	11^1
9 $p-20$	7935.986	7935.837(09)*	(9,7)u	02^2	7 $p+22$	8176.919		(7,4)	20^0	10 $o+10$	8445.678		(10,9)u	11^1
12 $p-10$	7954.901		(12,4)l	01^1	6 $p-21$	8181.377		(6,8)	03^3	6 $p+27$	8447.143		(6,8)	12^2
8 $p+24$	7956.627	7956.409(15)	(8,2)l	02^2	8 $p-22$	8182.966	8182.943(16)	(8,1)u	02^2	8 $o+14$	8447.999		(8,3)u	11^1
1 $p+5$	7958.502	7958.833(10)	(1,2)	12^2	8 $o+11$	8183.324	8182.737(20)	(8,3)l	11^1	16 $o+2$	8449.967		(16,15)l	01^1
8 $o+10$	7959.597	7959.452(19)	(8,0)	02^2	12 $p+14$	8197.456		(12,1)l	01^1	7 $p-29$	8458.186		(7,1)	20^0
2 $p+16$	7963.525		(2,2)	12^0	15 $o+3$	8197.917		(15,6)	00^0	13 $o-6$	8468.234		(13,6)l	01^1
5 $p+19$	7964.453		(5,7)	03^3	11 $p-19$	8203.419		(11,1)	10^0	15 $p+5$	8472.890		(15,4)	00^0
5 $o+11$	7964.573	7963.581(70)*	(5,3)l	03^1	11 $o+9$	8218.112		(11,0)	10^0	7 $o+15$	8476.591		(7,0)	20^0
4 $p+21$	7966.380		(4,1)u	03^1	3 $p+16$	8221.093		(3,2)	12^0	12 $p-14$	8477.374		(12,11)	02^0
11 $p+14$	7975.338		(11,10)	02^0	13 $p+8$	8224.778		(13,10)	10^0	6 $p+28$	8482.606		(6,7)	03^3
3 $p+14$	7977.777		(3,1)	03^3	8 $p+27$	8225.035		(8,11)	03^3	14 $p-8$	8482.722		(14,10)l	01^1
9 $p-21$	7980.439		(9,8)l	11^1	5 $o+12$	8230.298	8229.545(15)	(5,3)u	03^1	4 $o-11$	8484.009		(4,3)	12^0
9 $o-10$	7984.334		(9,3)	02^0	12 $p-13$	8237.880		(12,7)	10^0	5 $p+22$	8485.982		(5,5)	03^3
11 $p+15$	7984.584		(11,4)	10^0	9 $o+12$	8237.934	8237.796(09)	(9,6)u	02^2	0 $p+6$	8488.013		(0,1)	21^1
1 $p-12$	7989.277	7989.534(11)	(1,1)	12^2	4 $o-10$	8247.865		(4,0)	03^3	9 $o-13$	8492.697		(9,12)	03^3
3 $p-18$	7991.546	7991.670(11)	(3,5)	12^2	11 $o-10$	8253.293	8251.782(12)	(11,9)	02^0	8 $p-25$	8496.564		(8,2)u	11^1
7 $p-26$	7993.597		(7,10)	03^3	8 $p-23$	8253.742		(8,2)l	11^1	9 $o-14$	8500.207	8499.940(12)	(9,3)l	02^2
17 $p+2$	7994.364		(17,14)	00^0	18 $p+1$	8254.233		(18,16)	00^0	14 $o+4$	8502.347		(14,12)	10^0
16 $p-2$	8002.762		(16,11)	00^0	5 $p-25$	8256.823		(5,7)	12^2	11 $o-11$	8505.700	8505.370(12)	(11,9)l	02^2
12 $p+13$	8003.329		(12,8)	10^0	10 $o+9$	8260.234		(10,6)	02^0	19 $o+1$	8506.101		(19,18)	00^0
7 $p-27$	8003.851		(7,5)	20^0	3 $p-20$	8260.436		(3,1)	12^0	12 $p-15$	8506.621		(12,4)u	01^1
10 $p+20$	8006.507	8006.247(12)	(10,8)l	02^2	15 $p-6$	8266.460		(15,14)u	01^1	6 $p-23$	8517.159		(6,2)l	03^1
2 $p-11$	8013.644		(2,1)	12^0	5 $p-26$	8269.548		(5,2)l	03^3	1 $p-13$	8519.809		(1,2)	21^1
15 $p-5$	8017.246		(15,7)	00^0	3 $o+10$	8275.007		(3,0)	12^0	4 $p+26$	8523.090	8522.615(21)	(4,4)	12^2

TABLE 3 (continued)

Q. N.[a]					Label[d]		Q. N.[a]					Label[d]		Q. N.[a]					Label[d]	
J	I	P	n	E_{calc}[b] (cm^{-1})	E_{exp}[c] (cm^{-1})	Rot.	Vib.	J	I	P	n	E_{calc}[b] (cm^{-1})	E_{exp}[c] (cm^{-1})	Rot.	Vib.	J	I	P	n	E_{calc}[b] (cm^{-1})	E_{exp}[c] (cm^{-1})	Rot.	Vib.
4	p	+	27	8532.944	8532.448(12)	(4,2)l	12^2	8	p	−	27	8719.623		(8,10)	03^3	13	p	+	13	8898.676		(13,8)	10^0
15	o	−	4	8538.865		(15,3)	00^0	7	p	−	30	8723.372		(7,4)l	03^1	14	p	+	12	8915.420		(14,14)	02^0
20	p	+	1	8539.875		(20,20)	00^0	7	o	−	16	8729.497		(7,6)u	03^1	15	p	−	9	8918.591		(15,17)	02^2
5	o	+	13	8540.141	8539.642(12)	(5,6)	12^2	16	p	+	5	8733.833		(16,16)	10^0	16	o	+	3	8919.168		(16,15)u	01^1
10	p	+	22	8543.308		(10,4)	02^0	12	p	−	17	8734.530		(12,2)u	01^1	8	o	−	13	8919.473		(8,3)	20^0
10	p	−	19	8545.624		(10,8)l	11^1	18	o	−	1	8737.452		(18,15)	00^0	9	p	−	30	8924.988	8924.601(21)	(9,2)l	11^1
9	p	+	22	8548.456		(9,8)	20^0	8	p	−	28	8738.991		(8,8)	03^1	11	p	+	20	8930.701		(11,8)l	02^2
6	o	+	13	8550.179		(6,3)l	03^3	10	p	−	20	8740.025	8739.733(12)	(10,7)u	02^2	10	o	−	11	8931.540		(10,9)	20^0
5	p	+	23	8557.172		(5,1)u	03^1	2	p	+	19	8744.402		(2,1)u	21^1	10	p	−	23	8935.174	8934.919(13)	(10,5)l	02^2
11	p	−	20	8561.525		(11,10)l	11^1	12	p	+	18	8746.539		(12,10)l	02^2	5	p	+	26	8938.948		(5,2)	12^0
8	p	+	29	8561.972		(8,1)u	11^1	4	o	+	11	8748.979	8748.137(21)	(4,0)	12^2	8	p	+	32	8939.808		(8,10)	12^2
9	o	−	15	8565.006	8564.715(15)	(9,6)u	11^1	4	p	+	29	8752.192	8751.462(20)	(4,2)u	12^2	9	o	+	14	8940.205	8940.065(14)	(9,0)	02^2
1	p	+	6	8572.720		(1,1)	21^1	17	o	+	1	8756.619		(17,12)	00^0	3	p	−	25	8942.914		(3,2)u	21^1
4	p	+	28	8573.375		(4,2)	12^0	6	o	−	12	8757.929		(6,6)	03^3	11	p	−	22	8945.891		(11,10)u	11^1
1	o	−	6	8574.403		(1,0)	21^1	5	p	+	24	8759.484		(5,1)u	03^3	3	p	+	18	8946.610		(3,1)l	21^1
16	o	−	2	8575.190		(16,9)	00^0	2	o	−	6	8761.535		(2,0)	21^1	6	p	−	27	8946.897		(6,2)u	03^1
14	p	+	11	8575.666		(14,11)u	01^1	9	o	−	16	8762.271	8762.094(11)	(9,3)u	02^2	6	o	+	15	8948.553	8946.888(12)*	(6,6)	12^0
9	p	−	25	8575.676		(9,1)l	02^2	10	p	+	24	8763.050		(10,2)	02^0	12	o	−	9	8949.021		(12,3)	10^0
10	p	+	23	8578.169		(10,10)	20^0	9	o	+	13	8765.826		(9,3)l	11^1	9	p	+	27	8952.113		(9,1)l	11^1
4	p	−	20	8579.827		(4,1)	12^0	11	p	−	21	8772.922		(11,7)	02^0	14	p	−	10	8955.250		(14,10)u	01^1
12	p	−	16	8582.886		(12,5)	10^0	15	o	−	5	8773.852		(15,12)l	01^1	9	p	−	31	8957.405		(9,8)l	03^1
8	o	−	12	8583.064		(8,0)	11^1	5	p	−	30	8774.892	8774.058(31)	(5,5)	12^2	9	o	−	17	8959.407		(9,0)	11^1
13	p	−	13	8587.078		(13,8)u	01^1	6	p	−	25	8777.967		(6,7)	12^2	5	p	+	27	8962.886	8961.863(13)	(5,4)	12^2
2	o	+	7	8590.380		(2,3)	21^1	9	p	+	25	8780.294	8780.023(20)	(9,5)u	11^1	3	o	−	13	8971.474		(3,0)	21^1
11	p	+	18	8594.359		(11,10)	02^2	10	p	−	21	8786.124		(10,8)u	11^1	5	p	−	32	8971.972		(5,1)	12^0
11	p	+	19	8605.314		(11,8)	02^0	14	o	+	5	8786.369		(14,9)l	01^1	6	o	−	13	8973.388		(6,0)	03^1
6	p	+	29	8605.757		(6,1)l	03^1	13	p	−	14	8787.329		(13,4)l	01^1	5	o	+	15	8979.321		(5,0)	12^0
13	p	+	10	8611.877		(13,14)	02^2	13	p	−	15	8787.748		(13,14)	11^1	8	o	−	14	8980.344	8978.305(13)†	(8,6)l	03^1
7	p	+	25	8611.959		(7,5)l	03^1	8	p	+	31	8789.389		(8,4)	20^0	17	p	+	3	8981.093		(17,17)	01^1
8	p	+	30	8615.863		(8,7)l	03^1	4	p	−	22	8791.144	8790.446(21)	(4,1)u	12^2	11	o	−	12	8982.013	8981.477(12)	(11,9)u	02^2
9	p	+	23	8618.836		(9,4)u	02^2	7	p	−	31	8792.745		(7,8)	03^3	13	p	−	16	8983.051		(13,2)l	01^1
5	p	−	28	8620.874		(5,4)	03^3	5	p	−	31	8793.409		(5,2)u	03^3	10	p	+	27	8983.186		(10,11)	03^1
6	p	−	24	8624.270		(6,4)u	03^1	15	p	+	8	8794.725		(15,13)u	01^1	6	p	+	31	8985.268		(6,1)l	03^3
9	p	−	26	8626.456		(9,10)	03^1	5	p	+	25	8794.729		(5,4)	12^0	12	p	+	20	8986.242		(12,2)	10^0
8	p	−	26	8629.365		(8,5)	20^0	10	p	+	25	8795.279		(10,13)	03^3	7	p	+	26	8987.697		(7,1)l	03^1
5	p	−	29	8636.047	8634.652(14)	(5,5)	12^0	6	p	−	26	8795.648		(6,2)l	03^3	19	p	−	2	8993.902		(19,17)	00^0
12	o	+	9	8641.551		(12,3)u	01^1	5	o	−	15	8808.177	8807.586(18)	(5,3)l	12^2	11	p	−	23	8997.677		(11,11)	20^0
9	p	+	24	8645.701	8645.499(29)	(9,2)l	02^2	16	p	+	6	8809.895		(16,8)	00^0	10	o	+	12	9017.962	9017.824(11)	(10,6)u	02^2
13	o	−	7	8650.911		(13,9)	10^0	10	p	+	26	8819.788		(10,7)l	11^1	5	o	−	17	9050.652	9049.264(18)*	(5,6)	21^1
13	p	+	11	8651.186		(13,5)l	01^1	12	p	+	19	8820.198		(12,4)	10^0	5	o	−	18	9078.301	9077.153(32)	(5,3)u	12^2
12	o	+	10	8651.889		(12,12)	02^2	10	p	−	22	8828.587		(10,1)	02^0	9	o	+	17	9165.074	9164.618(22)	(9,3)u	11^1
5	o	−	14	8652.117		(5,0)	03^3	6	o	+	14	8834.528	8833.688(09)	(6,3)u	03^1	5	p	+	29	9186.991	9185.774(37)	(5,2)u	12^2
15	p	+	6	8654.498		(15,2)	00^0	9	p	−	28	8835.646		(9,7)	20^0	5	o	+	16	9241.971	9241.090(21)	(5,0)	12^2
7	o	−	15	8671.382		(7,9)	12^2	18	p	+	2	8837.258		(18,19)	01^1	11	p	−	26	9252.173	9251.699(15)	(11,7)u	02^2
12	p	+	17	8676.488		(12,1)u	01^1	3	o	+	12	8841.826		(3,3)	21^1	10	o	−	13	9268.164	9267.795(13)	(10,3)l	02^2
4	o	−	12	8680.186	8679.526(12)	(4,3)	12^2	13	p	+	12	8847.726		(13,7)u	01^1	6	o	+	17	9290.552	9289.879(12)	(6,3)u	03^3
5	o	+	14	8683.673	8682.938(12)	(5,3)	03^3	4	p	+	30	8852.976	8852.149(12)	(4,5)	21^1	6	p	+	36	9314.461	9313.066(21)	(6,4)u	12^2
2	p	−	13	8688.456		(2,2)	21^1	14	p	−	9	8859.933		(14,11)	10^0	10	o	−	14	9347.534	9346.886(15)	(10,6)u	11^1
10	o	+	11	8691.214	8690.955(11)	(10,6)l	02^2	13	o	+	7	8861.412		(13,3)l	01^1	7	o	+	18	9366.462	9364.720(14)	(7,3)u	03^1
15	p	−	8	8691.410		(15,1)	00^0	7	p	−	32	8868.239		(7,4)l	03^3	6	o	−	16	9410.563	9409.489(09)	(6,0)	03^3
15	p	+	7	8691.807		(15,14)	10^0	3	p	−	24	8869.083		(3,2)l	21^1	6	p	+	37	9429.922	9428.608(13)	(6,1)u	03^3
4	p	−	21	8696.975		(4,1)l	12^2	12	o	−	8	8869.733		(12,12)	11^1	8	o	−	16	9448.280	9446.240(10)*	(8,6)u	03^1
3	p	−	23	8700.697		(3,4)	21^1	9	p	−	29	8872.506	8872.119(21)	(9,1)u	02^2	12	o	−	11	9497.654	9497.272(14)	(12,9)u	02^2
2	p	+	18	8704.167		(2,1)l	21^1	9	p	+	26	8873.489	8873.350(23)	(9,2)u	02^2	10	o	−	16	9564.168	9564.295(15)	(10,3)u	02^2
15	o	+	4	8704.195		(15,0)	00^0	7	o	+	16	8885.813		(7,3)l	03^1	12	p	−	21	9644.523	9643.344(22)	(12,7)l	02^2
12	o	−	7	8706.587	8706.844(26)	(12,0)	01^1	5	o	−	16	8887.790	8886.456(13)	(5,3)	12^0	11	o	+	15	9886.631	9886.079(13)	(11,6)u	02^2
9	p	−	27	8707.442		(9,4)l	11^1	11	o	+	10	8894.796		(11,9)l	11^1								
10	o	−	10	8712.267		(10,3)	02^0	6	p	+	30	8898.674		(6,1)u	03^1								

[a] Quantum numbers J, I (o for $I = 3/2$ and p for $I = 1/2$), and parity (P). The column labeled n is an index for levels with the same J, I, and P ordering them by energy.
[b] Calculated energy value from Watson (*52*).
[c] Experimentally determined energy with its uncertainty in the last digits (2σ) in parentheses.
[d] Rotational and vibrational labels assigned as described in Section 3.1.
† Unusually large deviation from *ab initio* calculations.
* Level constructed using only transitions verified by combination differences.

this occurs, levels will have to be labeled by the only good quantum numbers $(J, I, \pm)$ and the energy-ordering index n.

The results of our energy level labeling scheme are listed in Table 3. Every ro-vibrational level below 9000 cm^{-1} has been labeled with J, G, v_1, v_2, ℓ, and (where appropriate), u or l. A few levels have been labeled above 9000 cm^{-1}, corresponding to the upper states of some of the experimentally observed transitions. We have related these labels to the quantum numbers usually used in the theoretical calculations, J, I, parity, and n. Note that our assignment of n, the index ordering levels with the same J, I, and parity by energy, is not necessarily final. We based n on the ordering of the energy levels in the calculations of Watson. It is possible, though unlikely, that for very closely spaced energy levels, the ordering of these levels may change in more accurate calculations, thus changing the assigned values of n. Also included in this table are the experimentally determined energy levels, which are the subject of section 3.3.

Our work is not the first attempt at labeling the energy levels. In 1994, Majewski *et al.* (which we refer to as Maj94 for the remainder of the paper) labeled each of the experimentally determined levels available at the time. This list was later expanded by Dinelli *et al.* (Din97) (*33*) to include many of the levels below 9000 cm^{-1}. The list of Din97 is not complete however; 273 levels were left unlabeled. Of the roughly 720 levels that our work and Din97 have in common, 79 levels differ in assignment. Ten of these discrepancies can be blamed on the arbitrary assignment of the highly mixed levels in Table 2. Most of the remaining disagreements appear to be errors in the assignments of Din97. During our analysis, we found that some of their labels violated parity and symmetry requirements, some levels were labeled as a being part of a pair of G levels when there was only one way to form G, and one label was assigned to two separate levels. Probably most of these misassignments were caused by not considering all of the levels simultaneously, which was essential to our analysis.

III.2. Compilation and assignment of laboratory data

Once the energy levels were given unique labels, the next step was to compile and analyze the frequency, uncertainty, and assignment for every transition reported. Every study in Table 1 was included in our analysis. (Please note that reference to each of these works for the remainder of the paper will be made using the labels assigned in Table 1.)

Instead of reviewing every assignment made (many transitions have been assigned and reassigned more than three times), we decided to consider all of the data simultaneously and make our own assignments independently. To make the assignments, we compared the transition frequencies to the variational calculations of Watson (*55*) and Neale, Miller, and Tennyson (NMT) (*56*), which are both based on spectroscopically fitted potential energy surfaces. We found that a combination of both calculations was necessary in our analysis. The NMT calculations were very good, generally differing from experiment by ~ 0.05 cm^{-1}. There is a serious problem with these predictions, however, for levels with $J > 9$, and the error can be as high as several cm^{-1} (see Section 4.2). Watson's calculations, though not as precise, are very reliable and were used to assign levels of high J.

The intensity predictions[3] of both calculations were very similar, with NMT's, on average, lower than Watson's by $\sim 1\%$ (with a standard deviation of 8%). H_3^+ is known to exhibit non-thermal population distributions in laboratory discharges, but can be described effectively as having thermal distributions among vibrational states and rotational levels, individually (*31*). We adjusted the theoretical intensities accordingly, assuming a vibrational temperature of 1200 K and a rotational temperature of 500 K. While the discharges used in each of the experiments had different temperatures, the values that we chose are roughly the average, and served to predict the order of magnitude of each transition's intensity.

Transition intensities were only reported in the literature for a few of the studies. Fortunately, we had access to all of the previous laser scans performed in Chicago (Baw90, Xu90, Lee91, Xu92, Ven94, Uy94, Joo00, McC01, and Lin01), and it was very important to our assignments to look at the transition intensities. By comparing the experimental intensities to the theoretically calculated intensities, we were able to determine roughly the sensitivity cutoff, limiting the number of possible lines available for each assignment. For lines that were very close together, it was useful to look at the original scans to see if some features were hidden on the shoulder of other transitions. In several cases we concluded that two calculated transitions were completely overlapped and were observed as a single feature. Studying these scans also enabled us to judge the quality of each line, and make an estimate of the uncertainty on a line by line basis. We did not have access to the raw data from the FTIR emission studies, and were not able to make such judgements on those lines.

During our analysis, we found that the uncertainties reported in the literature did not account for the discrepancies between different measurements of transition frequencies. This prompted us to re-examine the uncertainty for every experiment, and in most circumstances to increase them. We were rather conservative in our assignment of uncertainties, preferring to overestimate rather than underestimate the error. It is probably safe to consider our values as roughly two times the standard deviation.

A few systematic errors were identified which also have led to an increase in the uncertainty. As recently reported in McC00, it was found that the rate at which a scan needs

to be performed is much slower than had previously been thought. In this work, the authors observed small shifts in the transition frequency due to the scan rate and the lock-in detection time constant. We have studied this phenomenon carefully and have concluded that one needs to spend at least 30 time constants on a velocity modulated transition to avoid a frequency shift in the absorption feature. This requirement was not met in previous laser scans (in Chicago) and must be taken into account by increasing the uncertainty in every transition to 0.01 cm^{-1}. This error will not apply to the FTIR emission and absorption data (Maj87, Maj89, Nak90, Maj94, McK98). Another frequency error was noticed in the work of Uy94, in which several of the reported transitions disagreed with other reported values by 0.02–0.03 cm^{-1}.

Finally, there seemed to be a larger than expected difference in some of the reported FTIR emission transition frequencies (Maj89, Maj94) when compared to the theory and laser absorption experiments. Some of the lines that we were unable to assign (Table 4) from Maj89 and Maj94 were within 0.2 cm^{-1} of theoretically predicted lines that should be very strong. One difficulty with the FTIR emission experiments is the ubiquitous Rydberg H_2 emission. While these background features were identified by their strong pressure dependence (the Rydbergs are quenched at higher pressure), the apparent H_3^+ line position could be displaced if it were on the side of a strong H_2 signal. It is also possible that some of the lines attributed to H_3^+ are in fact H_2 lines which happen to increase in intensity with pressure.

It became apparent during our work that many of the lines assigned in Din97 were based on frequency alone. While the differences between the calculated and observed transition frequencies were usually small, sometimes assignments were made to transitions predicted to have intensities orders of magnitude weaker than the experimental sensitivity. This may partly be due to the fact that observed intensities are rarely published in the literature, and we urge experimenters to publish this information in the future. Frequently our reassignment of such lines increased the frequency difference from theory but ultimately made a much more reasonable assignment.

Once all of the assignments were made, we verified many of them by checking for combinations of other transitions that led to the same energy differences (combination differences). A program was written to search for all possible combinations of transitions that created closed "loops" of up to 6 transitions. The frequency of every verified transition agreed within 1.5 times the uncertainty in the frequency calculated by a combination of other transitions.

To label the transitions, we have extended the energy level notation from Section 3.1 using the band symbol

$$v_1'\nu_1 + v_2'\nu_2^{|\ell'|} \leftarrow v_1''\nu_1 + v_2''\nu_2^{|\ell''|} \qquad [7]$$

TABLE 4

Remaining unassigned transitions. Some of these lines were previously assigned but have been 'unassigned' during our analysis. Transitions marked with asterisks do not have any reasonable assignment and are likely not due to H_3^+. Lines without an asterisk had one or more candidate assignments whose frequency and/or intensity difference from theory was too large to make a confident assignment.

Frequency (cm^{-1})	Ref[a]	Frequency (cm^{-1})	Ref[a]	Frequency (cm^{-1})	Ref[a]
1980.367	Maj94	2702.321*	Baw90	3124.264*	Lin01
2028.198	Maj94	2708.432	Baw90	3128.912*	Xu92
2134.607	Maj94	2708.778	Baw90	3137.325	Xu92
2174.478	Maj94	2716.843*	Baw90	3161.895*	Xu92
2405.031	Baw90	2754.319	Baw90	3175.891	Maj94
2483.977	Baw90	2807.248*	Baw90	3177.467*	Maj94
2579.828	Baw90	2882.795*	Baw90	3180.420*	Xu92
2611.471*	Baw90	2915.872	Xu92	3182.593	Xu92
2612.538	Baw90	2918.157	Xu92	3182.605*	Lin01
2614.022*	Baw90	2932.711	Baw90	3188.562*	Maj94
2622.894*	Baw90	2942.920*	Maj94	3205.732*	Maj94
2623.274*	Baw90	2950.516	Maj94	3206.893*	Xu92
2626.289	Baw90	2958.735	Xu92	3235.521*	Lin01
2630.492	Baw90	2958.899	Xu92	3241.009	Maj94
2630.603*	Baw90	2965.791*	Xu92	3249.591*	Lin01
2653.290*	Baw90	2987.381	Maj94	3357.525*	Lin01
2653.559*	Baw90	2990.280*	Maj94	4394.944	Maj94
2653.692*	Baw90	2995.601*	Xu92	4587.373	Maj89
2672.862	Baw90	3005.898	Xu92	4756.345	Maj89
2673.229	Baw90	3022.332	Xu92	4788.544	Maj89
2674.344*	Baw90	3023.904*	Maj94	4823.315	Xu90
2680.330	Baw90	3104.125*	Lin01	4823.348	Maj89
2680.485	Baw90	3120.826	Xu92	4823.892	Maj94
2699.334*	Baw90	3121.475*	Xu92	4942.862	Maj89

[a] Reference from which the transition frequency was taken. Labels used in this column are defined in Table 1.

or more compactly

$$v_1' v_2'^{|\ell'|} \leftarrow v_1'' v_2''^{|\ell''|} \qquad [8]$$

and the branch symbol

$$^{\{n|t|\pm 6|\pm 9|\ldots\}}\{P|Q|R\}(J'', G'')^{\{u|l\}}_{\{u|l\}} \qquad [9]$$

where P, Q, and R correspond to the usual $\Delta J = -1, 0, +1$. As was done for the level labels, u and l are appended to the end of the symbol, when appropriate, as a superscript and/or subscript referring to the upper and lower states in the transition, respectively. The preceding superscript specifies ΔG when it is not 0. For overtone and forbidden bands ΔG can equal ± 3 (or ± 1, see footnote [4]), signified by t and n for the + and −, respectively. For highly mixed levels $|\Delta G| > 3$ are possible and these are labeled by $\pm 6, \pm 9$, etc.

A total of 895 unique transition frequencies have been reported in the literature, and we were able to assign 823 of them to transitions of H_3^+. Table 5 lists the adopted frequency, estimated uncertainty, assignment, and literature reference for each assigned transition. The assignments of 486 of these transitions were verified by their combination differences and are denoted by asterisks. For transitions that have been reported multiple times, we used the

TABLE 5
Observed and assigned laboratory transitions of H_3^+.

Frequency[a] (cm^{-1})	Assignment[b] Label	Band	Ref[c]	Frequency[a] (cm^{-1})	Assignment[b] Label	Band	Ref[c]	Frequency[a] (cm^{-1})	Assignment[b] Label	Band	Ref[c]
1546.901 (10)	$P(12,12)$	$01^1 \leftarrow 00^0$	Joo00	2134.241 (10)*	$Q(7,6)_u$	$02^0 \leftarrow 01^1$	Maj94	2395.500 (10)*	$Q(8,3)^l$	$01^1 \leftarrow 00^0$	Baw90
1798.396 (02)*	$P(9,9)$	$01^1 \leftarrow 00^0$	Maj87	2134.922 (10)*	$P(5,5)$	$01^1 \leftarrow 00^0$	Maj87	2397.911 (10)*	$Q(9,5)^l$	$01^1 \leftarrow 00^0$	Maj94
1826.160 (02)	$P(9,8)$	$01^1 \leftarrow 00^0$	Maj87	2137.039 (10)*	$P(5,3)_u$	$02^2 \leftarrow 01^1$	Maj94	2398.519 (10)*	$Q(8,7)^l$	$01^1 \leftarrow 00^0$	Maj87
1843.560 (10)*	$P(10,7)^u$	$01^1 \leftarrow 00^0$	Maj94	2140.348 (10)*	$P(5,4)$	$01^1 \leftarrow 00^0$	Maj87	2399.749 (10)*	$Q(1,1)$	$11^1 \leftarrow 10^0$	Baw90
1865.199 (10)*	$P(9,7)^u$	$01^1 \leftarrow 00^0$	Maj94	2142.328 (10)*	$P(5,4)_u$	$02^2 \leftarrow 01^1$	Maj94	2402.621 (10)*	$Q(6,0)$	$02^2 \leftarrow 01^1$	Baw90
1867.905 (10)	$P(11,6)^u$	$01^1 \leftarrow 00^0$	Maj94	2152.615 (10)	$P(3,0)$	$11^1 \leftarrow 10^0$	Maj94	2403.350 (20)*	$Q(2,3)$	$12^2 \leftarrow 11^1$	Baw90
1868.703 (10)*	$P(9,10)$	$02^2 \leftarrow 01^1$	Maj94	2152.887 (10)*	$P(5,3)^u$	$01^1 \leftarrow 00^0$	Maj87	2406.029 (10)*	$Q(2,1)^u$	$11^1 \leftarrow 10^0$	Baw90
1876.392 (10)*	$P(9,9)$	$02^2 \leftarrow 01^1$	Maj94	2160.320 (10)*	$P(5,5)$	$02^2 \leftarrow 01^1$	Maj94	2408.730 (10)*	$Q(8,6)^l$	$01^1 \leftarrow 00^0$	Maj87
1882.985 (10)	$P(8,8)$	$01^1 \leftarrow 00^0$	Maj94	2164.278 (10)*	$P(5,2)^u$	$01^1 \leftarrow 00^0$	Maj87	2411.518 (10)*	$Q(8,5)^l$	$01^1 \leftarrow 00^0$	Maj87
1883.755 (10)*	$P(10,6)^u$	$01^1 \leftarrow 00^0$	Maj94	2168.349 (10)*	$P(5,6)$	$02^2 \leftarrow 01^1$	Baw90	2412.859 (10)*	$Q(2,2)$	$11^1 \leftarrow 10^0$	Baw90
1904.235 (10)*	$P(8,7)$	$01^1 \leftarrow 00^0$	Maj94	2168.698 (10)*	$P(3,3)$	$11^1 \leftarrow 10^0$	Baw90	2413.314 (10)*	$Q(5,1)^l_u$	$02^2 \leftarrow 01^1$	Baw90
1905.488 (10)*	$P(9,6)^u$	$01^1 \leftarrow 00^0$	Maj94	2172.815 (10)*	$P(5,1)^u$	$01^1 \leftarrow 00^0$	Maj87	2413.922 (10)*	$R(1,1)$	$02^0 \leftarrow 01^1$	Baw90
1916.714 (10)	$P(10,5)^u$	$01^1 \leftarrow 00^0$	Maj94	2175.780 (10)*	$P(5,0)$	$01^1 \leftarrow 00^0$	Maj87	2416.289 (10)*	$R(1,0)$	$21^1 \leftarrow 20^0$	Baw90
1921.286 (10)*	$P(8,6)_u$	$02^2 \leftarrow 01^1$	Maj94	2182.348 (10)*	$P(4,2)_u$	$02^2 \leftarrow 01^1$	Maj94	2417.764 (10)*	$Q(7,4)^l$	$01^1 \leftarrow 00^0$	Maj87
1925.254 (10)	$P(11,4)^u$	$01^1 \leftarrow 00^0$	Maj94	2197.743 (10)*	$P(4,3)_u$	$02^2 \leftarrow 01^1$	Maj94	2418.899 (10)	$Q(7,0)$	$01^1 \leftarrow 00^0$	Baw90
1927.291 (10)	$P(11,0)$	$01^1 \leftarrow 00^0$	Maj94	2202.691 (10)	$P(4,6)$	$03^3 \leftarrow 02^2$	Maj94	2419.558 (30)	$Q(7,1)^l$	$01^1 \leftarrow 00^0$	Baw90
1927.792 (10)	$P(7,2)^u$	$11^1 \leftarrow 10^0$	Maj94	2217.451 (10)*	$P(4,4)$	$01^1 \leftarrow 00^0$	Wat84	2420.207 (10)	$Q(3,2)^u$	$11^1 \leftarrow 10^0$	Baw90
1933.653 (10)*	$P(4,3)_l$	$02^0 \leftarrow 01^1$	Maj94	2218.129 (10)*	$P(4,3)$	$01^1 \leftarrow 00^0$	Wat84	2420.728 (10)	$Q(7,3)^l$	$01^1 \leftarrow 00^0$	Baw90
1935.714 (10)*	$P(8,6)^u$	$01^1 \leftarrow 00^0$	Maj94	2223.965 (10)*	$P(4,2)^u$	$01^1 \leftarrow 00^0$	Wat84	2421.888 (10)*	$Q(7,2)^l$	$01^1 \leftarrow 00^0$	Baw90
1937.873 (10)*	$P(8,7)_u$	$02^2 \leftarrow 01^1$	Maj94	2229.895 (10)*	$P(4,1)^u$	$01^1 \leftarrow 00^0$	Wat84	2422.983 (10)*	$Q(3,1)^l_u$	$02^2 \leftarrow 01^1$	Baw90
1939.934 (10)*	$P(9,5)^u$	$01^1 \leftarrow 00^0$	Maj94	2229.912 (10)*	$P(4,4)$	$02^2 \leftarrow 01^1$	Maj94	2423.646 (10)*	$Q(7,6)^l$	$01^1 \leftarrow 00^0$	Maj87
1944.087 (10)*	$P(8,9)$	$02^2 \leftarrow 01^1$	Maj94	2241.077 (10)*	$P(2,2)$	$11^1 \leftarrow 10^0$	Baw90	2423.675 (20)*	$Q(4,1)^l_u$	$02^2 \leftarrow 01^1$	Baw90
1945.254 (10)	$P(10,4)^u$	$01^1 \leftarrow 00^0$	Maj94	2241.347 (10)*	$P(4,5)$	$02^2 \leftarrow 01^1$	Baw90	2424.797 (10)*	$Q(3,3)$	$11^1 \leftarrow 10^0$	Baw90
1947.467 (10)*	$P(8,8)$	$02^2 \leftarrow 01^1$	Maj94	2250.525 (10)	$Q(7,0)$	$02^0 \leftarrow 01^1$	Maj94	2431.821 (10)*	$Q(7,5)^l$	$01^1 \leftarrow 00^0$	Maj87
1958.420 (10)	$P(10,1)^u$	$01^1 \leftarrow 00^0$	Maj94	2253.633 (10)*	$Q(1,0)$	$02^0 \leftarrow 01^1$	Maj94	2433.901 (10)*	$Q(4,3)^u$	$11^1 \leftarrow 10^0$	Baw90
1959.957 (50)*	$P(3,1)_u$	$02^0 \leftarrow 01^1$	Maj94	2260.480 (10)	$Q(11,3)^l$	$01^1 \leftarrow 00^0$	Maj94	2436.653 (10)*	${}^tQ(6,3)_u$	$11^1 \leftarrow 01^1$	Baw90
1967.450 (02)*	$P(7,7)$	$01^1 \leftarrow 00^0$	Maj87	2260.480 (10)	$Q(1,1)$	$03^1 \leftarrow 02^0$	Maj94	2438.509 (10)*	$Q(4,4)$	$11^1 \leftarrow 10^0$	Baw90
1968.800 (02)*	$P(8,5)^u$	$01^1 \leftarrow 00^0$	Maj87	2265.551 (10)	$Q(6,2)_l$	$02^0 \leftarrow 01^1$	Maj94	2446.632 (10)*	$Q(6,5)^l$	$01^1 \leftarrow 00^0$	Maj87
1969.319 (10)*	$P(9,4)^u$	$01^1 \leftarrow 00^0$	Maj94	2271.405 (10)*	$Q(6,3)_l$	$02^0 \leftarrow 01^1$	Maj94	2447.903 (10)*	$Q(6,1)^l$	$01^1 \leftarrow 00^0$	Maj87
1977.313 (10)	$P(9,2)^u$	$01^1 \leftarrow 00^0$	Maj94	2274.262 (10)	$Q(11,0)$	$01^1 \leftarrow 00^0$	Maj94	2449.533 (10)*	$Q(6,2)^l$	$01^1 \leftarrow 00^0$	Maj87
1981.672 (10)*	$P(7,3)^u_u$	$02^2 \leftarrow 01^1$	Maj94	2277.104 (10)*	$Q(5,3)_l$	$02^0 \leftarrow 01^1$	Maj94	2449.800 (10)*	$Q(4,0)$	$02^2 \leftarrow 01^1$	Baw90
1982.486 (10)*	$P(6,6)$	$11^1 \leftarrow 10^0$	Maj94	2279.406 (30)*	$Q(3,1)_l$	$02^0 \leftarrow 01^1$	Maj94	2449.885 (10)	$P(1,2)$	$02^2 \leftarrow 01^1$	Baw90
1982.874 (02)*	$P(7,6)$	$01^1 \leftarrow 00^0$	Maj87	2279.406 (30)*	$Q(3,2)_l$	$02^0 \leftarrow 01^1$	Maj94	2452.718 (10)*	$Q(6,3)^l$	$01^1 \leftarrow 00^0$	Maj87
1984.067 (10)*	$P(7,5)_u$	$02^2 \leftarrow 01^1$	Maj94	2279.632 (10)*	$Q(3,0)$	$02^0 \leftarrow 01^1$	Maj94	2453.408 (10)*	$Q(6,4)^l$	$01^1 \leftarrow 00^0$	Maj87
1990.807 (10)*	$P(6,0)$	$02^2 \leftarrow 01^1$	Maj94	2279.913 (10)	$Q(5,0)$	$02^0 \leftarrow 01^1$	Maj94	2454.417 (10)*	${}^tQ(7,4)$	$10^0 \leftarrow 00^0$	Baw90
1996.884 (10)*	$P(8,4)^u$	$01^1 \leftarrow 00^0$	Maj94	2280.547 (10)	$Q(5,1)_l$	$02^0 \leftarrow 01^1$	Maj94	2456.273 (20)*	$Q(4,2)^l_l$	$02^2 \leftarrow 01^1$	Baw90
1997.172 (10)	$P(9,1)^u$	$01^1 \leftarrow 00^0$	Maj94	2284.000 (10)*	$Q(4,2)_l$	$02^0 \leftarrow 01^1$	Maj94	2457.290 (05)	$P(1,1)$	$01^1 \leftarrow 00^0$	McK98
2001.479 (10)	$P(9,0)$	$01^1 \leftarrow 00^0$	Maj94	2284.333 (10)	$Q(4,1)_l$	$02^0 \leftarrow 01^1$	Maj94	2457.613 (10)*	$Q(5,5)$	$11^1 \leftarrow 10^0$	Baw90
2002.045 (10)*	$P(9,3)^u$	$01^1 \leftarrow 00^0$	Maj94	2295.577 (10)*	$P(3,1)^u$	$01^1 \leftarrow 00^0$	Wat84	2457.912 (10)*	$R(1,0)$	$03^1 \leftarrow 02^0$	Baw90
2006.615 (10)*	$P(7,6)_u$	$02^2 \leftarrow 01^1$	Maj94	2295.947 (10)*	$P(3,2)$	$01^1 \leftarrow 00^0$	Wat84	2458.850 (10)	$R(1,1)^u$	$03^1 \leftarrow 02^0$	Baw90
2007.290 (10)*	$P(7,5)^u$	$01^1 \leftarrow 00^0$	Maj87	2295.980 (10)*	$P(3,0)$	$01^1 \leftarrow 00^0$	Wat84	2464.652 (10)*	$R(2,3)$	$02^0 \leftarrow 01^1$	Baw90
2011.400 (10)*	$P(6,3)^u_u$	$02^2 \leftarrow 01^1$	Maj94	2298.930 (10)*	$P(3,3)$	$01^1 \leftarrow 00^0$	Wat84	2467.553 (10)*	$Q(5,4)^l$	$01^1 \leftarrow 00^0$	Baw90
2018.029 (10)*	$P(8,3)^u$	$01^1 \leftarrow 00^0$	Maj94	2304.343 (10)*	$P(3,3)$	$02^2 \leftarrow 01^1$	Maj94	2469.235 (10)	$Q(5,3)_u$	$03^3 \leftarrow 02^2$	Baw90
2018.760 (10)*	$P(7,7)$	$02^2 \leftarrow 01^1$	Maj94	2312.918 (10)*	$P(3,4)$	$02^2 \leftarrow 01^1$	Maj94	2470.605 (10)	${}^tQ(8,4)$	$10^0 \leftarrow 00^0$	Baw90
2019.376 (10)*	$P(7,8)$	$02^2 \leftarrow 01^1$	Maj94	2314.681 (10)	$Q(10,4)^l$	$01^1 \leftarrow 00^0$	Maj94	2471.384 (10)	$R(3,3)^l$	$03^1 \leftarrow 02^0$	Baw90
2020.914 (10)*	$P(5,4)$	$11^1 \leftarrow 10^0$	Maj94	2324.698 (10)	$Q(10,3)^l$	$01^1 \leftarrow 00^0$	Maj94	2471.923 (10)	$Q(5,0)$	$01^1 \leftarrow 00^0$	Baw90
2022.011 (10)*	$P(5,3)^u$	$11^1 \leftarrow 10^0$	Maj94	2331.823 (10)	$Q(11,9)^l$	$01^1 \leftarrow 00^0$	Maj94	2472.325 (10)*	$Q(5,1)^l$	$01^1 \leftarrow 00^0$	Maj87
2023.165 (10)	$P(8,2)^u$	$01^1 \leftarrow 00^0$	Maj94	2333.983 (10)	$Q(5,0)$	$11^1 \leftarrow 10^0$	Maj94	2472.846 (10)*	$Q(5,3)^l$	$01^1 \leftarrow 00^0$	Maj87
2032.182 (10)*	$P(5,5)$	$11^1 \leftarrow 10^0$	Maj94	2334.544 (10)	$Q(5,1)^l$	$11^1 \leftarrow 10^0$	Maj94	2473.238 (10)*	$Q(5,2)^l$	$01^1 \leftarrow 00^0$	Maj87
2033.318 (10)*	$P(7,4)^u$	$01^1 \leftarrow 00^0$	Maj87	2335.567 (10)*	$Q(5,3)^l$	$11^1 \leftarrow 10^0$	Maj94	2474.054 (10)*	$Q(2,0)$	$02^2 \leftarrow 01^1$	Baw90
2036.291 (10)	$P(8,1)^u$	$01^1 \leftarrow 00^0$	Maj94	2341.498 (10)	$Q(10,9)^l$	$01^1 \leftarrow 00^0$	Maj94	2477.797 (10)†	$Q(4,2)_u$	$03^3 \leftarrow 02^2$	Baw90
2051.510 (10)*	$P(6,6)$	$01^1 \leftarrow 00^0$	Maj87	2348.355 (10)*	$Q(9,3)^l$	$01^1 \leftarrow 00^0$	Maj94	2483.553 (10)*	$Q(3,1)^l_l$	$02^2 \leftarrow 01^1$	Baw90
2054.047 (10)*	$P(6,4)_u$	$02^2 \leftarrow 01^1$	Maj94	2350.775 (10)	$Q(4,1)^l$	$11^1 \leftarrow 10^0$	Maj94	2486.559 (05)*	$Q(4,3)^l$	$01^1 \leftarrow 00^0$	McK98
2057.444 (10)*	$P(2,0)$	$02^0 \leftarrow 01^1$	Maj94	2351.639 (10)	$Q(9,0)$	$01^1 \leftarrow 00^0$	Maj94	2486.844 (10)*	$R(2,2)$	$02^0 \leftarrow 01^1$	Baw90
2060.200 (10)*	$P(7,3)^u$	$01^1 \leftarrow 00^0$	Maj87	2353.250 (10)	$Q(9,2)^l$	$01^1 \leftarrow 00^0$	Maj94	2491.745 (05)*	$Q(4,2)^l$	$01^1 \leftarrow 00^0$	McK98
2061.680 (10)*	$P(6,5)$	$01^1 \leftarrow 00^0$	Maj87	2354.125 (10)*	$Q(9,4)^l$	$01^1 \leftarrow 00^0$	Maj94	2491.906 (10)*	$Q(6,6)$	$11^1 \leftarrow 10^0$	Baw90
2067.366 (10)*	$P(10,8)_l$	$01^1 \leftarrow 00^0$	Maj87	2357.951 (10)*	$Q(10,7)^l$	$01^1 \leftarrow 00^0$	Maj94	2491.976 (10)*	$R(2,1)_u$	$02^0 \leftarrow 01^1$	Baw90
2073.951 (10)*	$P(6,5)_u$	$02^2 \leftarrow 01^1$	Maj94	2360.957 (10)*	$Q(10,6)^l$	$01^1 \leftarrow 00^0$	Maj94	2492.537 (05)*	$Q(4,1)^l$	$01^1 \leftarrow 00^0$	McK98
2077.500 (10)*	$P(7,1)^u$	$01^1 \leftarrow 00^0$	Maj87	2362.676 (10)	$Q(3,1)^l$	$11^1 \leftarrow 10^0$	Maj94	2492.728 (10)*	$R(2,0)$	$02^0 \leftarrow 01^1$	Baw90
2079.433 (10)*	$P(6,4)^u$	$01^1 \leftarrow 00^0$	Maj87	2364.814 (10)	$Q(3,0)$	$11^1 \leftarrow 10^0$	Maj94	2497.349 (10)	$R(1,0)$	$12^2 \leftarrow 11^1$	Baw90
2080.683 (10)	$P(7,0)$	$01^1 \leftarrow 00^0$	Maj94	2371.155 (10)	$Q(9,8)^l$	$01^1 \leftarrow 00^0$	Maj94	2498.080 (10)†	$P(1,3)$	$03^3 \leftarrow 02^2$	Baw90
2089.305 (10)*	$P(4,3)$	$11^1 \leftarrow 10^0$	Baw90	2372.185 (10)*	$P(2,1)$	$01^1 \leftarrow 00^0$	Wat84	2503.350 (05)*	$Q(3,2)^l$	$01^1 \leftarrow 00^0$	McK98
2089.764 (10)*	$P(6,6)$	$02^2 \leftarrow 01^1$	Baw90	2378.869 (10)*	$P(2,2)$	$01^1 \leftarrow 00^0$	Wat84	2508.134 (05)*	$Q(3,1)^l$	$01^1 \leftarrow 00^0$	McK98
2094.236 (10)*	$P(6,7)$	$02^2 \leftarrow 01^1$	Maj94	2380.555 (10)*	$P(2,3)$	$02^2 \leftarrow 01^1$	Maj94	2508.757 (10)*	$Q(4,1)^u_u$	$02^2 \leftarrow 01^1$	Baw90
2095.263 (10)*	$P(5,2)^u_u$	$02^2 \leftarrow 01^1$	Maj94	2384.252 (10)*	$Q(9,7)^l$	$01^1 \leftarrow 00^0$	Maj94	2509.078 (05)	$Q(3,0)$	$01^1 \leftarrow 00^0$	McK98
2096.629 (10)*	$P(6,3)^u$	$01^1 \leftarrow 00^0$	Maj87	2384.802 (10)*	$Q(9,6)^l$	$01^1 \leftarrow 00^0$	Maj94	2509.726 (10)	$R(3,3)^l$	$21^1 \leftarrow 20^0$	Baw90
2097.745 (10)*	$P(4,4)$	$11^1 \leftarrow 10^0$	Baw90	2387.602 (10)	$Q(8,1)^l$	$01^1 \leftarrow 00^0$	Maj94	2510.291 (10)*	$Q(3,1)^u_u$	$02^2 \leftarrow 01^1$	Baw90
2113.241 (10)*	$P(6,2)^u$	$01^1 \leftarrow 00^0$	Maj87	2388.452 (10)	$Q(8,2)^l$	$01^1 \leftarrow 00^0$	Maj94	2514.619 (10)*	$Q(2,1)_u$	$02^2 \leftarrow 01^1$	Baw90
2120.357 (10)*	$P(4,0)$	$02^2 \leftarrow 01^1$	Maj94	2389.257 (10)*	$Q(8,4)^l$	$01^1 \leftarrow 00^0$	Maj94	2515.755 (10)*	$Q(1,1)$	$02^2 \leftarrow 01^1$	Baw90
2122.513 (10)*	$P(6,1)^u$	$01^1 \leftarrow 00^0$	Maj87	2394.556 (10)	$R(1,2)$	$02^0 \leftarrow 01^1$	Baw90	2518.211 (05)*	$Q(2,1)^l$	$01^1 \leftarrow 00^0$	McK98

TABLE 5 (continued)

Frequency[a] (cm^{-1})	Assignment[b] Label	Band	Ref[c]	Frequency[a] (cm^{-1})	Assignment[b] Label	Band	Ref[c]	Frequency[a] (cm^{-1})	Assignment[b] Label	Band	Ref[c]
2520.677 (10)*	$Q(4,1)_l^l$	$02^2 \leftarrow 01^1$	Baw90	2617.809 (10)*	$Q(5,6)$	$03^3 \leftarrow 02^2$	Baw90	2769.393 (10)*	$R(3,3)^u$	$11^1 \leftarrow 10^0$	Baw90
2529.724 (05)	$Q(1,0)$	$01^1 \leftarrow 00^0$	McK98	2620.589 (10)*	$Q(8,6)^u$	$01^1 \leftarrow 00^0$	Baw90	2769.863 (10)	$R(3,1)^u$	$11^1 \leftarrow 10^0$	Baw90
2532.253 (10)	$R(3,4)$	$02^0 \leftarrow 01^1$	Baw90	2621.514 (10)	$R(4,4)$	$02^0 \leftarrow 01^1$	Baw90	2770.196 (10)†	$R(7,8)$	$02^0 \leftarrow 01^1$	Baw90
2534.922 (10)*	$Q(5,2)_u^u$	$02^2 \leftarrow 01^1$	Baw90	2624.967 (10)*	$Q(6,3)^u$	$01^1 \leftarrow 00^0$	Baw90	2770.940 (10)	$R(3,0)$	$11^1 \leftarrow 10^0$	Baw90
2536.931 (10)*	$Q(4,2)_u^u$	$02^2 \leftarrow 01^1$	Baw90	2626.220 (10)*	$Q(6,7)$	$02^2 \leftarrow 01^1$	Baw90	2771.586 (10)	$R(6,3)_l$	$02^0 \leftarrow 01^1$	Baw90
2538.253 (10)	$R(1,1)^l$	$11^1 \leftarrow 10^0$	Baw90	2628.097 (30)*	$Q(4,2)_l^u$	$02^2 \leftarrow 01^1$	Baw90	2783.325 (10)*	$R(3,1)_u^l$	$02^2 \leftarrow 01^1$	Baw90
2539.451 (10)*	$Q(1,2)$	$02^2 \leftarrow 01^1$	Baw90	2628.119 (20)*	$Q(7,7)$	$02^2 \leftarrow 01^1$	Baw90	2783.417 (10)*	$R(2,1)_u^u$	$02^2 \leftarrow 01^1$	Baw90
2539.744 (10)*	$Q(5,3)_u^u$	$02^2 \leftarrow 01^1$	Baw90	2630.814 (10)	$Q(10,8)^u$	$01^1 \leftarrow 00^0$	Baw90	2785.121 (10)*	$R(3,2)_l^l$	$02^2 \leftarrow 01^1$	Baw90
2541.293 (10)*	$Q(3,2)_u$	$02^2 \leftarrow 01^1$	Baw90	2639.806 (10)*	$Q(7,8)$	$02^2 \leftarrow 01^1$	Baw90	2787.400 (10)	$R(4,0)$	$12^2 \leftarrow 11^1$	Baw90
2541.433 (10)*	$Q(3,0)$	$02^2 \leftarrow 01^1$	Baw90	2640.172 (10)*	$Q(8,8)$	$02^2 \leftarrow 01^1$	Baw90	2789.736 (10)	$R(6,4)_l$	$02^0 \leftarrow 01^1$	Baw90
2542.467 (10)*	$Q(2,2)$	$02^2 \leftarrow 01^1$	Baw90	2648.105 (10)*	$R(2,3)$	$12^2 \leftarrow 11^1$	Baw90	2795.213 (10)	$R(4,3)^u$	$03^1 \leftarrow 02^0$	Baw90
2545.420 (05)*	$Q(1,1)$	$01^1 \leftarrow 00^0$	McK98	2648.692 (10)*	$Q(5,0)$	$02^2 \leftarrow 01^1$	Baw90	2798.620 (10)	$R(7,7)$	$02^0 \leftarrow 01^1$	Baw90
2552.988 (05)*	$Q(2,1)^u$	$01^1 \leftarrow 00^0$	McK98	2649.315 (10)	$R(4,3)_l^l$	$12^2 \leftarrow 11^1$	Baw90	2801.108 (10)	$R(5,4)^l$	$11^1 \leftarrow 10^0$	Baw90
2554.276 (10)*	$Q(3,3)$	$02^2 \leftarrow 01^1$	Baw90	2650.561 (10)	${}^{-6}P(4,6)$	$03^3 \leftarrow 02^2$	Baw90	2809.767 (10)*	$R(2,2)$	$02^2 \leftarrow 01^1$	Baw90
2554.475 (10)*	$Q(4,3)$	$03^3 \leftarrow 02^2$	Baw90	2650.954 (10)*	$Q(9,9)$	$02^2 \leftarrow 01^1$	Baw90	2810.597 (10)*	$R(5,3)^l$	$11^1 \leftarrow 10^0$	Baw90
2554.666 (05)*	$Q(2,2)$	$01^1 \leftarrow 00^0$	McK98	2653.095 (10)*	$Q(8,9)$	$02^2 \leftarrow 01^1$	Baw90	2816.843 (10)*	$R(2,3)$	$02^2 \leftarrow 01^1$	Baw90
2557.484 (10)	$R(3,3)$	$02^0 \leftarrow 01^1$	Baw90	2653.885 (10)*	$R(5,5)^l$	$21^1 \leftarrow 20^0$	Baw90	2817.349 (10)*	$R(5,6)$	$12^0 \leftarrow 11^1$	Baw90
2561.497 (05)*	$Q(3,3)$	$01^1 \leftarrow 00^0$	McK98	2657.652 (10)	$R(5,6)$	$02^0 \leftarrow 01^1$	Baw90	2818.072 (10)*	$R(4,2)_u^l$	$02^2 \leftarrow 01^1$	Baw90
2564.418 (05)*	$Q(3,2)^u$	$01^1 \leftarrow 00^0$	McK98	2660.373 (10)*	$Q(5,3)_l^u$	$02^2 \leftarrow 01^1$	Baw90	2818.196 (10)*	$R(2,1)_l^u$	$02^2 \leftarrow 01^1$	Baw90
2566.904 (10)*	$Q(2,3)$	$02^2 \leftarrow 01^1$	Baw90	2660.638 (10)*	${}^tQ(4,2)_l$	$11^1 \leftarrow 01^1$	Baw90	2821.518 (10)*	$R(8,9)$	$02^0 \leftarrow 01^1$	Baw90
2567.288 (05)*	$Q(4,4)$	$01^1 \leftarrow 00^0$	McK98	2664.213 (10)*†	$R(1,2)$	$03^3 \leftarrow 02^2$	Baw90	2822.357 (30)	$R(4,2)_u^u$	$12^2 \leftarrow 11^1$	Baw90
2568.708 (05)*	$Q(3,1)^u$	$01^1 \leftarrow 00^0$	McK98	2665.729 (10)*	$Q(4,3)_l$	$02^2 \leftarrow 01^1$	Baw90	2822.448 (30)	$R(4,3)_u^u$	$12^2 \leftarrow 11^1$	Baw90
2569.726 (10)*	${}^tQ(6,3)$	$10^0 \leftarrow 00^0$	Xu92	2666.142 (10)†	$R(7,6)^l$	$03^1 \leftarrow 02^0$	Baw90	2822.730 (20)	$R(7,5)_l$	$02^0 \leftarrow 01^1$	Baw90
2570.858 (10)*	$Q(3,1)_l^u$	$02^2 \leftarrow 01^1$	Baw90	2666.500 (10)	$Q(9,10)$	$02^2 \leftarrow 01^1$	Baw90	2823.138 (05)*	$R(2,2)^u$	$01^1 \leftarrow 00^0$	McK98
2570.987 (10)*	$Q(4,6)$	$03^3 \leftarrow 02^2$	Baw90	2670.234 (10)*	$R(1,0)$	$02^2 \leftarrow 01^1$	Baw90	2824.754 (10)	$R(7,4)_l$	$02^0 \leftarrow 01^1$	Baw90
2571.118 (05)*	$Q(5,5)$	$01^1 \leftarrow 00^0$	McK98	2671.142 (10)	$R(2,1)^u$	$11^1 \leftarrow 10^0$	Baw90	2825.956 (10)*	$R(4,3)_l^l$	$02^2 \leftarrow 01^1$	Baw90
2572.220 (10)	$R(1,0)$	$11^1 \leftarrow 10^0$	Baw90	2672.799 (10)	$R(2,2)^u$	$11^1 \leftarrow 10^0$	Baw90	2826.117 (05)*	$R(2,1)^u$	$01^1 \leftarrow 00^0$	McK98
2572.357 (10)*	$Q(6,4)_u^u$	$02^2 \leftarrow 01^1$	Baw90	2672.958 (10)	$R(3,3)^l$	$11^1 \leftarrow 10^0$	Baw90	2829.925 (05)*	$R(3,3)^l$	$01^1 \leftarrow 00^0$	McK98
2573.057 (10)*	$Q(6,3)_u^u$	$02^2 \leftarrow 01^1$	Baw90	2679.487 (10)	$R(4,2)_l$	$02^0 \leftarrow 01^1$	Baw90	2831.340 (10)*	$R(3,1)^l$	$01^1 \leftarrow 00^0$	Wat84
2573.582 (10)*	$Q(6,6)$	$01^1 \leftarrow 00^0$	Maj87	2680.631 (10)	$R(3,2)^l$	$11^1 \leftarrow 10^0$	Baw90	2832.198 (05)*	$R(3,2)^l$	$01^1 \leftarrow 00^0$	McK98
2574.659 (05)*	$Q(4,3)^u$	$01^1 \leftarrow 00^0$	McK98	2681.500 (10)	$R(3,1)^l$	$11^1 \leftarrow 10^0$	Baw90	2836.028 (10)*	${}^nR(5,5)^l$	$02^2 \leftarrow 10^0$	Baw90
2574.893 (10)*	$Q(7,7)$	$01^1 \leftarrow 00^0$	Baw90	2683.755 (10)	$R(5,5)$	$02^0 \leftarrow 01^1$	Baw90	2838.041 (10)	$R(6,6)^l$	$11^1 \leftarrow 10^0$	Baw90
2575.112 (30)*	$Q(9,9)$	$01^1 \leftarrow 00^0$	Baw90	2685.157 (10)*	$R(4,3)_l$	$02^0 \leftarrow 01^1$	Baw90	2841.148 (10)	${}^tQ(2,0)$	$11^1 \leftarrow 01^1$	Baw90
2575.112 (10)*	$R(1,1)^u$	$11^1 \leftarrow 10^0$	Baw90	2685.942 (10)*	${}^tQ(5,2)_l$	$11^1 \leftarrow 01^1$	Xu92	2842.191 (10)*	$R(5,3)_u^l$	$02^2 \leftarrow 01^1$	Baw90
2575.312 (10)	$Q(8,8)$	$01^1 \leftarrow 00^0$	Baw90	2691.443 (05)*	$R(1,1)^l$	$01^1 \leftarrow 00^0$	McK98	2843.898 (20)*	$R(3,1)_l^l$	$02^2 \leftarrow 01^1$	Baw90‖
2577.492 (10)†	$Q(2,3)$	$03^3 \leftarrow 02^2$	Baw90	2695.420 (10)*	$R(1,1)$	$02^2 \leftarrow 01^1$	Baw90	2844.464 (10)*	${}^nR(5,4)^u$	$02^2 \leftarrow 10^0$	Baw90‡
2577.629 (10)*	$Q(4,3)_u$	$02^2 \leftarrow 01^1$	Baw90	2696.110 (10)*	$R(2,1)_u^l$	$02^2 \leftarrow 01^1$	Baw90	2851.433 (10)	$R(8,8)$	$02^0 \leftarrow 01^1$	Baw90
2577.694 (10)*	$R(1,1)$	$03^3 \leftarrow 02^2$	Baw90	2700.573 (10)*	$R(3,0)$	$12^2 \leftarrow 11^1$	Baw90	2852.156 (10)	${}^tR(2,0)$	$12^0 \leftarrow 02^2$	Baw90
2579.390 (10)	$R(2,0)$	$03^3 \leftarrow 02^2$	Baw90	2704.382 (10)	$R(3,2)^u$	$03^1 \leftarrow 02^0$	Baw90	2853.598 (10)*	$R(4,1)_u^l$	$02^2 \leftarrow 01^1$	Baw90
2579.672 (10)*	$Q(5,4)_u$	$02^2 \leftarrow 01^1$	Baw90	2709.405 (10)*	${}^nR(4,4)^u$	$02^2 \leftarrow 10^0$	Baw90	2854.191 (10)*	${}^tR(5,4)_l$	$11^1 \leftarrow 01^1$	Baw90
2579.748 (10)*	$Q(3,4)$	$02^2 \leftarrow 01^1$	Baw90	2709.479 (10)	$R(3,1)_u^u$	$12^2 \leftarrow 11^1$	Baw90	2862.151 (10)*	$R(4,4)^u$	$11^1 \leftarrow 10^0$	Baw90
2581.184 (10)*	$Q(5,4)^u$	$01^1 \leftarrow 00^0$	Maj87	2713.789 (10)	$R(4,5)$	$12^0 \leftarrow 11^1$	Baw90	2864.369 (10)	$R(4,2)^u$	$11^1 \leftarrow 10^0$	Baw90
2582.909 (10)*	$Q(4,2)^u$	$01^1 \leftarrow 00^0$	Baw90	2715.559 (10)	$R(6,7)$	$02^0 \leftarrow 01^1$	Baw90	2868.040 (10)	$R(4,1)^u$	$11^1 \leftarrow 10^0$	Baw90
2583.155 (10)*	$Q(4,4)$	$02^2 \leftarrow 01^1$	Baw90	2715.827 (10)	$R(3,3)^u$	$03^1 \leftarrow 02^0$	Baw90†	2868.404 (10)*	$R(3,1)_u^u$	$02^2 \leftarrow 01^1$	Baw90
2586.985 (10)*	$Q(6,5)^u$	$01^1 \leftarrow 00^0$	Maj87	2718.262 (10)*	$R(1,2)$	$02^2 \leftarrow 01^1$	Baw90	2869.535 (10)	$R(9,10)$	$02^0 \leftarrow 01^1$	Baw90
2589.541 (10)*	$Q(4,1)^u$	$01^1 \leftarrow 00^0$	Baw90	2719.437 (10)*†	${}^{-6}Q(2,4)$	$03^3 \leftarrow 02^2$	Baw90	2870.890 (10)*	$R(3,0)$	$02^2 \leftarrow 01^1$	Baw90
2590.071 (10)*	$R(2,0)$	$12^2 \leftarrow 11^1$	Baw90	2724.058 (10)*	$R(3,2)_u^l$	$02^2 \leftarrow 01^1$	Baw90	2884.148 (10)*	${}^tQ(3,0)$	$11^1 \leftarrow 01^1$	Xu92
2590.315 (10)*	$Q(6,5)_u$	$02^2 \leftarrow 01^1$	Baw90	2725.342 (10)*	$R(3,0)$	$03^1 \leftarrow 02^0$	Baw90	2889.052 (10)*	$R(4,1)^l$	$01^1 \leftarrow 00^0$	Baw90
2591.323 (10)*	$Q(7,6)^u$	$01^1 \leftarrow 00^0$	Baw90	2725.898 (05)*	$R(1,0)$	$01^1 \leftarrow 00^0$	McK98	2890.993 (10)*	${}^tR(4,3)_l$	$21^1 \leftarrow 11^1$	Baw90
2593.460 (10)*	$Q(5,3)^u$	$01^1 \leftarrow 00^0$	Maj87	2726.220 (05)*	$R(1,1)^u$	$01^1 \leftarrow 00^0$	McK98	2891.867 (10)*	$R(4,2)^l$	$01^1 \leftarrow 00^0$	Wat84
2594.477 (10)*	$Q(8,7)^u$	$01^1 \leftarrow 00^0$	Baw90	2730.887 (10)*	$R(2,1)_l^l$	$02^2 \leftarrow 01^1$	Baw90	2893.103 (10)	$R(5,0)$	$12^2 \leftarrow 11^1$	Baw90
2595.880 (10)†	$R(6,6)^l$	$03^1 \leftarrow 02^0$	Baw90	2733.639 (10)*	${}^tR(8,7)_l$	$11^1 \leftarrow 01^1$	Baw90	2893.369 (10)*	$R(5,4)_u^l$	$02^2 \leftarrow 01^1$	Baw90
2596.520 (20)	$R(4,5)$	$02^0 \leftarrow 01^1$	Baw90	2734.526 (10)	$R(5,2)_l$	$02^0 \leftarrow 01^1$	Baw90	2894.488 (10)*	$R(4,4)^l$	$01^1 \leftarrow 00^0$	Oka81
2596.520 (20)	$Q(4,5)$	$02^2 \leftarrow 01^1$	Baw90	2735.515 (10)	$R(3,2)_u^u$	$12^2 \leftarrow 11^1$	Baw90	2894.610 (10)*	$R(4,3)^l$	$01^1 \leftarrow 00^0$	Oka81
2597.058 (10)*	$R(4,3)_u$	$02^0 \leftarrow 01^1$	Baw90	2737.851 (10)*	$R(4,3)_u^l$	$02^2 \leftarrow 01^1$	Baw90	2895.600 (10)	$R(7,7)^l$	$11^1 \leftarrow 10^0$	Baw90
2597.702 (10)	$Q(10,9)^u$	$01^1 \leftarrow 00^0$	Baw90	2740.568 (10)*	${}^tR(5,4)_u$	$11^1 \leftarrow 01^1$	Baw90	2895.874 (10)*	$R(3,2)_u^u$	$02^2 \leftarrow 01^1$	Baw90
2599.268 (10)*	$Q(5,5)$	$02^2 \leftarrow 01^1$	Baw90	2742.697 (10)*	$R(6,6)$	$02^0 \leftarrow 01^1$	Baw90	2896.161 (10)*	${}^tR(4,3)_u$	$11^1 \leftarrow 01^1$	Baw90
2600.886 (20)*	$Q(8,6)_u^u$	$02^2 \leftarrow 01^1$	Baw90‖	2743.418 (10)	$R(4,4)^l$	$11^1 \leftarrow 10^0$	Baw90	2898.614 (10)*	$R(7,6)^l$	$11^1 \leftarrow 10^0$	Baw90
2602.367 (10)*	$Q(3,2)_l$	$02^2 \leftarrow 01^1$	Baw90	2744.586 (10)	$R(4,2)^l$	$11^1 \leftarrow 10^0$	Baw90	2901.516 (10)	$R(9,9)$	$02^0 \leftarrow 01^1$	Baw90
2603.883 (10)*	$R(0,1)$	$02^2 \leftarrow 01^1$	Baw90	2744.719 (10)	$R(5,4)_l$	$02^0 \leftarrow 01^1$	Baw90	2901.653 (10)	$R(8,8)^u$	$11^1 \leftarrow 10^0$	Baw90
2605.063 (10)*	$Q(6,4)^u$	$01^1 \leftarrow 00^0$	Baw90	2745.307 (10)	$Q(6,3)_u^u$	$02^2 \leftarrow 01^1$	Baw90	2902.523 (10)	$R(5,4)_u^u$	$12^2 \leftarrow 11^1$	Baw90
2605.763 (10)*	$Q(4,1)_l^u$	$02^2 \leftarrow 01^1$	Baw90	2747.457 (10)*	$R(4,3)^l$	$11^1 \leftarrow 10^0$	Baw90	2909.239 (10)*	$R(4,2)_l^l$	$02^2 \leftarrow 01^1$	Xu92
2605.921 (10)*	$Q(5,2)^u$	$01^1 \leftarrow 00^0$	Baw90	2748.106 (10)*	$R(5,3)_l$	$02^0 \leftarrow 01^1$	Baw90	2918.026 (10)*	$R(3,3)^u$	$01^1 \leftarrow 00^0$	Oka81
2606.154 (10)*	$Q(7,6)_u$	$02^2 \leftarrow 01^1$	Baw90	2754.535 (10)*	$R(2,0)$	$02^2 \leftarrow 01^1$	Baw90	2923.361 (10)*	$R(3,2)^u$	$01^1 \leftarrow 00^0$	Oka81
2606.296 (10)	$R(2,2)^l$	$11^1 \leftarrow 10^0$	Baw90	2756.142 (10)	${}^tR(7,6)_l$	$11^1 \leftarrow 01^1$	Baw90	2924.414 (10)*	$R(6,3)_u^l$	$02^2 \leftarrow 01^1$	Oka81
2611.838 (10)*	$Q(5,6)$	$02^2 \leftarrow 01^1$	Baw90	2762.070 (05)*	$R(2,2)^l$	$01^1 \leftarrow 00^0$	McK98	2928.351 (10)*	$R(3,1)^u$	$01^1 \leftarrow 00^0$	Oka81
2612.842 (10)*	$R(3,2)_l$	$02^0 \leftarrow 01^1$	Baw90	2762.250 (10)*†	$R(5,5)^l$	$11^1 \leftarrow 10^0$	Baw90	2928.470 (10)	${}^nR(6,5)^l$	$02^2 \leftarrow 10^0$	Xu92
2613.540 (10)*	$Q(7,5)^u$	$01^1 \leftarrow 00^0$	Baw90	2765.545 (05)*	$R(2,1)^l$	$01^1 \leftarrow 00^0$	McK98	2930.163 (10)*	$R(3,0)$	$01^1 \leftarrow 00^0$	Oka81
2613.932 (10)	$R(2,1)^l$	$11^1 \leftarrow 10^0$	Baw90	2766.032 (10)*	${}^tR(6,5)_l$	$11^1 \leftarrow 01^1$	Baw90	2931.917 (30)	$R(7,6)_l$	$02^0 \leftarrow 01^1$	Carbo‖
2615.068 (10)*	$Q(6,6)$	$02^2 \leftarrow 01^1$	Baw90	2767.678 (10)	$R(3,2)^u$	$11^1 \leftarrow 10^0$	Baw90	2932.988 (10)*	$R(3,4)$	$02^2 \leftarrow 01^1$	Baw90

TABLE 5 (continued)

Frequency[a] (cm^{-1})	Assignment[b] Label	Band	Ref[c]	Frequency[a] (cm^{-1})	Assignment[b] Label	Band	Ref[c]	Frequency[a] (cm^{-1})	Assignment[b] Label	Band	Ref[c]
2934.155 (10)*	$R(3,3)$	$02^2 \leftarrow 01^1$	Baw90	3042.578 (10)	$R(6,4)^u$	$11^1 \leftarrow 10^0$	Xu92	3152.951 (05)	$R(6,2)^u_u$	$02^2 \leftarrow 01^1$	Lin01
2934.355 (10)*†	$R(3,3)$	$03^3 \leftarrow 02^2$	Baw90	3046.045 (05)	$R(5,1)^l_l$	$02^2 \leftarrow 01^1$	Lin01	3159.015 (05)	$R(9,8)^l$	$01^1 \leftarrow 00^0$	Lin01
2938.491 (10)*	$R(5,1)^l$	$01^1 \leftarrow 00^0$	Xu92	3050.552 (05)*	$R(8,4)^l$	$01^1 \leftarrow 00^0$	Lin01	3160.236 (05)	$R(10,7)^l$	$01^1 \leftarrow 00^0$	Lin01
2941.187 (10)*	$R(7,6)^l_u$	$02^2 \leftarrow 01^1$	Xu92	3051.407 (05)	$R(6,5)^l_l$	$02^2 \leftarrow 01^1$	Lin01	3162.430 (05)	$R(10,6)^l$	$01^1 \leftarrow 00^0$	Lin01
2942.209 (10)*	$R(5,2)^l$	$01^1 \leftarrow 00^0$	Maj87	3052.077 (05)	$R(5,1)^u_u$	$03^3 \leftarrow 02^2$	Lin01	3163.198 (05)	${}^tR(5,1)^l_l$	$11^1 \leftarrow 01^1$	Lin01
2944.828 (10)*	$R(4,0)$	$02^2 \leftarrow 01^1$	Baw90	3053.355 (05)	$R(6,1)^u$	$11^1 \leftarrow 10^0$	Lin01	3167.596 (05)	$R(9,9)^l$	$01^1 \leftarrow 00^0$	Lin01
2949.555 (10)*	$R(5,3)^l$	$01^1 \leftarrow 00^0$	Maj87	3053.562 (05)	$R(10,9)_l$	$02^0 \leftarrow 01^1$	Lin01	3172.045 (05)	$R(8,7)^l_l$	$02^2 \leftarrow 01^1$	Lin01
2950.605 (10)*	$R(4,1)^l_l$	$02^2 \leftarrow 01^1$	Xu92	3056.252 (05)*	$R(7,5)^l$	$01^1 \leftarrow 00^0$	Lin01	3175.189 (05)	$R(7,5)^l_l$	$02^2 \leftarrow 01^1$	Lin01
2951.438 (20)	$R(5,3)^u$	$11^1 \leftarrow 10^0$	Carbo‖	3059.381 (10)	$R(9,5)^l$	$01^1 \leftarrow 00^0$	Xu92	3177.167 (05)*	$R(10,8)^l$	$01^1 \leftarrow 00^0$	Lin01
2953.405 (10)*	$R(4,1)^u_u$	$02^2 \leftarrow 01^1$	Xu92	3059.512 (10)	${}^nP(3,4)^l$	$11^1 \leftarrow 01^1$	Xu92	3177.167 (05)*	$R(7,3)^u$	$11^1 \leftarrow 10^0$	Lin01
2955.154 (10)*	$R(5,4)^l$	$01^1 \leftarrow 00^0$	Uy94	3060.507 (05)*	$R(5,0)$	$02^2 \leftarrow 01^1$	Lin01	3177.628 (05)	${}^nR(7,5)^u$	$02^2 \leftarrow 10^0$	Lin01
2956.073 (10)*	$R(5,5)^l$	$01^1 \leftarrow 00^0$	Oka81	3061.287 (10)*	$R(4,6)$	$03^3 \leftarrow 02^2$	Xu92	3179.115 (05)*	${}^tR(6,3)^u_l$	$11^1 \leftarrow 01^1$	Lin01
2956.222 (10)	${}^{-6}R(6,2)^u$	$01^1 \leftarrow 00^0$	Uy94‖	3062.110 (05)*	$R(6,6)^u$	$11^1 \leftarrow 10^0$	Lin01	3179.998 (05)*	$R(6,4)^u_u$	$02^2 \leftarrow 01^1$	Lin01
2956.843 (30)	${}^tR(7,5)$	$10^0 \leftarrow 00^0$	Xu92‖	3062.813 (10)*	${}^nR(0,1)$	$11^1 \leftarrow 01^1$	Xu92	3182.038 (05)	$R(6,6)^u$	$01^1 \leftarrow 00^0$	Lin01
2956.947 (30)*	$R(3,2)^u_l$	$02^2 \leftarrow 01^1$	Xu92	3063.078 (10)	$R(11,6)^l$	$11^1 \leftarrow 00^0$	Xu92	3182.281 (05)*	${}^tR(5,2)^u_l$	$11^1 \leftarrow 01^1$	Lin01
2962.822 (10)*	$R(5,3)^l_l$	$02^2 \leftarrow 01^1$	Xu92	3063.273 (10)	$R(6,3)^u$	$03^1 \leftarrow 02^0$	Xu92	3187.488 (05)	$R(11,8)^l$	$01^1 \leftarrow 00^0$	Lin01
2964.705 (10)	$R(5,0)$	$11^1 \leftarrow 10^0$	Xu92‖	3063.935 (05)	${}^tR(6,2)^l_l$	$11^1 \leftarrow 01^1$	Lin01	3188.423 (05)	$R(6,2)^l_l$	$02^2 \leftarrow 01^1$	Lin01
2964.987 (10)*	${}^tR(5,3)_u$	$11^1 \leftarrow 01^1$	Xu92	3064.356 (05)*	$R(7,6)^l$	$01^1 \leftarrow 00^0$	Lin01	3193.232 (05)*	$R(6,5)^u$	$01^1 \leftarrow 00^0$	Lin01
2966.864 (10)	$R(6,4)^l_u$	$02^2 \leftarrow 01^1$	Xu92	3064.356 (05)*	$R(5,2)^l_l$	$02^2 \leftarrow 01^1$	Lin01	3194.796 (05)*	${}^tR(6,0)^l$	$11^1 \leftarrow 01^1$	Lin01
2974.534 (20)*	${}^tR(2,1)_u$	$11^1 \leftarrow 01^1$	Xu92	3065.578 (05)*	$R(5,2)^u_u$	$02^2 \leftarrow 01^1$	Lin01	3199.631 (05)*	${}^nR(7,7)^l$	$02^2 \leftarrow 10^0$	Lin01
2974.682 (20)*	${}^nQ(1,1)$	$11^1 \leftarrow 01^1$	Xu92	3065.777 (05)*	$R(5,1)^u_u$	$02^2 \leftarrow 01^1$	Lin01	3200.723 (05)	$R(10,9)^l$	$01^1 \leftarrow 00^0$	Lin01
2975.656 (10)*	${}^tR(5,3)_l$	$12^0 \leftarrow 02^2$	Xu92	3066.565 (05)*	${}^tR(5,3)$	$10^0 \leftarrow 00^0$	Lin01	3201.386 (05)	$R(7,1)^l_l$	$02^2 \leftarrow 01^1$	Lin01
2976.080 (10)	$R(8,7)^l$	$02^2 \leftarrow 01^1$	Xu92	3067.733 (05)*	$R(4,2)^u$	$02^2 \leftarrow 01^1$	Lin01	3201.672 (05)	$R(6,5)^u_u$	$02^2 \leftarrow 01^1$	Lin01
2976.566 (10)*	$R(4,2)^u_u$	$02^2 \leftarrow 01^1$	Xu92‡	3069.176 (05)*	$R(7,7)^l$	$01^1 \leftarrow 00^0$	Lin01	3202.174 (05)	${}^tR(5,2)$	$10^0 \leftarrow 00^0$	Lin01
2977.488 (10)†	$R(8,7)_l$	$02^0 \leftarrow 01^1$	Xu92	3076.175 (10)	$R(5,3)^u_u$	$03^3 \leftarrow 02^2$	Lin01	3203.158 (10)*	${}^tR(4,1)^u_l$	$11^1 \leftarrow 01^1$	Xu92‡
2979.325 (10)	${}^tR(6,4)_l$	$11^1 \leftarrow 01^1$	Xu92	3077.457 (10)†	${}^tR(6,3)$	$20^0 \leftarrow 10^0$	Lin01	3203.513 (10)	$R(8,6)^u$	$11^1 \leftarrow 10^0$	Xu92
2979.507 (10)	$R(6,1)^l$	$01^1 \leftarrow 00^0$	Xu92	3078.892 (05)	$R(9,3)^l$	$01^1 \leftarrow 00^0$	Lin01	3205.308 (05)	$R(6,4)^u$	$01^1 \leftarrow 00^0$	Lin01
2979.658 (10)*	${}^nR(6,6)^l$	$02^2 \leftarrow 10^0$	Xu92	3085.617 (05)*	${}^tR(5,3)_l$	$11^1 \leftarrow 01^1$	Lin01	3209.072 (05)*	$R(11,9)^l$	$01^1 \leftarrow 00^0$	Lin01
2980.327 (10)*	$R(4,3)^u_u$	$02^2 \leftarrow 01^1$	Carbo‖	3086.072 (05)*	${}^tR(4,2)_l$	$11^1 \leftarrow 01^1$	Lin01	3210.543 (05)	$R(12,9)^l$	$01^1 \leftarrow 00^0$	Lin01
2984.082 (10)*	$R(6,2)^l$	$01^1 \leftarrow 00^0$	Xu92	3091.891 (10)*	${}^nQ(2,2)^u$	$11^1 \leftarrow 01^1$	Xu92	3210.801 (05)	$R(10,10)^l$	$01^1 \leftarrow 00^0$	Lin01
2984.259 (10)*	${}^tR(4,3)_l$	$11^1 \leftarrow 01^1$	Xu92	3092.324 (10)*	${}^nQ(1,2)$	$11^1 \leftarrow 01^1$	Xu92‡	3212.252 (05)	$R(6,2)^u$	$01^1 \leftarrow 00^0$	Lin01
2985.494 (10)*	$R(6,3)^l$	$01^1 \leftarrow 00^0$	Xu92	3093.669 (05)	$R(7,7)^u$	$11^1 \leftarrow 10^0$	Lin01	3214.612 (05)	$R(6,6)$	$02^2 \leftarrow 01^1$	Lin01
2989.507 (20)*	$R(6,4)^l$	$01^1 \leftarrow 00^0$	Xu92	3096.416 (05)*	$R(5,5)^u$	$01^1 \leftarrow 00^0$	Lin01	3216.361 (05)*	$R(6,3)^u$	$01^1 \leftarrow 00^0$	Lin01
2989.507 (30)*	${}^tR(3,2)_l$	$11^1 \leftarrow 01^1$	Xu92	3096.665 (05)*	$R(6,3)^l_l$	$02^2 \leftarrow 01^1$	Lin01	3219.108 (05)	${}^tR(7,3)$	$10^0 \leftarrow 00^0$	Lin01
2989.618 (10)	${}^tR(4,0)$	$12^0 \leftarrow 02^2$	Xu92	3097.259 (05)*	${}^tR(2,0)$	$11^1 \leftarrow 01^1$	Lin01	3220.181 (05)	$R(7,0)$	$02^2 \leftarrow 01^1$	Lin01
2990.585 (10)*†	${}^tR(5,2)^l_l$	$11^1 \leftarrow 01^1$	Xu92	3097.985 (05)*	$R(5,4)^u_u$	$02^2 \leftarrow 01^1$	Lin01	3220.816 (05)	$R(6,1)^u$	$01^1 \leftarrow 00^0$	Lin01
2993.467 (10)*	$R(7,5)^l_u$	$02^2 \leftarrow 01^1$	Xu92	3099.905 (05)*	$R(8,6)^l$	$01^1 \leftarrow 00^0$	Lin01	3221.086 (05)	${}^nQ(2,3)$	$11^1 \leftarrow 01^1$	Lin01
2994.903 (10)*	${}^tR(4,2)_u$	$11^1 \leftarrow 01^1$	Xu92	3100.131 (05)*	${}^tR(7,3)$	$20^0 \leftarrow 10^0$	Lin01	3221.214 (05)*	$R(7,1)^u_u$	$02^2 \leftarrow 01^1$	Lin01
2998.347 (15)*	$R(11,7)^l_l$	$02^2 \leftarrow 01^1$	Lin01	3100.871 (05)	${}^nR(7,6)^l$	$02^2 \leftarrow 10^0$	Lin01	3222.022 (05)	$R(5,3)^u_l$	$02^2 \leftarrow 01^1$	Lin01
3000.105 (10)	${}^tR(8,6)_l$	$11^1 \leftarrow 01^1$	Xu92	3101.397 (05)	$R(5,3)^u_u$	$02^2 \leftarrow 01^1$	Lin01	3228.754 (05)*	${}^tR(3,0)^u$	$11^1 \leftarrow 01^1$	Lin01
3002.355 (10)	$R(10,10)^l$	$11^1 \leftarrow 10^0$	Xu92	3102.368 (05)*	$R(8,5)^l$	$01^1 \leftarrow 00^0$	Lin01	3235.574 (05)*	$R(6,7)$	$02^2 \leftarrow 01^1$	Lin01
3002.750 (10)	${}^nR(8,8)$	$02^0 \leftarrow 10^0$	Xu92	3102.736 (05)*	${}^tR(3,1)_l$	$11^1 \leftarrow 01^1$	Lin01	3235.813 (05)	$R(12,10)^l$	$01^1 \leftarrow 00^0$	Lin01
3003.253 (05)	$R(5,3)^u$	$03^1 \leftarrow 02^0$	Lin01	3103.873 (05)*	$R(6,0)$	$02^2 \leftarrow 01^1$	Lin01	3236.270 (05)	$R(7,4)^l_l$	$02^2 \leftarrow 01^1$	Lin01
3006.996 (05)	$R(5,4)^l_l$	$02^2 \leftarrow 01^1$	Lin01	3106.804 (05)	$R(5,4)^u$	$01^1 \leftarrow 00^0$	Lin01	3238.614 (05)*	$R(11,10)^l$	$01^1 \leftarrow 00^0$	Lin01
3008.108 (05)*	$R(4,4)^u$	$01^1 \leftarrow 00^0$	Lin01	3108.871 (05)*	$R(7,6)^l_l$	$02^2 \leftarrow 01^1$	Lin01	3238.662 (05)	$R(9,8)^l_l$	$02^2 \leftarrow 01^1$	Lin01
3009.317 (05)*	${}^tR(2,1)_l$	$11^1 \leftarrow 01^1$	Lin01	3110.877 (10)*	${}^nP(5,6)^l$	$11^1 \leftarrow 01^1$	Lin01	3240.385 (05)*	$R(8,6)^l_l$	$02^2 \leftarrow 01^1$	Lin01
3011.509 (05)*	$R(6,5)^l$	$01^1 \leftarrow 00^0$	Lin01	3111.038 (10)	${}^nR(9,9)$	$02^0 \leftarrow 10^0$	Lin01	3247.272 (05)	${}^tR(8,2)^u_u$	$11^1 \leftarrow 01^1$	Lin01
3014.364 (05)*	$R(6,6)^l$	$01^1 \leftarrow 00^0$	Lin01	3113.532 (05)*	$R(8,7)^l$	$01^1 \leftarrow 00^0$	Lin01	3247.694 (05)	$R(7,2)^u_u$	$02^2 \leftarrow 01^1$	Lin01
3015.241 (05)*	$R(4,3)^u$	$01^1 \leftarrow 00^0$	Lin01	3115.615 (05)*	$R(5,5)$	$02^2 \leftarrow 01^1$	Lin01	3247.800 (05)	${}^tR(6,1)^l_l$	$11^1 \leftarrow 01^1$	Lin01
3017.629 (05)	$R(5,0)$	$03^3 \leftarrow 02^2$	Lin01	3118.511 (05)	$R(6,4)^l_l$	$02^2 \leftarrow 01^1$	Lin01	3247.891 (05)	$R(7,4)^u_u$	$02^2 \leftarrow 01^1$	Lin01
3018.586 (05)	$R(9,8)_l$	$02^0 \leftarrow 01^1$	Lin01	3120.210 (05)	${}^tR(4,2)$	$10^0 \leftarrow 00^0$	Lin01	3249.704 (05)	$R(11,11)^l$	$01^1 \leftarrow 00^0$	Lin01
3020.495 (05)	$R(4,4)$	$02^2 \leftarrow 01^1$	Lin01	3120.321 (05)*	$R(8,8)^l$	$01^1 \leftarrow 00^0$	Lin01	3249.794 (05)	$R(7,3)^u_u$	$02^2 \leftarrow 01^1$	Lin01
3021.862 (05)*	$R(6,4)^u_u$	$12^2 \leftarrow 11^1$	Lin01	3121.216 (05)	${}^tR(4,0)^l$	$11^1 \leftarrow 01^1$	Lin01	3259.835 (05)*	$R(7,3)^l_l$	$02^2 \leftarrow 01^1$	Lin01
3022.424 (05)*	${}^tR(5,1)^l_u$	$11^1 \leftarrow 01^1$	Lin01	3121.814 (05)*	$R(5,3)^u$	$01^1 \leftarrow 00^0$	Lin01	3261.336 (05)	$R(8,5)^l_l$	$02^2 \leftarrow 01^1$	Lin01
3023.674 (10)	$R(6,3)^u$	$11^1 \leftarrow 10^0$	Xu92	3122.252 (05)*	$R(5,2)^u$	$01^1 \leftarrow 00^0$	Lin01	3265.138 (05)	$R(7,7)^u$	$01^1 \leftarrow 00^0$	Lin01
3024.439 (10)	${}^tR(8,5)$	$10^0 \leftarrow 00^0$	Lin01	3128.068 (05)*	$R(5,1)^u$	$01^1 \leftarrow 00^0$	Lin01	3265.304 (05)	$R(8,1)^u_u$	$02^2 \leftarrow 01^1$	Lin01
3024.558 (10)*	$R(4,2)^u$	$01^1 \leftarrow 00^0$	Lin01	3128.296 (05)	$R(7,2)^u$	$11^1 \leftarrow 10^0$	Lin01	3266.017 (05)	$R(7,5)^u_u$	$02^2 \leftarrow 01^1$	Lin01
3025.941 (05)*	$R(7,4)^l$	$01^1 \leftarrow 00^0$	Lin01	3129.516 (10)	$R(6,1)^l_l$	$02^2 \leftarrow 01^1$	Lin01	3269.095 (05)	${}^nR(8,5)^u$	$02^2 \leftarrow 10^0$	Lin01
3026.162 (05)*	${}^tR(6,4)$	$10^0 \leftarrow 00^0$	Lin01	3129.811 (05)	$R(5,0)$	$01^1 \leftarrow 00^0$	Lin01	3269.496 (05)	$R(8,3)^u$	$11^1 \leftarrow 10^0$	Lin01
3028.543 (05)*	$R(8,6)^l_u$	$02^2 \leftarrow 01^1$	Lin01	3130.216 (05)*	$R(9,6)^l$	$01^1 \leftarrow 00^0$	Lin01	3270.571 (05)	$R(14,12)^l$	$01^1 \leftarrow 00^0$	Lin01
3028.977 (05)*	$R(7,3)^l_u$	$02^2 \leftarrow 01^1$	Lin01	3134.077 (05)*	$R(7,6)^u$	$03^1 \leftarrow 02^0$	Lin01	3272.713 (05)	$R(12,11)^l$	$01^1 \leftarrow 00^0$	Lin01
3029.075 (10)*	$R(7,3)^l$	$01^1 \leftarrow 00^0$	Lin01	3136.793 (05)	$R(7,1)^u$	$11^1 \leftarrow 10^0$	Lin01	3276.197 (05)*	$R(7,6)^u$	$01^1 \leftarrow 00^0$	Lin01
3029.832 (05)*	$R(4,1)^u$	$01^1 \leftarrow 00^0$	Lin01	3137.145 (05)	$R(5,6)$	$02^2 \leftarrow 01^1$	Lin01	3277.429 (05)*	${}^tR(8,3)$	$10^0 \leftarrow 00^0$	Lin01
3033.304 (10)	$R(6,5)^u$	$11^1 \leftarrow 10^0$	Xu92	3137.814 (05)*	$R(6,3)^u_u$	$02^2 \leftarrow 01^1$	Lin01	3282.308 (05)	${}^tR(6,2)$	$10^0 \leftarrow 00^0$	Lin01
3033.746 (05)*	$R(8,3)^l$	$01^1 \leftarrow 00^0$	Lin01	3138.979 (05)	$R(7,0)$	$11^1 \leftarrow 10^0$	Lin01	3282.997 (05)	${}^{-6}R(8,6)_u$	$02^0 \leftarrow 01^1$	Lin01
3035.475 (05)*	$R(4,5)$	$02^2 \leftarrow 01^1$	Lin01	3140.641 (05)	$R(9,7)^l$	$01^1 \leftarrow 00^0$	Lin01	3284.093 (05)	$R(12,12)^l$	$01^1 \leftarrow 00^0$	Lin01
3036.720 (10)	$R(12,12)$	$02^0 \leftarrow 01^1$	Lin01	3144.458 (05)	${}^tR(6,3)$	$10^0 \leftarrow 00^0$	Lin01	3285.768 (05)*	$R(7,6)^u_u$	$02^2 \leftarrow 01^1$	Lin01
3037.319 (05)*	${}^tR(1,0)$	$11^1 \leftarrow 01^1$	Lin01	3146.461 (10)*	${}^nR(1,1)$	$11^1 \leftarrow 01^1$	Xu92	3288.443 (05)	${}^tR(7,3)^u_l$	$11^1 \leftarrow 01^1$	Lin01
3038.913 (10)	${}^tR(10,6)$	$10^0 \leftarrow 00^0$	Xu92	3150.724 (05)*	$R(6,1)^u_u$	$02^2 \leftarrow 01^1$	Lin01	3289.115 (05)	$R(7,5)^u$	$01^1 \leftarrow 00^0$	Lin01
3042.157 (10)*	${}^tR(3,1)_u$	$11^1 \leftarrow 01^1$	Xu92	3151.824 (05)	$R(7,4)^u$	$11^1 \leftarrow 10^0$	Lin01	3290.752 (10)	$R(7,2)^u$	$01^1 \leftarrow 00^0$	Xu92

TABLE 5 (continued)

Frequency[a] (cm^{-1})	Assignment[b] Label	Band	Ref[c]	Frequency[a] (cm^{-1})	Assignment[b] Label	Band	Ref[c]	Frequency[a] (cm^{-1})	Assignment[b] Label	Band	Ref[c]
3292.521 (05)	$R(7,2)^l_l$	$02^2 \leftarrow 01^1$	Lin01	3473.764 (05)	$R(10,6)^u_u$	$02^2 \leftarrow 01^1$	Lin01	4900.393 (10)*	${}^tR(3,3)$	$02^2 \leftarrow 00^0$	Xu90
3293.790 (05)	$R(9,6)^u$	$11^1 \leftarrow 10^0$	Lin01	3476.189 (05)	$R(9,4)^u$	$01^1 \leftarrow 00^0$	Lin01	4907.871 (10)*	${}^tQ(1,0)$	$02^2 \leftarrow 00^0$	Xu90
3296.014 (05)	$R(9,9)^u$	$11^1 \leftarrow 10^0$	Lin01	3486.049 (05)	$R(9,9)$	$02^2 \leftarrow 01^1$	Lin01	4908.672 (20)*	${}^nP(4,3)$	$02^2 \leftarrow 00^0$	Xu90
3298.990 (05)	$R(8,3)^u_u$	$02^2 \leftarrow 01^1$	Lin01	3497.971 (05)	$R(9,3)^u$	$01^1 \leftarrow 00^0$	Lin01	4914.248 (10)*	${}^tQ(3,0)$	$02^2 \leftarrow 00^0$	Xu90
3300.111 (10)*	${}^tR(5,0)^l$	$11^1 \leftarrow 01^1$	Lin01	3498.764 (05)	${}^{-6}R(9,5)^l$	$01^1 \leftarrow 00^0$	Lin01	4930.981 (20)	${}^nP(6,5)^l$	$02^2 \leftarrow 00^0$	Maj89
3301.694 (05)	${}^{-6}R(8,5)_l$	$02^0 \leftarrow 01^1$	Lin01	3499.417 (05)	$R(10,10)^u$	$01^1 \leftarrow 00^0$	Lin01	4931.596 (20)*	${}^tR(6,5)$	$02^2 \leftarrow 00^0$	Xu90
3302.423 (05)*	$R(7,4)^u$	$01^1 \leftarrow 00^0$	Lin01	3503.306 (10)	$R(10,9)^u$	$01^1 \leftarrow 00^0$	Lin01	4936.000 (20)*	${}^tR(2,2)$	$02^2 \leftarrow 00^0$	Xu90
3303.093 (05)*	$R(13,12)^l$	$01^1 \leftarrow 00^0$	Lin01	3513.541 (05)	$R(10,8)^u$	$01^1 \leftarrow 00^0$	Lin01	4955.991 (10)*	${}^nP(2,2)$	$02^2 \leftarrow 00^0$	Xu90
3305.935 (05)	$R(7,1)^u$	$01^1 \leftarrow 00^0$	Lin01	3516.951 (05)	$R(9,2)^u$	$01^1 \leftarrow 00^0$	Lin01	4966.838 (20)*	${}^tR(5,4)$	$02^2 \leftarrow 00^0$	Xu90
3307.150 (05)	$R(10,9)^l_l$	$02^2 \leftarrow 01^1$	Lin01	3521.044 (05)	$R(9,10)$	$02^2 \leftarrow 01^1$	Lin01	4968.272 (10)*	${}^tR(1,1)$	$02^2 \leftarrow 00^0$	Xu90
3308.650 (10)	$R(9,7)^l_l$	$02^2 \leftarrow 01^1$	Lin01	3523.742 (05)	${}^tR(8,1)$	$10^0 \leftarrow 00^0$	Lin01	4971.561 (10)*	${}^nP(3,3)$	$02^2 \leftarrow 00^0$	Xu90
3308.685 (05)	$R(7,0)$	$01^1 \leftarrow 00^0$	Lin01	3523.998 (05)	$R(10,7)^u$	$01^1 \leftarrow 00^0$	Lin01	4975.338 (20)*	${}^nP(6,6)^l$	$02^2 \leftarrow 00^0$	Xu90
3309.924 (05)	$R(7,7)$	$02^2 \leftarrow 01^1$	Lin01	3527.047 (05)	$R(10,9)^u_u$	$02^2 \leftarrow 01^1$	Lin01	5000.499 (10)*	${}^tR(4,3)$	$02^2 \leftarrow 00^0$	Xu90
3311.009 (05)	$R(8,0)$	$02^2 \leftarrow 01^1$	Lin01	3531.279 (05)	$R(10,6)^u$	$01^1 \leftarrow 00^0$	Lin01	5023.496 (10)*	${}^nQ(1,1)$	$02^2 \leftarrow 00^0$	Xu90
3313.752 (05)	$R(13,13)^l$	$01^1 \leftarrow 00^0$	Lin01	3546.576 (05)	$R(10,5)^u$	$01^1 \leftarrow 00^0$	Lin01	5029.071 (10)*	${}^nQ(2,1)$	$02^2 \leftarrow 00^0$	Xu90
3317.786 (05)	${}^nR(8,1)^l_u$	$11^1 \leftarrow 01^1$	Lin01	3551.579 (15)	$R(10,3)^u$	$01^1 \leftarrow 00^0$	Lin01	5032.447 (10)*	${}^tR(3,2)$	$02^2 \leftarrow 00^0$	Xu90
3321.010 (05)	$R(7,3)^u$	$01^1 \leftarrow 00^0$	Lin01	3552.313 (15)	$R(10,4)^u$	$01^1 \leftarrow 00^0$	Lin01	5054.742 (100)*	${}^nQ(4,1)^u$	$02^2 \leftarrow 00^0$	Maj89
3325.674 (10)	${}^tR(5,1)$	$10^0 \leftarrow 00^0$	Lin01	3553.705 (15)	$R(11,0)$	$01^1 \leftarrow 00^0$	Lin01	5061.882 (20)*	${}^tR(2,1)$	$02^2 \leftarrow 00^0$	Xu90
3328.773 (05)	$R(8,3)^l_l$	$02^2 \leftarrow 01^1$	Lin01	3571.295 (15)	$R(11,10)^u$	$01^1 \leftarrow 00^0$	Lin01	5094.218 (20)*	${}^tR(1,0)$	$02^2 \leftarrow 00^0$	Xu90
3329.924 (05)	$R(14,13)^l$	$01^1 \leftarrow 00^0$	Lin01	3572.419 (15)	$R(11,11)^u$	$01^1 \leftarrow 00^0$	Lin01	6806.665 (70)*	$P(3,1)^u$	$03^1 \leftarrow 00^0$	Ven94
3331.374 (05)	$R(8,4)^l_l$	$02^2 \leftarrow 01^1$	Lin01	3574.750 (15)	${}^tR(7,0)$	$10^0 \leftarrow 00^0$	Lin01	6807.297 (70)*	$P(3,3)$	$03^1 \leftarrow 00^0$	Ven94
3331.571 (05)	$R(8,5)^u_u$	$02^2 \leftarrow 01^1$	Lin01	3579.301 (15)	$R(11,9)^u$	$01^1 \leftarrow 00^0$	Lin01	6807.724 (70)*	$P(3,2)$	$03^1 \leftarrow 00^0$	Ven94
3332.520 (05)	$R(7,8)$	$02^2 \leftarrow 01^1$	Lin01	3586.139 (15)	$R(10,2)^u$	$01^1 \leftarrow 00^0$	Lin01	6811.374 (70)*	$P(3,0)$	$03^1 \leftarrow 00^0$	Ven94‡
3338.534 (05)	$R(14,14)^l$	$01^1 \leftarrow 00^0$	Lin01	3588.381 (15)	$R(11,8)^u$	$01^1 \leftarrow 00^0$	Lin01	6865.731 (70)*	$P(2,1)$	$03^1 \leftarrow 00^0$	Ven94
3343.327 (05)	${}^tR(9,3)$	$10^0 \leftarrow 00^0$	Lin01	3596.217 (15)	$R(11,7)^u$	$01^1 \leftarrow 00^0$	Lin01	6866.340 (70)*	$Q(5,0)$	$03^1 \leftarrow 00^0$	Ven94
3345.710 (05)	$R(8,8)^u$	$01^1 \leftarrow 00^0$	Lin01	3642.547 (10)	$R(12,12)^u$	$01^1 \leftarrow 00^0$	Maj94	6877.546 (70)*	$P(2,2)$	$03^1 \leftarrow 00^0$	Ven94
3348.845 (05)	$R(9,6)^l_l$	$02^2 \leftarrow 01^1$	Lin01	4434.861 (10)*	${}^tQ(5,4)$	$02^2 \leftarrow 00^0$	Maj94	6883.091 (70)*	$Q(5,3)^l$	$03^1 \leftarrow 00^0$	Ven94
3355.517 (05)*	$R(8,7)^u$	$01^1 \leftarrow 00^0$	Lin01	4465.095 (10)*	${}^tQ(6,4)$	$02^2 \leftarrow 00^0$	Maj94	6891.619 (70)*	$Q(4,3)^l$	$03^1 \leftarrow 00^0$	Ven94
3356.747 (05)*	$R(8,2)^u$	$01^1 \leftarrow 00^0$	Lin01	4539.759 (20)*	${}^tP(5,0)$	$02^2 \leftarrow 00^0$	Maj89	7144.212 (70)*	$R(1,1)^l$	$03^1 \leftarrow 00^0$	Ven94
3358.400 (05)	$R(15,15)^l$	$01^1 \leftarrow 00^0$	Lin01	4553.340 (10)*	${}^tQ(4,3)_u$	$03^3 \leftarrow 01^1$	Maj94	7192.908 (70)*	$R(2,2)^l$	$03^1 \leftarrow 00^0$	Ven94
3362.256 (10)	${}^tR(7,2)$	$10^0 \leftarrow 00^0$	Lin01	4557.020 (20)*	${}^tQ(4,3)$	$02^2 \leftarrow 00^0$	Xu90	7234.957 (70)*	$R(3,3)^l$	$03^1 \leftarrow 00^0$	Ven94
3368.118 (05)*	$R(8,6)^u$	$01^1 \leftarrow 00^0$	Lin01	4557.731 (10)*	${}^nP(7,1)^u$	$02^2 \leftarrow 00^0$	Maj94	7237.285 (70)*	$R(1,1)^u$	$03^1 \leftarrow 00^0$	Ven94
3368.560 (05)*	$R(8,7)^u_u$	$02^2 \leftarrow 01^1$	Lin01	4578.735 (20)*	${}^tQ(5,3)$	$02^2 \leftarrow 00^0$	Xu90	7241.245 (70)*	$R(1,0)$	$03^1 \leftarrow 00^0$	Ven94
3369.664 (05)	$R(9,5)^l_l$	$02^2 \leftarrow 01^1$	Lin01	4607.205 (20)*	${}^tQ(6,3)$	$02^2 \leftarrow 00^0$	Maj89	7265.882 (70)*	$R(4,4)^l$	$03^1 \leftarrow 00^0$	Ven94
3375.003 (05)	$R(8,6)^u_u$	$02^2 \leftarrow 01^1$	Lin01	4637.992 (50)*	${}^nP(5,1)^u$	$02^2 \leftarrow 00^0$	Maj89	7785.233 (10)*	${}^tQ(3,0)$	$12^2 \leftarrow 00^0$	McC00
3376.775 (05)	$R(11,10)^u_l$	$02^2 \leftarrow 01^1$	Lin01	4638.331 (10)	${}^tR(9,9)$	$02^2 \leftarrow 00^0$	Xu90	7785.701 (10)	${}^tQ(1,0)$	$12^2 \leftarrow 00^0$	McC00
3377.047 (05)	${}^tR(10,3)$	$10^0 \leftarrow 00^0$	Lin01	4641.987 (20)*	${}^tQ(7,3)$	$02^2 \leftarrow 00^0$	Maj89	7789.878 (10)	${}^tR(3,3)$	$12^2 \leftarrow 00^0$	McC00
3380.010 (05)	$R(8,5)^u$	$01^1 \leftarrow 00^0$	Lin01	4661.576 (10)*	${}^nP(7,3)$	$02^2 \leftarrow 00^0$	Maj94	7805.893 (10)†	${}^nP(1,1)$	$12^2 \leftarrow 00^0$	McC00
3381.399 (05)	$R(8,1)^u$	$01^1 \leftarrow 00^0$	Lin01	4664.306 (10)*	${}^tP(3,0)$	$02^2 \leftarrow 00^0$	Xu90	7820.239 (10)	${}^nP(2,2)$	$12^2 \leftarrow 00^0$	McC00
3388.155 (05)	$R(8,2)^l_l$	$02^2 \leftarrow 01^1$	Lin01	4677.273 (15)*	${}^tQ(3,2)$	$02^2 \leftarrow 00^0$	Xu90	7822.375 (10)	${}^tR(2,2)$	$12^2 \leftarrow 00^0$	McC00
3389.119 (05)	$R(9,3)^u_u$	$02^2 \leftarrow 01^1$	Lin01	4685.564 (10)	${}^tR(8,8)$	$02^2 \leftarrow 00^0$	Xu90	7826.739 (10)	${}^nP(3,3)$	$12^2 \leftarrow 00^0$	McC00
3392.547 (05)	$R(8,4)^u$	$01^1 \leftarrow 00^0$	Lin01	4691.962 (100)	${}^tQ(4,2)$	$02^2 \leftarrow 00^0$	Maj89	7833.249 (20)	${}^nP(4,4)^l$	$12^2 \leftarrow 00^0$	McC00
3395.752 (05)	${}^tR(6,1)$	$10^0 \leftarrow 00^0$	Lin01	4700.139 (20)*	${}^nP(4,1)$	$02^2 \leftarrow 00^0$	Maj89	7850.959 (10)	${}^tR(1,1)$	$12^2 \leftarrow 00^0$	McC00
3399.510 (05)	$R(8,3)^u$	$01^1 \leftarrow 00^0$	Lin01	4712.282 (10)*	${}^tQ(5,2)$	$02^2 \leftarrow 00^0$	Maj94	7880.921 (10)	${}^tR(4,3)$	$12^2 \leftarrow 00^0$	McC00
3399.872 (05)	$R(8,8)$	$02^2 \leftarrow 01^1$	Lin01	4721.019 (10)*	${}^nP(4,3)_l$	$03^3 \leftarrow 01^1$	Maj94	7894.711 (10)	${}^nQ(1,1)$	$12^2 \leftarrow 00^0$	McC00
3407.501 (05)	$R(9,6)^u_u$	$02^2 \leftarrow 01^1$	Lin01	4732.041 (10)*	${}^tR(7,7)$	$02^2 \leftarrow 00^0$	Maj94	7898.371 (10)*	${}^nQ(2,1)$	$12^2 \leftarrow 00^0$	McC00
3408.984 (10)	$R(10,7)^u_l$	$02^2 \leftarrow 01^1$	Lin01	4735.941 (100)*	${}^tQ(6,2)$	$02^2 \leftarrow 00^0$	Maj89	7905.717 (10)*	${}^nQ(3,1)$	$12^2 \leftarrow 00^0$	McC00
3411.415 (05)	$R(9,7)^u_u$	$02^2 \leftarrow 01^1$	Lin01	4744.767 (10)*	${}^nP(5,2)^u$	$02^2 \leftarrow 00^0$	Maj94	7912.047 (10)	${}^tR(3,2)$	$12^2 \leftarrow 00^0$	McC00
3411.859 (05)	${}^tR(9,2)$	$10^0 \leftarrow 00^0$	Lin01	4766.167 (100)*	${}^nP(7,4)^l$	$02^2 \leftarrow 00^0$	Maj94	7939.619 (10)	${}^tR(2,1)$	$12^2 \leftarrow 00^0$	McC00
3423.809 (05)	$R(9,9)^u$	$01^1 \leftarrow 00^0$	Lin01	4771.641 (100)*	${}^nP(3,1)$	$02^2 \leftarrow 00^0$	Maj89	7970.413 (10)*	${}^tR(1,0)$	$12^2 \leftarrow 00^0$	McC00
3427.667 (05)*	$R(8,9)$	$02^2 \leftarrow 01^1$	Lin01	4777.226 (10)*	${}^tR(6,6)$	$02^2 \leftarrow 00^0$	Xu90	7998.890 (10)	${}^nQ(2,2)$	$12^2 \leftarrow 00^0$	McC00
3431.295 (05)	$R(9,8)^u$	$01^1 \leftarrow 00^0$	Lin01	4795.030 (10)*	${}^tQ(2,1)$	$02^2 \leftarrow 00^0$	Maj94	8005.582 (30)	${}^tR(4,2)$	$12^2 \leftarrow 00^0$	McC00
3439.825 (05)	$R(11,9)^u_l$	$02^2 \leftarrow 01^1$	Lin01	4804.406 (50)*	${}^tQ(3,1)$	$02^2 \leftarrow 00^0$	Maj89	8007.410 (10)	${}^nQ(3,2)^u$	$12^2 \leftarrow 00^0$	McC00
3441.416 (05)	${}^tR(8,2)$	$10^0 \leftarrow 00^0$	Lin01	4805.287 (20)*	${}^nP(4,2)^u$	$02^2 \leftarrow 00^0$	Maj89	8022.012 (20)	${}^nQ(4,2)^u$	$12^2 \leftarrow 00^0$	McC00
3443.148 (05)	$R(9,7)^u$	$01^1 \leftarrow 00^0$	Lin01	4814.521 (20)*	${}^nP(6,3)$	$02^2 \leftarrow 00^0$	Maj89	8027.840 (20)	${}^tR(3,1)$	$12^2 \leftarrow 00^0$	McC00
3443.466 (10)	${}^tR(7,0)^l$	$11^1 \leftarrow 01^1$	Lin01	4816.353 (10)*	${}^nP(5,3)$	$02^2 \leftarrow 00^0$	Xu90	8037.673 (10)	${}^nR(3,1)^l$	$12^2 \leftarrow 00^0$	McC00
3445.702 (05)	$R(9,1)^u$	$01^1 \leftarrow 00^0$	Lin01	4818.901 (20)*	${}^tQ(4,1)$	$02^2 \leftarrow 00^0$	Maj89	8053.382 (10)*	$P(6,6)$	$21^1 \leftarrow 00^0$	McC00
3448.014 (05)	${}^tR(5,0)$	$10^0 \leftarrow 00^0$	Lin01	4820.598 (10)*	${}^tR(5,5)$	$02^2 \leftarrow 00^0$	Xu90	8071.617 (10)*	${}^nR(1,1)$	$12^2 \leftarrow 00^0$	McC00
3450.711 (05)	$R(9,8)^u_u$	$02^2 \leftarrow 01^1$	Lin01	4839.508 (20)*	${}^tQ(5,1)$	$02^2 \leftarrow 00^0$	Maj89	8089.406 (10)	${}^nQ(4,3)$	$12^2 \leftarrow 00^0$	McC00
3452.852 (05)	$R(9,0)$	$01^1 \leftarrow 00^0$	Lin01	4850.264 (20)*	${}^nP(2,1)$	$02^2 \leftarrow 00^0$	Xu90	8110.069 (10)*	${}^nQ(3,3)$	$12^2 \leftarrow 00^0$	McC00
3455.008 (05)	$R(9,6)^u$	$01^1 \leftarrow 00^0$	Lin01	4859.212 (20)*	${}^tR(8,7)$	$02^2 \leftarrow 00^0$	Xu90	8123.128 (10)	$P(5,5)$	$21^1 \leftarrow 00^0$	McC00
3457.772 (05)	${}^tR(10,2)$	$10^0 \leftarrow 00^0$	Lin01	4861.790 (20)*	${}^tR(4,4)$	$02^2 \leftarrow 00^0$	Xu90	8128.280 (10)	${}^tR(4,1)$	$12^2 \leftarrow 00^0$	McC00
3458.383 (05)	$R(9,3)^l_l$	$02^2 \leftarrow 01^1$	Lin01	4876.938 (10)*	${}^nP(3,2)$	$02^2 \leftarrow 00^0$	Xu90	8162.653 (10)	${}^tR(3,0)$	$12^2 \leftarrow 00^0$	McC00
3461.308 (05)	$R(9,5)^u$	$01^1 \leftarrow 00^0$	Lin01	4895.518 (20)*	${}^tR(7,6)$	$02^2 \leftarrow 00^0$	Xu90	8163.129 (10)*	${}^nR(2,1)$	$12^2 \leftarrow 00^0$	McC00
3461.643 (05)	${}^tR(7,1)$	$10^0 \leftarrow 00^0$	Lin01								

[a] Recommended transition frequency and uncertainties in the last decimal places (in parentheses) in cm^{-1}. Transitions marked with an asterisk were confirmed by combination differences with other transitions.

[b] Recommended assignments using the transition notation defined in Section 3.2.

[c] Reference from which the recommended frequency is based. "Carbo" refers to unpublished transitions observed during carbo-cation studies (*51*). Labels defined in Table 1.

† Unusually large deviation from *ab initio* calculations.

‡ Corrected frequency. There was an error in the previously reported value.

‖ Transition not reported in paper, but was identified and measured by us from the original data.

least uncertain measurement for the frequency. In cases where more than one equally accurate measurement was available, we chose the earliest measurement to include in this table. Many of the previous assignments have been changed due to both the new labeling scheme of energy levels and the reassignment of lines to different transitions. Some lines that had been previously assigned are no longer assigned. An electronic version of this table is available online which includes the calculated lower state energies and Einstein A coefficients. An online intensity calculator is also available at the authors' website (*39*).

The remaining 72 unassigned transitions are listed in Table 4 and should be considered carefully before being assigned in the future. Many of them (marked with an asterisk) had no reasonable theoretically predicted lines of sufficient intensity within ~ 1 cm^{-1} of the reported transition, and are likely due to a species other than H_3^+. Lines without an asterisk had one or more candidate assignments whose frequency and/or intensity difference from theory was too large to allow a confident assignment.

III.3. Construction of experimentally determined energy levels

One of the goals of this work was to determine the energy levels from experimental transitions. Constructing all of the relationships between the levels is only possible by combining transitions from different bands. For example, the fundamental band (with the selection rule $\Delta G = 0$) can relate individual J levels within a G "stack" with a combination of P, Q, and R transitions. Relating different G stacks requires transitions with a selection rule other than $\Delta G = 0$. This is the case for overtone and forbidden bands which have the selection rule $\Delta G = \pm 3$. Using a combination of the $\nu_2 \leftarrow 0$, $2\nu_2^2 \leftarrow \nu_2$, and $2\nu_2^2 \leftarrow 0$ transitions, Baw90 and Xu90 experimentally determined the first term values of the ground state in 1990.

We wrote a program to automatically extract from the transition data the relative energies of each level. First, combinations of $\nu_2 \leftarrow 0$, $2\nu_2^2 \leftarrow \nu_2$ and $2\nu_2^2 \leftarrow 0$ bands were used to determine as many ground vibrational state energy relationships as possible. Once this was done, the program examined every transition, searching for transitions whose upper or lower level had already been "determined". The other level in the transition was then calculated. This process was then iterated until no additional levels could be determined. Uncertainties in the transitions were added in quadrature and propagated through the calculation. We performed the entire process twice, once with all of the assigned transitions and once with only the transitions that had been confirmed by combination differences. Levels that were calculated in the first list but not in the second list were necessarily determined by only one transition and are susceptible to mistakes in transition assignments.

At this stage, only the relative values of the energies have been determined and an absolute standard is needed.

TABLE 6
Determined molecular constants for the ground vibrational state of H_3^+.[a]

$E_{1,1}$ [†]	64.1214(116)
E_{o-p} [†]	22.8389 (56)
B	43.5605 (16)
C	20.6158 (20)
D_{JJ}	4.1400 (63) $\times 10^{-2}$
D_{JG}	-0.7496 (14) $\times 10^{-1}$
D_{GG}	0.3700 (14) $\times 10^{-1}$
h_3	-0.4846 (26) $\times 10^{-5}$
H_{JJJ}	0.6745 (86) $\times 10^{-4}$
H_{JJG}	-0.2919 (28) $\times 10^{-3}$
H_{JGG}	0.4145 (38) $\times 10^{-3}$
H_{GGG}	-0.1942 (29) $\times 10^{-3}$
L_{JJJJ}	-0.1015 (36) $\times 10^{-6}$
L_{JJJG}	0.0769 (15) $\times 10^{-5}$
L_{JJGG}	-0.1964 (27) $\times 10^{-5}$
L_{JGGG}	0.1934 (31) $\times 10^{-5}$
L_{GGGG}	-0.0594 (22) $\times 10^{-5}$

[a] All values are in units of cm^{-1}. The numbers in parentheses are the 2σ uncertainties in the lastdigits. See text for a warning about the use of these values.
[†] Coefficients used to adjust the absolute energy of the experimental energy levels. These terms in equation 10 should be set to zero when simulating the energy structure with the other coefficients.

Additionally, the energy differences between between *ortho* ($G = 3n$) and *para* ($G = 3n \pm 1$) levels are not determined because transitions between them are forbidden. In the past (*21, 22*), the relationship between *ortho* and *para* levels and the offset from the forbidden level $(J, G) = (0, 0)$ were taken from theoretical calculations. To remain independent from calculations, we instead performed a fit on the ground vibrational state to determine the relationship between the *ortho* and *para* levels as well as their relationship to the (0,0) level. To do this, we initially computed the absolute values of all of the *ortho* and *para* levels assuming that the lowest populated energy level in each set had zero energy. Next, we performed a least-squares fit of every determined energy level in the ground vibrational state to the following, modified symmetric top energy level expression:

$$\begin{aligned} E(J,G) = \; & -E_{1,1} - \delta_{G,3n}E_{o-p} + BJ(J+1) + (C-B)G^2 \\ & -D_{JJ}J^2(J+1)^2 - D_{JG}J(J+1)G^2 - D_{GG}G^4 \\ & -\delta_{G,3}(-1)^J h_3 \left\{ \tfrac{(J+3)!}{(J-3)!} \right\} \\ & +H_{JJJ}J^3(J+1)^3 + H_{JJG}J^2(J+1)^2G^2 \\ & +H_{JGG}J(J+1)G^4 + H_{GGG}G^6 \\ & +L_{JJJJ}J^4(J+1)^4 + L_{JJJG}J^3(J+1)^3G^2 \\ & +L_{JJGG}J^2(J+1)^2G^4 + L_{JGGG}J(J+1)G^6 \\ & +L_{GGGG}G^8. \end{aligned} \qquad [10]$$

The first fitted parameter, $E_{1,1}$, gives the energy of the lowest populated *ortho* level (1,1) relative to the forbidden (0,0) level, and the second parameter, E_{o-p}, gives the energy separation between the (1,1) and the (1,0) levels (the relationship between *ortho* and *para* levels). Each energy level was weighted by the inverse of its uncertainty for the fit. The results of the fit and the 2σ uncertainties in the

parameters are listed in Table 6. With this information, we adjusted the absolute value of the $G = 3n$ and $G = 3n \pm 1$ levels by the fit parameters, defining the forbidden (0,0) level as zero energy. Please note that expression 10 does not behave properly outside of the energy levels used in the fit. As pointed out in Watson *et al.* (*17*), the effective Hamiltonian converges very slowly, making extrapolation difficult. One may be able to overcome this problem by using a Padè-type expression (*57–60*) as done in Ref. (*17*). The energy levels included in the fit, however, do behave properly, justifying our use of expression 10 to determine $E_{1,1}$ and E_{o-p}.

The values of the determined energy levels are listed in Table 3. Levels that were determined using only transitions verified with combination differences are marked with an asterisk. The values in parentheses correspond to the 2σ uncertainty (in the last digits) in the energy of each level due to the uncertainties in the transition frequencies used to construct the level. This can be thought of as the relative uncertainty for each level. There is an additional uncertainty in the systematic shift that must be considered when comparing the absolute energy of each level. The error in the value of the fit parameter $E_{1,1}$ must be included in the uncertainty for every level. The energy values for levels with $G = 3n$ also depend on the fit parameter E_{o-p} which adds an additional uncertainty which must be accounted for. However, the uncertainties in $E_{1,1}$ and E_{o-p} do not affect the calculations of transitions using these energy levels.

IV. APPLICATION OF RESULTS

The comprehensive list of assigned transitions and observed energy levels presented here will find many applications in the theoretical, laboratory, and astrophysical spectroscopy of H_3^+. In this section, we briefly outline two such applications: the search for the "forbidden" rotational spectrum and the evaluation of theoretical energy level calculations.

IV.1. Forbidden rotational transitions

At its potential minimum, H_3^+ is a perfect equilateral triangle with no dipole moment, and consequently does not possess an allowed pure rotational spectrum. However, as pointed out by Pan and Oka (*61*), the centrifugal distortion of the molecule due to rotation will break its C_3 symmetry and induce a small dipole moment in the plane of the molecule. The resulting dipole moment will give rise to a weak rotational spectrum which obeys the selection rules $\Delta J = 0, \pm 1$ and $\Delta G = \pm 3$. The general theory of forbidden rotational transitions in polyatomic molecules was developed by Watson (*62*). In the case of a nonpolar molecule like H_3^+, the rotational transition $|J, G+3\rangle \leftarrow |J-1, G\rangle$ can be thought of as arising from a mixing between $|J, G+3\rangle$ in the ground state and $|J, G\rangle$ in the ν_2 state, which leads to an intensity borrowing from the allowed rovibrational transition $R(J-1, G)$ of the fundamental band.

The transition dipole of such rotational transitions is proportional to the derivative of the dipole moment with respect to the ν_2 coordinate. This quantity is much larger for H_3^+ than for other molecules — in fact, the line strengths of H_3^+ transitions are orders of magnitude larger than those of CH_4, which have been observed in the laboratory. Although the transition dipole moments are small by the usual standards of rotational spectroscopy (most ranging between 1–30 mD), they approach the infrared transition moment (158 mD) at higher J levels. With the rapid development of quantum cascade lasers in the far-infrared, the rotational transitions of H_3^+ may soon be detected in the laboratory.

These rotational transitions are also of fundamental importance in the relaxation of H_3^+ in the interstellar medium, where their spontaneous emission lifetimes are shorter than collision times. Black (*63*) has pointed out that the flux of such H_3^+ transitions would be orders of magnitude lower than the thermal continuum from warm dust grains, making their detection infeasible. Draine and Woods (*64*) have suggested that H_3^+ rotational transitions may be observable in X-ray heated regions such as the starburst galaxy NGC 6240. Black (*65, 63*) has further suggested that, under the right conditions, the ${}^tR(3,1)$ transition could become an astrophysical maser.

In order to enable (laboratory and astronomical) searches for the rotational spectrum of H_3^+, we have estimated the transition frequencies using our experimentally determined energy levels from Table 3. These are given in Table 7, along with the most recent intensity calculations by Neale, Miller, and Tennyson (*56*).

IV.2. Evaluation of theoretical calculations

Variational calculations of H_3^+ have substantially improved in recent years with the introduction of adiabatic, relativistic, and non-adiabatic corrections to the theory. The experimentally determined energy levels provide a powerful tool to diagnose the behavior of these calculations, and to compare and contrast the different computational approaches. Before doing so, we give a brief overview of the development of the most recent H_3^+ theoretical calculations.

IV.2.1. Computational overview

The first calculations to effectively account for non-Born-Oppenheimer behavior did so by taking an *ab initio* potential energy surface (PES) and adjusting its fitting parameters to better match the experimental values. This semi-empirical approach was used by Watson (*55*) using the Meyer-Botschwina-Burton PES (*67*) and similarly by Dinelli *et al.* (*68*) using the Lie and Frye (*69*) PES. Later, Dinelli, Polyansky, and Tennyson(DPT) (*53*) introduced a

TABLE 7
Pure rotational transition frequencies in the ground vibrational state determined from experimentally determined energy levels.

Label[a]	Frequency[b] (cm^{-1})	$\|\mu_{ij}\|$[c] (mD)	A_{ij} [c] (s^{-1})	Label[a]	Frequency[b] (cm^{-1})	$\|\mu_{ij}\|$[c] (mD)	A_{ij} [c] (s^{-1})	Label[a]	Frequency[b] (cm^{-1})	$\|\mu_{ij}\|$[c] (mD)	A_{ij} [c] (s^{-1})
$^tR(3,1)$	7.255 (10)	4.23[†]	2.78×10^{-9} [†]	$^nQ(5,3)$	190.756 (13)	17.7	6.80×10^{-4}	$^nR(5,2)$	553.791 (19)	9.24	5.37×10^{-3}
$^tR(6,3)$	9.261 (13)	14.7[†]	6.22×10^{-8} [†]	$^nQ(3,3)$	201.524 (09)	5.37	7.40×10^{-5}	$^nQ(7,6)$	555.500 (14)	13.6	9.93×10^{-3}
$^nP(8,7)$	29.655 (18)	22.3	3.59×10^{-6}	$^tR(7,2)$	220.891 (25)	22.7	1.98×10^{-3}	$^nR(7,1)$	568.013 (34)	20.0	2.59×10^{-2}
$^nP(5,5)$	39.453 (12)	8.33	1.10×10^{-6}	$^tR(6,1)$	261.550 (21)	17.3	1.93×10^{-3}	$^nQ(6,6)$	581.450 (11)	6.99	3.00×10^{-3}
$^tR(5,2)$	51.347 (16)	11.3	6.38×10^{-6}	$^nQ(8,4)$	286.320 (42)	29.3	6.35×10^{-3}	$^nR(4,3)$	612.525 (12)	5.86	3.03×10^{-3}
$^nQ(8,2)$	56.563 (47)	32.5	5.94×10^{-5}	$^nQ(7,4)$	298.423 (24)	22.1	4.05×10^{-3}	$^nR(6,2)$	621.074 (25)	13.1	1.47×10^{-2}
$^nQ(7,2)$	58.880 (28)	25.6	4.19×10^{-5}	$^tR(5,0)$	306.088 (14)	17.3	3.18×10^{-3}	$^nQ(8,7)$	666.334 (20)	15.4	2.19×10^{-2}
$^nQ(6,2)$	61.101 (21)	19.4	2.68×10^{-5}	$^nQ(6,4)$	310.199 (19)	15.5	2.25×10^{-3}	$^nR(7,2)$	683.456 (44)	17.4	3.44×10^{-2}
$^nQ(5,2)$	63.197 (16)	13.9	1.53×10^{-5}	$^nQ(5,4)$	321.347 (15)	9.83	1.00×10^{-6}	$^nQ(7,7)$	700.315 (17)	7.95	6.80×10^{-3}
$^nQ(4,2)$	65.107 (13)	9.17	7.27×10^{-6}	$^nR(2,2)$	325.482 (09)	1.52	3.51×10^{-5}	$^nR(6,3)$	743.039 (18)	14.8	3.25×10^{-2}
$^nQ(3,2)$	66.758 (11)	5.33	2.64×10^{-6}	$^nQ(4,4)$	331.549 (12)	4.97	2.81×10^{-4}	$^nR(4,4)$	748.280 (13)	2.16	7.51×10^{-4}
$^nQ(2,2)$	68.062 (07)	2.40	5.66×10^{-7}	$^tR(7,1)$	338.256 (26)	22.6	7.00×10^{-3}	$^nR(5,4)$	811.941 (18)	4.62	4.22×10^{-3}
$^nP(6,6)$	84.606 (10)	10.6	1.81×10^{-5}	$^nR(4,1)$	353.533 (15)	7.58	9.73×10^{-4}	$^nQ(8,8)$	815.622 (20)	8.93	1.35×10^{-2}
$^tR(4,1)$	95.383 (14)	8.07	2.16×10^{-5}	$^nR(3,2)$	405.563 (12)	3.47	3.23×10^{-4}	$^nR(6,4)$	870.172 (23)	7.69	1.41×10^{-2}
$^tR(7,3)$	100.112 (15)	21.5	1.65×10^{-4}	$^nQ(8,5)$	406.002 (31)	25.7	1.38×10^{-2}	$^nR(7,4)$	922.999 (41)	11.3	3.58×10^{-2}
$^nR(1,1)$	105.173 (04)	0.84	4.26×10^{-7}	$^nQ(7,5)$	423.844 (24)	18.3	8.00×10^{-3}	$^nR(5,5)$	950.783 (17)	2.34	1.75×10^{-3}
$^nP(7,7)$	128.566 (15)	13.1	9.85×10^{-5}	$^nR(5,1)$	429.493 (19)	11.1	3.62×10^{-3}	$^nR(6,5)$	1003.537 (23)	4.98	9.00×10^{-3}
$^tR(6,2)$	138.350 (20)	16.8	2.70×10^{-4}	$^nQ(6,5)$	441.343 (19)	11.7	3.72×10^{-3}	$^nR(7,5)$	1050.737 (30)	8.22	2.57×10^{-2}
$^tR(3,0)$	141.847 (10)	7.20	5.97×10^{-5}	$^tR(7,0)$	455.294 (20)	30.5	3.15×10^{-2}	$^nR(6,6)$	1146.211 (12)	2.48	3.34×10^{-3}
$^nP(8,8)$	170.887 (18)	15.7	3.40×10^{-4}	$^nQ(5,5)$	458.093 (13)	6.00	1.08×10^{-3}	$^nR(7,6)$	1189.072 (16)	5.22	1.63×10^{-2}
$^nQ(7,3)$	178.278 (19)	34.6	2.13×10^{-3}	$^nR(4,2)$	481.837 (15)	6.05	1.57×10^{-3}	$^nR(7,7)$	1336.994 (19)	2.57	5.61×10^{-3}
$^tR(5,1)$	180.395 (16)	12.4	3.36×10^{-4}	$^nR(6,1)$	501.093 (25)	15.2	1.05×10^{-2}				
$^nR(2,1)$	190.662 (09)	2.41	1.76×10^{-5}	$^nQ(8,6)$	533.460 (17)	21.0	2.09×10^{-2}				

[a] Labels for pure rotational transitions using the transition notation defined in Section 3.2.
[b] Transition frequencies using energy data from Table 3. Reported uncertainty in the last digits (in parenthesis) is the quadrature sum of the uncertainties from Table 3.
[c] Dipole moments and Einstein coefficients from reference (*56*) except when marked otherwise.
[†] Dipole moment and Einstein coefficient taken from (*66*). The error in the reported values of A_{ij} and μ_{ij} have been corrected as pointed out in Ref. (*19*).

slightly different approach: a new semi-empirical surface is built by adding a purely *ab initio* Born-Oppenheimer PES to another surface (which they call the "adiabatic surface") of the same functional form whose parameters are determined from the fit to experimental data. In their work the PES of Röhse-Kutzelnigg-Jaquet-Klopper (RKJK) (*70*) was used as the Born-Oppenheimer surface. Energy level calculations using Watson's spectroscopically determined potential were reported by Majewski *et al.* (Maj94) (*27*), and Neale, Miller, and Tennyson (NMT) (*56*) calculated energy levels using the DVR3D (*71*) suite from the DPT surface. The transitions calculated from these energy levels proved to be invaluable in the assignment of laboratory spectra.

The first attempt to calculate the adiabatic effects *ab initio* was by Dinelli *et al.* (Din95) (*72*) who added a mass dependent function to the RKJK surface, which accounts for the diagonal adiabatic contributions. Energy levels were calculated from the modified surface using the TRIATOM program suite (*73*). Results of these calculations gave the best *ab initio* values at the time, but were still inferior to the calculations using the fitted potentials.

Three years later Cencek, Rychlewski, Jaquet, and Kutzelnigg (CRJK) calculated a new *ab initio* PES (*12*), taking into account both the diagonal adiabatic and relativistic corrections, and claimed an accuracy of a few hundredths of a cm^{-1}. Jaquet *et al.* (Jaq98) (*74*) then calculated energies from this surface using TRIATOM. Jaquet *et al.* considered the different choices of mass: the average mass (proton mass plus 2/3 electron mass denoted **NU23**), nuclear mass (**NU**), atomic mass (**AT**), and the reduced mass (**RE**). Using the same PES and DVR3D, Polyansky and Tennyson (Pol99) (*75*) calculated energy levels but attempted to simulate the nonadiabatic effects by using a different mass for rotational and vibrational motion. The rotational masses in their work were set to the nuclear value and the vibrational masses were set to a scaled atomic mass. Similarly, Jaquet (*15*) (Jaq99) calculated energies of the CRJK PES using NU23 masses for motion along the R(H-H_2) and $r(H_2)$ coordinates and NU masses for motion along the $\theta(R,r)$ coordinate (Jacobi type scattering coordinates), which he denotes as **NUVR**.

The coordinate systems used in Watson's as well as TRIATOM and DVR3D calculations cannot handle the kinetic energy singularity that occurs at the barrier to linearity ($\sim 10,000$ cm^{-1}) when using the usual Morse oscillator basis functions.[5] In 1989, Whitnell and Light (*79*) introduced hyperspherical coordinates, which properly treat the linear regions of the potential, to the calculations of H_3^+. Their methodology limited the calculations to $J = 0$ levels, but this limitation was later overcome by Bartlett and

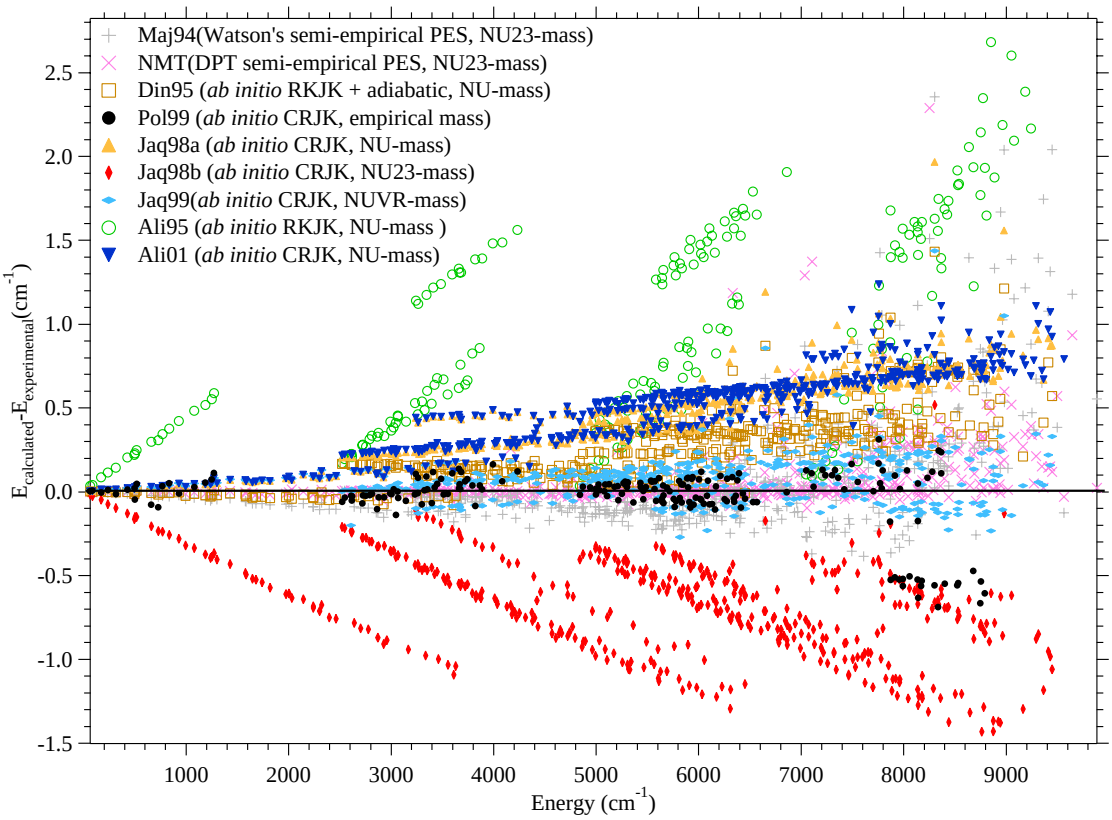

FIG. 3. Comparison of the latest calculated energy levels to experiment. Labels used in the legend are defined in Section 4.2. A printable color version of this Figure is available online (*39*).

Howard (*80*). Initially, calculations using hypershperical coordinates were performed on the MBB PES (*79–82*) but later used the more accurate RKJK surface (Ali95) (*83*) and very recently the CRJK surface (Ali01) (*84*). Ali95 and Ali01 were performed using nuclear masses, and in Ref. (*13*) the authors discuss the merits of this approach.

IV.2.2. Qualitative comparison

To evaluate each of the calculations, we have plotted the difference in the calculated and experimental values for all experimentally determined levels (Figure 3). This diagram clearly depicts the dependence of each calculation on vibrational state, rotational energy, and general scatter, which is useful in analyzing the effects of the various theoretical approaches. While a detailed analysis of each of these calculations is beyond the scope of this paper, we would like to make several qualitative remarks that are apparent from our comparison to experimental data:

1. Semi-empirical vs. ab initio approaches. The semi-empirical calculations give the most accurate results at energies where data was available at the time of the fit. At higher energies, where experimental data was sparse, the agreement is considerably poorer. In these cases, *ab initio* calculations perform better due to their more systematic residuals. *2. PES and non-BO corrections.* There is considerable difference between Din95 and Ali01 (and Jaq98a) which both use NU-mass, but use different PESs. This suggests that the introduction of relativistic effects (as done in CRJK, but not in RKJK + adiabatic) may increase the energy residuals or that the diagonal adiabatic contribution is treated differently in the two calculations. *3. Choice of mass.* The large rotational dependence of the residuals of Jaq98b implies that NU23 calculations produce too large a moment of inertia and consequently underestimates the rotational dependence of the the energies. While the scaled mass systems (NUVR and empirical mass) give smaller residuals and a flatter rotational dependence, the NU-mass calculations seem to give much

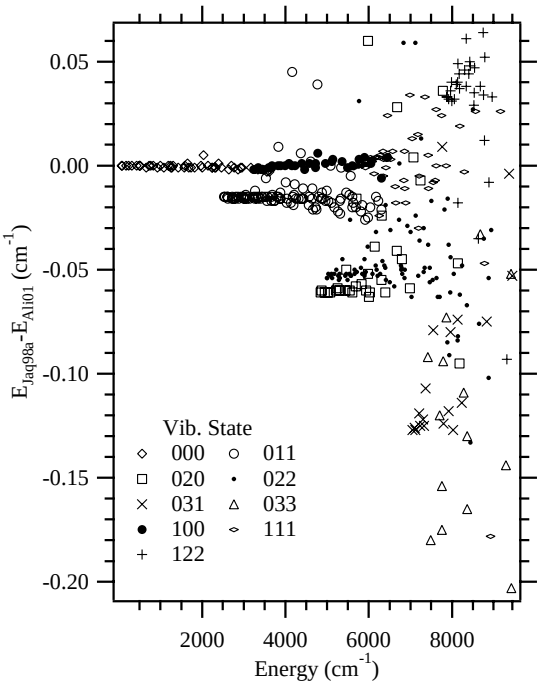

FIG. 4. Comparison of the energy level calculations of Ali95 and Jaq98a versus energy. Labels are defined in Section 4.2

more systematic residuals. We cannot rule out the possibility that the scatter in Pol99 and Jaq99 is due to convergence problems. *4. Differences in similar approaches.* To verify that the observed differences in calculations are indeed due to the different approaches (and not simply due to variances from one group's calculation to another) we compared Ali01 and Jaq98a which use the same choice of mass and same PES. Their results compared quite nicely, confirming that the differences in each of the other calculations are significant. Upon close inspection, the differences between Ali01 and Jaq98a show a slight dependence on the vibrational state (see Fig. 4). This difference is on the order of 0.05 cm^{-1} and is significant when compared to the most accurate calculations of Pol99 and Jaq99. The source of this vibrational dependence is unclear, but may be due to the choice of coordinate system and/or basis set.

It is difficult to pinpoint the source of the differences in results between each computational approach due to the limited amount of computational data available. Further "experiments on the calculations" need to be performed — systematic comparisons of the energies calculated with different coordinate systems, basis sets, mass choices, and non-BO corrections will be necessary to iron out the remaining discrepancies. The experimentally determined energy levels will be instrumental in this endeavor as a powerful tool to probe the rotational, vibrational, and energy dependences, as well as the general scatter of the various computational methodologies.

V. CONCLUSION

This work represents the end of a chapter in the laboratory spectroscopy study of H_3^+. Energy levels for nearly every vibrational band below the barrier to linearity have been probed and determined experimentally, many of them up to $J = 9$. Almost all of the observed lines have been assigned, and those that have not are probably due to species other than H_3^+ or have an error in the frequency measurement. While there are still transitions to be measured in this energy regime — higher J transitions in the $2\nu_2$ and $3\nu_2$ bands should be achievable with the better diode lasers and higher sensitivity available today — these will likely not lead a to better understanding of H_3^+ behavior at low energies or produce a qualitatively better diagnostic tool for theoretical calculations.

The next step for laboratory work is to make observations of states above the barrier to linearity, where some of the theoretical calculations are expected to break down. This is also the regime where the approximate quantum numbers begin to fail, and a new formalism may need to developed to describe such levels. Such experiments are currently underway in Chicago where the $5\nu_2 \leftarrow 0$ band is being studied with a high-power Ti:Sapphire laser.

ACKNOWLEDGMENTS

We gratefully acknowledge T. Oka for his assistance and encouragement during the course of this work. We also acknowledge J. K. G. Watson, J. Tennyson, R. Jaquet, and A. Alijah for many helpful conversations about theoretical calculations and for supplying us with their transition and energy level lists, in several cases before publication. Additionally, we appreciate their comments on an early version of the manuscript. B.J.M. wishes to thank the Fannie and John Hertz Foundation for their financial support. This work was also supported by NSF grant PHYS-9722691 and NASA grant NAG5-9583.

NOTES

1. This near degeneracy is evident from the first three terms in the rotational energy expression, $E_{rot} \approx BJ(J+1) + (C-B)k^2 - 2C\zeta k\ell$. Consider the levels $|J,k,\ell\rangle = |J,g+\ell,\ell\rangle$ and $|J,g-\ell,-\ell\rangle$. In this approximation, the energy separation between these levels is $4g\ell(C - B - \zeta C)$, which is nearly zero because $B \approx 2C$ (due to the planarity of the molecule) and $\zeta = -1$ (for the triatomic equilateral triangle (*36*)). Because these levels have the same symmetry and a small energy difference, they will be strongly mixed (the mixing is particularly strong for $|\ell| = 1$ due to the $\ell-$resonance term $q(q_+^2 J_+^2 + q_-^2 J_-^2)/4$).
2. The selection rule $\Delta v_1 = 0$ requires some qualification. The band $\nu_1 \leftarrow 0$ has the vibrational symmetry $A_1 \leftarrow A_1$ which is forbidden, but can become allowed via the rotation-vibration interaction. Bands such as $\nu_1 + \nu_2 \leftarrow \nu_2$ are qualitatively different in that they have vibrational symmetry $E \leftarrow E$, which is allowed through a vibration interaction alone (*24*). All of these bands are very weak because the change in the dipole moment is small upon excitation of totally symmetric mode, but $\nu_1 \leftarrow 0$ is by far the weakest, since it relies on an accidental degeneracy for the rotation-vibration interaction to be effective.

3. Note that in the paper of Neale, Miller, and Tennyson (*56*), the upper and lower values of J are switched in the equations relating transition probabilities to the Einstein A-coefficients. In their equations (2) and (3), each J' should be changed to J'', and vice versa.
4. This 'rule' is somewhat misleading and deserves more explanation. The signed G, denoted $g \equiv k - \ell$, carries the selection rule of $\Delta g = 0, \pm 3, \pm 6, ...$ due to the parity and nuclear spin selection rules. The confusion begins when g goes from a positive to a negative value or vice versa. Take for example an overtone transition where $k'' = \pm 1, \ell'' = 0$ and $k' = 0, \ell' = \pm 2$. In this case $g'' = \pm 1, g' = \mp 2, G'' = 1$, and $G' = 2$. The transition $\Delta g = \mp 3$ is clearly allowed but ΔG appears to be a misleading $+1$. Both transitions are properly labeled with an n; a label of t would denote the transition $g'' = \pm 1$ to $g' = \pm 4$ where $\Delta g = \pm 3$ and $\Delta G = +3$.
5. At the barrier to linearity one of the moments of inertia vanishes, causing some of the terms in the kinetic energy Hamiltonian to become singular. The terms that become singular depend on the coordinate system used. These singularities impose boundary conditions on the basis functions which are not met when using the common coordinate systems with the convenient Morse oscillators. Instead, artificial barriers must be applied to the potential to keep the calculations from diverging (consequently these calculations are expected to give poor results at energies near and above the the barrier to linearity) (*52*), or alternative basis functions such as spherical oscillators (which are much harder to make converge) are used (*56*). Refs. (*76–78*) discuss this computational problem in more detail.

REFERENCES

1. B. J. McCall and T. Oka, *Science* **287**, 1941-1942 (2000).

2. T. Oka, *Phys. Rev. Lett.* **45**, 531-534 (1980).

3. T. R. Geballe, and T. Oka, *Nature* **384**, 334-335 (1996).

4. B. J. McCall, T. R. Geballe, K. H. Hinkle, and T. Oka, *Astrophys. J.* **522**, 338-348 (1999).

5. B. J. McCall, T. R. Geballe, K. H. Hinkle, and T. Oka, *Science* **279**, 1910-1912 (1989).

6. L. Trafton, D. F. Lester, and K. L. Thompson, *Astrophys. J.* **343**, L73-76 (1989).

7. P. Drossart, *et al.*, *Nature* **340**, 539-541 (1989).

8. T. R. Geballe, M. F. Jagod, and T. Oka, *Astrophys. J.* **408**, L109-112 (1993).

9. L. M. Trafton, T. R. Geballe, S. Miller, J. Tennyson, and G. E. Ballester, *Astrophys. J.* **405**, 761-766 (1993).

10. J. E. P. Connerney and T. Satoh, *Philos. Trans. R. Soc. London* **358**, 2471-2483 (2000).

11. K. H. Hinkle, R. R. Joyce, N. Sharp, J. A. Valenti, *Proc. SPIE* **4008**, 720-728 (2000).

12. W. Cencek, J. Rychlewski, R. Jaquet, W. Kutzelnigg, *J. Chem. Phys.* **108**, 2831-2836 (1998).

13. J. Hinze, A. Alijah, and L. Wolniewicz, *Polish J. Chem.* **72**, 1293-1303 (1998).

14. A. Aguado, O. Roncero, C. Tablero, C. Sanz,M. Paniagua, *J. Chem. Phys.* **112**, 1240-1254 (2000).

15. R. Jaquet, *Chem. Phys. Lett.* **302**, 27-34 (1999).

16. T. Oka, *Phil. Trans. R. Soc. Lond. A* **303**, 543-549 (1981).

17. J. K. G. Watson, S. C. Foster, A. R. W. McKellar, P. Bernath, T. Amano, F. S. Pan, M. W. Crofton, R. S. Altman, and T. Oka, *Can. J. Phys.* **62**, 1875-1885 (1984).

18. W. A. Majewski, M. D. Marshall, A. R. W. McKellar, J. W. C. Johns, and J. K. G. Watson, *J. Mol. Spectrosc.* **122**, 341-355 (1987).

19. W. A. Majewski, P. A. Feldman, J. K. G. Watson, S. Miller, and J. Tennyson, *Astrophys. J.* **347**, L51-L54 (1989).

20. T. Nakanaga, F. Ito, K. Sugawara, H. Takeo, and C. Matsumura, *Chem. Phys. Lett.* **169**, 269-273 (1990).

21. M. G. Bawendi, B. D. Rehfuss, and T. Oka, *J. Chem. Phys.* **93**, 6200-6209 (1990).

22. L.-W. Xu, C. M. Gabrys, and T. Oka, *J. Chem. Phys.* **93**, 6210-6215 (1990).

23. S. S. Lee, B. F. Ventrudo, D. T. Cassidy, T. Oka, S. Miller, J. Tennyson, *J. Mol. Spectrosc.* **145**, 222-224 (1991).

24. L.-W. Xu, M. Rösslein, C. M. Gabrys, and T. Oka, *J. Mol. Spec.* **153**, 726-737 (1992).

25. B. Ventrudo, D. T.Cassidy, Z. Y. Guo, S. Joo, S. S. Lee, and T. Oka, *J. Chem. Phys.* **100**, 6263-6266 (1994).

26. D. Uy, C. M. Gabrys, M.-F. Jagod, and T. Oka, *J.Chem.Phys* **100**, 6267-6274 (1994).

27. W. A. Majewski, A. R. W. McKellar, D. Sadovskiĭ, and J. K. G. Watson, *Can. J. Phys.* **72**, 1016-1027 (1994).

28. A. R. W. McKellar and J. K. G. Watson, *J. Mol. Spectrosc.* **191**, 215-217 (1998).

29. S. Joo, F. Kühnemann, M.-F. Jagod, and T. Oka *The Royal Society Discussion Meeting on Astronomy, Physics, and Chemistry of H_3^+, London* February 9-10, (2000) (poster).

30. B. J. McCall and T. Oka, *J. Chem. Phys.* **113**, 3104-3110 (2000).

31. C. M. Lindsay, R. M. Rade, Jr., and T. Oka, *J. Mol. Spectrosc.* **Previous paper**, XXX-XXX (2001).

32. L. Kao, T. Oka, S. Miller, and J. Tennyson, *Astrophys. J. Suppl. Ser.* **77**, 317-329 (1991).

33. B. M. Dinelli, L. Neale, O. L. Polyansky, and J. Tennyson, *J. Mol. Spectrosc.* **181**, 142-150 (1997).

34. J. K. G. Watson, *J. Molec. Spectrosc.* **103**, 350-363 (1984).

35. I. R. McNab, *Adv. Chem. Phys.* **LXXXIX**, 1-87 (1995).

36. E. Teller, *Hand- und Jahrb. d. Chem. Phys.* **9**, 43-188 (1934).

37. J. T. Hougen, *J. Chem. Phys.* **37**, 1433-1441 (1962).

38. L. D. Landau and E. M. Lifshitz,*Quantum Mechanics (Non-relativistic Theory)*Pergamon Press, Oxford, 4th edition, (1989).

39. Energy level figures and tables of the transitions, energy levels, labels, and unassigned lines are available an the authors' website at "http://h3plus.uchicago.edu" and on the publishers site "???".

40. B. J. McCall, *Philos. Trans. R. Soc. London* **358**, 2385-2400 (2000).

41. A. Carrington, J. Buttenshaw, and R. A. Kennedy, *Mol. Phys.* **45**, 753-758 (1982).

42. A. Carrington and R. A. Kennedy, *J. Chem. Phys.* **41**, 91-112 (1984).

43. A. Carrington, I. R. McNab, and Y. D. West, *Mol. Phys.* **98**, 1073-1092 (1993).

44. F. Kemp, C. E. Krik, and I. R. McNab, *Phil. Trans. R. Soc. Lond. A* **358**, 2403-2418 (2000).

45. G. Herzberg, *Trans. Roy. Soc. Can.* **5**, 3-36 (1967).

46. A. Pine, *J. Opt. Soc. Amer.* **66**, 97-108 (1976).

47. R. C. Woods, *Rev. Sci. Instr.* **44**, 282-288 (1973).

48. Y. Endo, K. Nagai, C. Yamada, and E. Hirota, *J. Mol. Spectrosc.* **97**, 213-219 (1983).

49. C. S. Gudeman, M. H. Begemann, J. Pfaff, and R. J. Saykally, *Phys. Rev. Lett.* **50**, 727-31 (1983).

50. S. Miller and J. Tennyson, *J. Mol. Specrosc.* **128**, 530-539 (1988).

51. T. Oka, *in* "Frontiers of Laser Spectroscopy of Gases" (A. C. P. Alves, J. M. Brown, J. M. Hollas, Ed.) Vol. 234, pp. 353-377, Kluwer, Amsterdam, 1988.

52. J. K. G. Watson, *Can. J. Phys.* **72**, 238-249 (1994).

53. B. M. Dinelli, O. L. Polyansky, and J. Tennyson, *J. Chem. Phys.* **103**, 10433-10438 (1995).

54. J. K. G. Watson, private communication.

55. J. K. G. Watson, *Chem. Phys.* **190**, 291-300 (1995).

56. L. Neale, S. Miller, and J. Tennyson, *Astrophys. J.* **464**, 516-520 (1996).

57. S. P. Belov, A. V. Burenin, O. L. Polyansky, and S. M. Shapin, *J. Mol. Spectrosc.* **90**, 579-589 (1981).

58. A. V. Burenin, O. L. Polyanskii, and S. M. Shchapin, *Opt. Spektrosk.* **53**, 666-672 (1982).

59. A. V. Burenin, T. M. Fevral'skikh, E. N. Karyakin, O. L. Polyansky, and S. M. Shapin, *J. Mol. Spectrosc.* **100**, 182-192 (1983).

60. A. V. Burenin, O. L. Polyanskii, and S. M. Shchapin, *Opt. Spektrosk.* **54**, 436-41 (1983).

61. F.-S. Pan and T. Oka, *Astrophys. J.* **305**, 518-525 (1986).

62. J. K. G. Watson, *J. Mol. Spectrosc.* **40**, 536-544 (1971).

63. J. H. Black, *Philos. Trans. R. Soc. London* **358**, 2515-2521 (2000).

64. B. T. Draine and D. T. Woods, *Astrophys. J.* **363**, 464-479 (1990).

65. J. H. Black, *Faraday Discuss.* **109**, 257-266 (1998).

66. S. Miller and J. Tennyson, *Astrophys. J.* **335**, 486-490 (1988).

67. W. Meyer, P. Botschwina, and P. G. Burton, *J. Chem. Phys.* **84**, 891-900 (1986).

68. B. M. Dinelli, S. Miller, and J. Tennyson, *J. Mol. Spectrosc.* **163**, 71-79 (1994).

69. G. C. Lie, and D. Frye, *J. Chem. Phys.* **96**, 6784-6790 (1992).

70. R. Röhse, W. Kutzelnigg, R. Jaquet, and W. Klopper, *J. Chem. Phys.* **101**, 2231-2243 (1994).

71. J. Tennyson, J. R. Henderson, and N. G. Fulton, *Comput. Phys. Comm.* **86**, 175-198 (1995).

72. B. M Dinelli, C. R. Le Sueur, J. Tennyson, and R. D. Amos, *Chem. Phys. Lett.* **232**, 295-300 (1995).

73. J. Tennyson, S. Miller, and C. R. Le Sueur, *Comput. Phys. Comm.* **75**, 339-364 (1993).

74. R. Jaquet, W. Chencek, W. Kutzelnigg, and J. Rychlewski, *J. Chem. Phys.* **108**, 2837-2846 (1998).

75. O. L. Polyansky and J. Tennyson, *J. Chem. Phys.* **110**, 5056-5064 (1999).

76. J. R. Henderson and J. Tennyson, *Chem. Phys. Lett.* **173**, 133-138 (1990).

77. S. Carter and W. Meyer, *J. Chem. Phys.* **96**, 2424-2425 (1992).

78. J. R. Henderson, J. Tennyson, and B. Sutcliffe, *J. Chem. Phys.* **96**, 2426-2427 (1992).

79. R. M. Whitnell and J. C. Light, *J. Chem. Phys.* **90**, 1774-1786 (1989).

80. P. Bartlett and B. J. Howard, *Mol. Phys.* **70**, 1001-1029 (1990).

81. S. Carter and W. Meyer, *J. Chem. Phys.* **93**, 8902-8914 (1990).

82. L. Wolniewicz and J. Hinze, *J. Chem. Phys.* **101**, 9817-9829 (1994).

83. A. Alijah, J. Hinze, and L. Wolniewicz, *Ber. Bunsenges. Phys. Chem.* **99**, 251-253 (95).

84. A. Alijah and P. Schiffels, in preparation.

APPENDIX E

H_3^+ ENERGY LEVEL DIAGRAMS UP TO 9000 CM^{-1}

This appendix contains energy level diagrams for H_3^+ versus the approximate quantum number G. The energy levels are separated into the ideal bands and plotted against the ideal value of G, as assigned in Appendix D. Levels which have experimentally determined energies are shown with thick lines. The expectation values of the approximate quantum numbers used in our assignments and the energies displayed here are from the calculations of Watson. The four numbers above each energy level are the labels used by Watson: J, M, S, n—where J and n are the same as in the Appendix D. M and S are related to I and parity as follows:

M	S	I	P
0	-1	3/2	$+1$
1	0	1/2	-1
2	0	1/2	$+1$
3	-1	3/2	-1

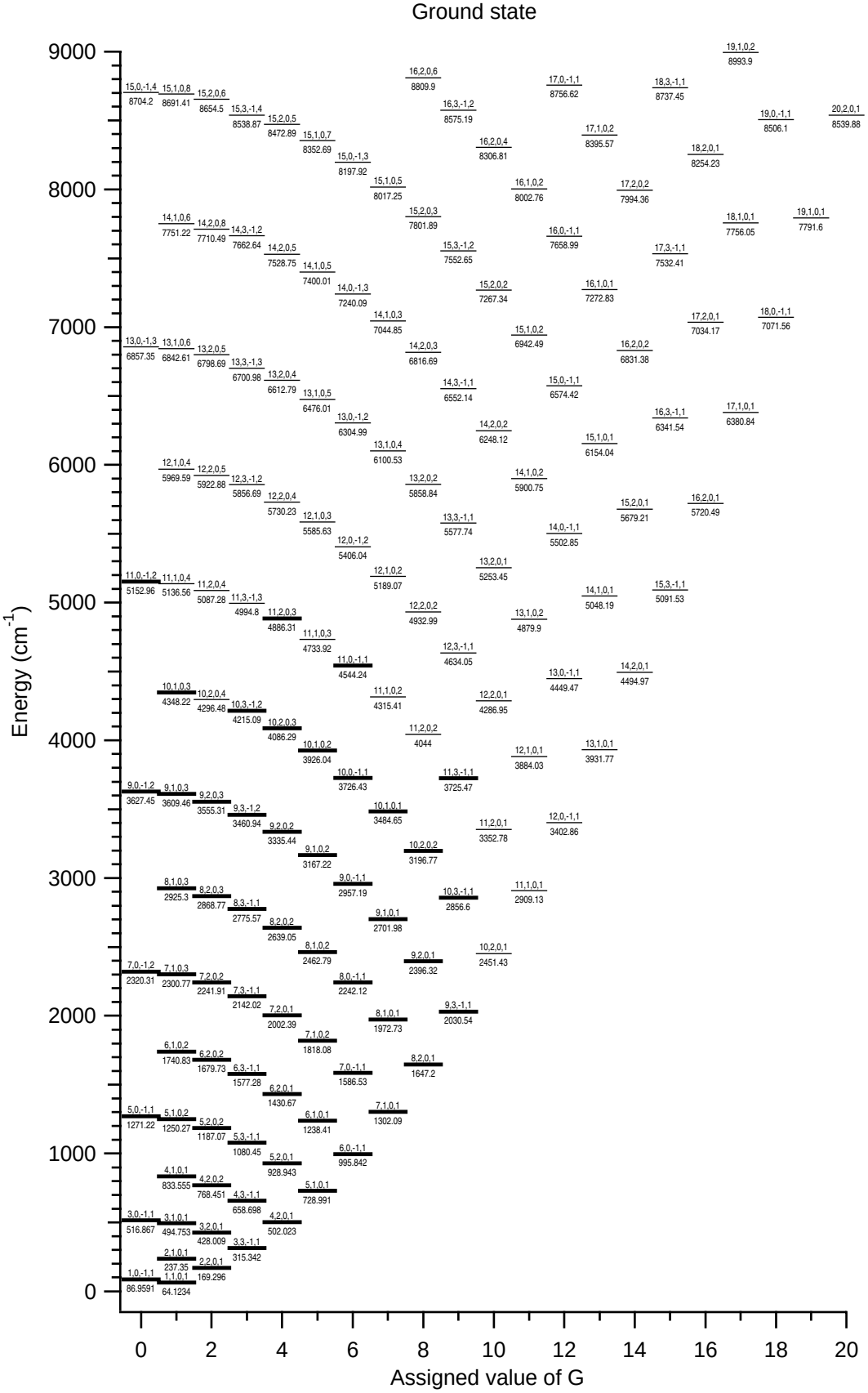
Ground state
Energy (cm-1)
Assigned value of G
0
1000
2000
3000
4000
5000
6000
7000
8000
9000
0
2
4
6
8
10
12
14
16
18
20
1,0,-1,1 86.9591
1,1,0,1 64.1234
2,1,0,1 237.35
2,2,0,1 169.296
3,0,-1,1 516.867
3,1,0,1 494.753
3,2,0,1 428.009
3,3,-1,1 315.342
4,1,0,1 833.555
4,2,0,2 768.451
4,3,-1,1 658.698
4,2,0,1 502.023
5,0,-1,1 1271.22
5,1,0,2 1250.27
5,2,0,2 1187.07
5,3,-1,1 1080.45
5,2,0,1 928.943
5,1,0,2 1238.41
6,0,-1,1 995.842
5,1,0,1 728.991
6,1,0,2 1740.83
6,2,0,2 1679.73
6,3,-1,1 1577.28
6,2,0,1 1430.67
6,1,0,1 1302.09
7,0,-1,2 2320.31
7,1,0,3 2300.77
7,2,0,2 2241.91
7,3,-1,1 2142.02
7,2,0,1 2002.39
7,1,0,2 1818.08
7,0,-1,1 1586.53
7,1,0,1 1302.09
8,1,0,3 2925.3
8,2,0,3 2868.77
8,3,-1,1 2775.57
8,2,0,2 2639.05
8,1,0,2 2462.79
8,0,-1,1 2242.12
8,1,0,1 1972.73
8,2,0,1 1647.2
9,0,-1,2 3627.45
9,1,0,3 3609.46
9,2,0,3 3555.31
9,3,-1,2 3460.94
9,2,0,2 3335.44
9,1,0,2 3167.22
9,0,-1,1 2957.19
9,1,0,1 2701.98
9,2,0,1 2396.32
9,3,-1,1 2030.54
10,1,0,3 4348.22
10,2,0,4 4296.48
10,3,-1,2 4215.09
10,2,0,3 4086.29
10,1,0,2 3926.04
10,0,-1,1 3726.43
10,1,0,1 3484.65
10,2,0,2 3196.77
10,3,-1,1 2856.6
11,0,-1,2 5152.96
11,1,0,4 5136.56
11,2,0,4 5087.28
11,3,-1,3 4994.8
11,2,0,3 4886.31
11,1,0,3 4733.92
11,0,-1,1 4544.24
11,1,0,2 4315.41
11,2,0,2 4044
11,3,-1,1 3725.47
11,2,0,1 3352.78
11,1,0,1 2909.13
12,1,0,4 5969.59
12,2,0,5 5922.88
12,3,-1,2 5856.69
12,2,0,4 5730.23
12,1,0,3 5585.63
12,0,-1,2 5406.04
12,1,0,2 5189.07
12,2,0,2 4932.99
12,3,-1,1 4634.05
12,2,0,1 4286.95
12,1,0,1 3884.03
12,0,-1,1 3402.86
13,0,-1,3 6857.35
13,1,0,6 6842.61
13,2,0,5 6798.69
13,3,-1,3 6700.98
13,2,0,4 6612.79
13,1,0,5 6476.01
13,0,-1,2 6304.99
13,1,0,4 6100.53
13,2,0,2 5858.84
13,3,-1,1 5577.74
13,2,0,1 5253.45
13,1,0,2 4879.9
13,0,-1,1 4449.47
13,1,0,1 3931.77
14,1,0,6 7751.22
14,2,0,8 7710.49
14,3,-1,2 7662.64
14,2,0,5 7528.75
14,1,0,5 7400.01
14,0,-1,3 7240.09
14,1,0,3 7044.85
14,2,0,3 6816.69
14,3,-1,1 6552.14
14,2,0,2 6248.12
14,1,0,2 5900.75
14,0,-1,1 5502.85
14,1,0,1 5048.19
14,2,0,1 4494.97
15,0,-1,4 8704.2
15,1,0,8 8691.41
15,2,0,6 8654.5
15,3,-1,4 8538.87
15,2,0,5 8472.89
15,1,0,7 8352.69
15,0,-1,3 8197.92
15,1,0,5 8017.25
15,2,0,3 7801.89
15,3,-1,2 7552.65
15,2,0,2 7267.34
15,1,0,2 6942.49
15,0,-1,1 6574.42
15,1,0,1 6154.04
15,2,0,1 5679.21
15,3,-1,1 5091.53
16,2,0,6 8809.9
16,3,-1,2 8575.19
16,2,0,4 8306.81
16,1,0,2 8002.76
16,0,-1,1 7658.99
16,1,0,1 7272.83
16,2,0,2 6831.38
16,3,-1,1 6341.54
16,2,0,1 5720.49
17,0,-1,1 8756.62
17,1,0,2 8395.57
17,2,0,2 7994.36
17,3,-1,1 7532.41
17,2,0,1 7034.17
17,1,0,1 6380.84
18,3,-1,1 8737.45
18,2,0,1 8254.23
18,1,0,1 7756.05
18,0,-1,1 7071.56
19,1,0,2 8993.9
19,0,-1,1 8506.1
19,1,0,1 7791.6
20,2,0,1 8539.88

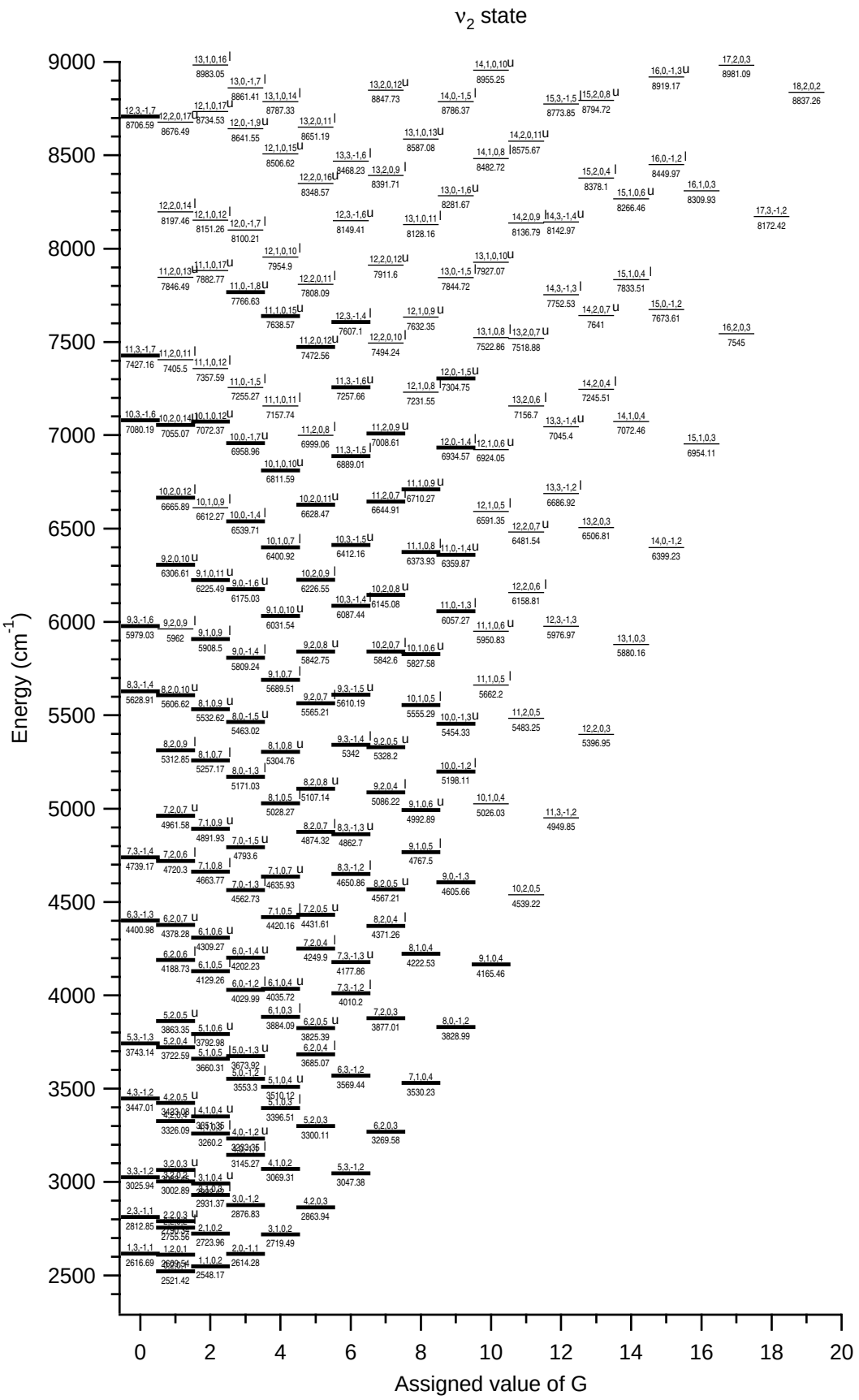
ν_2 state
Energy (cm^{-1})
Assigned value of G
9000
8500
8000
7500
7000
6500
6000
5500
5000
4500
4000
3500
3000
2500
0
2
4
6
8
10
12
14
16
18
20

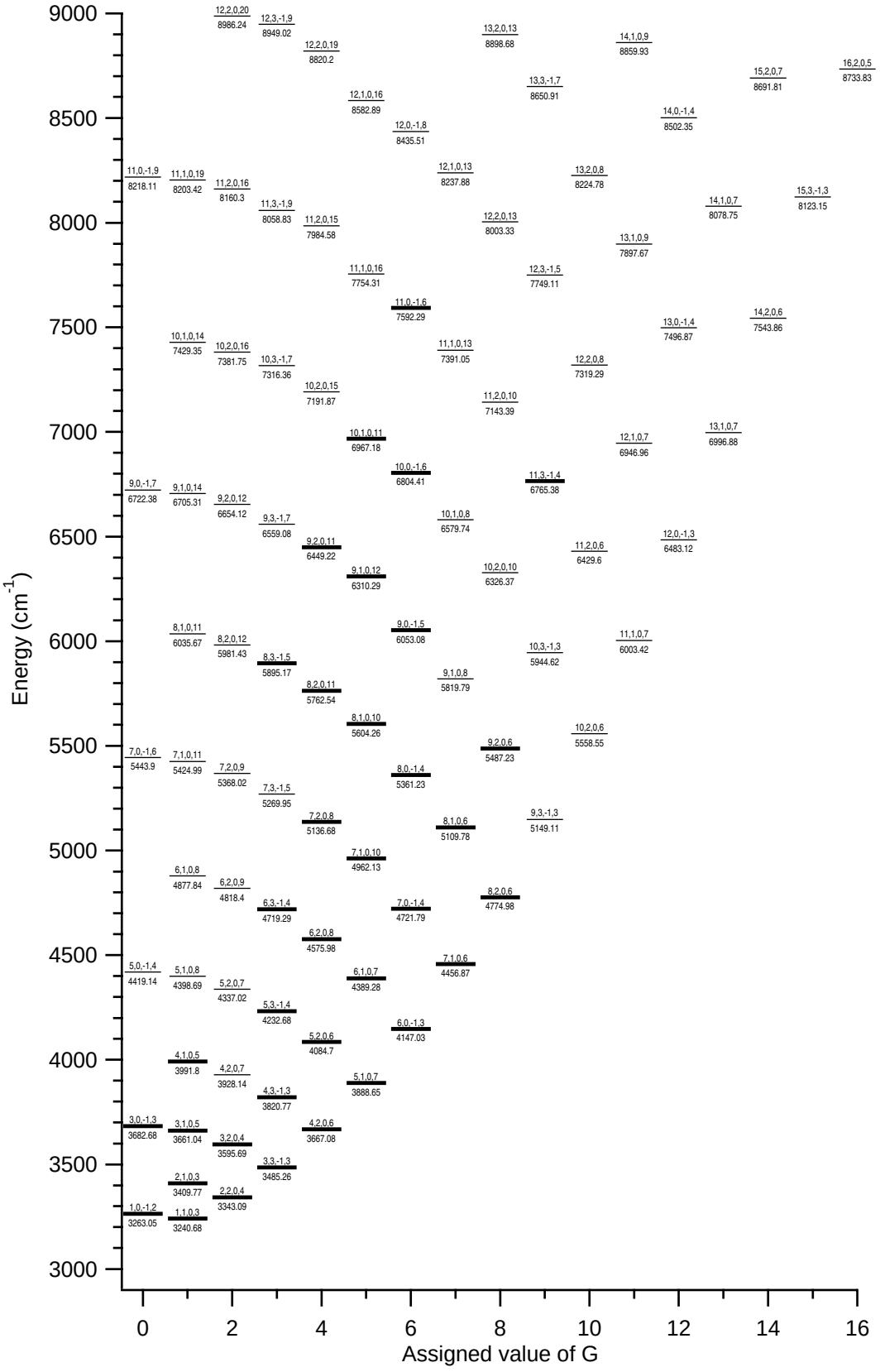
Energy (cm-1)
Assigned value of G
9000
8500
8000
7500
7000
6500
6000
5500
5000
4500
4000
3500
3000
0
2
4
6
8
10
12
14
16
12,2,0,20 8986.24
12,3,-1,9 8949.02
12,2,0,19 8820.2
13,2,0,13 8898.68
14,1,0,9 8859.93
16,2,0,5 8733.83
13,3,-1,7 8650.91
15,2,0,7 8691.81
12,1,0,16 8582.89
14,0,-1,4 8502.35
12,0,-1,8 8435.51
11,0,-1,9 8218.11
11,1,0,19 8203.42
12,1,0,13 8237.88
13,2,0,8 8224.78
11,2,0,16 8160.3
15,3,-1,3 8123.15
11,3,-1,9 8058.83
14,1,0,7 8078.75
12,2,0,13 8003.33
11,2,0,15 7984.58
13,1,0,9 7897.67
11,1,0,16 7754.31
12,3,-1,5 7749.11
11,0,-1,6 7592.29
14,2,0,6 7543.86
13,0,-1,4 7496.87
10,1,0,14 7429.35
11,1,0,13 7391.05
10,2,0,16 7381.75
10,3,-1,7 7316.36
12,2,0,8 7319.29
10,2,0,15 7191.87
11,2,0,10 7143.39
13,1,0,7 6996.88
10,1,0,11 6967.18
12,1,0,7 6946.96
9,0,-1,7 6722.38
10,0,-1,6 6804.41
11,3,-1,4 6765.38
9,1,0,14 6705.31
9,2,0,12 6654.12
10,1,0,8 6579.74
9,3,-1,7 6559.08
12,0,-1,3 6483.12
11,2,0,6 6429.6
9,2,0,11 6449.22
10,2,0,10 6326.37
9,1,0,12 6310.29
8,1,0,11 6035.67
9,0,-1,5 6053.08
11,1,0,7 6003.42
8,2,0,12 5981.43
10,3,-1,3 5944.62
8,3,-1,5 5895.17
9,1,0,8 5819.79
8,2,0,11 5762.54
10,2,0,6 5558.55
8,1,0,10 5604.26
9,2,0,6 5487.23
7,0,-1,6 5443.9
7,1,0,11 5424.99
8,0,-1,4 5361.23
7,2,0,9 5368.02
7,3,-1,5 5269.95
9,3,-1,3 5149.11
7,2,0,8 5136.68
8,1,0,6 5109.78
7,1,0,10 4962.13
6,1,0,8 4877.84
8,2,0,6 4774.98
6,2,0,9 4818.4
6,3,-1,4 4719.29
7,0,-1,4 4721.79
6,2,0,8 4575.98
5,0,-1,4 4419.14
5,1,0,8 4398.69
7,1,0,6 4456.87
6,1,0,7 4389.28
5,2,0,7 4337.02
5,3,-1,4 4232.68
6,0,-1,3 4147.03
5,2,0,6 4084.7
4,1,0,5 3991.8
4,2,0,7 3928.14
5,1,0,7 3888.65
4,3,-1,3 3820.77
3,0,-1,3 3682.68
3,1,0,5 3661.04
4,2,0,6 3667.08
3,2,0,4 3595.69
3,3,-1,3 3485.26
2,1,0,3 3409.77
2,2,0,4 3343.09
1,0,-1,2 3263.05
1,1,0,3 3240.68

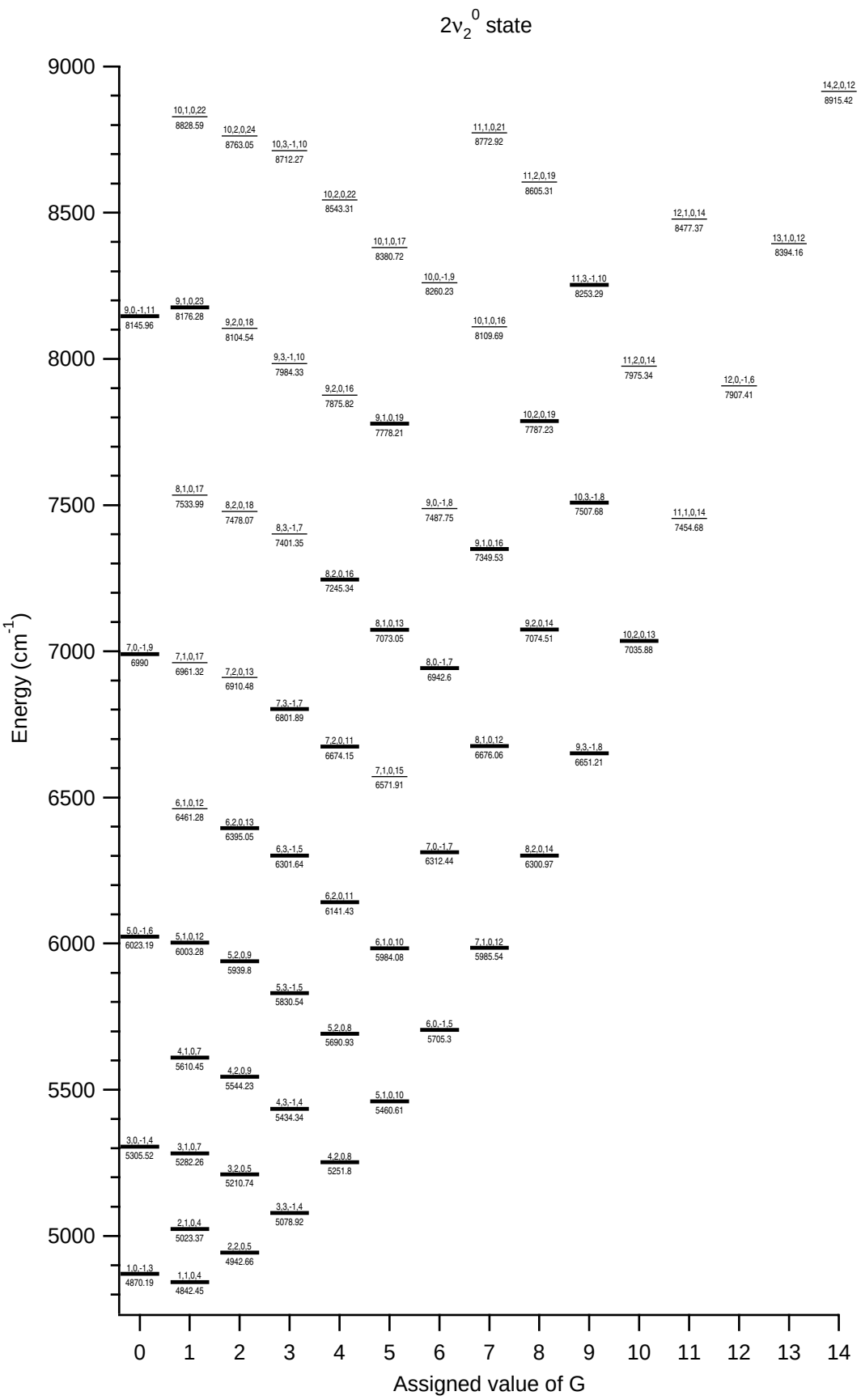
2ν2 0 state
Energy (cm-1)
Assigned value of G
9000
8500
8000
7500
7000
6500
6000
5500
5000
0
1
2
3
4
5
6
7
8
9
10
11
12
13
14
9,0,-1,11 8145.96
10,1,0,22 8828.59
10,2,0,24 8763.05
10,3,-1,10 8712.27
10,2,0,22 8543.31
10,1,0,17 8380.72
10,0,-1,9 8260.23
11,1,0,21 8772.92
11,2,0,19 8605.31
11,3,-1,10 8253.29
12,1,0,14 8477.37
13,1,0,12 8394.16
14,2,0,12 8915.42
9,1,0,23 8176.28
9,2,0,18 8104.54
9,3,-1,10 7984.33
9,2,0,16 7875.82
9,1,0,19 7778.21
10,1,0,16 8109.69
11,2,0,14 7975.34
12,0,-1,6 7907.41
10,2,0,19 7787.23
8,1,0,17 7533.99
8,2,0,18 7478.07
8,3,-1,7 7401.35
8,2,0,16 7245.34
8,1,0,13 7073.05
9,0,-1,8 7487.75
9,1,0,16 7349.53
10,3,-1,8 7507.68
11,1,0,14 7454.68
9,2,0,14 7074.51
10,2,0,13 7035.88
7,0,-1,9 6990
7,1,0,17 6961.32
7,2,0,13 6910.48
7,3,-1,7 6801.89
7,2,0,11 6674.15
7,1,0,15 6571.91
8,0,-1,7 6942.6
8,1,0,12 6676.06
9,3,-1,8 6651.21
6,1,0,12 6461.28
6,2,0,13 6395.05
6,3,-1,5 6301.64
6,2,0,11 6141.43
7,0,-1,7 6312.44
8,2,0,14 6300.97
5,0,-1,6 6023.19
5,1,0,12 6003.28
5,2,0,9 5939.8
5,3,-1,5 5830.54
5,2,0,8 5690.93
6,1,0,10 5984.08
6,0,-1,5 5705.3
7,1,0,12 5985.54
4,1,0,7 5610.45
4,2,0,9 5544.23
4,3,-1,4 5434.34
5,1,0,10 5460.61
3,0,-1,4 5305.52
3,1,0,7 5282.26
3,2,0,5 5210.74
3,3,-1,4 5078.92
4,2,0,8 5251.8
2,1,0,4 5023.37
2,2,0,5 4942.66
1,0,-1,3 4870.19
1,1,0,4 4842.45

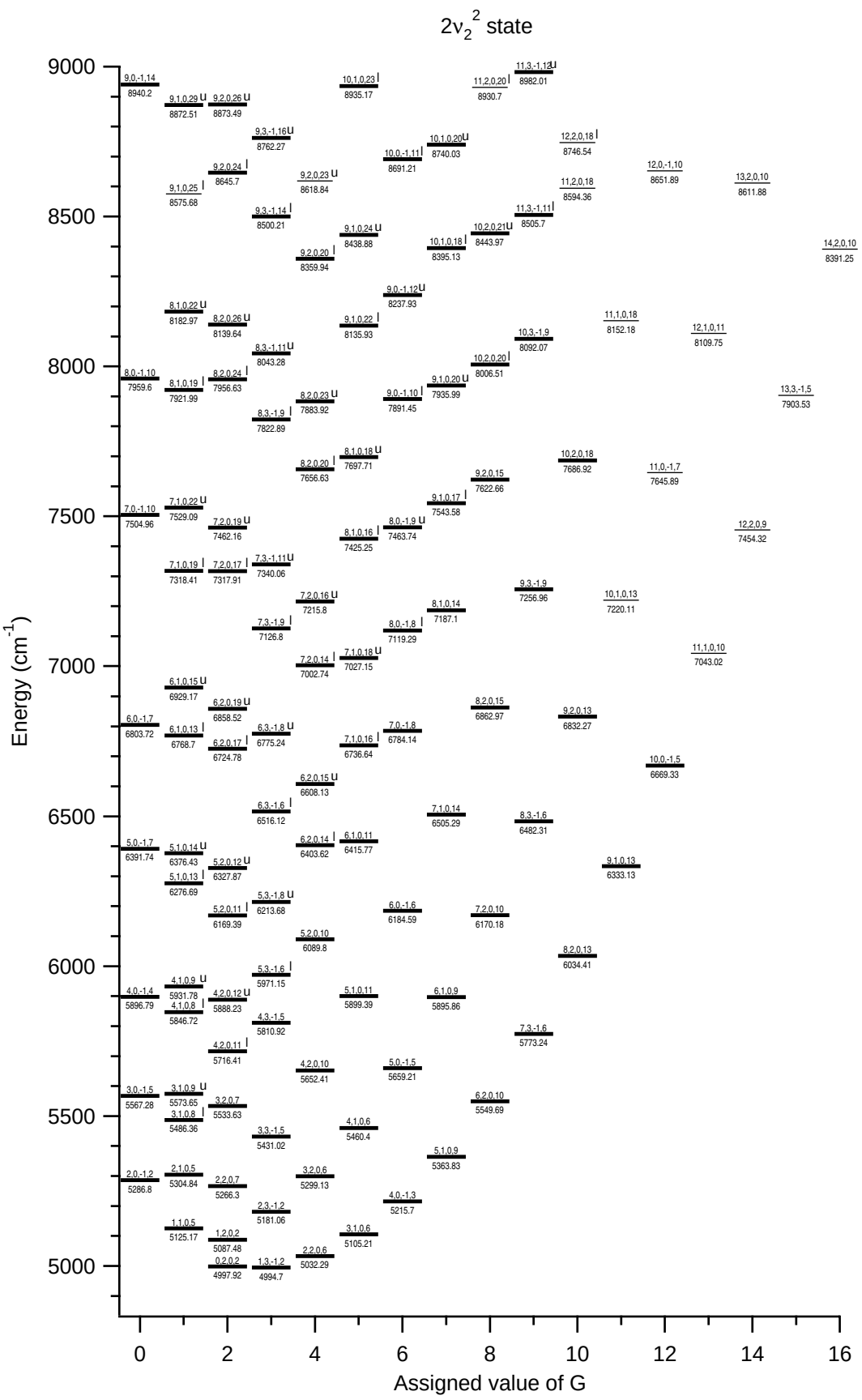
2ν2 2 state
Energy (cm-1)
Assigned value of G
9000
8500
8000
7500
7000
6500
6000
5500
5000
0
2
4
6
8
10
12
14
16
9,0,-1,14 8940.2
9,1,0,29 U 8872.51
9,2,0,26 U 8873.49
9,3,-1,16 U 8762.27
9,2,0,24 8645.7
9,1,0,25 8575.68
9,3,-1,14 8500.21
9,2,0,23 U 8618.84
9,2,0,20 8359.94
9,1,0,24 U 8438.88
10,1,0,23 8935.17
10,0,-1,11 8691.21
10,1,0,20 U 8740.03
10,1,0,18 8395.13
11,3,-1,12 U 8982.01
11,2,0,20 8930.7
10,2,0,21 U 8443.97
11,3,-1,11 8505.7
12,2,0,18 8746.54
11,2,0,18 8594.36
12,0,-1,10 8651.89
13,2,0,10 8611.88
14,2,0,10 8391.25
9,0,-1,12 U 8237.93
8,1,0,22 U 8182.97
8,2,0,26 U 8139.64
8,3,-1,11 U 8043.28
9,1,0,22 8135.93
10,3,-1,9 8092.07
10,2,0,20 8006.51
11,1,0,18 8152.18
12,1,0,11 8109.75
8,0,-1,10 7959.6
8,1,0,19 7921.99
8,2,0,24 7956.63
8,2,0,23 U 7883.92
8,3,-1,9 7822.89
9,1,0,20 U 7935.99
9,0,-1,10 7891.45
13,3,-1,5 7903.53
8,1,0,18 U 7697.71
8,2,0,20 7656.63
9,2,0,15 7622.66
10,2,0,18 7686.92
11,0,-1,7 7645.89
7,0,-1,10 7504.96
7,1,0,22 U 7529.09
7,2,0,19 U 7462.16
9,1,0,17 7543.58
8,0,-1,9 U 7463.74
8,1,0,16 7425.25
12,2,0,9 7454.32
7,1,0,19 7318.41
7,2,0,17 7317.91
7,3,-1,11 U 7340.06
9,3,-1,9 7256.96
10,1,0,13 7220.11
7,2,0,16 U 7215.8
8,1,0,14 7187.1
7,3,-1,9 7126.8
8,0,-1,8 7119.29
11,1,0,10 7043.02
7,2,0,14 7002.74
7,1,0,18 U 7027.15
6,1,0,15 U 6929.17
6,2,0,19 U 6858.52
8,2,0,15 6862.97
9,2,0,13 6832.27
6,0,-1,7 6803.72
6,1,0,13 6768.7
6,2,0,17 6724.78
6,3,-1,8 U 6775.24
7,0,-1,8 6784.14
7,1,0,16 6736.64
10,0,-1,5 6669.33
6,2,0,15 U 6608.13
6,3,-1,6 6516.12
7,1,0,14 6505.29
8,3,-1,6 6482.31
5,0,-1,7 6391.74
5,1,0,14 U 6376.43
5,2,0,12 U 6327.87
6,2,0,14 6403.62
6,1,0,11 6415.77
9,1,0,13 6333.13
5,1,0,13 6276.69
5,3,-1,8 U 6213.68
5,2,0,11 6169.39
6,0,-1,6 6184.59
7,2,0,10 6170.18
5,2,0,10 6089.8
8,2,0,13 6034.41
5,3,-1,6 5971.15
4,1,0,9 U 5931.78
4,2,0,12 U 5888.23
4,1,0,8 5846.72
5,1,0,11 5899.39
6,1,0,9 5895.86
4,3,-1,5 5810.92
7,3,-1,6 5773.24
4,2,0,11 5716.41
4,2,0,10 5652.41
5,0,-1,5 5659.21
3,0,-1,5 5567.28
3,1,0,9 U 5573.65
3,2,0,7 5533.63
6,2,0,10 5549.69
3,1,0,8 5486.36
3,3,-1,5 5431.02
4,1,0,6 5460.4
5,1,0,9 5363.83
2,0,-1,2 5286.8
2,1,0,5 5304.84
2,2,0,7 5266.3
3,2,0,6 5299.13
4,0,-1,3 5215.7
2,3,-1,2 5181.06
1,1,0,5 5125.17
1,2,0,2 5087.48
3,1,0,6 5105.21
0,2,0,2 4997.92
1,3,-1,2 4994.7
2,2,0,6 5032.29

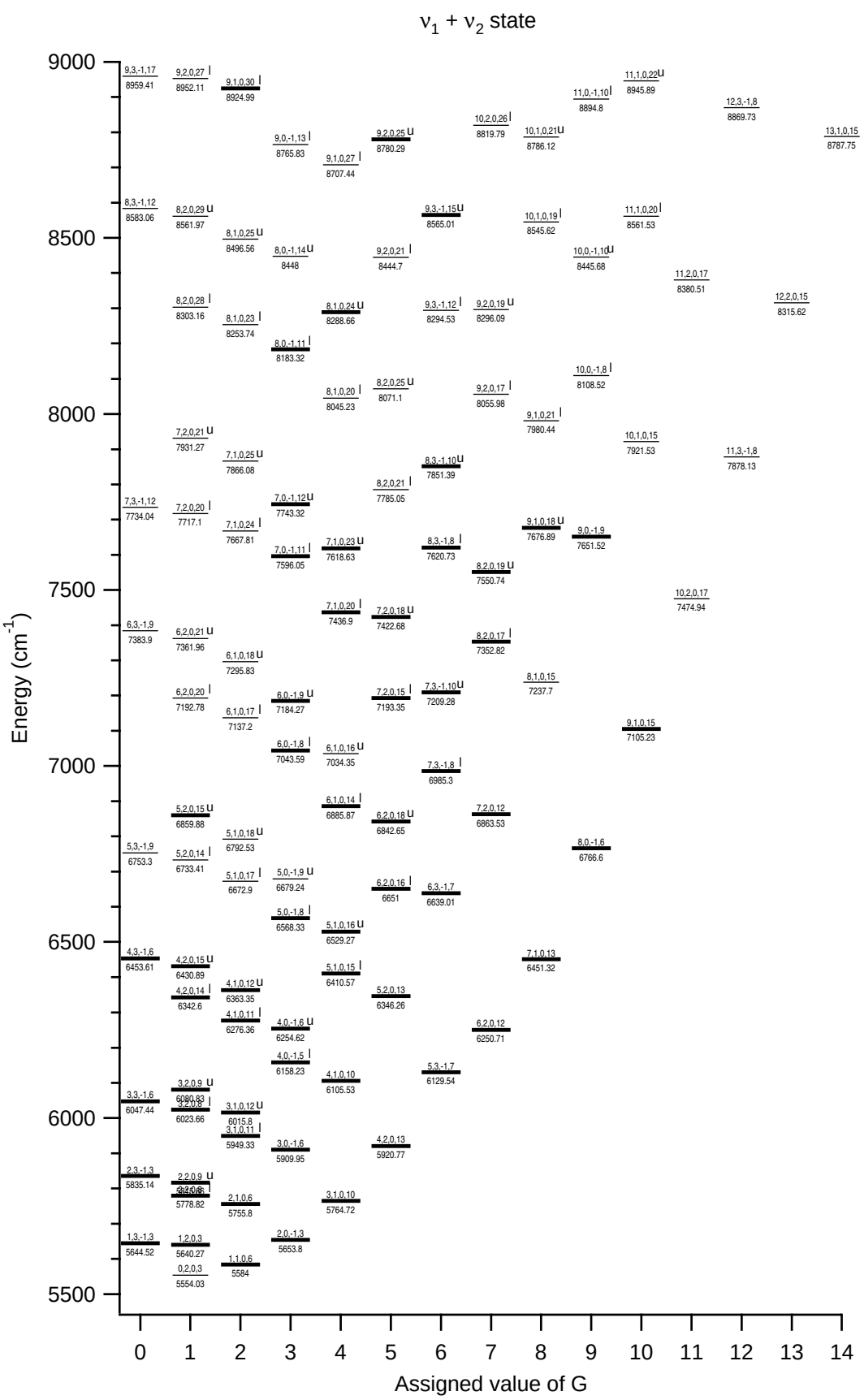
ν1 + ν2 state
Energy (cm-1)
Assigned value of G
9000
8500
8000
7500
7000
6500
6000
5500
0
1
2
3
4
5
6
7
8
9
10
11
12
13
14
9,3,-1,17 8959.41
9,2,0,27 l 8952.11
9,1,0,30 l 8924.99
9,0,-1,13 l 8765.83
9,1,0,27 l 8707.44
9,2,0,25 u 8780.29
10,2,0,26 l 8819.79
10,1,0,21 u 8786.12
11,0,-1,10 l 8894.8
11,1,0,22 u 8945.89
12,3,-1,8 8869.73
13,1,0,15 8787.75
8,3,-1,12 8583.06
8,2,0,29 u 8561.97
8,1,0,25 u 8496.56
8,0,-1,14 u 8448
9,3,-1,15 u 8565.01
9,2,0,21 l 8444.7
10,1,0,19 l 8545.62
10,0,-1,10 u 8445.68
11,1,0,20 l 8561.53
11,2,0,17 8380.51
8,2,0,28 l 8303.16
8,1,0,23 l 8253.74
8,0,-1,11 l 8183.32
8,1,0,24 u 8288.66
9,3,-1,12 l 8294.53
9,2,0,19 u 8296.09
12,2,0,15 8315.62
10,0,-1,8 l 8108.52
8,1,0,20 l 8045.23
8,2,0,25 u 8071.1
9,2,0,17 l 8055.98
7,2,0,21 u 7931.27
7,1,0,25 u 7866.08
8,3,-1,10 u 7851.39
9,1,0,21 l 7980.44
10,1,0,15 7921.53
11,3,-1,8 7878.13
7,3,-1,12 7734.04
7,2,0,20 l 7717.1
7,1,0,24 l 7667.81
7,0,-1,12 u 7743.32
8,2,0,21 l 7785.05
7,0,-1,11 l 7596.05
7,1,0,23 u 7618.63
8,3,-1,8 l 7620.73
9,1,0,18 u 7676.89
9,0,-1,9 7651.52
8,2,0,19 u 7550.74
10,2,0,17 7474.94
6,3,-1,9 7383.9
6,2,0,21 u 7361.96
6,1,0,18 u 7295.83
7,1,0,20 l 7436.9
7,2,0,18 u 7422.68
8,2,0,17 l 7352.82
6,2,0,20 l 7192.78
6,1,0,17 l 7137.2
6,0,-1,9 u 7184.27
7,2,0,15 l 7193.35
7,3,-1,10 u 7209.28
8,1,0,15 7237.7
9,1,0,15 7105.23
6,0,-1,8 l 7043.59
6,1,0,16 u 7034.35
7,3,-1,8 l 6985.3
5,2,0,15 u 6859.88
5,1,0,18 u 6792.53
6,1,0,14 l 6885.87
6,2,0,18 u 6842.65
7,2,0,12 6863.53
8,0,-1,6 6766.6
5,3,-1,9 6753.3
5,2,0,14 l 6733.41
5,1,0,17 l 6672.9
5,0,-1,9 u 6679.24
6,2,0,16 l 6651
6,3,-1,7 6639.01
5,0,-1,8 l 6568.33
5,1,0,16 u 6529.27
4,3,-1,6 6453.61
4,2,0,15 u 6430.89
4,2,0,14 l 6342.6
4,1,0,12 u 6363.35
4,1,0,11 l 6276.36
5,1,0,15 l 6410.57
5,2,0,13 6346.26
7,1,0,13 6451.32
6,2,0,12 6250.71
4,0,-1,6 u 6254.62
4,0,-1,5 l 6158.23
5,3,-1,7 6129.54
4,1,0,10 6105.53
3,3,-1,6 6047.44
3,2,0,9 u 6080.83
3,2,0,8 l 6023.66
3,1,0,12 u 6015.8
3,1,0,11 l 5949.33
3,0,-1,6 5909.95
4,2,0,13 5920.77
2,3,-1,5 5835.14
2,2,0,9 u
2,2,0,8 l 5778.82
2,1,0,6 5755.8
3,1,0,10 5764.72
1,3,-1,5 5644.52
1,2,0,3 5640.27
0,2,0,3 5554.03
1,1,0,6 5584
2,0,-1,3 5653.8

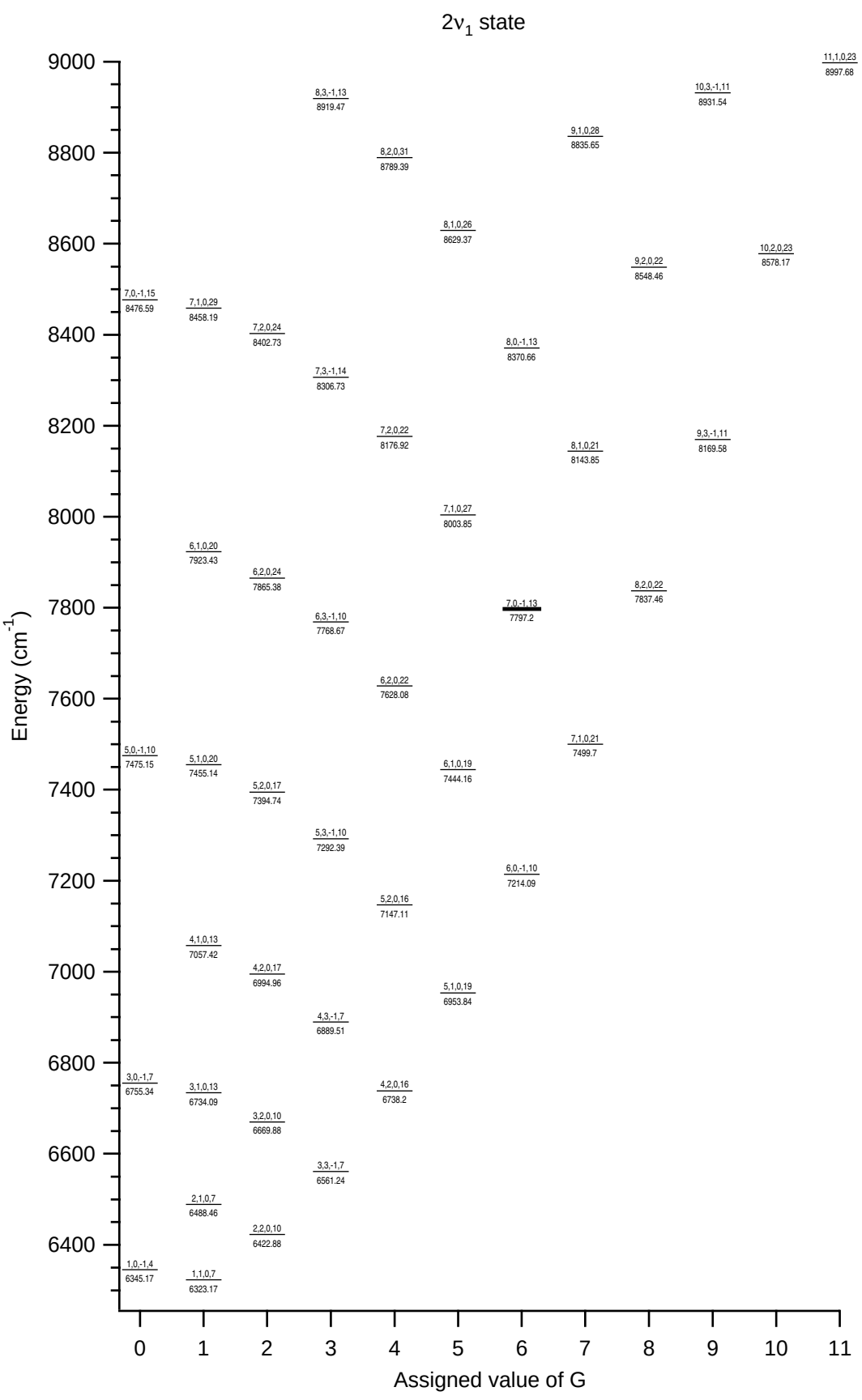
2ν1 state
Energy (cm-1)
Assigned value of G
9000
8800
8600
8400
8200
8000
7800
7600
7400
7200
7000
6800
6600
6400
0
1
2
3
4
5
6
7
8
9
10
11
11,1,0,23 8997.68
10,3,-1,11 8931.54
9,1,0,28 8835.65
8,3,-1,13 8919.47
8,2,0,31 8789.39
8,1,0,26 8629.37
10,2,0,23 8578.17
9,2,0,22 8548.46
7,0,-1,15 8476.59
7,1,0,29 8458.19
7,2,0,24 8402.73
8,0,-1,13 8370.66
7,3,-1,14 8306.73
9,3,-1,11 8169.58
7,2,0,22 8176.92
8,1,0,21 8143.85
7,1,0,27 8003.85
6,1,0,20 7923.43
6,2,0,24 7865.38
8,2,0,22 7837.46
7,0,-1,13 7797.2
6,3,-1,10 7768.67
6,2,0,22 7628.08
7,1,0,21 7499.7
5,0,-1,10 7475.15
5,1,0,20 7455.14
6,1,0,19 7444.16
5,2,0,17 7394.74
5,3,-1,10 7292.39
6,0,-1,10 7214.09
5,2,0,16 7147.11
4,1,0,13 7057.42
4,2,0,17 6994.96
5,1,0,19 6953.84
4,3,-1,7 6889.51
3,0,-1,7 6755.34
3,1,0,13 6734.09
4,2,0,16 6738.2
3,2,0,10 6669.88
3,3,-1,7 6561.24
2,1,0,7 6488.46
2,2,0,10 6422.88
1,0,-1,4 6345.17
1,1,0,7 6323.17

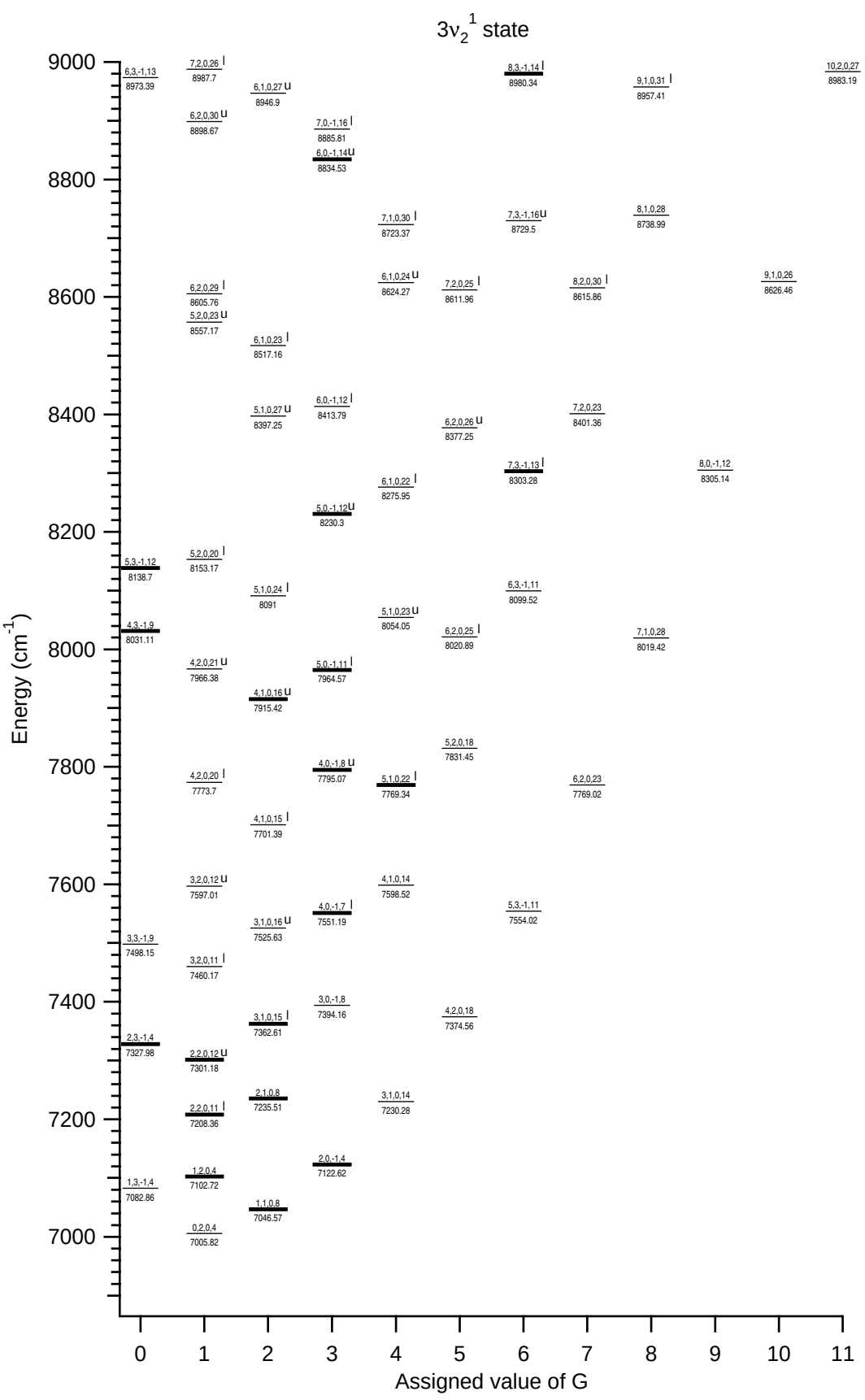
3ν2 1 state
Energy (cm-1)
Assigned value of G
9000
8800
8600
8400
8200
8000
7800
7600
7400
7200
7000
0
1
2
3
4
5
6
7
8
9
10
11
6,3,-1,13 8973.39
7,2,0,26 l 8987.7
6,1,0,27 u 8946.9
6,2,0,30 u 8898.67
7,0,-1,16 l 8885.81
6,0,-1,14 u 8834.53
8,3,-1,14 l 8980.34
9,1,0,31 l 8957.41
10,2,0,27 8983.19
7,1,0,30 l 8723.37
7,3,-1,16 u 8729.5
8,1,0,28 8738.99
6,2,0,29 l 8605.76
5,2,0,23 u 8557.17
6,1,0,24 u 8624.27
7,2,0,25 l 8611.96
8,2,0,30 l 8615.86
9,1,0,26 8626.46
6,1,0,23 l 8517.16
6,0,-1,12 l 8413.79
5,1,0,27 u 8397.25
7,2,0,23 8401.36
6,2,0,26 u 8377.25
7,3,-1,13 l 8303.28
8,0,-1,12 8305.14
6,1,0,22 l 8275.95
5,0,-1,12 u 8230.3
5,3,-1,12 8138.7
5,2,0,20 l 8153.17
5,1,0,24 l 8091
6,3,-1,11 8099.52
5,1,0,23 u 8054.05
4,3,-1,9 8031.11
6,2,0,25 l 8020.89
7,1,0,28 8019.42
4,2,0,21 u 7966.38
5,0,-1,11 l 7964.57
4,1,0,16 u 7915.42
5,2,0,18 7831.45
4,0,-1,8 u 7795.07
4,2,0,20 l 7773.7
5,1,0,22 l 7769.34
6,2,0,23 7769.02
4,1,0,15 l 7701.39
3,2,0,12 u 7597.01
4,1,0,14 7598.52
4,0,-1,7 l 7551.19
5,3,-1,11 7554.02
3,1,0,16 u 7525.63
3,3,-1,9 7498.15
3,2,0,11 l 7460.17
3,0,-1,8 7394.16
3,1,0,15 l 7362.61
4,2,0,18 7374.56
2,3,-1,4 7327.98
2,2,0,12 u 7301.18
2,1,0,8 7235.51
2,2,0,11 l 7208.36
3,1,0,14 7230.28
2,0,-1,4 7122.62
1,3,-1,4 7082.86
1,2,0,4 7102.72
1,1,0,8 7046.57
0,2,0,4 7005.82

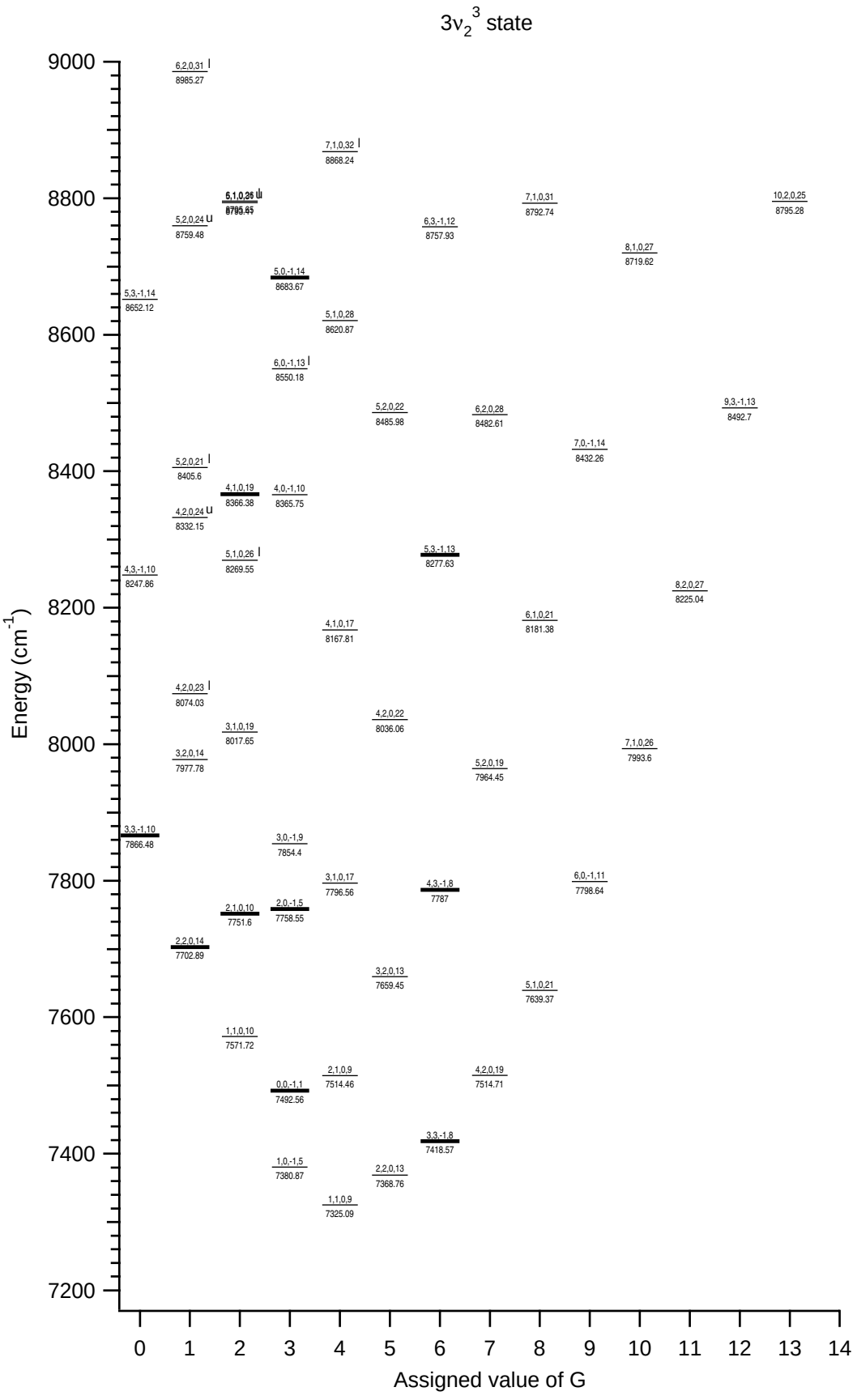
3ν2 3 state
Energy (cm-1)
Assigned value of G
9000
8800
8600
8400
8200
8000
7800
7600
7400
7200
0
1
2
3
4
5
6
7
8
9
10
11
12
13
14
6,2,0,31
8985.27
7,1,0,32
8868.24
5,2,0,24 u
8759.48
6,3,-1,12
8757.93
7,1,0,31
8792.74
10,2,0,25
8795.28
8,1,0,27
8719.62
5,3,-1,14
8652.12
5,0,-1,14
8683.67
5,1,0,28
8620.87
6,0,-1,13
8550.18
9,3,-1,13
8492.7
5,2,0,22
8485.98
6,2,0,28
8482.61
7,0,-1,14
8432.26
5,2,0,21
8405.6
4,1,0,19
8366.38
4,0,-1,10
8365.75
4,2,0,24 u
8332.15
5,3,-1,13
8277.63
4,3,-1,10
8247.86
5,1,0,26
8269.55
8,2,0,27
8225.04
6,1,0,21
8181.38
4,1,0,17
8167.81
4,2,0,23
8074.03
4,2,0,22
8036.06
3,1,0,19
8017.65
7,1,0,26
7993.6
3,2,0,14
7977.78
5,2,0,19
7964.45
3,3,-1,10
7866.48
3,0,-1,9
7854.4
6,0,-1,11
7798.64
3,1,0,17
7796.56
4,3,-1,8
7787
2,1,0,10
7751.6
2,0,-1,5
7758.55
2,2,0,14
7702.89
3,2,0,13
7659.45
5,1,0,21
7639.37
1,1,0,10
7571.72
2,1,0,9
7514.46
4,2,0,19
7514.71
0,0,-1,1
7492.56
3,3,-1,8
7418.57
1,0,-1,5
7380.87
2,2,0,13
7368.76
1,1,0,9
7325.09

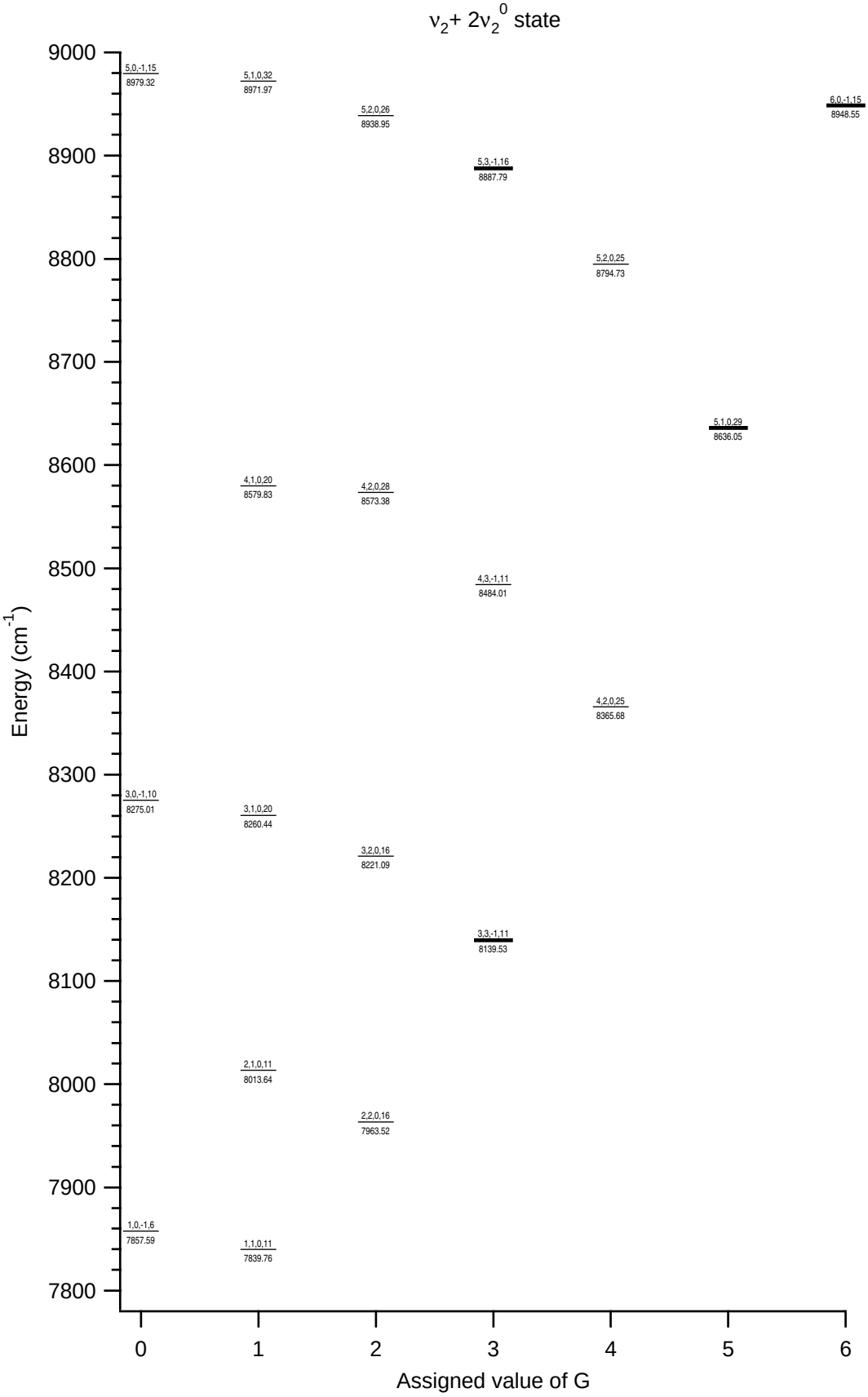
ν_2+ 2ν_2^0 state
Energy (cm^{-1})
9000
8900
8800
8700
8600
8500
8400
8300
8200
8100
8000
7900
7800
0
1
2
3
4
5
6
Assigned value of G
5,0,-1,15
8979.32
5,1,0,32
8971.97
5,2,0,26
8938.95
5,3,-1,16
8887.79
5,2,0,25
8794.73
5,1,0,29
8636.05
6,0,-1,15
8948.55
4,1,0,20
8579.83
4,2,0,28
8573.38
4,3,-1,11
8484.01
4,2,0,25
8365.68
3,0,-1,10
8275.01
3,1,0,20
8260.44
3,2,0,16
8221.09
3,3,-1,11
8139.53
2,1,0,11
8013.64
2,2,0,16
7963.52
1,0,-1,6
7857.59
1,1,0,11
7839.76

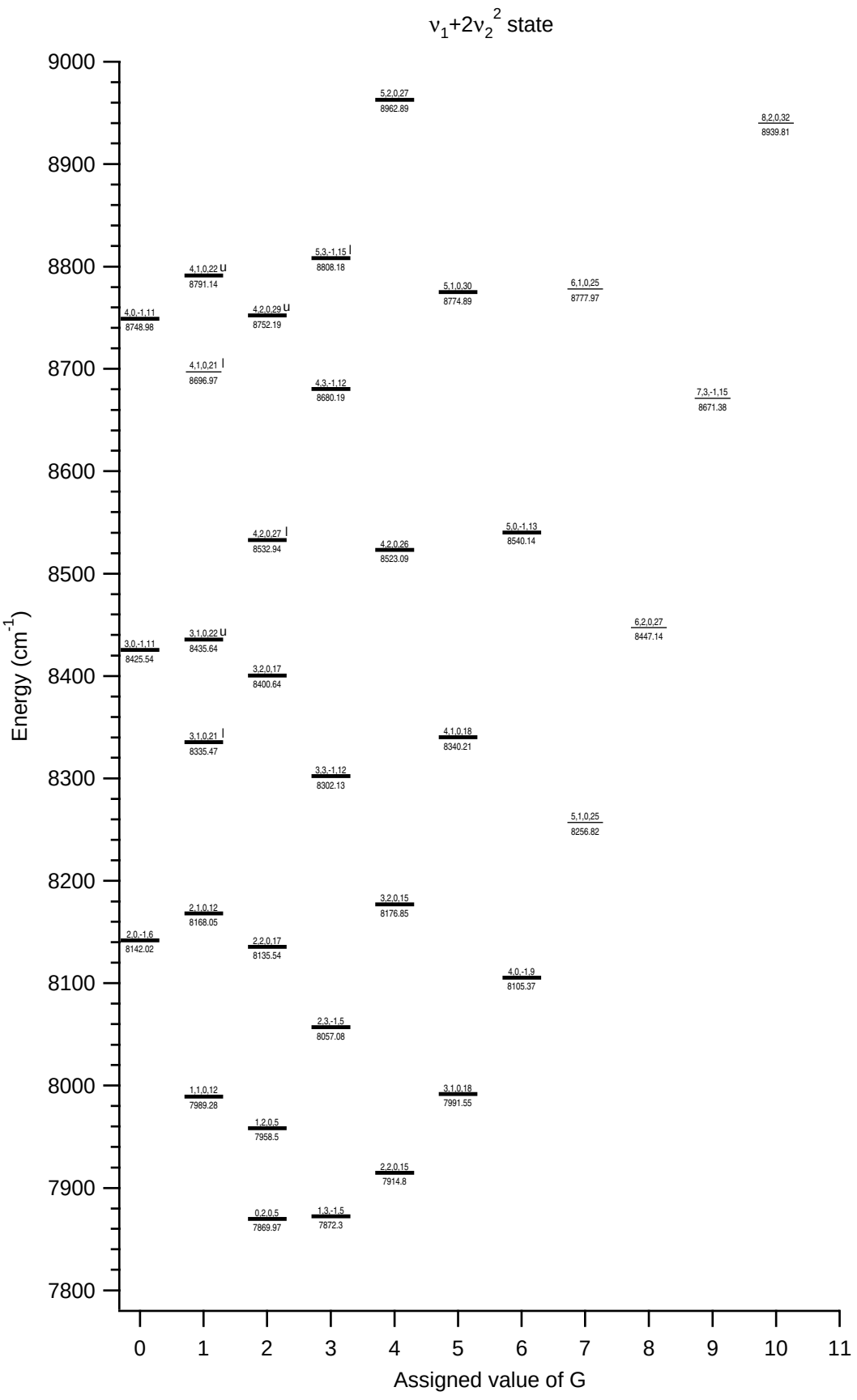
$\nu_1+2\nu_2^2$ state
Energy (cm^{-1})
Assigned value of G
9000
8900
8800
8700
8600
8500
8400
8300
8200
8100
8000
7900
7800
0
1
2
3
4
5
6
7
8
9
10
11
5,2,0,27
8962.89
8,2,0,32
8939.81
5,3,-1,15 l
8808.18
4,1,0,22 u
8791.14
5,1,0,30
8774.89
6,1,0,25
8777.97
4,0,-1,11
8748.98
4,2,0,29 u
8752.19
4,1,0,21 l
8696.97
4,3,-1,12
8680.19
7,3,-1,15
8671.38
4,2,0,27 l
8532.94
5,0,-1,13
8540.14
4,2,0,26
8523.09
6,2,0,27
8447.14
3,0,-1,11
8425.54
3,1,0,22 u
8435.64
3,2,0,17
8400.64
4,1,0,18
8340.21
3,1,0,21 l
8335.47
3,3,-1,12
8302.13
5,1,0,25
8256.82
3,2,0,15
8176.85
2,1,0,12
8168.05
2,0,-1,6
8142.02
2,2,0,17
8135.54
4,0,-1,9
8105.37
2,3,-1,5
8057.08
1,1,0,12
7989.28
3,1,0,18
7991.55
1,2,0,5
7958.5
2,2,0,15
7914.8
0,2,0,5
7869.97
1,3,-1,5
7872.3

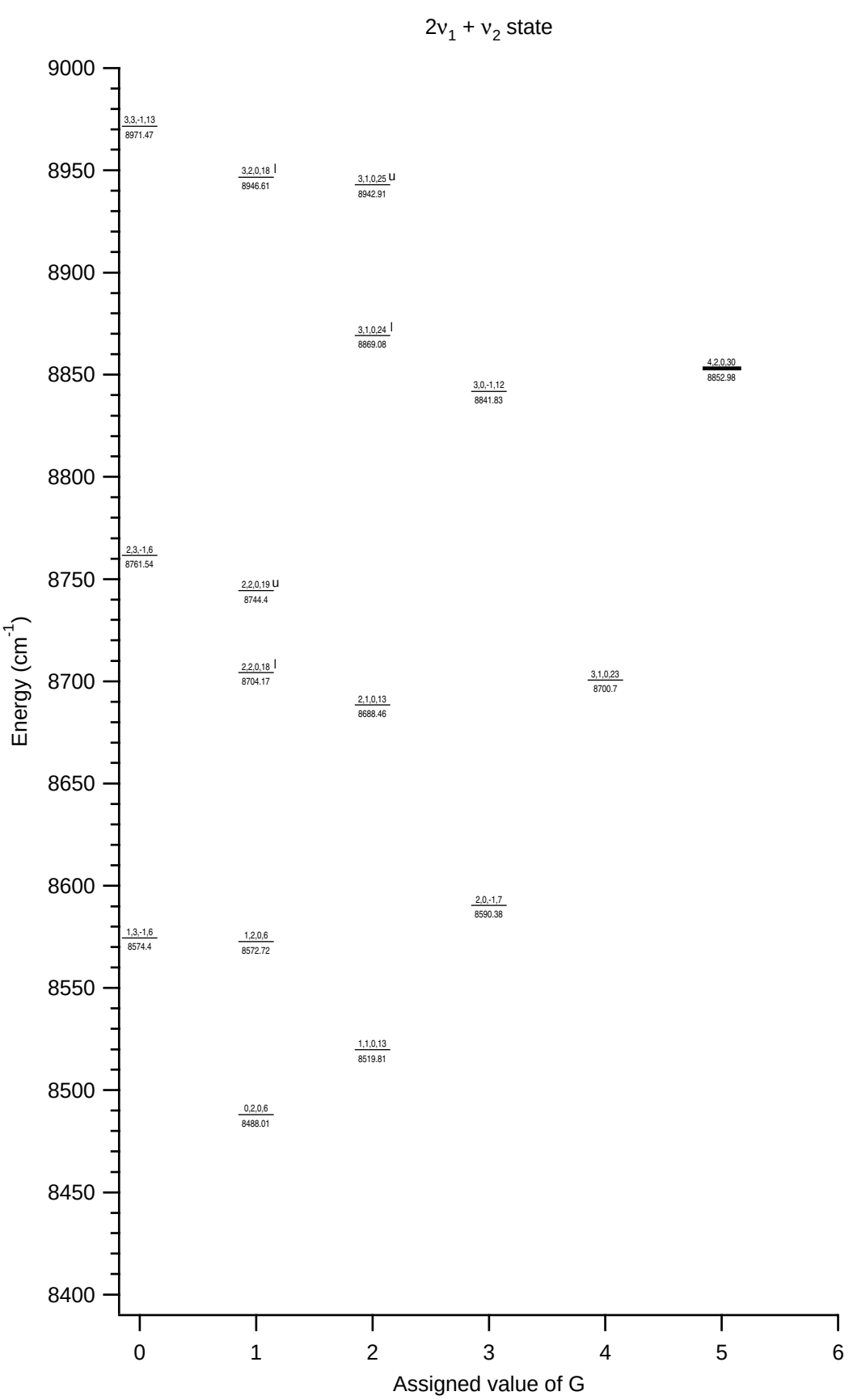
2ν1 + ν2 state
Energy (cm-1)
Assigned value of G
9000
8950
8900
8850
8800
8750
8700
8650
8600
8550
8500
8450
8400
0
1
2
3
4
5
6
3,3,-1,13
8971.47
3,2,0,18 l
8946.61
3,1,0,25 u
8942.91
3,1,0,24 l
8869.08
4,2,0,30
8852.98
3,0,-1,12
8841.83
2,3,-1,6
8761.54
2,2,0,19 u
8744.4
2,2,0,18 l
8704.17
3,1,0,23
8700.7
2,1,0,13
8688.46
2,0,-1,7
8590.38
1,3,-1,6
8574.4
1,2,0,6
8572.72
1,1,0,13
8519.81
0,2,0,6
8488.01

REFERENCES

[1] J. J. Thomson, Phil. Mag. **21**, 225 (1911).

[2] T. Oka, Phys. Rev. Lett. **45**, 531 (1980).

[3] S. S. Lee, B. F. Ventrudo, D. T. Cassidy, T. Oka, S. Miller, and J. Tennyson, J. Mol. Spect. **145**, 222 (1991).

[4] C. A. Coulson, Proc. Cambridge Phil. Soc. **31**, 244 (1935).

[5] R. E. Christoffersen, J. Chem. Phys. **41**, 960 (1964).

[6] G. D. Carney and R. N. Porter, J. Chem. Phys. **65**, 3547 (1976).

[7] G. D. Carney and R. N. Porter, Phys. Rev. Lett. **45**, 537 (1980).

[8] W. Meyer, P. Botschwina, and P. Burton, J. Chem. Phys. **84**, 891 (1986).

[9] B. T. Sutcliffe and J. Tennyson, J. Chem. Soc. Faraday Trans. **83**, 1663 (1987).

[10] S. Miller and J. Tennyson, J. Mol. Spectrosc. **136**, 223 (1989).

[11] D. W. Martin, E. W. McDaniel, and M. L. Meeks, Astrophys. J. **134**, 112 (1961).

[12] E. Herbst and W. Klemperer, Astrophys. J. **185**, 505 (1973).

[13] W. D. Watson, Astrophys. J. **183**, L17 (1973).

[14] T. R. Geballe and T. Oka, Nature **384**, 334 (1996).

[15] P. A. M. Dirac, Proc. Roy. Soc. Lond. **A112**, 661 (1926).

[16] L. D. Landau and E. M. Lifshitz, *Quantum Mechanics (Non-relativistic Theory)*, Butterworth-Heinemann, Oxford, 4th edition, 1997.

[17] J. Tennyson, Rep. Prog. Phys. **58**, 421 (1995).

[18] O. Friedrich, A. Alijah, Z. Xu, and A. J. C. Varandas, Phys. Rev. Lett. **86**, 1183 (2001).

[19] H. M. Edwards, *Galois Theory*, Springer-Verlag, New York, 1984.

[20] G. Herzberg, *Molecular Spectra and Molecular Structure*, volume II, Krieger, Malabar, Florida, 2nd edition, 1991.

[21] E. Teller, Hand- und Jahrb. d. Chem. Phys. **9, II**, 43 (1934).

[22] E. B. Wilson, Jr., J. C. Decius, and P. C. Cross, *Molecular Vibrations*, Dover, New York, 2nd edition, 1980.

[23] P. R. Bunker, *Molecular Symmetry and Spectroscopy*, Academic Press, New York, 1979.

[24] T. Oka, J. Molec. Spectrosc. **48**, 503 (1973).

[25] R. Röhse, W. Kutzelnigg, R. Jaquet, and W. Klopper, J. Chem. Phys. **101**, 2231 (1994).

[26] B. Dinelli, S. Miller, and J. Tennyson, J. Mol. Spect. **153**, 718 (1992).

[27] H. H. Nielsen and D. M. Dennison, Phys. Rev. **72**, 1101 (1947).

[28] J. K. G. Watson, J. Mol. Spect. **103**, 350 (1984).

[29] W. Klemperer, K. K. Lehmann, J. K. G. Watson, and S. C. Wofsy, J. Phys. Chem. **97**, 2413 (1993).

[30] B. J. McCall, Phil. Trans. R. Soc. Lond. **A358**, 2385 (2000).

[31] B. J. McCall and T. Oka, J. Chem. Phys. **113**, 3104 (2000).

[32] T. Oka, The H_3^+ ion, in *Molecular Ions: Spectroscopy, Structure, and Chemistry*, edited by T. A. Miller and V. E. Bondybey, pages 73–90, North-Holland Publishing Company, Amsterdam, 1983.

[33] A. von Engel, *Ionized Gases*, AIP Press, Woodbury, NY, reprint edition, 1994.

[34] M. G. Bawendi, B. D. Rehfuss, and T. Oka, J. Chem. Phys. **93**, 6200 (1990).

[35] W. H. Flygare, Acc. Chem. Res. **1**, 121 (1968).

[36] C. S. Gudeman, M. H. Begemann, J. Pfaff, and R. J. Saykally, Phys. Rev. Lett. **50**, 727 (1983).

[37] J. U. White, J. Opt. Soc. Am. **32**, 285 (1942).

[38] D. R. Herriott and H. J. Schulte, Appl. Opt. **4**, 883 (1965).

[39] E. T. White, *High Resolution Infrared Laser Spectrosocpy of* CH_5^+, PhD thesis, University of Chicago, 1999.

[40] P. C. D. Hobbs, Appl. Opt. **36**, 903 (1997).

[41] J. K. G. Watson, *private communication*, 1996.

[42] See AIP Document No. E-PAPS: E-JCPSA6-113-021032 for a file containing the frequencies and intensities of the observed Rydberg transitions. EPAPS document files can be retrieved from the FTP server (http://www.aip.org/epaps/epaps.html) or from ftp.aip.org in the directory /epaps/. For further information, e-mail: paps@aip.org or fax: 516-576-2223. The table is also available on the author's web site (at http://h3plus.uchicago.edu/data/rydbergs.html).

[43] D. Uy, *Infrared Spectroscopic and Kinetic Studies of Molecular Ions and* H_2 *in Glow Discharges with a Difference Frequency Laser System*, PhD thesis, University of Chicago, 1996.

[44] D. Uy, C. M. Gabrys, T. Oka, B. J. Cotterell, R. J. Strickland, C. Jungen, and A. Wüest, J. Chem. Phys. **113**, 10143 (2000).

[45] B. M. Dinelli, S. Miller, and J. Tennyson, J. Mol. Spect. **163**, 71 (1994).

[46] L.-W. Xu, C. Gabrys, and T. Oka, J. Chem. Phys. **93**, 6210 (1990).

[47] L. Neale, S. Miller, and J. Tennyson, Astrophys. J. **464**, 516 (1996).

[48] B. M. Dinelli, L. Neale, O. L. Polyansky, and J. Tennyson, J. Mol. Spect. **181**, 142 (1997).

[49] L. Wolniewicz and J. Hinze, J. Chem. Phys. **101**, 9817 (1994).

[50] O. L. Polyansky and J. Tennyson, J. Chem. Phys. **110**, 5056 (1999).

[51] R. Jaquet, *private communication*, 1999.

[52] W. A. Majewski, A. R. W. McKellar, D. Sadovskiĭ, and J. K. G. Watson, Can. J. Phys. **72**, 1016 (1994).

[53] B. M. Dinelli, O. L. Polyansky, and J. Tennyson, J. Chem. Phys. **103**, 10433 (1995).

[54] B. M. Dinelli, C. R. L. Sueur, J. Tennyson, and R. D. Amos, Chem. Phys. Lett. **232**, 295 (1995).

[55] W. Cencek, J. Rychlewski, R. Jaquet, and W. Kutzelnigg, J. Chem. Phys. **108**, 2831 (1998).

[56] R. Jaquet, Chem. Phys. Lett. **302**, 27 (1999).

[57] A. Alijah and P. Schiffels, *manuscript in preparation*, 2001.

[58] B. T. Sutcliffe and J. Tennyson, Int. J. Quant. Chem. **39**, 183 (1991).

[59] J. K. G. Watson, Can. J. Phys. **72**, 702 (1994).

[60] J. K. G. Watson, Chem. Phys. **190**, 291 (1995).

[61] J. Tennyson and B. T. Sutcliffe, J. Molec. Spect. **101**, 71 (1983).

[62] J. K. G. Watson, Phil. Trans. R. Soc. Lond. **A358**, 2371 (2000).

[63] A. Alijah, J. Hinze, and L. Wolniewicz, Ber. Bunsenges. Phys. Chem. **99**, 251 (1995).

[64] R. M. Dickson, *Vibrational Overtones in Solid Parahydrogen*, PhD thesis, University of Chicago, 1996.

[65] S. Gerstenkorn, J. Verges, and J. Chevillard, *Atlas du Spectre d'Absorption de la Molecule d'Iode*, Laboratoire Aimé Cotton, Orsay (France), 1982.

[66] I. H. Bachir, H. Bolvin, C. Demuynck, J. L. Destombes, and A. Zellagui, J. Molec. Spectrosc. **166**, 88 (1994).

[67] F. Kemp, C. E. Kirk, and I. R. McNab, Phil. Trans. R. Soc. Lond. **A358**, 2403 (2000).

[68] C. F. McKee and J. P. Ostriker, Astrophys. J. **218**, 148 (1977).

[69] J. E. Gunn and B. A. Peterson, Astrophys. J. **142**, 1633 (1965).

[70] R. C. Bohlin, B. D. Savage, and J. F. Drake, Astrophys. J. **224**, 132 (1978).

[71] P. M. Solomon and M. W. Werner, Astrophys. J. **165**, 41 (1971).

[72] H.-H. Lee, R. P. A. Bettens, and E. Herbst, Astr. Astrophys. Suppl. Ser. **119**, 111 (1996).

[73] J. Lyman Spitzer, *Physical Processes in the Interstellar Medium*, Wiley Interscience, New York, classics library edition, 1998.

[74] E. F. van Dishoeck and J. H. Black, Astrophys. J. Suppl. Ser. **62**, 109 (1986).

[75] T. P. Snow, B. L. Rachford, J. Tumlinson, J. M. Shull, D. E. Welty, W. P. Blair, R. Ferlet, S. D. Friedman, C. Gry, E. B. Jenkins, A. Lecavelier, M. Lemoine, D. C. Morton, B. D. Savage, K. R. Sembach, A. Vidal-Madjar, D. G. York, B. . Andersson, P. D. Feldman, and H. W. Moos, Astrophys. J. **538**, L65 (2000).

[76] M. T. Bowers, D. D. Elleman, and J. King, Jr., J. Chem. Phys. **50**, 4787 (1969).

[77] V. G. Anicich and W. T. Huntress, Jr., Astrophys. J. Suppl. Ser. **62**, 553 (1986).

[78] F. C. Fehsenfeld, Astrophys. J. **209**, 638 (1976).

[79] D. B. Millgan and M. J. McEwan, Chem. Phys. Lett. **319**, 482 (2000).

[80] T. Amano, Astrophys. J. **329**, L121 (1988).

[81] G. Sundström, J. R. Mowat, H. Danared, S. Datz, L. Broström, A. Filevich, A. Källberg, S. Mannervik, K. G. Rensfelt, P. Sigray, M. af Ugglas, and M. Larsson, Science **263**, 785 (1994).

[82] N. G. Adams and D. Smith, Chem. Phys. Lett. **105**, 604 (1984).

[83] C. M. Mountain, D. J. Robertson, T. J. Lee, and R. Wade, Proc. SPIE **1235**, 25 (1990).

[84] K. H. Hinkle, R. R. Joyce, N. Sharp, and J. A. Valenti, Proc. SPIE **4008**, 720 (2000).

[85] B. J. McCall, T. R. Geballe, K. H. Hinkle, and T. Oka, Astrophys. J. **522**, 338 (1999).

[86] J. H. Lacy, R. Knacke, T. R. Geballe, and A. T. Tokunaga, Astrophys. J. **428**, L69 (1994).

[87] C. A. Kulesa, J. H. Black, and C. K. Walker, Infrared and submillimeter spectroscopy of molecular clouds, in *American Astronomical Society Meeting 194, #47.09*, volume 194, page 4709, 1999.

[88] J. H. Black, Phil. Trans. R. Soc. Lond. **A358**, 2515 (2000).

[89] A. G. G. M. Tielens, A. T. Tokunaga, T. R. Geballe, and F. Baas, Astrophys. J. **381**, 181 (1991).

[90] S. P. Willner, F. C. Gillett, T. L. Herter, B. Jones, J. Krassner, K. M. Merrill, J. L. Pipher, R. C. Puetter, R. J. Rudy, R. W. Russell, and B. T. Soifer, Astrophys. J. **253**, 174 (1982).

[91] P. F. Roche and D. K. Aitken, Monthly Not. Roy. Astr. Soc. **208**, 481 (1984).

[92] S. Beckwith, N. J. Evans, E. E. Becklin, and G. Neugebauer, Astrophys. J. **208**, 390 (1976).

[93] G. F. Mitchell, J.-P. Maillard, M. Allen, R. Beer, and K. Belcourt, Astrophys. J. **363**, 554 (1990).

[94] G. F. Mitchell, S. W. Lee, J.-P. Maillard, H. Matthews, T. I. Hasegawa, and A. I. Harris, Astrophys. J. **438**, 794 (1995).

[95] F. F. S. van der Tak, E. F. van Dishoeck, N. J. Evans, and G. A. Blake, Astrophys. J. **537**, 283 (2000).

[96] F. F. S. van der Tak and E. F. van Dishoeck, Astron. Astrophys. **358**, L79 (2000).

[97] T. R. Geballe, B. J. McCall, K. H. Hinkle, and T. Oka, Astrophys. J. **510**, 251 (1999).

[98] B. J. McCall, T. R. Geballe, K. H. Hinkle, and T. Oka, Science **279**, 1910 (1998).

[99] C. Cecchi-Pestellini and A. Dalgarno, Monthly Not. Roy. Astr. Soc. **313**, L6 (2000).

[100] K. A. van der Hucht, P. W. Morris, P. M. Williams, D. Y. A. Setia Gunawan, D. A. Beintema, D. R. Boxhoorn, T. de Graauw, A. Heras, D. J. M. Kester, F. Lahuis, K. J. Leech, P. R. Roelfsema, A. Salama, E. A. Valentijn, and B. Vandenbussche, Astron. Astrophys. **315**, L193 (1996).

[101] L. F. Smith, M. M. Shara, and A. F. J. Moffat, Astrophys. J. **358**, 229 (1990).

[102] Y. J. Pendleton, S. A. Sandford, L. J. Allamandola, A. G. G. M. Tielens, and K. Sellgren, Astrophys. J. **437**, 683 (1994).

[103] L. M. Hobbs, Astrophys. J. **181**, 79 (1973).

[104] D. L. Lambert, Y. Sheffer, and P. Crane, Astrophys. J. **359**, L19 (1990).

[105] R. Gredel, Astron. Astrophys. **351**, 657 (1999).

[106] E. F. van Dishoeck and J. H. Black, Astrophys. J. **258**, 533 (1982).

[107] R. Gredel and G. Münch, Astron. Astrophys. **285**, 640 (1994).

[108] E. F. van Dishoeck and J. H. Black, Astrophys. J. **340**, 273 (1989).

[109] L. Magnani and J. S. Onello, Astrophys. J. **443**, 169 (1995).

[110] A. C. Danks, S. R. Federman, and D. L. Lambert, Astron. Astrophys. **130**, 62 (1984).

[111] S. M. V. Aldrovandi and D. Pequignot, Astron. Astrophys. **25**, 137 (1973).

[112] J. A. Cardelli, D. M. Meyer, M. Jura, and B. D. Savage, Astrophys. J. **467**, 334 (1996).

[113] U. J. Sofia, J. A. Cardelli, K. P. Guerin, and D. M. Meyer, Astrophys. J. **482**, L105 (1997).

[114] B. J. McCall, K. H. Hinkle, T. R. Geballe, and T. Oka, Faraday Discuss. **109**, 267 (1998).

[115] A. V. Torres-Dodgen, M. Carroll, and M. Tapia, Monthly Not. Roy. Astr. Soc. **249**, 1 (1991).

[116] D. H. Schulte, Astrophys. J. **128**, 41 (1958).

[117] T. P. Snow, D. G. York, and D. E. Welty, Astron. J. **82**, 113 (1977).

[118] R. Racine, Astron. J. **73**, 233 (1968).

[119] H. J. G. L. M. Lamers, M. de Groot, and A. Cassatella, Astron. Astrophys. **128**, 299 (1983).

[120] W. Wegner, Mon. Not. Royal Astr. Soc. **270**, 229 (1994).

[121] M. A. C. Perryman, L. Lindegren, J. Kovalevsky, E. Hoeg, U. Bastian, P. L. Bernacca, M. Crézé, F. Donati, M. Grenon, F. van Leeuwen, H. van der Marel, F. Mignard, C. A. Murray, R. S. Le Poole, H. Schrijver, C. Turon, F. Arenou, M. Froeschlé, and C. S. Petersen, Astron. Astrophys. **323**, L49 (1997).

[122] E. F. van Dishoeck and J. H. Black, Astrophys. J. **334**, 771 (1988).

[123] S. Lepp and A. Dalgarno, Astrophys. J. **335**, 769 (1988).

[124] S. Hayakawa, S. Nishimura, and T. Takayanagi, Publ. Astr. Soc. Jap. **13**, 184 (1961).

[125] M. Larsson, Phil. Trans. R. Soc. Lond. **A358**, 2433 (2000).

[126] A. E. Orel, I. F. Schnieder, and A. Suzor-Weiner, Phil. Trans. R. Soc. Lond. A **358**, 2445 (2000).

[127] D. C. B. Whittet, A. C. A. Boogert, P. A. Gerakines, W. Schutte, A. G. G. M. Tielens, T. de Graauw, T. Prusti, E. F. van Dishoeck, P. R. Wesselius, and C. M. Wright, Astrophys. J. **490**, 729 (1997).

[128] M. G. Rawlings, A. J. Adamson, and D. C. B. Whittet, Astrophys. J. Suppl. Ser. **131**, 531 (2000).

[129] K. Hinkle, L. Wallace, and W. Livingston, *Infrared Atlas of the Arcturus Spectrum, 0.9–5.3μm*, Astronomical Society of the Pacific, San Francisco, 1995.